THE PHYSICAL REVIEW

VOLUME 96 Second Series NUMBER 1

OCTOBER 1, 1954

Published for the

AMERICAN PHYSICAL SOCIETY

by the

AMERICAN INSTITUTE OF PHYSICS

LANCASTER, PA., AND NEW YORK, N. Y.

THE
PHYSICAL REVIEW

A journal of experimental and theoretical physics established by E. L. Nichols in 1893

SECOND SERIES, VOL. 96, NO. 1 OCTOBER 1, 1954

Secondary Electron Emission by Photoelectric Action and Ion Bombardment at the Cathode in Corona Breakdown of Argon

LAURA COLLI* AND UGO FACCHINI*
Department of Physics, University of California, Berkeley, California
(Received June 22, 1954)

Differences between the secondary cathode mechanisms active in coaxial cylindrical argon-filled counter tubes with positive central wire at various gas pressures observed by E. J. Lauer at Berkeley and the authors at Milan, have been resolved as a result of recent work by the authors at Berkeley. It appears that at pressures ranging from 1000 to about 150 mm Hg, with spectroscopically pure argon, the dominant mechanism is a photoelectric liberation from the cathode caused by photons with some microseconds of time delay and of energy about 10 ev. These lead to a corona threshold with γ_p ranging from 1 to 5×10^{-4}, uncorrected for electron back diffusion. At pressures between 25 and 100 mm Hg an electron liberation by impact of A^+ and A_2^+ ions on the Ni cathode was confirmed to be important in the corona current, in agreement with Lauer's findings. This effect seems to be very dependent on the conditions of the surface and was found to be active only after a degassing at 900°C for hours.

A NUMBER of papers have been published in recent years on the mechanisms of production of secondary electrons which take place in the electrical breakdown in argon, either in a plane parallel geometry or in cylindrical geometry.[1–7] These studies were carried out under varying conditions and revealed different aspects of the mechanisms involved.

Because of notable differences between the results obtained at Milan[5] and at Berkeley,[4] and through the courtesy of the Fulbright Award Committee and the U. S. Office of Naval Research, it became possible for the authors to extend their investigations in the laboratory of Professor L. B. Loeb in the Physics Department of the University of California at Berkeley. The purpose of this note is to report and analyze critically the results obtained with positive wire coaxial cylindrical geometry at both places and to show how the results can be brought into agreement and the differences explained.

In the first Milan paper,[1] the action of a photoelectric effect at the cathode was observed, by analyzing the shape of α-particle pulses in the pre-corona amplification region. However, in that work, the argon purity was not satisfactory and the impurities contained in argon (about 10^{-3} parts of CO_2) seriously influenced the results.[8] Subsequently, and independently, two studies were carried on, by the authors in Milan[5] and by Lauer in Berkeley,[4] utilizing the same method and with argon of high purity. In the next sections we will discuss these studies, which will be denoted in what follows as M and B, respectively.

THE PHOTOELECTRIC EFFECT; RESULTS AT MILAN

The cathode tube used was of brass, 6 cm in diameter, and was outgassed at 200°C. Argon of initial purity 98 to 99.9 percent was introduced into the discharge tube and circulated over a Ca-Mg alloy, heated to 450° for purification purposes. The pressures which were found convenient for study ranged between 150 and 1000 mm Hg. In a further unpublished study at Milan, the same measurements were repeated using a nickel cathode 5 cm in diameter, outgassed to 350°C, with no change in results.

The results which are of significance for this discussion can be summarized as follows:

* On the staff of Laboratori C.I.S.E., Via Procaccini 1, Milan, Italy.

[1] Colli, Facchini, and Gatti, Phys. Rev. **80**, 92 (1950).
[2] J. A. Hornbeck, Phys. Rev. **83**, 374 (1951).
[3] J. P. Molnar, Phys. Rev. **83**, 933, 940 (1951).
[4] E. J. Lauer, J. Appl. Phys. **23**, 300 (1952), referred to as B in the text.
[5] L. Colli and U. Facchini, Phys. Rev. **88**, 987 (1952), referred to as M in the text.
[6] L. H. Fisher and G. A. Kachickas, Phys. Rev. **91**, 775 (1953).
[7] R. N. Varney, Phys. Rev. **93**, 1156 (1954).
[8] Colli, Facchini, and Gatti, Phys. Rev. **84**, 606 (1951).

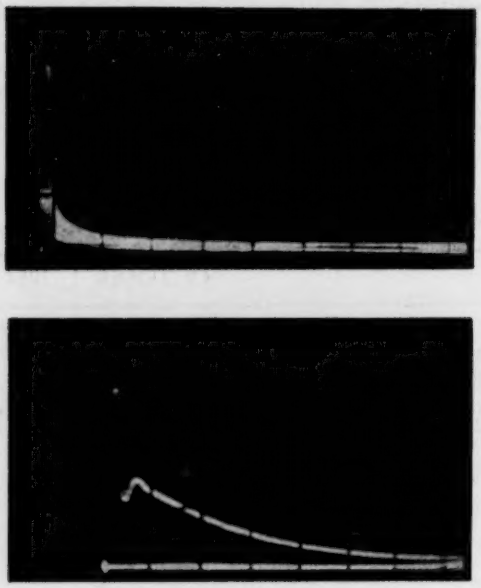

FIG. 1. α-particle pulses. Experimental conditions as in B. Cathode: nickel well outgassed, 2.9 cm in diameter; argon pressure: 400 mm Hg; corona threshold: 1660 volts; sweep time: 100 μsec. The upper pulse, taken 100 volts below the corona threshold, shows the electronic shape of the primary avalanche with no secondary effect. The lower pulse, taken at the corona threshold, shows the peak and the continuous slope due to the diffused photoelectric effect.

1. The corona current is due, mostly, to a secondary photoelectric effect produced at the cathode by photons generated in the Townsend avalanches near the wire. This statement is supported by the shape of α-particle pulses observed just below the corona threshold (see Figs. 4–7 in M).

2. The Townsend multiplication coefficient at the corona threshold, N_s, has a value of 200–300 with the various pressures and surfaces used. Denote by γ_p the number of photoelectrons extracted from the cathode and reaching the wire for each electron present in the Townsend avalanche. The values of γ_p are determined from the well-known equation, $N_s\gamma_p=1$, at corona threshold.

From the data γ_p was evaluated as $\gamma_p \simeq 3\text{–}5\times10^{-3}$, not very dependent on the pressure used, and it appeared to be of the same order of magnitude for nickel and brass.[9]

3. The α pulses near the corona threshold at pressures over $\sim$300 mm Hg, were followed by a convergent succession of pulses corresponding to the successive avalanches produced by photoelectrons. The successive pulses were diffused in time and the diffusion became greater as the pressure decreased, until at pressures below 300 mm Hg the successive avalanches overlapped to a continuous slope following the α primary pulse.

To explain this effect, it was assumed that the active photons were produced during a period of the order of few microseconds which increased as the pressure decreased.

THE DELAYED PHOTON PRODUCTION

In a recent paper, one of us[10] directly studied the time of production of the photons and established their energy as about 10 ev. It was found that in a Townsend avalanche lasting less than 5×10^{-7} sec, photons are emitted obeying the law $[\exp(-9p^2t)-\exp(-3\times10^6t)]$, which gives the emission rate *versus* time, with p the pressure in mm Hg and t the time in seconds. This law corresponds to a photon burst with a rise time of about 1 μsec and a delay time of 3.4 μsec at pressures above 300 mm Hg, and to a burst with both the rise time and the delay time longer at lower pressure. In that paper, it was suggested these photons might be produced by the decay of excited argon molecules A_2^*, formed by metastable atoms in three-body collisions. These results furnish a satisfactory explanation of the γ_p pulse shapes mentioned in the previous section.

THE PHOTOELECTRIC EFFECT; RESULTS AT BERKELEY

Turning to the appropriate sections of the paper B, it should be noted that the cathode used was nickel well outgassed by electron bombardment and with a diameter of 2.9 cm. Spectroscopically pure argon was directly introduced in the discharge tube, at a pressure ranging from 25 to 400 mm Hg. In this work, the action of an ion cathode γ_i effect was observed. The α-particle pulses near the corona threshold were followed by secondary pulses at time intervals of 100–600 μseconds depending on pressure corresponding to the ion transit-time across the gap. The values of γ_i (number of electrons extracted from the cathode per incident ion), were found to be about 10^{-3} at the lower pressures ($\sim$100 mm Hg), and much smaller at higher pressures, i.e., 6×10^{-5} at 200 mm Hg and 2×10^{-5} at 600 mm Hg. At these pressures, the values of N_s (threshold multiplication), were found about 400 to 600.[11]

DISCUSSION OF BERKELEY RESULTS

It appears, at pressures above 200 mm Hg, that $N_s\gamma_i \ll 1$, and that this secondary ion process could not have been responsible for the corona current at threshold. The most probable explanation was that the diffused photoeffect observed in M, was responsible for the corona mechanism in the B study as well. The tube used in B had a diameter of 2.9 cm, smaller than the one used in M, and consequently the transit time of electrons in B was 2–3 microseconds instead of 6–8

[9] A decrease in γ_p of roughly a factor 2 was noted after the outgassing at 350°.

[10] L. Colli, Phys. Rev. **95**, 892 (1954).

[11] E. J. Lauer (private communication).

microseconds as in M. It is therefore to be expected that in a counter such as used in B the successive avalanches, even at a pressure of 400 mm Hg, completely overlapped

RECENT EXPERIMENTAL VERIFICATION

When the authors undertook a study at Berkeley of the α-particle pulses at an appropriate sweep rate with the apparatus used in B, at pressures of 400 and 200 mm Hg, Figs. 1 and 2 were obtained, which are in good agreement with the assumptions made. Under the assumption that the photoeffect is the most important effect acting above 200 mm Hg from the values of N_s, found in B, the values of $\gamma_p \simeq 1.5\text{–}2.5 \times 10^{-3}$ were obtained, in good agreement with the ones found in Milan.

ION CATHODE EFFECT

At pressures between 25 and 100 mm Hg, the values of $N_s\gamma_i$ found in B are of the order of $\frac{1}{2}$ and the ion-cathode effect plays an important role in the corona current. However, in M, the ion-cathode effect was not observed. It must be noted that the lowest pressure used in M was 150 mm Hg. Recently much work has been done by Hagstrum[12] and by the Berkeley group[13] on the extraction of electrons from metals bombarded with ion beams under conditions of high purity and outgassing techniques. Hagstrum used a beam of helium ions having energies between 10 and 1000 ev against "flashed" surfaces of Mo, Ta, and W. Parker[13] studied, among others, argon ions with energy between 2 and 150 ev against "flashed" surfaces of Ta and Pt. It was found by Hagstrum and confirmed by Parker[13] and Huber[14] that γ_i is generally strongly dependent on the surface conditions; particularly Parker, with argon ions of low energy, found a reduction in γ_i by a factor of 10 or so when the surface was covered by a molecular gas layer. Hagstrum also observed that the complete cleaning of the surface is not achieved by heating it in vacuum up to 500°C, but only by heating the target above 900°C. After cooling, the gas layer reforms in a time dependent on the residual gases pressure and on the metal considered. It varies, for instance, from seconds at a pressure of 10^{-6} mm Hg with tungsten to hours under better conditions. The gas layer is also quickly reformed when the clean surface is exposed to a noble gas containing small amounts of molecular impurities. These results readily explain the failure to observe a γ_i effect in M. In fact, (1) the brass and nickel used there were outgassed only to 350°C; (2) argon which was not completely purified was introduced into the tube, the purification requiring a few hours of circulation over Ca-Mg. It must be concluded that the cathode surface was thus not very clean but covered by a thick gas layer and consequently the γ_i values expected should have been less than those observed in B, taken with a more thoroughly outgassed surface. In this connection, it is of importance to note the observations made on a nickel surface contaminated in the course of the recent studies with the apparatus used in B. The nickel surface was initially outgassed ten hours at orange-red heat (900 to 1000°C), and after cooling in good vacuum was exposed for a few hours to spectroscopically pure argon. It then showed a nice succession of γ_i pulses at 50 to 100 mm Hg. On the other hand, if the same cathode was exposed for a few minutes to air or to 99.5 percent pure argon, the gas being subsequently removed and the tube filled with the spectroscopically pure argon the γ_i pulses then completely disappeared. With such contamination, the threshold voltage is increased about 20 volts and the threshold multiplication by a factor 2 or so. Under these conditions the photoelectric effect appeared to be the most important action. In fact, γ_p appeared to be little altered by the surface treatment. It is interesting to note that the photoelectric emission from surfaces does not parallel the ion bombardment emission and may vary in quite different fashion with the surface conditions.[15,16]

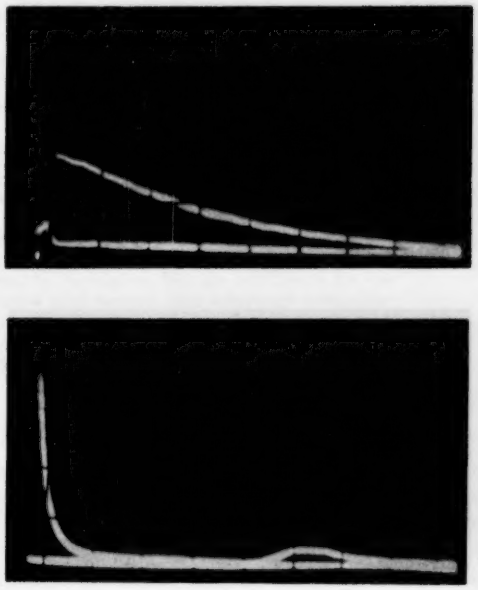

FIG. 2. α pulses at the corona threshold. Experimental conditions as in B. Argon pressure: 200 mm Hg; corona threshold: 1265 volts. The upper pulse, taken with a sweep time of 100 μsec, shows the diffused photoelectric effect following the primary avalanche. In the lower pulse, taken with a sweep time of 1300 μsec, it is possible to see the primary avalanche, the following slow photoeffect, and also the secondary peak at about 600 μsec due to the ion-cathode effect. At this pressure, the ion-cathode effect is estimated to be of the order of few percent of the photoelectric effect.

[12] H. D. Hagstrum, Phys. Rev. **89**, 244, 338 (1953); **91**, 543 (1953).
[13] J. H. Parker, Phys. Rev. **93**, 1148 (1954).
[14] E. Huber, Ph.D. thesis, University of California, June, 1954 (unpublished).
[15] Wainfan, Walker, and Weissler, J. Appl. Phys. **24**, 1318 (1953).
[16] Barch, Irick, and Geballe, Sixth Gaseous Electronics Con-

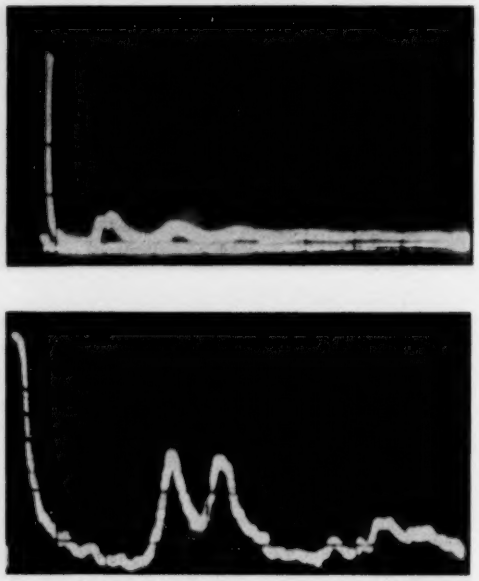

FIG. 3. α-particle pulses near the corona threshold. Experimental conditions as in B. Argon pressure: 50 mm Hg; corona threshold: 765 volts. The upper pulses, taken with a 2000-μsec sweep time, shows the γ_i pulse succession. The first secondary pulse is composed of two distinct peaks due to two different kinds of ions. The lower pulse shows the first part of the upper pulse enlarged. At higher pressure, the separation between the two peaks was not clear.

CONCLUSION

In argon of high purity and with cylindrical electrodes, at pressures above 150 mm Hg, the most important secondary process in the determination of the corona threshold is the photoelectric effect. The γ_p values are of the order of magnitude $1\text{–}5\times10^{-3}$ for brass and nickel cathodes and are not strongly dependent on the conditions of the cathodes surfaces or on the pressures used up to 1000 mm Hg. At pressures between 25 and 150 mm Hg, with the "clean" nickel cathode, the ion-cathode effect plays an important role. γ_i seems to be very dependent on the conditions of the surface. When the surface is not clean enough but is covered by molecular gases, the γ_i is strongly reduced and γ_p remains the only important effect seen at these pressures. It seems interesting to note that in the γ_i process there may be two kinds of argon ions involved, atomic A^+ and molecular A_2^+ ions.[17] The existence of these ions has been discussed extensively elsewhere.[18–20] It is interesting to note that the γ_i pulses shown in Fig. 3 give evidence of the presence of two ions in comparable proportions, at a pressure of 50 mm Hg.

The authors wish to express their gratitude to the Fulbright Committee and the U. S. Office of Naval Research for making possible this clarification of the fundamental mechanisms outlined. They desire to express their thanks to Professor L. B. Loeb for his assistance in this study, for his useful suggestions, and for the hospitality shown in his laboratory. They are furthermore deeply appreciative of the assistance given by all the members of Professor Loeb's Gaseous Electronics group and, in particular, to Mr. Peter Wagner and Miss Elsa Huber for their cooperation. The cooperation of Dr. E. J. Lauer in the interpretation of his work is also much appreciated.

ference, Washington, D. C., October 22–24, 1953, Paper B-9 (unpublished). See also similar effect in J. K. Theobald, J. Appl. Phys. **24**, 123 (1953).

[17] M. A. Biondi in discussion holds that at these pressures only A_2^+ ions exist.

[18] J. A. Hornbeck, Phys. Rev. **84**, 615 (1951).

[19] J. A. Hornbeck and J. P. Molnar, Phys. Rev. **84**, 621 (1951).

[20] A. V. Phelps and S. C. Brown, Phys. Rev. **86**, 102 (1952).

Spherically Symmetric Solutions in Nonsymmetrical Field Theories. II

P. C. VAIDYA
Vallabh Vidyanagar, Anand, India

(Received September 14, 1953; revised manuscript received January 4, 1954)

The skew symmetric tensors satisfying the general criterion of spherical symmetry, derived in Part I, contain certain arbitrary functions which indicate axial symmetry. These functions are removed. It is found that in addition to the "radial" components found by Papapetrou, the tensor has "transverse" components. In Maxwell's electrodynamics and in general relativity there are solutions which represent spherically symmetric fields of skew tensors with these transverse components. But in the unified field theories of Einstein or Schrödinger it is found that such solutions describing fields of skew tensors with nonvanishing transverse components do not exist. Thus the solutions found by Papapetrou, Wyman, and Bonnor are the only spherically symmetric solutions allowed by the unified field theories. The spherically symmetric solution found in general relativity for a radiating star has no counterpart in the unified field theories.

For comparison, it is noted that the same is the case with the field equations of Dirac's new electrodynamics. Spherically symmetric nonstatic solutions of Maxwell's electrodynamics have no counterpart in Dirac's electrodynamics.

1. INTRODUCTION

IN I,[1] we have shown that a spherically symmetric tensor field g_{ik} must satisfy the criterion

$$\xi^{\alpha}{}_{,i}g_{\alpha k}+\xi^{\alpha}{}_{,k}g_{i\alpha}+g_{ik,\alpha}\xi^{\alpha}=0, \tag{1.1}$$

where the ξ^{μ} are the contravariant components of an infinitesimal rotation of a sphere about a diameter.

$$\xi^1=0, \quad \xi^2=A\cos(\varphi+B),$$

$$\xi^3=-A\sin(\varphi+B)\cot\theta+C, \quad \xi^4=0, \tag{1.2}$$

where A, B, and C are constants.

We have given one tensor field which is skew symmetric and satisfies the criterion (1.1). It is

$$g_{\underset{\sim}{ik}}=\begin{Vmatrix} 0 & Pv & -Pu\sin\theta & Hh \\ -Pv & 0 & Ek\sin\theta & Qv \\ Pu\sin\theta & -Ek\sin\theta & 0 & -Qu\sin\theta \\ -Hh & -Qv & Qu\sin\theta & 0 \end{Vmatrix}. \tag{1.3}$$

Here capital letters stand for arbitrary functions of (r,t) while small letters are functions of θ, φ, whose forms are specified in I. In addition to the well-known radial components $g_{\underset{\sim}{14}}$ and $g_{\underset{\sim}{23}}$, this tensor also contains the transverse components $g_{\underset{\sim}{12}}$, $g_{\underset{\sim}{24}}$, $g_{\underset{\sim}{13}}$, and $g_{\underset{\sim}{34}}$. Now the transverse components of a skew spherically symmetric field will lie on the tangent plane to the sphere through the field point. From the familiar case of an electromagnetic field, we know that in this tangent plane the transverse components may take up any two orthogonal directions depending on the polarization of the corresponding wave. Thus a polarized electromagnetic wave can choose a preferential direction through polarization even when it is spherically symmetric. This polarization (or preferential choice of a direction) will be exhibited in the tangent plane to the sphere at any field point. Hence effects of polarization will be found on these new transverse components and are not to be traced in the earlier radial components found by Papapetrou. The functions u and v of θ and φ, which occur only in the transverse components of $g_{\underset{\sim}{ik}}$, can therefore be taken to indicate the corresponding polarization of the field.

But there is another way in which functions of θ and φ may occur in our tensor field. If the infinitesimal rotation (1.2) is given about a diameter QOQ' of the sphere, it is clear that those tensor fields which have only axial symmetry round QOQ', but which are not centrally symmetric round O, will also satisfy the criterion (1.1) and so may be present in a solution of Eq. (1.1). It is easy to see that functions indicating axial symmetry round QOQ' will also be functions of θ, φ. The function $w(\theta,\varphi)$, arbitrary functions of which occur in our solution (1.3), can easily be seen to be such a function. We have noted in I that w is proportional to the cosine of the angle POQ, where P is the field point on the sphere at which the value of the tensor is taken. It is therefore clear that arbitrary functions of w (which occur in the radial as well as the transverse components) are indicative of the axial symmetry round the axis of rotation. In I we had taken w, along with u and v, as indicating polarization of the field. This was a mistake. We now remove these functions of w by putting them equal to unity in our tensor. We then get a spherically symmetric skew tensor field of the following form:

$$g_{\underset{\sim}{ik}}=\begin{Vmatrix} 0 & 0 & p\sin\theta & H \\ 0 & 0 & E\sin\theta & 0 \\ -p\sin\theta & -E\sin\theta & 0 & -q\sin\theta \\ -H & 0 & q\sin\theta & 0 \end{Vmatrix}, \tag{1.4}$$

where p, q, E, and H are functions of r and t. The form (1.4) is obtained by so choosing the orientations of the axes of our polar coordinates that we get simplified values of the functions $u(\theta,\varphi)$ and $v(\theta,\varphi)$:

$$v=0, \quad u=1. \tag{1.5}$$

[1] P. C. Vaidya, Phys. Rev. **90**, 695 (1953). This paper is referred to hereafter as I.

In order to gain increased confidence in these new transverse components of the tensor, we shall give in the next section the spherically symmetric solution in general relativity which describes skew tensor fields with nonzero transverse components. That solution will also provide the background for the corresponding solution of the unified field theory which we are investigating in this paper.

2. SKEW TENSOR FIELDS IN GENERAL RELATIVITY

A spherically symmetric field, in the scheme of general relativity, will be expressible in terms of a line element

$$ds^2=-e^{\lambda}dr^2-r^2(d\theta^2+\sin^2\theta d\varphi^2)+e^{\nu}dt^2, \qquad (2.1)$$
$$\lambda=\lambda(r,t), \quad \nu=\nu(r,t).$$

From this line element we can calculate

$$T_{\mu}^{\nu}=-\frac{1}{8\pi}(R_{\mu}^{\nu}-\tfrac{1}{2}g_{\mu}^{\nu}R). \qquad (2.2)$$

It is, however, known from Maxwell's electrodynamics that

$$T_{\mu}^{\nu}=-F_{\mu\alpha}F^{\nu\alpha}+\tfrac{1}{4}g_{\mu}^{\nu}F_{\alpha\beta}F^{\alpha\beta}, \qquad (2.3)$$

where $F_{\mu\nu}$ is the skew symmetric electromagnetic field tensor obtained from a potential four-vector A_{μ}:

$$F_{\mu\nu}=A_{\mu,\nu}-A_{\nu,\mu}. \qquad (2.4)$$

Equating the two values of T_{μ}^{ν}, we shall find that[2]

$$F_{14}=0, \quad F_{23}=0,$$
$$F_{12}=-(m'/\dot{m})F_{24}=m'(4\pi f)^{-\frac{1}{2}}u, \qquad (2.5)$$
$$F_{13}=-(m'/\dot{m})F_{34}=m'(4\pi f)^{-\frac{1}{2}}v\sin\theta,$$

where $2m=r(1-e^{-\lambda})$, $m'=\partial m/\partial r$, $\dot{m}=\partial m/\partial t$, and f is a function of m. This spherically symmetric skew field has nonvanishing transverse components of the form (1.4). This field satisfies all the equations of Maxwell and the charge current vector J_{μ} is not zero, but it is null.

$$J_{\mu}J^{\mu}=0. \qquad (2.6)$$

The gravitational field represented by it is the field outside a radiating star.[3] However, our interest in this solution, at present, is that it gives the same form of the spherically symmetric skew tensor as the one obtained by us geometrically in I.

It is further found that it is not necessary to introduce the curved space-time of general relativity to obtain such a spherically symmetric skew field in the scheme of Maxwell's electrodynamics. It can be verified that

$$F_{14}=0, \quad F_{23}=0, \quad F_{13}=0, \quad F_{34}=0,$$
$$F_{12}=F_{24}=f(t-r),$$

satisfy all the field equations of Maxwell. Here again the charge-current vector J_{μ} is not zero, but

$$J_{\mu}J^{\mu}=0. \qquad (2.6)$$

This last relation suggests that solutions of this type cannot exist in the scheme of classical electrodynamics recently proposed by Dirac.[4] For in that scheme the vector J_{μ} is proportional to a unit vector v_{μ} and therefore it cannot be a null vector as in (2.6). We have actually verified that spherically symmetric solutions with nonvanishing transverse components of the skew tensor $F_{\mu\nu}$ do not exist in Dirac's electrodynamics. This may be a consequence of the nonlinearity introduced by Dirac in the originally linear Maxwell scheme. We now proceed to show that even though the nonlinearity introduced by general relativity allows such solutions, the unified field theories do not allow spherically symmetric skew fields with nonvanishing transverse components.

3. SOLUTIONS IN THE UNIFIED FIELD THEORY OF EINSTEIN

In this section we shall search for solutions in the unified field theories which will correspond to the solution giving the gravitational field of a radiating star mentioned in the foregoing section. For that purpose we take the complete tensor g_{ik} of the form

$$g_{ik}=\begin{Vmatrix} -\alpha & 0 & p\sin\theta & a+H \\ 0 & -\beta & E\sin\theta & 0 \\ -p\sin\theta & -E\sin\theta & -\beta\sin^2\theta & -q\sin\theta \\ a-H & 0 & q\sin\theta & \gamma \end{Vmatrix}. \qquad (3.1)$$

The different functions introduced here are functions of r and t. It will be seen that we have taken g_{ik} from general relativity and g_{ik} from (1.4). In general, we can impose four coordinate conditions on this g_{ik}. Two of them have already been imposed when we took the orientations of our axes of coordinates for which $v=0$, $u=1$. Two more coordinate conditions can be imposed by properly choosing r and t. Consider an arbitrary transformation,

$$r=r(r',t'), \quad t=t(r',t'), \qquad (3.2)$$

of the coordinates (r,t) to the coordinates (r',t'). It is easy to verify that if we choose r and t of (3.2) to satisfy the equations

$$p(\partial r/\partial t')+q(\partial t/\partial t')=0, \qquad (3.3)$$
$$(pa+q\alpha)(\partial r/\partial r')-(q a-p\gamma)(\partial t/\partial r')=0, \qquad (3.4)$$

then after the transformation we shall find that $g_{34}'=0$ and $g_{14}'=0$. But this is possible only if the Jacobian of the transformation does not vanish, that is, if

$$p^2\gamma+2pqa-q^2\alpha\neq 0. \qquad (3.5)$$

Similarly it is possible to find transformations of (r,t)

[2] V. V. Narlikar and P. C. Vaidya, Proc. Natl. Inst. Sci. (India) 14, 153 (1948).
[3] P. C. Vaidya, Proc. Indian Acad. Sci. A33, 264 (1951).
[4] P. A. M. Dirac, Proc. Roy. Soc. (London) A212, 330 (1952).

which will lead to $g_{13}'=0$ and $g_{14}'=0$, again only if (3.5) holds.

However, there is another simplification possible whether the condition (3.5) is satisfied or not. We choose our r and t of (3.2) to satisfy the equations

$$p(\partial r/\partial t')+q(\partial t/\partial t')=0, \tag{3.6}$$

$$\gamma(\partial t/\partial r')^2+2\alpha(\partial t/\partial r')(\partial r/\partial r')-\alpha(\partial r/\partial r')^2=0. \tag{3.7}$$

Then after the transformations we shall find that $g_{34}'=0$, $g_{11}'=0$. We can factorize the quadratic left-hand member of (3.7) into distinct factors each of which will be linear in the partial derivatives. Now it is always possible to choose one or the other of these two factors in such a way that the selected factor equated to zero, together with Eq. (3.6), will define a transformation of (r,t) into (r',t') whose Jacobian will not vanish. Hence this type of transformation is always possible. It may be noted that these coordinates (r',t') are similar to what we have called "Newtonian" coordinates in general relativity.[5]

We use these "Newtonian" coordinates and take our g_{ik} of the form

$$g_{ik}=\begin{Vmatrix} 0 & 0 & p\sin\theta & a+H \\ 0 & -\beta & E\sin\theta & 0 \\ -p\sin\theta & -E\sin\theta & -\beta\sin^2\theta & 0 \\ a-H & 0 & 0 & \gamma \end{Vmatrix}. \tag{3.8}$$

One of the field equations is

$$\underset{\sim}{G}^{is}{}_{,s}=0. \tag{3.9}$$

For $i=4$, this leads to

$$\frac{\partial}{\partial r}[H(\beta^2+E^2)A]-[pEHA]\cot\theta=0, \tag{3.10}$$

$$A^2[\det|g_{ik}|]=-1.$$

It is therefore clear that, as $A\neq 0$,

$$\frac{\partial}{\partial r}[H(\beta^2+E^2)A]=0, \tag{3.11}$$

$$pEH=0. \tag{3.12}$$

The case $p=0$ gives the known solutions of Bonnor. Therefore, from (3.12) we conclude that $EH=0$. We have worked out the detailed solutions in all the three cases (i) $E=0$, $H=0$; (ii) $E=0$, $H\neq 0$; (iii) $E\neq 0$, $H=0$. We found the quantities $\Gamma_{ij}{}^k$ by writing its defining equation,

$$g_{ik,l}-g_{is}\Gamma_{lk}{}^s-g_{sk}\Gamma_{il}{}^s=0, \tag{3.12}$$

in the form

$$g_{is}\Gamma_{kl}{}^s=-\tfrac{1}{2}g_{kl,i}+\tfrac{1}{2}g_{li,k}+\tfrac{1}{2}g_{ik,l}+g_{ks}\Gamma_{il}{}^s+g_{sl}\Gamma_{ki}{}^s, \tag{3.13}$$

and

$$g_{is}\Gamma_{kl}{}^s=\tfrac{1}{2}g_{kl,i}-\tfrac{1}{2}g_{li,k}-\tfrac{1}{2}g_{ik,l}-g_{ks}\Gamma_{il}{}^s-g_{sl}\Gamma_{ki}{}^s. \tag{3.14}$$

Having found $\Gamma_{kl}{}^i$ from (3.13) and (3.14) for all the three cases mentioned above, we calculated R_{ik} from

$$R_{ik}=\Gamma_{ik}{}^s{}_{,s}-\Gamma_{is}{}^t\Gamma_{tk}{}^s-\tfrac{1}{2}(\Gamma_{is}{}^s{}_{,k}+\Gamma_{ks}{}^s{}_{,i})+\Gamma_{ik}{}^s\Gamma_{st}{}^t. \tag{3.15}$$

It was found that R_{ik} contained terms in $\cot^2\theta$. This means that though g_{ik} is spherically symmetric, while R_{ik} is not. The situation is similar to the one discussed by Takeno and others,[6] who were using Papapetrou's form of spherically symmetric g_{ik}. Now in all the unified field theories, there is one field equation of the form

$$R_{ik}=\lambda g_{ik}. \tag{3.16}$$

[In Schrödinger's theory $\lambda\neq 0$, while in Einstein's theories $\lambda=0$.] In all the cases mentioned above, we have found[7] that (3.16) eventually leads to equations of the type (3.10):

$$f(r,t)+\varphi(r,t)\cot^2\theta=0,$$

which, in their turn, have eventually led to $p=0$ in all cases. Hence solutions with nonvanishing transverse components do not exist under any scheme of field equations which contain equations of the type (3.16).

4. CONCLUSION

We have shown here that spherically symmetric solutions with nonvanishing transverse components of the skew tenor g_{ik} are not allowed by the unified field theories of Einstein. Corresponding to a solution of the point charge in general relativity there are the solutions of Papapetrou, Wyman, and Bonnor in the unified field theory; but corresponding to the solution of a radiating star in general relativity there are no solutions in the unified field theory.

Here we have an analog in the classical electrodynamics. Corresponding to the well-known solution for a point charge in Maxwell's electrodynamics, we have a solution in the new electrodynamics proposed by Dirac. (It is only a gauge transform of the Maxwellian solution.[8]) However, corresponding to the non-static spherically symmetric solution of Maxwell's electrodynamics given here in Sec. 2, there is no solution in Dirac's scheme.

If, however, we want axially symmetric solutions, we can introduce arbitrary functions of w in our g_{ik} as in Eq. (1.3). Solutions of this type are now being investigated.

[5] P. C. Vaidya, Nature **171**, 260 (1953).

[6] Takeno, Ikeda, and Abe, Progr. Theoret. Phys. Japan **6**, 842 (1951).

[7] The detailed calculations for the three cases are appended here as appendixes I, II, and III.

[8] K. J. Le Couteur, Nature **169**, 146 (1952).

APPENDIX I

Case (i): $E=0$, $H=0$

The tensor is

$$g_{ik}=\begin{Vmatrix} 0 & 0 & p\sin\theta & a \\ 0 & -\beta & 0 & 0 \\ -p\sin\theta & 0 & -\beta\sin^2\theta & 0 \\ a & 0 & 0 & \gamma \end{Vmatrix}$$

so that

$$g=\det\|g_{ik}\|=-\beta(\beta a^2+\gamma p^2)\sin^2\theta.$$

The 3-index symbols which will ultimately give terms containing $\cot^2\theta$ in R_{11} are Γ_{1k}^2, Γ_{12}^k, Γ_{21}^k, where k may be 1, 3, or 4. Their values can be easily obtained from (3.13), (3.14). We have found that

$$\Gamma_{11}^2=(p^2a^2/\beta A)\cot\theta,$$

$$\Gamma_{13}^2=-\Gamma_{31}^2=(p/2\beta)\cot\theta\sin\theta, \quad \Gamma_{14}^2=\Gamma_{41}^2=0,$$

$$\Gamma_{13}^1=\Gamma_{21}^1=-(p^2\gamma/2A)\cot\theta,$$

$$\Gamma_{13}^3=-\Gamma_{21}^3=(pa^2/2A)\cot\theta\csc\theta,$$

$$\Gamma_{12}^4=\Gamma_{21}^4=(p^2a/2A)\cot\theta,$$

where $A=a^2\beta-p^2\gamma$. The value of R_{11} is of the following form:

$$R_{11}=f_{11}(r,t)+\frac{p^2a^2(a^2\beta+p^2\gamma)}{2\beta A^2}\cot^2\theta.$$

$R_{11}=\lambda g_{11}$ will now demand that the coefficient of $\cot^2\theta$ in R_{11} should vanish. Since $a^2\beta+p^2\gamma\neq0$ (because $g\neq0$), this forces the conclusion $p=0$.

APPENDIX II

Case (ii): $E=0$, $H\neq0$

The fundamental tensor is

$$g_{ik}=\begin{Vmatrix} 0 & 0 & p\sin\theta & a+H \\ 0 & -\beta & 0 & 0 \\ -p\sin\theta & 0 & -\beta\sin^2\theta & 0 \\ a-H & 0 & 0 & \gamma \end{Vmatrix}.$$

Of the 64 symbols Γ_{ik}^l there are 27 (for which either i, k, or l is 2) which contain $\cot\theta$ as a factor in their values. These symbols ultimately lead up to $\cot^2\theta$ terms in R_{ik}. We give here the main results of calculations of these 27 symbols. First, eighteen symbols are evaluated by solving a closed set of eighteen simultaneous equations obtained from Eqs. (3.13) and (3.14). The method of writing these eighteen equations is a simple one. We begin with any one symbol, say Γ_{23}^2. We write down its value from (3.14). Then on the right-hand side Γ_{23}^1 will appear. Next we write the value of Γ_{23}^1 from (3.13). Its value will involve two new symbols Γ_{23}^4 and Γ_{24}^1. We write down their values again, using (3.13) and (3.14). We proceed in this way till we come ultimately to an equation which does not involve any further new symbol. The solution of these eighteen equations is a straightforward process. The following values are obtained for the eighteen symbols coming in this set of simultaneous equations:

$$\Gamma_{23}^3=\Gamma_{23}^1=\Gamma_{24}^3=\Gamma_{24}^1=0,$$

$$\Gamma_{24}^4=(H/\gamma)\Gamma_{24}^1=(H/a)\Gamma_{21}^1=(-H/a)\Gamma_{24}^4$$

$$=(H/p)\csc\theta\Gamma_{23}^4=(H^2/a^2)\Gamma_{21}^1$$

$$=(-2H\gamma/a^2)\Gamma_{21}^4=(-p^2H^2\gamma/2Aa^2)\cot\theta,$$

$$\Gamma_{24}^3\sin\theta=(H\gamma/a\beta)\Gamma_{23}^4\csc\theta=(-H/\beta)\Gamma_{23}^1\csc\theta$$

$$=(H/p)(\Gamma_{23}^3-\cot\theta)=(\gamma/a)\Gamma_{21}^3\sin\theta$$

$$=(-H\gamma/a^2)\Gamma_{21}^3\sin\theta$$

$$=[pH\gamma(a^2+H^2)/2a^2A]\cot\theta,$$

$$\Gamma_{21}^4=[p^2(a^2-H^2)/2aA]\cot\theta,$$

where $A=(a^2+H^2)\beta-p^2\gamma$. The following five symbols can then be obtained by solving the single equation obtained for each of them from (3.13) or (3.14).

$$\Gamma_{11}^2=[p^2(a^2-H^2)/\beta A]\cot\theta,$$

$$\Gamma_{13}^2=[Hp\{\beta(a^2+H^2)+p^2\gamma\}/2aA\beta]\cot\theta\sin\theta,$$

$$\Gamma_{13}^2=(p/2\beta)\cot\theta, \quad \Gamma_{14}^2=(-p^2H^2\gamma/2aA\beta)\cot\theta,$$

$$\Gamma_{14}^2=0.$$

The values of R_{11} and R_{22} are of the following form:

$$R_{11}=f_{11}(r,t)+\frac{p^2(a^2+H^2)^2\beta+a^2p^4\gamma(a^2-H^2)}{2\beta a^2A^2}\cot^2\theta,$$

$$R_{22}=f_{22}(r,t)-\frac{p^2\gamma(a^2+H^2)}{2a^2A}\cot^2\theta.$$

$R_{ik}=\lambda g_{ik}$ will now demand that the coefficients of $\cot^2\theta$ in the above should vanish. This again leads to $p=0$, unless we take $a^2+H^2=0$ and $\gamma=0$ which will make $A=0$ and so the values of the 3-index symbols will need revaluation. We do this. Beginning with $a^2+H^2=0$, $\gamma=0$, we work out the values of these 27 symbols. Most of them become zero. But when we try to find Γ_{21}^4 and Γ_{21}^4, we are faced with the two equations:

$$a\Gamma_{21}^4-H\Gamma_{21}^4=(Hp^2/2a\beta)\cot\theta,$$

$$H\Gamma_{21}^4+a\Gamma_{21}^4=(p^2/2\beta)\cot\theta.$$

If neither of Γ_{21}^4, Γ_{21}^4 is to be infinite in value, Hp^2/β must vanish, which again leads to $p=0$ because with $a^2+H^2=0$, H cannot vanish.

Hence in this case the only conclusion is $p=0$.

APPENDIX III

Case (iii): $E\neq 0$, $H=0$

In this case, if we use the "Newtonian" form (3.8) for g_{ik}, it becomes very difficult to isolate the symbols which involve $\cot\theta$ terms from symbols not involving them. Hence we do not use the form (3.8) but, beginning with the general form (3.1) we take two cases according as (3.5) is satisfied or not.

Sub-Case (i): When (3.5) Is Satisfied

The tensor g_{ik} can be taken in the form

$$g_{ik}=\begin{pmatrix} -\alpha & 0 & p\sin\theta & 0 \\ 0 & -\beta & E\sin\theta & 0 \\ -p\sin\theta & -E\sin\theta & -\beta\sin^2\theta & 0 \\ 0 & 0 & 0 & \gamma \end{pmatrix}.$$

It is now found that all the 37 symbols $\Gamma_{ik}{}^{l}$ for which either i or k or l is 4, do not contain $\cot\theta$. $\Gamma_{11}{}^{1}$ is $\alpha'/2\alpha$. These 38 symbols do not contain $\cot\theta$. Of the remaining 26 symbols, $\Gamma_{11}{}^{3}$, $\Gamma_{22}{}^{2}$, $\Gamma_{22}{}^{3}$, and $\Gamma_{33}{}^{3}$ vanish. The following are the values of the rest.

$$(-\beta/2p)\Gamma_{11}{}^{2}=(\alpha/p)\Gamma_{12}{}^{1}=(-\beta/E)(\Gamma_{12}{}^{2}-\beta'/2\beta)$$
$$=\Gamma_{21}{}^{3}\sin\theta=(\alpha/2E)(\Gamma_{22}{}^{1}+\beta'/2\alpha)$$
$$=(-\alpha/p)(\Gamma_{23}{}^{3}-\cot\theta)=x-y\cot\theta,$$

$$\Gamma_{12}{}^{1}=\Gamma_{12}{}^{2}=\Gamma_{21}{}^{3}=\Gamma_{23}{}^{3}=0,$$

$$\Gamma_{13}{}^{1}=-\Gamma_{31}{}^{1}=(p/a)[\gamma'/2\gamma+\beta'/2\beta - (E/\beta)(x-y\cot\theta)]\sin\theta,$$

$$\Gamma_{31}{}^{2}=-\Gamma_{13}{}^{2}=(E/\beta)[(-p/2E)\cot\theta+E'/2E - \beta'/2\beta+(E/\beta)(x-y\cot\theta)]\sin\theta,$$

$$\Gamma_{31}{}^{3}=\Gamma_{13}{}^{3}=B'/B-\alpha'/2\alpha-\beta'/2\beta+(E/\beta)(x-y\cot\theta),$$

$$\Gamma_{32}{}^{1}=-\Gamma_{23}{}^{1}=(E/\alpha)[E'/2E-B'/B+\alpha'/2\alpha + (p/2E)\cot\theta-(p^2/E\alpha)(x-y\cot\theta)]\sin\theta,$$

$$\Gamma_{32}{}^{2}=-\Gamma_{23}{}^{2}=(p/\alpha)[\beta'/2\beta-(E/\beta)(x-y\cot\theta)]\sin\theta,$$

$$\Gamma_{33}{}^{1}=[-\beta'/2\alpha+(2p^2/\alpha^2)(\gamma'/2\gamma+\beta'/2\beta) - (2E^2/\alpha\beta)(E'/2E-\beta'/2\beta)+(Ep/\alpha\beta)\cot\theta - 2E(p^2\beta+E^2\alpha)(x-y\cot\theta)/\alpha^2\beta^2]\sin^2\theta,$$

$$\Gamma_{33}{}^{2}=[-(1+p^2/\alpha\beta)\cot\theta-(2Ep/\alpha\beta) \times(E'/2E-B'/B+\alpha'/2\alpha+\beta'/2\beta) + p(p^2\beta+E^2\alpha)(x-y\cot\theta)/\alpha^2\beta^2]\sin^2\theta,$$

where

$$x=(2Ey/p)(B'/B+E'/2E-\alpha'/2\alpha-\beta'/2\beta),$$
$$2y=\alpha\beta p/[\alpha(\beta^2-E^2)-\beta p^2],$$
$$B^2=\alpha(\beta^2+E^2)-\beta p^2,$$

and a prime indicates differentiation with regard to r (e.g., $\alpha'\equiv\partial\alpha/\partial r$). Now R_{ik} will contain terms in $\cot\theta$ and $\cot^2\theta$. Here again we shall require these terms to vanish. Once again we shall be led to $p=0$, or else $\alpha(\beta^2-E^2)+\beta p^2=0$ from R_{11} and $\alpha(\beta^2-3E^2)-\beta p^2=0$ from R_{22}. Then, when we write down the value of R_{33} and use the above two results, we get the coefficient of $\cot^2\theta$ therein as $-\frac{1}{4}$ which does not vanish. Hence the other alternative does not hold. The only conclusion s $p=0$.

Sub-Case (2): When (3.5) Is Not Satisfied

In this case we can remove both g_{11} and g_{44} along with g_{34}.[9] Thus we take our tensor as

$$g_{ik}=\begin{pmatrix} 0 & 0 & p\sin\theta & a \\ 0 & -\beta & E\sin\theta & 0 \\ -p\sin\theta & -E\sin\theta & -\beta\sin^2\theta & 0 \\ a & 0 & 0 & 0 \end{pmatrix}.$$

The following 13 nonzero symbols lead to $\cot^2\theta$ terms in R_{11}.

$$\Gamma_{11}{}^{2}=(p^2/A)\cot\theta+(r,t),$$
$$\Gamma_{12}{}^{2}=\Gamma_{21}{}^{2}=(pE/2A)\cot\theta+(r,t),$$
$$\Gamma_{12}{}^{3}\sin\theta=-\Gamma_{21}{}^{3}\sin\theta=(p\beta/2A)\cot\theta+(r,t),$$
$$\Gamma_{13}{}^{2}\csc\theta=-\Gamma_{31}{}^{2}\csc\theta=(p\beta/2A)\cot\theta+(r,t),$$
$$\Gamma_{13}{}^{3}=\Gamma_{31}{}^{3}=(-pE/2A)\cot\theta+(r,t),$$
$$\Gamma_{12}{}^{4}=\Gamma_{21}{}^{4}=(p^2\beta/2aA)\cot\theta+(r,t),$$
$$-\Gamma_{13}{}^{4}\csc\theta=+\Gamma_{31}{}^{4}\csc\theta=(p^2E/2aA)\cot\theta+(r,t),$$
$$A=\beta^2-E^2,$$

where the (r,t)'s indicate some additional functions of r and t.

The coefficient of $\cot^2\theta$ in R_{11} turns out to be $p^2/2A$, so that the inevitable conclusion is $p=0$.

---

[9] If (3.5) is not satisfied, g_{44} automatically becomes zero when we make the transformation for which g_{34} is zero. We can use the other coordinate condition to make $g_{11}=0$.

Space Charge Formation and the Townsend Mechanism of Spark Breakdown in Gases

R. W. Crowe, J. K. Bragg,* and Virginia G. Thomas
General Electric Research Laboratory, Schenectady, New York

(Received April 21, 1954; revised manuscript received June 15, 1954)

The Townsend criterion for electrical breakdown in gases is based upon a singularity in the Townsend expression for the current as a function of voltage. The conventional derivation of this equation involves the assumption that space charges are absent. A more precise expression of this criterion, involving the effects of space charge, removes the singularity and describes a current that is finite at every finite point. Beyond a certain current, however, the derivative of the current with respect to voltage becomes negative, indicating that the system is incapable of withstanding a voltage larger than that at which the negative characteristic develops. In most cases, the breakdown voltage so established should not differ appreciably from that given by the ordinary Townsend equation.

The second Townsend coefficient is normally determined from the curvature found, as the sparking separation is approached, in plots of the logarithm of the current *versus* electrode separation at constant electric field. The extent of this curvature can be influenced somewhat by distortion of the electric field by space charges if the initial photocurrent from the cathode is sufficiently large.

I. INTRODUCTION

According to the Townsend theory of electrical breakdown in gases, the steady-state current flowing in a uniform-field gap is given by

$$i=i_0e^{\alpha\delta}/[1-(\omega/\alpha)(e^{\alpha\delta}-1)], \tag{1}$$

where i_0 is the initial photocurrent, δ is the electrode separation, and α and (ω/α) are the primary and secondary ionization coefficients, respectively.[1,2] Because both ω and α are increasing functions of the electric field, E, the equation describes a current which increases, as E increases, toward an unbounded value reached when

$$(\omega/\alpha)(e^{\alpha\delta}-1)=1. \tag{2}$$

This condition is taken to define implicitly the breakdown (threshold) electric field.

The derivation of Eq. (1) involves the assumption that the densities of positive and negative charges in the gap are sufficiently low that the electric field is not distorted. Under such conditions, α will be constant throughout the gap. However, as the sparking threshold is approached, this situation clearly no longer obtains. In fact, the formation of field-distorting space charge must be an essential feature of the mechanism of gas breakdown, rather than "following after" the spark in some poorly defined way as has often been assumed. Actually, this fact was pointed out many years ago by von Engel and Steenbeck.[3] In order to account for the results of recent measurements of formative time lags in gas breakdown, other investigators have also recognized, in a qualitative manner, the importance of positive space charge in the initiation of the spark in slightly overvolted gaps.[4,5]

It is the purpose of this paper to show that the buildup of positive space charge in a gas can be described by the appropriate modification of the Townsend equation. It is demonstrated that this buildup occurs as the voltage approaches the threshold voltage predicted by Eq. (1), providing i_0 is not too large. Varney, White, Loeb, and Posin[6] have done a similar calculation for the case where $(\omega/\alpha)=0$ (no secondary mechanism), and our study is essentially an extension of theirs.

II. THE SPACE CHARGE EQUATION

In the steady state the currents of positive and negative charges in the spark gap (cathode at origin, anode at δ) must satisfy the following equations:

$$\begin{aligned}\nabla\cdot\mathbf{i}_-&=\alpha i_-,\\ \nabla\cdot\mathbf{i}_+&=-\alpha i_-,\\ \mathbf{i}&=\mathbf{i}_++\mathbf{i}_-=\text{constant}.\end{aligned} \tag{3}$$

Furthermore, they are related to the charge densities n_+ and n_- by the relations

$$\begin{aligned}\mathbf{i}_-&=n_-e\mu_-\mathbf{E},\\ \mathbf{i}_+&=n_+e\mu_+\mathbf{E},\end{aligned} \tag{4}$$

where μ_- and μ_+ are the *magnitudes* of the charge mobilities and e is the magnitude of the electronic charge. Finally, n_+ and n_- determine the divergence of the electric field:

$$\nabla\cdot\mathbf{E}=4\pi e(n_+-n_-). \tag{5}$$

We will specialize these equations to a situation in which the field is directed along the x axis, the properties of the system being independent of y and z.

The generalized secondary mechanism, characterized

* Present address: Operations Research, Inc., 8416 Georgia Avenue, Silver Spring, Maryland.

[1] See, for example, L. B. Loeb, *Fundamental Processes of Electrical Discharge in Gases* (John Wiley and Sons, Inc., New York, 1939), Chap. IX.

[2] Dutton, Haydon, Llewellyn Jones, and Davidson, Brit. J. Appl. Phys. 4, 170 (1953).

[3] A. von Engel and M. Steenbeck, *Elektrische Gasentladungen* (Julius Springer, Berlin, 1932), Vol. II, p. 50.

[4] L. H. Fisher and B. Bederson, Phys. Rev. 81, 109 (1951).

[5] G. A. Kachickas and L. H. Fisher, Phys. Rev. 88, 878 (1952).

[6] Varney, White, Loeb, and Posin, Phys. Rev. 48, 818 (1935).

by (ω/α), is introduced by the expression,

$$i_-(0)=i_0+\int_0^\delta \omega(x)i_-(x)dx. \tag{6}$$

Combination of this with Eq. (3) and the introduction of a new independent variable,

$$u=\int_0^x \alpha dx, \quad du=\alpha dx, \tag{7}$$

yield the generalized Townsend equation,

$$i_-(x)=i_0e^u\Big/\left[1-\int_0^{\bar{u}}(\omega/\alpha)e^u du\right], \tag{8}$$

$$\bar{u}=\int_0^\delta \alpha dx.$$

If we assume, as is usually done, that (ω/α) is approximately independent of the electric field, then we have

$$i_-(x)=i_0e^u/[1-(\omega/\alpha)(\exp\bar{u}-1)]. \tag{9}$$

Equations (4), (5), and (9) may now be combined to give

$$\alpha E dE=\frac{[(4\pi i_0/\mu_+)(\exp\bar{u}-\exp u)du]}{[1-(\omega/\alpha)(\exp\bar{u}-1)]}. \tag{10}$$

In arriving at Eq. (10), $1/\mu_-$ has been considered to be negligible compared with $1/\mu_+$.

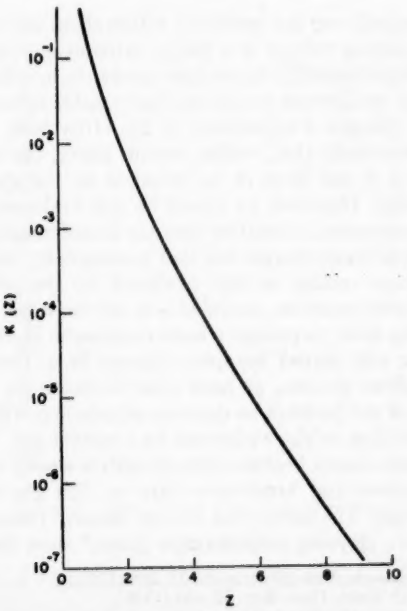

FIG. 1. Calculated curve of $K(z)$ *vs* z.

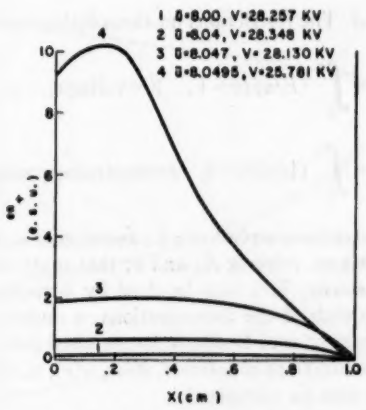

FIG. 2. Distribution of positive ions across the spark gap for various voltages near threshold.

Now to integrate Eq. (10), it is necessary to assume a functional form for the dependence of α upon E. For many gases, it has been demonstrated that α can be sufficiently approximated by an expression of the form,

$$\alpha/P=Ae^{-BP/E}, \tag{11}$$

in the greater part of the region of E/P significant to discharge phenomena. In this expression, P is the gas pressure, and A and B are constants characteristic of the gas. To be sure, Eq. (11) is not the only functional relation which can be applied accurately to this limited range of E/P. We use it here not only because it appears to have some theoretical significance,[7] but also because it contributes to the ease of computation. Thus, it is possible to show that

$$K(1/\eta)=K(1/\eta_0)+\frac{[(4\pi i_0/\beta\mu_+)(u\exp\bar{u}-\exp u+1)]}{[1-(\omega/\alpha)(\exp\bar{u}-1)]}, \tag{12}$$

where

$$\beta=AP(BP)^2,$$

$$\eta=E/BP, \quad \eta_0=E_0/BP, \quad E_0=E(0),$$

$$K(z)=\tfrac{1}{2}[e^{-z}/z^2-e^{-z}/z-\mathrm{Ei}(-z)],$$

$$-\mathrm{Ei}(-z)=\int^\infty (e^{-t}/t)dt.$$

The function $K(z)$ is plotted in Fig. 1.

We have then for the electric field

$$E=BP/K^{-1}\left\{K_0+\frac{[(4\pi i_0/\beta\mu_+)(u\exp\bar{u}-e^u+1)]}{[1-(\omega/\alpha)(\exp\bar{u}-1)]}\right\}. \tag{13}$$

Here K^{-1} is the inverse of the K function, and K_0

[7] T. Kihara, Revs. Modern Phys. 24, 45 (1952).

$=K(1/\eta_0)$. The restrictions on the solutions are

$$\int_0^\delta E dx = \int_0^{\hat{u}} (E/\alpha) du = V, \quad V = \text{voltage};$$
$$\int_0^\delta dx = \int_0^{\hat{u}} (1/\alpha) du = \delta, \quad \delta = \text{electrode spacing}. \tag{14}$$

These restrictions serve to fix K_0 and $\hat{u}$; that is, they are two equations, relating K_0 and $\hat{u}$, that must be solved simultaneously. This may be done by introducing Eq. (13) into each of the two equations; a numerical procedure must be used to obtain the required pair, $(K_0,\hat{u})$. All of the functions of interest, $E(x)$, $\alpha(x)$, $n_+(x)$, $i_-(x)$, etc., can then be calculated.

Equation (13) shows clearly the role of space charges in a Townsend breakdown process. It gives $E(x)$ as essentially equal to E_0 when

$$\left| \frac{4\pi i_0}{\beta \mu_+} \cdot \frac{u \exp\hat{u} - \exp u + 1}{1 - (\omega/\alpha)(\exp\hat{u} - 1)} \right| \ll K_0.$$

Insertion of physically reasonable numbers shows that in most cases the inequality is violated only when the generalized Townsend threshold, defined by

$$(\omega/\alpha)(\exp\hat{u} - 1) = 1,$$

is approached. Numerical illustrations of the influence of space charges on the Townsend current are presented in the following sections.

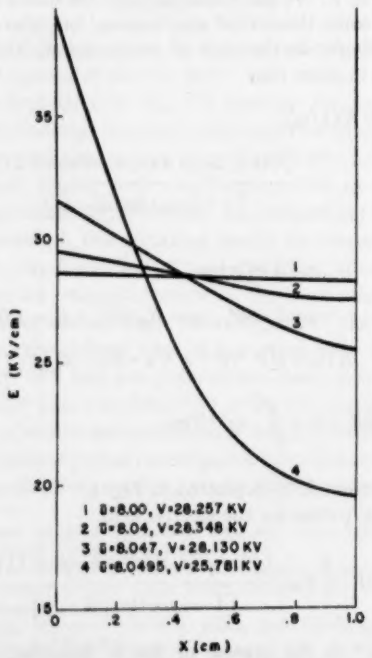

FIG. 3. Distribution of the electric field across the spark gap for various voltages near threshold.

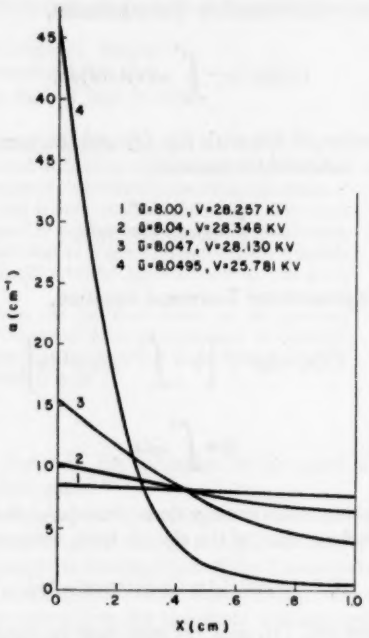

FIG. 4. Distribution of α across the spark gap for various voltages near threshold.

III. NUMERICAL ILLUSTRATIONS

A. Space Charge and the Townsend Threshold

Normally one can predict to within about 0.5 percent the sparking voltage of a gas by introducing Eq. (11), with experimentally determined constants, into Eq. (2); that is, by ignoring completely the possible influence of space charges. Furthermore, it has often been shown experimentally that, within certain limits, the magnitude of i_0 has little or no influence on the sparking potential. Therefore, we should be able to demonstrate by a numerical calculation that the introduction of the effects of space charges will lead to essentially the same threshold voltage as that predicted by the ordinary Townsend equation, provided i_0 is not too large.

In an effort to present a more meaningful illustration of the role played by space charges in a Townsend breakdown process, we have tried to choose the conditions of the problem so that our calculations will yield results close to those expected for a specific gas. Nitrogen was chosen because there is such a wealth of prebreakdown and breakdown data on this gas in the literature. The conduction data of Masch,[8] Posin,[9] and Dutton, Haydon, and Llewellyn Jones,[10] show that the

[8] K. Masch, Arch. Elektrotech. **22**, 589 (1932).
[9] D. Q. Posin, Phys. Rev. **50**, 650 (1936).
[10] Dutton, Haydon, and Llewellyn Jones, Proc. Roy. Soc. (London) **A213**, 203 (1952).

Townsend α can be expressed conveniently by the relation

$$\alpha/P = 7.0e^{-260P/E}, \qquad (15)$$

provided E/P is less than about 120 (volts/cm) per mm Hg. Introduction of this result into Eq. (2) leads to an expression which describes the variation of the sparking potential with $P\delta$. By fitting this expression to the sparking data of Ehrenkrantz,[11] we obtain a value of 3.19×10^{-4} for (ω/α), in good agreement with the recent direct measurements of Dutton, Haydon, and Llewellyn Jones[10] in the region $40<E/P<45$.

The conditions we have chosen are: $P=700$ mm Hg, $\delta=1.0$ cm, $(\omega/\alpha)=3.19\times10^{-4}$, $B=260$ (volts/cm) per mm Hg, $A=7.0$ (cm×mm Hg)$^{-1}$, $\mu_+=3.0\times760/P$ cm^2/volt sec, and $i_0=6.36\times10^{-11}$ amperes/cm^2. Our calculations, based on these values, show that space charges do not become important until the voltage is less than one percent below threshold; in this case the ordinary Townsend condition for breakdown is adequate.

However, the behavior of current and voltage sheds much light on the mechanism of the spark. Figures 2 through 5 detail the results of calculations for four voltages near threshold. The first three show the variation of n_+, E, and α across the gap. Note the increasing inhomogeneity as $\bar{u}$ increases. Figure 5 shows the plot of log$i$ *versus* V; the *approach* to threshold is essentially that described by the ordinary Townsend equation. A fundamental feature of the plot is the negative $i-V$ characteristic that develops beyond $i\approx10^{-5}$ ampere/cm^2; this illustrates the instability of the system beyond this point. Points on the negative characteristic represent states that are in principle steady states, but probably could not be realized experimentally.[12] The criterion for breakdown appropriate to this situation is that the slope of the log$i$ *versus* V curve become infinite, and not that the current itself reach some specified value as demanded by the ordinary Townsend equation. That is, if the external circuit is capable of supplying *at least* the current corresponding to the onset of the negative characteristic, the breakdown will not be influenced by the external circuit.

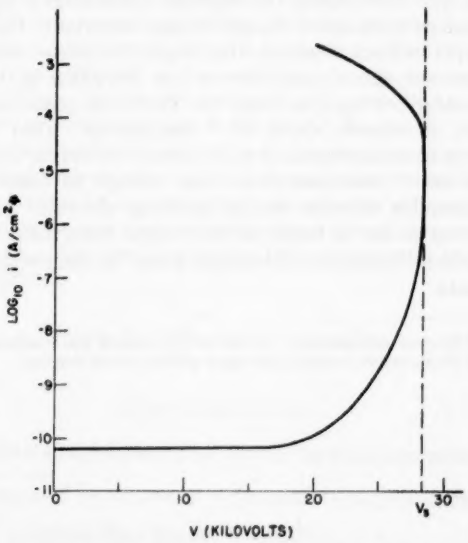

FIG. 5. Variation of the steady-state current with voltage.

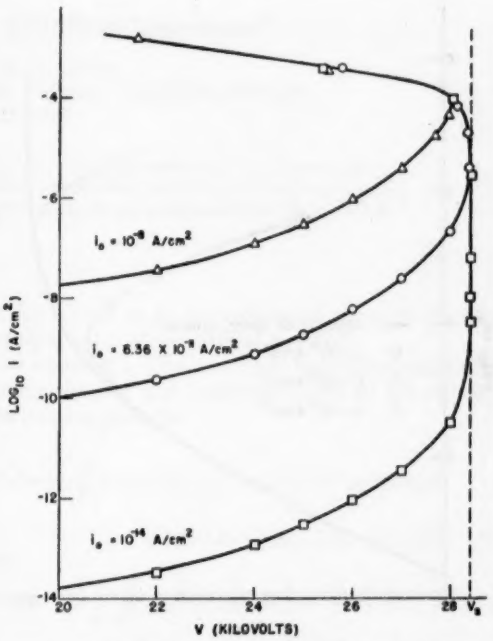

FIG. 6. The influence of the magnitude of i_0 on the sparking threshold.

In order to demonstrate the influence of i_0 on the sparking threshold, we have carried out similar calculations with i_0 equal to 10^{-14} and 10^{-8} ampere/cm^2. The results, shown in Fig. 6, indicate that the influence of space charges on the threshold voltage is negligible unless i_0 is significantly larger than 10^{-8} ampere/cm^2.

It is important to mention that the negative $i-V$ characteristic can develop only if α increases with some power of E greater than one; otherwise the function is single-valued. This has been shown qualitatively by von Engel and Steenbeck.[3] Varney, White, Loeb, and Posin[6] also noted that such a dependence of α upon E could lead to the development of breakdown through space charge formation by α alone. However, the process was not discussed in terms of the negative characteristic.

[11] Florence Ehrenkrantz, Phys. Rev. **55**, 219 (1939).

[12] It should be pointed out that the existence of the negative characteristic, as calculated, much beyond the point of instability depends upon the applicability of the Townsend mechanism in this region. The space charge which gives rise to the negative characteristic may, under certain circumstances, result in the formation of a streamer, as has often been observed.

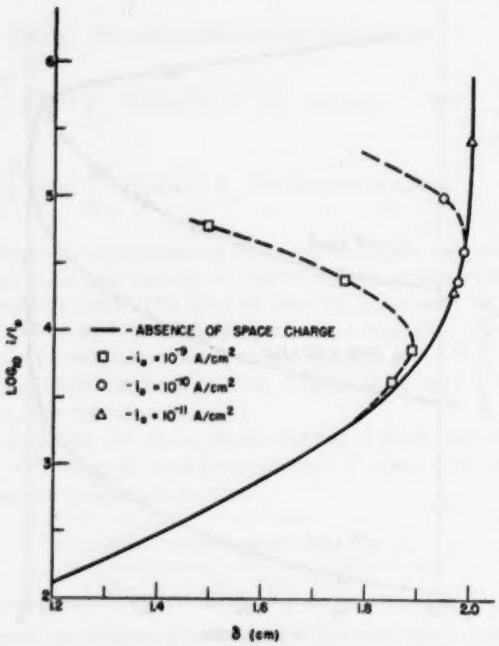

FIG. 7. The influence of space charges on the curvature of log$i$ *vs* δ plots at constant V/δ.

B. The Influence of Space Charge on Measurements of (ω/α)

There has been considerable discussion in the past concerning the possible influence of space charges on measurements of the secondary ionization coefficient, (ω/α). Equation (1) predicts a certain curvature in the plot of log$i$ *versus* δ at constant E/P as the sparking distance is approached. Experimental values of (ω/α) are usually obtained from the extent of this curvature. However, because space charges also become important as threshold is approached, their effects might complicate such measurements.

In 1936 Posin[9] found that it was impossible to evaluate accurately the secondary coefficient for N_2 from pre-breakdown current measurements unless i_0 was kept below about 10^{-13} ampere/cm². He attributed this to the effects of space charge. At about the same time, Varney, White, Loeb, and Posin[6] showed that such a field distortion can cause an increase in current more rapid than that predicted by the equation, $i=i_0e^{\alpha\delta}$, when i_0 is sufficiently large. However, secondary processes were omitted in their calculations.

In a recent paper, Dutton, Haydon, and Llewellyn Jones[10] have reported the results of a study of pre-breakdown currents in N_2, measured for various values of i_0. They found that the initial photocurrent could be varied from 6×10^{-15} amperes to 1.8×10^{-12} ampere[13] without any noticeable effect on the measured value of (ω/α). For these measurements, the gas pressure was 300 mm Hg, and the sparking distance 2.09 cm. For the highest value of i_0, the current became as high as 10^{-7} ampere as δ approached the sparking distance. This current is considerably in excess of that for which space charge distortion was commonly believed to be important.

In order to show numerically the effect of space charge distortion on the curvature of log$i$ as a function of δ, we must introduce Eq. (13) into the expression

$$\int_0^{\bar{u}}(E/\alpha)du \Big/ \int_0^{\bar{u}}(1/\alpha)du = V/\delta = \text{constant} \quad (16)$$

and again determine pairs $(K_0,\bar{u})$ that satisfy this condition. The current in the gap can then be calculated for various values of δ approaching threshold.

To illustrate, we have again chosen N_2, under approximately the same conditions used by Dutton, Haydon, and Llewellyn Jones[10] in their experimental measurements ($P=300$ mm Hg, $\delta_s=2.0$ cm, $V/\delta=1.245\times10^4$ volts/cm, and the same values of A, B, μ_+, and (ω/α) used in the previous calculation). The results are plotted in Fig. 7 for three values of i_0 (10^{-11}, 10^{-10}, and 10^{-9} ampere/cm²), and compared with the predictions of Eq. (1). Note again the negative characteristic that develops when space charges become important. These results indicate, however, that under the above conditions one should not observe any deviation of the curvature of $\log(i/i_0)$ from the Townsend prediction, until i_0 exceeds about 10^{-10} ampere/cm². That is, errors in measurement of (ω/α) should not appear until the initial photocurrent is large enough to cause a measurable decrease in the sparking distance. This current is far in excess of the largest value used by Dutton, Haydon, and Llewellyn Jones[10] in their experiments.

[13] Because approximately 0.5 cm² of the cathode was irradiated, this photocurrent is nearly the same as the current density.

Properties of the Quantum Statistical Impedance*

J. L. JACKSON AND M. C. YOVITS
Applied Physics Laboratory, The Johns Hopkins University, Silver Spring, Maryland
(Received April 22, 1954)

The transfer function of a general linear dissipative system, which had previously been derived, is examined. It is shown that its real and imaginary parts satisfy relationships which must be true for general passive systems. Examination of the transfer function at low frequencies gives expressions for the equivalent resistance and capacitance.

IN a recent paper by one of the writers[1] the direct response of a linear dissipative system to an external generalized driving force was computed. The transfer function deduced from this computation had a real part which agreed with a previous result of Callen and Welton;[2] a new expression for the imaginary part was obtained. Callen and Welton showed that the real part of the transfer function was always positive, as indeed it should be for a dissipative system. It is the purpose of this note to point out some further properties of this transfer function.

It will be shown that the transfer function satisfies the requirement that it have no poles in the lower half of the ω plane. Expressions will be obtained for the expansion coefficients of the transfer function about zero frequency. This expansion is consistent with the physically expected behavior.

A linear system can be characterized by its transfer function, $F(\omega)$, which has the property that a periodic input, $\exp(i\omega t)$, yields the output $F(\omega)\exp(i\omega t)$. The singularities of $F(\omega)$ are the values of ω for which the homogeneous system equation has solutions. These singularities will in general occur for complex values of ω. The existence of such a singularity in the lower half of the ω plane would imply a temporal exponentially increasing solution of the homogeneous system equation. Thus, the transfer function of a passive system can have no singularities in the lower half ω plane.

As a consequence of this fact, the use of Cauchy's integral theorem gives a necessary and sufficient condition (except for an arbitrary constant in the real part) which must exist between the real and imaginary parts of such a transfer function for real frequencies.[3] This condition is

$$B(\omega)=(2\omega/\pi)\int_0^\infty [A(x)/(x^2-\omega^2)]dx, \tag{1}$$

where

$$F(\omega)\equiv A(\omega)+iB(\omega); \tag{1.1}$$

the functions $A(\omega)$ and $B(\omega)$ are real for real frequencies. In Eq. (1) it is to be understood that the Cauchy principal value of the integral is meant.

In reference 1, it is shown that, for a linear dissipative system the real and imaginary parts of the transfer function are given by

$$A(\omega)=\pi\omega\int f(E)\rho(E)[|\langle E+\hbar\omega|Q|E\rangle|^2\rho(E+\hbar\omega) - |\langle E-\hbar\omega|Q|E\rangle|^2\rho(E-\hbar\omega)]dE, \tag{2}$$

and

$$B(\omega)=-2\omega\int\int [f(E)\rho(E)\rho(E')(E-E')|\langle E|Q|E'\rangle|^2 \times[(E-E')^2-(\hbar\omega)^2]^{-1}dEdE'. \tag{2.1}$$

The notation used is that of reference 1. In order to verify that this transfer function satisfies Eq. (1) the transformation,

$$|E-E'|\equiv\hbar x, \tag{3}$$

is used to replace E' in Eq. (2.1); Eq. (1) is identically obtained.

It is of interest to note the behavior of this transfer function at low frequencies. The real and imaginary parts have the zero frequency expansions

$$A(\omega)=\alpha\omega^2+O(\omega^4), \tag{4}$$

$$B(\omega)=\beta\omega+O(\omega^3), \tag{4.1}$$

where

$$\alpha=(\pi\hbar/kT)\int f(E)\rho^2(E)|\langle E|Q|E\rangle|^2dE, \tag{4.2}$$

and

$$\beta=2\int\int [f(E)\rho(E)\rho(E')|\langle E|Q|E'\rangle|^2 \times(E'-E)^{-1}dEdE'. \tag{4.3}$$

The expression for α can be obtained readily from Eq. (4.6) of reference 2. It should be observed that α and β are both positive, the latter because $f(E)$ is smaller than $f(E')$ when E' is less than E. Equations (4) and (4.1) specify an impedance that has a zero frequency expansion of the form

$$Z(\omega)=(i\omega\beta)^{-1}+(\alpha/\beta^2)+O(\omega). \tag{5}$$

* Supported by the Bureau of Ordnance, Department of the Navy.
[1] J. L. Jackson, Phys. Rev. **87**, 471 (1952).
[2] H. B. Callen and T. A. Welton, Phys. Rev. **83**, 34 (1951).
[3] See, e.g., H. W. Bode, *Network Analysis and Feedback Amplifier Design* (D. Van Nostrand Company, Inc., New York, 1945), Chap. XIV.

In the language of circuit theory this means that the dissipative system has capacitance β and resistance (α/β^2). Higher order circuit elements can be found by taking into account the higher order terms in the expansion of $A(\omega)$ and $B(\omega)$.

The zero frequency behavior of the transfer function is that which is to be expected for a dissipative system. The resistance is shown to be finite and different from zero. The current vanishes at zero frequency due to the presence of the capacitive term in the impedance.

One might also consider the transfer function $F_n(\omega)$ which gives the response of a single member of the ensemble with unperturbed energy, E_n. The corresponding real and imaginary parts are then clearly

$$A_n(\omega)=\pi\omega[|\langle E_n+\hbar\omega|Q|E_n\rangle|^2\rho(E_n+\hbar\omega) - |\langle E_n-\hbar\omega|Q|E_n\rangle|^2\rho(E_n-\hbar\omega)], \quad (6)$$

and

$$B_n(\omega)=-2\omega\int(E_n-E')|\langle E_n|Q|E'\rangle|^2 \times[(E_n-E')^2-(\hbar\omega)^2]^{-1}dE'. \quad (6.1)$$

It is not here apparent that the real part of this transfer function, which gives the response of a single member of the ensemble, must be positive. However, it is clear that the relationship of Eq. (1) is fulfilled, even for a single member of the ensemble.

PHYSICAL REVIEW VOLUME 96, NUMBER 1 OCTOBER 1, 1954

The Virial Series of the Ideal Bose-Einstein Gas*

B. WIDOM†
Department of Chemistry, University of North Carolina, Chapel Hill, North Carolina
(Received May 17, 1954)

It is suggested that the ideal Bose-Einstein gas be used as the prototype of an imperfect gas in investigating a possible connection between divergence of the virial series and the condensation phenomenon. An explicit expression is obtained for the virial coefficients in this case. Obtaining the radius of convergence of this series appears to be a formidable mathematical problem, and only a lower bound for this radius is established. It is conjectured, however, that the radius of convergence is infinite.

THE ideal Bose-Einstein gas is imperfect, in the sense that its equation of state is not $p=\rho kT$. The imperfection is a quantum effect, and it gives rise to the well-known Einstein condensation. In many respects the p-v isotherms[1] resemble those of an ordinary condensing gas, though there are, of course, important differences.

The problem of finding a possible relationship between the extreme limit of convergence of the virial series, and the point of condensation, is one of considerable importance in the mathematical theory of ordinary imperfect gases.[2] In this connection it would be interesting to find the radius of convergence of the virial series of the ideal Bose gas and observe whether or not it is equal to the density at which condensation is known to occur. I have succeeded in obtaining explicit expressions for the coefficients in this series, but I have only been able to establish a lower bound for the radius of convergence. It may be conjectured, however, that the radius of convergence is infinite, and that the function defined by the virial series bears the same relation to the pressure of the system that a function of van der Waals type (including the unstable portions) bears to the pressure in an ordinary condensing gas.[2]

The dimensionless density $x_1=(h^2/2\pi mkT)^{\frac{3}{2}}\rho$ and the dimensionless pressure $x_2=(1/kT)(h^2/2\pi mkT)^{\frac{3}{2}}p$ are two members of the set of functions[3] x_s given by

$$x_s=\sum_1^\infty n^{-(s+\frac{1}{2})}y^n, \quad (1)$$

where $y=\exp(\mu/kT)$. The virial series is obtained by eliminating y from the expressions for x_2 and x_1, expressing the former as a power series in the latter.[4] From Bürmann's expansion,[5]

$$x_{s+1}(y)=x_{s+1}(0)+\sum_1^\infty\frac{1}{n!}\left\{\frac{d^{n-1}}{dy^{n-1}}\left[\left(\frac{y}{x_s}\right)^n\frac{dx_{s+1}}{dy}\right]\right\}_{y=0}x_s^n.$$

* Work supported by the U. S. Office of Naval Research.
† Present address: Department of Chemistry, Cornell University, Ithaca, New York.
[1] O. K. Rice, Phys. Rev. **93**, 1161 (1954).
[2] H. N. V. Temperley, Proc. Phys. Soc. (London) **A67**, 233 (1954).
[3] These functions have been studied by E. W. Barnes, Proc. London Math. Soc. (2) **4**, 284 (1906); C. Truesdell, Ann. Math. **46**, 144 (1945); and others.
[4] A general problem of this kind was considered by J. C. Glashan, Am. J. Math. **3**, 190 (1880), but his results are of too implicit a nature to be useful here.
[5] E. T. Whittaker and G. N. Watson, *Modern Analysis* (Cambridge University Press, London, 1927), fourth edition, pp. 128–129.

But by Eq. (1), $x_{s+1}(0)=0$ and $dx_{s+1}/dy=x_s/y$. Hence,

$$x_{s+1}=x_s\left\{1+\sum_1^\infty \frac{1}{(n+1)!}\left[\frac{d^n}{dy^n}\left(\frac{x_s}{y}\right)^{-n}\right]_{y=0} x_s{}^n\right\}.$$

Segar[6] has shown how to express, in determinantal form, any derivative of any power of a function.[7] Applying Segar's result, one obtains

$$\left[\frac{d^n}{dy^n}\left(\frac{x_s}{y}\right)^{-n}\right]_{y=0}=(-1)^n D_n,$$

where D_n is the following determinant of order n:

$$D_n=\begin{vmatrix} \frac{n}{2^{s+1}} & 1 & 0 & 0 & \cdots \\ \frac{2n}{3^{s+1}} & \frac{n+1}{2^{s+1}} & 2 & 0 & \cdots \\ \frac{3n}{4^{s+1}} & \frac{2n+1}{3^{s+1}} & \frac{n+2}{2^{s+1}} & 3 & \cdots \\ \frac{4n}{5^{s+1}} & \frac{3n+1}{4^{s+1}} & \frac{2n+2}{3^{s+1}} & \frac{n+3}{2^{s+1}} & \cdots \\ \cdot & \cdot & \cdot & \cdot & \\ \cdot & \cdot & \cdot & \cdot & \\ \cdot & \cdot & \cdot & \cdot & \end{vmatrix}. \quad (2)$$

Finally, then,

$$x_{s+1}=x_s\left[1+\sum_1^\infty (-1)^n\frac{D_n}{(n+1)!}x_s{}^n\right]. \quad (3)$$

When $s=1$, Eq. (3) is the virial series. Having found an explicit formula for the coefficients amounts to having solved the recurrence relations by means of which these coefficients are usually obtained.[8] Note that condensation is known[8] to occur at $x_1=\zeta(3/2)=2.612\cdots$. ($\zeta$ is the Riemann zeta function.)

By writing $y=r\exp(it)$, it is seen from Eq. (1) that, for $r<1$, $|x_1(y)|\leq x_1(r)$, the equality holding when $t=0$. But for $r<1$, $x_1(r)$ is an increasing function of r, and as $r\to 1$, $x_1(r)\to\zeta(3/2)$. Thus, in the circle $|y|=1$, $|x_1(y)|<\zeta(3/2)$. Also, $x_1(y)$ is regular in this circle. Therefore, by Landau's theorem,[9] the inverse function $y(x_1)$ is regular, and $|y(x_1)|<1$, when $|x_1|<\zeta(3/2)\times\{\zeta(3/2)-[\zeta(3/2)^2-1]^{\frac{1}{2}}\}^2\equiv Q$. But $x_2(y)$ is regular for $|y|<1$. Then, since a regular function of a regular function is regular, the radius of convergence R of the virial series must satisfy $R\geq Q=0.103\cdots$.

Better estimates of R can be obtained by considering the magnitude of D_n. There are only 2^{n-1} nonvanishing terms in the full expansion of D_n. When $s=1$, the largest element of D_n is the element in the $(n-1)$th row and the nth column, *viz.*, $(n-1)$. Consequently, $|D_n|\leq 2^{n-1}(n-1)^n$, or $R\geq 1/2e=0.184\cdots$.

Widom[10] has pointed out that for $s=1$ the largest nonzero element of the kth row of D_n is $\leq k$ when $k\geq 2(n-1)/3$ and is $\leq 2(n-1)/3$ when $k<2(n-1)/3$, and that, as a consequence,

$$|D_n|\leq\frac{2^{n-1}[2(n-1)/3]^{2(n-1)/3}n!}{(\{2(n-1)/3\}-1)!},$$

where $\{A\}$ means "smallest integer $\geq A$." Thus, $R\geq 1/2e^{\frac{1}{2}}=0.257\cdots$.

I am indebted to Professor O. K. Rice, under whose direction this work was done.

[6] H. W. Segar, Messenger of Math. (2) **21**, 177 (1891–2).

[7] A different, though equivalent, result was obtained by S. Mangeot, Ann. Sci. l'École Norm. Sup. (3) **14**, 247 (1897), but his determinant is slightly less convenient for our purposes.

[8] J. E. Mayer and M. G. Mayer, *Statistical Mechanics* (John Wiley and Sons, Inc., New York, 1940), pp. 288–290, 416–426.

[9] L. Bieberbach, *Lehrbuch der Funktionentheorie* (B. G. Teubner, Leipzig, 1934), fourth edition, Vol. I, pp. 189–190.

[10] H. Widom (private communication).

Approximate Variational Principle in Quantum Statistics*

WILLIAM M. MACDONALD, III,† AND JOHN M. RICHARDSON‡
Explosives and Physical Sciences Division, Bureau of Mines, Pittsburgh, Pennsylvania
(Received May 19, 1954)

The density matrix of von Neumann can be used to formulate an exact variational principle for quantum statistics which embodies the principle of maximization of entropy. Using the formalism of second quantization, we can write this variational principle for fermions or bosons and can then derive from it an approximate variational procedure which yields the particle states of a system of interacting bosons or fermions as well as the distribution of particles in these states. These equations yield the generalization of the Hartree-Fock equations for nonzero temperature and the corresponding extension to bosons.

I. INTRODUCTION

THE quantum statistics of interacting identical particles was first attacked from the point of view of the density matrix by Dirac[1] who derived the Hartree-Fock equations for fermions at zero temperature in this way. The problem of a system of interacting fermions at nonzero temperatures has been studied by Husimi[2] in his long paper on the density matrix and, more recently, by Husimi and Nishiyama.[3,4] These authors used the principle of maximization of entropy to derive their results, although the minimization of free energy has been suggested by Lidiard,[5] who has used the method to derive the approximate free energy used by Koppe[6] in a calculation of the influence of the exchange energy on the specific heat of free electrons in metals. Kubo[7] has also minimized the free energy in his treatment of antiferromagnetism.

The purpose of this paper is the formulation of a general approximate variational method in the quantum statistics of fermions and bosons using the grand canonical ensemble of Gibbs and the procedures of second quantization. The emphasis in this treatment is no longer on the individual particles but on the states,[8] and we shall speak appropriately of correlations and interactions between these states for example. After first discussing the exact variational principle, which is equivalent to the entropy maximization principle, we derive its formulation for identical particles by the use of second quantization. In treating the variational principle for identical particles, we introduce the approximation that correlations between particle states are to be neglected. By "no correlation" we mean that the number of particles in one state does not depend strongly upon the number of particles occupying other states. More explicitly, we set the density matrix equal to a product of factors each referring to a particular particle state. We then introduce the further approximation that each factor is a function only of the operator for the number of particles in the particle state to which the factor refers. The now approximate variational principle gives the best form for each factor, in the sense of minimizing the quantum mechanical partition function for the grand canonical ensemble.

Even though correlations between particle states are neglected, the interactions between them are present in a manner like that of the familiar "effective field" theories. This fact appears when we vary the functional form of the particle states in our variational expressions; the equations which emerge are a generalization of the Hartree-Fock equations for fermions at nonzero temperature. These equations have already been given by Husimi[2] for fermions in a somewhat similar derivation. From the point of view adopted in this paper we can also justify the application of our procedure to the boson case in which we obtain a similar set of equations. Although the distributions of particles and the particle states are a natural extension of the fermion case, these latter equations have not been given previously.

II. GENERAL FORMULATION

In quantum statistics the grand canonical ensemble of Gibbs is introduced by taking the density matrix of von Neumann[9] in the form

$$\rho=\exp[\beta(\mu N-H)]/\text{Trace}\sum_{N=0}^{\infty}\exp[\beta(\mu N-H)], \quad (1)$$

where $\beta=(kT)^{-1}$, μ is the chemical potential, H (an ordinary Schrödinger operator) is the Hamiltonian for a system of the ensemble, and N (a scalar) is the number of particles in a system. The trace is to be taken over the space spanned by the eigenstates of the system. It is

* This research is part of the work which was carried out at the Bureau of Mines, supported by the U. S. Office of Naval Research.
† Present address: Department of Physics, Princeton University, Princeton, New Jersey.
‡ Present address: Hughes Research and Development Laboratories, Culver City, California.
[1] P. A. M. Dirac, Proc. Cambridge Phil. Soc. **26**, 376 (1930).
[2] K. Husimi, Proc. Phys.-Math. Soc. Japan **22**, 264 (1940).
[3] T. Nishiyama, Progr. Theoret. Phys. Japan **5**, 135 (1950); **6**, 1 (1950).
[4] K. Husimi and T. Nishiyama, Progr. Theoret. Phys. Japan **5**, 909 (1950).
[5] A. B. Lidiard (private communication).
[6] H. Koppe, Z. Naturforsch. **2a**, 429 (1947).
[7] Ryo Kubo, Revs. Modern Phys. **25**, 344 (1953).
[8] The term "state" here is intended to denote a possible state for a single particle and not a state of the whole system composed of many particles. To avoid confusion we will call the first-mentioned state a particle state.
[9] J. von Neumann, *Die Mathematische Grundlagen der Quantenmechanik* (Dover Publications, New York, 1943).

well known that Eq. (1) can be derived from the variational principle:

$$\Theta=\mathrm{Trace}\rho(\log\rho-\beta\mu N+\beta H),\quad \delta\Theta=0, \tag{2}$$

where we minimize Θ with respect to ρ subject to the constraint

$$\mathrm{Trace}\rho=1. \tag{3}$$

If the system is homogeneous it can be shown that $\Theta_{\min}=-\beta pV$, where p is the pressure and V is the volume of the system. This variational principle is related to the entropy maximization principle which leads to the Gibbs petite canonical ensemble. The use of the n-particle Hamiltonian and wave functions which are the product of single-particle wave functions in Eq. (2) will lead to the proper wave functions and distributions for Maxwell-Boltzmann particles.

For a system of n identical particles the wave functions for the system must be symmetric or antisymmetric combinations of some single particle states $\psi_k(s)$, where s denotes space and spin coordinates. This restriction is easily incorporated by the use of the second quantization procedure developed by Jordan and Wigner[10] and discussed more fully by Fock.[11] In second quantization we first introduce the ordered orthonormal set of single-particle wave functions $\psi_k(s)$. The symmetric or antisymmetric combinations of the $\psi_k(s)$ which form the permissible states of the n-particle system can then be characterized by the number of particles N_k occupying each state $\psi_k(s)$ and therefore denoted by $\Psi(N_1,\cdots,N_r)$. In so designating the wave functions of this so-called Fock space, we have shifted our emphasis from the particles to the particle states $\psi_k(s)$. Two operators a_m and a_m^* logically appear in the theory as generators of these states:

$$\begin{aligned}a_m^*\Psi(\cdots,N_m,\cdots)&=\epsilon_m(N_m+1)^{\frac{1}{2}}\Psi(\cdots,N_m+1,\cdots),\\ a_m\Psi(\cdots,N_m,\cdots)&=\epsilon_m(N_m)^{\frac{1}{2}}\Psi(\cdots,N_m-1,\cdots).\end{aligned} \tag{4}$$

The factor ϵ_m depends on the statistics of the particles; for bosons $\epsilon_m=1$, whereas for fermions

$$\epsilon_m=(-1)^{\eta},\quad \eta=\sum_{r=0}^{m-1}N_r.$$

The operators a_m and a_m^* (annihilation and creation operators) satisfy the commutation $[\ ]$ and anticommutation relations $[\ ]_+$:

$$\begin{aligned}&\text{(bosons):}\quad [a_m,a_n]=[a_m^*,a_n^*]=0,\quad [a_m,a_n^*]=\delta_{mn};\\ &\text{(fermions):}\quad [a_m,a_n]_+=[a_m^*,a_n^*]_+=0,\quad [a_m,a_n^*]_+=\delta_{mn}.\end{aligned} \tag{5}$$

[10] P. Jordan and E. Wigner, Z. Physik **47**, 631 (1928).
[11] V. Fock, Z. Physik **75**, 622 (1932); **76**, 852 (1932).

The operator whose eigenvalue is the number of particles in the particle-state $\psi_k(s)$ is

$$N_k=a_k^*a_k, \tag{6}$$

and the operator for the total number of particles is then

$$N=\sum N_k=\sum a_k^*a_k. \tag{7}$$

It follows from the commutation relations of Eq. (5) that the eigenvalues of N_k are 0, 1 for fermions whereas for bosons they are the entire set of non-negative integers.

Let the Hamiltonian for interacting particles be expressed in the particle formalism as

$$H=\sum H_1(s)+\tfrac{1}{2}\sum_{s\neq s'}H_2(s,s'), \tag{8}$$

where $H_1(s)$ is an operator depending only on the coordinates of s, whereas $H_2(s,s')$ is a two-particle interaction term depending on the coordinates of s and s'. The Hamiltonian for interacting identical particles can be shown to be

$$\begin{aligned}H=&\sum_{m,n}a_m^*(m|H_1|n)a_n\\ &+\tfrac{1}{2}\sum_{mnpq}a_m^*a_n^*(mn|H_2|pq)a_qa_p,\end{aligned} \tag{9}$$

where

$$\begin{aligned}(m|H_1|n)&=\int d(1)\psi_m^*(1)H_1(1)\psi_n(1),\\ (mn|H_2|pq)&=\int d(1)d(2)\psi_m^*(1)\psi_n^*(2)\\ &\quad\times H_2(1,2)\psi_p(1)\psi_q(2).\end{aligned} \tag{10}$$

We can now substitute the expressions for N and H given by (7) and (9) into Eq. (2) and can proceed to minimize Θ with respect to ρ.

We now make the assumption

$$\rho=\prod_m\rho_m(N_m). \tag{11}$$

This equation can be regarded as containing two approximations: (1) ρ is the product of operators each referring to a particle state $\psi_m(s)$, and (2) each of these factors is a function only of N_m. The first approximation is of the same type as that made by Hartree for the wave functions of atomic electrons. This factorization implies the neglect of correlations between particle states. We emphasize that this does not imply a neglect of correlations between two bosons in the same particle state. For the case of fermions, the neglect of correlation between particle states is obviously equivalent to the neglect of correlations between particles since there can be, at most, one particle in a state. For the sake of uniqueness we shall take each factor as individually normalized so that

$$\begin{aligned}&\text{(bosons):}\quad \mathrm{Trace}\,\rho_m(N_m)=\sum_{N_m=0}^{\infty}\rho_m(N_m)=1;\\ &\text{(fermions):}\quad \mathrm{Trace}\,\rho_m(N_m)=\rho_m(0)+\rho_m(1)=1.\end{aligned} \tag{12}$$

Even though the results of minimizing the exact variational expression are invariant to the choice of particle state, the minimum of the approximate variational expression which incorporates Eq. (12) depends on the choice of the orthonormal set. For this reason we shall minimize Θ not only with respect to the ρ_m but also with respect to the functional form of the set ψ_m, with the orthonormality condition (5) as the only constraint.

III. INTERACTING FERMIONS

For the case of fermions we can take $\rho_m(N_m)$ in the form

$$\rho_m(N_m)=(1-w_m)(1-N_m)+w_mN_m, \tag{13}$$

in which w_m is clearly the probability for the occupation of the particle state ψ_m. We can combine Eqs. (2), (11), and (12) to obtain

$$\Theta=\sum_m (1-w_m)\log(1-w_m)+\sum_m w_m[\log w_m-\beta\mu+(m|H_1|n)]+\tfrac{1}{2}\sum_{m,n} w_mw_n[(mn|H_2|mn)-(mn|H_2|nm)]. \tag{14}$$

Carrying out the variation on w_m we find

$$w_m=\{\exp[\beta(\epsilon_m-\mu)]+1\}^{-1}, \tag{15}$$

where ϵ_m is an effective energy which includes the direct and exchange interaction energy

$$\epsilon_m=(m|H_1|n)+\sum_n w_n\times[(mn|H_2|mn)-(mn|H_2|nm)]. \tag{16}$$

Aside from the fact that ϵ_m is an effective energy, Eq. (15) is what one obtains for noninteracting fermions.

The variation of ψ_m^* subject to the orthonormality constraint yields

$$H_1(1)\psi_m(1)+\sum_n w_n\int d(2)\psi_n^*(2)H_2(1,2)\psi_n(2)\psi_m(1)-\sum_n w_n\left[\int d(2)\psi_n^*(2)H_2(1,2)\psi_m(2)+\lambda_{mn}\right]\psi_n(1)=0. \tag{17}$$

We emphasize that the integral represents summation over spin as well as integration over space. λ_{mn} is a Lagrange multiplier for the orthonormality condition. The variation of ψ_m gives the complex conjugate of Eq. (17). The Hartree-Fock equation is a special case of Eq. (17) obtained by letting the temperature go to zero ($\beta\to\infty$) so that $w_m=1$ if $\epsilon_m<\mu$ and $w_m=0$ if $\epsilon_m>\mu$.

Husimi has derived Eqs. (15), (16), and (17) from a different point of view. He asserts, therefore, that Eq. (11) implies the neglect of correlations between *particles* and that this approximation makes the treatment of the boson case unreasonable by this approach. We have pointed out that the approximation neglects correlations only between particle states and in the boson case will also provide reasonable results.

IV. INTERACTING BOSONS

In treating interacting bosons we do not have a simple form for $\rho_m(N_m)$ but instead must carry along the normalization of Eq. (12) by Lagrange multipliers. In the representation in which the N_m are diagonal, Eq. (14) reduces to

$$\Theta=\sum_m\sum_{N_m}\rho_m(N_m)\{\log\rho_m(N_m)+\beta[-\mu+(m|H_1|n)]N_m+\tfrac{1}{2}\beta(mm|H_2|mm)N_m(N_m-1)\}+\tfrac{1}{2}\sum_{m\neq n}\sum_{N_m,N_n}\rho_m(N_m)\rho_n(N_n)\times[(mn|H_2|mn)+(mn|H_2|nm)]N_mN_n. \tag{18}$$

Upon minimizing this with respect to $\rho_m(Nm)$ and ψ_m^*, we find

$$\rho_m(N_m)=\rho_m(0)\exp[-\beta(N_m\epsilon_m-\mu)], \tag{19}$$

where, for bosons,

$$\epsilon_m=(m|H_1|n)+(mm|H_2|mm)(N_m-1)+\sum_n\rho_n(N_n)[(mn|H_2|mn)+(mn|H_2|nm)], \tag{20}$$

$$H_1(1)\psi_m(1)+2N_m\int d(2)\psi_m^*(2)H_2(1,2)\psi_m(2)\psi_m(1)+\lambda_m\psi_m(1)+\sum_{n\neq m}\sum_{N_n}\rho_n(N_n)N_n\times\left[\int d(2)\psi_n^*(2)H_2(1,2)\psi_n(2)\psi_m(1)+\int d(2)\psi_n^*(2)H_2(1,2)\psi_m(2)\psi_n(1)+\lambda_{mn}\psi_n(1)\right]=0. \tag{21}$$

Again the integral represents integration over space and summation over spin. The Lagrange multipliers λ_m and λ_{mn} are again the result of the orthonormality conditions. Equation (21) then constitutes a "consistent field" or Hartree-Fock equation for bosons. We note that the most significant differences between Eqs. (17) and (21) are in the presence of an interaction term between bosons in the same particle state and in the sign of the exchange term. We can easily see that in the case of no interaction Eqs. (19) and (20) lead to the Bose-Einstein distribution, for these equations become

$$\rho_m(N_m)=\rho_m(0)\exp\{-\beta N_m[\mu-(m|H_1|n)]\}. \tag{22}$$

The average number of particles in the particle state

ψ_m is then

$$\langle N_m\rangle=\sum_{N_m}\rho_m(N_m)N_m$$
$$=\{\exp\beta[(m|H_1|n)-\mu]-1\}^{-1}. \quad (23)$$

SUMMARY

The approximate variational procedure described herein has enabled us to obtain suitable wave functions for the description of the individual particle states of a system of "weakly" interacting bosons or fermions and to give the distribution of particles in these states. The procedure is not limited to these two cases, which are to be considered merely as illustrative of the general procedure. An application to ferromagnetism or antiferromagnetism can be made and a quantum theory of liquids can be derived along the lines of the classical cell theory as developed by Richardson and Brinkley.[12] In a discussion of helium II, however, one should expect the correlation between different particle states to play an important part, and this requires a modification of the simple assumption of Eq. (11).

One of us (WMM) is indebted to Professor J. A. Wheeler and Professor A. S. Wightman and to L. van Hove for several interesting discussions of this paper.

[12] J. M. Richardson and S. R. Brinkley, Jr., Phys. Rev. **87**, 199 (1952); *High Speed Aerodynamics and Jet Propulsion* (Princeton University Press, Princeton, 1953), Vol. I, Sec. F.

PHYSICAL REVIEW VOLUME 96, NUMBER 1 OCTOBER 1, 1954

Mobility of Impurity Ions in Germanium and Silicon*

C. S. FULLER AND J. C. SEVERIENS†
Bell Telephone Laboratories, Murray Hill, New Jersey

(Received May 14, 1954)

Lithium has been shown to migrate as a singly-charged positive ion in single crystals of both Ge and Si in temperature ranges of 150–600°C and 360–860°C, respectively. The mobility of the Li^+ in crystalline Ge and Si has been measured as a function of temperature. Through the use of the Einstein relation between diffusion constant and mobility, values of the diffusion constants in cm²/sec of Li^+ in Ge and Si are obtained as follows: $D=25\times10^{-4}\exp\{(-11\,800)/RT\}$ for Ge and $D=23\times10^{-4}\exp\{(-15\,200)/RT\}$ for Si, in satisfactory agreement with previously published results on the thermal diffusion of Li^+. A curious reversion of conductivity type of solid solutions of Li in Ge is discussed. Copper has likewise been found to move as a positive ion in germanium in the temperature range 800°–900°C leading to diffusivities in agreement with previously published results.

INTRODUCTION

LITHIUM has already been shown to diffuse rapidly into crystalline germanium and silicon, behaving as a donor element in these semiconductors,[1] and the diffusion constants for these processes have been determined by means of a method involving the measurement of *p-n* junction positions.[2] An alternative method, capable of greater experimental accuracy, and based on fewer assumptions consists of measuring the mobilities of the Li^+ ions under an applied electric field. In theory, the diffusivity D can then be determined from the Einstein relationship between diffusion constant and mobility. The sign of the ionic charge (positive in the case of Li as required by its donor properties) can also be ascertained by noting the direction the impurity ion moves in the electric field. The activation energies for diffusion can be obtained in the usual way from the slopes of plots of the logarithm of the diffusion constant against reciprocal of the absolute temperature. In the present work this method has been applied successfully to Li in solution in Ge and Si.

THEORY

The basic principle of the method (see Fig. 1) is the diffusion of a hemispherical cloud of impurity ions into the semiconductor. We shall refer to such an ion cloud as a "pulse" because of its similarity to the analogous pulses employed in the measurement of electron and hole mobilities by the Haynes-Shockley method.[3] The impurity ion pulse is put in at a temperature chosen so as to obtain a relatively high concentration of Li in solution. The location of the diffusion region in the semiconductor is then determined from the location of the *p-n* junction. Thereupon the sample is subjected at a given temperature to a dc electric field for a fixed time after which the pulse, now less concentrated due to thermal diffusion is again located from the new *p-n* junction position. If the net drift motion of the center of the pulse is x, then the mobility is obtained from the relation $\mu=x/Et$; where t is the drift time in seconds and

* A brief report of this work first appeared as a Letter to the Editor, Phys. Rev. **92**, 1322 (1953).

† Present address: The Johns Hopkins University, Baltimore, Maryland.

[1] C. S. Fuller and J. A. Ditzenberger, Phys. Rev. **91**, 193 (1954).

[2] Fuller, Theuerer, and van Roosbroeck, Phys. Rev. **85**, 678 (1952); C. S. Fuller, Phys. Rev. **86**, 136 (1952).

[3] J. H. Haynes and W. Shockley, Phys. Rev. **81**, 835 (1951). This analogy was first pointed out to the authors by W. Shockley.

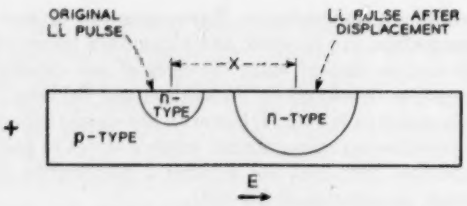

FIG. 1. Sketch of p-type semiconductor bar showing original pulse (small circle) and pulse after migration for a time, t, in field E.

E the field in volts/cm. The diffusion constant is then obtained from the Einstein relationship giving $D=(kT/q)(x/Et)$; where k is Boltzmann's constant, T the absolute temperature, and q the ionic charge. Since the quantities T, x, E, and t can all be measured to within a few percent, this method provides an accurate means of determining D. The method, if taken in conjunction with the thermal diffusion measurements,[2] can also serve to prove that these ions do obey the Einstein relation, at least to within the experimental error of both methods.

A difficulty in the method arises from the fact that thermal diffusion makes the pulses less concentrated and therefore their location becomes less precise for longer times. Large fields are therefore desirable so as to move the center of the pulses for appreciable distances (20 mils is sufficient for a measurement to within 5 percent) before they have spread out so much thermally as to cause inaccuracies in location. Solubility considerations likewise put a lower temperature limit on the method. These considerations apply particularly to copper in Ge for which the maximum solubility is about 4×10^{16} cm^{-3} and the diffusivity is high (3×10^{-5} cm^2/sec) in the temperature range investigated (800°–900°C).

EXPERIMENTAL TECHNIQUE WITH LITHIUM

Single crystals[4] of Ge and Si (p type, since Li is a donor) were cut into bars 0.7 in.×0.1 in.×0.06 in. by means of a diamond saw. The samples were then dry-ground and small cubes [approx 15 mils (0.038 cm) on a side] of metallic Li were placed near the midpoint of the bars, one cube of Li per bar. The bars, with the metallic Li on them, were then heated for about 30 seconds in a tubular furnace in a helium atmosphere at a temperature of 800°C±10°C. At this temperature most of the Li fuses into the semiconductor to form a Li-rich alloy while some of the Li (about 10^{18} atoms per cm^3) diffuses into the lattice to give a hemispherical diffusion region. After this short heating period the samples were quenched on a large steel block. The surface was thereupon reground and etched to remove surface contaminants. The etching process completely removed the Li-rich alloy region, leaving a pit of about 5–10 mils (0.0125–0.0250 cm) deep and about 20 mils (0.050 cm) in diameter. Concentric with this pit there remained the hemispherical diffusion region into which the Li had diffused and which was thereby converted from p-type to n-type. The p-n boundary, which is a circle on the surface concentric with the pit, was then made visible by the deposition of barium titanate under reverse voltages of about 40 volts.[5] The diameter of the diffusion pulses thus prepared varied from 35 mils (0.089 cm) to 55 mils (0.140 cm). The ends of the bars were finally plated so as to provide good electrical contact for the electrodes.

The specimen was then placed in a series circuit consisting of storage batteries and current limiting slide wire resistors. It was supported (as shown in Fig. 2) between two steel cooling rods, electrically insulated therefrom by thin mica separators. Electrical contact was made through pressure contacts on the plated end areas. An ammeter was placed in the circuit and currents ranging from 0.3 to 10 amp were passed through the specimen, the current serving to heat up the specimen as well as to provide the electric field. The electric field acting on the ions was determined by measuring the voltage across two tungsten probes, 1.0 cm apart, which could be brought in pressure contact with the sample. Knowing the current and voltage across the sample, the resistivity, and in turn the temperature, can be found. Data of Morin were used for this purpose.[6] The drift times during which the samples were exposed to the field varied from 5 minutes to 5 hours, depending on the temperatures at which the runs were made. After exposing the pulse to the field for a definite time, the sample was cooled down to room temperature as quickly as possible. This required about

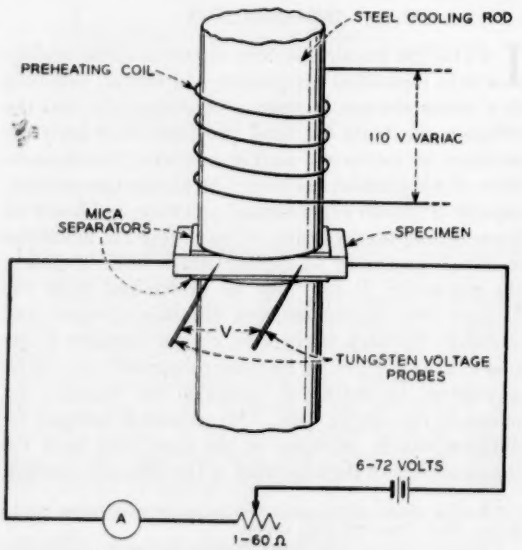

FIG. 2. Experimental arrangement.

[4] G. K. Teal and J. B. Little, Phys. Rev. 78, 637 (1951); G. K. Teal and E. Buehler, Phys. Rev. 81, 637 (1951).

[5] G. L. Pearson, U. S. Patent No. 2,669,692, February 16, 1954.

[6] F. J. Morin (private communication).

40 seconds. The surface was re-cleaned and the *p-n* boundaries brought out again by means of barium titanate. The circular trace of the displaced pulse was then located optically under a microscope, and the drift distance measured by means of a micrometer eyepiece. The drift distances ranged from 3 to 20 mils (0.0076 to 0.0508 cm). All the necessary information is thus available to determine the ion mobilities.

It has been found as was expected from its donor properties[2] that Li moves as a positive, singly-charged ion in Ge and Si. The diffusion constant as a function of temperature was calculated and the results are shown in Table I and plotted in Fig. 3. For comparison, this plot also shows the thermal diffusion measurements.[2] Good agreement obtains between the two methods, showing that the Einstein relation is valid for these ions in the concentration and temperature ranges investigated. The curves can best be described by the equations:

$$D = 25\times10^{-4}\exp(-11\,800/RT) \text{ for Ge;}$$
$$D = 23\times10^{-4}\exp(-15\,200/RT) \text{ for Si.}$$

The activation energies are therefore 11 800 and 15 200 cal/mole for Ge and Si, respectively.

TABLE I. Tabulation of experimental data.

T(°C)	$E\left(\frac{\text{volts}}{\text{cm}}\right)$	t(sec)	x(cm)	$\mu\left(\frac{\text{cm}^2}{\text{volt sec}\times10^6}\right)$	$D\left(\frac{\text{cm}^2}{\text{sec}\times10^7}\right)$
			Germanium		
150	6.00	1500	0.0076	0.085	0.031
174	9.00	8400	0.0153	0.201	0.078
203	5.45	13 200	0.0178	0.248	0.102
227	6.15	1000	0.0263	0.430	0.183
254	4.27	1000	0.0238	0.560	0.255
274	4.00	9000	0.0330	0.97	0.458
295	3.70	7200	0.0312	1.36	0.667
313	3.25	7200	0.0500	2.17	1.10
334	2.52	3800	0.0216	2.23	1.17
358	2.26	6300	0.0558	3.92	2.14
373	2.56	4620	0.0554	4.68	2.61
400	2.06	4500	0.0554	5.98	3.48
418	2.22	3600	0.0576	7.22	4.31
451	1.60	3000	0.0432	10.0	6.50
460	2.20	600	0.0140	10.6	6.70
473	1.65	2760	0.0605	13.3	8.56
491	1.33	2400	0.0522	16.3	11.4
524	1.71	1500	0.0578	22.6	15.5
554	1.50	1680	0.0623	24.6	17.6
574	1.49	900	0.0432	32.2	23.6
600	1.24	600	0.0320	43.0	32.4
			Silicon		
360	12.0	4500	0.0139	0.258	0.147
390	13.0	4200	0.0246	0.452	0.258
422	11.3	3600	0.0274	0.675	0.405
460	8.15	4200	0.0381	1.11	0.70
494	7.55	3600	0.0444	1.64	1.08
527	5.95	3000	0.0464	2.61	1.80
564	6.23	2040	0.0554	4.36	3.15
620	5.20	1500	0.0515	6.60	5.10
670	4.21	1200	0.0556	11.0	8.95
707	4.75	660	0.0436	14.0	11.8
780	3.68	360	0.0305	23.0	20.9
877	3.40	300	0.0368	36.0	27.3

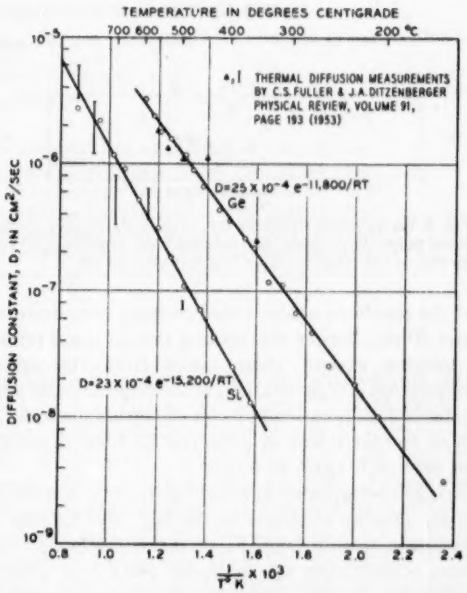

FIG. 3. Plots of diffusivity against reciprocal of absolute temperature for Li in Ge and Si.

REVERSION PHENOMENON SHOWN BY LITHIUM IN Ge

A curious effect, which incidentally permits a graphic demonstration of the drift, was observed for the case of Li in Ge. This is illustrated in Fig. 4. After the pulse had been exposed to the electric field, it was found that the barium titanate would bring out not only the displaced diffusion area, but also an image of the original spot, i.e., the original pulse position. Upon probing this region with a tungsten point and examining the characteristic rectification curves on an oscilloscope, it was found that this original spot had returned to *p* type, the same type as the body of the Ge specimen, whereas the area into which the Li had been moved under the action of the electric field was *n* type. This phenomenon was observed over the entire temperature range and is shown for two cases in the photograph of Fig. 5. These show the small original circle which has reconverted to *p* type after exposure to the field, inside of (A) or partially inside of (B) a larger *n* type pulse after it has been moved. The rest of the sample is of course still *p* type.

The following is offered as an explanation of the above observations: Upon quenching rapidly from the temperature (800°C), at which the original pulse is produced, the Li remains, at room temperature, in a supersaturated state. However, upon re-heating in the mobility apparatus, the temperature rise is of necessity slower (several minutes). It is believed that precipitation of some of the Li occurs throughout the original region during this stage. Upon reaching the experimental temperature, all of the Li, except for some residual nucleation centers, is again in solution, the field is then applied for a fixed time

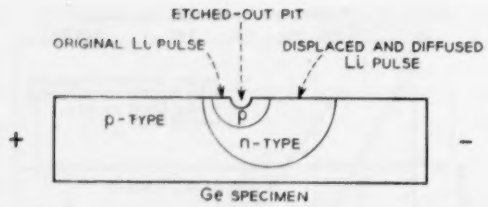

FIG. 4. Ge specimen after exposure to dc field, showing displaced diffused pulse (large circle) and original pulse (small circle) where reversion to the original p-type conductivity occurs.

and the specimen again cooled to room temperature in about 40 sec. During this cooling the ion cloud remains in solution except where nuclei from the original precipitation still persist, i.e., in the original pulse where crystallization occurs rapidly on the residual nuclei. The almost complete loss of dissolved Li from this region thus returns it again to p type.

No such behavior as described above was observed for silicon. This we attribute to the fact that Li does not precipitate readily from Si in the temperature range (room temperature up to about 100°C) in which it precipitates rapidly from Ge. Thus, the warming-up period in the mobility apparatus does not precipitate enough Li to leave nucleation centers and no reversion to the original conductivity type takes place. In the silicon experiments, therefore, care was taken to preserve the original etched-out pit (Fig. 4) so that determination of the drift distance x could be determined.

A final comment might be made regarding a peculiar wiggly appearance of the diffused and migrated pulses when made visible with barium titanate. One of these is evident in Fig. 5(A). We are uncertain as to the cause of these fluctuations in pulse radius. One explanation is that they correspond to resistivity variations in the specimens. There is some evidence against this, however, and in support of structural variations in the single crystal lattice. Further work will be required to establish this point.

MOBILITY OF COPPER IN Ge

Experiments similar to those described above have also been performed using copper particles instead of Li to produce p-type[7,8] pulses in n-type Ge. Because of the small solubility of copper in Ge, (approximately 10^{16} cm^{-3}) the precise location of the copper pulses after migration presents considerable difficulty. In addition, the danger of contamination and the high diffusivity of copper in Ge (3×10^{-5} cm^2/sec)[7] require that short times (about 45 to 60 seconds) be employed. This greatly reduces the precision. Successful experiments have however, been performed at 800°C and 900°C which show that copper moves as a positively charged ion in Ge at these temperatures. The drift distances were 0.011 and 0.020 cm for fields of 1.0 and 1.3 volts/cm, respectively. The calculated diffusivities are 2.4×10^{-5} and 3.0×10^{-5} cm^2/sec in satisfactory agreement with previously reported thermal measurements of 2.8×10^{-5} cm^2/sec. One test at 700°C showed no essential motion. However, the solubility at this temperature is just at the detection limit. Large boundary fluctuations also exist. Because of these and other inaccuracies we are unable to be entirely certain whether the ion is singly or doubly charged, although the above figures for the diffusivities are based on the assumption of a single positive charge.

The above finding that copper behaves as a positive ion in Ge at temperatures of 800°–900°C is interesting in view of the reported acceptor properties of copper.[7] It suggests the possibility that the ionization of copper is

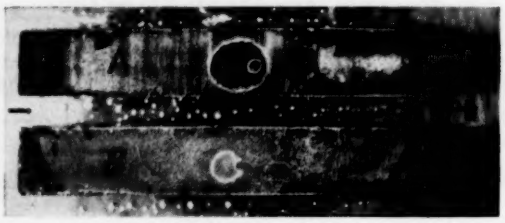

FIG. 5. Two Ge bars showing original pulses (small circles) and drifted pulses (large circles). (A) Shows original pulse within the drifted one. (B) Shows the drifted pulse partially separated. In each case the negative electrode is to the left. The pulses were made visible by means of barium titanate deposition.

dependent upon temperature in such a way that it acts as a negative ion at room temperatures and as a positive ion at the higher temperatures of these experiments. The single result at 700°C in which no motion was observed, lends some further support to this hypothesis, since it might be expected that intermediate temperatures might favor neutrality of the copper.

It has not been possible to investigate the behavior of copper in silicon by this method inasmuch as its acceptor properties in silicon are too feeble to allow the p-n junction method to be employed. In addition, J. D. Struthers has found copper to precipitate readily in silicon.

ACKNOWLEDGMENT

The authors wish to thank J. A. Ditzenberger for help with the measurements and E. Buehler and E. Kolb for supplying single crystals of germanium and silicon. Mr. F. G. Foster kindly provided the photograph in Fig. 5.

[7] C. S. Fuller and J. D. Struthers, Phys. Rev. **87**, 526 (1952).
[8] Fuller, Struthers, Ditzenberger, and Wolfstirn, Phys. Rev. **93**, 1182 (1954).

Adiabatic Magnetization of a Superconducting Sphere

R. L. DOLECEK
United States Naval Research Laboratory, Washington, D. C.
(Received June 14, 1954)

Measurements are reported of the temperature changes accompanying suppression of the superconductivity of a lead sphere by adiabatic magnetization. Observations were made in the temperature range 2.1°K to 4.3°K for magnetizations into the complete range of the intermediate state. The magnetic fields were applied as step functions of time, and allowance was made for the resulting eddy-current heating. After magnetization, practically complete temperature equilibrium was established in the order of 15 seconds. Temperature changes observed on magnetization were in quantitative agreement with values predicted from calorimetric data and demonstrate a linear relationship between the applied magnetic field and the fraction of normal metal produced in the intermediate state.

INTRODUCTION

At a given temperature, the molar entropy of a metal in the superconducting state is smaller than the molar entropy of the metal in the normal state produced by the application of a magnetic field in excess of the critical field at that temperature. This entropy difference accrues only during increase of the magnetic field from a threshold-field value determined by specimen geometry to the critical-field value for bulk material.[1] The manner of variation of the entropy during this intermediate state transition has received theoretical attention.[2] Thus, utilizing specific heat and critical-field data, one can predict the cooling to occur upon the isentropic magnetization of a superconducting sphere. It has been observed by other investigators[3–5] that cooling of a superconductor results from the application of a magnetic field sufficient to produce the intermediate state. However, experimental verification of the predicted cooling was not accomplished. This paper is a report of an experiment designed to measure the temperature changes induced in a superconducting sphere by adiabatic magnetizations and to test the predicted linear relationship between the applied-magnetic field (H) and the fraction (x) of normal metal produced in the intermediate state; *viz.*, $x=(3H/H_c-2)$, where H_c is the critical-magnetic field for bulk material at the specimen temperature.

EXPERIMENTAL PROCEDURE

Measurements were taken of the cooling produced by adiabatic magnetization of a superconducting lead sphere. Observations were made in the temperature range 2.1°K to 4.3°K for fields in the range $0<h\leq 1.03$, where h is the ratio of applied field to critical-magnetic field. This range of applied fields corresponds to $0<x\leq 1$, where x is the fraction of the sphere that becomes normal when the sphere is subjected to a magnetic field sufficient to produce the intermediate state, *viz.* $\frac{2}{3}<h<1$. A carbon thermometer[6] was employed to measure temperature, the resistance of the thermometer being automatically recorded by a system having a response time of about five seconds. Temperature changes could be measured to approximately ±0.005°K. Practically complete equilibrium was reached in approximately 15 seconds after the application of the magnetic field. The fact that equilibrium was established in such a short time is in agreement with previous observations[7,8] and indicative of good thermal contact between the thermometer and the specimen. Figure 1 presents a typical record obtained on magnetization.

Since the conditions for reversibility were difficult to realize, changes in magnetic field were applied as step functions of time, and allowance was made for induced eddy-current heating. The eddy currents induced in the sphere were calculated and the excess magnetic energy was used, together with the isentropic cooling predicted by calorimetric data, to calculate the expected theoretical temperature change. The experimental conditions of measurement were the same as those reported in a previous publication[9] except that since the sample temperature changed, the magnetizations were adiabatic rather than isothermal. Thus, the eddy-current heating was calculated by the method previously outlined,[9] but an ideal isentropic-magnetization curve was used rather than an ideal isothermal-magnetization curve. In these

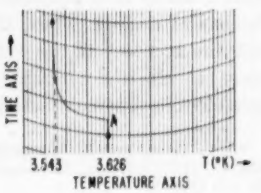

FIG. 1. Typical temperature record obtained on magnetization of a superconducting sphere. Markers on the time axis are at 15-second intervals. The magnetic field was turned on at A. Intervals along the temperature axis are only approximately equal as thermometer resistance is recorded. This record is of trial No. 43 of Table II.

[1] R. L. Dolecek, Phys. Rev. **82**, 102 (1951).
[2] D. Shoenberg, *Superconductivity* (Cambridge University Press, London, 1938), Chap. V; see also second edition (1952), Chap. III.
[3] K. Mendelssohn and J. R. Moore, Nature **133**, 413 (1934).
[4] W. H. Keesom and J. A. Kok, Physica **1**, 595 (1934).
[5] Mendelssohn, Daunt, and Pontius at Congres Internacionale du Froid, Le Haye, 1936 (unpublished).
[6] J. R. Clement and E. H. Quinnell, Rev. Sci. Instr. **23**, 213 (1952).
[7] D. Shoenberg, Proc. Cambridge Phil. Soc. **33**, 559 (1937).
[8] W. H. Keesom and P. Van Laer, Physica **3**, 173 (1936).
[9] R. L. Dolecek, Phys. Rev. **94**, 540 (1954).

TABLE I. Magnetization measurements at various initial temperatures.

Trial No.	Initial temperature °K	Applied h	Computed eddy-current heating °K	Computed isentropic cooling °K	Theoretical temperature change expected °K	Experimental temperature change observed °K	Deviation °K
35	4.378	1.02	0.084	0.256	−0.172	−0.174	−0.002
36	3.988	0.98	0.085	0.275	−0.190	−0.187	+0.003
37	3.755	0.95	0.094	0.287	−0.193	−0.186	+0.007
56	3.625	0.93	0.100	0.280	−0.180	−0.179	+0.001
61	3.241	0.97	0.213	0.382	−0.169	−0.179	−0.010
60	2.937	0.97	0.315	0.442	−0.127	−0.153	−0.026
59	2.670	1.03	0.555	0.579	−0.024	−0.078	−0.054
58	2.057	1.02	1.074	0.707	+0.367	+0.262	−0.105

calculations the critical-field data of Daunt *et al.*[10] were used and it was assumed that the critical-field curve was parabolic. The isentropic temperature changes for magnetization were computed using specific-heat data for lead[11–13] adjusted to yield, at the transition temperature, zero entropy difference between the superconducting and normal states. Also used were some recent measurements[14] of the atomic heat and latent heat of transition of superconducting lead which indicate a quartic dependence of the critical-magnetic field on temperature.[9] Since the Debye temperature of lead is not constant in the temperature interval studied, a lattice atomic heat of the form AT^3+BT^5 was employed.[15] The equations assumed for the entropies were

$$\text{Molar entropy of superconducting lead} = (1.377T^3+0.0118T^5+1.01\times10^{-6}T^7)\times10^{-4}\ \text{cal/°K},$$

$$\text{Molar entropy of normal lead} = (8.07T+1.267T^3+0.011T^5)\times10^{-4}\ \text{cal/°K}.$$

These equations yield entropy differences between the superconducting and normal states in good agreement with the values obtained by Daunt and Mendelssohn.[10]

EXPERIMENTAL RESULTS

In Table I typical measurements made on magnetizations from zero magnetic field to h, computed at the final temperature, are given together with temperature changes resulting from eddy-current heating and computed values of theoretical temperature changes expected. The value of the eddy-current heating ranges from a small to a predominant part of the expected theoretical cooling. Thus, the measurements test not only the accuracy of the eddy-current heating calculations but also the correctness of interpretation of the behavior of a superconducting sphere in the intermediate state and the accuracy of the functions assumed for the entropy and magnetic behavior of lead. The deviations encountered in these observations are quite large in absolute value and, at the lower temperatures, there appears to be systematic discrepancy. However, in all instances the deviation is less than ten percent of the sum of the calculated temperature changes involved. In the computation of the theoretical temperature change expected, experimental data for specific heats and critical-magnetic fields were employed, the magnetization curve for a perfect sphere was used, and no allowance was made for hysteresis effects. In view of these limitations, the data obtained are in good agreement with theory and verify (within 10 percent) the current interpretation of the behavior of a superconducting sphere in the intermediate state.

The predicted linear relationship between the applied magnetic field and the fraction of normal metal produced in the intermediate state can be tested by a calorimetric experiment in which magnetizations throughout the range of the intermediate state are all performed from a fixed initial temperature. The energy per mole absorbed by a conversion of superconducting metal to the normal state is given by the latent heat Q multiplied by the fraction converted dx, and this under adiabatic conditions will result in an absorption of heat energy of CdT from the metal, where C is the molar specific heat. If the magnetizations are all performed from the same initial temperature, then $Q/C\simeq$constant and one would expect $dT/dx\simeq$constant. Thus, if the fraction (x) converted is linearly related to the applied field H, a plot of temperature change resulting from magnetization *versus* x calculated from the magnitude of the applied magnetic field should yield a straight line of slope Q/C.

From an initial temperature of 3.62 ± 0.02°K, measurements were taken of the cooling produced by adiabatic magnetization into the complete range of the intermediate state. The measurements are given in Table II. Except for the small temperature changes near $x=0$, the deviations again are generally less than ten percent of the temperature changes involved. The eddy-current corrections in Table II include a small vibration heating incurred upon the sudden application of the magnetic field to the spherical specimen. This correction

[10] J. G. Daunt and K. Mendelssohn, Proc. Roy. Soc. (London) **160**, 127 (1937); Daunt, Horseman, and Mendelssohn, Phil. Mag. **27**, 754 (1939).
[11] W. H. Keesom and J. N. van den Ende, Leiden Comm. **19**, No. 213C (1931).
[12] J. R. Clement and E. H. Quinnell, Phys. Rev. **85**, 502 (1952).
[13] Horowitz, Silvidi, Malaker, and Daunt, Phys. Rev. **88**, 1182 (1952).
[14] These measurements, performed at the Naval Research Laboratory, are in preparation for publication.
[15] M. Blackman, Proc. Roy. Soc. (London) **A159**, 416 (1937).

TABLE II. Magnetization measurements at fixed initial temperatures.

Trial No.	Initial temperature °K	$x=\left(\frac{3H}{H_c}-2\right)$	Computed eddy current heating °K	Computed isentropic cooling °K	Theoretical cooling computed °K	Experimental cooling observed °K	Deviation °K
49	3.633	0.024	0.015	0.008	−0.007	0.002	−0.009
47	3.595	0.068	0.015	0.023	0.008	0.008	0.00
48	3.641	0.090	0.015	0.030	0.015	0.013	+0.002
51	3.633	0.135	0.015	0.046	0.031	0.028	+0.003
44	3.618	0.182	0.015	0.064	0.049	0.050	−0.001
53	3.624	0.238	0.015	0.084	0.069	0.065	+0.004
43	3.626	0.298	0.017	0.106	0.089	0.083	+0.006
54	3.624	0.400	0.026	0.143	0.117	0.110	+0.007
42	3.622	0.497	0.040	0.178	0.138	0.132	+0.006
55	3.621	0.565	0.050	0.201	0.151	0.139	+0.012
41	3.621	0.677	0.072	0.242	0.170	0.166	+0.004
56	3.625	0.786	0.100	0.280	0.180	0.179	+0.001
40	3.588	0.823	0.116	0.299	0.183	0.187	−0.004
57	3.630	0.893	0.132	0.315	0.185	0.183	+0.002
39	3.654	1.00	0.171	0.354	0.183	0.192	−0.009

is a predominant part of the eddy-current correction near $x=0$. In the computation of the temperature changes, experimental data for specific heats and critical-magnetic fields were employed, the magnetization curve for a perfect sphere was used, and no allowance was made for hysteresis effects. In view of these limitations, the data obtained are in good agreement with theory and verify (within 10 percent) the linear dependence of the fraction of the sphere in the normal state upon the average magnetic induction of the whole specimen. For test of the predicted linear dependence, the fraction (x) computed from the value of magnetic field applied is to be plotted against the total temperature change which is obtained by summing the eddy-current heating and the observed experimental cooling. This plot is presented in Fig. 2.

Except near the ends, the relationship is quite linear and since the fraction (x) was computed from the value of the applied magnetic field, the agreement substantiates the assumption that the fraction (x) of normal metal produced in the intermediate state of a superconducting sphere is a linear function of the applied magnetic field. This confirms the observations of Keesom and Van Laer[16] who have demonstrated the linear dependence for a tin ellipsoid having a demagnetizing coefficient of 0.056. That departures occur near the ends of the curve may be related to the fact that, in the calculations, an ideal magnetization curve was assumed for the sphere with no discontinuities on entering or leaving the intermediate state and no hysteresis. Variation of the latent and specific heat might produce the deviation from linearity at the larger values of x.

The slope of the curve for $x<0.6$, where eddy-current corrections are negligible, is about 0.34. As previously shown, this slope should equal Q/C. From calorimetric data one calculates an expected value of $Q/C\simeq 0.32$. This is in reasonably good agreement with the slope of the curve.

The effect of eddy-current heating was nominal for magnetizations involving $h<0.9$. However, it should be pointed out that there is an inversion at a temperature of about one-third the superconducting transition temperature and that below this temperature the eddy-current heating accompanying magnetization by the abrupt application of a magnetic field will exceed the isentropic cooling. See, for example, the eddy-current heating incurred for point No. 58 of Table I. It can be seen that at low temperatures the eddy-current heating of metals under magnetization (and demagnetization) can be of considerable magnitude and should be recognized as a possible source of serious heating. Magnetic cooling cycles should be designed to minimize the effect.

To realize most of the available cooling one may minimize eddy-current heating either by reducing the demagnetization factor of the sample or by applying the magnetic field slowly. For a lead sphere at 3.6°K it was found possible to obtain ninety percent of the theoretical isentropic cooling by traversing the intermediate state in about three minutes.

CONCLUSIONS

Measurements were performed on the adiabatic magnetization of a superconducting sphere, and the

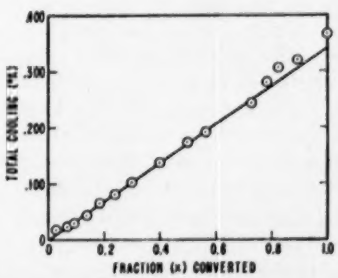

FIG. 2. Demonstration of the linear relationship between the applied magnetic field and the fraction of normal metal produced in the intermediate state. The straight line is drawn with a slope to fit best the data $x\leq 0.6$ for which eddy-current corrections are small.

[16] W. H. Keesom and P. H. Van Laer, Physica 4, 487 (1937).

results confirm the gross aspects of current interpretation of the behavior of a superconducting sphere in the intermediate state. Temperature changes observed on magnetization were in quantitative agreement with values predicted from calorimetric data and demonstrate a linear relationship between the applied magnetic field and the fraction of normal metal produced in the intermediate state.

PHYSICAL REVIEW VOLUME 96, NUMBER 1 OCTOBER 1, 1954

Electrical Properties of Silicon Containing Arsenic and Boron

F. J. MORIN AND J. P. MAITA
Bell Telephone Laboratories, Murray Hill, New Jersey
(Received April 28, 1954)

Electrical conductivity and Hall effect have been measured from 10° to 1100° Kelvin on single-crystal silicon containing arsenic and boron. Extrinsic carrier concentration is computed from Hall coefficient. Analysis of extrinsic carrier concentration indicates the ionization energy of arsenic donor levels to be 0.049 ev and of boron acceptor levels to be 0.045 ev for low impurity concentrations. Fermi degeneracy is found to occur in the range 10^{18} to 10^{19} cm^{-3} impurity concentration. Extrinsic Hall mobility is computed from Hall coefficient and conductivity. Curves of Hall mobility against resistivity at 300°K are computed from theory and compared with experiment. The temperature dependence of lattice-scattering mobility is found from conductivity to be $T^{-2.6}$ for electrons and $T^{-2.3}$ for holes. From conductivity mobility and intrinsic conductivity, it is found that carrier concentration at any temperature below 700°K is given by the expression: $np=1.5\times10^{33}T^3\exp(-1.21/kT)$. The temperature dependence of the ratio Hall mobility/conductivity mobility is determined for holes and electrons.

1. INTRODUCTION

AN extensive investigation of the fundamental electrical properties of silicon has not been published since 1949, when Pearson and Bardeen reported on silicon containing boron and phosphorus.[1] Their experimental work was necessarily limited because neither single crystals nor the means for measuring below 77°K were then available. Recently, it seemed opportune to reinvestigate silicon: good quality single crystals were available; it became possible to make the low temperature measurements necessary to locate precisely the impurity levels; there was considerable interest in silicon and fundamental information was needed.

Electrical conductivity and Hall effect have been measured from 10° to 1100°K on single crystals of silicon containing arsenic and boron. Unfortunately a complete analysis of the data is not possible at present. For example, one needs to know more about the scattering processes which produce the departure from the $T^{-1.5}$ law of lattice scattering mobility found for both holes and electrons; it is shown that electron-hole scattering is probably negligible below 1200°K; only a very rough estimate of optical mode scattering can be made; the possibility of scattering by multiple constant energy surfaces and by band splitting due to spin-orbit coupling was suggested by C. Herring but is neglected because theory is lacking. The meaning of the low temperature Hall effect in some samples is uncertain. Behavior of computed Hall mobility suggests the presence of impurity level conduction for which theory is unavailable. Determination of the mass parameter by fitting carrier concentration data in the extrinsic range is faced with two new problems for which theory is unavailable: the apparent dependence of the mass parameter on impurity concentration and the possible existence of excited states associated with the impurity atoms.

1.1 Methods

Crystals were prepared by E. Shannon of these laboratories using the Teal-Little pull technique.[2] In each case two crystals were pulled from du Pont silicon and then combined with the added impurity in a melt from which the final crystal was pulled. Samples were bridge shape[3] cut with the [110] direction along the length of the sample. The samples were sandblasted. Contact was made to n-type samples by bonding through gold plate with Sb-doped gold wire. Contacts to p-type samples were pressure contacts on rhodium plate.

1.2 Symbols

The symbols used have been defined previously by the authors.[4]

2. EXPERIMENTAL RESULTS

Conductivity and Hall coefficient in the intrinsic range of silicon are shown in Fig. 1. The Hall coefficient

[1] G. L. Pearson and J. Bardeen, Phys. Rev. **75**, 865–883 (1949).

[2] G. K. Teal, Phys. Rev. **78**, 647 (1950); Teal, Sparks, and Buehler, Phys. Rev. **81**, 637 (1951).

[3] P. Debye and E. Conwell, Phys. Rev. **93**, 693–706 (1954).

[4] F. J. Morin and J. P. Maita, Phys. Rev. **94**, 1525 (1954). See Sec. 3 for definition of symbols.

is negative, indicating that electron mobility is greater than hole mobility. The rapid downward curvature of the Hall coefficient suggests that electron and hole mobilities are converging at high temperature. Conductivity from ~400° to 600°K is a combination of intrinsic and extrinsic. At high temperature, conductivity is intrinsic and follows a straight line. This is in contrast to the curvature found in the intrinsic range of germanium and attributed to electron-hole scattering.[4] Extrinsic conductivity and Hall coefficient in silicon containing arsenic are shown in Figs. 2 and 4 and in silicon containing boron in Figs. 3 and 5. The sign of the Hall effect indicates arsenic to be a donor and boron to be an acceptor. The curves are displaced in the expected way by the change in amount of added impurity. Sample 159 represents the control to which no impurity was intentionally added. Samples 140 and 125 contain the highest concentration of impurity and show Fermi degeneracy. In the temperature range 10°–100°K the remaining curves have slopes indicating ionization of impurity centers with increasing temperature. Near 300° impurity centers are almost completely ionized and carrier concentration is constant. In this range conductivity changes with the temperature variation of mobility, and Hall coefficient changes with the temperature variation of the ratio μ_H/μ_c. Samples 126 and 141 depart at low temperature from the behavior common to the other nondegenerate samples. This result is not understood. It is shown later to include anomalous behavior of computed carrier concentration and Hall mobility.

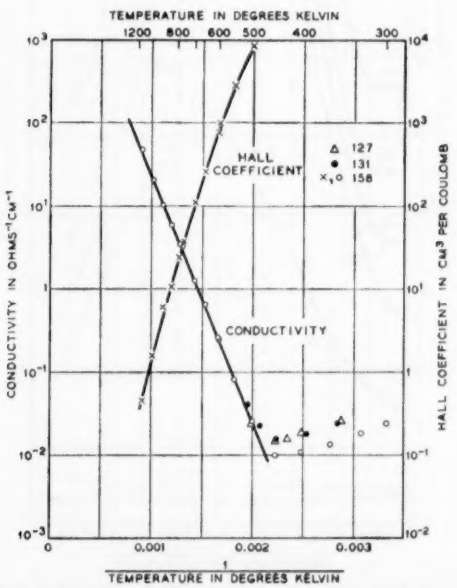

FIG. 1. Conductivity and Hall coefficient in the intrinsic range of silicon as a function of reciprocal absolute temperature.

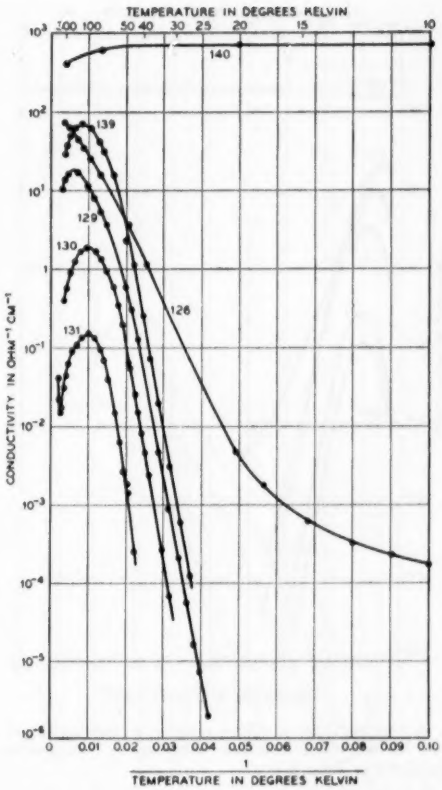

FIG. 2. Conductivity of silicon samples containing arsenic as a function of reciprocal absolute temperature. Composition of samples given in Table I.

3. EXTRINSIC RANGE

It is the plan of this paper to consider first the extrinsic range data and then to use some of the results obtained to analyze the intrinsic range. Carrier concentration and Hall mobility are computed from extrinsic conductivity and Hall coefficient. The concentration and ionization energies of impurities and the mass parameters for holes and electrons are determined from carrier concentration results. Curves of Hall mobility as a function of resistivity at 300°K are computed from theory, assuming lattice scattering and ionized impurity scattering and using the impurity concentrations determined from the carrier concentration analysis. This serves as a rough check on the impurity concentrations as determined, and on the general perfection of the samples.

3.1 Carrier Concentration

Carrier concentration has been computed from the Hall coefficient using the relations

$$R_H = 3/8en \text{ (or } p) \quad \text{(impurity range)},$$
$$R_H = 1/en \text{ (or } p) \quad \text{(degenerate range)},$$

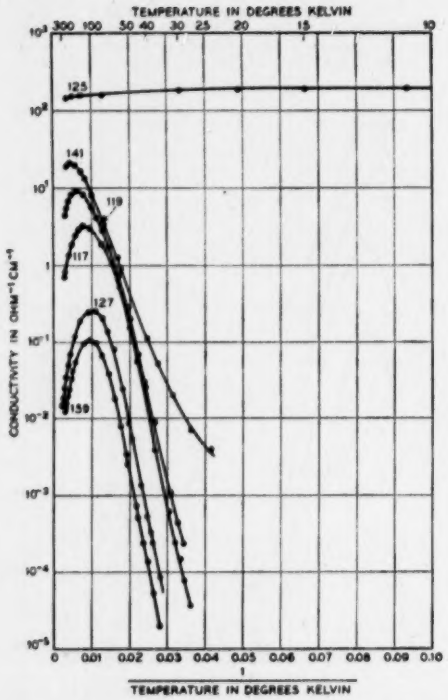

FIG. 3. Conductivity of silicon samples containing boron as a function of reciprocal absolute temperature. Composition of samples given in Table I.

and is shown in Fig. 6 for electrons and Fig. 7 for holes. The solid lines have been computed to fit the data by a method similar to that described in reference 1. The values found by this computation for concentrations and ionization energies of impurities and for the mass parameters of electrons and holes are shown in Table I. The ionization energy of arsenic levels appears to be 0.049 ev and of boron levels 0.045 ev under condition of high dilution of the impurities. These values are about the same as those found by Pearson and Bardeen, ~0.046 ev, for both donors (phosphorus) and acceptors (boron) if their sample 1 results are neglected on the grounds (suggested by its behavior) that the sample probably contained n-p junctions. The value of 0.056 ev for sample 131 seems out of line and the following possible explanation is given for this result. Crystals grown from undoped silicon are p type. In preparing 131, an amount of arsenic (donor) was added which together with the unknown donors normally present, compensated the acceptors and produced an n-type sample. Compensation may have been sufficient to ionize all of the arsenic (0.049 ev levels) plus some of the unknown donor (0.056 ev levels) with the consequence that the 0.049 ev levels were undetected by the Hall effect measurement. It is possible, therefore, that there is a higher concentration of impurities in sample 131 than shown in Table I. As shown by the mobility analysis in Sec. 3.2, the concentration of impurities may be as high as 2×10^{15} cm^{-3}.

TABLE I. Composition of samples and summary of extrinsic range results.

Sample No.	Majority impurity ionization energy ev	Net impurity concentration cm^{-3}	Minority impurity concentration cm^{-3}	Mass parameter	Added impurity
		n type			
131	0.056	1.75×10^{14}	1.0×10^{14}	0.5	arsenic
130	0.049	2.1×10^{15}	5.25×10^{14}	1.0	arsenic
129	0.048	1.75×10^{16}	1.48×10^{15}	1.2	arsenic
139	0.046	1.3×10^{17}	2.2×10^{15}	1.0	arsenic
126	?	2.2×10^{18}	...	...	arsenic
140	degenerate	2.7×10^{19}	...	...	arsenic
		p type			
159	0.045	3.1×10^{14}	4.1×10^{14}	0.4	none
127	0.045	7.0×10^{16}	2.2×10^{15}	0.4	boron
117	0.043	2.4×10^{16}	2.3×10^{15}	0.6	boron
119	0.043	2.0×10^{17}	4.9×10^{15}	0.7	boron
141	?	1×10^{18}	...	...	boron
125	degenerate	1.5×10^{19}	...	...	boron

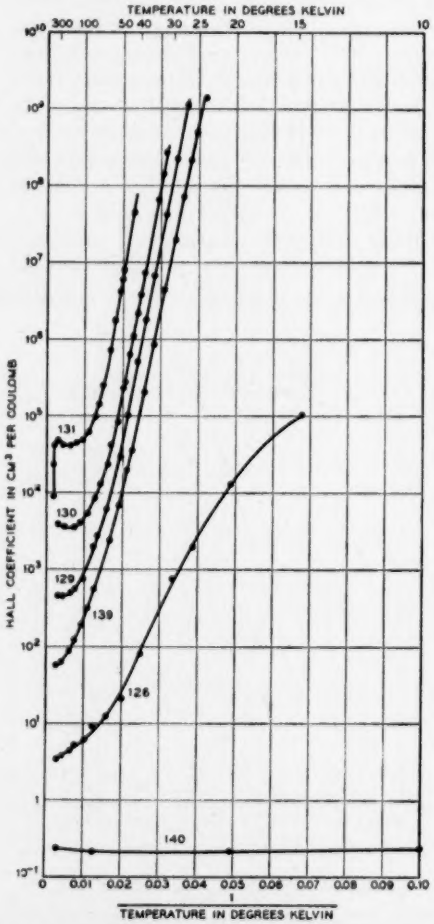

FIG. 4. Hall coefficient of silicon samples containing arsenic as a function of reciprocal absolute temperature. Composition of samples given in Table I.

It is not clear from the analysis of carrier concentrations how impurity ionization energy varies with impurity concentration. The effect is obscured by some new process occurring at low temperatures and superimposed upon the normal impurity ionization process. This can be seen as curvature in the low temperature carrier concentration results for samples 126 and 141. Evidence that this is not due to transition into Fermi degeneracy is given by their apparent Hall mobility which at low temperature drops well below that of the degenerate samples. Fermi degeneracy occurs at an impurity concentration between 10^{18} and 10^{19} cm^{-3}. It occurs in germanium at about one decade less in impurity concentration.

The analysis of carrier concentration does not give a very useful value for the inertial mass of the carriers. As shown in Table I, the mass parameter is found to vary with impurity concentration. Theory has not been developed for such a dependence. It is also probable that impurity levels have excited states. These cause the carrier concentration and, therefore, the computed mass parameter to be less than that predicted by the simple theory which assumes only a ground state.

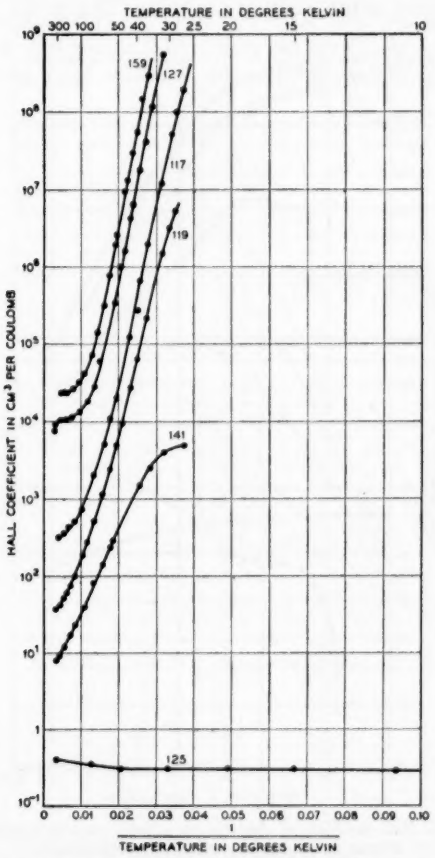

FIG. 5. Hall coefficient of silicon samples containing boron as a function of reciprocal absolute temperature. Composition of samples given in Table I.

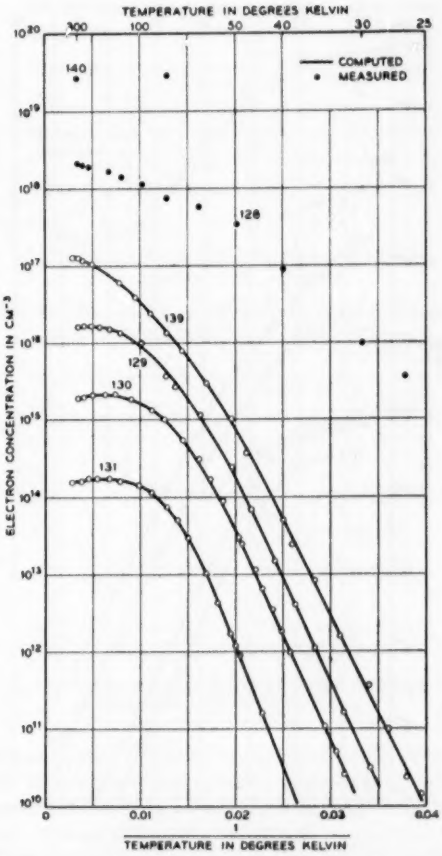

FIG. 6. Charge carrier concentration in silicon samples containing arsenic as a function of reciprocal absolute temperature.

3.2 Hall Mobility

Hall mobility, the product of conductivity and Hall coefficient, is shown in Figs. 8 for electrons and 9 for holes. The low temperature behavior of samples 139, 126, 119, and 141 is anomalous. No ordinary scattering mechanism predicts the rapid drop in mobility with decreasing temperature found in these samples. This result suggests the presence of a different conduction process, probably impurity level conduction, occurring at low temperatures and with low mobility carriers.

Hall mobility as a function of resistivity, both taken at 300°K, is shown in Figs. 10 and 11. The solid lines were computed by combining[5] lattice scattering and ionized impurity scattering mobilities. This computation was intended as a rough check on the impurity concentrations determined from carrier concentration. In making the computation it was assumed that

[5] Using the method of Conwell in reference 3.

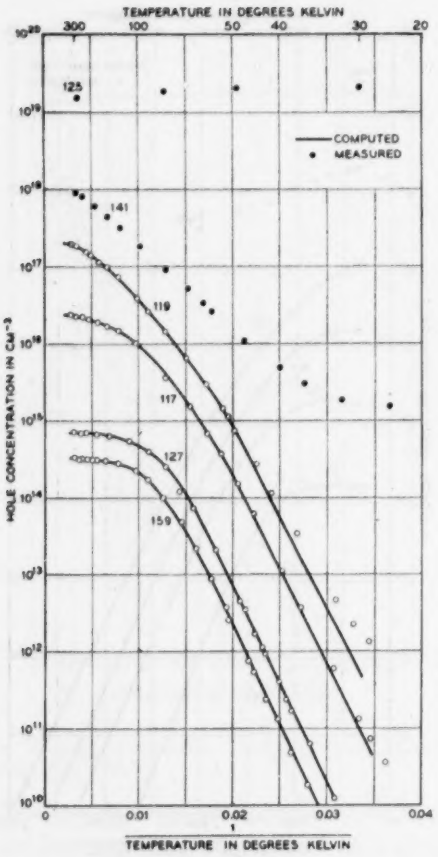

FIG. 7. Charge carrier concentration in silicon samples containing boron as a function of reciprocal absolute temperature.

$\mu_H/\mu_e = 1.0$ and is constant with impurity concentration. Lattice scattering mobility was used as an adjustable parameter to move the curve along the mobility axis and give the best fit to measured values. For the computation lattice scattering mobility was taken to be 1700 cm²/volt sec for electrons and 350 cm²/volt sec for holes. Ionized impurity scattering was computed using the modified Conwell-Weisskopf formula[5] and the impurity concentrations determined in Sec. 3.1. The resulting fit to the data suggests that the ionized impurities observed by the Hall effect make up the majority of scattering centers in the samples investigated. Sample 131 is the exception. Its mobility lies below the computed value by a significant amount. It is consistent with the carrier concentration results described in Sec. 3.1 to assume the low mobility to be due to ionized impurity scattering. The observed lowering of lattice scattering mobility requires a concentration of 2×10^{15} cm^{-3} ionized impurities, about seven times the amount detected by the Hall effect.

4. INTRINSIC RANGE

In this section intrinsic carrier concentration is computed from conductivity and conductivity mobility. From these results an empirical expression for the temperature dependence of carrier concentration is obtained. An estimate is made of the temperature behavior of μ_H/μ_e necessary to bring carrier concentration from Hall coefficient into agreement with that determined from conductivity.

4.1 Lattice Scattering Mobility

Conductivity mobility has been determined by the method described by Morin[6] using the conductivity of *n*-type samples 130 and 131 and *p*-type samples 127 and 159, together with drift mobilities at 300°K measured by Prince[7] (1300 cm²/volt sec for electrons and 500 cm²/volt sec for holes). The results are shown as plotted points in Fig. 12. Using the impurity concentrations determined in Sec. 3.1 it can be shown that impurity scattering in samples 127 and 159 is negligible above 150°K and that the results in Fig. 12 for holes represent lattice scattering mobility. This is not true

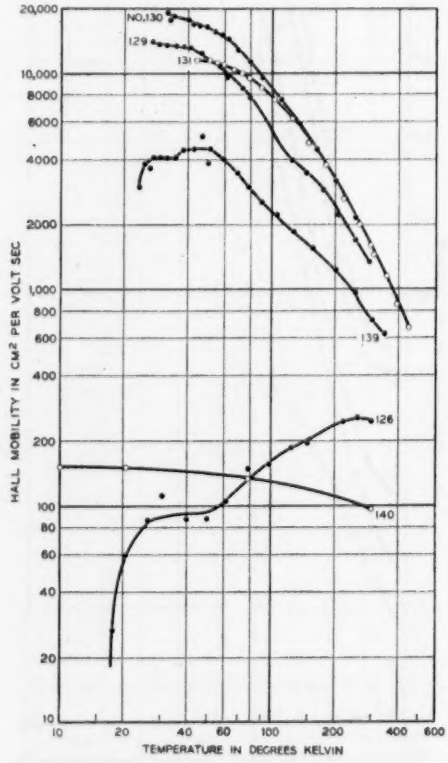

FIG. 8. Hall mobility of electrons in silicon samples containing arsenic as a function of absolute temperature.

[6] F. J. Morin, Phys. Rev. **93**, 62–63 (1954).
[7] M. Prince, Phys. Rev. **93**, 1204–1206 (1954).

for the electron results which must be corrected for impurity scattering. Electron lattice scattering mobility has been determined from measured mobility and computed ionized impurity scattering mobility. For this computation ionized impurity concentration was assumed to be 2.6×10^{15} cm^{-3}, that found in Sec. 3.1 for sample 130 and which is also a reasonable value for sample 131. The results are given by the relations

$$\mu_{Ln}=4.0\times10^{9}T^{-2.6}, \quad (1)$$

$$\mu_{Lp}=2.5\times10^{8}T^{-2.3}, \quad (2)$$

and shown by the straight lines in Fig. 12. The temperature dependence of μ_L departs from the $T^{-1.5}$ law expected for acoustical mode scattering. According to Herring, these results may be due to optical mode scattering, to the band edges being located at some point other than the center of the Brillouin zone, to bands split by spin-orbit coupling, or to a combination of these effects.

A computation has been made to find out what effect the presence of optical modes might have on an extrapolation of μ_L to higher temperatures. The optical mode temperature θ for silicon has been computed by Herring to be ~1200°K, using optical mode frequency

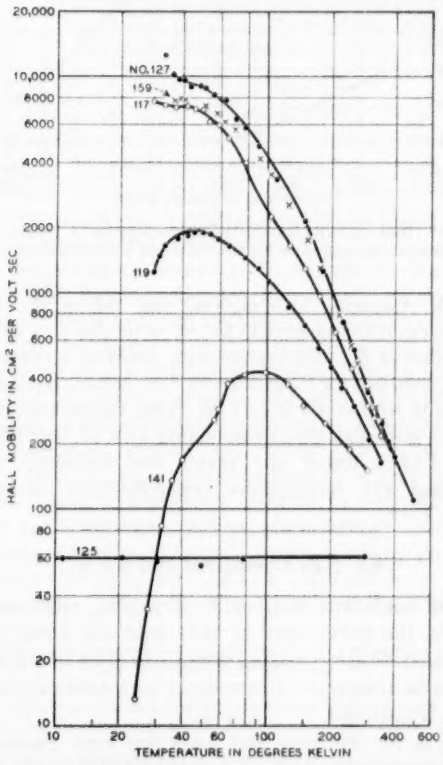

FIG. 9. Hall mobility of holes in silicon samples containing boron as a function of absolute temperature.

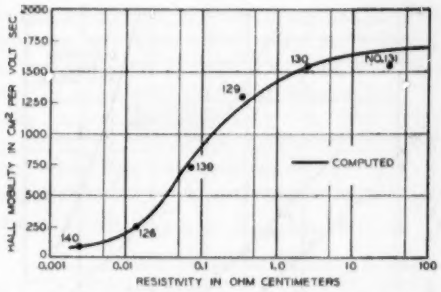

FIG. 10. Hall mobility of electrons as a function of resistivity in silicon samples containing arsenic.

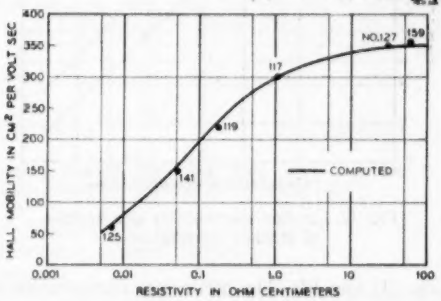

FIG. 11. Hall mobility of holes as a function of resistivity in silicon samples containing boron.

results of Smith.[8] From this result and Eq. (2), reference 4, the optical mode temperature dependence has been computed and is shown in Fig. 12. It is evident that if optical modes make an appreciable contribution to scattering at high temperatures (as they are expected to) they will also contribute appreciably to the scattering in the range where μ_L has been measured. A computation similar to that described is Sec. 4.1, reference 4, indicates that a large part (but probably not all) of the departure of the mobility temperature dependence from the $T^{-1.5}$ law might be due to optical modes. However, the results indicate that a large optical mode contribution does not cause the lattice scattering mobility to depart importantly from the linear extrapolation shown in Fig. 12.

4.2 Electron-Hole Scattering

Electron hole scattering has been computed using using the equation in Sec. 5.1 of reference 4 with $m_n=m_p=m$ and $\kappa=12$. Results are shown in Fig. 12. The effect of electron-hole scattering on mobility is negligible below 1200°K.

4.3 Carrier Concentration

Carrier concentration in the intrinsic range has been computed from conductivity and from mobility given

[8] H. M. J. Smith, Trans. Roy. Soc. (London) **241**, 105 (1948–1949).

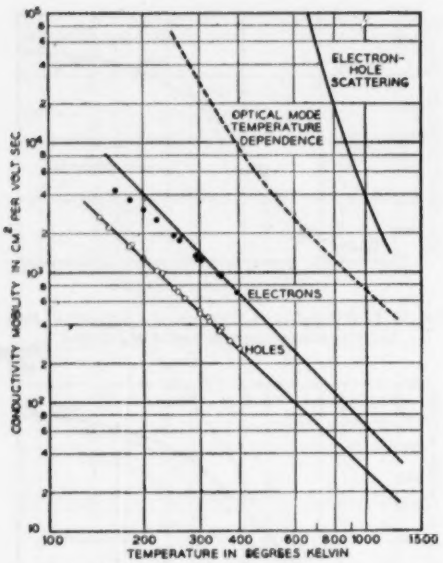

FIG. 12. Conductivity mobility as a function of absolute temperature.

by Eqs. (1) and (2). The method of computation used in the region of mixed intrinsic and extrinsic conductivity has been described in reference 4, Sec. 4.2. Results are shown in Fig. 13 as plotted points. From these the following empirical expression has been derived:

$$np = 1.5\times10^{33}T^3\exp(-1.21/Tk), \qquad (3)$$

which fits the measured points below 700°K. Above this temperature the width of the forbidden region

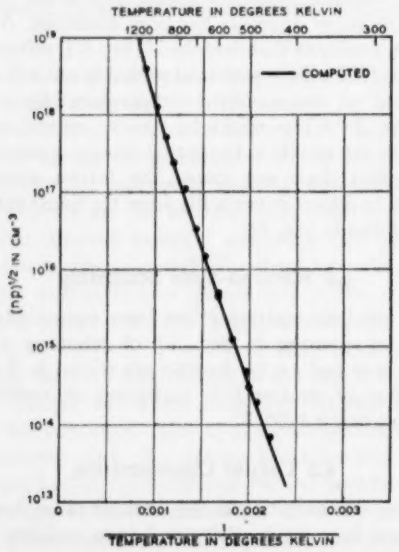

FIG. 13. Carrier concentration in the intrinsic range of silicon as a function of reciprocal absolute temperature.

depends appreciably upon the electrostatic interaction of charge carriers. The effect of this dependence on np has been determined as described in reference 4, Sec. 5.2, using the relation

$$\Delta E_G = -7.1\times10^{-10}(np)^{\frac{1}{4}}T^{-\frac{1}{2}}. \qquad (4)$$

From Eqs. (3) and (4) the solid line shown in Fig. 13 has been computed. The value of $(np)^{\frac{1}{2}}$ at 1000°K computed from Eqs. (3) and (4) is 13 percent greater than $(np)^{\frac{1}{2}}$ computed from Eq. (3) alone.

From lattice scattering conductivity mobility of Fig. 12 and $(np)^{\frac{1}{2}}$ from Eq. (3), intrinsic resistivity of silicon is found to be 2.3×10^5 ohm cm at 300°K.

4.4 Temperature Dependence of E_G

The theoretical formula for carrier concentration in the intrinsic range, Eq. (16), reference 4, has the same form as empirical equation (3) but the numerical factor in (3) is larger than the theoretical value by a factor

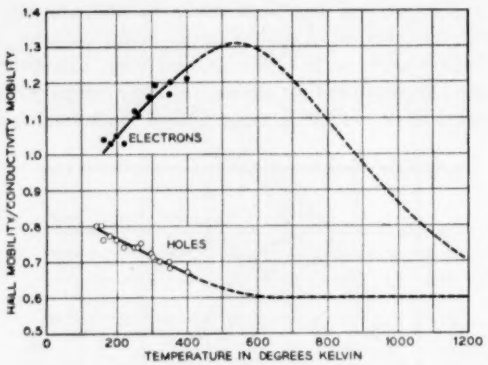

FIG. 14. Hall mobility/conductivity mobility as a function of absolute temperature for electrons and holes in silicon.

of 63. Assuming $m_n = m_p = m$, and taking the discrepancy in the numerical factor to be due to a linear variation of E_G with temperature, leads to a temperature coefficient for E_G of 3.6×10^{-4} ev/degree. $E_G(T=0)$ found in section 4.3 is 1.21 ev. These values are somewhat higher than the corresponding 3.0×10^{-4} ev/degree and 1.12 ev found by Pearson and Bardeen,[1] who assumed the temperature dependence of mobility to be $T^{-1.5}$.

4.5 Hall Coefficient and μ_H/μ_e

Hall coefficient is given by Eq. (15), reference 4. All of the parameters in that equation have been determined except μ_{Hn}/μ_{cn} and μ_{Hp}/μ_{ep}. In this section a possible temperature dependence for these two parameters is discussed.

μ_H/μ_e for electrons and holes has been computed from measured μ_H and μ_e for samples 130, 131, 127, and 159 and is shown as plotted points in Fig. 14. It was

assumed that the μ_{Hp}/μ_{ep} temperature dependence is given by the dotted line for holes in Fig. 14. With this extrapolation and the carrier concentration and mobility results of the preceding sections, the Hall coefficient relation was used to compute μ_{Hn}/μ_{en}. This result is shown by the dotted line for electrons in Fig. 14. According to Herring these results are what one would expect if the conduction band were composed of multiple surfaces of minimum energy, and the valence band of some structure other than a spherical energy surface. However, on this basis, μ_{Hp}/μ_{ep} is lower than the expected $\mu_H/\mu_e>1$. A similar result was found at one time for electrons in germanium.[9] This discrepancy disappeared as improved germanium crystals were made. Presumably this same effect may be lowering the μ_H/μ_e values found for both electrons and holes in silicon.[10] It is assumed that, with improvement of the material, μ_{Hp}/μ_{ep} will approach $\sim$1, then the peak value for μ_{Hn}/μ_{en} increasing proportionally may approach $\sim$2.2. This is reasonable in the light of the germanium results[6] where the highest value measured was $\mu_{Hp}/\mu_{ep}\sim$1.8.

ACKNOWLEDGMENT

The authors wish to thank C. Herring for his considerable assistance in interpreting the data.

[9] W. Shockley, *Electrons and Holes in Semiconductors* (D. Van Nostrand Company, Inc., New York, 1950), first edition, p. 338.

[10] *Note added in proof.*—See the more recent Hall mobility results of P. P. Debye and T. Kohane, Phys. Rev. **94**, 724 (1954).

PHYSICAL REVIEW VOLUME 96, NUMBER 1 OCTOBER 1, 1954

Secondary Electron Yield from Al by High-Energy Primary Electrons*

G. W. TAUTFEST AND H. R. FECHTER†
W. W. Hansen Laboratories of Physics, Stanford University, Stanford, California
(Received June 3, 1954)

The yield of secondary electrons from thin (1.71 mg/cm²) aluminum foils by high-energy primary electrons is reported. The value is 0.0397±0.0003 secondary electron per primary electron from both sides of the foil. The result is independent of the primary-electron energy in the range 111–235 Mev.

IN connection with the development of a nonsaturable monitor[1] for electron beams, we have measured the yield of secondary electrons from thin (1.71 mg/cm²) aluminum foils under bombardment by 150-Mev electrons. A general diagram of the experimental arrangement is shown in Fig. 1.

A monoenergetic beam of electrons from the Stanford Mark III linear accelerator is stripped to $\frac{1}{16}$-inch diameter by a uranium collimator, and, after passing through the double-deflection system[2] of the linear accelerator at the 130-ft station, is brought to a focus on a set of twenty aluminum foils, each 2½ inches by 4 inches in size and 0.00025 inch thick. Alternate foils are connected together and mounted in a vacuum (10^{-6} mm Hg) on polystyrene insulators. One set of foils is biased to a negative potential of 1 kv with respect to the second set which is connected via a vacuum feed-through to a grounded condenser. After passing through the foils, the beam is collected in a lead Faraday-cup integrator. The ratio of the charge integrated on the condenser to the charge collected in the Faraday cup when averaged over the ten foils gives directly the number of secondary electrons liberated from both sides of the foil by a primary electron. The ratio we obtain is 0.0397±0.0003 secondary electron per primary electron, which is in qualitative agreement with low-energy experimental data.[3] No theory of secondary-electron yields at these energies exists.

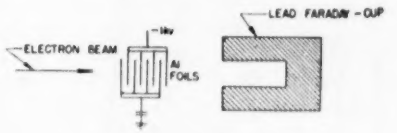

FIG. 1.

Since the theoretical energy distribution of secondary electrons with kinetic energy $W>2$ kev varies as $1/W^2$, the high-energy secondaries which are not collected in our arrangement give negligible correction to the above ratio. The ratio was found to be independent of the bias voltage from 300 volts to 2 kv and to be independent of the primary-electron energy in the range 111–235 Mev.

* The research reported in this document was supported jointly by the U. S. Office of Naval Research and the U. S. Atomic Energy Commission.

† Now at the Stanford Research Institute, Stanford, California.

[1] G. W. Tautfest and H. R. Fechter, Rev. Sci. Instr. (to be published).

[2] W. K. H. Panofsky and J. A. McIntyre, Rev. Sci. Instr. **25**, 287 (1954).

[3] Shatas, Marshall, and Pomerantz, Phys. Rev. **94**, 757 (1954).

Paramagnetic Resonance in Uranium Salts*

S. N. Ghosh,† Walter Gordy, and D. G. Hill‡
Department of Physics, Duke University, Durham, North Carolina
(Received November 5, 1953; revised manuscript received July 2, 1954)

Paramagnetic resonance has been observed in U^{+3} and U^{+4} ions in powdered samples of UF_3 and UF_4, respectively. The resonance curve in UF_3 was found to be asymmetric, with two unresolved peaks yielding $g_\perp \approx 2.1$ and $g_\parallel \approx 2.8$. The resonance is broad and weak; the over-all half-width is about 5 kilogauss at room temperature. The curve obtained for UF_4 is symmetric and yields $g = 2.1_5$. Its half-width is about 3.5 kilogauss at room temperature. Although the resonance in UF_3 appeared somewhat stronger at liquid air than at room temperature, that in UF_4 could be detected only at room and at elevated temperatures. The results favor the interpretation that the two unpaired electrons in U^{+4} are $6d$ electrons, that the crystalline field in UF_4 is essentially cubic, and that either the lowest component of the Stark multiplet is a nonmagnetic singlet or that the electrons have a high degree of antiferromagnetic alignment. The results on UF_3 show that the crystalline field has an axially symmetric component.

THE magnetic properties of the uranium compounds are of special interest because of the light they throw on the electronic structure of the uranium atom and its ionized forms. Numerous measurements have been made on the magnetic susceptibilities of the uranium salts.[1] Supplementary information from paramagnetic resonances is obviously desirable, but previous attempts to observe such resonances in a large number of uranium salts have met with failure.

We have been able to detect paramagnetic resonance at microwave frequencies in both UF_3 and UF_4 at room temperature, but only in UF_3 at the temperature of liquid air. Both resonances were abnormally weak and broad. The reported detection[2] of resonance in UF_4 at liquid air temperature proved to be erroneous. The spurious signal was caused by the increased instability of the balanced wave-guide bridge when the cell was cooled by liquid air. With the more stable spectrometer employed in the later work, the resonance in UF_4 could be detected at room or at elevated temperatures, but not at the temperature of liquid air. That in UF_3 appeared to be slightly stronger at liquid air than at room temperature, as mentioned in the preliminary report. Attempts made to detect paramagnetic resonance in UCl_4 at 90°K and at 300°K were unsuccessful. The spectrometer employed was the balanced microwave bridge type described by Lancaster and Gordy.[3] All measurements were made at frequencies near 30 kMc/sec on samples in powder form. The results are summarized in Table I. The samples, which were obtained from the Oak Ridge National Laboratory, had an estimated purity better than 99 percent.

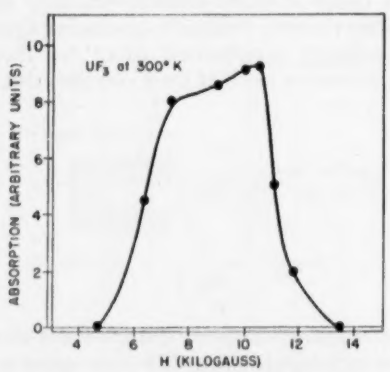

FIG. 1. Paramagnetic resonance in UF_3 powder at 30 kMc/sec and room temperature.

UF_3

Figure 1 shows the resonance curve obtained for UF_3 powder at room temperature. The curve is noticeably asymmetric, with its highest peak on the high field side. A plausible interpretation of the asymmetric shape is that the internal field around the U^{+3} ion has a cylindrically symmetric component which resolves the g factor into distinguishable components parallel ($g_\parallel$) and perpendicular ($g_\perp$) to the axis of the field symmetry. In a powder where all orientations of the polycrystalline axes are equally probable, the $g_\perp$ has for geometric reasons the greater weight. From the stronger peak we tentatively assign $g_\perp = 2.1$–2.2, and from the position of the shoulder on the low-field side $g_\parallel = 2.8$–2.9, approximately.

At the temperature of liquid air the strength of the absorption in UF_3 appeared to be greater than at room

TABLE I. Summary of results.

Substance	Ion	g factor	Half-width kilogauss
UF_3	U^{+3}	$g_{Av}=2.4$ $\begin{cases} g_\perp = 2.1-2.2 \\ g_\parallel = 2.8-2.9 \end{cases}$	5.0 (unsymmetrical)
UF_4	U^{+4}	2.1_5	3.5 (symmetrical)
UCl_4	U^{+4}	Resonance not observed	

* This research was supported by the U. S. Air Force under a contract monitored by the Office of Scientific Research, Air Research and Development Command.
† Now at the Air Force Cambridge Research Center.
‡ Department of Chemistry, Duke University, Durham, North Carolina.
[1] J. K. Dawson, Nucleonics **10**, 39 (1952).
[2] Ghosh, Gordy, and Hill, Phys. Rev. **87**, 229 (1952).
[3] F. Lancaster and W. Gordy, J. Chem. Phys. **19**, 1181 (1951).

temperature, but the amount of increase could not be quantitatively measured. Although the curve shows the same tendency for doubling at the lower temperature, the peak on the high-field side appears to be stronger relative to that on the low-field side (see Fig. 2). The average g factor obtained for the lower temperature is slightly higher than that for room temperature, but this may be a spurious effect resulting from the change in shape of the curve upon cooling. From such broad and asymmetric curves it is obviously not possible to obtain anything but approximate g values.

The U^{+3} ion has three unpaired electrons. The orbitals which they occupy are uncertain. Dawson[1] has reviewed the evidence from magnetic susceptibilities for uranium and related elements, and he concludes that the $5f$ and $6d$ shells are very close in U^{+3}. It is possible that the ground state represents an admixture of these states. The present results are not sufficient to resolve

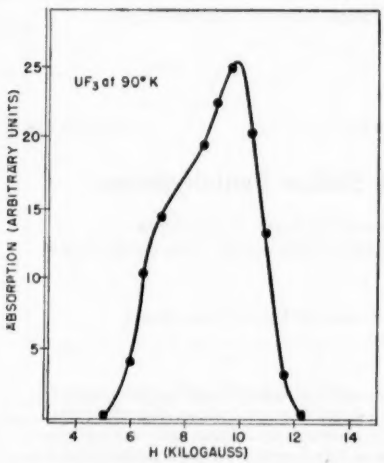

FIG. 2. Paramagnetic resonance in UF_3 powder at 30 kMc/sec and liquid air temperature.

the question of the ground state. They do show that the unpaired electrons are not in orbitals which are effectively shielded from the crystalline field effects. Considerable internal Stark interaction is evident. Evidently, the orbital motions are not completely quenched by the internal field since the observed g factor is different from the free spin value of 2.

Even if there were no spin-orbit decoupling, the internal field could resolve the g factor into distinguishable $g_\perp$ and $g_\parallel$ components. In the latter case, the vector $\mathbf{J}=\mathbf{L}+\mathbf{S}$ is resolved into components J_z along the axis of symmetry z of the crystalline field as in certain of the rare earth salts.[4] The observed transitions then occur between certain of the J_z levels which happen to be populated at room temperature and which are degenerate, or nearly degenerate, in the absence of

[4] R. J. Elliott and K. W. H. Stevens, Proc. Phys. Soc. (London) **A64**, 205 (1951).

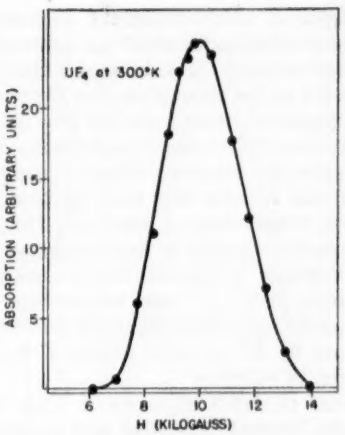

FIG. 3. Paramagnetic resonance in UF_4 powder at 30 kMc/sec and room temperature.

an external field. Also the selection rules must allow transitions between the particular levels considered, which in general means that $J_z=J_z'\pm1$.

It is possible that the resonances which we observed in UF_3 arise from two sets of electronic levels which are sufficiently close for both to be populated significantly at room temperature. This might explain the variation in the shape of the resonance curves upon cooling. Measurements on single crystals of UF_3 at different orientations are highly desirable, but we have not been able to obtain such crystals.

UF_4

The curve observed for UF_4 is symmetric (see Fig. 3) and yields a g value of 2.1_5. The resonance was easily observed at temperatures of 300, 420, and 450°K, but it could not be detected at the temperature of liquid air. Unsuccessful attempts were made to detect resonance in UCl_4 at room temperature.

In the U^{+4} ions there are only 2 unpaired electrons. According to the Seaborg,[5] representation of the ground state of the uranium atom $5f^36d7s^2$, the unpaired electrons would be expected to reside in the $5f$ orbitals. From a consideration of the available magnetic susceptibility data, Dawson[1] has concluded, however, that they are probably $6d$ electrons. The present paramagnetic resonance results tend to confirm Dawson's conclusions. The observed g factor is essentially isotropic and near the free spin value of 2. This suggests that the orbital motions are effectively quenched by an internal field of cubic symmetry.

The fact that the resonance in UF_4 could not be observed at liquid air temperature, together with the fact that it is not as strong at room temperature as would be expected from its width, suggests either that the resonance arises from electrons which are not in the lowest level of the Stark multiplet or that there is

[5] G. T. Seaborg, Nucleonics **5**, 16 (1949).

a high degree of antiferromagnetic alignment. In a private communication Herzfeld[6] has informed us that magnetic susceptibility data obtained by him can best be interpreted on the assumption that the lowest state in UF_4 is single and hence could not give rise to paramagnetic resonance. Our results might be interpreted on the assumption that the lowest state is a "nonmagnetic" singlet and that it is the only state significantly populated at the temperature of liquid air. The weakness of the resonance observed at room temperature would then be attributed to the relatively low population of the "magnetic state" at room temperature. The observed magnetic state would lie above the nonmagnetic ground state by kT or more (where T is the room temperature, $kT \approx 200$ cm^{-1}).

Our failure to detect resonance in UCl_4 may be a result of the internal crystalline field splittings. This does not mean that the crystalline field splitting in UCl_4 would necessarily be larger than that in UF_4 and hence, that the magnetic state would be less populated. The failure to detect resonance in UCl_4 could be caused by too short a relaxation time (line too broad to detect), which might result from a closer spacing of the Stark multiplet.

The most likely cause of the weakness of paramagnetic resonance in UF_3 and UF_4 and the failure to detect resonance in other uranium salts is strong exchange interaction which could cause significant antiferromagnetic alignment of the electron spins. Many of the uranium salts, including the ones investigated here, have been found to have relatively large Weiss constants.[1] Paramagnetic resonance studies on magnetically diluted salts are needed, and are being planned.

Dr. E. E. Schneider, at our request, has checked the existence of paramagnetic resonance in both UF_3 and UF_4 at room temperature. He used a method of detection which depends on magnetic modulation. We wish to thank him for this assistance.

[6] We are indebted to Dr. C. M. Herzfeld for communicating his results to us before publication.

PHYSICAL REVIEW VOLUME 96, NUMBER 1 OCTOBER 1, 1954

Paramagnetic Resonance in Chromous Sulfate Pentahydrates

KAZUO ONO, *Institute of Science and Technology, University of Tokyo, Tokyo, Japan*
SHOICHIRO KOIDE AND HISAO SEKIYAMA, *College of General Education, University of Tokyo, Tokyo, Japan*
AND
HIDETARO ABE, *Institute of Science and Technology, University of Tokyo, Tokyo, Japan*

(Received April 30, 1954)

Paramagnetic resonance absorption in single crystals of chromous sulfate pentahydrate has been observed at room temperature and at wavelengths of 11 mm, 6.5 mm, and 5.4 mm. The result shows that this crystal has a structure similar to that of copper sulfate pentahydrate. The observed data have been analyzed by the so-called spin Hamiltonian, and the parameters determined have been found to be quite consistent with the values of the spin-orbit coupling constant and the spin-spin interaction constant obtained from spectroscopic data.

PARAMAGNETIC resonance absorption in single crystals of chromous sulfate pentahydrate has been investigated at room temperature and at wavelengths of $\lambda = 11$ mm, 6.5 mm, and 5.4 mm. Few measurements have heretofore been made of the magnetic properties of the Cr^{++} ion, because the Cr^{++} ion, especially in aqueous solution, has a strong tendency to oxidize. The specimens were, therefore, prepared in an evacuated vessel. Large crystals were obtained, which were blue and transparent. This crystal is triclinic and each unit cell seems to contain two unequivalent ions.

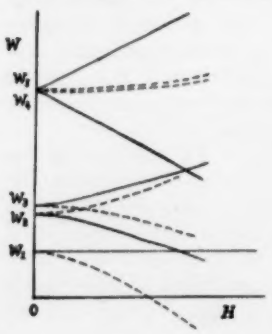

FIG. 1. Relative positions of the lowest energy levels of the Cr^{++} ion in $CrSO_4 \cdot 5H_2O$. The full lines are those for $\mathbf{H} \| z$ axis and the dashed lines for $\mathbf{H} \| y$ axis.

The ground state of the free Cr^{++} ion is $3d^4\ {}^5D$. The fivefold orbital degeneracy is split by the cubic component of the crystalline field into a lower doublet Γ_3 and an upper triplet Γ_5, both of them being split into singlets by the additional rhombic component. These circumstances are the same as in the case of the $3d^9\ {}^2D$ ion (Cu^{++}). The fine structure Hamiltonian for the lowest spin quintuplet becomes

$$\mathcal{H} = D(S_z^2 - \tfrac{1}{3}S(S+1)) + E(S_x^2 - S_y^2) + \beta(g_x H_x S_x + g_y H_y S_y + g_z H_z S_z), \quad (1)$$

where D and E are constant parameters, β the Bohr

magneton, g the g factor, and $\mathbf{H}$ is the applied magnetic field. Since D is comparable to $g\beta H$ in this case, the spacings of the spin quintuplet vary with H in a complicated way as shown in Fig. 1. The transition $W_2 \leftrightarrow W_1$ can be observed when $\mathbf{H}$ is parallel to the z axis and that between $W_2 \leftrightarrow W_3$ when $\mathbf{H}$ is applied in the xy plane. The transition $W_2 \leftrightarrow W_3$ is energetically possible in the case of $\mathbf{H} \| z$, but is forbidden by selection rules. Examples of the angular dependence of the resonance field are shown in Fig. 2 and Fig. 3. In Fig. 2, the magnetic field is in the yz plane with $\lambda = 5.4$ mm, and in Fig. 3, $\mathbf{H}$ lies in the $z_1 z_2$ plane (the subscripts 1 and 2 indicate the two dissimilar ions, respectively) with $\lambda = 6.5$ mm. In these figures, dashed lines are used to indicate that the resonance absorption is small. We can see in Fig. 3 that the angle α between the two z axes is 86°. This angle is just the same as that obtained by one of the present authors[1] for copper sulfate.

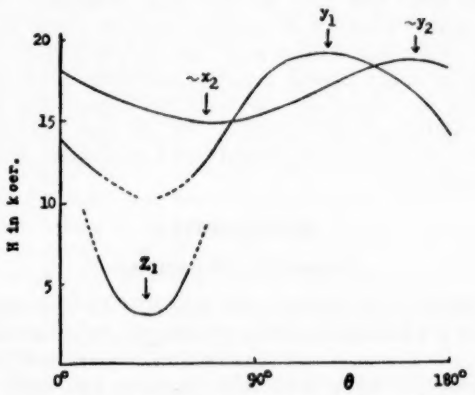

FIG. 2. The angular dependence of the resonance field in the $z_1 - y_1$ plane with $\lambda = 5.4$ mm. x_1, y_1, z_1 and x_2, y_2, z_2 indicate the rhombic axes of the crystalline fields corresponding to the two kinds of ions, respectively.

Using some appropriate approximations, it can be shown that

$$
\begin{aligned}
D &= -3(l^2 - m^2)\left(\frac{\lambda^2}{\Delta E} + \rho\right), \\
E &= -2\sqrt{3} lm \left(\frac{\lambda^2}{\Delta E} + \rho\right), \\
g_x &= 2 - 2(l - \sqrt{3}m)^2 \lambda / \Delta E, \\
g_y &= 2 - 2(l + \sqrt{3}m)^2 \lambda / \Delta E, \\
g_z &= 2 - 8l^2 \lambda / \Delta E,
\end{aligned}
\tag{2}
$$

where λ is the spin-orbit coupling coefficient, ρ is the spin-spin coupling constant between $3d$ electrons, ΔE is the spacing between Γ_3 and Γ_5, and l and m satisfy the relations

$$
2lm / [\sqrt{3}(l^2 - m^2)] = E/D, \quad l^2 + m^2 = 1. \tag{3}
$$

[1] K. Ono (unpublished work).

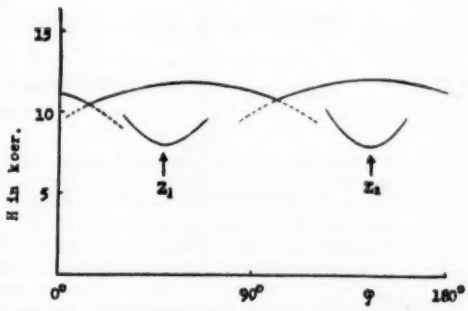

FIG. 3. Angular dependence of the resonance field in the $z_1 - z_2$ plane with $\lambda = 6.5$ mm.

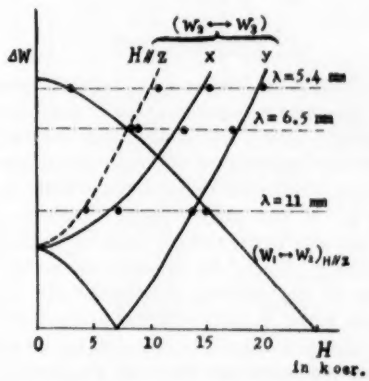

FIG. 4. ΔW as a function of H. The full lines indicate the theoretical values and the circles the experimental ones.

The best agreement of the experimental resonance frequencies with the calculated ones is obtained by taking $|D| = 2.24$ cm^{-1} and $|E| = 0.10$ cm^{-1} for both dissimilar ions. Since the g's are considered to be very close to 2 on account of the smallness of the spin orbit coupling constant compared to ΔE, the above calculation was tentatively made by assuming $g_x \fallingdotseq g_y \fallingdotseq g_z \fallingdotseq 2$. Spectroscopic data indicated $\lambda = 58$ cm^{-1} and $\rho = 0.42$ cm^{-1} for the free Cr^{++} ion.[2,3] These values are quite consistent with the values of $|D|$ and $|E|$ determined above, if we assume $\Delta E = 10\,000$ cm^{-1}. In the above formula we have two alternative cases, i.e., $l \simeq 1$, $m \simeq 0$ and $m \simeq 1$, $l \simeq 0$. Since copper sulfate corresponds to the former, it is reasonable to assume that for chromous sulfate it is also the case. Then we obtain $g_x \fallingdotseq g_y = 1.99$ and $g_z = 1.95$, and these values improve the agreement between the calculated and the observed ΔW (see Fig. 4). We have made preliminary measurements of the anisotropy of the static susceptibility of this crystal. The results are consistent with the anisotropy espected from the above values of D and the g's.

The authors' thanks are due to Professor H. Kumagai for his continuous encouragement.

[2] O. Laporte, Z. Physik **47**, 761 (1928).
[3] M. H. L. Pryce, Phys. Rev. **80**, 1107 (1950).

Properties of Zinc-, Copper-, and Platinum-Doped Germanium*

W. C. DUNLAP, JR.
General Electric Research Laboratory, Schenectady, New York
(Received June 28, 1954)

Hall effect and resistivity measurements have been made on a number of samples of single-crystal germanium containing additions of zinc, platinum, and copper. All three were found to be acceptors with energy of ionization 0.029, 0.040, and 0.036-ev electron volt, respectively. Measurements were made in the temperature range 15°K to about 400°K. All the Hall and resistivity curves showed a tendency to flatten out at the lowest temperatures, rather than to continue on an exponential curve. Possible explanations include (a) surface conductivity with low activation energy, (b) traces of low-ionization energy acceptors, (c) internal leakage due to imperfections or dislocations. Studies were made looking for acceptor states in the upper part of the forbidden band, such as have been found for gold. Evidence was found for a platinum acceptor level 0.2 ev below the conduction band and for a copper acceptor level just below the middle of the forbidden band.

INTRODUCTION

A NUMBER of studies have recently been made of acceptors in germanium not in the third column of the periodic table. First of these was zinc,[1] which was found, by low-temperature resistivity measurements, to be an electron acceptor in germanium with an ionization energy of the carrier equal to about 0.03 ev. Copper has also been studied, both by doping of the crystal during growth,[2] by diffusion methods,[3] and by the study of heat-treated specimens.[4] An ionization energy was found in the vicinity of about 0.04 ev. The equality of values found for heat-treated as compared to diffused specimens has been one important piece of evidence for the theory that traces of copper account for all the main heat-treatment phenomena of germanium.

In the present work, a new low-temperature cryostat for the measurement of Hall coefficient and resistivity of semiconductor specimens was designed and built. The first work carried out with this new equipment was done on zinc-doped specimens. It was considered desirable to extend the previous resistivity measurements to determine the ionization energy from Hall measurements. Following this study, Hall measurements were made to study heat-treated samples and thus to extend the previous resistivity measurements of DeSorbo and Dunlap. Studies have also been made with platinum-doped germanium. Unlike the other agents studied, this is apparently the first work done with platinum. Besides determination of the acceptor action and the ionization energy of platinum, estimates were made of the segregation coefficient ($\sim 10^{-6}$), and the solubility ($\sim 10^{14}$ atoms/cm^3) of platinum in germanium as determined from the properties of the grown crystals.

Of particular interest in the study of new doping agents in germanium is the possibility of second states of the impurity center. Such states were first found with gold,[5] and more recently Tyler, Woodbury, and Newman[6] have found evidence for such states with iron and cobalt. Burton *et al.*[7] have also indicated that copper might possess a second ionization level just below the middle of the forbidden region. The investigation of this possibility for the three elements zinc, copper, and platinum formed a chief object of the present study.

EXPERIMENTAL

Preparation of Samples

Single crystals were grown especially for this work, with a Czochralski furnace of essentially conventional design. The melt was contained in a quartz crucible surrounded by a ½-in. thick graphite liner used to improve axial thermal symmetry. The furnace consisted of a quartz jar containing a viewing window, and surrounded by a nichrome furnace winding. The heating current was controlled manually by a Variac autotransformer. Crystals were generally grown from (111) seeds, held in a stainless steel chuck. The pulling head provided independent lifting and rotating motions. The rotation speeds were, generally, 3–4 revolution/sec, the pulling speed generally 1–2 in. per hour. Forming gas (nitrogen +10 percent hydrogen) was used as the atmosphere.

Addition of the desired impurity was made by insertion of a small funnel into the top of the furnace. The metallic impurity was then added in the form of one or two weighed pellets. The seed was withdrawn during this process and the melt allowed to stand a few minutes so that uniform distribution of the impurity might more easily take place.

In many of the melts, the original crystals contained appreciable quantities of arsenic or antimony impurities.

* Presented in preliminary form at the Michigan meeting of the American Physical Society, March, 1954 [Phys. Rev. 94, 1419 (1954)].

[1] W. C. Dunlap, Jr., Phys. Rev. 85, 945 (1952).

[2] F. J. Morin and J. P. Maita, Phys. Rev. 90, 337 (1953).

[3] Fuller, Theurer, and Van Roosbroeck, Phys. Rev. 85, 678 (1952).

[4] W. DeSorbo and W. C. Dunlap, Jr., Phys. Rev. 83, 869, 879 (1951).

[5] W. C. Dunlap, Jr., Phys. Rev. 91, 1282 (1953).

[6] Tyler, Woodbury, and Newman, Phys. Rev. 94, 1419 (1954).

[7] Burton, Hull, Morin, and Severiens, J. Phys. Chem. 57, 853 (1953).

In others, the original crystal was nearly intrinsic in resistivity. All samples designed to show the direct effect of the impurities contained negligible quantities of other impurities.

The samples used were rectangular plates, sawed out of the ingots in planes normal to the axis of growth. The six connections for measurement were made by soldering techniques, in most cases. Indium was found to be a satisfactory solder for low-temperature work with *p*-type specimens, while arsenic-doped indium was used for soldering contacts to *n*-type specimens.

Measurement Methods

The methods of measurement were quite conventional. The cryostat involved a few new features and is shown in Fig. 1. The metal Dewar contained an inner can of stainless steel from which hung a 9-in. copper bar, $\frac{3}{4}$ in. in diameter. The inner can also contained carbon black, which, when pumped on, aided cooling by the energy of desorption. The sample was cemented inside this copper bar, the leads and thermocouple passing up through the center of the copper bar and through a stainless steel tube extending up through the inner can and out the top of the Dewar. A heater coil was wound around the copper bar between the sample and the inner can, which could be filled either with liquid helium or hydrogen. With hydrogen in the can, the temperature of the sample could be easily controlled between 15°K and 65°K, and temperatures above this range caused no problem. Two liters of liquid hydrogen were sufficient to cool the system from 77°K, and to maintain it at 20°K for 6–8 hours.

The copper bar was surrounded by a radiation shield at 78°K and an outer brass case, total diameter about $1\frac{3}{4}$ in., although the thickness of the main part of the Dewar was about 10 in. The sample thus could be mounted in a permanent magnet with a field of 1500 gauss. Rotation of the magnet served to reverse the magnetic field.

Temperature was measured by means of copper-constantan thermocouples, calibrated against the Ohio State gas thermometer. Thermocouples were indium-soldered to the samples. The thermal emf's were measured with a Type B Rubicon potentiometer. Thermal emf's in the potentiometer and associated circuit often caused errors, at 20°K, of a few microvolts. Consequently, a calibration was usually made at 20°K with the sample maintained at liquid hydrogen temperature. It was assumed that the extraneous few microvolts would remain constant during a run. The few times this was checked by repeat calibrations this was found to be so. It is estimated that temperatures measured are accurate to about 0.2°C in the worst part of the range, between 15 and 20°K.

The samples themselves were used as the measure of the constancy of temperature for each measurement. To obtain a given temperature, it will be remembered

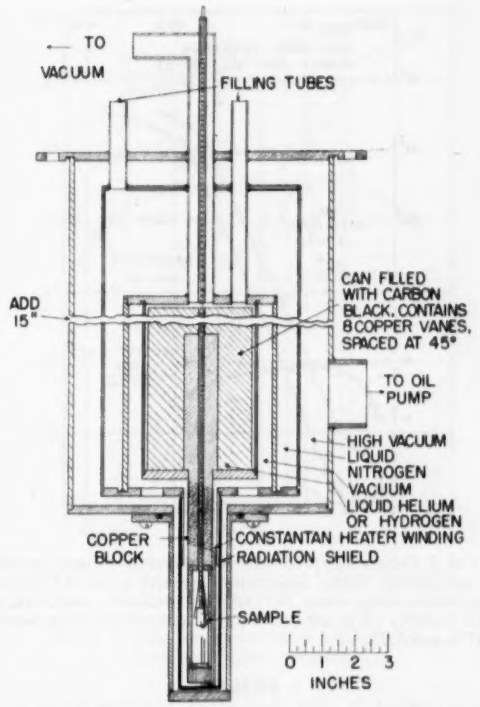

FIG. 1. Diagram of cryostat and sample connections.

from the above, the flow of heat into the hydrogen can was compensated by the heater between the sample and the can. The heating current was adjusted until the potential drop across the sample was constant during the time needed for Hall and resistivity measurements. This was often not easy because of the extreme sensitivity of some of the samples to temperature variation in the temperature range 15–78°K. In most cases, the temperature had to be held constant to less than 0.01°K during the time of measurement.

Purity of the Doping Agents

In experiments such as the present ones, purity of the doping agents can be a critical problem. This is particularly true of elements with a very small segregation coefficient—defined as the ratio of the concentration of the element in the solid to that in the liquid. If the element should be contaminated with a very small percentage of an element, such as arsenic, with a much larger segregation coefficient (about 0.1 for As), the results can be completely erroneous. The best check on this problem is to obtain the purest possible materials, with 99.99-percent purity a minimum, and to make many repetitions of the growth of crystals with material from several sources.

All the impurity agents used in the present work were 99.99 percent or better in purity, and consistent results were obtained.

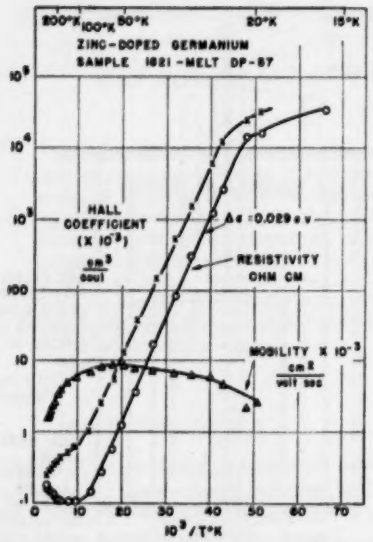

FIG. 2. Conduction properties of a p-type zinc-doped specimen of germanium. Room temperature resistivity was 0.2 ohm cm, the carrier density about 10^{18} cm^3. Hall coefficient, resistivity, and Hall mobility (R/ρ) are shown in the temperature range between 300°K and 15°K.

RESULTS

Zinc

Figure 2 shows typical results on zinc. Hall coefficient, resistivity, and mobility are all plotted on the same chart. The ionization energy found from the relation

$$n \sim 1/R \sim n_0 \exp(-\Delta E/kT),$$

was about 0.029 ev. This is to be compared with the value 0.031 previously found by the author from resistivity measurements on other samples. The agreement is quite satisfactory.

The room temperature resistivity of this particular sample was about 0.2 ohm cm. Other samples have been made with resistivities as low as 0.05 ohm cm. No direct information on solubility of zinc in germanium has been sought. The above facts indicate, since samples of less than 0.05 ohm cm have not been found even in heavily doped melts, that the solubility is about 10^{17} atoms/cm^3.

Likewise, good values of segregation coefficient have been somewhat difficult to obtain, primarily because of the high vapor pressure of zinc at the melting point of germanium, 940°C. Burton has estimated 0.01 for the segregation coefficient, and our results are not inconsistent with this figure.

The Hall coefficient and resistivity tend to flatten out at temperatures below 40°K. This is a phenomenon that has been observed with many widely different samples of germanium and other semiconductors. The nature of the effect is not clear and may arise from a number of possible sources, such as traces of ordinary acceptors such as indium or boron, surface conductivity, a conductivity associated with dislocations, or other effects. Because the effective number of centers required to produce these effects is so small relative to the 0.03-zinc state, they do not appear to be related to any state of the zinc atoms.

The mobility of zinc-doped specimens tends to be somewhat less than that for most p-type specimens of comparable resistivity. In the present case, the Hall mobility at 25°C was 1506 cm^2/volt sec, whereas indium-doped specimens of the same resistivity are usually in the range 2400–2600 cm^2/volt sec.

No evidence has been found that zinc produces any acceptor levels in the upper half of the forbidden band, such as are found for gold. The methods of investigating this point are discussed more fully in the section on platinum.

Platinum

The purity of the platinum used is a critical part of the study, since the segregation coefficient is about 5×10^{-6}. Platinum of claimed 99.999-percent purity obtained from Sigmund Cohn was used. Because of the large segregation, amounts of the order 25–50 mg were added to melts of the order 100 g weight. In all tests made using this and other platinum samples, evidence for acceptor action was found. Twenty platinum-doped melts were made.

Figure 3 shows the low-temperature Hall and resistivity data for a sample of platinum-doped material made by adding 41-mg platinum during growth of an ingot with 75-g germanium. The resistivity before the platinum was added was 40 ohm cm n type, afterwards

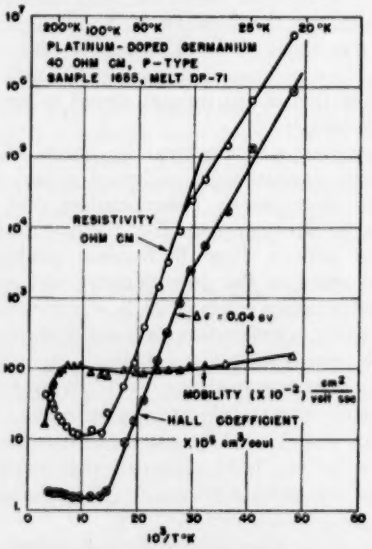

FIG. 3. Conduction properties of a platinum-doped specimen of germanium. The platinum content was about 10^{14} atoms/cm^3, the room temperature resistivity 40 ohm cm.

40 ohm cm p type. The segregation coefficient calculated from the change in electrical resistivity was 5×10^{-6}. Since the minimum resistivity (p type) found with any of the ingots prepared in these studies was about 10 ohm cm, it is presumed that the solubility is about 2×10^{14} atoms/cm^3.

The slope of the Hall coefficient curve gives an ionization energy of 0.04 ev. This is taken from the higher temperature range, since it can be seen that the curve apparently breaks into a section of smaller slope. Rather than ascribe any significance to this low-temperature portion, we shall tentatively classify it with the corresponding result in the zinc case and assume that it results from an extraneous effect.

Because of the similarity in many respects between platinum and gold, an intensive search was made for high-lying acceptor states in platinum-doped germanium. The procedure was to start with low-resistivity n-type material and add platinum in steps, about 30–40 mg each, until 150–200 mg had been added. Samples were cut from each successive section, and tested for evidence of acceptor states in the upper half of the band. Figure 4 shows results on several samples. One of these went to high resistance, with a slope indicating an ionization energy of 0.18 ev. The other, while of low resistivity, showed a "hump" in the Hall and resistivity curves that indicated an ionization energy of 0.22 ev. Thus it is concluded, contrary to the preliminary findings, that there is a second acceptor level in Pt-doped Ge, at about 0.2 ev below the conduction band. This is at the same level as for gold. It is presumed that the second level is associated with the Pt^{--} ion, although

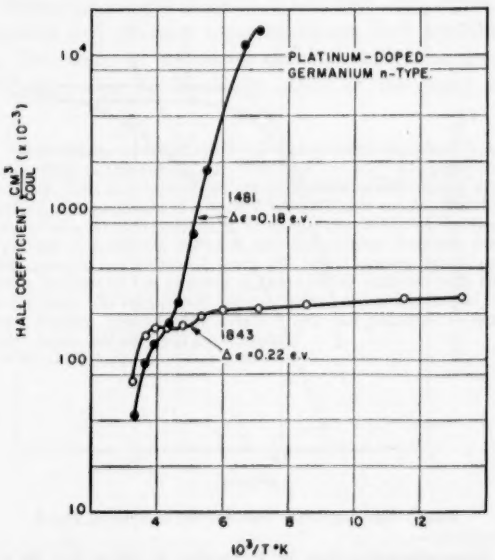

FIG. 4. Experimental results indicating high-lying acceptor levels in Pt-doped germanium. The ionization energy for the high-resistivity sample was obtained directly from the slope, while a more extended analysis was needed for the other case.

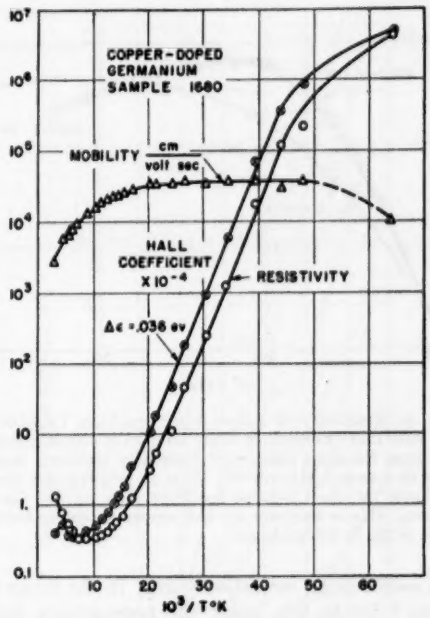

FIG. 5. Conduction properties of p-type copper-doped germanium specimen.

it is quite possibly associated with a lattice defect accompanying the Pt center.

Copper

A number of copper-doped melts were prepared, using 99.999-percent pure copper, kindly put at our disposal by Dr. D. Turnbull of this laboratory. The problem of doping with copper is complicated by the large diffusion coefficient of copper, and sectional doping, as described above, is ineffective.

Figure 5 shows the properties of one copper-doped specimen. The ionization energy from the slope of the Hall curve was about 0.036 ev.

Evidence for additional copper states was sought. Some evidence was found of an acceptor state close to the center of the forbidden region, as suggested by Burton *et al.* Figures 6 and 7 show results on several samples of germanium close to the intrinsic region. In all samples of Cu-doped Ge, the Hall and resistivity curves break down into the intrinsic line at temperatures lower than that for ordinary samples, shown in both Figs. 6 and 7 for comparison. These results are consistent with the presence of acceptor states close to the middle of the band. The number of such states, and their exact energy level, is difficult to estimate from such experiments as these.

By annealing such samples, or by doping in such a way that the Fermi level is close to the middle of the band, even at low temperature, one can see the upper copper states more directly. Results are shown in Fig. 8. The slope increases continually on annealing, until the

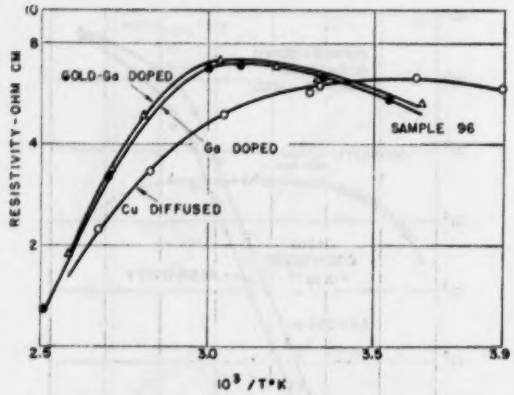

FIG. 6. Resistivity of copper-doped specimen (p type) compared with that of several ordinary samples of p-type germanium with about the same resistivity. Resistivity reaches a peak and begins to approach the intrinsic value at temperatures considerably lower for the Cu-doped specimen than for the Ga-doped specimen. This is evidence for the copper acceptors below the middle of the forbidden band.

slope indicates an ionization energy in the range 0.20–0.25 ev.† Up to this point the homogeneity has remained acceptable, as indicated by the mobility value. Further annealing led to drastic drop in mobility, evidence of p-n junctions being formed in the sample.

DISCUSSION

Ionization Energies

The hydrogen-like model[8] has been moderately successful in accounting for the ionization energies of third and fifth column impurities in germanium. To obtain agreement with experiment, it is necessary to assume that the effective mass of the carriers is in the range 0.2–0.3 of the electron mass. However, these values are consistent with effective mass values obtained by other means, such as the variation of mobility with resistivity,[9] and the cyclotron resonance effect.[10]

In the case of the elements zinc, copper, and platinum, theoretical correlation is likely to be somewhat more difficult. The closest simplification is that of the helium-like model. In this model, two valence electrons move in a field of the doubly charged impurity ion. The effect of the germanium lattice is taken account of through the reduction of all energy levels, relative to the ionization limit, by the square of the dielectric constant ($K=16$).[11]

Since the first ionization potential of helium is 24.5 ev, the ionization energy ΔE for carriers with an effective mass of 0.2 the electron mass is

$$\Delta E=(24.5/K^2)(m^*/m)=0.02 \text{ ev}.$$

This figure is in reasonable agreement with the value for zinc, but the agreement becomes progressively worse for copper and platinum. It is probable that the details of the binding between ion and lattice, and of such effects as screening, must be calculated more closely to obtain better agreement. It is doubtful, also, whether the effective mass for free carriers is exactly the same as that for bound carriers moving about an impurity atom, and the value of the effective mass may very easily depend upon the nature and strength of the binding forces. We conclude that the helium-like model is, at best, only a very crude approximation.

Diffusion Coefficients

Studies have been made upon the diffusion of zinc[12] and copper[13] into germanium, although no such work has yet been done using platinum. Although the electrical properties of zinc- and copper-doped germanium are similar in some respects, the diffusion properties are completely different. Zinc diffuses very slowly, and copper very rapidly in germanium. For Zn, D at 900°C is about 10^{-11} cm²/sec, and the activation energy for diffusion is about 2.5 ev. These values are quite comparable to those for indium, gallium, and other acceptors in germanium. Copper, on the other hand, has a diffusion coefficient of $\sim 10^{-5}$ cm²/sec

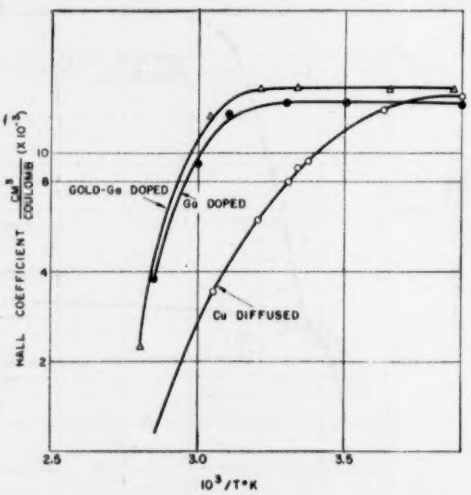

FIG. 7. Hall coefficient data for the samples of Fig. 5.

† *Note added in proof.*—A more exact determination of this level has been made by J. F. Batten and R. M. Baum [Phys. Rev. **94**, 1393 (1954)], who find $\Delta\epsilon=0.32$ ev above the valence band.

[8] First discussed by H. A. Bethe. See, for example, W. Shockley, *Electrons and Holes in Semiconductors* (D. Van Nostrand Company, Inc., New York, 1950), p. 224.

[9] P. P. Debye and E. Conwell, Phys. Rev. **93**, 693 (1954).

[10] Dresselhaus, Kip, and Kittel, Phys. Rev. **92**, 827 (1953).

[11] H. B. Briggs, Phys. Rev. **77**, 287 (1950); a new low-frequency value of 15.8 is given by W. C. Dunlap, Jr., and R. L. Watters, Phys. Rev. **92**, 1396 (1953).

[12] See reference 1. Also, W. C. Dunlap, Jr., Phys. Rev. **86**, 615 (1952); C. S. Fuller, Phys. Rev. **86**, 136 (1952); and W. C. Dunlap, Jr., Phys. Rev. **94**, 1531 (1954).

[13] Fuller, Struthers, Ditzenberger, and Wolfstirn, Phys. Rev. **93**, 1182 (1954).

at 600°C, and the apparent activation energy is 0.2 ev or less.

These discrepancies can be accounted for if it is assumed that at room temperature both zinc and copper are substitutional acceptors and that, furthermore, at higher temperatures copper leaves its substitutional sites, presumably by losing one or more electrons, and becomes interstitial. Only a relatively small fraction of the copper ions need to do this in order that one may account for the observed effects. Zinc, on the other hand, retains its electrons even at high temperatures, and remains substitutional. Here, again, the lack of better understanding of the coupling between impurity and the lattice prevents closer correlation of these ideas. A pertinent contradiction, perhaps, is that the tetrahedral radius of copper is 1.35 A, that of zinc only 1.30 A. A change in electronic state of copper is probably needed to reduce its size to the point where it can become interstitial, and evidence of Fuller *et al.*[13] does indicate that copper does diffuse as a *positive*, rather than a negative ion.

SUMMARY[14]

The present work shows that several elements besides the "3–5" elements are active in germanium. With other recent work, there are now eight or ten such active elements. Many others may be found, provided they are sufficiently soluble that electrical effects can be seen. Silver, for example, can be seen in germanium from autoradiographs, but the solubility is apparently too small for there to be a direct effect on conduction properties.[15]

From the present work it is also seen that crystal-growing and diffusion experiments are both valuable in the study of unknown elements in germanium. Diffusion may be especially useful in the study of insoluble elements, since their solubility is often much greater at 700° or 800° than at the melting point.

There remains a large field in the interpretation of such data as have been presented here. The correlation between atomic properties of the impurity, and the band structure of germanium so as to obtain the correct value of ionization energy, and diffusion coefficient has not yet been made.

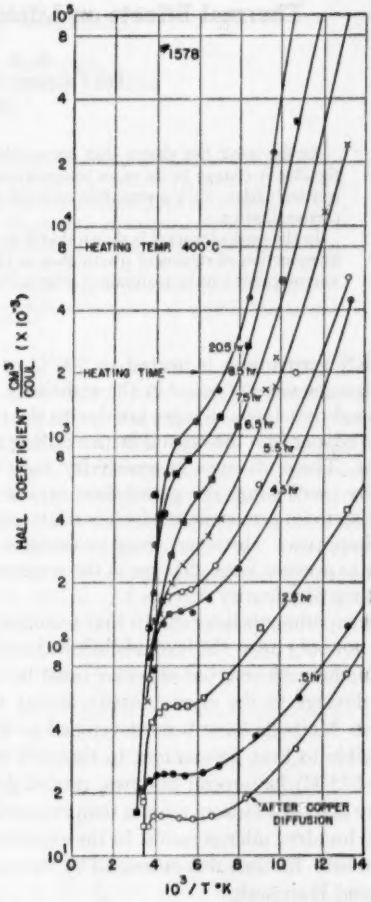

FIG. 8. Hall coefficient for an *n*-type sample that had been quenched, then annealed in stages at 400°C. The increase in slope with annealing shows the existence of high-lying acceptor states, probably at about 0.25 ev.

[14] The results obtained with all the present materials have applications to the question of "electrical forming" of germanium rectifiers. Zinc and copper are constituents of most brasses and bronzes, and platinum is a widely used whisker material, either pure, or alloyed with ruthenium. It is clear that if any of the three is present in a whisker material, and the whisker is pulsed with high currents, or "formed," there will be a tendency for *p*-type action because of the alloying of the whisker material with the germanium. The copper will have a further action because of its fast diffusion. The diffusion effect of zinc and platinum is relatively small, but may not be negligible.

[15] W. C. Dunlap, Jr. (to be published).

Thermal Effects on Lifetime of Minority Carriers in Germanium

R. A. LOGAN AND M. SCHWARTZ
Bell Telephone Laboratories, Murray Hill, New Jersey
(Received May 28, 1954)

Earlier work has shown that germanium may be heated to elevated temperatures (~875°C) without significant change in its room temperature resistivity, provided special care is taken to prevent chemical contamination. Such precautions were not sufficient, however, to prevent a drastic decrease in the minority carrier lifetime.

In the present work it is shown that if, in addition to cleanliness, special precautions are taken to avoid the introduction of strains or plastic flow in the germanium crystal, minority carrier lifetimes in excess of 100 microseconds can be maintained after such heat treatments.

WHEN germanium is heated to 500°C or higher, changes usually occur in the resistivity.[1] It has been shown[2] that these changes are due to the entrance of atomic copper into the crystal lattice during the heat treatment. These changes in resistivity may be prevented[3] by precleaning the germanium crystal surface and heating in an atmosphere which is relatively free of volatile impurities. However, these procedures are not sufficient to prevent large changes in the room temperature lifetime of minority carriers.[4]

Recent experiments have shown that to maintain high lifetime, not only must the level of chemical contamination be further reduced, but also care must be taken to prevent damage to the crystal lattice during the heat treatment. Methods have been developed so that it is now possible to heat germanium to elevated temperatures (~875°C) for several minutes, retaining original resistivity and, in addition, a room temperature lifetime of several hundred microseconds. In the experiments reported on here, lifetime was measured by the method of Haynes and Hornbeck.[5]

If electrons and holes were to recombine only by a radiative annihilation process, then the lifetime would be about one second at room temperature.[6] Observed lifetimes, being much smaller than this, indicate the presence of recombination centers. Three types of recombination centers are known: (1) chemical impurities;[7] (2) dislocations introduced into crystals by plastic deformation;[8] and (3) crystal imperfections[9] such as vacancies or interstitial atoms whose high-temperature equilibrium concentration may be "frozen in" if the crystal is rapidly quenched[4] after heating.

The following procedures were applied in the successful attempt to prevent the introduction of these three respective types of centers.

1. To remove chemical contamination, the germanium surface was cleaned by methods already described.[4] The heating was performed in a large stainless steel vacuum system with a residual pressure of about 2×10^{-5} mm Hg. Germanium specimens were heated by clamping them between chemically cleaned molybdenum electrodes and passing current through the specimen.

2. To avoid plastic deformation during heating, one electrode was made as flexible and as lightweight as possible to minimize the stress exerted on the sample. The sample was suspended in a vertical position between this electrode and a fixed upper electrode. With this heating arrangement germanium rods with cross section 0.1 in.×0.1 in. (or larger) were heated to high temperature (~875°C) for several minutes. They retained their original resistivity and had a lifetime in excess of 100 μsec. Rods of smaller cross section, e.g., 0.05 in.×0.1 in., could not be heated successfully in this way due, presumably, to the deformation caused by the small residual stress exerted by the electrodes. However, such rods could be heated on a flat horizontal molybdenum strip which was held between similar electrodes and maintained at 935°C for 10 minutes. The rods, heated in this way, retained their original room temperature lifetime ($\tau\sim150$ μsec).

3. To avoid quenching effects, the samples were cooled slowly (approximately 100°C/min). However, if the rods were rapidly cooled by shutting off the power after the heat cycle, the lifetime was lowered. For example, a rod, rapidly cooled in this way after heating on the molybdenum strip as described above, had the lifetime reduced from 150 μsec to 50 μsec.

The results presented here may be applied in the design of a heating system in which germanium may be heated to elevated temperature for extended times without impairing resistivity, and in addition, maintaining a high lifetime.

[1] H. C. Theuerer and J. H. Scaff, Trans. Am. Inst. Mining Met. Engrs. **191**, 59 (1951).
[2] C. S. Fuller and J. D. Struthers, Phys. Rev. **87**, 526 (1952); W. P. Slichter and E. D. Kolb, Phys. Rev. **87**, 527 (1952).
[3] R. A. Logan, Phys. Rev. **91**, 757 (1953).
[4] J. R. Haynes and J. A. Hornbeck, Phys. Rev. **90**, 152 (1953).
[5] Navon, Bray, and Fan, Proc. Inst. Radio Engrs. **40**, 1342 (1952); R. A. Logan, Phys. Rev. **91**, 757 (1953).
[6] W. Shockley, *Electrons and Holes in Semiconductors* (D. Van Nostrand Company, Inc., New York, 1950), Chap. 3.
[7] Burton, Hull, Morin, and Severiens, J. Phys. Chem. **57**, 853 (1953).
[8] Pearson, Read, and Morin, Phys. Rev. **93**, 666 (1954).
[9] G. L. Pearson (private communication); also, see reference 5, p. 347.

Optical Properties of Lead Telluride*

MARVIN E. LASSER AND HENRY LEVINSTEIN
Physics Department, Syracuse University, Syracuse, New York
(Received June 21, 1954)

Optical constants of lead telluride films as a function of both temperature and oxygen content have been investigated. The films were evaporated onto sapphire disks subsequently exposed to air and also on sapphire disks maintained at pressures lower than 10^{-6} mm of Hg. Film thickness, determined by Tolansky interference techniques and by weighing techniques, indicated that the density of evaporated layers of PbTe is about 10 percent smaller than for bulk. The optical constants were calculated from the reflection and transmission curves of the film. The addition of oxygen to the film was shown to give rise to an increase in absorption and a slight increase in the index of refraction. The optical properties were then shown to be strongly dependent on the temperature of the film. A mechanism has been proposed to explain the results.

I. INTRODUCTION

THIN evaporated layers of PbTe are found to be photosensitive to radiation in the near infrared. The photoconductive properties have been described by Bode and Levinstein.[1] When the film is exposed to successive traces of oxygen, the resistance increases at first, then decreases, the thermoelectric power changes sign, and the material becomes sensitive to infrared radiation. The photosensitivity is low at room temperature, but when the film is cooled to liquid air temperature, the photosensitivity is increased by many orders of magnitude. The photoeffect at this temperature extends to about 5.5 microns. This upper wavelength limit shifts toward the visible as the temperature is raised.

The only detailed investigations of the optical properties of PbTe films reported to date were performed by Gibson.[2] He did not correlate them with the photoconductive properties of the films. Curve *C* of Fig. 1 shows the absorption coefficients of PbTe films as determined by Gibson.

The results of Vernier[3] on the absorption and photoconductivity of PbS films should also be noted since many similarities have been found between PbTe and PbS. Vernier reported large variations among different films of both the spectral sensitivity and the absorption spectra and found a correspondence between the over-all shape of the sensitivity and absorption curves. He did not attempt experiments on unoxidized films nor did he perform experiments at temperatures other than room temperature.

Gibson theorized that the absorption by films in the long-wavelength region is mainly attributable to the scattering of light by individual crystallites in the film. This would render the true absorption undetectable. To eliminate this factor he began investigations on PbTe bulk crystals.[4] This does not permit measurement of both absorption and photoconductivity on the same sample since bulk PbTe crystals show no photoconductive properties. The main portion of his experiment was performed on thin cleaved or polished crystals. Absorption in these crystals for wavelengths below 4 microns is high and no measurement of the absorption coefficient could be made. The 4-micron edge moves linearly toward longer wavelength with temperature as the material is cooled. Gibson was able to obtain one extremely thin crystal, about 1 micron in thickness, and was able to measure the transmission to wavelengths below 2 microns. (Curve *A*, Fig. 1.)

Avery[5,6] recently published two reports in which he

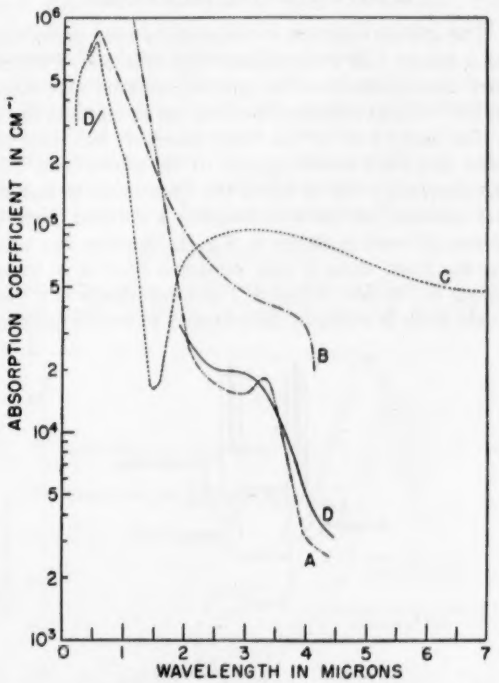

FIG. 1. Absorption coefficient as a function of wavelength: *A*. crystals (Gibson); *B*. crystals (Avery); *C*. films (Gibson); *D*. films (present work).

* This work was supported by the Wright Air Development Center.
[1] D. Bode and H. Levinstein, Phys. Rev. (to be published).
[2] A. F. Gibson, Proc. Phys. Soc. (London) **B63**, 756 (1950).
[3] P. Vernier, J. phys. radium **14**, 175 (1953).
[4] A. F. Gibson, Proc. Phys. Soc. (London) **B65**, 378 (1952).
[5] D. G. Avery, Proc. Phys. Soc. (London) **B66**, 133 (1953).
[6] D. G. Avery, Proc. Phys. Soc. (London) **B67**, 2 (1954).

obtained values for the optical constants of single crystals by means of a reflection technique. Curve *B* in Fig. 1 shows his results on the absorption constant. Avery also found that heating of a PbS crystal caused a decrease in both the absorption and the index of refraction at longer wavelengths. The measurements of the effects of temperature were restricted to PbS, since Avery was unable to obtain cleavage faces of PbTe crystals smooth enough to give reproducible data.

Thin films have been used in the present study of the optical constants because they have the following advantages over bulk crystals of PbTe.

1. It is possible to obtain correlations between photosensitivity and absorption on the same samples. Photosensitivity has not been found in bulk crystals of PbTe.
2. The absorption coefficients in the region examined are high. This gives rise to very low percentages of transmission in crystals.
3. If reflection measurements of bulk crystals are used to determine the optical constants, surface conditions seriously affect the results.
4. It is possible to control the amount of oxygen impurities added to thin layers. The present arrangement allows for the measurement of the optical constants with different oxygen impurity concentrations.

II. EXPERIMENTAL TECHNIQUES

The optical constant measurements were performed on a Model 12B Perkin-Elmer Spectrometer. Preliminary measurements of the optical constants were made on PbTe films evaporated in a bell jar on sapphire disks.

The major part of the work, however, was done on films that were never exposed to the atmosphere. For this purpose, a cell in which the films could be formed was mounted on the spectrometer. A detailed drawing of the cell used is shown in Fig. 2. Sapphire was used for the front window and substrate since it is transparent in the near infrared. The transmission of a disk 1 mm thick is constant (88 percent) to wavelengths up to 4 microns and then falls slowly to about 50 percent at 6 microns.

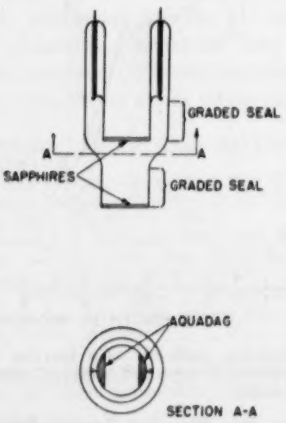

FIG. 2. Sketch of cell blank.

Approximately 5 mg of powdered PbTe was introduced into the cell. The cell was attached to an all-glass vacuum system which used a three-stage oil diffusion pump backed by a Welch forepump. A glass reservoir of oxygen was separated from the system by stopcocks such that pulses of oxygen could be admitted. The system was trapped with liquid oxygen. Pressures lower than 5×10^{-7} mm of Hg could be obtained. The pulses were adjusted to produce a pressure increase of about 1 micron.

Before the film was formed, the cell was heated to 550°C for over an hour in order to outgas the cell. Some of the PbTe was vaporized in the process but it condensed outside of the cell. An air stream was then directed against the inside sapphire, cooling it to about 50°C, thus allowing the PbTe to condense on the substrate. This process was continued until a desired thickness was obtained. The thickness was determined by noting the wavelength of the interference peaks. A film of 5000A thickness could be formed in about 2 hours.

Brattain and Briggs[7] have derived equations for the transmission and reflection of radiation incident on a film of index n, extinction coefficient k, and thickness t.

The equation for transmission is:

$$T=\frac{16n_1n_2(n^2+k^2)}{r^2\{[e^x-(\rho/r)e^{-x}]^2+4(\rho/r)\sin^2[y+\frac{1}{2}(\phi-\theta)]\}}, \quad (1)$$

where

$$r^2=[(n_1+n)^2+k^2][(n_2+n)^2+k^2],$$

$$\rho^2=[(n_1-n)^2+k^2][(n_2-n)^2+k^2],$$

$$\tan\phi=\frac{[-k(2n+n_1+n_2)]}{[(n_1+n)(n_2+n)-k^2]},$$

$$\tan\theta=\frac{[-k(2n-n_1-n_2)]}{[(n_1-n)(n_2-n)-k^2]},$$

$$x=2\pi kt/\lambda,$$

$$y=2\pi nt/\lambda,$$

where n_1 represents the index of refraction of air and n_2 is the index of refraction of the nonabsorbing film substrate.

For very large k the e^x term in the denominator is much greater than either the e^{-x} term or the sine term. Equation (1) thus reduces to

$$T=Ae^{-4\pi kt/\lambda}. \quad (2)$$

Hammer[8] has shown that for the reflected energy only, in the range of values of optical constants found in this experiment, the use of the relationship $2nt=m\lambda$

[7] W. H. Brattain and H. B. Briggs, Phys. Rev. 75, 1705 (1949).
[8] K. Hammer, Z. tech. Phys. 24, 169 (1943).

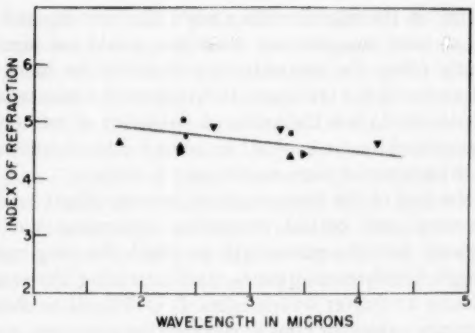

FIG. 3. Room temperature index of refraction as a function of wavelength (thickness determined by Tolansky method).

to determine the locations of maxima and minima is valid.

Since the determination of the index of refraction requires a knowledge of the thickness of the film, this thickness had to be carefully measured. Two different accepted methods of thickness determination were used. One method consists of weighing the film and determining the film thickness by assuming a bulk density of PbTe. The other method makes use of the Tolansky interference technique.

Thicknesses of films determined by the Tolansky method averaged about 10 percent greater than those determined by the weighing method. This result indicates that the density of the material when it is evaporated and then condensed in the form of films is less (by about 10 percent) than the density of bulk crystals. Since Wilman[9] has found from x-ray data that lattice constants in films of PbS and PbSe are the same as in the bulk crystals, the change in apparent density is probably attributable to the presence of spaces between the crystallites.

The thickness of films formed inside of the cell cannot be measured directly. However, if the index of refraction is known from the measurements above, the thickness can be calculated from the location of the interference peaks.

Equation (1) was used for the calculation of the extinction coefficient k. The evaluation of k at wavelengths where the absorption is not large enough to damp out the effect of interference is based on the assumption that both n and t at a given wavelength are known, being found as above. Thus we have an equation with one unknown which cannot be solved explicitly for k.

In order to obtain an approximation solution, the transmission equation is divided into a number of parts and the individual relationships are plotted as a function of n for different values of k. The three relationships are: $16n_1n_2(n^2+k^2)/r^2$, ρ/r, and $\frac{1}{2}(\phi-\theta)$. Through the choice of a value of k and the assumption that the values of the above three relationships calculated from it are correct, the only equation remaining to be solved for k is: $e^x-(\rho/r)e^{-x}=C$, where ρ/r is found from the graph of this value and C is calculated from T and values obtained from all the graphs.

Graphs of $16n_1n_2(n^2+k^2)/r^2$ and ρ/r show that these relationships do not depend strongly on k. The phase angle is proportional to k but the evaluation of Eq. (1) is not affected greatly by the value of the phase angle.

The method, therefore, was to assume a value of k at a given n, t, and λ and then solve $e^x-(\rho/r)e^{-x}=C$ for k. If this calculated value of k was greatly different from the value assumed, it in turn could be used as the assumed value. It was usually found that this process did not have to be repeated more than once, the two calculated values agreeing closely.

III. RESULTS

A. Films Exposed to Air

1. Index of Refraction

The values of n as a function of wavelength obtained from the thicknesses determined by the Tolansky method are shown in Fig. 3. The value of the index calculated from the thickness determined by the weighing technique was found to be higher than the index based on the Tolansky thickness method. The error in both methods is not greater than ± 5 percent. This error is believed to be based almost entirely on the uncertainty of the thickness calculations.

Values of index based on the assumption of bulk densities (weighing methods) agree within experimental error with the values found by Avery on bulk crystals. Avery found that n increases slightly with increasing wavelength, while the present results show a definite decrease in index at longer wavelengths.

2. Extinction Coefficient

Since the value of the extinction coefficient in the visible region is found to be high, Eq. (2) is valid in

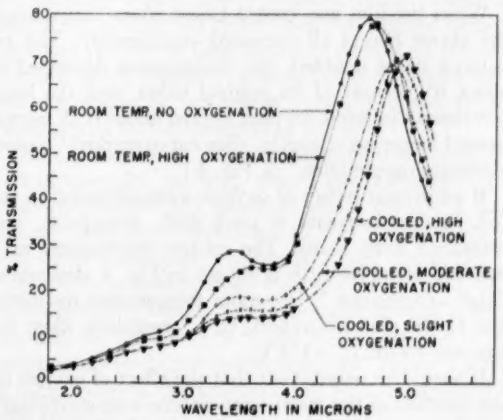

FIG. 4. Percent transmission of a typical film for different temperatures and different degrees of oxygenation.

[9] H. Wilman, Proc. Phys. Soc. (London) **60**, 117 (1948).

this region. A Welch Densichron with three different Wrattain Filters was used to determine the percentage transmission at wavelengths of 0.45, 0.53, and 0.65 micron. The values of $\ln T$ *vs* t were plotted for the three wavelengths measured. The values of the extinction coefficient determined from the slopes of these curves are: 1.03 at 0.45 micron, 1.32 at 0.53 micron, and 1.82 at 0.65 micron. These values, expressed in terms of the absorption coefficient α, where $\alpha=4\pi kl/\lambda$, are shown in curve *D* of Fig. 1. The measurements in this region were performed only to obtain an order of magnitude value of the absorption constant, so that these values could be compared with the absorption measured at longer wavelengths.

B. Films in High Vacuum

1. Effects of Oxygen and Temperature on Transmission Properties

A typical transmission curve of a film maintained in vacuum is shown in Fig. 4. The transmission peaks at 3.4 microns and at 4.7 microns arise from the presence of interference. When the substrate was cooled to −158°C (the lowest temperature achieved with the cooling techniques used) there was no appreciable change in either the transmission curve or the resistance. However, if one pulse of oxygen was allowed to enter the cell, the following very noticeable effects on both the electrical and optical properties of the film were obtained:

a. The resistance of the film suddenly increased from 150 to 300 ohms.

b. The transmission in the 3-micron wavelength region decreased about 10 percent.

c. The wavelength at which the 4.7-micron interference peak appeared was shifted about 0.02 micron toward longer wavelengths. This shift is below the resolving power of the instrument, but the change in peak can definitely be seen for all samples investigated.

When the film was cooled below room temperature the above effects all increased considerably. The resistance value doubled, the transmission decreased to about 65 percent of its original value, and the long-wavelength interference peak moved about 0.15 micron toward longer wavelengths. (See curve marked "cooled, moderate oxygenation" in Fig. 4.)

If additional pulses of oxygen were admitted to the cell, further increases in peak shift, absorption, and resistance were noted. The energy transmitted as a function of wavelength is shown in Fig. 4, designated "high oxygenation." The room temperature resistance was 11 000 ohms, increasing to 1.7 megohms when the film was cooled to −158°C.

It should be pointed out that the effect of oxygen on the location of the room temperature long-wavelength interference peak is small in magnitude (less than 1 percent). The shift in interference peak that probably occurs on the sapphire disks when they are exposed to air at room temperature, therefore, would not significantly affect the determination of either the index of refraction or the thickness. It is this result which makes it possible to use the value of the index of refraction determined on the exposed sapphire for the calculation of thicknesses of films maintained in vacuum.

Heating of the films produced reverse effects on the electrical and optical properties, decreasing the resistance and the wavelength at which the long-wavelength interference appears, and increasing the transmission at shorter wavelengths. It is difficult to obtain accurate values for films at elevated temperatures, since heating of the film for the time required to take transmission measurements usually changed the properties of the films. Only a few cases were found where it was possible to raise the temperature of the film without producing a permanent change in film properties.

Although no careful measurements were made on the film in the vacuum cell at wavelengths below 1.8 microns, experiments were performed to see if additions of oxygen and changes in temperature affected the transmission between 1 and 1.8 microns. Within the limits of oxygenation and temperature variations used in the present investigation, no effects have been noted in this region below 1.7 microns.

2. Effects of Oxygen and Temperature on the Index of Refraction

Figure 5 is a plot of the index of refraction as a function of wavelength for films at different temperatures and with different oxygen content. The addition of oxygen did not affect the index of a film at room temperature sufficiently to make it observable on the graph. As indicated in the curves, the index variation begins at wavelengths near 2.5 microns and increases with wavelength. The change in index, therefore, could not be due to a thickness change of the film, since this

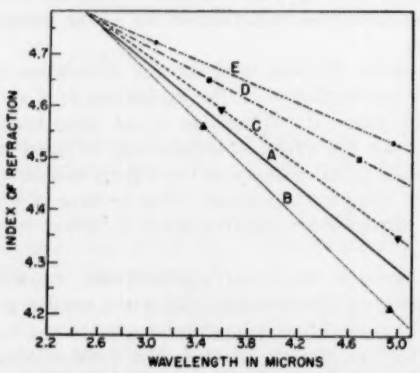

FIG. 5. Index of refraction as a function of wavelength for different degrees of oxygenation: *A*. Room temperature; *B*. heated —225°C (slight oxygenation); *C*. cooled——158°C (slight oxygenation); *D*. cooled——158°C (moderate oxygenation); *E*. cooled——158°C (high oxygenation).

would give rise to a peak shift in all regions of the spectrum investigated. Since the thickness does remain constant, and the location of the peaks is given by the relationship $2nt=m\lambda$, the change in index is proportional to the change in wavelength. On the basis of this fact the values shown in Fig. 5 were determined. Figure 6 shows the linear decrease in the index with temperature, at a particular wavelength. This result is in contrast to germanium, where the index increases with increasing temperature as reported by Briggs[10] for crystals and as measured on films of germanium in this laboratory.

3. Effects of Oxygen and Temperature on the Extinction Coefficient

Typical values for the extinction coefficient are shown in Fig. 7. The curves were calculated on the basis of values for the refractive index and thickness determined by the Tolansky method. Curves calculated on the basis of index and thickness values obtained from the weighing technique are very similar.

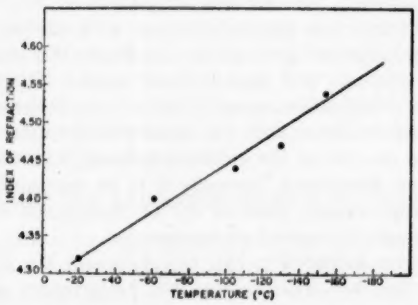

FIG. 6. Index of refraction at $\lambda=4.9$ microns as a function of temperature for a film after high oxygenation.

The absorption curves for different films show one common characteristic. The long-wavelength absorption edge moves toward longer wavelengths when the film is cooled. This is very similar to the effect on bulk crystals observed by Gibson.[11] In Fig. 1 the magnitude of a typical absorption curve of a photosensitive cell is compared with the results obtained, by both Avery and Gibson, on bulk crystals. Avery's values were obtained from radiation reflected from bulk crystals; Gibson obtained his results from measurements of transmitted radiation. The present results agree more closely with those of Gibson, but it should be pointed out that Gibson does not claim very good accuracy in his results. The similarity of the magnitudes and shapes shown in all three curves indicates that absorption obtained in bulk and films is essentially due to the same mechanism, and that scattering by crystallites does not play a significant role at the wavelengths under consideration.

[10] H. B. Briggs, Phys. Rev. **77**, 287 (1950).
[11] A. F. Gibson, Proc. Phys. Soc. (London) **B65**, 378 (1952).

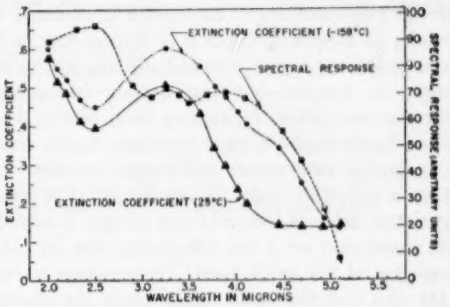

FIG. 7. Extinction coefficient and spectral response as a function of wavelength.

IV. DISCUSSION

The similarity between the absorption curves at low temperatures and the spectral sensitivity curves indicates that the two are related. The sensitivity curves are displaced toward longer wavelengths, but Moss[12] shows that this is often to be expected in regions where the absorption is high. The fact that the absorption cutoff at long wavelengths varies with temperature in much the same way as the long-wavelength limit of sensitivity as reported by Bode and Levinstein[1] also helps to substantiate the theory that absorption and sensitivity are interrelated.

The results indicate that the absorption below 1.7 microns is intrinsic in nature, the absorption arising from excitation of electrons from the valence band to the conduction band. Two mechanisms are conceived as possible causes of the absorption at longer wavelengths. The first is that the absorption in this longer wavelength region is still intrinsic. This assumption is supported by the high absorption values and also by the comparatively small variations of both the absorption and spectral response from their respective values in the shorter-wavelength region.

This long-wavelength region may also be considered an impurity region, the absorption being caused by excitation of electrons either from the valence band to impurity centers or from impurity centers to the conduction band. Impurity absorption is indicated since the absorption in this region varies with the oxygen content and the temperature of the film.

An explanation in terms of impurity levels still does not account for the high absorption coefficient. It is perhaps possible that the films would contain a large enough number of impurities to give rise to the high extinction coefficient. If, however, the absorption is considered as arising from the same mechanism as in bulk crystals, where the impurity concentration is much smaller, the similarity of shape and magnitude of absorption curves is not easily explained. Figure 1 shows a comparison of the absorption in films as obtained in this study.

[12] T. S. Moss, Proc. Phys. Soc. (London) **A64**, 590 (1951).

If the long-wavelength absorption is assumed to be intrinsic, no simple description of the conduction band can be proposed. A simple model will not illustrate how changes in temperature and oxygen contamination affect the absorption. To explain these effects the conduction band should have a structure that is sensitive to changes in temperature and oxygen content.

Such a proposal might be avoided if it is assumed that a new oxide is formed when oxygen is added, the high absorption at 3 microns being due to intrinsic absorption of the oxide itself. Temperature variations of the film and the oxide might cause the changes in absorption noted, but it is difficult to see how the various effects reported would be explained. If it is assumed that the absorption characteristics in the film do arise mainly from an oxide, the similarity with absorption in bulk crystals is also not easily understood.

The supposition that the absorption spectra result from structure of the conduction band therefore appears to be the only way to describe an intrinsic phenomenon. In order to explain the long-wavelength cutoff at about 5 microns at low temperatures, the energy gap between the valence and the conduction band must be of the order of 0.25 ev. This value disagrees with the results of Hall measurements as reported by Chasmar and Putley.[13] However, Scanlon[14] has recently pointed out that the energy gap derived from Hall constant measurements at high temperatures may be in error.

By producing purer crystals of PbS, Scanlon can measure the activation energy of PbS at lower temperatures, and he finds that it is about 0.37 ev as compared with earlier results of 1.17 ev obtained at temperatures above 900°K.[15] It could therefore be expected that when purer crystals of PbTe are available with activation energies measurable at lower temperatures, a similar decrease in activation energy will be observed.

To explain the observed effects, one might assume a conduction band which would lie 0.25 ev above the valence band. The density of states might be quite low to a point about 0.7 ev above the valence band, at which point the density would increase rapidly. The tail in the conduction band could thus explain the decreased absorption beyond 2 microns. Since freshly evaporated films are always *n* type,[16] part of the tail of the conduction band would be filled with electrons, probably excited from interstitial Pb centers, close to the conduction band. Oxygen added to the film is adsorbed on the film surface,[17] and, by acting as a trap for electrons, removes them from the tail of the conduction band, thus increasing absorption beyond 2 microns. A decrease in temperature prevents thermal excitation from the valence band to the tail of the conduction band, resulting in both an increase in absorption and an extension of the high absorption region to longer wavelengths. Photoconductivity is then produced when the electron and hole density is increased as electrons are excited to the conduction band.

Although this picture disagrees with the interpretation suggested by Chasmar and Putley,[18] a model of this type can still explain their results. Their high value of activation energy (0.62 ev) would arise from thermal excitation from the valence band to the region above the tail of the conduction band. The value of 0.62 ev determined thermally is to be compared with the approximate value of 0.7 ev determined in this experiment by optical measurements.

We are indebted to Mr. Eric Ellis and Mr. Donald Cole for their assistance in the performance of this work.

[13] R. P. Chasmar and E. H. Putley, *Semiconducting Materials* (Butterworth Scientific Publications, London, 1951), p. 216.
[14] W. W. Scanlon, Phys. Rev. **92**, 1573 (1953).
[15] E. H. Putley and J. B. Arthur, Proc. Phys. Soc. (London) **B64**, 616 (1951).
[16] S. J. Silverman and H. Levinstein, Phys. Rev. **94**, 871 (1954).
[17] R. A. Smith, *Semiconducting Materials* (Butterworth Scientific Publications London, 1951), p. 198.
[18] R. P. Chasmar and E. H. Putley, *Semiconducting Materials* (Butterworth Scientific Publications, London, 1951), p. 216.

Magnetic Resonance Absorption of Diphenyl-Picryl Hydrazyl at Low Magnetic Fields

M. A. GARSTENS, L. S. SINGER, AND A. H. RYAN
United States Naval Research Laboratory, Washington, 25 D. C.
(Received June 30, 1954)

Measurements of the magnetic resonance absorption line shapes and g factors of diphenyl-picryl hydrazyl have been made at several frequencies below 15 Mc/sec using a linearly polarized rf field. An approximately inverse fourth power dependence of the g factor with frequency was found. The frequency dependence of both the g factor and line shape are found to be in agreement with a theory for the low-field case developed in a previous paper.

I. INTRODUCTION

THE shapes of magnetic resonance lines at magnetic fields large compared to the line width can generally be interpreted quite successfully by the use of the Bloch absorption equation.[1,2] However, the fact that this equation does not reduce to the Debye expression for absorption in zero magnetic field suggests that Bloch's equation is not applicable to the low-field case, where the magnetic field for maximum absorption is of the same magnitude as the line width.

In order to investigate the low-field case in more detail, we have measured the magnetic resonance absorption line shapes and g factors of diphenyl-picryl hydrazyl in a linearly polarized rf field at several frequencies below 15 Mc/sec. The experimental results are then compared with the theory developed for the low-field case in a previous paper.[3]

II. APPARATUS AND EXPERIMENTAL PROCEDURE

To obtain the high sensitivity required for accurate g-factor measurements, a magnetic field modulation scheme which included a coherent detector was used. The sample consisted of approximately 3 g of polycrystalline diphenyl-picryl hydrazyl. All measurements were made at room temperature. A block diagram of the apparatus is shown in Fig. 1.

A. The Static Magnetic Field

A large solenoid supplied by storage batteries produced the static magnetic field. For the line shape measurements, a motor-driven potentiometer produced a gradual change of magnetic field of about 5 gauss in 3 minutes. The voltage drop across a resistance in series with the magnet served as the input to one axis of a Leeds and Northrup $X-Y$ recording potentiometer. For the g-factor measurements, the magnet current was determined by measuring the voltage drop across a standard resistance in series with the magnet by means of a Leeds and Northrup type "K" potentiometer.

The solenoid was mounted so that its axis could be aligned with the direction of the magnetic field in the room, a dip-needle and compass serving as direction indicators. The center of the solenoid at which the sample was placed was kept about 5 feet above the partially magnetized steel beams supporting the floor. For the g-factor measurements, no attempt was made to determine the absolute value of the magnetic field. The procedure, which required only relative values of field, was as follows. Assuming the solenoid field to be parallel to and in the same sense as the ambient field, the magnetic field H at the sample can be written $H=mP+b$, where P is the potentiometer reading in volts, m is the solenoid constant in gauss/volt, and b is the magnitude of the ambient field. If the oscillator frequency ν, the potentiometer reading P, and the potentiometer reading P_r upon current reversal are observed at the absorption maximum; then the ratio of the g-factor g_ν to that at 15 Mc/sec, g_{15}, measured under the same conditions, is given by

$$\frac{g_\nu}{g_{15}}=\left(\frac{\nu}{H}\right)\Big/\left(\frac{\nu_{15}}{H_{15}}\right)=\left(\frac{\nu}{\nu_{15}}\right)\left(\frac{P_{15}+P_{r15}}{P+P_r}\right). \quad (1)$$

Assuming that g_{15} is equal to the high-field value 2.0036,[4] the g factor at a frequency ν can be calculated from the

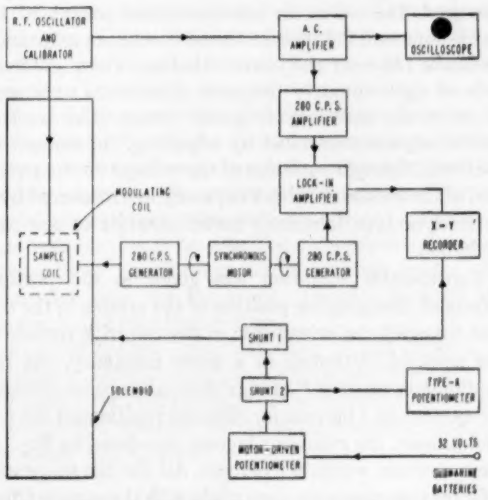

FIG. 1. Block diagram of the apparatus.

[1] F. Bloch, Phys. Rev. **70**, 460 (1946).
[2] G. E. Pake, Am. J. Phys. **18**, 438 (1950).
[3] M. A. Garstens, Phys. Rev. **93**, 1228 (1954).
[4] Holden, Kittel, Merritt, and Yager, Phys. Rev. **77**, 147 (1950).

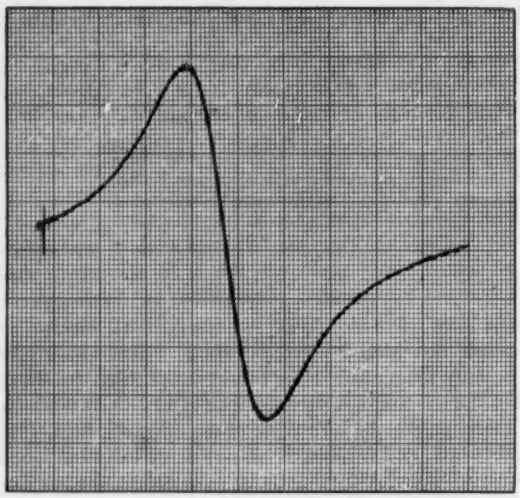

FIG. 2. A recorder chart showing the resonance at 5 mc/sec. The two curves which appear essentially superimposed were obtained immediately before and after calibration.

experimentally determined quantities in Eq. (1). A number of measurements made at different solenoid orientations showed that above 3 Mc/sec the g factors had a mean deviation of a few parts in 10^4 when the angle between the solenoid axis and the ambient field direction was less than 3°. The compass and dip-needle which could be read to $\pm 1°$ were thus adequate as orientation indicators.

B. The Radio-Frequency Field

A conventional electron coupled oscillator-detector[5] incorporating a calibrator of the Watkins-Pound type[6] was used. The coil of the resonant circuit was about 2.5 inches long and 0.8 inch in diameter with an additional feedback tap near the center winding. Three different coils of approximately the same dimensions were used to cover the necessary frequency range. The level of oscillation was controlled by adjusting the amount of feedback, through variation of the voltage on the screen grid of the oscillator tube. Frequency was measured by a heterodyne-type frequency meter accurate to one part in 20 000.

Considerable attention was given to the possible effects of changing the position of the sample in the coil and changing the orientation of the coil with respect to the solenoid. Although at a given frequency, the potentiometer reading P at maximum absorption changed by as much as 1 percent for different positions of the coil and sample, the relative g factors calculated by Eq. (1) were constant within 0.1 percent. All the line shape and g-factor measurements were made with the sample filling the center $\frac{2}{3}$ of the coil and with the coil perpendicular to the solenoid axis within 1°.

C. Detection System

In the detection scheme used, a small 280-cycle/sec modulation field supplied by an auxiliary coil parallel to the solenoid axis, produced across a variable resistance in the plate circuit of the oscillator a 280-cycle/sec component due to the magnetic absorption. This signal was then amplified and fed into a coherent detector. The dc output was connected to the X axis and the magnet current to the Y axis of an X−Y recorder.

For sufficiently small modulating fields, the signal amplitude will be proportional to the slope of the absorption curve. An approximate calculation for small modulations shows that for either a Lorentzian or Gaussian shaped absorption curve, a peak-to-peak modulation amplitude of 10 percent of the full width at half-maximum absorption will give signals having 280-cycle/sec components proportional to slopes within 2 percent over the entire absorption. Since two stages of tuned amplification preceded the coherent detector, the 560-cycle/sec component of the signal which is large near the absorption peak is not detected. For all the measurements made, the peak-to-peak modulation amplitude was 0.04 gauss or less; i.e., less than 3 percent of the full width at half-maximum absorption. For the g-factor measurements at the lower frequencies, the absorption curves were quite unsymmetrical so that even smaller modulations were required. The decreased sensitivity resulting from the small sweep was the limiting factor in determining the minimum radio frequency at which one could measure a g-factor within 0.1 percent. This frequency was about 2.7 Mc/sec.

D. Experimental Procedure

The procedure for measuring g factors already described was used at frequencies above 5 Mc/sec. Below this frequency, since a different coil was required, the g factors were measured relative to g_5 and then corrected for the deviation of g_5 from g_{15}.

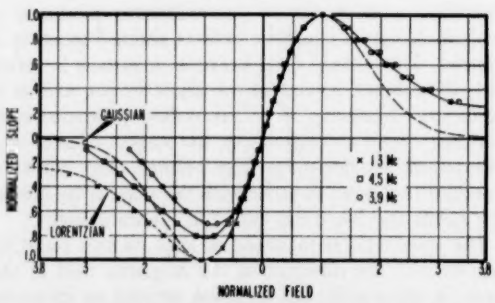

FIG. 3. A comparison of the resonance line shapes at three different frequencies. The magnitudes of the high-field extreme slopes, and the difference in field between the points of zero slope and high-field extreme slope, are normalized to unity.

[5] J. B. Dow, Proc. Inst. Radio Engrs. **19**, 2095 (1931).
[6] G. D. Watkins and R. B. Pound, Phys. Rev. **82**, 343 (1951).

The procedure for measuring line shapes was as follows. A curve was first traced on the recorder as the field was increased. The magnet current was observed at both the beginning and end of the trace. The magnet was then set at a high field value where there was no absorption and the X axis of the recorder calibrated by means of the Watkins-Pound calibrator. The absorption was then retraced on the same chart as the field was decreased, the acceptable runs being those in which the forward and reverse traces were essentially superimposed. The apparent g factor was then measured by observing the magnet current and frequency at the point of zero slope. A recorder tracing made in this manner at 5 Mc/sec is shown in Fig. 2.

III. EXPERIMENTAL RESULTS

A comparison of some of the results of the line shape measurements is shown in Fig. 3. The solid curves drawn through the experimental points were adjusted so that the points of zero slope coincided with zero on the magnetic field axis. The magnitudes of the high-field extreme slopes, and the difference in field between the points of zero slope and high-field extreme slope, were normalized to unity. The dotted curves are the first derivatives of Gaussian and Lorentzian shaped curves drawn in the same manner. For the particular hydrazyl sample used, the width in gauss between extreme slope points was found to be constant between 10 and 15 Mc/sec and had the value 1.00 ± 0.02 gauss.

A plot of the g factors as a function of frequency is shown in Fig. 4. Each experimental point is the average of 3 measurements taken in rapid succession. The g factors were found to be independent of the strength of the rf field at the low levels of oscillation employed. Figure 5 is a plot of $-\log_{10}(\Delta g/g)$ *vs* $\log_{10}\omega$, where $(\Delta g/g)=(g_p-2.0036)/2.0036$ and ω is the angular frequency. The vertical bars drawn through some of the experimental points indicate the error in $\log_{10}(\Delta g/g)$ which would result from a 0.1 percent error in g_p. The dashed curves are calculated as described in Sec. IV.

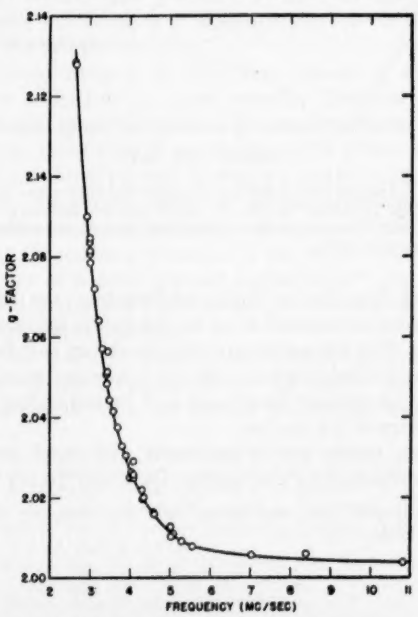

FIG. 4. Variation of the g factor with frequency.

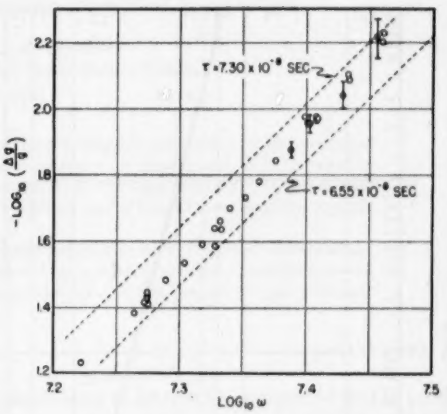

FIG. 5. Fractional deviation of the g factor as a function of angular frequency. The dashed curves were calculated from Eq. (3).

IV. DISCUSSION

In a previous paper[3] a theory was developed for magnetic resonance in gases at low fields. This theory is found to fit the experimental data very closely. The gas model is applicable in this instance since one may envisage the magnetic dipoles as suffering repeated random collisions with the lattice phonon field via the exchange system.[7] A parameter τ may be introduced defining the mean time between interactions or collisions of the dipoles with the lattice via the exchange system. The times of last collision, assuming random occurrence of such, are distributed according to the weighting function $(1/\tau)e^{-t/\tau}$, as in a gas.

Bloembergen and Wang[7] have shown that for diphenyl-picryl hydrazyl, where the exchange is very strong, the relaxation process between the spins and the lattice occurs via the exchange spin system. The gas model may still be applied here, the effect of exchange in this instance being to give rise to a narrow line described by a single relaxation parameter $\tau=t_{He}$, the relaxation time for the energy transfer between the magnetic and exchange system.

For the linearly polarized case, in the absence of saturation, the following steady state solution for χ'' is obtained if the lateral effects of the magnetization in the x and y directions due to the radio-frequency field are not taken into account.[3]

$$\chi''=\tfrac{1}{2}\chi_0\omega_0\tau\left(\frac{1}{1+\tau^2(\omega_0-\omega)^2}-\frac{1}{1+\tau^2(\omega_0+\omega)^2}\right). \quad (2)$$

[7] N. Bloembergen and S. Wang, Phys. Rev. **93**, 72 (1954).

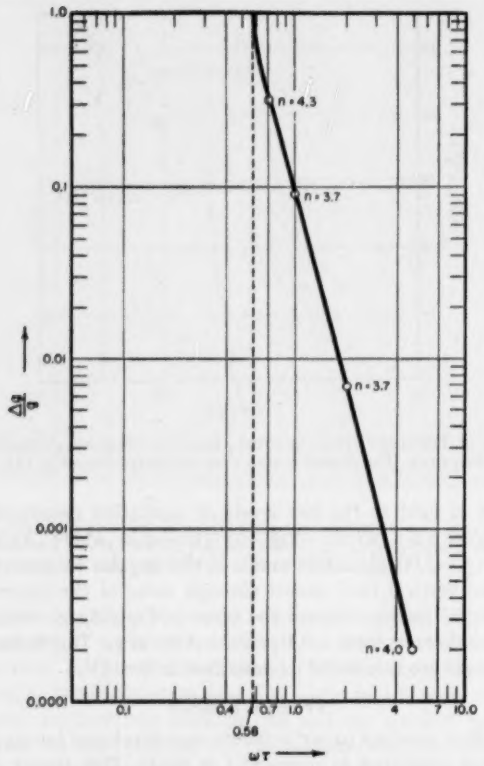

FIG. 6. A log-log plot of the fractional deviation of g as a function of $\omega\tau$. The slope of this curve for different values of $\omega\tau$ are indicated by the letter n. Below $\omega\tau=0.58$ no maxima occur in the absorption lines.

The first term is the Bloch solution for the circularly polarized case.[3] Both the circularly and linearly polarized solutions under the above assumptions lead to incorrect predictions of absorption and g-value shifts at low fields. Thus χ'' approaches zero as H_0 does, instead of reducing to a non zero value as experiment indicates.

At low fields the magnetization in the x and y directions due to the radio-frequency field becomes important. If these are taken into account, one obtains for χ'':

$$\chi''=\tfrac{1}{2}\chi_0\omega\tau\left(\frac{1}{1+\tau^2(\omega_0-\omega)^2}+\frac{1}{1+\tau^2(\omega_0+\omega)^2}\right). \quad (3)$$

Figure 6 is a log-log plot of $\Delta g/g$ *versus* $\omega\tau$. Its slope is indicated at several points by n which corresponds to the exponent in the expression $\Delta g/g\sim 1/(\omega\tau)^n$ obtained from Eq. (3) by maximizing it as a function of $\omega_0\tau$ at constant $\omega\tau$.

The agreement between the experimental results and this theory is shown in Figs. 5 and 7. In Fig. 5, the dashed curves show the relative deviation in the apparent g factors predicted by (3) for two values of the inverse line width parameter.

From the comparison in Fig. 5, one would deduce a τ of about $(6.9\pm0.4)\times10^{-8}$ sec. This is in substantial agreement with the τ of $(6.6\pm0.2)\times10^{-8}$ sec determined directly from line width measurements between 10 and 15 Mc/sec. Over the frequency range shown, the dashed curves are apparently linear with slopes of about 3.7. The experimentally determined slope is 3.9 ± 0.3.

The solid curves in Fig. 7 are plots of $(d\chi''/d\omega_0)$ calculated from equation (3), as a function of magnetic field. The same value of τ was used for the three curves, namely 6.6×10^{-8} sec as determined experimentally from the line width. The magnitude of the high-field extreme slope was normalized to unity in each case. The circles are experimental points normalized in the same manner. Note that at the lowest frequency, the point of zero slope corresponding to an absorption maximum is absent. This is in agreement with the theory as indicated in Fig. 6 which predicts that no absorption maximum should be present below $\omega\tau=0.58$ corresponding to a frequency of 1.3 Mc/sec.

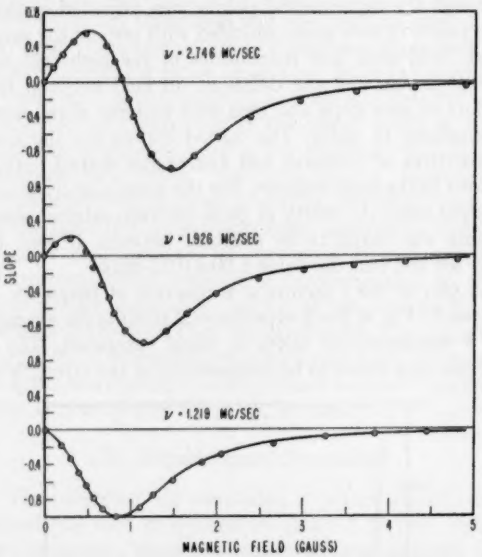

FIG. 7. Comparison of some of the observed resonances (points) with those predicted by Eq. (3) (solid curves), assuming $\tau=6.6\times10^{-8}$ sec. The magnitudes of the high-field extreme slopes are normalized to unity.

These results are in agreement with those also recently reported by Codrington, Olds, and Torrey.[8]

[8] Codrington, Olds, and Torrey, Bull. Am. Phys. Soc. **29**, No. 4, 19 (1954).

Vibrational Anharmonicity and Lattice Thermal Properties

J. S. DUGDALE AND D. K. C. MACDONALD
Division of Physics, National Research Council, Ottawa, Canada
(Received June 1, 1954)

It has been believed for some time that anharmonicity of lattice vibrations is responsible for the continued rise of the specific heats of certain solids in the classical temperature region. A general analysis is here carried out of the linear chain model interacting through a Morse potential. All the major thermal properties, such as specific heats, thermal expansion, and compressibility are derived, and a tentative comparison is made with observed properties of the alkali metals.

It is found that the linear chain then exists in two widely different states with properties characteristic of condensed and gas-like phases; these two states are separated by a relatively narrow transition region in temperature where the specific heat passes through a rather sharp maximum (except at high pressures when the maximum ultimately disappears).

1. INTRODUCTION

THE atomic heats of the alkali metals Li, Na, K, and Rb all show anomalous behavior at temperatures greater than their characteristic temperatures. Apart from the sharp increase in specific heats as the melting temperature is approached (this and the corresponding behavior of the electrical resistance are attributed to the formation of defects in the lattice),[1,2] there is also a steady rise in atomic heat at constant volume above the value $3R$ which is the classical limit if only harmonic vibrations of the lattice are considered. Furthermore, this excess atomic heat is too large to be accounted for on the basis of a free electron contribution. It was suggested by Lindemann[3] that such anomalous behavior might be due to the anharmonicity of the lattice vibrations and this explanation has generally been regarded as probably correct. Born and Brody, Born,[4] Waller,[5] and Damköhler[6] have all made estimates of the influence of anharmonicity on the specific heat of a lattice.

Anharmonicity is an important feature of the behavior of lattices for other reasons. There are many significant properties of a lattice such as thermal expansion, the change of specific heat with pressure, etc., which are zero if a purely harmonic potential is assumed. Finally the anharmonicity of lattice vibrations is responsible for the establishment of thermal equilibrium among the modes of vibration of the lattice and for the existence of a finite thermal conductivity.[7,8] For these reasons further study of the influence of anharmonicity was considered desirable.

In the treatment of anharmonicity given by Born and Brody (Waller's conclusions are essentially the same) the precise model is not defined well enough to enable the conclusions to be clearly interpreted and in addition there are problems of convergence which were not considered (see also reference 5). Damköhler, on the other hand, considered a precise model (a linear chain) with specified boundary conditions, and because this makes the problem directly tractable a linear chain model is considered in this paper. The treatment here is, we believe, considerably simpler and more direct than that of Damköhler; we evaluate the Gibbs free energy analytically instead of by numerical approximation, and consequently our results can be carried to any desired degree of precision. The analysis is also readily extended to include next-nearest neighbor interaction in good approximation. Moreover, the procedure adopted here reveals certain other properties of the model which are of interest in their own right. It is found that at low pressures there exists a relatively narrow temperature region in which the specific heat at constant pressure passes through a sharp maximum (at higher pressures the maximum ultimately disappears), above which the equation of state of the chain approximates to that of a perfect linear "gas", while below this "transition" the chain has the properties of a condensed state.

2. GENERAL ANALYSIS

The linear chain model has been considered in a large number of papers.[9–11] In the treatment given here, a single physically realistic interatomic potential (the Morse potential) is employed and all the important thermodynamic properties of such a chain are derived for temperatures high enough that classical statistics are applicable. Although the application to three dimensions of results derived on a one-dimensional model is necessarily very tentative, we have, in order to keep in touch with physical reality, interpreted some of the quantities appearing in the analysis in terms of the physical properties of sodium, since we are particularly interested in the alkali metals.

[1] L. G. Carpenter, J. Chem. Phys. **21**, 2244 (1953).
[2] D. K. C. MacDonald, J. Chem. Phys. **21**, 177 (1953).
[3] F. A. Lindemann, Phil. Mag. **45**, 1119 (1923).
[4] M. Born and E. Brody, Z. Physik **6**, 132 (1921); M. Born, *Handbuch der Physik* (Springer Publishing Company, Inc., Berlin, 1933), Vol. 24, Part 2, p. 675.
[5] I. Waller, Ann. Physik **83**, 153 (1927).
[6] G. Damköhler, Ann. Physik **24**, 1 (1935).
[7] R. Peierls, Ann. Physik **3**, 1055 (1929).
[8] R. Peierls, Ann. inst. Henri Poincaré **5**, 177 (1935).
[9] T. Nagamiya, Proc. Phys.-Math. Soc. Japan **22**, 705, 1034 (1940).
[10] H. Takahasi, Proc. Phys.-Math. Soc. Japan **24**, 63 (1942).
[11] F. Gürsey, Proc. Cambridge Phil. Soc. **46**, 182 (1950).

We consider then a system of $(N+1)$ identical particles of mass m equally separated (at 0°K and under zero tension) by a distance A_0 (see Fig. 1). These initial

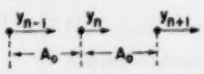

FIG. 1. System of identical particles.

positions of the particles are then chosen as the origins of measurement for the displacements of the respective particles, and that of the nth particle from its origin is denoted by y_n. Without loss of generality, we may consider as fixed the zeroth particle so that y_0 is always zero. The interatomic potential of two particles separated by a distance r is $\Phi(r)$. Thus the energy of interaction between the nth and the $(n-1)$th particle is $\Phi(A_0+y_n-y_{n-1})$, and the potential energy of the whole system is

$$V=\sum_{n=1}^{N} D(e^{-a(y_n-y_{n-1})}-1)^2, \tag{1}$$

where we use the Morse potential and initially restrict the analysis to nearest-neighbor interaction. Hence, if we write

$$x_n=y_n-y_{n-1},$$

then

$$V=\sum_{n=1}^{N} D(e^{-ax_n}-1)^2. \tag{2}$$

We now set up what may be called the partition function at constant force, $Z_G(P,N,T)$, (see for example, Fowler and Guggenheim[12]) where P is the applied force, analogous to pressure in a three-dimensional problem. Then

$$Z_G(P,N,T)\equiv\int_{-\infty}^{+\infty}\cdots\int_{-\infty}^{+\infty}\times e^{[-H(p_0,\cdots,q_0,\cdots)+PL]/kT}dp_n\cdots dq_n\cdots, \tag{3}$$

where $L=NA_0+\sum_1^N x_n$. Takahasi[10] and Gürsey[11] have also shown analytically that this form of partition function may be derived from the more usual form, Z_F, the partition function at constant length (volume). Thus

$$Z_G=m^N\int_{-\infty}^{+\infty}\cdots\int_{-\infty}^{+\infty}\exp\{-[(\sum_n D(e^{-ax_n}-1)^2+P(NA_0+\sum_n x_n)+m\sum_n \dot{y}_n^2/2]/kT\}d\dot{y}_1\cdots\times d\dot{y}_n dy_1\cdots dy_n; \tag{4}$$

that is,

$$Z_G=K\left[\int_{-\infty}^{+\infty}\exp\left(-\frac{Pz}{akT}+\frac{D}{kT}(e^{-z}-1)^2\right)dz\right]^N, \tag{5}$$

where

$$K=(2\pi mkT)^{N/2}e^{-NPA_0/kT}a^{-N}.$$

[12] R. H. Fowler and E. A. Guggenheim, *Statistical Thermodynamics* (Cambridge University Press, London, 1939), p. 254.

Thus, if we set $u=e^{-z}$, we have[13]

$$Z_G=K\left\{\int_0^{\infty} u^{(P/akT)-1}\exp[-D(u-1)^2/kT]du\right\}^N \equiv KI^N. \tag{5a}$$

If we write $v=u-1$, and integrate by parts, then

$$I=\frac{2aD}{P}\int_{-1}^{\infty}(1+v)^{P/akT}v\exp(-Dv^2/kT)dv$$
$$=\frac{2D}{kT}\int_{-1}^{+1}\exp(-Dv^2/kT)\left\{v^2+\left(\frac{P}{akT}-1\right)\times\left(\frac{P}{akT}-2\right)\frac{v^4}{3!}+\cdots\right\}dv$$
$$+\frac{2aD}{P}\int_1^{\infty}v^{P/akT+1}\exp(-Dv^2/kT)dv$$
$$+\frac{2D}{kT}\int_{+1}^{\infty}v^{P/akT}\exp(-Dv^2/kT)\times\left\{1+\left(\frac{P}{akT}-1\right)\cdot\frac{1}{2!v}+\cdots\right\}dv \tag{6}$$
$$\equiv\frac{2D}{kT}(I_1+I_3)+\frac{2aD}{P}I_2. \tag{6a}$$

It should be noted that so far no approximations have been made. In (6a) it may now be shown that I_3 is certainly entirely negligible in comparison with I_1 except for $(P/akT)\gg 1$. For the compressible metal sodium at ~300°K, the equivalent pressure corresponding to the equality $P/akT=1$ is about 3000 atmos. We shall therefore assume meanwhile that $P/akT<1$ and so ignore I_3. Now as $P\to 0$ it is evident that the first term converges uniformly to a finite limit while the second term does not; in fact, then

$$I\approx(\pi kT/D)^{\frac{1}{2}}+(akT/P)e^{-D/kT}. \tag{7}$$

The second term is then only comparable with the first for

$$P\lesssim(a^2DkT)^{\frac{1}{2}}e^{-D/kT}. \tag{7a}$$

For sodium again at room temperature, this value of P corresponds to an equivalent pressure of about 10^{-16} atmos, and consequently from this standpoint we may entirely neglect the second term in (7) at normal temperatures and pressures. The second term in (7) corresponds to a gas-like behavior as we shall see later. We might regard (7a) as corresponding to a vapor-pressure equation, and, although in the linear chain the thermo-

[13] We are grateful to Dr. H. C. Schweinler for suggesting this transformation.

dynamic functions remain continuous and consequently no discontinuity presents itself, we shall see that there is, in general, a sharp maximum in the specific heat when the two terms in (7) are comparable.

3. CONDENSED STATE

Thus, except under the extreme conditions discussed, we have $I=(2D/kT)I_1$, corresponding to a condensed state. Assuming that $D/kT\gg 1$ (e.g., $D/kT\sim 45$ for sodium at room temperature, with D interpreted as the latent heat of vaporization at absolute zero), we may replace the limits (± 1) in I_1 by $(\pm\infty)$. The presence of the exponential factor with the large index ensures that we then make negligible errors by this approximation in the constituent integrals until we reach terms containing very high powers of v which are already of no physical interest.[14] Thus,

$$Z_G=K\left(\frac{\pi kT}{D}\right)^{N/2}\left\{1+\frac{1}{4}\left(\frac{P}{akT}-1\right)\times\left(\frac{P}{akT}-2\right)\frac{kT}{D}+\cdots\right\}^N. \quad (8)$$

Now $G=-kT\ln Z_G$ and hence, after some reduction,

$$G=-NkT\ln\left(\frac{2\pi^2mk^2}{a^2D}\right)^{\frac{1}{2}}-NkT\ln T+PNA_0 - \frac{1}{2}\frac{N(kT)^2}{D}-\frac{5}{8}\frac{N(kT)^3}{D^2}-\cdots + \frac{P}{aD}\left\{\frac{3}{4}NkT+\frac{19}{16}\frac{N(kT)^2}{D}+\cdots\right\} - \left(\frac{P}{aD}\right)^2\left\{\tfrac{1}{4}ND+\cdots\right\}. \quad (9)$$

Although [following (6a)] we confined ourselves to $P/akT<1$, it may be shown that this equation remains applicable for the less restrictive condition $P/aD\ll 1$, so long as $kT/D\ll 1$. Thus

$$C_P\equiv -T\left(\frac{\partial^2 G}{\partial T^2}\right)_P=Nk\left\{1+\frac{kT}{D}+\frac{15}{4}\left(\frac{kT}{D}\right)^2+\cdots - \frac{P}{aD}\left(\frac{19}{8}\frac{kT}{D}+\cdots\right)+\cdots\right\}. \quad (10)$$

[14] This approximation is, of course, not imperative.

Also,

$$\left(\frac{\partial L}{\partial P}\right)_T\equiv\left(\frac{\partial^2 G}{\partial P^2}\right)_T = -\frac{N}{a^2D}\left\{\frac{1}{2}+\frac{11}{8}\frac{kT}{D}+\cdots-\frac{3}{4}\frac{P}{aD}\cdots\right\}, \quad (11)$$

essentially the compressibility;

$$\left(\frac{\partial L}{\partial T}\right)_P=\frac{Nk}{aD}\left\{\frac{3}{4}+\frac{19}{8}\frac{kT}{D}+\cdots-\frac{11}{8}\frac{P}{aD}\cdots\right\}, \quad (12)$$

essentially the thermal expansion;

and

$$C_{L_{(P=0)}}=Nk\left\{1-\frac{1}{8}\frac{kT}{D}-\frac{9}{32}\left(\frac{kT}{D}\right)^2-\cdots\right\}. \quad (13)$$

Damköhler, using his first analytical method (based on the partition function at constant length) obtained the leading terms of Eqs. (11) and (12), and Eqs. (10) and (13) as far as the terms linear in (kT/D). Since, however, he felt unable to extend this approach to give the higher terms in the expansions, he used a second method to obtain results intended to be valid at higher temperatures, which involved a numerical computation of the partition function at constant pressure which we have here evaluated analytically. These results differed appreciably from those he obtained by his first method, presumably because of inaccuracy in computations, and consequently those conclusions which he bases solely on his second method are incorrect.

The foregoing analysis may also be carried through with the inclusion of second-neighbor interaction if we neglect the repulsive part of the potential for these neighbors and ignore end effects on the assembly. Under these conditions, Eq. (7) becomes:

$$I=\left(\frac{\pi kT}{D(1+\Lambda)^2}\right)^{\frac{1}{2}}+\frac{akT}{P}\exp\left[-\frac{D}{kT}(1-\Lambda)^2\right],$$

where

$$\Lambda=2e^{-a\Lambda_0}, \quad (7')$$

and Eqs. (10) to (13) retain the same form with D replaced by $D(1+\Lambda)^2$.

Since the electrical resistivity in a solid at classical temperatures is approximately proportional to the mean-square amplitude of atomic vibrations, we shall assume that in this model the resistance would correspondingly be proportional to $\langle(x-\bar{x})^2\rangle_{Av}$. Then, in general,

$$\langle(x-\bar{x})^2\rangle_{Av}=-kT\frac{\partial^2}{\partial P^2}\left(\frac{G}{N}\right),$$

which from (11) gives

$$\langle(x-\bar{x})^2\rangle_{Av}=\frac{kT}{2a^2D}\left\{1+\frac{11}{4}\frac{kT}{D}+\cdots-\frac{3}{2}\frac{P}{aD}\cdots\right\}. \quad (14)$$

TABLE I. Morse constants derived from molecular data.

Element	A_0(A)	D (kcal/mole)	a(A^{-1})	$10^5\alpha$ [lin. exp. calc. from (12)]	$10^5\alpha$ (exptl.)	Ratio: $\frac{\alpha_{exptl.}}{\alpha_{calc.}}$
Li_2	2.67	26.4	0.83	2.52	5.6	2.2_2
Na_2	3.07	17.6	0.84	3.24	7.2	2.2_2
K_2	3.91	11.8	0.78	4.08	8.3	2.0_4

Under the condition that the length is maintained at the equilibrium value at $T=0$ (i.e., $L=NA_0$) we have, therefore,

$$R_{T,\,L=L_0}=B\left\{\frac{kT}{2a^2D}\left(1+\frac{1}{2}\frac{kT}{D}+\cdots\right)\right\}, \qquad (15)$$

where B represents the electron-lattice interaction which may be considered constant if L is fixed.

Finally, there is one further relationship which is of value. If the lattice potential were purely harmonic (i.e., expanding only to the quadratic term in x), its characteristic frequency would be proportional to $a\sqrt{D}$. Because of the higher-power (anharmonic) terms, however, this characteristic frequency depends on the compression or extension of the chain and, for an imposed relative atomic displacement x_0, the characteristic frequency for small vibrations is now proportional to $\sqrt{(a^2D-3a^3Dx_0)}$. From this it readily follows that the Grüneisen parameter, defined as $\gamma=-d\log\nu_c/d\log L$ (where ν_c is the characteristic frequency),[16] now has the value

$$\gamma=\tfrac{3}{2}aA_0. \qquad (16)$$

It can then be seen, using the leading terms of Eqs. (11), (12), and (13), that the Grüneisen relationship

$$\gamma=\alpha L/\beta C_v,$$

where

$$\alpha=\frac{1}{L}\left(\frac{dL}{dT}\right)_P, \quad \beta=\frac{1}{L}\left(\frac{dL}{dP}\right)_T,$$

is valid as a first approximation.

Equations (10) to (13) then represent the chief thermodynamic properties of what we may call the "condensed" state of the linear chain. Any comparison between these properties and those of a real solid must, at best, be very tentative. The solid inert gases very closely satisfy the condition of short-range forces which we have assumed, and if the transition from one to three dimensions introduces no qualitative features which are completely absent in the linear chain then these equations should indicate the kind of behavior which is to be expected when account is taken of an anharmonic potential function. Unfortunately, the data on such solids are at present meager in the region of temperatures where classical statistics are valid.

[16] For a discussion of the significance of γ in 1, 2 and 3 dimensions, see J. S. Dugdale and D. K. C. MacDonald, Phys. Rev. **89**, 832 (1953).

In making comparison with metals, the representation of the interatomic forces by a potential is obviously a much grosser approximation. To illustrate that, nevertheless, this model can provide a useful correlation, we compare in Tables I and II the observed thermal expansion coefficients at room temperature for the alkali metals with those derived using Eq. (12).

Qualitatively, it might appear that the foregoing analysis of the linear chain model could account rather well for the observed deviations from classical harmonic behavior. For example, the model predicts a specific heat at zero "pressure" which increases monotonically with temperature [Eq. (10)] and suggests an electrical resistance at zero "pressure" which rises more rapidly than linearly [Eq. (14)]—features found in a number of metals (for example, see MacDonald[2] for data on sodium). If, however, we make a closer examination, serious discrepancies arise. Taking sodium as probably the "best-behaved" of the monovalent metals —at least in an electronic sense (see MacDonald and Mendelssohn[16] and MacDonald and Pearson[17])—one finds that C_p is already rising much more rapidly than linearly with T in the room-temperature region where the factor $(15/4)(kT/D)^2$ in Eq. (10) should still be very small compared with (kT/D). Furthermore, C_v also *increases* with temperature (a feature common to sodium, potassium, and rubidium[18]) while in the present model C_L *diminishes* with rising temperature. In making comparison with the electrical resistance it is perhaps even more vital to do so under constant-volume conditions, since it is not yet known with certainty how the electron-lattice interaction energy [characterized by B in (15)] varies with volume. For sodium, the temperature variation of electrical resistance is significantly *less* rapid than linear when corrected to the

TABLE II. Morse constants derived from bulk metal data.[a]

Element	A_0(A)	D (kcal/mole)	a(A^{-1})	$10^5\alpha$ [lin. exp. calc. from (12)]	$10^5\alpha$ (exptl.)	Ratio: $\frac{\alpha_{exptl.}}{\alpha_{calc.}}$
Li	3.03	36.0	0.80	1.68	5.6	3.3_2
Na	3.72	26.2	0.67	2.25	7.2	3.2
K	4.50	21.9	0.53	2.82	8.3	2.9_4
Rb	4.9*	20.6	0.47	3.10	9.0	2.9_0
Cs	5.2*	18.7	0.44	3.44	9.7	2.8_2

[a] *Sources of data:* Morse constants (except those marked*): See J. C. Slater, *Introduction to Chemical Physics* (McGraw-Hill Book Company, Inc., New York and London, 1939), pp. 454–455; Morse constants (marked*): See W. Hume-Rothery, *Atomic Theory for Students of Metallurgy* (Institute of Metals, London, 1946), p. 216; Experimental expansion coefficients: See A. E. van Arkel, *Reine Metalle* (Springer, Berlin, 1939).

[16] D. K. C. MacDonald and K. Mendelssohn, Nature **161**, 972 (1948); Proc. Roy. Soc. (London) **A202**, 103 (1950).

[17] D. K. C. MacDonald and W. B. Pearson, Proc. Roy. Soc. (London) **A219**, 373 (1953).

[18] See, for sodium and potassium, F. E. Simon and W. Zeidler, Z. physik Chem. **123**, 383 (1926); for sodium, Dauphinee, MacDonald, and Preston-Thomas, Proc. Roy. Soc. (London) **A221**, 267 (1954); for rubidium, H. Preston-Thomas in Proceedings of the Third International Congress on Low Temperature Physics, Houston, 1953 (unpublished).

volume at absolute zero by using Bridgman's data.[19] The linear model, on the other hand, still predicts a positive deviation under these conditions [see Eq. (15)].

As we have already emphasized, it is not easy to say immediately whether such discrepancies are an intrinsic consequence of a one-dimensional model, or whether in fact one ought already to seek other sources than anharmonicity for the behavior observed. In anticipation of later work we may, however, mention that the falling specific heat at constant L appears to be a very general prediction of the one-dimensional model [see also Damköhler[6]].

Nevertheless, two relationships of interest can be derived which, because of their form, we may expect to translate into three dimensions without essential change. If dB/dV is neglected,

$$\left(\frac{d\log R}{d\log V}\right)_{p=0}=2\gamma, \tag{17a}$$

and

$$\left(\frac{d\log R}{d\log T}\right)_{p=0}\doteq 1+2\cdot 4\alpha\gamma T. \tag{17b}$$

Mott and Jones[20] derive analogous relations starting from the expression $R\propto T/M\theta^2$; their first is in agreement with ours, while they give essentially $1+2\alpha\gamma T$ for the second.[21] The small difference arises because the relationship $R\propto T/M\theta^2$ is only strictly valid for harmonic vibrations, while a part of the resistance variation in (17b) is due to the anharmonicity.

4. THE GAS-LIKE STATE AND THE TRANSITION REGION

It is clear from Eq. (7) that as $P\to 0$ the second term will ultimately become dominant, and if this term alone is considered, the partition function yields the free energy of a perfect linear "gas" whose specific heat at constant pressure is $\frac{3}{2}Nk$ and whose equation of state is $PL=NkT$. Let us therefore examine the behavior when the two terms of Eq. (7) are comparable. We have now

$$G=-NkT\ln\left(\frac{2\pi^2mk^2}{a^2D}\right)^{\frac{1}{2}}-NkT\ln T+PNA_0$$
$$-NkT\ln\left(1+\left(\frac{a^2DkT}{\pi}\right)^{\frac{1}{2}}\frac{1}{P}e^{-D/kT}\right). \tag{18}$$

Writing $p=P\sqrt{\pi}/aD$, $t=kT/D$, we have for the entropy

$$S=Nk\left\{\ln\left(\frac{2\pi^2mk^3}{a^2D}\right)^{\frac{1}{2}}+\ln t+1+\ln\left(1+\frac{\sqrt{t}}{p}e^{-1/t}\right)\right.$$
$$\left.+\left(\frac{1}{(p/\sqrt{t})e^{1/t}+1}\right)\left(\frac{1}{2}+\frac{1}{t}\right)\right\}, \tag{19}$$

and

$$C_P=Nk\left\{1+\left[2\left(1+\frac{p}{\sqrt{t}}e^{1/t}\right)\right]^{-1}\right.$$
$$\left.+\frac{p}{\sqrt{t}}e^{1/t}\left(\frac{1}{2}+\frac{1}{t}\right)\Big/\left(1+\frac{p}{\sqrt{t}}e^{1/t}\right)^2\right\}. \tag{20}$$

From this equation it can be seen immediately that as $t\to 0$, $C_p\to Nk$ and as $t\to\infty$, $C_p\to\frac{3}{2}Nk$. When, however, $(p/\sqrt{t})e^{1/t}=1$, i.e., on what we may term the vapor-pressure curve,

$$P=\left(\frac{a^2DkT}{\pi}\right)^{\frac{1}{2}}e^{-D/kT}\quad\text{and}\quad C_P=\frac{Nk}{4}\left\{5+\left(\frac{1}{2}+\frac{1}{t}\right)^2\right\}.$$

In the region for which the expression is valid, i.e., for $t\ll 1$, this gives very nearly $C_P=Nk/4t^2$, so that for $t=1/50$ (corresponding to about 0°C for sodium), $C_P=625Nk$. In Figs. 2 and 3 the specific-heat curves are shown for a force such that the transition is centered on 0°C, and it is evident that this specific-heat anomaly approximates to a latent heat. Correspondingly, from (19), we can see readily that as the temperature is increased through this critical range, the entropy rises rapidly by about ND/T, and hence that the equivalent latent heat is ND.

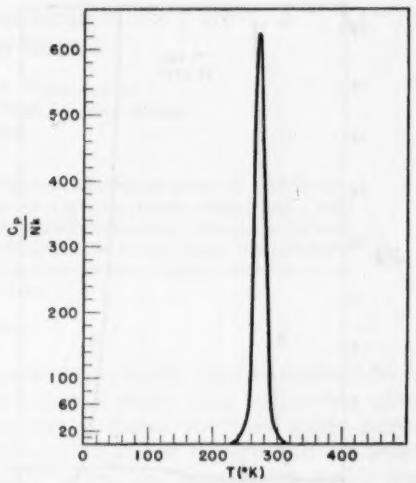

FIG. 2. Specific heat at constant force showing transition region from condensed to gas-like state. This figure shows the third term of Eq. (20); the first two terms are negligible on this scale.

[19] P. W. Bridgman, *The Physics of High Pressure* (Bell Publishing Company, London and New York, 1946).

[20] N. F. Mott and H. Jones, *Theory of Properties of Metals and Alloys* (Oxford University Press, London, 1936), pp. 268, 271.

[21] In fact, on their assumptions, Mott and Jones's Eq. (66) should read

$$\frac{R}{T}=\frac{R_0}{T_0}\{1+2\alpha\gamma(T-T_0)\},$$

where T_0 is some arbitrary reference temperature within the "classical" region. Their previous equation is of course correct.

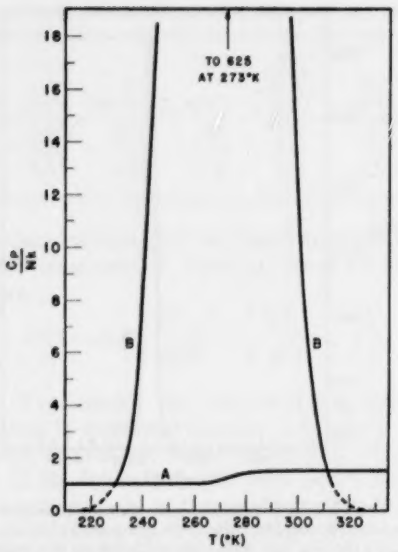

FIG. 3. Specific heat at constant force showing transition region from condensed to gas-like state. Curve A shows the first two terms of Eq. (20). Curve B shows the third term.

From Eq. (18) it also follows that the length is given by

$$L=NA_0+\frac{NkT}{P}\left\{1\Big/\left(1+\frac{p}{\sqrt{t}}e^{1/t}\right)\right\}, \qquad (21a)$$

which may also be written as an equation of state,

$$P(L-NA_0)=NkT\Big/\left\{1+\frac{P\sqrt{\pi}}{\sqrt{(a^2DkT)}}e^{D/kT}\right\}. \qquad (21b)$$

While it is evident from (21a) that L changes isothermally from NA_0 (characteristic of the condensed state) to NkT/P (characteristic of the gas-like state) as p runs from high to low values, it should be noted that the *compressibility* increases monotonically, showing no anomaly at the transition, in contrast to the striking behavior of the specific heat.

We are grateful to Professor J. C. Slater for helpful discussions and to Dr. S. K. Roy for help in checking the calculations. We are also indebted to Drs. C. Domb, R. B. Dingle, and A. B. Bhatia for useful criticisms.

APPENDIX

Since it has been suggested in the past (e.g., Peierls,[8] Domb[22]) that a linear chain would be inherently unstable due to thermal vibrations, we append an elementary proof that this is not the case.

Consider the propagation of a wave of thermal motion through any lattice of particles such that the *displacement* of the ith particle from its equilibrium position is given by

$$\xi_i=A\sin\{\omega(t+x_i/v)\}, \qquad (A1)$$

where x_i is the equilibrium position of the ith particle, v the velocity of sound, and ω the angular frequency. Then the mean square relative *displacement* of any two particles is given by

$$\langle(\xi_i-\xi_j)^2\rangle_{Av}=2A^2\sin^2\left(\frac{2\pi}{\lambda}\frac{\Delta x}{2}\right),\leqslant\frac{2\pi^2A^2\Delta x^2}{\lambda^2}$$

$$\text{for } \Delta x\leqslant\lambda/2, \qquad (A2)$$

where

$$\Delta x\equiv x_i-x_j.$$

If (A1) be a normal mode of the lattice, ignoring anharmonicity, then

$$(\tfrac{1}{2}mN\omega^2)(\tfrac{1}{2}A^2)=\tfrac{1}{2}kT,$$

where m is the mass of a particle and N is the number of particles in the lattice. Therefore,

$$\langle\Delta\xi^2\rangle_{Av}/\Delta x^2\leqslant 4\pi^2kT/mN\omega^2\lambda^2=kT/mNv^2. \qquad (A3)$$

If we now ignore dispersion so that v is not a function of frequency it is clear that (A3) is independent of frequency, and since the individual displacements due to each normal mode are themselves uncorrelated, the total fluctuation due to all normal modes, say $\mathfrak{N}$ in number, is given by

$$\langle\Delta\xi^2_{\text{tot}}\rangle_{Av}/\Delta x^2\leqslant\mathfrak{N}/N(kT/mv^2). \qquad (A4)$$

In the case of a one-dimensional lattice, $\mathfrak{N}/N\approx 1$, while for a three-dimensional lattice $\mathfrak{N}/N\approx 3$, and thus in general

$$\langle\Delta\xi^2_{\text{tot}}\rangle_{Av}/\Delta x^2\sim kT/mv^2$$

and the total relative displacement of neighboring atoms (setting $\Delta x=a$, the lattice constant) is given by

$$\langle\Delta\xi_n^2\rangle_{Av}\sim kTa^2/mv^2\sim h^2T/mk\theta^2.$$

It may be of interest (see also Frenkel[23]) to recall that the Lindemann theory of melting corresponds essentially to setting the dimensionless parameter $kT/mv^2\sim\frac{1}{10}$ at the melting point. However, the factor kT/mv^2 may also be considered immediately as the ratio $(V_i/v)^2$, where V_i is the thermal agitation velocity of the atoms; consequently the general success of the Lindemann theory could also thus be interpreted as evidence of a critical velocity (-ratio) involved in the melting process equally well with its derivation in terms of the displacement of atoms from their equilibrium positions.

[22] C. Domb, *Changements de Phase* (Society of Chemical Physics, Paris, 1952), p. 338.

[23] J. Frenkel, *Kinetic Theory of Liquids* (Oxford University Press, London, 1946), p. 138.

Probability Curves near Threshold for the Formation of He^+, Ne^{++}, A^{++}, Kr^{++}, and Xe^{++} by Electron Impact

W. M. Hickam, R. E. Fox, and T. Kjeldaas, Jr.
Westinghouse Research Laboratories, East Pittsburgh, Pennsylvania

(Received June 23, 1954)

The formation of He^+, Ne^{++}, A^{++}, Kr^{++}, and Xe^{++} as a function of electron energy is studied with essentially monoenergetic electrons. The He^+ curve obtained in this way for an energy range of eight volts above the ionization threshold does not exhibit any detectable departure from linearity. The accuracy is such that the difference between a 1.0 and 1.1 power curve is detectable for this energy range. The ionization probability curves of the doubly charged ions is interpreted as the superposition of linear excitation curves arising from each of the $^3P_2$, $^3P_1$, $^3P_0$, $^1D_2$, and $^1S_0$ states of the ions.

I. INTRODUCTION

IONIZATION probability curves obtained with monoenergetic electrons[1,2] for singly charged ions exhibit a threshold law which varies linearly with the excess electron energy. When this linear threshold law was applied to the analysis of ionization probability curves of Xe^+ and Kr^+ it was demonstrated that the observed structure could be correlated to energy levels of the ions.[3] For at least a few volts above threshold, the total ionization cross section could be treated as the sum of linearly increasing cross sections for each state of the ion. Certain departures from linearity over restricted regions were adequately explained by the autoionization of excited states of the atoms. More recently, Wannier[4] has extended the work of Wigner to ionization processes and has given theoretical arguments for a general threshold law applicable to singly charged ions formed by direct electron impact. Since the earlier reported work, instrumental modifications have made it possible to study ionization probability curves over a somewhat wider energy range. Because the singly charged helium ion has no energy levels within some 40 volts of the ionization potential, it was chosen for a further study of the threshold law.

A natural extension of these studies is the examination of ionization probability curves resulting from the formation of doubly charged ions of the rare gases. Curves obtained for doubly charged rare gas ions by other investigators[5–7] exhibited a considerably larger amount of curvature or "tailing" near the ionization threshold than did those for the singly charged ions. Since the tailing due to the electron energy spread should have been comparable for the two cases, the excessive tailing for doubly charged ions was believed to be characteristic of the formation of these ions.

The retarding potential difference method[8] developed by the authors[1,2] substantially reduces the effects of electron energy spread and thus makes possible a detailed examination of the structure of ionization probability curves. The fact that the doubly charged rare gas ions (except He^{++}) have five energy levels near the ground state allows one to extend the studies of the effects of energy levels on these curves.

II. EXPERIMENTAL RESULTS AND DISCUSSION

The experiments were performed with a mass spectrometer employing the RPD method of obtaining relative ionization probability curves. The instrument and procedure was similar to that employed in the study of singly charged ions[1,3] with the exception that an electron multiplier was used as the ion detector in order to obtain greater sensitivity.[9]

1. Ionization Probability of He^+

The ionization probability curve for He^+ is shown in Fig. 1 for an energy range of some 8 ev. The energy scale of this curve, as well as all subsequent curves, has been adjusted so as to make the appearance potential agree with the spectroscopically determined ionization

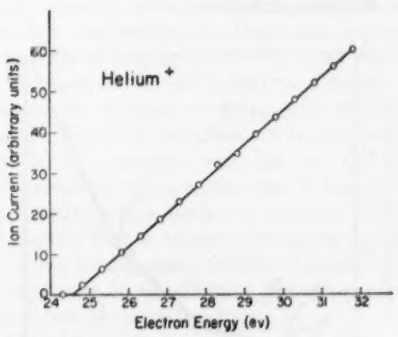

FIG. 1. Ionization probability curve for He^+. The onset has been made to agree with the spectroscopically determined ionization potential.

[1] Fox, Hickam, Kjeldaas, and Grove, Phys. Rev. **84**, 859 (1951)
[2] Fox, Hickam, Kjeldaas, and Grove, National Bureau of Standards Circular 522 (U. S. Government Printing Office, Washington, D. C., 1953), p. 211.
[3] Fox, Hickam, and Kjeldaas, Phys. Rev. **89**, 555 (1953).
[4] G. Wannier, Phys. Rev. **90**, 817 (1953).
[5] W. Bleakney, Phys. Rev. **36**, 1303 (1930).
[6] D. P. Stevenson and J. A. Hipple, Phys. Rev. **62**, 237 (1942).
[7] Dibeler, Mohler, and Reese, Bur. Standards J. Research **38**, 617 (1947).
[8] Hereinafter referred to as the RPD method.
[9] A detailed description of the apparatus and method is being prepared for publication as a separate paper.

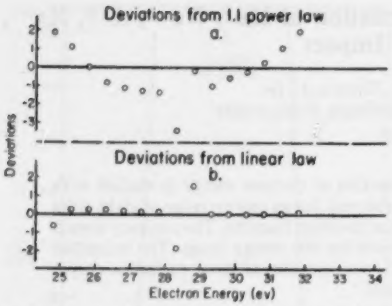

FIG. 2. (a) The deviation of the experimental points of Fig. 1 from the best fit by least squares to a 1.1 power curve. (b) The deviation of the same points from a linear (1.0) curve.

potential. In general, this correction was 0.3 ev or less. Figure 2 was prepared to exhibit quantitatively the degree of linearity obtained. The bottom curve shows the deviations of the points from a linear law, while the top curve shows the deviations of these same points from a 1.1 power law. These deviations were determined by least-squares fit in both cases. Wannier's[4] theory for a threshold law predicts that for an energy range small compared to the Rydberg energy,

$$I^+ = AE^{1.127},$$

where A is a constant of proportionality, and E is the electron energy in excess of the ionization potential. The curves in Fig. 2 definitely show that the 1.1 power law does not fit the data as well as the linear law. It must be noted, however, that this curve covers an energy range of 8 volts and thus may not be a true test of Wannier's law. If the energy range is limited to one or two electron volts, the scatter in the experimental points makes it impossible to determine which of the two power laws gives the best fit to the data. Thus, a comparison of the 1.1 power law and the linear law for other gases did not lead to a definite conclusion.

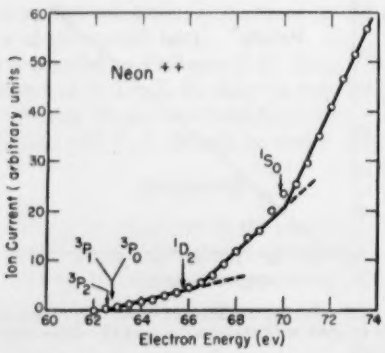

FIG. 3. An ionization probability curve for the formation of Ne^{++}. The onset has been made to agree with the spectroscopically determined ionization potential. The location of the energy levels are determined by spectroscopic data.

2. Ionization Probability of Ne^{++}, A^{++}, Kr^{++}, and Xe^{++}

The ionization probability curves for Ne^{++}, A^{++}, Kr^{++}, and Xe^{++} are shown in Figs. 3, 4, 5, and 6, respectively. The positions of the energy levels above the $^3P_2$ ground state as given by spectroscopic data[10] are shown on each curve by appropriately placed arrows.

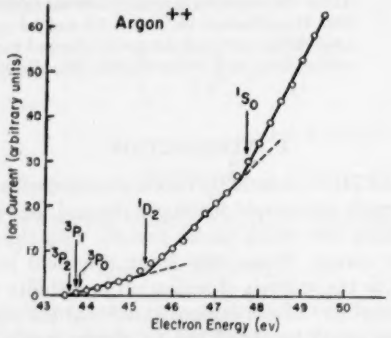

FIG. 4. Ionization probability curve for the formation of A^{++}. The energy scale has been adjusted to make the designated energy states agree with the spectroscopically determined values.

Actually, several runs were made for each gas, the curves shown here are believed to be typical. The curves are analyzed on the same basis as were the singly charged ions, i.e., the assumption is made that they are the sums of linearly rising cross sections for each level of the ion formed. In the present case, however, five states are involved: $^3P_2$, $^3P_1$, $^3P_0$, $^1D_2$, and $^1S_0$; and since the

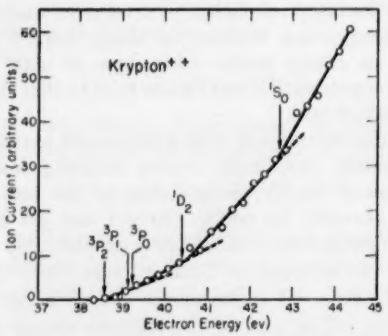

FIG. 5. Ionization probability curve for the formation of Kr^{++}. The energy scale has been adjusted to make the designated energy states agree with the spectroscopically determined values.

scatter is more severe, the correctness of this assumption cannot be demonstrated by using it to locate the energy levels and then comparing the results with spectroscopic

[10] All identified states are taken from C. E. Moore, *Atomic Energy Levels*, National Bureau of Standards Circular 467 (U. S. Government Printing Office, Washington, D. C., 1952); Landolt-Börnstein, *Zahlenwerte und Funktionen* (Springer, Berlin, 1950), Vol. I. The conversion factor used is 8066.8 cm^{-1} per volt from J. W. M. DuMond and E. A. Cohen, Phys. Rev. 82, 555 (1951).

data. Instead, the levels are located on the curves from the spectroscopic information, thus dividing the curves into successive energy regions. Within any one energy region the points should fall on a straight line. Figures 3 through 6 were prepared by fitting the best straight line to the data within each energy region. The relatively good fit of the points to the straight lines, and the agreement of the intersections of these straight lines with the marked levels is an indication that the assumption is at least approximately valid. The largest discrepancy occurs in the Ne^{++} curve where the average of three runs disagrees with the $^1D_2$ and $^1S_0$ levels by about 0.5 ev. In the other cases the agreement was usually better than 0.2 ev. Furthermore, a certain amount of departure from linearity is evident in the vicinity of the breaks for the neon and argon curves. Perhaps these deviations may be explained on the basis of contributions from autoionization. This effect would be similar to that observed in the case of the singly charged ions.[3]

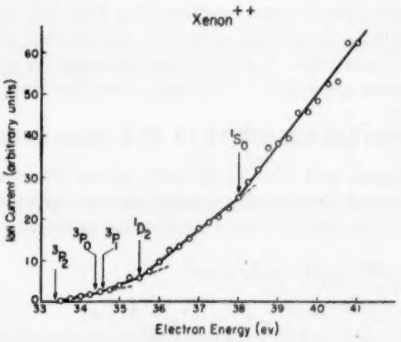

FIG. 6. Ionization probability curves for the formation of Xe^{++}. The energy scale has been adjusted to make the designated energy states agree with the spectroscopically determined values.

This method of analyzing the data implies that the threshold law for the formation of doubly charged ions in a single state goes linearly with the excess electron energy just as for singly charged ions. The initial portion of the ionization probability curve for Xe^{++} was studied in great detail and is shown in Fig. 7. This curve gives the most direct information of the group studied since the first excited energy level of this ion is about one volt higher than its ground state. A number of curves were taken in this region of which Fig. 7 is typical. It is apparent from the curve that there is no evidence for other than a linear threshold law. Wannier has reported in a private communication that the arguments which led to the 1.127 power law[4] for single ionization would

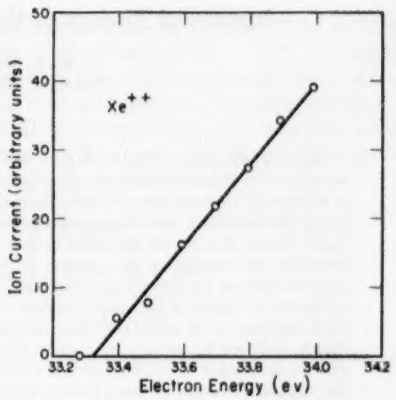

FIG. 7. The ionization probability curve for the formation of Xe^{++} taken between the $^3P_2$ ground state and the $^3P_0$ state to demonstrate the linearity of the ionization threshold law. The energy scale has been adjusted to make the onset of the curve agree with the spectroscopically determined ionization potential.

lead to a threshold law which varies approximately as the square of the excess electron energy in the case of double ionization.

Additional evidence for a linear rather than a higher power law is found in the early work of Bleakney[5] on the multiply charged ions of argon and neon. In his work the straight line sections of the ionization probability curves for A^{+++} and Ne^{+++} yield pronounced breaks which are in good agreement with the spectroscopically determined energy levels for the removal of two p electrons and a single s electron.

The results of the work reported here coupled with Bleakney's work provide evidence that a linear threshold law holds for doubly as well as singly charged ions. The deviations of the points from linearity in some of the curves are attributed to additional ionization processes such as autoionization. It is evident from the data that an appreciable electron energy spread would yield a smoothly varying curve and hence result in a loss of information concerning the ionization processes associated with the energy levels. The most positive test of the threshold law for the formation of doubly charged ions would be obtained from a study of He^{++}. Unfortunately, however, interferences from a background current of H_2^+, coupled with the low ion yield for $(He)^{++}$ prevented this investigation. It is hoped that in the near future such a study can be made using He^3.

The authors wish to express their appreciation to Dr. D. J. Grove for his many helpful discussions, and to other colleagues in the Physics Department for their critical review of the manuscript.

Improved Theory of the Zeeman Effect of Atomic Oxygen

K. KAMBE* AND J. H. VAN VLECK
Harvard University, Cambridge, Massachusetts
(Received June 9, 1954)

The previous calculations of Abragam and Van Vleck on the g factors of the $2p^4\ ^3P$ terms of atomic oxygen are refined by including exchange, using better wave functions, and not assuming that the charge distribution in which a $2p$ electron moves is spherically symmetric. In Sec. 2, a general technique is developed for calculating the relativistic and diamagnetic corrections to the g factors of complex atoms (Breit-Margenau and Lamb terms, etc.) by an expansion in spherical harmonics which is an extension of the well-known Slater procedure for computing the angular dependence of electrostatic energy. The integrals encountered are usually either of the Condon and Shortley F, G type, or variants thereof. The most important members are computed by means of the wave functions of Hartree, Hartree, and Swirles, based on a Fock self-consistent field, but some of the minor contributions are estimated with Slater wave functions improved by introducing slightly different screening constants for the $2s$ and $2p$ terms. When all corrections are comprised, including also the Schwinger electrodynamic shift, motion of nucleus, and deviations from Russell-Saunders coupling, the calculated values of the g factors for the $^3P_1$ and $^3P_2$ terms are, respectively, 1.500974, 1.500913, in excellent agreement with Rawson and Beringer's experimental determinations 1.500971, 1.500905.

I. INTRODUCTION

THE gyromagnetic ratios or g values have been measured quite accurately for a number of atoms by molecular beam or microwave techniques in several laboratories.[1] The precision is high enough to detect perceptible departures from the values given by simple vector-coupling theory. The deviations arise from a variety of causes, *viz.* (I) the Schwinger quantum-electrodynamical effect, (II) motion of the nucleus, (III) departures from Russell-Saunders coupling, (IV) relativistic or diamagnetic corrections, including modulation by the magnetic field of spin orbit and the velocity dependent part of the orbit-orbit interaction. The theory has been given for the helium atom by Perl and Hughes,[2] and extended to the n-electron case by Perl.[3] Abragam and Van Vleck[4] have independently developed the theory with particular reference to the oxygen atom. The reader is referred to the latter paper, henceforth called AVV for detailed explanation of the mechanisms underlying the various corrections (I)–(IV) mentioned above. Abragam and Van Vleck made certain approximations, *viz.*, they neglected exchange terms, and in treating the Zeeman contribution of a given electron, they assumed that the charge distribution of the remaining electrons is centro-symmetric, whereas in complex atoms such as oxygen it is not. Also in some places they used rather crude Slater wave functions. It is the purpose of the present article to refine their theory by not making these approximations. A general procedure will be presented in Sec. II, which is not confined to the particular case of the oxygen atom. It does not duplicate Perl's theory, as he was concerned mainly with deriving the basic Hamiltonian function [our Eq. (1)] and with applications to systems with only one valence electron. Our analysis in Sec. II furnishes an expansion in spherical harmonics applicable to arbitrary complex atoms.

II. MATRIX ELEMENTS IN THE nlm_lm_s SCHEME

Abragam and Van Vleck have shown that the relativistic and diamagnetic corrections are given by the expectation value of the Hamiltonian operator

$$\begin{aligned}\delta Z=&-\beta\mathbf{H}\cdot\textstyle\sum_i(\mathbf{l}_i+\boldsymbol{\sigma}_i)T_i/mc^2\\&-(\beta e^2Z/2mc^2)\textstyle\sum_i[\nabla_i(1/r_i)\times\mathbf{A}_i]\cdot\boldsymbol{\sigma}_i\\&+(\beta e^2/2mc^2)\textstyle\sum_{i\neq k}[\nabla_i(1/r_{ik})\times\mathbf{A}_i]\cdot\boldsymbol{\sigma}_i\\&+(\beta e^2/2mc^2)\textstyle\sum_{i\neq k}[\nabla_i(1/r_{ik})\times\mathbf{A}_i]\cdot 2\boldsymbol{\sigma}_k\\&-(e^3/2m^2c^3)\textstyle\sum_{i\neq k}[r_{ik}^{-1}(\mathbf{A}_i\cdot\mathbf{p}_k)\\&\qquad+r_{ik}^{-3}(\mathbf{r}_{ik}\cdot\mathbf{A}_i)(\mathbf{r}_{ik}\cdot\mathbf{p}_k)].\end{aligned}\quad(1)$$

The explanation of the notation used in Eq. (1) is given in AVV, and will not be repeated here, as the various symbols have their usual significance. We take the magnetic field along the z axis, whence

$$A_x=-\tfrac{1}{2}yH,\quad A_y=\tfrac{1}{2}xH,\quad A_z=0.$$

As shown in AVV the first term of (1), proportional to the kinetic energy T, is the relativistic correction proper; the second and third terms derive from spin orbit, the fourth from the spin-other orbit, and the fifth from the magnetic orbit-orbit interaction. The sum of the first three terms is called the Breit-Margenau, the fourth the Lamb correction.

We will show that it is possible to follow a procedure analogous to that in the theory of complex spectra. This analogy is not explicitly brought out in AVV, but is very helpful. The operators involved in (1) are

* Now at the College of Electro-Communications, Tokyo, Japan.

[1] P. Kusch and A. M. Foley, Phys. Rev. **74**, 250 (1948); Koenig, Prodell, and Kusch, Phys. Rev. **88**, 191 (1952); E. B. Rawson and R. Beringer, Phys. Rev. **88**, 677 (1952); Hughes, Tucker, Rhoderick, and Weinreich, Phys. Rev. **91**, 828 (1953); Brix, Eisinger, Lew, and Wessel, Phys. Rev. **92**, 647 (1953).

[2] W. Perl and V. Hughes, Phys. Rev. **91**, 842 (1953).

[3] W. Perl, Phys. Rev. **91**, 852 (1953).

[4] A. Abragam and J. H. Van Vleck, Phys. Rev. **92**, 1448 (1953), referred to as AVV.

generalizations of a quantity either of type F or G in the terminology of Condon and Shortley's book[6] (henceforth called TAS). Matrix elements of δZ in the nlm_lm_s scheme can be calculated by making expansions which are similar to those in TAS, but usually considerably more complicated. Transformation to the $SLJM$ scheme will be made in Sec. 3 by the method of diagonal sums.

In the nlm_lm_s scheme a state A can be specified by a complete ordered set $a^1, a^2, \cdots a^N$ of one-electron quantum numbers, where a^i stands for a set of four quantum numbers $n^il^im_l^im_s^i$. The corresponding orbital function is $R(nl)\Theta(lm_l)\Phi(m_l)$. The first two terms of (1) are of one-electron type, and so easy to evaluate. One readily finds that

$$(A|\delta Z_1|A)=-(\beta H/mc^2)\textstyle\sum_i(m_l^i+2m_s^i)(n^il^i|T|n^il^i), \tag{2}$$

$$(A|\delta Z_2|A)=\frac{\beta HZe^2}{mc^2}\textstyle\sum_i\left(n^il^i\left|\frac{1}{r}\right|n^il^i\right)\frac{[l^i(l^i+1)-1+(m_l^i)^2]m_s^i}{(2l^i-1)(2l^i+3)}. \tag{3}$$

Here, $(n^il^i|T|n^il^i)$ denotes the kinetic energy of a single n^il^i electron. The contributions from a closed shell to (2) or (3) vanish.

The third and fourth term of δZ will be treated simultaneously. Their combined diagonal element is

$$(A|\delta Z_3+\delta Z_4|A)=(\beta e^2/2mc^2)\textstyle\sum_{i\neq k}[(2m_s^i+4m_s^k)J(a^ia^k;a^ia^k)+6m_s^i\delta(m_s^i,m_s^k)J(a^ia^k;a^ka^i)], \tag{4}$$

where

$$J(ab;cd)=(ab|[\nabla_i(1/r_{ik})\times\mathbf{A}_i]_s|cd). \tag{5}$$

The spin dependence of (4) is such that the contributions from interactions within closed shells cancel out, but this is not true of the interactions between closed shells and valence electrons. We calculate the requisite values of (5) in the followlng way. We first note that

$$\left[\nabla_1\left(\frac{1}{r_{12}}\right)\times\mathbf{A}_1\right]_s=\frac{H}{2}\left[r_1\sin^2\theta_1\frac{\partial}{\partial r_1}+\cos\theta_1\sin\theta_1\frac{\partial}{\partial\theta_1}\right]\left(\frac{1}{r_{12}}\right), \tag{6}$$

and then make the standard expansion (notation as in TAS):

$$\frac{1}{r_{12}}=\sum_{k=0}^{\infty}\frac{r_<^k}{r_>^{k+1}}\frac{4\pi}{2k+1}\sum_{m=-k}^{k}\Theta_1(km)\Theta_2(km)\Phi_1(m)\Phi_2^*(m). \tag{7}$$

By appropriate recursion formulas (TAS p. 53), we express $\sin^2\theta_1\Theta_1(km)$, and $\cos\theta_1\sin\theta_1\partial\Theta_1/\partial\theta_1$ as linear combinations of $\Theta_1(k+2m)$, $\Theta_1(km)$, and $\Theta_1(k-2m)$. We thus obtain the result,

$$\left[\nabla_1\left(\frac{1}{r_{12}}\right)\times\mathbf{A}_1\right]_s=\frac{H}{2}\sum_{k=0}^{\infty}\frac{r_<^k}{r_>^{k+1}}\frac{4\pi}{2k+1}\sum_{m=-k}^{k}\left\{\mp\frac{(k\pm1)(k+1\pm1)+m^2}{2k+1\pm2}\Theta_1(km)\right.$$
$$\left.\pm\frac{(2k+1)}{(2k+1\pm2)}\left(\frac{[(k\pm1)^2-m^2][(k+1\pm1)^2-m^2]}{(2k-1\pm2)(2k+3\pm2)}\right)^{\frac{1}{2}}\Theta_1(k\pm2m)\right\}\Theta_2(km)\Phi_1(m)\Phi_2^*(m). \tag{8}$$

Here the upper or lower choice of sign applies according as $r_1>r_2$ or $r_1<r_2$. The integrations over φ involved in taking the expectation values are elementary. Those over θ lead to the well-known expressions of Condon and Shortley, *viz.*,

$$C^k(lm_l,l'm_l')=[2/(2k+1)]^{\frac{1}{2}}\int_0^{\pi}\Theta(km_l-m_l')\Theta(lm_l)\Theta(l'm_l')\sin\theta d\theta, \tag{9}$$

whose numerical values are tabulated in TAS, p. 178. The radial integrals involved in the direct in distinction from exchange terms are of the form

$$F_>^k(nl,n'l')=\int_0^{\infty}dr_1\int_0^{r_1}\frac{r_2^k}{r_1^{k+1}}R_1^2(nl)R_2^2(n'l')dr_2. \tag{10}$$

Our expressions $F_>^k$ are somewhat different from the Condon and Shortley integrals F^k, which can be defined in terms of the $F_>^k$ as follows:

$$F^k(nl,n'l')=F_>^k(nl,n'l')+F_>^k(n'l',nl).$$

[6] E. V. Condon and G. H. Shortley, *The Theory of Atomic Spectra* (Cambridge University Press, Cambridge, 1935), referred to as TAS.

For the special case $n'=n$, $l'=l$, this relation becomes

$$F_>{}^k(nl,nl)=\tfrac{1}{2}F^k(nl,nl). \tag{11}$$

We find

$$J(ab;ab)=\tfrac{1}{2}H\sum_{k=0}^{\infty}\frac{(k+1)(k+2)}{(2k+3)}[F_>{}^k(n^al^a,n^bl^b)C^k(l^bm_l{}^b,l^bm_l{}^b)$$
$$+F_>{}^{k+2}(n^bl^b,n^al^a)C^{k+2}(l^bm_l{}^b,l^bm_l{}^b)][C^{k+2}(l^am_l{}^a,l^am_l{}^a)-C^k(l^am_l{}^a,l^am_l{}^a)]. \tag{12}$$

In a similar fashion we find that the exchange integrals are given by the following expressions:

$$J(ab;ba)=\frac{H}{4}\sum_{k=0}^{\infty}\sum\nolimits_{\pm}G^k(n^al^a;n^bl^b)\left\{\frac{2(m_l{}^a-m_l{}^b)^2-(2k^2+2k-1)}{(2k-1)(2k+3)}C^k(l^am_l{}^a,l^bm_l{}^b)\right.$$
$$\left.\pm\left(\frac{[(k\pm1)^2-(m_l{}^a-m_l{}^b)^2][(k+1\pm1)^2-(m_l{}^a-m_l{}^b)^2]}{(2k+1\pm2)^2}\right)^{\frac{1}{2}}C^{k\pm2}(l^am_l{}^a,l^bm_l{}^b)\right\}C^k(l^am_l{}^a,l^bm_l{}^b), \tag{13}$$

where G^k is defined as in Condon and Shortley. [There is no need to introduce also an exchange integral $G_>{}^k$ analogous to (10), as $G_>{}^k=\frac{1}{2}G^k$.] In (13) and elsewhere the symbol $\sum_\pm$ means that there is to be a summation sign over both sign choices.

The calculation of the fifth or orbit-orbit term of δZ is based on the same general sort of procedure as for the other terms, but is considerably more laborious. The final result is[6]

$$(A\,|\,\delta Z_5\,|\,A)=-(\beta e^2/mc^2h)\sum\nolimits_{i\neq k}[M(a^ia^k;a^ia^k)-\delta(m_s{}^i,m_s{}^k)M(a^ia^k;a^ka^i)], \tag{14}$$

with

$$M(ab;ab)=\tfrac{1}{2}hH\sum_{k=1}^{\infty}[F_>{}^{k-1}(n^al^a,n^bl^b)+F_>{}^{k+1}(n^bl^b,n^al^a)]\left[\frac{k(k+1)(2l^b+1)}{(2k+1)^2(2l^b-1)}\right]^{\frac{1}{2}}[\textstyle\sum_\pm\pm C^{k\pm1}(l^am^a,l^am^a)]$$
$$\times[\textstyle\sum_\pm\pm(l^b\mp m_l{}^b)^{\frac{1}{2}}(l^b\mp m_l{}^b-1)^{\frac{1}{2}}C^k(l^bm_l{}^b,l^b-1m_l{}^b\pm1)], \tag{15}$$

$$M(ab;ba)=\tfrac{1}{2}hH\sum_{k=0}^{\infty}(\textstyle\sum_\pm G^{k\pm1}(n^al^a,n^bl^b))$$
$$\times\left\{\textstyle\sum_\pm(m_l{}^a-m_l{}^b\pm2)\left[l_a\frac{(l^a\pm m_l{}^a+1)(l^a\pm m_l{}^a+2)}{(2l^a+1)(2l^a+3)}(C^k(l^a+1m_l{}^a\pm1,l^bm_l{}^b))^2\right.\right.$$
$$+\left(\frac{(l^a\mp m_l{}^a-1)(l^a\mp m_l{}^a)(l^a\pm m_l{}^a+1)(l^a\pm m_l{}^a+2)}{(2l^a-1)(2l^a+1)^2(2l^a+3)}\right)^{\frac{1}{2}}C^k(l^a+1m_l{}^a\pm1,l^bm_l{}^b)C^k(l^a-1m_l{}^a\pm1,l^bm_l{}^b)$$
$$\left.-(l^a+1)\frac{(l^a\mp m_l{}^a-1)(l^a\mp m_l{}^a)}{(2l^a-1)(2l^a+1)}(C^k(l^a-1m_l{}^a\pm1,l^bm_l{}^b))^2\right]$$
$$+2(m_l{}^a-m_l{}^b)\left[l_a\frac{(l^a+1-m_l{}^a)(l^a+1+m_l{}^a)}{(2l^a+1)(2l^a+3)}(C^k(l^a+1m_l{}^a,l^bm_l{}^b))^2\right.$$
$$-\left(\frac{(l^a-m_l{}^a)(l^a+m_l{}^a)(l^a+1-m_l{}^a)(l^a+1+m_l{}^a)}{(2l^a-1)(2l^a+1)^2(2l^a+3)}\right)^{\frac{1}{2}}C^k(l^a+1m_l{}^a,l^bm_l{}^b)C^k(l^a-1m_l{}^a,l^bm_l{}^b)$$
$$\left.\left.-(l^a+1)\frac{(l^a-m_l{}^a)(l^a+m_l{}^a)}{(2l^a-1)(2l^a+1)}(C^k(l^a-1m_l{}^a,l^bm_l{}^b))^2\right]\right\}$$
$$+\tfrac{1}{2}hH(m_l{}^a-m_l{}^b)\sum_{k=0}^{\infty}\left\{\int_0^\infty\int_0^\infty\left[\frac{(1-k)}{2k+1}r_1r_2\frac{r_<{}^k}{r_>{}^{k+1}}+r_2{}^2\frac{r_<{}^{k+1}}{r_>{}^{k+2}}-\frac{k+4}{2k+5}r_1r_2\frac{r_<{}^{k+2}}{r_>{}^{k+3}}\right]\right.$$
$$\left.\times R_1(n^al^a)R_1(n^bl^b)R_2(n^bl^b)\frac{d}{dr_2}\frac{R_2(n^al^a)}{r_2}dr_1dr_2\right\}[C^{k+1}(l^am_l{}^a,l^bm_l{}^b)]^2. \tag{16}$$

In concluding the present section, it should be mentioned that the sums over k in the various expressions which we have derived do not really involve an infinite number of terms and instead in any practical case are limited to a few terms, as is usual for spherical harmonic expansions in atomic spectra. The reason that this is true is that $C^k(lm,l'm')$ vanishes unless k, l, and l' satisfy the so-called triangular condition $k+l+l'=2q$ (q integral), $|l-l'|\leq k\leq l+l'$.

III. APPLICATION TO THE OXYGEN ATOM

The preceding section gives the general technique for calculating matrix elements in the nlm_sm_l system of representation. The application to oxygen proceeds by specializing the results to the configuration $2p^4$. In addition, it is necessary to transform the results to the *LSJM* system of representation. This is accomplished by using the invariance of the diagonal sum, together with the fact that the transformation properties of all the first-order Zeeman terms under rotations are such that they must be proportional to the magnetic quantum number M. This feature or trick is explained in AVV and so need not be described here. Some of the manipulations involved in δZ_5 are fairly complicated, and as a check on the accuracy of the calculations they have been reduced to the final form by grouping the integrals in two different ways in the intermediate steps, of which we omit the details.

The final forms for the corrections to the g factors of the $^3P_1$ and $^3P_2$ terms, which as in AVV we denote by Δg_1 and Δg_2, prove to be[6]

$$\Delta g_1=(8mc^2)^{-1}\{-12\langle T\rangle_{Av}+2Z\langle 1/r\rangle_{Av}-[5F^0(2p,2p)-(11/5)F^2(2p,2p)$$
$$+\textstyle\sum_{n=1,2}(4F_>{}^2(2p,ns)+(16/3)F_>{}^0(ns,2p)-(8/5)F_>{}^2(2p,ns))]$$
$$-2[F^0(2p,2p)+F^2(2p,2p)+\textstyle\sum_{n=1,2}(4/3)(F_>{}^0(ns,2p)+F_>{}^0(2p,ns)$$
$$-(7/20)G^1(2p,ns)-\tfrac{1}{4}G^{-1}(2p,ns)-(1/10)G^3(2p,ns)-\tfrac{3}{4}R(2p,ns))]\}, \quad (17)$$

$$\Delta g_2=\Delta g_1-(5mc^2)^{-1}\{(Z/2)\langle 1/r\rangle_{Av}-[\tfrac{3}{4}F^0(2p,2p)+\tfrac{3}{4}F^2(2p,2p)$$
$$+\textstyle\sum_{n=1,2}(-F_>{}^0(2p,ns)+(4/3)F_>{}^2(2p,ns)-G^1(2p,ns)]\}. \quad (18)$$

Here, $\langle T\rangle_{Av}$ and $\langle 1/r\rangle_{Av}$ denote the mean values of the kinetic energy and $1/r$ for a $2p$ electron, and G^{-1} is the exchange integral G^k for $k=-1$. The definition of $R(2p,ns)$ is

$$R(2p,ns)=\tfrac{1}{3}\int_0^\infty\int_0^\infty\left(r_1r_2\frac{1}{r_>}+r_2{}^2\frac{r_<}{r_>{}^2}-\tfrac{1}{5}r_1r_2\frac{r_<{}^2}{r_>{}^3}\right)R_1(2p)R_1(ns)\left(R_2(2p)\frac{d}{dr_2}\frac{R_2(ns)}{r_2}-R_2(ns)\frac{d}{dr_2}\frac{R_2(2p)}{r_2}\right)dr_1dr_2. \quad (19)$$

In Table I we give the numerical values which we use for the various integrals, and also the methods by which these values are calculated. A few comments on the latter are in order. Many of the integrals have already been computed in the paper of Hartree, Hartree, and Swirles[7] (henceforth abbreviated to HHS), or can be estimated quite accurately from data in it. More of the integrals are given in an earlier article by Hartree and Black[8] (HB), which does not, however, include the Fock exchange terms. It is not consistent to calculate some integrals with wave functions which include exchange, and others with functions which do not, but the relatively minor modifications caused by exchange can be extrapolated by comparing the results for the integrals which have been computed by both methods. Some integrals such as G^1 are so small or have such

TABLE I. The numerical values of $\langle T\rangle_{Av}$ and various radial integrals involved in the expressions for Δg_1 and Δg_2. (All values are in atomic units.)

Integral	Numerical value	Integral	Numerical value
	$13^g\times10^{-6}$		1.11[a]
$F^0(2s,2p)$	0.773[b]	$F^0(1s,2p)$	1.099[c]
$F^0(2p,2p)$	0.754[b]	$F_>{}^0(2p,1s)$	1.089[d]
$F^2(2p,2p)$	0.336[b]	$F_>{}^0(2p,2s)$	0.409[c]
$G^1(1s,2p)$	0.092[f]	$F_>{}^2(2p,1s)$	0.207[d]
$G^1(2s,2p)$	0.472[b]	$F_>{}^2(2p,2s)$	0.179[c]
$G^{-1}(2p,1s)$	0.173[g]	$G^{-1}(2p,2s)$	1.354[g]
$G^3(2p,1s)$	0.032[g]	$G^3(2p,2s)$	0.291[g]
$R(2p,1s)$	−0.123[g]	$R(2p,2s)$	−0.042[g]

[a] Calculated by numerical integration of the HHS wave function, and also by integration of the Löwdin analytical function. The value 1.11 is obtained in both cases.
[b] Calculated by Hartree, Hartree, and Swirles.
[c] Extrapolated from HB by assuming $F^0(1s,2p)=F^0(1s,2p)_{HB}+\langle 1/r\rangle_{HHS}-\langle 1/r\rangle_{HB}$.
[d] Calculated by the formula $F_>{}^k(2p,1s)=\langle r^k\rangle_{1s}\langle r^{-k-1}\rangle_{2p}-F_>{}^{-k-1}(1s,2p)$. The first term is computed with Löwdin functions, while the second is small and is adequately calculated with the modified Slater functions.
[c] Derived from HHS by making a rough estimate of the small difference $F_>{}^k(2p,2s)-\frac{1}{4}F^k(2p,2p)$.
[f] Calculated by D. R. Hartree and M. M. Black.
[g] Calculated from the modified Slater functions.

[6] Mimeographed pages of the algebraic details of the derivation of Eqs. (13)–(18) can be obtained by writing to Miss Esther Reynolds, Librarian, Lyman Laboratory, Harvard University, Cambridge, Massachusetts. This supplementary material is also available as Document with the ADI Auxiliary Publications Project, Photoduplication Service, Library of Congress, Washington 25, D. C. A copy may be secured by citing the Document number 4326 and by remitting $1.25 for photoprints or $1.25 for 35-mm microfilm. Advance payment is required. Make checks or money orders payable to: Chief, Photoduplication Service, Library of Congress.

[7] Hartree, Hartree, and Swirles, Trans. Roy. Soc. (London) **A238**, 229 (1939), referred to as HHS.

[8] D. R. Hartree and M. M. Black, Proc. Roy. Soc. (London) **A139**, 311 (1933), referred to as HB.

small coefficients that the distinction between HHS and HB is immaterial. There are also available the elaborate analytical wave functions of Löwdin,[9] which are quite accurate analytical descriptions of the wave functions obtained numerically by HHS, but it is too laborious to calculate anything but one-electron integrals by means of them. When no other method is available, we have utilized a modified form of Slater wave function. The modification consists in using slightly different, rather than identical exponents, for the $2s$ and $2p$ wave functions, *viz.*,

$$R(2s)=Br^2e^{-2.195r}, \quad R(2p)=B'r^2e^{-2.075r}. \tag{20}$$

The exponents have been determined so as to yield the same values of $F^0(2s,2s)$ and $F^0(2p,2p)$ as those obtained numerically with HHS wave functions. Fortunately, all the terms which must be estimated only by means of the modified Slater functions are relatively minor, so that the absence of high precision therein will not vitiate our results.

By far the most important integral or expectation value to know accurately is that involving the mean kinetic energy. This has been calculated by the following three methods, which agree to within one percent:

(a) Direct integration of the kinetic energy operator with Löwdin wave functions.

(b) A method which utilizes the conservation of energy, and which expresses T as a difference between the total energy and an appropriate potential energy. The relevant formula is

$$\begin{aligned}\langle T\rangle_{Av}=&-\tfrac{1}{2}\epsilon_{2p,2p}+Z\langle 1/r\rangle_{Av}-2F^0(2p,1s)-2F^0(2p,2s)\\&-3F^0(2p,2p)+(3/10)F^2(2p,2p)\\&+\tfrac{1}{3}G^1(2p,1s)+\tfrac{1}{3}G^1(2p,2p),\end{aligned} \tag{21}$$

where $\epsilon_{2p,2p}$ is the energy parameter of HHS (the quantity conserved according to their wave equation—not to be confused with a physical ionization energy). The various integrals in this formula are calculated as shown in the table, mainly with the numerical data of HHS.

(c) A generalized virial theorem. Because of the Fock exchange terms, the virial theorem does not have its usual elementary form, but from the HHS wave equation one deduces that

$$\begin{aligned}\langle T\rangle_{Av}=&\tfrac{1}{2}Z\langle 1/r\rangle_{Av}-F_>{}^0(2p,1s)-F_>{}^0(2p,2s)\\&-\tfrac{3}{4}F^0(2p,2p)+(3/40)F^2(2p,2p)\\&+(1/6)[G^1(1s,2p)+G^1(2s,2p)]+\tfrac{1}{3}\sum_{n=1,2}\\&\times\int_0^\infty Y_1(ns,2p)R_1(ns)(dR_1(2p)/dr_1)dr_1,\end{aligned} \tag{22}$$

where

$$\begin{aligned}Y_1(ns,2p)=&\int_0^{r_1}(r_2/r_1)R_2(ns)R_2(2p)dr_2\\&+\int_{r_1}^\infty(r_1^2/r_2)R_2(ns)R_2(2p)dr_2.\end{aligned} \tag{23}$$

The agreement of the mean kinetic energy as obtained from (b) and (c) is a check on the accuracy of the HHS wave functions. This comparison is of interest for this reason quite irrespective of the application to oxygen, and furnishes a method of checking the accuracy of wave functions based on Hartree-Fock fields for other atoms than oxygen.[10] This is one reason why we have included formula (22). The numerical check is, of course, only on the numerical accuracy with which the equations are integrated, and supplies no information concerning the physical soundness of the mathematical model itself.

The values of $\langle T\rangle_{Av}$ obtained by methods (a), (b), and (c) are, respectively, 136, 135, and 133×10^{-6}.

TABLE II. Calculated and observed corrections Δg_1 and Δg_2 to the g factors of the $2p^4\,{}^3P_1$ and ${}^3P_2$ terms of oxygen. (The uncorrected value is $g=1.5$ for both terms.)

Correction		Δg_1 KVV[a]	Δg_1 AVV[b]	Δg_2 KVV[a]	Δg_2 AVV[b]
$\langle\delta Z_1\rangle$		−203		−203	
$\langle\delta Z_2\rangle$		+118	−158[c]	+71	−198[c]
$\langle\delta Z_1+\delta Z_2\rangle$	(direct)	−71		−70	
$\langle\delta Z_3+\delta Z_4\rangle$	(exchange)	+2	...	+8	...
$\langle\delta Z_3\rangle$	(direct)	−34	−31	−28	−31
$\langle\delta Z_4\rangle$	(exchange)	+15	...	+9	...
Relativistic and diamagnetic		−173	−189	−213	−229
Motion of nucleus		+2	+2	+2	+2
Departure from Russell-Saunders coupling		0	0	−21	−21
Schwinger-Karplus-Kroll		+1145	+1145	+1145	+1145
TOTAL		974	958	913	897
Observed		971		905	

[a] Kambe and Van Vleck (present work).
[b] Abragam and Van Vleck (see reference 4).
[c] Sum of the Breit-Margenau and Lamb corrections which is $\langle\delta Z_1+\delta Z_2\rangle+\langle\delta Z_3+\delta Z_4\rangle$ (direct) in the present calculation. The contribution of the Breit-Margenau corrections (without exchange) is
-142×10^{-6} (for Δg_1), -164×10^{-6} (Δg_2) (K. & V.V.)
-130×10^{-6} (Δg_1), -156×10^{-6} (Δg_2) (A. & V.V.)

IV. COMPARISON WITH EXPERIMENT FOR OXYGEN

In Table II we list the various corrections to the g factor which we have calculated. The earlier values obtained in AVV are appended for comparison. We also tabulate the various other corrections which must be included and are the same as given in AVV. The new grand total is seen to agree well with the measurements of Rawson and Beringer. The discrepancy is less than either the experimental or theoretical error.

The one fact which is a little disconcerting is that the difference $\Delta g_1-\Delta g_2$ is not given with higher precision than the absolute values themselves, *viz.*,

$$\Delta g_1-\Delta g_2=61\times10^{-6}\ \text{(calc)}, \quad \Delta g_1-\Delta g_2=66\times10^{-6}\ \text{(obs)}.$$

Experimentally, $\Delta g_1-\Delta g_2$ can probably be measured more accurately than g_1 or g_2, and this should also be

[9] P. O. Löwdin, Phys. Rev. **90**, 120 (1953).

[10] Our formulas (21) and (22) are specialized to the configuration $2p^4$, but there are analogous expressions in other cases.

true of the theoretical calculations. In fact, the orbit-orbit corrections (as well as the more certain electrodynamical corrections and those for the motion of the nucleus) cancel out entirely from $\Delta g_1 - \Delta g_2$ [see Eq. (18)], and these were the only corrections in which we had to resort to modified Slater wave functions. The deviations from Russell-Saunders coupling are involved solely in the difference $\Delta g_1 - \Delta g_2$, and it is natural to blame them for the discrepancy. However, the spin-orbit parameter involved therein can be estimated quite accurately by extrapolation from atomic spectra [unless perchance, the nondiagonal element $(^3P_2|\zeta_{2p}|^1D_2)$ differs markedly from the diagonal elements[11] $(^1P|\zeta_{2p}|^1P)$ or $(^3P|\zeta_{2p}|^3P)$]. In any case, a discrepancy of only 5×10^{-6} is, after all, very small. Complete reliance cannot be placed on even the most perfect Hartree-Fock wave functions used to compute F^k, etc., because of approximations basic to the self-consistent field model. The HHS wave functions, for instance, give a spin-orbit parameter about 10 percent too high. (The discrepancy in $\Delta g_1 - \Delta g_2$ would, incidentally, disappear almost completely if we used the HHS rather than spectroscopic value of ζ_{2p} in calculating the deviations from Russell-Saunders coupling, but there appears to be no logical grounds for so doing.) We are hence probably hoping for too much precision, and it certainly does not seem repaying to push further any calculations based on the Hartree-Fock model. The experimental measurements of Rawson and Beringer were originally essayed to see whether there was experimental evidence for the Schwinger electrodynamical corrections in complex atoms. As a result of the present paper we can certainly say that these corrections are confirmed in oxygen, though of necessity with less precision than in atoms with a single valence electron.

The authors wish to thank the U. S. Office of Naval Research for making it possible for one of them (K.K.) to be at Harvard during the writing of this paper.

[11] G. W. King and J. H. Van Vleck, Phys. Rev. **56**, 464 (1939), find that the diagonal and off-diagonal elements of ζ are appreciably different in mercury, but in light atoms like oxygen the difference may not be as great.

PHYSICAL REVIEW VOLUME 96, NUMBER 1 OCTOBER 1, 1954

Decay Scheme of I^{132}*

H. L. Finston and W. Bernstein
Brookhaven National Laboratory, Upton, New York
(Received June 8, 1954)

The radiations of 2.33-hr I^{132} have been investigated with magnetic lens and scintillation spectrometers. Beta rays of 2.12 (18 percent), 1.53 (24 percent), 1.16 (23 percent), and 0.9 (20 percent) Mev have been identified. Gamma rays of 0.528 (25 percent), 0.624 (6 percent), 0.673 (100 percent), 0.777 (75 percent), 0.96 (20 percent), 1.16 (8 percent), 1.40 (11 percent), 1.96 (5 percent), and 2.2 (2 percent) Mev have been observed, and their coincidences are tabulated. A possible decay scheme is proposed which is consistent with the experimental data.

INTRODUCTION

THE routine production[1] of 77-hr Te^{132}—2.33-hr I^{132} has made available high purity, high specific activity I^{132} sources for the first time. Previous investigations reported β rays[2] with maximum energies of 2.2 and 0.9 Mev, and γ rays[3] of 0.67, 1.41, and 1.99 Mev. A γ ray of energy greater than 2.23 Mev was reported[4] since photoneutron production in D_2O was observed. In view of the uncertainty in the existing information, it seemed advisable to undertake the present investigation.

Source Preparation

The radioactive Te was separated with carrier Te from pile-irradiated U by a series of hydrolytic precipitations of TeO_2 alternated with precipitation of elemental Te by means of $NaHSO_3$ solution. The final solution consisted of Na_2TeO_3 in NaOH.

Since the half-life of I^{132} is short, it was desirable to use a Te^{132}—I^{132} equilibrium source for the β-ray energy measurements. This source was prepared by evaporating a small aliquot of the above solution on 0.1 mg/cm² nylon one week after the initial Te separation; the I which had grown in during the one-week delay was driven off during the evaporation. Sufficient time was then allowed for the I^{132} to attain equilibrium with the Te^{132} before the measurements were begun. The one-week delay before the separation of Te from I allowed

* Work performed under the auspices of the U. S. Atomic Energy Commission.
[1] Stang, Tucker, Banks, Doering, and Mills, Nucleonics (to be published).
[2] Novey, Sullivan, Coryell, Newton, Sleight, and Johnson, in *Radiochemical Studies: The Fission Products* (McGraw-Hill Book Company, Inc., New York, 1951), Paper No. 135, National Nuclear Energy Series, Plutonium Project Record, Vol. 9, Book 2, part 5, p. 958.
[3] Maienschein, Bair, and Baker, Phys. Rev. **83**, 477 (1951).
[4] L. S. Goldring, Brookhaven National Laboratory Quarterly Progress Report, July 1-September 30, 1951 (unpublished); Brookhaven National Laboratory Report BNL-132 (S-11) (unpublished).

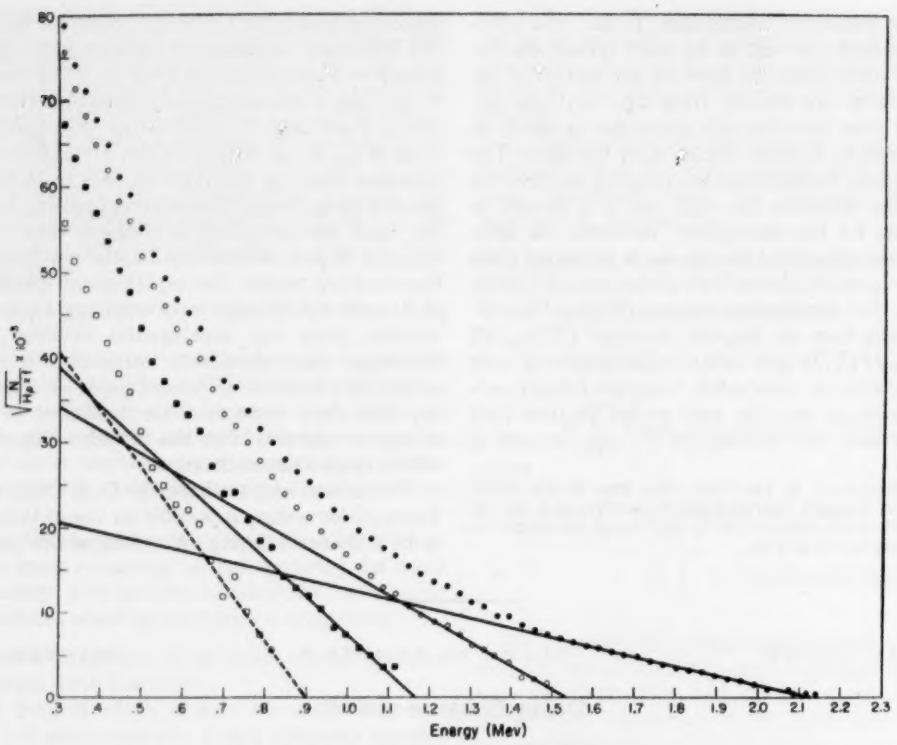

FIG. 1. Kurie plot analysis of the I^{132} β-ray spectrum.

for the decay of the primary short-lived Te fission product activities (2-min Te^{133}, 44-min Te^{134}, 2-min Te^{135}, 25-min Te^{131}, 72-min Te^{129}, and 9.3-hr Te^{127}). The Te isomers, 115-day Te^{127m}, 33-day Te^{129m} and 30-hr Te^{131m}, which are the parents of 9.3-hr Te^{127}, 72-min Te^{129} and 25-min Te^{131}, respectively, were not removed by this procedure. However, a consideration of the fission yields[5] and the half-lives indicates that the contribution from these activities could not be greater than 2 percent of that due to the I^{132}. The 77-hr Te^{132}, which was of course present, did not obscure the results for reasons which will be discussed later. A similar source was mounted in a stainless steel cup for investigation of the externally converted γ-ray spectrum.

In order to obtain an unambiguous picture of the I^{132} γ-ray spectrum, it was desirable to use "pure" I^{132} sources for these measurements. These sources were prepared from the final Te solution in the following manner: After an initial delay of at least 48 hours, which permitted the short-lived Te activities to decay, the daughter products were separated from the Te solution. Since this separation was performed at varying times after the initial Te separation, variable amounts of Te^{131m} and Te^{132} were present in the solution. A 2–4 hour growth period, after which the I was separated from the Te solution, resulted in a negligible contribution from the 8-day I^{131} arising from the Te^{131m} which may have been present. The I^{132} was precipitated as AgI and mounted.

β-RAY MEASUREMENTS

The β-ray spectrum was investigated using a lens spectrometer with a resolution of 2.7 percent. Figure 1 shows a Kurie plot analysis of the I^{132} β-ray spectrum. The experimental points were corrected for the decay during the experiment. Analysis of the Kurie plot gave the following β-ray energies and approximate intensities: 2.12±0.04 Mev (18 percent), 1.53±0.07 Mev (24 percent), and 1.16±0.07 Mev (23 percent). A more doubtful β-ray group with an energy of 0.9±0.1 Mev and an intensity of approximately 20 percent was also observed. The K-shell internal conversion electrons from the 0.673-Mev γ ray were carefully determined; the sources were too weak to permit accurate measurement of the other internal conversion electrons. It is obvious that the Te^{132} β rays, which are of much lower energy[6] (approximately 0.22 Mev), did not interfere with these energy and intensity determinations.

[5] A. C. Pappas, Technical Report No. 63, Laboratory for Nuclear Science, Massachusetts Institute of Technology, 1953 (unpublished).

[6] L. M. Langer and G. Ford, Atomic Energy Commission Report WASH-62, December, 1951 (unpublished), referred to in "Table of Isotopes" by Hollander, Perlman, and Seaborg, Revs. Modern Phys. 25, 469 (1953).

γ-RAY MEASUREMENTS

The energies and intensities of the γ rays were investigated with a scintillation spectrometer which consisted of a 1-in. high×1½-in. diameter cylindrical NaI(Tl) crystal, a DuMont K1186 photomultiplier tube, non-overloading amplifier,[7] stable high-voltage supply,[8] and a single-channel pulse-height analyzer.[9] The source was placed approximately six inches from the crystal to minimize spurious addition effects which result from the simultaneous detection of two cascaded γ rays. Be absorber was used to remove the β rays.

The γ-ray spectrum was divided into three overlapping regions to insure that all points were determined in the region of good amplifier linearity and constant channel width. The normalized composite curve is shown in Fig. 2. The experimental points were all corrected for the decay which had occurred during the run. Energy calibration was made with Co^{60}, Na^{22}, Cs^{137}, and Ce^{144}-Pr^{144} γ rays. Although there was a slight asymmetry in the shape of the 0.665-Mev γ-ray photoline, the resolution was too poor to identify another γ ray. However, a γ ray of 0.624 Mev, which is not seen in Fig. 2, was observed in the electron spectrum from a thin lead converter with the lens spectrometer; the resolution was again set to 2.7 percent. No γ rays with energy less than 0.500 Mev were observed; the absence of a 0.364-Mev γ ray indicates that the 8-day I^{131} contamination was negligible. Since no x-rays were observed, there are no abundant γ rays present which are converted to an appreciable extent.

The relative intensities of the individual γ rays were obtained in the following manner. The areas under each of the individual photolines were integrated after subtraction of the background and the Compton distribution from each of the higher energy γ rays. These areas, after correction for the crystal efficiency and yield in the photoline,[10] are proportional to the relative intensities of the γ rays. In the case of the 1.96- and 2.2-Mev γ rays, the efficiency curves were extrapolated to these energies. Although some error was introduced by this procedure, it is probably small compared to the other errors in obtaining the intensities of these lines. The intensity of the 0.624-Mev γ ray is estimated to be approximately 6 percent of the 0.673-Mev γ ray from the external conversion electron data. The energies and intensities of the γ rays are tabulated in columns 1 and 2, Table I.

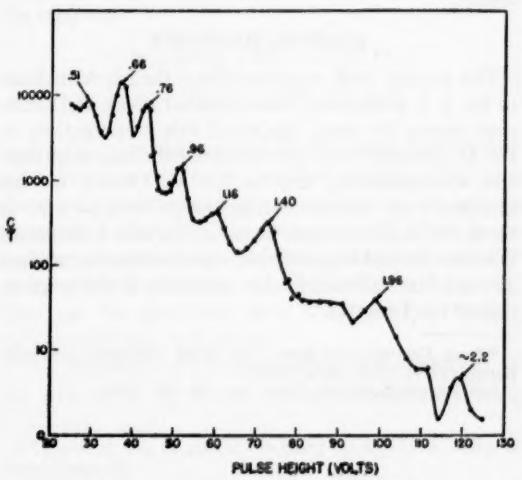

FIG. 2. I^{132} γ-ray spectrum observed with a scintillation spectrometer.

TABLE I. Energies, intensities, and γ-γ "coincidences" of I^{132} γ rays observed with scintillation spectrometers.

	Selecting γ-ray energy (Mev)	Rel. intensity (%) (including efficiency corrections)	γ rays observed in "coincidence" spectrum (Mev)
γ_1	0.510±0.03	25±5	0.665, 0.768
γ_2	0.665±0.03	100	0.510, 0.665, 0.768, 0.96, 1.16, 1.40, 1.96
γ_3	0.768±0.04	75±10	0.510, 0.665, 0.96, 1.16, 1.40
γ_4	0.96 ±0.05	20±4	0.665, 0.768
γ_5	1.16 ±0.06	8±3	0.665, 0.768
γ_6	1.40 ±0.07	11±4	0.665, 0.768
γ_7	1.96 ±0.10	~5	0.665
γ_8	2.2 ±0.10	~2	...

An equilibrium Te^{132}-I^{132} source was supplied to Dr. E. Church at the Argonne National Laboratory, who examined the internal conversion electrons in a 440-gauss β-ray spectrograph. He obtained the following more accurate energy measurements: 0.528±0.006 Mev, 0.673±0.006 Mev, 0.777±0.006 Mev. No significant data were obtained for the higher-energy γ rays because the source intensity was too low.

γ-γ AND β-γ COINCIDENCE MEASUREMENTS

The γ-γ and β-γ coincidence data were obtained using a coincidence scintillation spectrometer, the components of which were identical with those previously described, except that a gray-wedge coincidence spectrometer[11] replaced the single-channel analyzer. An anthracene crystal was used as the β-ray detector for the β-γ coincidence measurement. The essential feature of this coincidence spectrometer is that it displays either all events detected in one crystal, or only those events which occur in time coincidence (0.1 μsec) with events of a selected amplitude observed in another detector. Accidental effects were evaluated by the introduction of a 0.5-μsec delay line in one leg of the coincidence circuit. The γ-γ coincidences are tabulated in column 3, Table I.

[7] R. L. Chase and W. A. Higinbotham, Rev. Sci. Instr. **23**, 34 (1952).
[8] W. A. Higinbotham, Rev. Sci. Instr. **22**, 133 (1951).
[9] Model 510, Single Channel Pulse-Height Analyzer, Atomic Instrument Company, Cambridge, Massachusetts.
[10] P. R. Bell (unpublished).
[11] Bernstein, Chase, and Schardt, Rev. Sci. Instr. **24**, 437 (1953). R. L. Chase, Brookhaven National Laboratory Report BNL 262 (T-42), 1953 (unpublished).

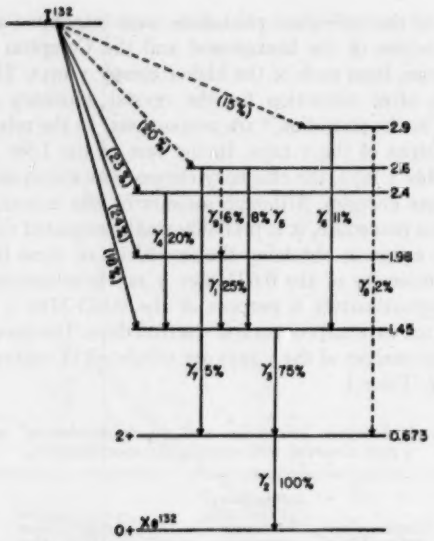

FIG. 3. Proposed decay scheme of I^{132}. The energies and intensities are the experimentally observed values.

By making intense exposures, it is possible to define the end point of a β-ray spectrum fairly accurately. Photographs were taken of the β rays in coincidence with each of the γ rays. The 2.12-Mev β ray was observed to be in coincidence with both the 0.665- and 0.768-Mev γ rays. Evidence for the other β-γ coincidences could not be obtained. The available source strength required that good geometry be used for these measurements, and consequently the intensity of the addition spectrum of the 0.665- and 0.768-Mev γ rays was comparable with that of the other γ rays. Although stronger sources could have been prepared, they would have been extremely difficult to work with, and it was felt that the Kurie plot analysis provided sufficient evidence for the proposed decay scheme. The β-γ coincidences obtained with the 1.96- and 2.2-Mev γ rays were doubtful because the low intensity of these γ rays limited the statistical accuracy of these measurements.

DISCUSSION

The decay scheme postulated in Fig. 3 is consistent with the experimental evidence; the indicated intensities and energies are the experimentally determined values. Doubtful or unobserved transitions are indicated by the dashed lines. The locations of both the 2.2- and 0.624-Mev (γ_9, Fig. 3) γ rays in the decay scheme are not implicit in the coincidence data. However, the 2.2-Mev γ ray, which is probably the γ ray observed to produce photoneutrons in D_2O, represents within the experimental error the crossover transition for the 1.4- and 0.77-Mev γ rays. The 1.16-Mev γ ray represents, within the experimental error, the crossover transition for the 0.53- and 0.62-Mev γ rays.

The energy and intensity of the 0.97-Mev β ray which was uncertain, and the 0.73-Mev β ray which was not observed in the Kurie plot analysis of the β-ray spectrum, are postulated on the basis of the γ rays. The β-γ coincidence data indicate that there are no β-ray transitions to either the ground state or the 0.67-Mev level, and that the 2.12-Mev β ray leads to the 1.45-Mev level. The $\log(ft)$ values for the 2.13, 1.53, 1.16, 0.97, and 0.73 Mev β-ray transitions are 7.5, 6.9, 6.4, 6.1, and 5.8, respectively; this indicates that all the β-ray transitions are probably first forbidden, with the possible exception of the 0.73-Mev β ray.

The K-shell internal conversion coefficient for the 0.673-Mev γ ray was determined to be 2.7×10^{-3}; this value appears to be in best agreement with the theoretical values for an $E2$ transition.[12]

The coincidence and intensity data indicate that the 0.673-Mev level represents the first excited state of Xe^{132}. The 2+ assignment for this level is consistent with the predictions of the systematics[13] of the first excited states of even-even nuclei. The spin assignment of the 1.45-Mev level is probably larger than 2, since no β-ray transitions to the 2+, 0.673-Mev level or the 0+ ground state are observed, and crossover transitions from the 1.45-Mev level to the ground state are absent.

ACKNOWLEDGMENTS

The authors wish to acknowledge their indebtedness to Dr. J. J. Kraushaar, who extended advice and assistance during the early phases of this investigation, to Dr. D. Alburger, who performed all the lens spectrometer measurements, and to Dr. E. Church for his accurate γ-ray energy measurements. We also wish to thank the Radioisotopes Group of the Hot Laboratory Division for making available separated fission product Te, and Mr. T. Prach for his assistance in the preparation of the I sources.

[12] Rose, Goertzel, and Perry, Oak Ridge National Laboratory Report ORNL-1023 (unpublished).
[13] G. Scharff-Goldhaber, Phys. Rev. **90**, 587 (1953).

Coulomb Wave Functions in the Transition Region*

MILTON ABRAMOWITZ, *Computation Laboratory, National Bureau of Standards, Washington, D. C.*

AND

H. A. ANTOSIEWICZ, *Mathematics Department, The American University, Washington, D. C.*

(Received June 28, 1954)

Expansions, involving the Airy integrals, of the functions $F_L(\eta,\rho)$, $G_L(\eta,\rho)$ are obtained from a study of the Coulomb wave equation. These expansions are convergent in the region $|\rho-\rho_1|<\rho_1$, where

$$\rho_1=\eta+[\eta^2+L(L+1)]^{\frac{1}{2}}.$$

1. INTRODUCTION

THE Coulomb wave functions $F_L(\eta,\rho)$, $G_L(\eta,\rho)$ which are defined as two linearly independent solutions of the differential equation

$$\frac{d^2y}{d\rho^2}+\left(1-\frac{2\eta}{\rho}-\frac{L(L+1)}{\rho^2}\right)y=0, \tag{1}$$

where L is a non-negative integer and $\eta>0$ is a parameter,[1] are of importance in many problems such as the separation of Schrödinger's wave equation for a Coulomb force field, the scattering of charged particles and the stability of laminar Poiseuille flow. They have been investigated intensively for the past several years and expansions of them have been obtained by various authors.[2]

In the present note, we establish first a representation of the general solution of (1) with $L=0$, valid in the region $|\rho-2\eta|<2\eta$, in terms of the well-known Airy integrals $\mathrm{Ai}(z)$, $\mathrm{Bi}(z)$ which, for $z\geq 0$, are defined[3] by the relations

$$\begin{aligned}\mathrm{Ai}(z)&=\tfrac{1}{3}z^{\frac{1}{2}}\{I_{-\frac{1}{3}}(\tfrac{2}{3}z^{\frac{3}{2}})-I_{\frac{1}{3}}(\tfrac{2}{3}z^{\frac{3}{2}})\},\\ \mathrm{Bi}(z)&=(z/3)^{\frac{1}{2}}\{I_{-\frac{1}{3}}(\tfrac{2}{3}z^{\frac{3}{2}})+I_{\frac{1}{3}}(\tfrac{2}{3}z^{\frac{3}{2}})\},\end{aligned} \tag{2}$$

where $I_{\pm\frac{1}{3}}(x)$ is the modified Bessel function of the first kind. We then outline our method briefly for the case $L\neq 0$ and not necessarily an integer. As far as the functions $F_L(\eta,\rho)$, $G_L(\eta,\rho)$ are concerned, there is no real loss of generality in considering the case $L=0$ only as these functions satisfy recurrence relations by which they can be generated from the functions $F_0(\eta,\rho)$, $G_0(\eta,\rho)$ and their derivatives.

The possibility of a representation of the solutions of (1) with $L=0$ in terms of Airy integrals becomes apparent if we transform Eq. (1) by the substitution

$$x=(2\eta-\rho)/(2\eta)^{\frac{1}{3}},\quad \mu=(2\eta)^{\frac{2}{3}}, \tag{3}$$

into the equation

$$y''-\frac{\mu x}{\mu-x}y=0; \tag{4}$$

for this equation resembles, the more so the larger μ, the equation

$$u''-xu=0, \tag{5}$$

whose general solution may be written in the form

$$u(x)=c_1\,\mathrm{Ai}(x)+c_2\,\mathrm{Bi}(x). \tag{6}$$

It seems reasonable, therefore, to presume that the general solution of (4) may be represented for all $\mu\neq 0$ in the form $y(x,\mu)=Y(x,\mu)u(x)$, where $Y(x,\mu)$ is suitably determined. Indeed, such a representation is possible but rather awkward to obtain. Rather, we attempt to find a representation in the form

$$y(x,\mu)=\phi(x,\mu)u(x)+\psi(x,\mu)u'(x), \tag{7}$$

where $u(x)$ is defined as in (6). This, as we shall see, will enable us to determine the functions $\phi(x,\mu)$, $\psi(x,\mu)$ as analytic functions of x for all $|x|\leq r<|\mu|$ whose series expansions have coefficients that are readily available from simple algebraic recurrence relations. It is this fact which makes the representation (7) extremely useful for numerical computations since the error in truncating the series expansions of $\phi(x,\mu)$, $\psi(x,\mu)$ can be estimated from a comparison with the expansion of $1/(1-x/\mu)$.

2. REPRESENTATION OF $y(x,\mu)$

Let

$$\begin{aligned}y_1(x,\mu)&=\phi(x,\mu)\,\mathrm{Ai}(x)+\psi(x,\mu)\,\mathrm{Ai}'(x),\\ y_2(x,\mu)&=\phi(x,\mu)\,\mathrm{Bi}(x)+\psi(x,\mu)\,\mathrm{Bi}'(x).\end{aligned} \tag{8}$$

We wish to determine the functions $\phi(x,\mu)$, $\psi(x,\mu)$ such that for every $\mu\neq 0$ and x in $|x|\leq r<|\mu|$ the functions $y_1(x,\mu)$, $y_2(x,\mu)$ are two linearly independent solutions of (4).

* This work was supported (in part) by the U. S. Office of Naval Research.

[1] *Tables of Coulomb Wave Functions*, National Bureau of Standards, Applied Mathematics Series 17 (U. S. Government Printing Office, Washington, D. C., 1952), Vol. 1.

[2] See, e.g., Bloch, Hull, Broyles, Bouricius, Freeman, and Breit, Phys. Rev. **80**, 553 (1950); T. D. Newton, Atomic Energy of Canada, Limited. Unclassified Report, CRT-526 (unpublished).

[3] *The Airy Integral* (British Association for the Advancement of Science, Cambridge, 1946).

On substituting either of the expressions (8) into Eq. (4) and equating to zero the coefficients of the respective Airy integral and its derivative, we obtain the system of differential equations,

$$\phi''-\frac{x^2}{\mu-x}\phi+2x\psi'+\psi=0, \quad \psi''-\frac{x^2}{\mu-x}\psi+2\phi'=0, \quad (9)$$

which we attempt to solve for $|x|\leq r<|\mu|$ by assuming that $\phi(x,\mu)$, $\psi(x,\mu)$ admit the expansions

$$\phi(x,\mu)=\sum_0^\infty a_n(\mu)x^n, \quad \psi(x,\mu)=\sum_0^\infty b_n(\mu)x^n. \quad (10)$$

Expanding $x^2/(\mu-x)$ in (9) in powers of x, we thus find the recurrence relations

$$\begin{aligned} &a_2=-\tfrac{1}{2}b_0, \quad a_3=-\tfrac{1}{2}b_1, \\ &b_2=-a_1, \quad b_3=\tfrac{2}{3}a_2, \end{aligned} \quad (11)$$

$$a_{n+4}=\frac{1}{(n+4)(n+3)}\left\{\sum_0^n \mu^{-j-1}a_{n-j}-(2n+5)b_{n+2}\right\},$$

$$b_{n+4}=\frac{1}{(n+4)(n+3)}\left\{\sum_0^n \mu^{-j-1}b_{n-j}-2(n+3)a_{n+3}\right\}, \quad (12)$$

$$n=0, 1, 2, \cdots.$$

Hence, the four constants a_0, a_1, b_0, b_1 are arbitrary within the restriction that $y_1(x,\mu)$, $y_2(x,\mu)$ be linearly independent. The simplest choice, satisfying this requirement, is to take

$$a_0=1, \quad a_1=b_0=b_1=0, \quad (13)$$

whence it follows that the Wronskian determinant of $y_1(x,\mu)$, $y_2(x,\mu)$ at $x=0$ becomes $W[y_1,y_2]=\pi^{-1}$. For convenience, we list a few terms in the resulting expansions (10):

$$\begin{aligned} \phi(x,\mu)=1&+\frac{1}{12\mu}x^4+\frac{1}{20\mu^2}x^5+\frac{1}{30\mu^3}x^6 \\ &+\frac{1}{42}\left(\frac{1}{\mu^4}+\frac{11}{30\mu}\right)x^7+\cdots, \\ \psi(x,\mu)=&-\frac{1}{30\mu}x^5-\frac{1}{60\mu^2}x^6-\frac{1}{105\mu^3}x^7 \\ &-\frac{1}{168}\left(\frac{1}{\mu^4}+\frac{11}{30\mu}\right)x^8+\cdots. \end{aligned} \quad (14)$$

Since the coefficients in the system (9) are analytic functions of x for all $|x|\leq r<|\mu|$, it follows from a well-known theorem that its solutions are likewise analytic functions of x for all $|x|\leq r<|\mu|$. Thus, the functions $\phi(x,\mu)$, $\psi(x,\mu)$ as defined in (14) are for every $\mu\neq 0$ analytic in x for all $|x|\leq r<|\mu|$.

3. CONCLUSION

The determination of a particular solution of Eq. (4) is straightforward. Choosing, for instance, $x=0$ as initial point, we obtain for the constants involved in the representation (7):

$$\begin{aligned} c_1&=\pi\sqrt{3}\{y'(0,\mu)\,\mathrm{Ai}(0)-y(0,\mu)\,\mathrm{Ai}'(0)\}, \\ c_2&=-\pi\{y'(0,\mu)\,\mathrm{Ai}(0)+y(0,\mu)\,\mathrm{Ai}'(0)\}. \end{aligned} \quad (15)$$

If we put $y(0,\mu)=F_0(\eta,2\eta)$, $y'(0,\mu)=(2\eta)^{\frac{1}{2}}(dF_0/d\rho)_{\rho=2\eta}$, these constants normalize (7) to represent $F_0(\eta,\rho)$ for all ρ in the region $|\rho-2\eta|<2\eta$, $\eta>0$; a similar set of constants may be obtained for $G_0(\eta,\rho)$.[4]

If $L\neq 0$ we can derive an analogous representation. Indeed, if in (1), we let

$$x=(\rho_1-\rho)/\rho_1^{\frac{1}{3}}, \quad \nu=\rho_1^{\frac{1}{3}}, \quad (16)$$

where ρ_1 is the larger of the two roots (assumed to be real) of the equation

$$\rho^2-2\eta\rho-L(L+1)=0, \quad (17)$$

namely,

$$\rho_{1,2}=\eta\pm[\eta^2+L(L+1)]^{\frac{1}{2}}, \quad (18)$$

we obtain the equation

$$\frac{d^2y}{dx^2}-\left\{\frac{\nu x}{\nu-x}-\frac{L(L+1)x}{\nu(\nu-x)^2}\right\}y=0, \quad (19)$$

whose "limiting" equation as $\nu\to\infty$ is

$$(d^2u/dx^2)-xu=0. \quad (20)$$

The above method yields the representation

$$y(x,\nu,L)=\phi_L(x,\nu)u(x)+\psi_L(x,\nu)u'(x), \quad (21)$$

where $u(x)$ is defined as in (6) and

$$\begin{aligned} \phi_L(x,\nu)&=\sum_0^\infty \alpha_n(\nu,L)x^n=1-\frac{L(L+1)}{6\nu^4}x^3+\cdots, \\ \psi_L(x,\nu)&=\sum_0^\infty \beta_n(\nu,L)x^n=\frac{L(L+1)}{12\nu^4}x^4+\cdots, \end{aligned} \quad (22)$$

with coefficients determined as follows:

$$\alpha_0=1, \quad \alpha_1=\alpha_2=0, \quad \alpha_3=-L(L+1)/6\nu^4,$$

$$\beta_0=\beta_1=\beta_2=\beta_3=0,$$

$$\alpha_{n+4}=\frac{1}{(n+4)(n+3)}\left\{\sum_0^n \nu^{-j-1}\alpha_{n-j}-(2n+5)\beta_{n+2}-L(L+1)\sum_0^{n+2} j\nu^{-j-3}\alpha_{n+2-j}\right\}, \quad (23)$$

[4] Asymptotic expansions of $F_0(\eta,2\eta)$, $G_0(\eta,2\eta)$ were obtained in the following paper: [M. Abramowitz and P. Rabinowitz, Phys. Rev. **96**, 77 (1954)].

$$\beta_{n+4}=\frac{1}{(n+4)(n+3)}\left\{\sum_{0}^{n}\nu^{n-j-1}\beta_{n-j}-(2n+6)\alpha_{n+3}\right.$$
$$\left.-L(L+1)\sum_{0}^{n+2}j\nu^{n-j-3}\beta_{n+2-j}\right\},$$
$$n=0,1,2,\cdots.$$

The functions $\phi_L(x,\nu)$, $\psi_L(x,\nu)$ are analytic in x for all $|x|<\nu$, i.e., $|\rho-\rho_1|<\rho_1$. Note that by (18) $\rho_1\to\infty$ with η while $\rho_2\to 0$ as $\eta\to\infty$, L being fixed.

The above results are contained in a general representation theorem for the solutions of an nth order linear ordinary differential equation with analytic coefficients.[5]

[5] H. A. Antosiewicz and M. Abramowitz, "A Representation for Solutions of Analytic Systems of Linear Differential Equations," J. Wash. Acad. Sci. (to be published).

PHYSICAL REVIEW VOLUME 96, NUMBER 1 OCTOBER 1, 1954

Evaluation of Coulomb Wave Functions along the Transition Line*

MILTON ABRAMOWITZ AND PHILIP RABINOWITZ
Computation Laboratory, National Bureau of Standards, Washington, D. C.

(Received June 28, 1954)

Asymptotic representations are obtained for the regular and irregular Coulomb wave functions and their derivatives for $\rho=2\eta$. A table of these functions is given, and a discussion is given to show how values may be obtained for $\rho\neq 2\eta$ by using Taylor's formula.

IN a recent paper Barfield and Broyles[1] evaluated the Coulomb wave functions F_0, G_0, and F_0' from their contour integral representations for $\rho=2\eta$ and gave a short table of these functions. They made the observation that a knowledge of the functions for $\rho=2\eta$ permitted the efficient use of local Taylor expansions for numerical computation. It is the purpose of this paper to exploit these suggestions and demonstrate a systematic method of computation over a wide range of values of ρ and η. Specifically, we provide in Table I values of these functions for 2η ranging from 0 to 50 and develop an asymptotic formula which may be used for larger values of the argument. The tabular values were computed on the National Bureau of Standards SEAC with the aid of programs prepared by Dr. C. E. Froberg of Sweden during his stay at the Computation Laboratory of the National Bureau of Standards. The results were obtained to nine decimal places by numerical quadrature of integral representations of the functions and checks were applied by differencing and calculation of the Wronskian. The table as given to seven decimals is correct to within a unit of the last place. The intervals were chosen so that the five-point Lagrangian interpolation formula will yield the full accuracy beyond $\rho=3$. For larger values of 2η, the representations obtained will yield equivalent results.

We restrict our discussion to the case $L=0$ since there is a convenient method of generating the functional values for $L>0$ for the pertinent range of values of ρ and η with the aid of the recurrence relations.

We start with the integral representation[2] employed by Newton,

$$F_0-iG_0=\rho C_0(\eta)\int_{-1}^{-i\infty}\exp(2\eta i\,\mathrm{arctanh}s-i\rho s)ds, \quad (1)$$

where $C_0(\eta)=(2\pi\eta)^{-\frac{1}{2}}(1-e^{-2\pi\eta})^{-\frac{1}{2}}$, in order to obtain asymptotic expansions for F_0 and G_0 and their derivatives for $\rho=2\eta$. In this case, we have

$$F_0(2\eta)-iG_0(2\eta)$$
$$=2\eta C_0\int_{-1}^{-i\infty}\exp[2\eta i(\mathrm{arctanh}s-s)]ds, \quad (2)$$

and evaluate this integral by the method of steepest descents. We note that if $f(s)=\mathrm{arctanh}s-s$, then $f'(s)$ has a double zero for $s=0$ and $f(s)=\frac{1}{3}s^3+\frac{1}{5}s^5+\cdots$. Thus, if $s=e^{i\theta}$, is^3 is real and negative for $\theta=5\pi/6$ and $\theta=-\pi/2$, the paths of steepest descent. We consequently deform the path from $s=-1$ to $s=-i\infty$ into the equivalent path

$$c_1:\ s=e^{i\theta},\quad \pi\geq\theta\geq 5\pi/6;$$
$$c_2:\ s=\zeta e^{5\pi i/6},\quad 1\geq\zeta\geq 0; \quad (3)$$
$$c_3:\ s=\zeta e^{-\pi i/2},\quad 0\leq\zeta\leq\infty.$$

It can then be shown that the contribution from the integral along c_1 is smaller in absolute value than $\frac{1}{6}\pi\exp\{-\eta(\frac{1}{2}\pi\eta-1)\}$. The integral along c_3 is

$$J_3=-i\int_0^{\infty}\exp[2\eta(\arctan\zeta-\zeta)]d\zeta, \quad (4)$$

and this can be represented asymptotically by the

* This work was supported (in part) by the U. S. Office of Naval Research.

[1] W. D. Barfield and A. A. Broyles, Phys. Rev. 88, 892 (1952).

[2] T. D. Newton, Chalk River Laboratory Report 526, December, 1952 (unpublished).

TABLE I. Coulomb functions for $\rho=2\eta$.

$\rho=2\eta$	F_0	F_0'	G_0	G_0'	$\rho=2\eta$	F_0	F_0'	G_0	G_0'
0.0	0.0000000	1.0000000	1.0000000	0.0000000	15.0	0.9847202	0.3052996	1.7171606	−0.4831337
0.5	0.3485125	0.7251403	1.1482085	−0.4802921	15.5	0.9902704	0.3033518	1.7263386	−0.4809919
1.0	0.5166015	0.5929246	1.1974870	−0.5613235	16.0	0.9956675	0.3014834	1.7352810	−0.4789166
1.5	0.6065420	0.5232290	1.2379327	−0.5807968	16.5	1.0009207	0.2996885	1.7440008	−0.4769040
2.0	0.6617816	0.4815575	1.2757788	−0.5827288	17.0	1.0060382	0.2979621	1.7525097	−0.4749507
2.5	0.7004111	0.4535470	1.3106041	−0.5790591	17.5	1.0110275	0.2962996	1.7608186	−0.4730536
3.0	0.7301291	0.4330004	1.3422906	−0.5735802	18.0	1.0158956	0.2946968	1.7689374	−0.4712097
3.5	0.7544607	0.4169974	1.3711212	−0.5676187	18.5	1.0206486	0.2931499	1.7768754	−0.4694163
4.0	0.7751972	0.4040078	1.3974834	−0.5616710	19.0	1.0252926	0.2916555	1.7846412	−0.4676709
4.5	0.7933518	0.3931476	1.4217412	−0.5559273	19.5	1.0298329	0.2902104	1.7922428	−0.4659712
5.0	0.8095520	0.3838640	1.4442027	−0.5504558	20	1.0342745	0.2888118	1.7996876	−0.4643149
5.5	0.8242151	0.3757900	1.4651204	−0.5452732					
6.0	0.8376341	0.3686700	1.4847003	−0.5403739					
6.5	0.8500228	0.3623195	1.5031110	−0.5357429					
7.0	0.8615430	0.3566012	1.5204917	−0.5313615					
7.5	0.8723199	0.3514106	1.5369583	−0.5272109	22	1.0511411	0.2836314	1.8280303	−0.4580862
8.0	0.8824527	0.3466662	1.5526082	−0.5232725	24	1.0667458	0.2790155	1.8543437	−0.4524127
8.5	0.8920214	0.3423035	1.5675239	−0.5195291	26	1.0812800	0.2748610	1.8789213	−0.4472086
9.0	0.9010915	0.3382706	1.5817760	−0.5159650	28	1.0948936	0.2710901	1.9019960	−0.4424062
9.5	0.9097174	0.3345251	1.5954254	−0.5125659	30	1.1077061	0.2676425	1.9237558	−0.4379512
10.0	0.9179449	0.3310321	1.6085246	−0.5093189	32	1.1198147	0.2644708	1.9443548	−0.4337994
10.5	0.9258127	0.3277625	1.6211196	−0.5062124	34	1.1312995	0.2615371	1.9639206	−0.4299144
11.0	0.9333539	0.3246917	1.6332507	−0.5032358	36	1.1422273	0.2588106	1.9825608	−0.4262657
11.5	0.9405973	0.3217989	1.6449537	−0.5003796	38	1.1526543	0.2562659	2.0003662	−0.4228279
12.0	0.9475677	0.3190663	1.6562601	−0.4976353	40	1.1626285	0.2538820	2.0174148	−0.4195792
12.5	0.9542871	0.3164785	1.6671980	−0.4949953	42	1.1721911	0.2516411	2.0337740	−0.4165011
13.0	0.9607746	0.3140223	1.6777927	−0.4924524	44	1.1813778	0.2495282	2.0495282	−0.4135776
13.5	0.9670473	0.3116858	1.6880668	−0.4900003	46	1.1902198	0.2475306	2.0646501	−0.4107947
14.0	0.9731203	0.3094591	1.6980407	−0.4876333	48	1.1987442	0.2456371	2.0792632	−0.4081403
14.5	0.9790072	0.3073330	1.7077331	−0.4853460	50	1.2069751	0.2438382	2.0933811	−0.4056037

expansion

$$J_3=\frac{-i}{3\beta}\left\{\Gamma(\tfrac{1}{3})+\sum_{n=5}^{\infty}\frac{a_n\Gamma(\frac{1}{3}n+\frac{1}{3})}{\beta^n}\right\},\quad \beta^3=\tfrac{3}{2}\eta, \tag{5}$$

where the coefficients a_n are given recursively by

$$a_5=(3/5)\beta^3,\quad a_6=0,\quad a_7=-(3/7)\beta^3,$$
$$a_8=0,\quad a_9=(1/3)\beta^6, \tag{6}$$
$$(n+2)a_{n+2}+na_n=3\beta^3a_{n-3}.$$

The integral along c_2 can be evaluated in exactly the same manner.

If we collect our results, making use of the fact that

$$2\eta C_0\cong(2\eta/\pi)^{\frac{1}{2}}=(3/\pi)^{\frac{1}{2}}\beta^{\frac{1}{2}},$$

we get

$$F_0(2\eta)\cong\frac{\Gamma(\frac{1}{3})\beta^{\frac{1}{2}}}{2\sqrt{\pi}}\left\{1-\frac{2}{35}\frac{\Gamma(\frac{2}{3})}{\Gamma(\frac{1}{3})}\frac{1}{\beta^4}-\frac{8}{2025}\frac{1}{\beta^8}-\cdots\right\},$$
$$G_0(2\eta)\cong\frac{\sqrt{3}\Gamma(\frac{1}{3})\beta^{\frac{1}{2}}}{2\sqrt{\pi}}\left\{1+\frac{2}{35}\frac{\Gamma(\frac{2}{3})}{\Gamma(\frac{1}{3})}\frac{1}{\beta^4}-\frac{8}{2025}\frac{1}{\beta^8}+\cdots\right\}. \tag{7}$$

The coefficient of β^{-8} in these expansions is zero, so that the error is smaller than β^{-10}.

The procedure may be carried out in an entirely similar manner to determine F_0' and G_0', since from (1) we get

$$\frac{dF_0}{d\rho}-i\frac{dG_0}{d\rho}=\frac{1}{\rho}(F_0-iG_0)$$
$$-i\rho C_0\int_{-1}^{-i\infty}\exp(2\eta i\,\operatorname{arctanh}s-i\rho s)s\,ds. \tag{8}$$

The results are

$$F_0'(2\eta)=\frac{\Gamma(\frac{2}{3})}{2\sqrt{\pi}\beta^{\frac{1}{2}}}\left\{1-\frac{4}{15}\frac{\Gamma(\frac{1}{3})}{\Gamma(\frac{2}{3})}\frac{1}{\beta^2}+\frac{272}{14175}\frac{1}{\beta^6}-\cdots\right\}+\frac{1}{3\beta^3}F_0(2\eta)$$
$$G_0'(2\eta)=\frac{-\sqrt{3}\Gamma(\frac{2}{3})}{2\sqrt{\pi}\beta^{\frac{1}{2}}}\left\{1+\frac{4}{15}\frac{\Gamma(\frac{1}{3})}{\Gamma(\frac{2}{3})}\frac{1}{\beta^2}+\frac{272}{14175}\frac{1}{\beta^6}+\cdots\right\}+\frac{1}{3\beta^3}G_0(2\eta). \tag{9}$$

For the convenience of the reader, the results in (7) and (9) are given in a form suitable for computation.

$$F_0(2\eta)=0.7063326373\eta^{1/6}\times\left[1-\frac{0.04959570165}{\eta^{4/3}}-\frac{0.0088888889}{\eta^2}-\cdots\right],$$

$$G_0(2\eta)=1.223404016\eta^{1/6}\times\left[1+\frac{0.04959570165}{\eta^{4/3}}-\frac{0.0088888889}{\eta^2}+\cdots\right],$$

$$F_0'(2\eta)=\frac{0.4086957323}{\eta^{1/6}}\left[1-\frac{0.6913041477}{\eta^{2/3}}+\frac{0.04317460317}{\eta^2}-\cdots\right]+\frac{0.5}{\eta}F_0(2\eta), \tag{10}$$

$$G_0'(2\eta)=\frac{-0.7078817734}{\eta^{1/6}}\left[1+\frac{0.6913041477}{\eta^{2/3}}+\frac{0.04317460317}{\eta^2}+\cdots\right]+\frac{0.5}{\eta}G_0(2\eta).$$

An examination of (7) and (9) shows that the expressions are useful for large values of η. Actually, they may be used even at $\eta=1$ to obtain results good to a few percent.

Let us now consider the problem of determining the functional values in the neighborhood of $\rho=2\eta$ by means of Taylor series.

To employ the Taylor expansion, one must compute the successive derivatives of F_0 and G_0. Thus, if $u=F_0$ or G_0, we have

$$u(\rho+\delta,\eta)=u(\rho)+\frac{\delta}{1!}u'+\frac{\delta^2}{2!}u''+\frac{\delta^3}{3!}u'''+\cdots,$$
$$u'(\rho+\delta,\eta)=u'(\rho)+\frac{\delta}{1!}u''+\frac{\delta^2}{2!}u'''+\frac{\delta^3}{3!}u^{iv}+\cdots. \tag{11}$$

However if we define

$$\sigma_n=\frac{\delta^n}{n!}\frac{d^nu}{d\rho^n}, \tag{12}$$

(11) can be written

$$u(\rho+\delta,\eta)=\sum_{n=0}^{\infty}\sigma_n,\quad u'(\rho+\delta,\eta)=\delta^{-1}\sum_{n=1}^{\infty}n\sigma_n. \tag{13}$$

For hand computation the form (11) may be preferred. However, if a computer is available, (13) may be used advantageously.

The successive derivatives follow immediately from the differential equation for the Coulomb wave functions, namely,

$$\rho u''+(\rho-2\eta)u=0,$$
$$\rho u'''+u''+(\rho-2\eta)u'+u=0, \tag{14}$$
$$\rho u^{(n+1)}+(n-1)u^{(n)}+(\rho-2\eta)u^{(n-1)}+(n-1)u^{(n-2)}=0.$$

In terms of the quantities σ_n, (14) may be rewritten

$$2\rho\sigma_2+\delta^2(\rho-2\eta)\sigma_0=0,$$
$$\rho n(n+1)\sigma_{n+1}+\delta(n^2-n)\sigma_n+\delta^2(\rho-2\eta)\sigma_{n-1}+\delta^3\sigma_{n-2}=0; \tag{15}$$

and since $\sigma_0=u$, $\sigma_1=\delta u'$, one may generate as many σ_n's as are needed. We note that when δ is not small, $u(\rho+\delta)$ may be computed in successive steps which are fractions of δ by a procedure which is essentially a numerical integration of the differential equation starting from $\rho=2\eta$. We shall demonstrate the method in the case of $u=G_0$ to obtain the value for $\rho=6$, $\eta=4$. From Table I we have

$$G_0(8,4)=1.5526082,\quad G_0'(8,4)=-0.5232725.$$

With the aid of (14), we get

$$G_0''=0,\qquad G_0^{viii}=0.1957515,$$
$$G_0'''=-0.1940760,\qquad G_0^{ix}=-0.2856133,$$
$$G_0^{iv}=0.1793371,\qquad G_0^{x}=0.4793638,$$
$$G_0^{v}=-0.0672514,\qquad G_0^{xi}=-0.7595047,$$
$$G_0^{vi}=0.1306637,\qquad G_0^{xii}=1.3063974.$$
$$G_0^{vii}=-0.1937505,$$

We thus find with $\delta=1$, $G(7,4)=2.1164851$, $G'(7,4)=-0.6544076$ and with $\delta=2$, $G(6,4)=3.01378$. Starting with $G(7,4)$ and $G'(7,4)$ with $\delta=1$, we arrive at the same value for $G(6,4)$. The value of $G_0(6,4)$ obtained by an independent method is 3.013787. The technique described is adapted for use with a large-scale computer. The table as given or the expressions in (10) would provide starting values for the stepwise procedure described. The recurrence relations could be used to obtain values for $L>0$. In applying the Taylor formula the truncating error can be controlled at each step by restricting the magnitudes of δ and σ_n. The integration may be extended to the regions where the asymptotic expansion for large values of ρ or the representation in terms of Bessel-Clifford functions for large η may be used conveniently.

Elastic Scattering of Deuterons by He^3†

R. J. S. Brown,* K. F. Famularo, H. D. Holmgren,‡ D. Rankin, and T. F. Stratton
University of Minnesota, Minneapolis, Minnesota

(Received June 28, 1954)

Differential cross sections for the elastic scattering of deuterons by He^3 have been measured at laboratory energies of 1.02, 1.50, 2.00, 2.50, 3.00, and 3.25 Mev for nine center-of-mass angles ranging from 45° to 125°. At each deuteron energy the cross section passes through a minimum in the vicinity of 90°, with the minimum shifting to slightly higher angles as the bombarding energy increases. The cross section decreases with increasing energy for each angle investigated. At 3.25 Mev the cross section passes through a minimum of 16 millibarns at 100° and rises to approximately 80 millibarns at 45° and 125°. A comparison of the results for the scattering of deuterons by He^3 and by the mirror nucleus H^3 shows the cross sections to be approximately the same except at the lowest energies and forward angles.

INTRODUCTION

MEASUREMENTS of differential cross sections for elastic scattering between pairs of light nuclei have been extended to include the scattering of deuterons by He^3. Data were taken for deuterons scattered at center-of-mass angles from 45° to 125° at laboratory bombarding energies from 1.02 Mev to 3.25 Mev.

Differential cross sections have been previously measured[1] in the above angle and energy range for the scattering of deuterons by H^3, the mirror nucleus of He^3, and results will be compared with those of the present experiment. In an earlier experiment[2] measurements of differential cross sections were made for the scattering of 10-Mev deuterons by He^3 and by H^3 with nearly identical results for the two scattering processes.

EQUIPMENT

The small volume scattering chamber employed in the present experiment was the one used for the scattering of protons by deuterons and is described by Brown *et al.*[3] A minor modification was made in the slit system defining the scattered beam to prevent high-energy protons due to the $He^3(d,p)He^4$ reaction from penetrating the original 6-mil tantalum slit material and entering the counter with reduced energy. The circular aperture next to the counter was replaced by one cut from 20-mil gold sheet. The original rectangular tantalum slits were backed by 20-mil gold strips. The aperture in the gold material was slightly wider than that in the tantalum, so that particles could not strike the gold slit edges without first penetrating the tantalum.

The beam entering the chamber was collimated to within a half-angle of 1.1°, while the defining slit system for the scattered beam permitted an rms angular deviation of 0.6° from the nominal laboratory scattering angle.

The electrical current carried by the deuteron beam was measured and integrated by an electronic instrument[4] instead of by the condenser and ballistic galvanometer system described in reference 3. After collecting a predetermined electrical charge, the instrument stopped the counters and placed a shutter in the path of the deuteron beam.

Scattered particles were detected in a proportional counter, and pulse-height distributions were recorded by a ten-channel discriminator[5] in the manner described in reference 3.

He^3 HANDLING

The He^3 handling system was adapted from the one previously described in connection with the study of the proton yield from the $He^3(d,p)He^4$ reaction.[6] The He^3 was stored and purified in a glass bulb containing activated charcoal and was transferred between the storage bulb and the scattering chamber by means of a mercury Toepler pump. To keep mercury and condensable vapors from passing into the scattering chamber, a liquid nitrogen trap was placed in the line from the He^3 handling system to the chamber.

The amount of He^4 impurity in the He^3 was measured at intervals by the mass spectrometer group at the University of Minnesota and was found to be 5.5 percent by volume. Over a period of about ten months this concentration was constant within the accuracy of the measurements, about 0.3 percent.

The pressure in the chamber was indicated by a Wallace and Tiernan differential manometer as in the experiment described in reference 3. A gradual rise in pressure of the order of 0.5 mm Hg (with a chamber pressure of about 40 mm Hg) was observed when data were taken over a period of several hours; the rise was

† Work supported in part by the joint program of the U. S. Office of Naval Research and the U. S. Atomic Energy Commission.

* Now at California Research Corporation, La Habra, California.

‡ Atomic Energy Commission Predoctoral Fellow during most of this work. Present address: Naval Research Laboratory, Washington, D. C.

[1] Stratton, Freier, Keepin, Rankin, and Stratton, Phys. Rev. 88, 257 (1952).

[2] Allred, Armstrong, Hudson, Potter, Robinson, Rosen, and Stovall, Phys. Rev. 88, 425 (1952).

[3] Brown, Freier, Holmgren, Stratton, and Yarnell, Phys. Rev. 88, 253 (1952).

[4] R. J. S. Brown, Rev. Sci. Instr. (to be published).

[5] W. C. Elmore and M. Sands, *Electronics* (McGraw-Hill Book Company, Inc., New York, 1949).

[6] Yarnell, Lovberg, and Stratton, Phys. Rev. 90, 292 (1953).

attributed to materials outgassing from the chamber walls. The effect of the pressure rise on the data was determined by repeating runs after the gas had been in the chamber for different lengths of time. In most cases it was necessary to repurify the gas after about three hours of use.

IDENTIFICATION OF PARTICLES

There were six groups of charged particles which entered the proportional counter when the mixture of He^3 and He^4 was bombarded with deuterons: deuterons scattered by He^3 and by the He^4 impurity, the He^3 and the He^4 recoil nuclei, and protons and alpha particles from the $He^3(d,p)He^4$ reaction. At each bombarding energy and angle of observation, the energies of the particles were computed and their ionization losses in the counter gas determined from known energy-loss relations.[7] The particle groups could then be identified by the magnitudes of the pulses which they produced in the proportional counter.

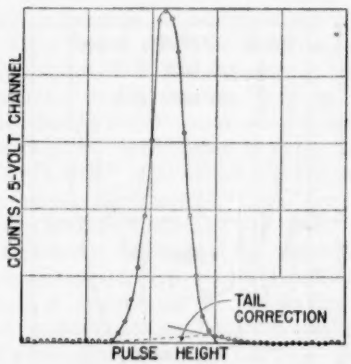

FIG. 1. Pulse-height distribution from 1.02-Mev deuterons scattered from He^3 at 27° (lab).

At most angles and energies, pulses from deuterons scattered by He^3 were not resolved from those due to deuterons scattered by He^4. In addition, it was seldom possible to separate the pulses produced by the recoil He^3 nuclei from those produced by the recoil He^4 nuclei. Pulses from the scattered deuterons were always resolved from those due to the recoil nuclei. The known amount of He^4 in the He^3 contributed counts which could be subtracted, since the cross sections for the elastic scattering of deuterons by He^4 were known.[8] Alpha-particle pulses from the $He^3(d,p)He^4$ reaction were resolved from those due to all other particle groups except at the bombarding energy of 1.02 Mev. Since the cross sections for this reaction were known,[6] counts due to the alpha particles could be subtracted when necessary. The high energy protons from this reaction had such small energy loss in the counter that they were not observed.

[7] M. Livingston and H. A. Bethe, Revs. Modern Phys. **9**, 270 (1937).

[8] Blair, Freier, Lampi, and Sleator, Phys. Rev. **75**, 1678 (1949).

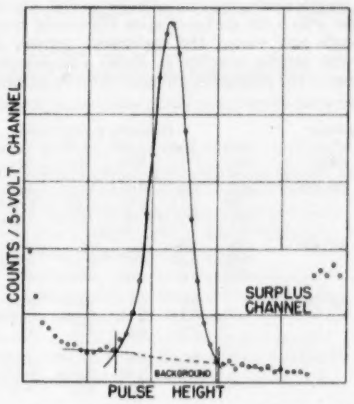

FIG. 2. Pulse-height distribution from 3.25-Mev deuterons scattered from He^3 at 50° (lab).

CORRECTIONS TO THE DATA

In previous work with the small volume scattering chamber,[1,3,9] it was found necessary to make corrections of the order of a few percent to the data taken at small angles. This correction subtracted counts due to particles which entered the counter after they had been doubly scattered, once by the gas and then again by the walls of the chamber.

Figure 1 shows a pulse-height distribution for d-He^3 scattering at a laboratory angle of 27° and a bombarding energy of 1.02 Mev. The tail on the high-pulse side of the peak is due to particles which have been scattered more than once. Counts of similar origin but appearing under the main peak are considered to be represented by the dashed line. The area under this line is subtracted from the peak.

The validity of this correction procedure was verified by applying it to the data obtained from scattering processes for which the cross sections were known from measurements with larger scattering chambers. Pulse-height distributions were taken for proton-proton scattering at representative angles and energies in the range of laboratory angles from 27° to 60° and energies from 1.5 Mev to 3.0 Mev. The data agreed within three percent of the accepted values[10,11] when corrected by the procedure followed for the d-He^3 scattering. Similar agreement was obtained from p-He^4 scattering[12] at 2.53 Mev for laboratory angles extending from 30° to 160°.

The incident deuteron beam produced neutrons at the collimating slits of the chamber. On the small volume chamber this source of neutrons was close to the counter, particularly when the counter was set at large angles. Figure 2 shows a pulse-height distribution in

[9] Claassen, Brown, Freier, and Stratton, Phys. Rev. **82**, 589 (1951).

[10] Herb, Kerst, Parkinson, and Plain, Phys. Rev. **55**, 998 (1939).

[11] Blair, Freier, Lampi, Sleator, and Williams, Phys. Rev. **74**, 553 (1948).

[12] Freier, Lampi, Sleator, and Williams, Phys. Rev. **75**, 1345 (1949).

TABLE I. Elastic scattering of deuterons by He^3. θ is the center-of-mass angle; $\sigma(\theta)$ is the center-of-mass differential cross section. For each angle and energy the uppermost number is $\sigma(\theta)$ in millibarns; the middle number is $k^2\sigma(\theta)$ (dimensionless); the lowest number is the estimated probable error in percent.

Scattering angle		Deuteron energy (lab)					
Lab angle	C.m. angle	1.02 Mev	1.5 Mev	2.0 Mev	2.5 Mev	3.0 Mev	3.25 Mev
27° 22′	45° 15′	406 1.44 6%	216 1.13 4%	128 0.87 4%	102 0.88 3%	80.9 0.843 3%	77 0.87 4%
33° 15′	54° 44′	226 0.80 4%	130 0.68 4%	82 0.57 4%	65 0.56 3%	55.8 0.581 3%	55 0.62 6%
40°	65° 25′		98 0.51 4%	59 0.41 4%	45.4 0.394 4%	38.2 0.398 4%	38.6 0.435 6%
45°	73° 11′		81 0.42 4%	55 0.38 4%	41.3 0.358 4%	32.2 0.335 4%	28.8 0.325 5%
50°	80° 46′		80 0.42 4%	50 0.35 4%	36 0.31 5%	23.3 0.243 5%	22.2 0.250 6%
56° 15′	90°		85 0.44 5%	52 0.36 5%	34 0.29 5%	21.1 0.220 6%	17.3 0.195 7%
62° 23′	98° 39′					20.5 0.213 8%	16.0 0.180 7%
70°	108° 52′		115 0.60 8%	82 0.57 4%	54.9 0.476 3%	31.5 0.328 5%	24.0 0.271 7%
83° 41′	125° 16′		155 0.80 5%	126 0.87 4%	106 0.92 3%	89.3 0.930 3%	84.8 0.957 3%

which the neutron background was high and the d-He^3 cross section was relatively small. The background, which was subtracted, is indicated by the dashed line.

ERRORS

Probable errors assigned to the following factors in the experiment are: correction for He^4 impurity in the He^3, 0.5 percent; geometry (including angle of scattering), 0.7 percent; charge measurement, 0.5 percent; pressure and temperature measurement, negligible; statistics, 1.0 percent or less; bombarding energy, 1.2 percent or less. If these errors are combined quadratically, the result is less than 2 percent.

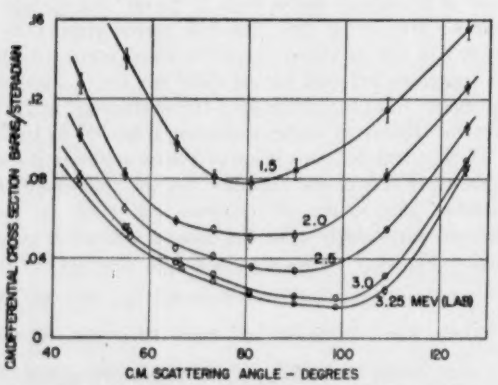

FIG. 3. Center-of-mass differential cross sections for the scattering of deuterons by He^3.

Since the estimated errors of the background corrections are several times as great as those from all other sources, the error which is assigned to each cross-section measurement is, in most cases, the estimated uncertainty of the background subtraction. In all cases, the assigned error is greater than the root-mean-square deviation of the individual measurements from their means, and greater than fifteen percent of the background correction.

RESULTS

The results are tabulated in Table I and shown graphically in Fig. 3. No distinction is made between values of cross sections obtained by detection of recoil and of directly scattered particles. Values obtained by the two methods agreed well within the assigned probable errors in cases where both direct and recoil data were taken.

The function $k^2\sigma(\theta)$ is tabulated, with k equal to the center-of-mass momentum divided by $\hbar$.

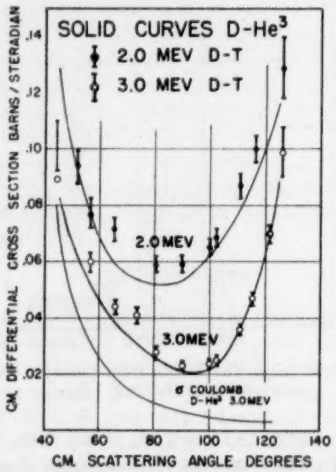

FIG. 4. Comparison of cross sections for the scattering of deuterons by He^3 and by H^3. The solid curve is the d-He^3 Coulomb cross section, calculated from the Rutherford formula.

In Fig. 4 the cross sections for the scattering of deuterons by H^3 and He^3 are compared. In addition, the Coulomb cross sections calculated from the Rutherford formula are shown. It is seen that the d-He^3 and d-H^3 scattering cross sections are essentially the same at large angles and high energies, where the Coulomb cross sections are small. At 10.0 Mev Allred *et al.*[2] found essentially the same cross sections for the two scatterings except at low angles, where the Coulomb cross sections are appreciable.

The authors are pleased to acknowledge the advice and assistance of Professors J. H. Williams and G. D. Freier, and of the members of the electrostatic generator group, Doctors D. M. Van Patter, W. R. Stratton, J. L. Yarnell, and Mr. B. E. Simmons.

Absolute Cross Section *Versus* Energy of the $Cu^{63}(\gamma,n)$ and $Cu^{63}(\gamma,2n)$ Reactions*

ARTHUR I. BERMAN AND KARL L. BROWN
Department of Physics and High Energy Physics Laboratory, Stanford University, Stanford, California

(Received June 29, 1954)

Experimental values were found for the absolute cross section of both $Cu^{63}(\gamma,n)$ and $(\gamma,2n)$ reactions *versus* quantum energy from threshold to 36 Mev. Statistical and systematic errors were limited by the use of (a) the direct electron beam of the Stanford 36-Mev linear accelerator, which produced bremsstrahlung immediately before and within the copper foils under bombardment, (b) an electron-beam collector which recorded the total accumulated charge in the incident flux, (c) a 4π scintillation counter which measured the activity of the resultant Cu^{62} and Cu^{61}, and (d) electroplated foils of separated Cu^{63} isotope.

The cross-section curves of the two reactions are similar—both rise rapidly to a maximum value about 6 Mev above threshold and then fall to zero almost as rapidly. The integrated cross sections were found to be 0.55 ± 0.03 and 0.081 Mev-barn for the (γ,n) and $(\gamma,2n)$ reactions, respectively. The $(\gamma,2n)$ threshold is 20.0 ± 0.5 Mev. A precision of 0.5 percent was attained in the relative (γ,n) activation points and 5 percent in the absolute cross section integrated over energy. The corresponding errors in the $(\gamma,2n)$ data were 5 and 20 percent; the latter value includes the effect of a 10 percent uncertainty in the currently published data on the electron-capture to positron-emission ratio of Cu^{61}.

I. INTRODUCTION

THE number of publications relating to photonuclear reactions has become so extensive in the past few years that no attempt is made here to provide a complete reference to this voluminous material, as an introduction to this research. There are, however, several articles of a review nature which should lead the reader to most of the published work in this field.[1–3]

The $Cu^{63}(\gamma,n)Cu^{62}$ cross section has been studied in detail by several investigators,[4–11] and the $Cu^{63}(\gamma,2n)$ cross section has been studied by Montalbetti *et al.*[2] The present experiment differs from the others principally in the energy range covered by the experiment and in the method of determining the photon flux initiating the reactions. With one exception,[9] the results of all the previous measurements of the $Cu^{63}(\gamma,n)$ and $(\gamma,2n)$ absolute cross sections were dependent upon the calculated response of an r meter or ionization chamber, whereas Krohn and Shrader used a pair spectrometer calibrated against the theoretical and experimental cross section for the photodisintegration of the deuteron.

In this experiment, the external electron beam of the Stanford 36-Mev linear accelerator[12] was used directly to activate a stack of Cu foils. The beam passed successively through a thin Cu correcting foil (explained in detail later), a relatively thick radiator, and a second identical thin foil, and then directly into a "Faraday cup" electron collector which permitted a precise measurement of the accumulated charge in the incident electron flux. From knowledge of the integrated charge and the Bethe-Heitler theory,[13] the effective photon spectrum passing through the second thin foil can be determined to good precision.

The number of photoneutrons ejected from the copper foil was determined in this experiment by counting the residual radioactivity of the Cu^{62} and Cu^{61} isotopes (resulting from the $Cu^{63}(\gamma,n)Cu^{62}$ and the $Cu^{63}(\gamma,2n)Cu^{61}$ reactions) with a 4π scintillation counter. To avoid interference from extraneous activities, the $(\gamma,2n)$ cross section was evaluated by using electroplated foils of Cu^{63} separated isotope.

II. EXPERIMENTAL TECHNIQUE

The Stacked-Foil Method

When photonuclear reactions are produced by quanta which are created within and immediately preceding the material under study, one is able to establish almost precisely the photon flux initiating the reactions. This flux is determined from knowledge of the incident electron-beam intensity and of Bethe-Heitler bremsstrahlung theory[13] (modified slightly to account for the finite radiator thickness).[14]

Unfortunately, the accuracy of this technique is modified somewhat by the existence of a background effect, namely, the similar reactions induced by the virtual quanta identified with the electromagnetic field of the moving electrons. These are in contradistinction to the bremsstrahlung quanta which are created by electrons as they decelerate in matter. Although the cross section for the electronuclear effect is only about one percent of the photonuclear process[15] for thin targets, there may be several hundred electrons striking

* The research reported in this document was supported jointly by the U. S. Navy (Office of Naval Research) and the U. S. Atomic Energy Commission.

[1] K. Strauch, Ann. Rev. Nuclear Sci. **2**, 110 (1953).
[2] Montalbetti, Katz, and Goldemberg, Phys. Rev. **91**, 659 (1953).
[3] A. I. Berman, Am. J. Phys. **22**, 277 (1954).
[4] G. C. Baldwin and G. S. Klaiber, Phys. Rev. **73**, 1156 (1948).
[5] B. C. Diven and G. M. Almy, Phys. Rev. **80**, 407 (1950).
[6] L. Katz and A. G. W. Cameron, Can. J. Phys. **29**, 518 (1951).
[7] P. R. Byerly and W. E. Stephens, Phys. Rev. **83**, 54 (1951).
[8] L. I. Newkirk, Phys. Rev. **86**, 249 (1952).
[9] V. E. Krohn and E. F. Shrader, Phys. Rev. **87**, 685 (1952).
[10] K. Strauch, Phys. Rev. **81**, 973 (1951).
[11] Marshall, Rosenfeld, and Wright, Phys. Rev. **83**, 305 (1951).
[12] R. Post and N. Shiren, Rev. Sci. Instr. (to be published).
[13] H. Bethe and W. Heitler, Proc. Roy. Soc. (London) **A146**, 93 (1934).
[14] R. Wilson, Proc. Phys. Soc. (London) **A66**, 638 (1953).
[15] K. L. Brown and R. Wilson, Phys. Rev. **93**, 443 (1954).

the sample for every effective bremsstrahlung photon produced, and so the two effects may be quite comparable in magnitude. To some extent, the difficulty can be lessened by extending the thickness of the radiator; however, a point is soon reached where the degeneration of both electron and photon energies in the mass of the radiator introduces a sizable uncertainty in the calculated photon flux.

The number of unwanted reactions—be they induced by the electrons, neutrons, or stray gamma radiation entering with the electrons—can be measured conveniently by placing a foil, equivalent to the sample, in front of the radiator and observing the reaction yield. Thus, the electron beam passes successively through a thin correcting foil, a relatively thick radiator, and a (second identical) thin rear sample foil. Of course, the front foil, being of finite thickness, acts as its own radiator, producing a small amount of "self-induced" photonuclear reactions, which are equivalent (except for a degeneration factor) to those induced similarly in the rear foil. The net difference in reaction yield (corrected for photon and electron degeneration) between the rear and front foils is then due only to bremsstrahlung quanta produced in the radiator and front foil, the sum being the "effective radiator."

In this experiment, the reaction yield is measured by determining the radioactivity of the ten-minute copper-62 and three-hour copper-61 nuclei which results from the (γ,n) and $(\gamma,2n)$ processes, respectively, in copper-63. Both radioisotopes emit positrons, whose end-point energies are 2.9 and 1.3 Mev, respectively.

Naturally occurring copper is composed of isotopes 63 and 65 in the proportion 69:31. Of all competing photon-induced activities which can occur in these isotopes, only the $Cu^{65}(\gamma,n)$ reaction appears to be of any consequence. This twelve-hour copper-64 activity conflicts so strongly with the weak three-hour $(\gamma,2n)$ activity to be measured, that it was necessary to perform the $Cu^{63}(\gamma,2n)$ experiment with highly-enriched copper-63 foils. Oxide containing 99.4 percent copper-63 was borrowed from Oak Ridge. Smooth foils were then electroplated from a weak (about 0.1 normal) nitric-acid solution on a polished, stainless-steel anode (rotated at one rps to stir the solution and insure uniformity); the foils were then easily stripped. Foils ranging in thickness from 3 to 16 mg/cm² and totaling 130 mg/cm² were made. They were reduced in a hydrogen atmosphere and weighed immediately. A beta-ray gauge was constructed to determine their uniformity, which in nearly all cases varied not more than 2 percent in standard deviation.

Incident Electron-Flux Measurement

The electrons from the Stanford 36-Mev linear accelerator were magnetically analyzed and collimated in high vacuum so that a fairly uniform beam of $\frac{1}{4}$-inch by $\frac{1}{8}$-inch cross section entered the foils. The foil holder was mounted in air at the entrance to a Faraday-cup electron collector.[16] This consisted of a graphite cylinder bored with a deep hole and backed by lead as illustrated in Fig. 1. The electrons are attenuated primarily by ionization in the graphite, and any photons produced are effectively absorbed by the lead. The lip at the front of the graphite serves two purposes. First, it narrows the aperture to a size more nearly consistent with the beam dimensions and hence helps to prevent loss of secondary particles. Second, those few electrons which would strike the inner surface of the graphite near the aperture at grazing angles and eject secondaries are forced to enter the carbon block at a more nearly normal angle of incidence, and thus eject fewer secondaries. The purpose of the ring magnet is to deflect the low-energy secondary particles generated at the base of the cup back into the collector. Thus, the emergent beam, with all its secondary products, is contained within the integrator; the net accumulated charge is therefore a direct measure of the number of electrons collected.

To test the efficiency of the collector, the beam was monitored with a hydrogen ion chamber preceding the foils, and the cup was biased through a range of +900 to −900 volts. Upon extrapolating the resultant collection yield (normalized to constant beam intensity) to saturation voltages, it was observed that the influence of low-energy secondary particles resulted in a change in total charge accumulation of less than ±2 percent. To verify that charged particles resulting from the electron shower were effectively trapped by the cup, a further test was made. The ionizing radiation leaving the end and sides of the cup was measured by calibrated x-ray film and also by a Victoreen ionization thimble. From this, it was possible to calculate the maximum loss of charged particles. This predicted that the total number of particles lost was less than one-half of one percent of the incident flux. Inasmuch as both electrons and positrons are generated in the cup, and the film and Victoreen thimble are insensitive to charge polarity, the actual loss is expected to be even less. This result is further verified by the work of Kantz on the penetration depth of electron-induced showers.[17]

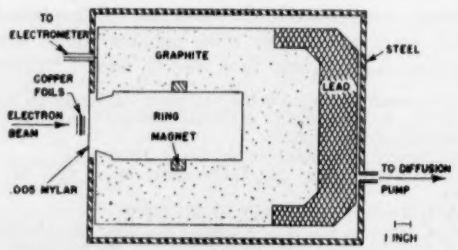

FIG. 1. Experimental arrangement showing the Faraday cup electron collector and bombardment position of the foils.

[16] A more complete description of this collector and its associated circuitry is discussed in a paper to be submitted to the *Review of Scientific Instruments* by K. L. Brown and G. W. Tautfest.

[17] A. D. Kantz, Stanford High Energy Physics Laboratory Technical Report HEPL-17, May 1954 (unpublished).

TABLE I. $\phi(\epsilon,\epsilon_M)/\phi_0$ in Mev^{-1} for 0.025-radiation-length copper.

$\epsilon \backslash \epsilon_M$	10	12	14	16	18	20	22	24	26	28	30	32	34	36	38	40
9	399	725	905	1037	1138	1220	1289	1348	1399	1442	1479	1512	1542	1570	1596	1621
11		346	590	730	824	897	957.5	1009	1054.5	1092.5	1126	1156	1183.5	1208.5	1232	1254
13			297	488	611	690	749	797	838.5	873.5	904.5	932	957	980	1001	1020.5
15				255	425	529	597	646.5	686.5	720	749	774	797	817.5	836.5	853.5
17					220	370	456.5	512.5	554.5	588	616	640	661	679.5	696.5	711.5
19						193	321	393	442	478	506	529	549	566.5	582	595.5
21							172	297	360.5	404	434.5	458	477	493	507	518.5
23								158	264	325.5	365	392.5	413	429.5	443	454
25									145	249	306.5	343	367	385.5	400	410.5
27										135	230	283	316	338	353.5	364.5
29											126	211	260	290.5	310	323
31												118	198	245	273	290.5
33													110	187	229	254
35														102.5	175.5	215.5
37															95	164
39																88

These facts demonstrate the reliability of the cup as an absolute beam-monitor in the energy range of the accelerator. The ion-chamber monitor was used also to correlate the beam emerging from the foils with the incident beam at the various primary-electron energies. An observed difference was caused by the primary-electron beam scattering foil electrons into the collector. This necessitated a correction of from 2.5 percent at 36 Mev to essentially zero at 12 Mev. Similar scattering in the 0.005-inch Mylar foil window of the collector required a correction of 2.3 percent (calculated from the Møller scattering formula).

The charge from the collector was accumulated on a condenser in an electrometer unit. A slide-back voltage was continuously applied through an electronic feedback circuit which maintained a zero net voltage across the Faraday-cup collector. Fluctuations in beam intensity during the run would introduce serious errors unless corrected for; for example, an increase in intensity is more serious near the end of a run than near the beginning, as activity induced near the beginning will be more likely to have decayed before the counting period starts. To offset this, a technique used by Snowdon was used.[18] A high resistance was placed across the condenser so that the accumulated charge leaked off at the rate of decay of the reaction being studied.

Photon-Flux Calculation

The Bethe-Heitler formula, including screening, as integrated over all angles of photon emission was employed to calculate the number of photons in each quantum-energy interval for an infinitesimal thickness of radiator.[13] This formula suffers from the fact that the Born approximation was used in its derivation. Thus, at the high-energy end of the spectral distribution, where the recoil electron has practically zero kinetic energy, the formula is invalid. Further, the over-all cross section is subject to a possible error which increases with Z.

[18] S. C. Snowdon, Phys. Rev. 78, 299 (1950).

In an attempt to relieve the first difficulty, the bremsstrahlung cross section was adjusted by a multiplying factor calculated by Sommerfeld for the nonrelativistic formula,[19] which causes the cross section to be finite rather than zero at the cut-off energy.

The second difficulty is alleviated by noting the recent work of Bethe *et al.*[20] which substantiates the validity of the Bethe-Heitler formula for large momentum transfers. This is not true of the pair production cross section, as has been shown by experiment.[21] Nevertheless, with a copper radiator as was used in this experiment, even if the error in the Bethe-Heitler bremsstrahlung formula were as large as the pair-production error, the net error to this experiment would not exceed one percent.

In order to adjust the Bethe-Heitler formula for the finite thickness of the radiator, it was necessary to account for the degeneration of the electrons and photons. Wilson's formula[14] was used for this purpose. At the high-energy end, errors resulting from the application of this formula become more serious than the uncertainty in the use of the Sommerfeld factor. These calculated values are tabulated in Table I. The bremsstrahlung cross section is given as $\phi(\epsilon,\epsilon_M)/\phi_0$ in Mev^{-1} for 0.025-radiation-length copper (0.3325 g/cm^2). $\phi_0=r_0^2/137$, where $r_0=2.818\times10^{-13}$ cm (classical electron radius); $\phi(\epsilon,\epsilon_M)$ = bremsstrahlung cross section per copper nucleus, integrated over all angles of emission, in an energy range ϵ and $\epsilon+d\epsilon$, per incident electron of kinetic energy ϵ_M. These values should be multiplied by $(Z+\delta)/Z$ to include the contribution to bremsstrahlung production by interactions with the field of atomic electrons. An approximate value of $\delta=1$ is used in this work.

It was necessary to know with some degree of accuracy the electron kinetic energy and therefore the maximum photon energy incident on the foils. At the

[19] W. Heitler, *The Quantum Theory of Radiation* (Clarendon Press, Oxford, 1936), p. 171.

[20] H. A. Bethe and L. C. Maximon, Phys. Rev. 93, 768 (1954); Davies, Bethe, and Maximon, Phys. Rev. 93, 788 (1954).

[21] A. I. Berman, Phys. Rev. 90, 210 (1953).

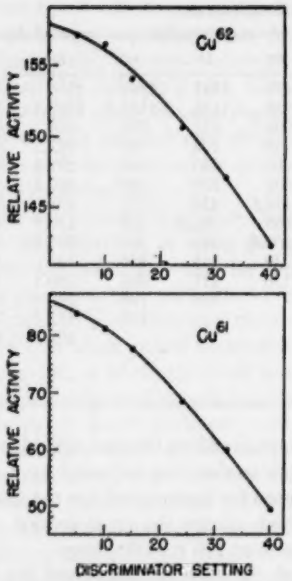

FIG. 2. Relative activity *vs* discriminator setting for a foil 6.9 mg/cm² thick.

exit point of the accelerator the electron beam was deflected by the field of an electromagnet, and a fraction, depending on the geometry, was transmitted through collimators to the foils. The energy calibration was obtained as follows. The relation between the field and magnet current was found to 0.1 percent accuracy by inserting a rotating coil into the magnetic field and comparing the induced voltage obtained with that from a permanent magnetic field. This function was then normalized to an absolute value by observing the magnet current at the threshold of the (γ,n) reaction in Cu^{63} and C^{12}. The former value, 10.61 Mev, is a result of a precise measurement of Birnbaum,[22] while the latter, 18.71 Mev, is found from nuclear mass spectrometer values.[23] Throughout the experiment, the magnet current, measured with a potentiometer, was reversed, raised, and lowered in a fixed manner to provide assurance that all settings followed a fixed hysteresis loop. Furthermore, the magnet was operated well below the saturation level resulting in an almost linear function of energy *versus* magnet current, which again assured reproducibility of the energy settings. The energy resolution of the electrons incident on the foils was found to be 1.5 percent by deflecting the beam with a second magnet through fine slits.

Measuring the Radioactivity

The activity induced in the front and rear foils was measured with a 4π scintillation counter. The foil was sandwiched between two flat anthracene crystals, 1-inch square and ¼-inch thick, backed by two DuMont 6292 photomultipliers. The natural-copper foils used in the (γ,n) runs were 1¼-inch diameter disks 40 mg/cm² thick, while the enriched foils were ½-inch×⅞-inch strips totaling 65 mg/cm². The cross section of the beam was shown by film exposure to be completely contained in the foils. Hence, any positrons of the induced activity which escaped the foils with finite energy would most certainly be absorbed in the anthracene and cause a light pulse to be produced. So long as the foil was reasonably centered between the crystals, it was impossible to detect changes in the counting rate as a function of the foil's position. However, every effort was made to duplicate the runs precisely by giving close attention to constants of the experiment, such as foil position, both in the beam and in the counter. The photomultiplier outputs were equalized and then connected in parallel. The pulses were fed successively into a Los Alamos-type 501 amplifier and Berkeley decimal scaler. Very small pulses, commensurate with the noise level, were eliminated by a discriminator. To account for the proportion of pulses lost, an extrapolation of a plot of activity *versus* discriminator setting was made for a thin foil (6.9 mg/cm²). In Fig. 2 this plot is shown for both Cu^{61} and Cu^{62}. The result was not at variance with the expected Fermi distribution, if one allows a 50 percent tolerance in the calibration of the discriminator. This calibration was made by using the 167-kev endpoint energy of S^{35}. During the experimental runs, a discriminator setting of 32 volts was chosen to reject unwanted low-energy activity and to decrease the background counting rate. The counter background was 0.6 count per second.

It was found that for thin foils the fraction lost by discrimination barely varies with foil thickness so that the result of the extrapolation can be assumed to be that for a foil of zero thickness. The 2–3 mil thickness of the foils used in the regular runs permitted some self-absorption to occur. Fortunately, in 4π geometry, a plot of specific activity *versus* thickness is semilogarithmic, and the extrapolation to zero thickness can be made without difficulty. This is shown in Fig. 3. The self-absorption factors found were essentially equal to those calculated from the self-absorption coefficients of Baker and Katz.[24]

Measurements of the half-lives of the two isotopes were made with the 4π counter. The results are 9.73 $\pm$0.02 minutes for Cu^{62}, and 3.32$\pm$0.03 hours for Cu^{61}. The latter result is in agreement with other workers, while the former is up to 7 percent lower than some of the previously published values. The shorter half-life was measured after bombarding the enriched foils below the $(\gamma,2n)$ threshold. Actually, ordinary copper could have been used in this determination provided the discriminator had been set high enough to eliminate

[22] M. Birnbaum, Phys. Rev. 93, 146 (1954).
[23] See, for example, E. Segrè, editor, *Experimental Nuclear Physics* (John Wiley and Sons, Inc., New York, 1953), p. 745.
[24] R. G. Baker and L. Katz, Nucleonics 11, 14 (1953).

the competing Cu^{64} activity. At any rate, the discriminator was set at a sufficiently high value to lower the background count. Paired runs of 45 minutes each were compared and the initial counting rate was chosen low enough to prevent uncertainties in the dead-time from seriously affecting the result. Other paired runs of 20-minutes and 2-minute duration were taken at different intervals with respect to the initial bombardment time and all results fall within the statistical error stated. This value of half-life was used to recompute the dead-time of the scalars (6.0 ± 0.5 microseconds at the 32 discriminator setting) at fast counting rates, which in turn allowed a more sensitive computation of the half-life to be made at moderate counting rates.

III. EXPERIMENTAL RESULTS

Activation Curves

Activation points were taken at 2-Mev intervals. Smaller intervals, which would permit fine rather than coarse structure determinations of the cross section, would require a higher-energy resolution of the incident electron beam, and further knowledge about the bremsstrahlung energy distribution near cutoff. For the (γ,n) measurements, five sets of front and rear foils of the ordinary copper were used. Five runs of 200 seconds each were made at a given energy and then repeated at a later date with the foil positions interchanged. Each foil was counted for 100 seconds and counting rates were of the order of 1000 counts per second. An additional run was made with the enriched foils to check on possible interference from activities induced in the copper-65 isotope in ordinary copper; in particular, the $Cu^{65}(\gamma,3n)$ reaction, which would produce an excess of 10-minute Cu^{62}. Since no excess was observed in the natural copper relative to the enriched foils, it was concluded that up to 36 Mev, activity from this reaction must be less than one percent of the $Cu^{63}(\gamma,n)$ activity. The $Cu^{65}(\gamma,2n)$ leads to the stable isotope Cu^{63} and therefore is not detectable by this experimental technique.

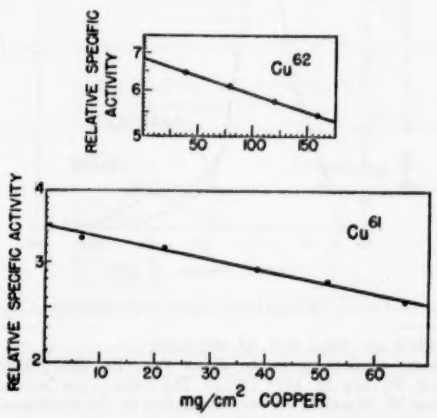

FIG. 3. Self-absorption curves in 4π geometry of Cu^{62} and Cu^{61} activities.

Experimental Corrections

The $(\gamma,2n)$ runs, two at each energy, were made exclusively with the enriched foils. The subtraction of counts due to competing reactions and to residual activity from previous runs was usually made without difficulty. Normally (for counting rates in excess of 20 counts per second) the competing Cu^{64} activity was evaluated by counting it after the decay of the three-hour Cu^{61} activity and then correcting by extrapolating back to the original Cu^{64} activity. However, at lower counting rates, although the Cu^{64} activity still represented a significant correction to the observed Cu^{61} activity, the usual procedure could not be followed as the amount of the Cu^{64} activity remaining after decay of the Cu^{61} was so small as to be completely obscured by the natural counter background. In this event, a $2\frac{1}{2}$-hour run of constant beam intensity was made and high counting rates were assured by using a $\frac{1}{8}$-inch lead converter. By following the decay of the sample over an extensive period, the resultant activities could be separated and the initial counting-rate ratio of Cu^{62}: Cu^{64} determined. Since the $Cu^{63}(\gamma,n)Cu^{62}$ and $Cu^{65}(\gamma,n)Cu^{64}$ cross sections occur at essentially the same effective quantum energy—well below the region of the $Cu^{63}(\gamma,2n)Cu^{61}$ cross section—it seemed reasonable to assume the above ratio to be essentially independent of energy above the $(\gamma,2n)$ threshold. This was indeed found to be the case. Thus, in the regular low-counting rate $(\gamma,2n)$ runs, the expected Cu^{62} activity was deduced from a knowledge of the average beam intensity and from the already determined $Cu^{63}(\gamma,n)Cu^{62}$ activation curve. This, combined with the above ratio, then determined the expected Cu^{64} background activity.

Multiple scattering of the primary electrons in the foils increases the effective path lengths of the bremsstrahlung quanta and electrons in the rear foil relative to the first. A correction for this was applied which varied from 4 to 0.4 percent from 12 to 36 Mev.[25] A further correction resulted from the fact that the electrons, which contribute nearly 80 percent of the background activity in the rear foil, are degenerated in energy while traversing the radiator. The remaining background consists of approximately 20 percent stray gamma-ray induced activity (as determined by magnetically removing the electrons before they strike the foils, and observing the resultant activity), and about 1 percent neutron-induced activity (about equal in each foil). Both the gamma and neutron backgrounds were precisely accounted for in each bombardment by the foil-subtraction process. Except for a slight degeneration correction, which can be made with only an order-of-magnitude knowledge of the background, it should be recalled that subtracting the front-foil activity from

[25] K. L. Brown, Ph.D. dissertation, Department of Physics, Stanford University, June, 1953 (unpublished).

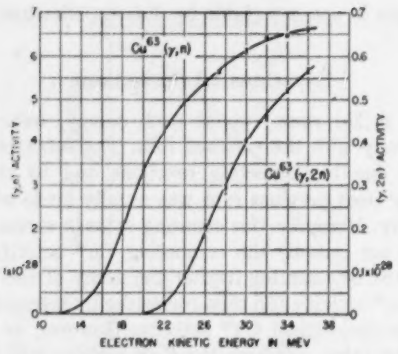

FIG. 4. Activations per Cu^{63} nucleus per electron per cm^2 incident on a 0.025-radiation-length (0.3325 g/cm^2) copper radiator for the $Cu^{63}(\gamma,n)$ and $(\gamma,2n)$ reactions.

the rear-foil activity eliminates the effect of any induced background which is the same in both foils. The validity of this method is borne out by the results of runs on the same set of foils at the same energy but on different occasions. The activity in the front and rear foils normalized to the integrated beam was not consistent from run to run (indicating different gamma backgrounds), whereas the difference in activity reproduced to better than 0.5 percent. Activity induced by foil electrons scattered from rest into an energy region above threshold was calculated to be negligible. The electron-degeneration correction was obtained through the use of the activation curve of the electron-induced reaction derived from the photonuclear activation curve and the photonuclear-electronuclear activation ratio of Brown and Wilson.[15] From this, and the theoretical value of the average electron-energy degeneration expected, the corrected rear-foil electron activation was computed.

The corrected activation curves for the two reactions are plotted in Fig. 4. The average standard deviation of the individual points is about 0.5 percent.

Cross-Section Curves

The cross sections at odd-Mev points were computed by applying the photon-difference method[6] to the activation curves using bremsstrahlung distributions calculated at even-Mev intervals for a 0.025-radiation-length copper radiator. The yield formula is

$$V(\epsilon_M)=n_e N_r N\int_{\epsilon_T}^{\epsilon_M}\phi(\epsilon,\epsilon_M,t)\sigma_\epsilon d\epsilon, \qquad (1)$$

where ϵ = quantum energy in Mev, ϵ_M = maximum quantum energy equal to electron kinetic energy, $V(\epsilon_M)$ = total activated nuclei in the foil corresponding to a maximum quantum energy ϵ_M, n_e = number of incident electrons, N_r = effective number of radiator nuclei per cm^2, N = number of nuclei per cm^2 in the sample, $\phi(\epsilon,\epsilon_M,t)$ = cross section in cm^2 per Mev interval for radiator of thickness t, and σ_ϵ = reaction cross section in cm^2 at energy ϵ.

In the determination of the absolute cross section for the $(\gamma,2n)$ process, the activation was adjusted for the number of Cu^{61} disintegrations which proceed through electron-capture, by the electron-capture to positron-emission ratio of Cook[26] of 0.47. This value is subject to an error of about 10 percent. The result is in excellent agreement with that obtained for the electron-capture to positron-emission ratio calculated theoretically from the decay scheme.[27] A 655-kev gamma ray is present in 20 percent of the Cu^{62} disintegrations, and a 284-kev gamma ray in 3 percent. For the anthracene crystals in the counter of 0.5-cm effective thickness, Compton interactions require a correction to the measured activity amounting to 1.0 ± 0.3 percent.

The copper-62 nucleus decays also partially by electron capture. A theoretical lower limit to the electron-capture to positron-emission ratio is 2.1 percent assuming that all disintegrations proceed directly to the ground state. On the other hand, the small amount of branching which may occur would increase the ratio by two or three times. However, as the precise decay scheme is not yet known, the lower limit was used in stating the final activation and cross-section values.

The cross sections are shown in Figs. 5 and 6. The conclusion may be drawn that in these reactions at the measured energies, the process is more reasonably described by a compound-nucleus model in which the neutrons are evaporated as a statistical fluctuation, than by a model in which the neutrons are ejected by a direct interaction with the incident photon. In the latter case, one would expect the cross section to decrease more slowly past the maximum.[28] The expected ratio of the $(\gamma,2n)$ cross section to the cross section of all reactions in which at least one neutron is emitted may be calculated from the statistical model

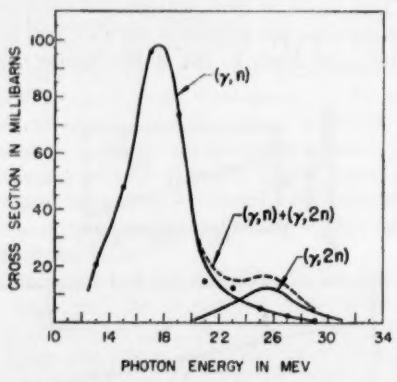

FIG. 5. $Cu^{63}(\gamma,n)$ and $(\gamma,2n)$ cross sections.

[26] C. S. Cook, Phys. Rev. **83**, 462 (1951).
[27] Owen, Cook, and Owen, Phys. Rev. **78**, 686 (1950); R. Bouchez, Physica **18**, 1171 (1952). The authors are indebted to Professor W. Meyerhof for his information on the latest available data on the electron-capture ratios.
[28] E. D. Courant, Phys. Rev. **82**, 703 (1951); C. Levinthal and A. Silverman, Phys. Rev. **82**, 822 (1951).

of Weisskopf and Ewing[29] as

$$\sigma(\gamma,2n)/[\sigma(\gamma,n)+\sigma(\gamma,2n)+\sigma(\gamma,pn)+\sigma(\gamma,3n)+\cdots] = 1-[1+(a/E)^{\frac{1}{2}}(E-E_b)] \times \exp[-(a/E)^{\frac{1}{2}}(E-E_b)], \quad (2)$$

where $a=2.2$ Mev^{-1} for copper, $E=\epsilon-\epsilon_T(\gamma,n) = \epsilon-10.6$ Mev, and $E_b=\epsilon_T(\gamma,2n)-\epsilon_T(\gamma,n)=20-10.6=9.4$ Mev.

Table II compares the calculated values with the results of this experiment at several quantum energies. The (γ,pn) cross section could readily account for the observed discrepancy.

The observed $(\gamma,2n)$ threshold is 20.0 ± 0.5 Mev. This is not quite at the maximum energy for the (γ,n) reaction, as might be expected on an evaporation model, probably because of competition from the (γ,pn) reaction. Judging from the small amount of information available on other isotopes,[2] this latter cross section is expected to be of the same order of magnitude as the $(\gamma,2n)$ cross section.

The cross sections integrated over all energies up to 35 Mev for the (γ,n) and $(\gamma,2n)$ reactions are 0.55 and 0.081 Mev-barn, respectively. The same values were found either from the area of the curves or from the values of the yield at 36 Mev and the bremsstrahlung cross section at the mean cross-section energy. The theoretical integrated cross sections for all reactions in copper were found by Levinger and Bethe[30] to be 0.95 $(1+0.8x)$ Mev-barns for Cu^{63}. The value of x, the fraction of neutron-proton exchange force quoted in the paper, is 0.55, so that the integrated cross section would then be 1.35 Mev-barns. This is considerably higher than the 0.63 Mev-barn found experimentally for the (γ,n) and $(\gamma,2n)$ integrated sum. The inequality may be due to (a) the presence of competing cross sections, notably the (γ,pn) and (γ,p), or (b) the probable increase of the cross sections at several hundred Mev.

TABLE II. $\sigma(\gamma,2n)/[\sigma(\gamma,n)+\sigma(\gamma,2n)+\cdots]$ calculated from the statistical model and compared with the experimental result of $\sigma(\gamma,2n)/[\sigma(\gamma,n)+\sigma(\gamma,2n)]$.

Energy (Mev)	Theory	Experiment
21	0.08	0.13
23	0.36	0.43
25	0.58	0.71
27	0.73	0.79

TABLE III. Integrated cross section for the reaction $Cu^{63}(\gamma,n)$.

$\sigma(\gamma,n)$ (Mev-barns)	Reference
0.60	5
0.63	6
0.76	10
0.77 ± 0.15	11
0.55 ± 0.03	this paper

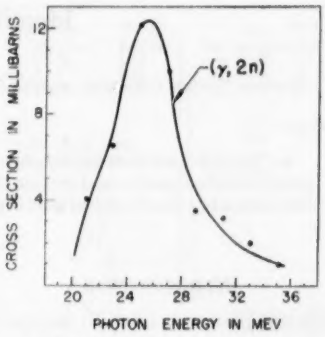

FIG. 6. $Cu^{63}(\gamma,2n)$ cross section.

In Table III, the (γ,n) cross section is compared with those of other workers.

The error in the values of the integrated cross section may be estimated as 5 percent for the (γ,n) reaction and 20 percent for the $(\gamma,2n)$ reaction. In the first reaction, an error of 1 to 2 percent arises from the calculation of the thick-target bremsstrahlung distribution. The precision of the integrated value would be sensitive only to the part of the bremsstrahlung distribution between 12 and 24 Mev, which is known to good accuracy for primary-electron energies in the neighborhood 30–36 Mev. The limit of accuracy of the electron collector is 2 percent, and fluctuations in foil mass per unit area constitute the remainder of the major errors. In the $(\gamma,2n)$ absolute determination, aside from the slightly poorer counting statistics, an additional error occurs due to the significant self-absorption of the lower-energy beta particles in the thicker foils. Furthermore, the published uncertainty in the ratio of electron-capture to positron-emission is about 10 percent.[26]

ACKNOWLEDGMENT

The authors wish to thank Professor W. K. H. Panofsky, under whose direction this research was carried out. Acknowledgment is made of the assistance on several phases of this work given by Dr. W. C. Barber and Wayland George. We also wish to thank many other members of the Hansen Laboratories staff who have contributed to the completion of this research; in particular, C. Newton, D. D. Reagan, C. Hsieh, and J. Helmer, who have helped in the development of the Faraday-cup integrator.

[29] V. F. Weisskopf and D. H. Ewing, Phys. Rev. **57**, 472 (1940).
[30] J. S. Levinger and H. A. Bethe, Phys. Rev. **78**, 115 (1950).

Identification of Platinum-188†

ROBERT A. NAUMANN
Palmer Physical Laboratory and Frick Chemical Laboratory, Princeton University, Princeton, New Jersey
(Received June 28, 1954)

An unstable even-even neutron-deficient platinum isotope with a half-life of 10.3±0.4 days has been prepared and assigned a mass number 188. The decay of this isotope results in unstable iridium 188, which in turn decays to a known excited state in stable osmium 188.

INTRODUCTION

THE lightest platinum ($Z=78$) isotope previously reported is stable platinum-190, occurring in nature to the extent of 0.012 percent.[1] In an attempt to prepare and identify lighter platinum radioisotopes, bombardments of metallic iridium foil with 50-Mev protons have been carried out in the Nevis and Harvard University synchrocyclotrons. The iridium foil was stated by the manufacturer[2] to be 99.8+ percent pure, and spectroscopic analysis[3] revealed only the presence of platinum to the extent of 0.1 percent as a heavy element impurity.

SEPARATION PROCEDURES

After bombardment a platinum fraction was chemically isolated by solvent extraction of the platinum as a platinum-tin complex into ethyl acetate from 6*N* hydrochloric acid, the iridium target having been previously dissolved in a fused mixture of KOH and KNO_3.[4] An iridium fraction could be prepared free from radioplatinum by repeated extraction of added inert platinum carrier solution. The method was checked by achieving a satisfactory separation of 3-day Pt^{191} and 4-day Pt^{193m} from 75-day Ir^{192} and 19-hour Ir^{194} formed by 22-Mev deuteron bombardment of natural iridium.

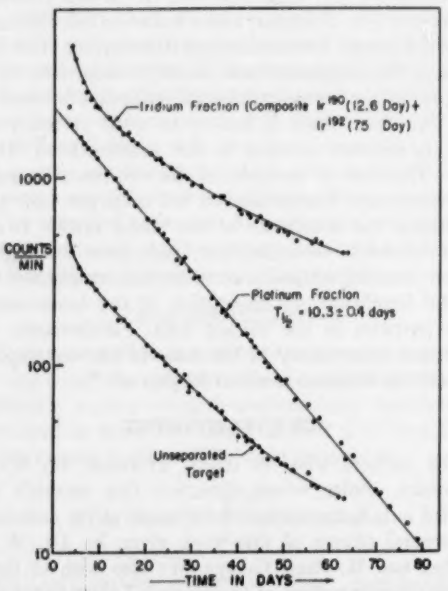

FIG. 1. Gross decay curves of fractions isolated from an iridium target bombarded with 50-Mev protons.

DECAY DATA

A typical decay curve of the platinum and iridium fractions separated from an iridium target after bombardment is shown in Fig. 1. The decay was followed with an Amperex 200C Geiger-Müller counter having an end window 1.4 mg/cm² thick. After 3 days the platinum fraction showed a simple exponential decay with a half-life of 10.3±0.4 days, which was followed for over 70 days. The iridium fraction shows a complex decay curve.

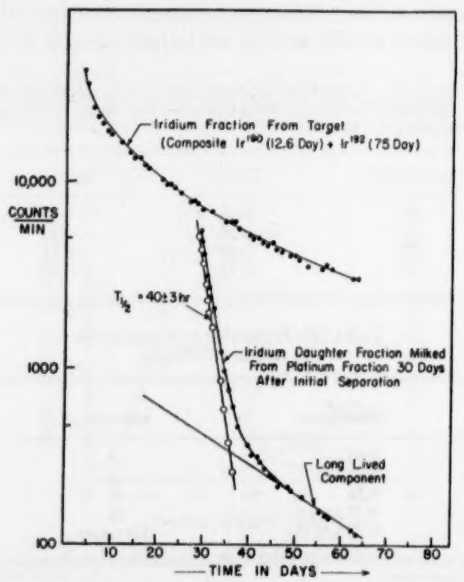
Iridium Fraction From Target
(Composite Ir190 (12.6 Day) + Ir192 (75 Day)
T½ = 40 ± 3 hr
Iridium Daughter Fraction Milked From Platinum Fraction 30 Days After Initial Separation
Long Lived Component
COUNTS MIN
10,000
1000
100
10 20 30 40 50 60 70 80
TIME IN DAYS

FIG. 2. Gross decay curves of the iridium fraction isolated directly after bombardment from the target (top curve) and the iridium fraction isolated from an aged sample of the 10.3-day platinum (bottom curve).

† This research was supported in part by the U. S. Atomic Energy Commission, the Higgins Scientific Trust Fund, the U. S. Office of Naval Research, and through a grant in aid by the E. I. du Pont de Nemours and Company, Inc.

[1] W. T. Leland, Phys. Rev. 76, 992 (1949).

[2] Baker and Company, Inc., Newark, New Jersey.

[3] We are indebted to the spectroscopy division of Brookhaven National Laboratory for performing this analysis.

[4] W. Wayne Meinke, University of California Radiation Laboratory Report UCRL-432 (unpublished).

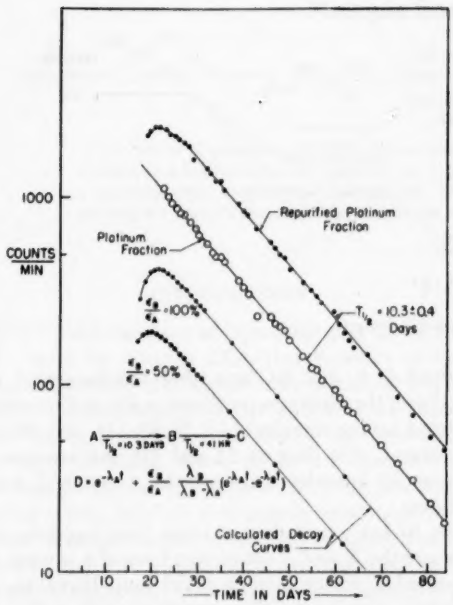
Repurified Platinum Fraction
Platinum Fraction
$T_{1/2}$ = 10.3±0.4 Days
$\frac{\epsilon_B}{\epsilon_A}$ =100%
$\frac{\epsilon_B}{\epsilon_A}$ =50%
A $T_{1/2}$ =10.3 DAYS B $T_{1/2}$ =41 HR C
$D = e^{-\lambda_A t} + \frac{\epsilon_B}{\epsilon_A} \frac{\lambda_B}{\lambda_B - \lambda_A}(e^{-\lambda_A t} - e^{-\lambda_B t})$
Calculated Decay Curves
COUNTS MIN
TIME IN DAYS

FIG. 3. Gross decay curves of a 10.3-day platinum fraction isolated directly after bombardment and of a repurified sample of the 10.3-day platinum (top 2 curves), for comparison the calculated gross decay curves of a 10.3-day isotope with 41-hour daughter isotope are shown (bottom 2 curves).

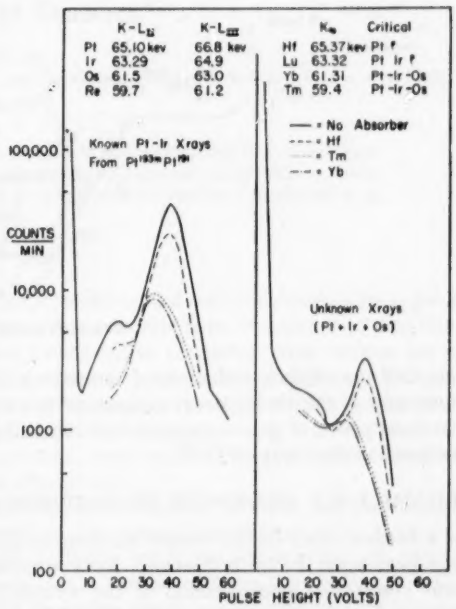
K-L_{II} K-L_{III} K_α Critical
Pt 65.10 kev 66.8 kev Hf 65.37 kev Pt f
Ir 63.29 64.9 Lu 63.32 Pt Ir f
Os 61.5 63.0 Yb 61.31 Pt-Ir-Os
Re 59.7 61.2 Tm 59.4 Pt-Ir-Os
— = No Absorber
- - - = Hf
= Tm
-·- = Yb
Known Pt-Ir Xrays From Pt^{193m} Pt^{79m}
Unknown Xrays (Pt + Ir + Os)
COUNTS MIN
PULSE HEIGHT (VOLTS)

FIG. 4. Comparison of the critical absorption of known platinum and iridium x-rays and the x-rays occurring in the decay of an aged sample of 10.3-day platinum.

In order to determine chemically the element to which this half-life was to be assigned, further individual separations of mercury, gold, platinum, iridium, and osmium were undertaken from the platinum fraction 36 days after its initial separation from the target. No activity was found to be present in the mercury, gold, or osmium fractions. However, the iridium and repurified platinum fractions both showed activity. The decay curves of the iridium fractions, isolated directly from the target and isolated from the aged platinum fraction, are shown in Fig. 2. The iridium fraction isolated from the aged platinum fraction shows a decay resolvable into a short-lived component having a half-life of 40±3 hours, and a longer-lived component having a half-life of approximately 10 days. The iridium fraction isolated directly from the target shows no short-lived decay component 36 days after bombardment. A 41-hour neutron-deficient iridium isotope, Ir^{188}, has been reported by Chu;[5] this suggests that the short-lived component in the iridium fraction isolated from the aged platinum is the Ir^{188} daughter of a long-lived Pt^{188} parent. The long-lived component is most probably platinum activity incompletely separated from this iridium fraction.

The decay of the repurified platinum fraction is shown in Fig. 3. A growth in total activity during the first 3 days after purification was followed by a simple exponential decay with a half-life of approximately 10 days. This decay curve is compatible with the total activity curve expected for the growth of a 41-hour daughter activity from a 10.3-day parent, if the disintegrations of the daughter are counted with approxi-

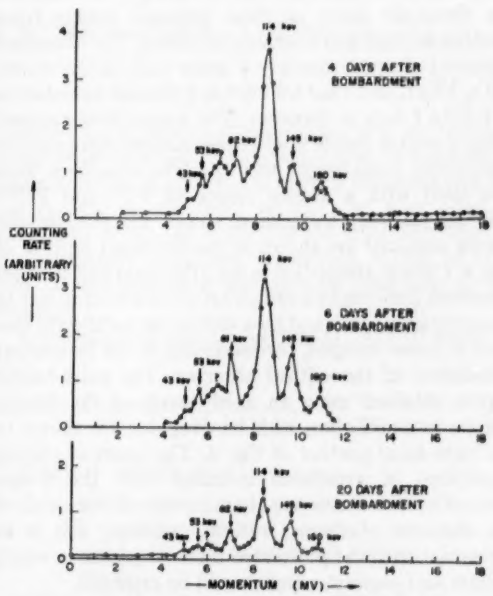

FIG. 5. Conversion electron peaks accompanying the decay of the 10.3-day platinum activity showing the initial increase of the electron lines at 82 and 145 kev.

[5] T. C. Chu, Phys. Rev. **79**, 582 (1950).

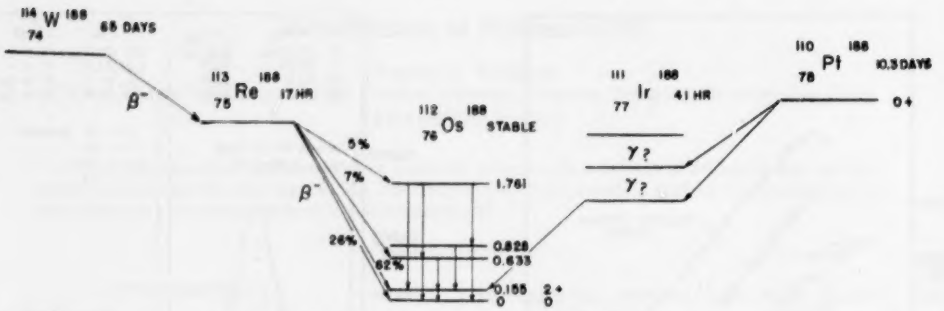

FIG. 6. Properties of the mass-188 isobars.

mately half the efficiency of those of the parent. The reappearance of the 10-day decay component preceded by the short period of growth suggests that this half-life be assigned to the decay of Pt^{188}.

CRITICAL X-RAY ABSORPTION MEASUREMENTS

As a further check on the atomic numbers involved in the postulated $Pt^{188}-Ir^{188}-Os^{188}$ decay sequence, critical absorption measurements of the x-radiations accompanying the decay of the 10-day activity were undertaken. The x-radiations expected in such a sequence would be those characteristic of iridium and osmium and would result from the filling of vacancies in the electronic shells of these elements arising from electron capture and internal conversion. The absorbers consisted of approximately ½ gram each of the oxides HfO_2, Yb_2O_3, and Tm_2O_3 spread in a circular indentation in Lucite 1 inch in diameter. The x-rays were counted using a sodium iodide scintillation counter equipped for differential pulse-height analysis. The absorbers were first used with a known source of Pt^{191} and Pt^{193m} emitting platinum and iridium x-rays. The pulse-height curves obtained are shown in the left-hand portion of Fig. 4. Critical absorption in the ytterbium and thulium absorbers is shown by a reduction of the counting rate in the x-ray photopeak and by a shift in the location of this peak to lower energies, corresponding to the fluorescent x-radiation of the critical absorber. The pulse-height curves obtained using an aged source of the 10-day isotope in equilibrium with its daughter are shown in the right-hand portion of Fig. 4. The onset of critical absorption in ytterbium indicates that the x-rays emitted by this source are characteristic of one or all of the elements platinum, iridium, osmium; this is in agreement with the postulated decay sequence in which iridium and osmium x-rays would be expected.

CONVERSION ELECTRONS

A preliminary study of the electron lines occurring in the decay of the 10-day platinum has been made with a thin-lens β-ray spectrometer. A thin source was prepared by electrolytic deposition of high specific activity material upon 0.2-mil platinum foil. The conversion lines observed 4, 6, and 20 days after bombardment and isolation of the platinum are shown in Fig. 5. Conversion electrons having energies of 43, 53, 82, 114, and 180 kev are present. The lines at 82 and 145 kev are seen to increase in intensity between the 4-day and 6-day readings.

The 63-kev separation of these lines suggests that these are the K and L conversion lines of a gamma ray converted in either osmium or iridium. However, the initial increase in intensity suggests that these lines are associated with the decay of a daughter activity, presumably due to a level in Os^{188} reached by decay of Ir^{188}. The energy of this transition is then found to be 156±3 kev from the known[6] K and L electron binding energies in osmium. This energy value is in good agreement with the values previously reported[7–11] for the lowest-lying $E2$ γ transition in Os^{188} which range from 152–160 kev. This level had been observed by the previous workers in the β^- decay of Re^{188} and its reoccurrence confirms a mass assignment of 188 to both the 10.3-day platinum and the 42-hour iridium.

The remaining conversion lines at 43, 53, 114, and 180 kev are associated with levels in Ir^{188}, the 53 and 114 or 114 and 180 may constitute a K, L conversion line pair. Figure 6 summarizes the present information available concerning the mass 188 isobars; the level scheme for Os^{188} is taken from McMullen and Johns.[11]

ACKNOWLEDGMENTS

It is a pleasure to acknowledge the assistance of Dr. W. Goodell and Dr. W. Preston, and the staffs of the Nevis and Harvard University synchrocyclotrons in carrying out these bombardments, the assistance of Dr. J. Mihelich who first carried out the critical x-ray absorption measurements at Brookhaven National Laboratory, and the assistance of Miss B. Bamman for her help in recording data.

[6] Hill, Church, and Mihelich, Rev. Sci. Instr. **23**, 523 (1952).
[7] L. C. Miller and L. F. Curtiss, Phys. Rev. **70**, 983 (1946).
[8] Cork, Schreffler, and Fowler, Phys. Rev. **74**, 1657 (1948).
[9] Beach, Peacock, and Wilkinson, Phys. Rev. **76**, 1585 (1949).
[10] Richmond, Grant, and Rose, Proc. Phys. Soc. (London) **A65**, 484 (1952).
[11] C. C. McMullen and M. W. Johns, Phys. Rev. **91**, 418 (1953).

Multiple Scattering of Neutrons*

GEORGE H. VINEYARD
Department of Physics, University of Missouri, Columbia, Missouri, and Brookhaven National Laboratory, Upton, New York
(Received June 24, 1954)

The theory of multiple scattering of neutrons is developed in cases of interest for diffraction experiments. Computations of second-order scattering for various plane slab sample arrangements are carried out, under a quasi-isotropic cross-section assumption. The relevance of recent computations by Chandrasekhar is pointed out, and these are also applied to the present problem.

INTRODUCTION

THE determination of crystalline and liquid structures by neutron diffraction depends on measuring single scattering. Higher-order scattering is always present in addition to first-order scattering, and in some cases the experimental data should be corrected accordingly. Although there exists an extensive and elaborate literature on multiple-scattering problems of various types, little of it is exactly applicable to the present situation. Some calculations by Chandrasekhar may be applied in several cases, and these will be considered subsequently. Blok and Jonker[1] have given an approximation method and worked it out numerically in a special application to hydrogenous scatterers. Their method requires rather specific numerical computations for each case, although it permits one to take account of anisotropic cross sections which are not too complicated.

We present in this paper an analysis in terms of orders of scattering. This yields a formal solution to the problem in terms of a sum of definite integrals, and applies to arbitrary sample geometries and for arbitrary scattering cross sections. Evaluation of the early terms of the series is possible for simple geometrical conditions, and gives an adequate approximation whenever the scattering is sufficiently small. The general solution may be used to show certain properties of the scattering, and suggests some approximations which allow one to cope with the very complex cross sections encountered in diffraction problems.

GENERAL ANALYSIS IN TERMS OF ORDERS OF SCATTERING

We consider a sample which consists of a crystalline powder or an amorphous material, so that we can deal exclusively with densities of neutrons instead of Schrödinger waves. We also consider the incident neutrons to be monoenergetic, and neglect the effect of any energy changes during scattering. Let $P_n(\mathbf{r},\mathbf{s})$, $n=0, 1, 2, 3, \cdots$, be defined as the number of neutrons per unit volume at $\mathbf{r}$ which have already been scattered just n times and which are now proceeding in the direction of the unit vector $\mathbf{s}$, within unit solid angle. The scatterer is described by the following parameters:

$\sigma_d(\mathbf{s},\mathbf{s}')$ = differential scattering cross section, per unit volume, for scattering from direction $\mathbf{s}$ to direction $\mathbf{s}'$;

$\sigma=\int\sigma_d d\Omega$ = total scattering cross section per unit volume (here and afterwards $\int d\Omega$ means integration over a solid angle of 4π with respect to the obvious angular variable);

σ_T = total cross section per unit volume (scattering plus absorption).

σ_d is meant to describe the scattering properties of a portion of the material small enough to involve only single scattering, yet large enough to include structural effects, and, in the case of crystalline powders, to contain many crystalline grains representing all orientations. It is thus a macroscopic cross section.

The scattering is governed by a set of transport equations,[2]

$$\mathbf{s}\cdot\nabla P_n(\mathbf{r},\mathbf{s})+\sigma_T P_n(\mathbf{r},\mathbf{s})=\int d\Omega'\sigma_d(\mathbf{s}',\mathbf{s})P_{n-1}(\mathbf{r},\mathbf{s}'),\qquad n=0, 1, 2, \cdots, \quad (1)$$

(where $P_{-1}\equiv 0$) which express the fact that scattering of neutrons of order $n-1$ provides a source, and scattering and absorption of neutrons of order n provide a sink for the current of nth order neutrons at each point $\mathbf{r}$. Equations (1) on the interior of the scatterer, together with boundary conditions prescribing $P_0(\mathbf{r},\mathbf{s})$ at each point of the surface of the scatterer determine all the densities P_n.

A formal set of solutions of Eqs. (1) may be shown to be

$$P_0(\mathbf{r},\mathbf{s})=P_0(\mathbf{r}-L\mathbf{s})\exp(-\sigma_T L), \quad (2a)$$

$$P_n(\mathbf{r},\mathbf{s})=\int d\Omega'\sigma_d(\mathbf{s}',\mathbf{s})\times\int_0^L d\xi\exp(-\sigma_T\xi)P_{n-1}(\mathbf{r}-\xi\mathbf{s},\mathbf{s}'),\qquad n=1, 2, \cdots. \quad (2b)$$

Here L is the distance from the point $\mathbf{r}$ to the surface of the sample in the direction $-\mathbf{s}$. It is assumed that the sample is nowhere concave. See Fig. 1.

* Work carried out under the auspices of the U. S. Atomic Energy Commission.

[1] J. Blok and C. C. Jonker, Physica **18**, 809 (1952).

[2] From the basic article by A. M. Weinberg, U. S. Atomic Energy Commission Report AEC-3405 (unpublished) "the derivation of these equations should be evident."

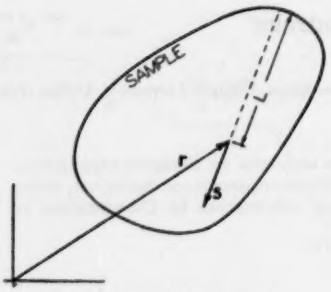

FIG. 1. Geometry of the general case.

Equations (2) state that particles constituting the nth-order component at $\mathbf{r}$ must have suffered their last scattering act somewhere along a line in the direction $-\mathbf{s}$, being at that stage members of the component of order $n-1$, and must then have proceeded to $\mathbf{r}$ without absorption or further scattering.

By iterating Eqs. (2), one can next express P_n as a multiple integral of P_0. In principle the problem is then solved, although the evaluation of these integrals for all but the simplest geometries and cross sections and for $n>2$ proves to be exceedingly tedious. Hereafter, attention will be mainly restricted to samples in the form of a plane slab.

INSTANCE OF THE PLANE SLAB

Suppose the sample to be a slab of indefinite lateral extent and thickness t. Suppose the incoming neutrons to be collimated and incident at an angle θ_0 with the slab normal. For convenience we suppose the incident beam to be of large cross-sectional area, uniformly distributed and containing unit density of neutrons. See Fig. 2.

The neutron densities now become functions of z, the depth below the surface, and θ, the direction of the vector $\mathbf{s}$. We find from Eqs. (2),

$$P_0(z,\theta)=\exp(-\sigma_T z\sec\theta_0)(2\pi)^{-1}\delta(\cos\theta-\cos\theta_0), \quad (3)$$

and

$$P_1(z,\theta)=\sigma_d(\mathbf{s},\mathbf{s}_0)\left[\frac{\exp(-\sigma_T z\sec\theta_0)}{\sigma_T\cos\theta}\right]\times\left[\frac{\exp[\sigma_T L(\sec\theta_0\cos\theta-1)]-1}{\sec\theta_0-\sec\theta}\right], \quad (4)$$

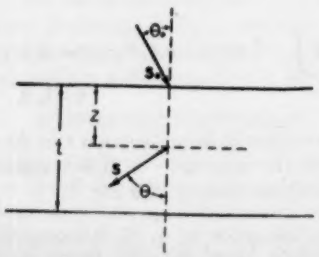

FIG. 2. Geometry of the plane slab.

where

$$L=z\sec\theta, \quad \theta<\pi/2; \quad L=(z-t)\sec\theta, \quad \theta>\pi/2, \quad (5)$$

and δ indicates the Dirac δ function. At the bottom of the slab, (4) gives, with $\sigma_T t=\tau$,

$$P_1(t,\theta)=\sigma_d(\mathbf{s},\mathbf{s}_0)\left[\frac{\exp(-\tau\sec\theta_0)}{\sigma_T\cos\theta}\right]\times\left[\frac{\exp[\tau(\sec\theta_0-\sec\theta)]-1}{\sec\theta_0-\sec\theta}\right], \quad \theta<\pi/2, \quad (6)$$

and at the top,

$$P_1(0,\theta)=\sigma_d(\mathbf{s},\mathbf{s}_0)\left[\frac{\exp[-\tau(\sec\theta_0-\sec\theta)]-1}{\sigma_T\cos\theta(\sec\theta_0-\sec\theta)}\right], \quad \theta>\pi/2. \quad (7)$$

To calculate the current density in nth-order scattering which leaves the surface of the slab, it is only necessary to multiply P_n, evaluated at the surface, by the velocity of the neutrons. The current is the current density multiplied by the cross-sectional area of the beam, and if $J_n(\theta)$ is the nth-order scattered current, per unit incident current, transmitted through the slab at direction θ, per unit solid angle, we find

$$J_n(\theta)=(\cos\theta/\cos\theta_0)P_n(t,\theta), \quad n=0, 1, 2, \cdots. \quad (8)$$

In the following, second-order scattering will be computed for three specific cases:[3] (a) angle of incidence equal to angle of transmission, (b) angle of incidence equal to zero, and (c) reflection at an angle equal to angle of incidence, sample infinitely thick.

Case (a): $\theta=\theta_0$

Equation (2b), with $n=2$, applied to Eq. (4) gives

$$P_2(t,\theta)=\sigma_T^{-2}\sec\theta e^{-\tau\sec\theta}\int d\Omega'\sigma_d(\mathbf{s},\mathbf{s}')\sigma_d(\mathbf{s}',\mathbf{s}_0)f(\theta'), \quad (9)$$

where $\mathbf{s}'$ is a unit vector making angle θ' with the (downward) slab normal, and

$$f(\theta')=\frac{|\sec\theta'|}{(\sec\theta-\sec\theta')^2}\{\exp[\tau|\sec\theta'|(\sec\theta\cos\theta'-1)]-1\}-\frac{\tau\sec\theta'}{\sec\theta-\sec\theta'}.$$

In general, this integral can be handled only by numerical methods. However, for most liquid and crystalline

[3] With the quasi-isotropic approximation it does not matter (in second- and higher-order scattering) whether the direction of emergence is co-planar with the slab normal and the direction of incidence. In developing the δ-function approximation this further restriction will be assumed.

samples, σ_d is a rapidly varying function of angle which, if averaged over a small range of angles about any angle, would be virtually a constant, equal to $\sigma/4\pi$. $f(\theta')$ is a relatively slowly varying function, and we thus find that a good approximation to P_2 is given by replacing the two differential cross sections by $\sigma/4\pi$ and removing them from the integral. This approximation is inadequate for θ very small, or for the case of x-ray scattering where, at not too long wavelengths, the atomic structure factor imparts a pronounced secular trend to σ_d. We call it the quasi-isotropic approximation.

With the quasi-isotropic approximation the integral in (9) may be evaluated, to give:

$$J_2(\theta)=P_2(t,\theta)=\left(\frac{\sigma}{\sigma_T}\right)^2\frac{e^{-\tau s}}{8\pi s}\Big[\left(\frac{s}{s-1}\right)(1-e^{(s-1)\tau})$$
$$+(s\tau+1)\{\bar{\mathrm{Ei}}([s-1]\tau)-\ln([s-1]\tau)\}$$
$$+\left(\frac{s}{s+1}\right)(1-e^{-(s+1)\tau})+(1-s\tau)$$
$$\times\{\mathrm{Ei}(-[s+1]\tau)-\ln([s+1]\tau)\}+2\ln\tau$$
$$-(e^{s\tau}+e^{-s\tau})\,\mathrm{Ei}(-\tau)\Big], \quad (10)$$

where $s=\sec\theta$,

$$\mathrm{Ei}(x)=\int_{-\infty}^{x}\frac{e^u}{u}du, \quad x<0,$$

and $\bar{\mathrm{Ei}}(x)$ is defined by the same integral as $\mathrm{Ei}(x)$, with $x>0$; the integral is understood in the sense of the Cauchy principal value.[4]

There is another form of σ_d, the δ function approximation, which allows rather simple evaluation of (9) and which approximates a variety of situations, including both isotropic and highly anisotropic examples. Let

$$\sigma_d(\chi)=\sum_{n=1}^{N}a_n\delta(\chi-b_n), \quad (11)$$

where χ is the scattering angle, and a_n and b_n are arbitrary. This form is well suited to the cross section of a crystalline powder, for example. Let the pole of a spherical coordinate system coincide with the downward slab normal. Let $\mathbf{s}$, $\mathbf{s}_0$, and the slab normal be co-planar. Let $\mathbf{s}'$ have polar angles θ' and φ', where φ' is measured from the plane of $\mathbf{s}$ and $\mathbf{s}_0$. Let the angle between $\mathbf{s}'$ and $\mathbf{s}_0$ be η, between $\mathbf{s}'$ and $\mathbf{s}$ be ζ. One finds, assuming $\theta=\theta_0$, $(\chi=2\theta)$,

$$\cos\eta=\cos\theta'\cos\theta-\sin\theta'\sin\theta\cos\varphi',$$
$$\cos\zeta=\cos\theta'\cos\theta+\sin\theta'\sin\theta\cos\varphi',$$
$$\theta'=\cos^{-1}[(\cos\eta+\cos\zeta)/2\cos\theta].$$

[4] E. Jahnke and J. Emde, *Table of Functions* (G. E. Stechert and Company, New York, 1938), pp. 1–3. A. Hammad, Phil. Mag. **38**, 515 (1947).

The solid angle $d\Omega'$ can be written: (when $\theta\neq 0$)

$$d\Omega'=\sin\theta'd\theta'd\varphi'=I(\eta,\zeta)d\eta d\zeta, \quad (12)$$

where

$$I(\eta,\zeta)=\left[1-\left(\frac{\cos2\theta-\cos\eta\cos\zeta}{\sin\eta\sin\zeta}\right)^2\right]^{-\frac{1}{2}}.$$

Inserting (11) and (12) in (9), we find

$$P_2(t,\theta)=\sigma_T^{-2}\sec\theta e^{-\tau\sec\theta}$$
$$\times\sum_{n=1}^{N}{\sum_m}^{*}a_na_mI(b_n,b_m)f(\theta_{nm}'), \quad (13)$$

where θ_{nm}' means θ' at $\eta=b_n,\zeta=b_m$, and $\sum_m{}^*$ means summation over all m for which $|b_n-2\theta|\leq b_m\leq|b_n+2\theta|$.

Equation (13) can be explicitly evaluated without much trouble for reasonable values of N. From its form one sees that the peaks in σ_d do not appear directly in J_2. The individual terms of (13) are not monotonic in θ, however, since $I(b_n,b_m)$ becomes infinite when $2\theta=|b_n\pm b_m|$. The resulting infinities in P_2 are caused by the infinitely sharp peaks assumed for σ_d. Allowing a small but finite width w (radians) for each peak of σ_d, and keeping the areas of each peak unchanged, one finds that at these infinities one should replace $I(b_n,b_m)$ in (13) by

$$[(9/32)|\cot b_n\pm\cot b_m|w]^{-\frac{1}{2}},$$

corresponding to the cases $|b_n\pm b_m|=2\theta$, respectively. Correction of I is unnecessary whenever $2\theta-|b_n\pm b_m|\gg w$.

For $w=0.01$ radian, $b_n=80°$, $b_m=90°$, this gives a peak only about 4 times as high as the minimum point on the curve of $I(b_n,b_m)$ *vs* θ. Thus, in typical crystalline cases these peaks are low and broad, and the superposition of all of them leads to a rather smooth curve resembling that of the quasi-isotropic approximation.

Case (b): $\theta_0=0$

A precisely similar calculation, again making the quasi-isotropic approximation, reveals that

$$J_2(\theta)=\cos\theta P_2(t,\theta)=\left(\frac{\sigma}{\sigma_T}\right)^2\frac{e^{-\tau s}}{8\pi}$$
$$\times\Big[-\frac{1}{s}(e^{\tau s}+e^{-\tau})\,\mathrm{Ei}(-\tau)+\frac{1}{s-1}\mathrm{Ei}(-2\tau)$$
$$-\frac{1}{s(s-1)}e^{\tau(s-1)}\,\mathrm{Ei}(-\tau[s+1])-\frac{1}{s(s-1)}$$
$$\times\{\bar{\mathrm{Ei}}(\tau[s-1])-\ln(\tau[s-1])+\ln\tau\}$$
$$+\frac{1}{s-1}e^{\tau(s-1)}\ln(\tfrac{1}{2}\gamma\tau)+\frac{1}{s(s-1)}$$
$$\times e^{\tau(s-1)}\ln(s+1)+\left(\frac{e^{\tau(s-1)}-1}{s-1}\right)\ln2\Big], \quad (14)$$

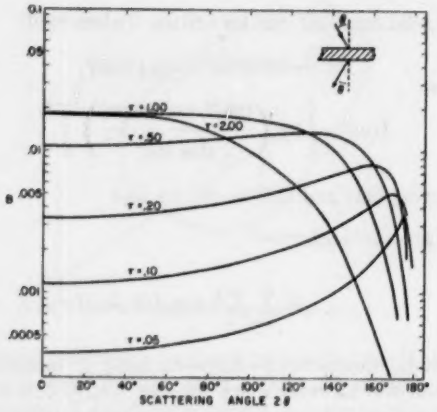

FIG. 3. Second scattering coefficient, B *vs* scattering angle, 2θ [case (a)].

where $\gamma = 1.78107\cdots$.

Case (c): Reflection at the Specular Angle, Thick Slab

This is the only case giving simple results. With the same procedure, and the quasi-isotropic approximation, we find

$$J_2(\theta) = P_2(0,\theta) = (\sigma/\sigma_T)^2(8\pi \sec\theta)^{-1} \ln(1+\sec\theta). \quad (15)$$

Here, contrary to the previous convention, θ has been measured from the upward normal, as pictured in Fig. 4.

Summary of Plane Slab Results

In all three cases, we find that the first- and second-order scattered currents can be written, respectively,

$$J_1 = (\sigma/\sigma_T)A 4\pi\sigma_d(\chi)/\sigma, \quad (16)$$

$$J_2 = (\sigma/\sigma_T)^2 B, \quad (17)$$

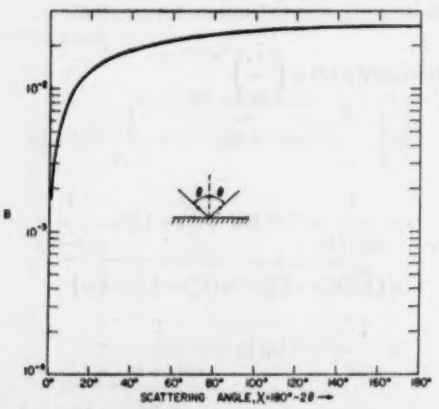

FIG. 4. Case (c) (back reflection) second scattering coefficient, B *vs* scattering angle, $\pi - 2\theta$.

where A and B may be called the first- and second-order scattering coefficients, and are defined by Eqs. (10), (14), and (15) in conjunction with the preceding expressions. The angle χ is the scattering angle, equal to 2θ, θ, and $\pi - 2\theta$, in cases (a), (b), and (c), respectively. Equation (16) has been cast into such a form that the mean value of the differential cross-section dependent factor, $4\pi\sigma_d(\chi)/\sigma$, is unity. A and B each depend on τ and $\sec\theta$ only.

Equations (16) and (17) indicate at once the role of the ratio σ/σ_T, which may be termed an "albedo," in fixing the magnitude of the various orders of scattering. One may further show, by a simple change of variables in the second integral of Eq. (2b), that P_n is quite generally proportional to $(\sigma/\sigma_T)^n$. From this it is clear that a sufficiently large absorption cross section can always reduce higher-order scattering indefinitely compared to first order scattering. With x-rays the albedo is typically from 0.1 to 0.01 and thus multiple scattering corrections are generally less important for x-rays than for neutrons.

The second scattering coefficient B (under the quasi-isotropic approximation) is plotted *vs* the scattering angle χ in Figs. 3 and 4, for cases (a) and (c), respectively. In Fig. 3, various values of the thickness parameter τ lead to the various curves. Here, a tendency of second-order scattering to be isotropic is apparent, especially for τ in the vicinity of 1.

In Fig. 5 is plotted the ratio of second-order scattering coefficient B to first-order coefficient A, for case (a), with quasi-isotropic approximation. The thickness parameter τ is abscissa. For modest scattering angles the ratio is nearly independent of scattering angle. From the curves, one sees that τ must be as small as 0.05 to make B/A equal $\frac{1}{10}$. With vanishing thickness, the ratio vanishes, but as $\tau \ln\tau$, rather than linearly with τ, as one might have at first supposed.

LIMITS OF VALIDITY OF THE RESULTS

The implicit assumption of the foregoing work has been that second-order scattering forms such a large share of the multiple scattering that third, fourth, etc., orders may be ignored. This assumption is valid only under special circumstances. Rough calculation shows that third-order scattering is about as much smaller than second order as second order is smaller than first, and this proportion extends to all higher orders as well. Consequently, if second-order scattering is much less than first order, we may generally conclude that second order is well representative of all higher orders. Two conditions, as has been noted, favor this: smallness of τ, and smallness of the albedo, σ/σ_T. From the curves given here one can immediately determine whether this condition is satisfied.

To demonstrate more fully the relative magnitudes of the various higher orders of scattering, suitable rela-

tions of inequality can be found. Define

$$Q_n(\mathbf{r}) = \int d\Omega P_n(\mathbf{r},\mathbf{s}), \tag{18}$$

the nth-order neutron density at $\mathbf{r}$. With the quasi-isotropic approximation, Eq. (2b) may be rewritten

$$P_n(\mathbf{r},\mathbf{s}) = (\sigma/4\pi)\int_0^L d\xi \exp(-\sigma_T\xi) Q_{n-1}(\mathbf{r}-\xi\mathbf{s}).$$

Now if the maximum value of $Q_n(\mathbf{r})$, for all $\mathbf{r}$, is denoted $Q_n^{\max}$, we have

$$P_n(\mathbf{r},\mathbf{s}) \leq (\sigma/4\pi) Q_{n-1}{}^{\max} \int_0^L d\xi \exp(-\sigma_T\xi)$$

$$= (\sigma/4\pi\sigma_T) Q_{n-1}{}^{\max}[1-\exp(-\sigma_T L)]. \tag{19}$$

Specializing now to the plane slab case, L is given by Eq. (5). Next, integrate Eq. (19) with respect to the solid angle associated with $\mathbf{s}$. One finds

$$Q_n(\mathbf{r}) \leq (\sigma/\sigma_T)[1-F(z)] Q_{n-1}{}^{\max},$$

TABLE I. Test of approximations.

σ/σ_T	τ	Error in using J_2	Error in using Eq. (23)
1	0.1	−20%	−4%
1	0.5	−45%	+5%
0.5	0.5	−21%	+1.5%

where

$$F(z) = \tfrac{1}{2}\{\exp[-\sigma_T z]+\exp[-\sigma_T(t-z)] + \sigma_T z \,\mathrm{Ei}(-\sigma_T z)+\sigma_T(t-z)\,\mathrm{Ei}[-\sigma_T(t-z)]\}.$$

The minimum value of $F(z)$ occurs at $z=t/2$, so finally,

$$Q_n{}^{\max} \leq (\sigma/\sigma_T) g(\tau) Q_{n-1}{}^{\max}, \tag{20}$$

where

$$g(\tau) = 1-F(t/2) = 1-\exp(-\tau/2)-(\tau/2)\,\mathrm{Ei}(-\tau/2). \tag{21}$$

$g(\tau)$ is plotted in Fig. 6.

Iterating the inequalities (20), we find

$$Q_n{}^{\max} \leq [(\sigma/\sigma_T) g(\tau)]^{n-m} Q_m{}^{\max}. \tag{22}$$

The general level of higher than second-order scattering cannot exceed $\sum_{n=3}^{\infty} Q_n{}^{\max}$; so by (22), this level cannot exceed

$$\sum_{n=3}^{\infty} [(\sigma/\sigma_T) g(\tau)]^{n-2} Q_2{}^{\max} = Q_2{}^{\max}[(\sigma/\sigma_T) g(\tau)][1-(\sigma/\sigma_T) g(\tau)]^{-1}.$$

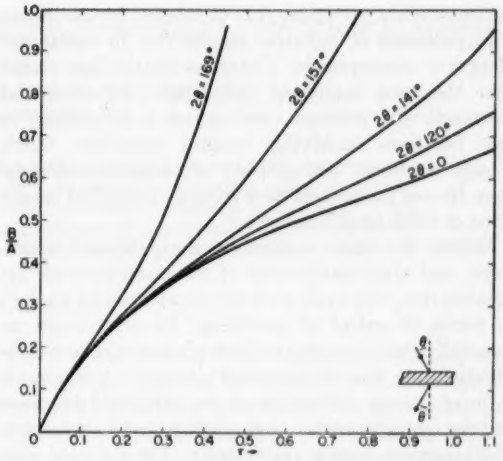

FIG. 5. Ratio of 2nd to 1st scattering coefficients, B/A vs τ [case (a)].

From this it is clear that smallness of $(\sigma/\sigma_T)g(\tau)$ compared to unity insures that second-order scattering is a close approximation to all of the multiple scattering. Comparison of Fig. 6 and Fig. 5 shows that this criterion is nearly the same as the previously described criterion that $(\sigma/\sigma_T)(B/A)$ be small.

From these calculations a rough tendency for the ratio J_{n+1}/J_n to be independent of n is apparent. This suggests an improved approximation for the multiple scattering. Assume $J_{n+1}/J_n = J_2/\bar{J}_1$, $n=2, 3, \cdots$, where $\bar{J}_1$ means the average of J_1 over angles. Employing (16) and (17), we have $J_2/\bar{J}_1 = (\sigma/\sigma_T)(B/A)$. Then

$$J_2+J_3+J_4+\cdots \cong J_2[1+(\sigma/\sigma_T)(B/A) + (\sigma/\sigma_T)^2(B/A)^2+\cdots],$$

or

$$J_2+J_3+J_4+\cdots \cong J_2/[1-(\sigma/\sigma_T)(B/A)]. \tag{23}$$

Equation (23) is an appreciable improvement over J_2 itself, as long as $(\sigma/\sigma_T)(B/A)<1$. A test of this is afforded by Chandrasekhar's exact calculation for isotropic scattering [case (b)]. For $\theta=0$, one finds errors as listed in Table I.

CHANDRASEKHAR'S COMPUTATIONS

The problem of multiple scattering without energy loss has already had considerable attention from

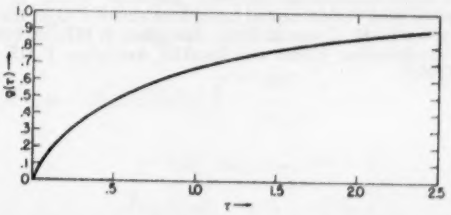

FIG. 6. $g(\tau)$ vs τ, plane slab case [see Eq. (21)].

astrophysicists, to whom it is of interest in connection with problems of radiative equilibrium in stellar and planetary atmospheres. Chandrasekhar[5,6] has shown that the total scattering (all orders) for plane-slab scatterers with isotropic cross section is determined by two functions satisfying integral equations which, though nonlinear, are adapted to numerical computation. He and co-workers have recently published tabulations of these basic functions.[7]

Within the realm covered by the published tabulations, and after justification of the quasi-isotropic approximation, this work is clearly superior to an analysis in terms of orders of scattering. Its advantages are especially great for cases of thick scatterers. There is the disadvantage that the scattered intensity appears as the ratio of certain differences of the tabulated functions and the quantity $\cos\theta_0 - \cos\theta$, where θ_0 and θ are incident and emergent angles, respectively. For the case most

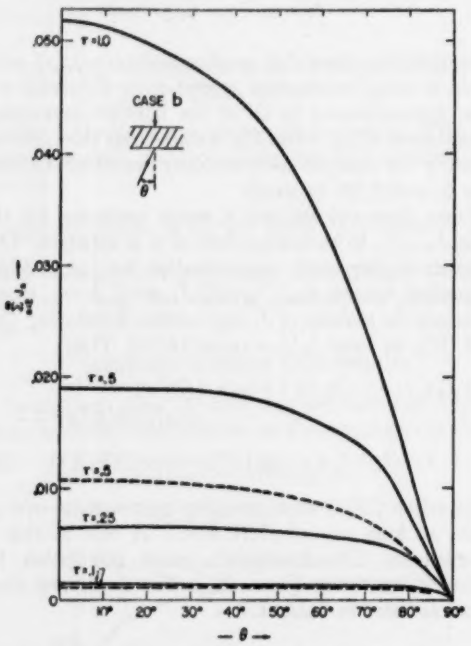

FIG. 7. Multiple scattering, $\Sigma_{n=2}^{\infty} J_n$, from Chandrasekhar. $\sigma/\sigma_T = 1$ [dotted lines give J_2, (Eq. (14)].

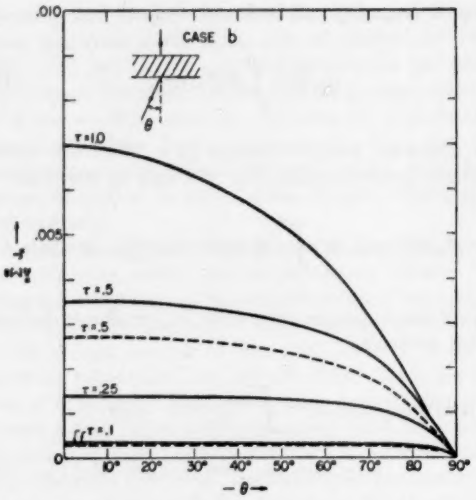

FIG. 8. Multiple scattering, $\Sigma_{n=2}^{\infty} J_n$, from Chandrasekhar. $\sigma/\sigma_T = 0.5$ [dotted lines give J_2, Eq. (14)].

important in neutron diffraction [our case (a)] this ratio is 0/0, and the limit as θ approaches θ_0 cannot be found with accuracy from the tabulated values.[8]

We have employed Chandrasekhar's tables to compute multiple scattering in our case (b), where, for the parameter ranges tabulated they are superior to our Eq. (14). Computing J_1 from Eqs. (4) and (8), we subtract this from the Chandrasekhar values (which give $\sum_{n=1}^{\infty} J_n$), and present the results in Figs. 7 and 8. Again the approximate isotropy for angles which are not too large can be seen, particularly for thin samples.

Also plotted in Figs. 7 and 8 are curves of J_2, computed from Eq. (14) for $\tau = 0.1$ and $\tau = 0.5$. Qualitatively, the second-order curves are entirely similar to the curves which include all higher orders. For $\tau = 0.5$, $\sigma/\sigma_T = 1$, the quantitative agreement is poor, for the other cases it is fair to good, as has been predicted by the foregoing considerations.

ACKNOWLEDGMENTS

The writer is indebted to D. A. Kleinman for valuable suggestions, to Miss Jean Snover for a great deal of help with the computations, to S. Chandrasekhar for comments, and to the Brookhaven National Laboratory for its hospitality during the course of this work.

[5] S. Chandrasekhar, *Radiative Transfer* (Clarendon Press, Oxford, 1950), Chap. IX.

[6] A multiple-scattering treatment somewhat similar to that presented here, but not carried beyond the abstract stage, has also been given by H. C. van de Hulst, Astrophys. J. **107**, 220 (1948).

[7] Chandrasekhar, Elbert, and Franklin, Astrophys. J. **115**, 244, 269 (1952).

[8] Chandrasekhar has also given analytic approximations to his two functions (reference 5, pages 202–207), and from these one can treat the case $\theta = \theta_0$ with an accuracy comparable to that of the present work. The formulas seem to be more cumbersome, however.

Indirect Exchange Coupling of Nuclear Magnetic Moments by Conduction Electrons*

M. A. RUDERMAN AND C. KITTEL
Department of Physics, University of California, Berkeley, California
(Received June 17, 1954)

A calculation is given of the indirect exchange $\mathbf{I}_i \cdot \mathbf{I}_j$ type coupling of nuclear magnetic moments in a metal by means of the hyperfine interaction with the conduction electrons. The interaction appears to account qualitatively for the broad nuclear spin resonance lines observed in natural metallic silver. It is expected that the interaction may sharpen the resonances in pure isotopic specimens. The line shape of the minority isotope in a binary mixture may tend to be Gaussian, while that of the majority isotope may tend to be Lorentzian, if the indirect exchange interaction is dominant.

INTRODUCTION

SEVERAL recent measurements suggest that the width of nuclear-spin resonance lines in the heavier metals may be greater than expected from magnetic dipolar interactions alone. The additional broadening for nuclei with spin $I > \frac{1}{2}$ might be caused in part by the interaction of the nuclear electric quadrupole moment with lattice imperfections, but nuclei with $I = \frac{1}{2}$ have zero quadrupole moment, so that here other broadening mechanisms must be effective. Among nuclei with $I = \frac{1}{2}$, Bloembergen and Rowland[1] report anomalous line widths in tin and thallium; the widths are of the order of five times the calculated dipolar widths. Sogo and Jeffries[2] find that the width peak-to-peak of the absorption derivative of the Ag^{109} resonance in natural silver is approximately 115 ± 15 cps, whereas the corresponding calculated dipolar width is only about 50 cps. While some of the examples might be explained by spin-lattice relaxation or the possible presence of paramagnetic impurities, we would like to suggest a more general mechanism.

There will exist in metals a coupling between the magnetic moments of two nuclei *via* their hyperfine interaction with the conduction electrons. Ramsey and others[3] have shown that a similar interaction exists between nuclear spins in molecules. Let us consider a metal crystal in which all but two of the nucleons are nonmagnetic. The electron wave functions of the perfectly periodic problem will be scattered by the hyperfine interaction with each of the magnetic nucleons. The total wave function seen by one magnetic nucleon will depend on the spin orientation of the other, thus establishing an indirect spin-dependent coupling between the two nucleons. We proceed to calculate the interaction by second-order perturbation theory. The interaction will be shown to have the form $\mathbf{I}_i \cdot \mathbf{I}_j$ of an exchange operator, suggesting that the interaction may sharpen[4] the line in pure isotopic specimens, while broadening the line in isotopic mixtures. The observed line width in natural silver appears to be in qualitative agreement with our calculations. We assume throughout that the contact part of the hyperfine interaction is dominant, and that the dipolar part of this interaction may be neglected.

CALCULATION

We consider first an electron moving in an exactly periodic lattice; interactions with nuclear spins and lattice vibrations are neglected. The electron can be described by the Bloch function $\phi_{\mathbf{k}}(\mathbf{r}) = e^{i\mathbf{k}\cdot\mathbf{r}} u_{\mathbf{k}}(\mathbf{r})$, where $u_{\mathbf{k}}(\mathbf{r})$ is periodic in the lattice. It is convenient to normalize ϕ so that for large volumes,

$$V^{-1} \int\int\int d\tau \phi_{\mathbf{k}}^* \phi_{\mathbf{k}} \rightarrow 1. \tag{1}$$

The interaction between nuclear and electron spins is manifest in hyperfine structure. This same interaction will of course couple Bloch functions of different $\mathbf{k}$, i.e., scatter conduction electrons. The matrix element for the scattering from $\mathbf{k}$ to $\mathbf{k}'$ by the moment μ on the nucleus at $\mathbf{r} = \mathbf{R}_i$ is

$$\mathbf{S} \cdot \mathbf{I}_i \Delta_{\mathbf{k}\mathbf{k}'} e^{i(\mathbf{k}-\mathbf{k}')\cdot\mathbf{R}_i}, \tag{2a}$$

$$\Delta_{\mathbf{k}\mathbf{k}'} \equiv \int\int\int d\tau \phi_{\mathbf{k}'}^*(\mathbf{r}) \Delta \phi_{\mathbf{k}}(\mathbf{r}) = \Delta_{\mathbf{k}'\mathbf{k}}^*. \tag{2b}$$

Here $\mathbf{S}$ and $\mathbf{I}$ are the spin operators for the electron and nucleus; Δ is the hyperfine interaction. Since the interaction (2) is so weak compared to the electron-lattice coupling it is sufficient to treat it as a small perturbation. We assume the conduction band is filled in both spin states from $k = 0$ to k_m. Then the interaction between the spins of nuclei i and j at $\mathbf{r} = \mathbf{R}_i$ and $\mathbf{R}_j$, via the double scattering of an electron $(\mathbf{k} \rightarrow \mathbf{k}' \rightarrow \mathbf{k})$, is

$$H(\mathbf{R}_{ij}) = -(\mathbf{S}\cdot\mathbf{I}_i)(\mathbf{S}\cdot\mathbf{I}_j) \int_0^{k_m} \frac{d\mathbf{k}}{(2\pi)^3} \times \int_{k_m}^{\infty} \frac{d\mathbf{k}'}{(2\pi)^3} \frac{\Delta_{\mathbf{k}\mathbf{k}'} \Delta_{\mathbf{k}'\mathbf{k}} e^{i(\mathbf{k}-\mathbf{k}')\cdot\mathbf{R}_{ij}}}{E(\mathbf{k}') - E(\mathbf{k})} + \text{c.c.} \tag{3}$$

* Assisted in part by the National Science Foundation.

[1] N. Bloembergen and T. J. Rowland, Acta Metallurgica **1**, 731 (1953).

[2] P. B. Sogo and C. D. Jeffries (private communication) the shape is approximately Gaussian.

[3] N. F. Ramsey, Phys. Rev. **91**, 303 (1953); N. F. Ramsey and E. M. Purcell, Phys. Rev. **85**, 143 (1952); E. L. Hahn and D. E. Maxwell, Phys. Rev. **88**, 1070 (1952); also work by Gutowsky, McCall, and Slichter, Phys. Rev. **84**, 589 (1951).

[4] C. J. Gorter and J. H. Van Vleck, Phys. Rev. **72**, 1128 (1947).

The restriction $k'>k_m$ is dictated by the exclusion principle. However, it will be evident that the exclusion principle can be neglected in the intermediate states k'.

The hyperfine interaction does not depend strongly on k. Since the largest contributions to Eq. (3) come when $k'\sim k\sim k_m$, we approximate

$$\Delta_{kk'}\Delta_{k'k} \quad \text{by} \quad |\Delta_{k_mk_m}|^2.$$

Summing over the electron spins and performing all angular integrations we obtain for (3):

$$\frac{\mathbf{I}_i\cdot\mathbf{I}_j|\Delta_{k_mk_m}|^2}{(2\pi)^4R_{ij}^2}\int_{-k_m}^{k_m}kdke^{ikR_{ij}} \times\left[\int_{k_m}^{\infty}+\int_{-\infty}^{-k_m}\frac{e^{ik'R_{ij}}k'dk'}{E(k')-E(k)}\right]. \quad (4)$$

In deriving (4) it has been assumed that $E(k)$ depends only upon the magnitude of k.

It is perhaps of some interest to show how the exclusion principle plays no real role in the k' integration. The bracket in (4) may be written:

$$\text{P.P.}\left[\int_{-\infty}^{\infty}\frac{e^{ik'R}k'dk'}{E(k')-E(k)}-\int_{-k_m}^{k_m}\frac{e^{ik'R}k'dk'}{E(k')-E(k)}\right]. \quad (5)$$

Putting the second integral of (5) into (4), we have a constant times

$$\text{P.P.}\int_{-k_m}^{k_m}dk\int_{-k_m}^{k_m}dk'e^{i(k+k')R}kk'[E(k')-E(k)]^{-1}. \quad (6)$$

Expression (6) vanishes because the integrand is antisymmetric in k and k'. Therefore we may replace the bracket in (4) by the first integral of (5) which is the result which would have obtained if the exclusion principle had been neglected in intermediate states in (3). This, of course, must be quite generally true since the conduction band could have been "filled" before or after introducing the perturbation (3).

If it is assumed that the effective mass does not vary appreciably for k in the neighborhood of k_m we may put $E(k)=\hbar^2k^2/2m^*$. Then (4) becomes

$$\frac{\mathbf{I}_i\cdot\mathbf{I}_j}{4}\frac{|\Delta_{k_mk_m}|^2m^*}{(2\pi)^3R_{ij}^4\hbar^2}[2k_mR_{ij}\cos(2k_mR_{ij})-\sin(2k_mR_{ij})]. \quad (7)$$

The quantity $\Delta_{k_mk_m}$ can be simply related to the observed atomic hyperfine structure splitting ν_a. From Eqs. (1) and (2) the hyperfine splitting for a conduction electron with wave number k is given by

$$[(2I+1)/2\Omega]\Delta_{kk}=2\pi\hbar\nu_{hfs}(k). \quad (8)$$

Ω is the atomic volume which enters because of the normalization (1). The observed hyperfine interaction in the free atom and crystal are comparable, differing because of the changed electron density in the vicinity of $r=0$, i.e.,

$$\nu_{hfs}(k)/\nu_a\approx\Omega^{-1}\phi_k^2(0)/\psi^2(0)\equiv\xi; \quad (9)$$

ξ is generally less than but of order one.

APPLICATIONS

We see that the interaction energy between nucleon spins in a metal is of the form

$$3\mathcal{C}=\sum_{i>j}\sum_j A_{ij}\mathbf{I}_i\cdot\mathbf{I}_j, \quad (10)$$

where

$$A_{ij}=\frac{\Omega^2m^*\xi_i\nu_a(i)\xi_j\nu_a(j)}{2\pi(2I_i+1)(2I_j+1)}\left(\frac{1}{R_{ij}}\right)^4 \times[2k_mR_{ij}\cos(2k_mR_{ij})-\sin(2k_mR_{ij})]. \quad (11)$$

This interaction is in addition to the usual dipolar and quadrupolar interactions. We note that A_{ij} depends on the product $\mu_i\mu_j$ of the nucleon magnetic moments. A qualitative estimate suggests that the new interaction will be of the same order of magnitude as the magnetic dipolar interaction when the electron density at the nucleon in the metal is of the order of a few hundred times greater than the density of a uniform distribution of charge, as in a plane wave. Using atomic hyperfine separations (with $\xi=1$), we estimate the following density ratios:

Li	Na	K	Ag	Rb	Cs
35	200	550	1100	1600	3100

We now consider the effect of a strong $\mathbf{I}_i\cdot\mathbf{I}_j$ interaction on the width and shape of nuclear resonance lines. That the interaction is of the form Eq. (10) follows from the matrix element (2) and is independent of any of the subsequent approximations. This interaction is of the same type as the electron exchange interaction $\mathbf{S}_i\cdot\mathbf{S}_j$, of which the properties with respect to electron resonance experiments have been studied in particular detail by Van Vleck,[5] whose results we use here. In a metal consisting entirely of one isotope the nuclear exchange interaction tends to sharpen the resonance line. The second moment $\langle(\Delta\nu)^2\rangle$ is not affected by the exchange interaction, while the fourth moment $\langle(\Delta\nu)^4\rangle$ is increased. As the line sharpens the shape is said approximately to go from Gaussian to Lorentzian. We have been unable to find accounts of nuclear resonance experiments in metals carried out under conditions which would provide a critical test of the predicted sharpening, although the corresponding effect is well known in electron spin resonance. When the line width is reduced, the reduction is roughly in the ratio of the dipolar interaction to the exchange interaction.†

[5] J. H. Van Vleck, Phys. Rev. 74, 1168 (1948); see also P. W. Anderson and P. R. Weiss, Revs. Modern Phys. 25, 269 (1953).

† *Note added in proof.*—In a private communication N. Bloembergen reports that he has observed effects of this nature in

An interesting situation arises when the crystal consists of two magnetic ingredients with gyromagnetic factors sufficiently different that the resonances for the two varieties of nuclei do not overlap. Here the nuclear exchange interaction between unlike nucleons tends to broaden each resonance line. We shall apply the results of Van Vleck to the nuclear resonance in natural silver, which consists of roughly equal parts Ag^{107} and Ag^{109}, both isotopes having $I=\frac{1}{2}$. The nuclear magnetic moments are[6]

$$\mu_{107}=-0.113 \text{ nm},$$

$$\mu_{109}=-0.130 \text{ nm};$$

the atomic ground-state hyperfine splittings are[7]

$$\nu_{107}=1713 \text{ Mc/sec},$$

$$\nu_{109}=1977 \text{ Mc/sec}.$$

The expression for $\langle(\Delta\nu)^4\rangle$, Van Vleck's Equation (29), is formidable. We shall evaluate it approximately for silver under three simplifying assumptions: (a) the dipolar interaction is neglected; (b) only nearest neighbor exchange interactions are considered; (c) all nearest neighbor nuclear exchange interactions are taken to be equal, independent of the isotopes involved. Thus $A_{jk}=A_{jk'}=A_{j'k}=A_{j'k'}=A$, for nearest neighbors, where the sites j, k may be occupied by primed or unprimed nuclear varieties.

We consider the moments of the resonance line of the unprimed nucleons, with $I=I'=\frac{1}{2}$. From Van Vleck's Equation (28),

$$h^2\langle(\Delta\nu)^2\rangle=(4N)^{-1}\sum_j\sum_{k'}A_{jk'}^2, \tag{12}$$

where N is the number of unprimed nucleons in the specimen. We calculate for a face-centered cubic lattice, for which each site has 12 nearest neighbor sites. We let f be the fraction of sites occupied by the primed variety and $(1-f)$ the fraction of sites occupied by the unprimed variety, the two varieties being distributed entirely at random. It is readily seen that the value of the double summation is $12NfA^2$, so that

$$h^2\langle(\Delta\nu)^2\rangle=3fA^2. \tag{13}$$

We have for the fourth moment, from Van Vleck's Equation (29), letting Σ' denote a sum over indices larger than those in the preceding summation,

$$\begin{aligned}h^4\langle(\Delta\nu)^4\rangle=&(8N)^{-1}\sum_{l'}\sum_j\sum_k{}'A_{jk}^2(A_{jl'}^2+A_{kl'}^2\\&-2A_{jl'}A_{kl'})+(8N)^{-1}\sum_j\sum_{k'}\sum_{l'}{}'\\&\times[A_{k'l'}^2(A_{jk'}^2+A_{jl'}^2-2A_{jk'}A_{jl'})\\&+3A_{jk'}^2A_{jl'}^2]+(16N)^{-1}\sum_j\sum_{k'}A_{jk'}^4.\end{aligned} \tag{14}$$

We discuss on the foregoing assumptions the several summations, letting $\sum$ denote the appropriate multiple summation:

$$\begin{aligned}&\sum A_{jk}^2A_{jl'}^2=\sum A_{jk}^2A_{kl'}^2=66N(f-f^2)A^4;\\&\sum A_{jk}^2A_{jl'}A_{kl'}=24N(f-f^2)A^4;\\&\sum A_{k'l'}^2A_{jk'}^2=\sum A_{k'l'}^2A_{jl'}^2=66Nf^2A^4;\\&\sum A_{k'l'}^2A_{jk'}A_{jl'}=24Nf^2A^4;\\&\sum A_{jk'}^2A_{jl'}^2=66Nf^2A^4;\\&\sum A_{jk'}^4=12fNA^4.\end{aligned} \tag{15}$$

We have then

$$h^4\langle(\Delta\nu)^4\rangle=(9/4)(5f+11f^2)A^4. \tag{16}$$

For equal proportions of the two varieties, as is approximately true of natural silver, $h^4\langle(\Delta\nu)^4\rangle=11.8A^4$, while $h^2\langle(\Delta\nu)^2\rangle=1.5A^2$. We have

$$\langle(\Delta\nu)^4\rangle^{\frac{1}{4}}/\langle(\Delta\nu)^2\rangle^{\frac{1}{2}}=1.51,$$

while with a Gaussian distribution the ratio would be 1.32. For small f the fourth moment tends to dominate the square of the second moment, and the line may approach an approximate Lorentzian distribution, just as in the dilution problem considered earlier.[8]

We now estimate the nearest neighbor nuclear exchange constant A for silver, taking $m^*=1$ and $\xi=1$. We find $A\cong2.5\times10^{-25}$ erg or $A/h\cong40$ cps. The rms width in natural silver from nearest neighbor exchange interactions alone is then 50 cps. This may be increased by about 20 percent when the exchange type interactions of more distant neighbors is taken into account. This estimated rms exchange width of ~60 cps is to be compared with a calculated rms width from the dipolar interaction of order 25 cps; the dipolar interaction will increase the over-all calculated width slightly. Taking the line shape to be Gaussian, as is observed, the experimental rms value is $\Delta\nu=55\pm8$ cps.[9] Of course any agreement would be certainly accidental; it is not necessarily true that $m=m^*$ and $\xi=1$. Interpretation of the Knight shift[10] in silver on the assumption $m^*=m$ leads to the value $\xi\cong0.7$. An estimate of the spin-lattice relaxation time using the observed Knight shift and the Korringa[11] relation leads to $T_1\cong0.02$ sec, so that this might contribute ~10 cps to the width. It appears that our interpretation of the silver line width would lead to ξ near 0.8.

If the nuclear spins are aligned the energy levels of the conduction electrons are split by the hyperfine interaction: those electrons whose moment is parallel to the nuclear magnetization have their energy lowered by $I\Delta(2\Omega)^{-1}$. This is of order kT for temperatures around

thallium metal specimens as the isotope ratio Tl^{205}/Tl^{203} is varied. He suggests that the dipolar part of the hyperfine interaction may make a contribution here.

[6] Brun, Oeser, Staub, and Telschow, Phys. Rev. **93**, 172 (1954).

[7] G. Wessel and H. Lew, Phys. Rev. **91**, 476 (1953).

[8] C. Kittel and E. Abrahams, Phys. Rev. **90**, 238 (1953).

[9] For a Gaussian, the rms width is one-half of the peak-to-peak absorption deviation.

[10] P. B. Sogo and C. D. Jeffries, Phys. Rev. **93**, 174 (1954).

[11] J. Korringa, Physica **16**, 601 (1950).

10^{-6} °K. Fröhlich and Nabarro[12] have investigated the behavior of the nuclear and electron spin systems below these temperatures including the slight change in population between the two electron spin states but neglecting the interaction Eq. (10). They conclude that below 10^{-6} °K the system of nuclear moments has ferromagnetic behavior. However, we see from Eq. (11) that the inclusion of the exchange interaction (which is essentially independent of the relative population of the electron spin states) makes the situation obscure. For nearest neighbors A_{ij} is positive and therefore gives a higher energy when spins are parallel than when antiparallel. This interaction energy is comparable to that from the Fröhlich-Nabarro effect. The exchange interaction varies at large distance as $R^{-3}\cos(k_mR)$, so that when the nuclear spins are ordered a nearest neighbor approximation is inadequate. We have made no attempt to calculate the nature of the lowest-energy state of the coupled-spin systems.

We are happy to thank E. Teller for contributing a number of pertinent questions and answers. We wish to express our appreciation to W. D. Knight for many helpful discussions of the experimental data. We are grateful to C. D. Jeffries and P. B. Sogo for permission to refer to their unpublished measurements on silver and to N. Bloembergen for communication of his results on metallic thallium. John Walsh has kindly checked our calculations.

[12] H. Fröhlich and F. R. N. Nabarro, Proc. Roy. Soc. (London) **A175**, 382 (1940).

PHYSICAL REVIEW VOLUME 96, NUMBER 1 OCTOBER 1, 1954

Identification of Gadolinium and Terbium Radioisotopes as Fission Products of U^{235}

E. C. Freiling, L. R. Bunney, and N. E. Ballou
U. S. Naval Radiological Defense Laboratory, San Francisco, California

(Received June 14, 1954)

The identification of Gd^{159} and Tb^{161} as products of the neutron-induced fission of U^{235} has been confirmed. By a comparison of counting rates with Mo^{99}, the fission yields have been estimated to be 1.1×10^{-3} and 8×10^{-4} percent, respectively.

THE radionuclides, Gd^{159} and Tb^{161}, have been found to be among the products of nuclear fission in numerous cation exchange resin separations[1] of rare earth fission products done over the past year. As expected from an extrapolation of the fission yield curve,[2] the fission yields of these radionuclides are rather low; however, development of quite efficient rare earth separation procedures[1] has made possible the ready identification of them among the other rare earth fission product radionuclides. Described below are summaries of experimental techniques used and preliminary estimates of yields of Gd^{159} and Tb^{161} formed in thermal neutron fission of U^{235}.

TABLE I. Fission yields of Gd^{159} and Tb^{161} relative to Mo^{99}.

Experiment	Fission yields Gd^{159} (in percent $\times10^3$)	Tb^{161} (in percent $\times10^4$)
1*a*	1.02	8.1
1*b*	1.07	(12.8)[a]
2*a*	1.19	7.6
2*b*	1.30	9.3
Average	1.14±0.13[b]	8.3±0.9

[a] Not included in average.
[b] Standard deviation.

Samples of both normal uranium and of uranium enriched in U^{235} were rigorously purified of rare earth impurities. (Gadolinium is of major concern here since neutron capture reactions in it lead to formation of the radionuclides being studied.) Purification was based on elution of uranium from a strongly acidic cation exchange resin with 1.0*M* ammonium lactate at *p*H 3.0. The uranium was eluted much ahead of any rare earth impurities.

The highly purified uranium samples were irradiated for one hour in the Materials Testing Reactor,[3] following which radiochemical analyses for rare earth radionuclides and Mo^{99} was performed. In addition to the previously known fission product radionuclides Nd^{147}, Pm^{149}, Sm^{153}, Eu^{156}, and Y^{91}, the radioisotopes of gadolinium and terbium, Gd^{159} and Tb^{161}, were also identified. Estimates of the fission yields of the latter were made by comparisons to Mo^{99}, whose fission yield was taken as 6.2 percent.[2] The values obtained in duplicate determinations on two different irradiated samples of uranium are given in Table I.

The fission yields of Gd^{159} and Tb^{161} lie on a smooth extrapolation of the previously established fission yield curve.[2] Although the standard error is about 10 percent, the absolute accuracy of the indicated fission yields may be no better than about 30 percent. Improvements in the absolute beta-ray counting measurements will materially improve the accuracy.

[1] E. C. Freiling and L. R. Bunney, J. Am. Chem. Soc. **76**, 1021 (1954).
[2] C. D. Coryell and N. Sugarman, Editors, *Radiochemical Studies: The Fission Products* (McGraw-Hill Book Company, Inc., New York, 1951), National Nuclear Energy Series, Plutonium Project Record, Vol. 9, Div. IV, p. 537.
[3] J. R. Huffman, Nucleonics **12**, No. 4, 21–26 (1954).

Angular Distributions of Protons from $Na^{23}(d,p)Na^{24}$ and $Ti^{47,48}(d,p)Ti^{48,49}$†

M. M. Bretscher, J. O. Alderman, A. Elwyn, and F. B. Shull
Department of Physics, Washington University, Saint Louis, Missouri

(Received June 21, 1954)

Sodium and titanium targets were bombarded with 10-Mev deuterons, and angular distributions of protons from the stripping reaction were observed with arrays of nuclear emulsions. Absorbing foils in front of each emulsion were arranged so that the integrated flux of protons in a limited energy range could be determined. Distributions were found for each of the four most energetic proton groups from sodium, corresponding to Q values of 4.731 (ground state), 4.259, 4.167, and 3.390 Mev. The data were compared with the Butler theory, and l_n values of 2, 2, 0, and 0, respectively, were necessary to fit theory to data. With Ti^{47} targets, l_n values of 3, 1 (and 3?), 1, and 1, respectively, were determined for proton groups corresponding to Q values of 8.14, 6.81, 5.83, and 4.83 Mev. With Ti^{48} targets, l_n values of 3, 1, 1, and either 1 or 2 were determined for proton groups corresponding to Q values of 5.81 (ground state), 4.46, 4.11, and 3.40 Mev, respectively. From these data, parity and possible spin values for the various states of Na^{24}, Ti^{48}, and Ti^{49} are deduced.

INTRODUCTION

It has been shown by Butler[1] that stripping reactions, produced by deuterons of moderate energy, can be used to obtain information about the spins and parities of the initial and final nuclei involved. The angular distribution of the protons or neutrons shows a strong general preference for emission in the forward direction, which is characteristic of stripping reactions. In the small-angle region, however, the yield fluctuates violently as a function of the angle, and has a prominent maximum at or near the forward direction as well as subsidiary maxima at larger angles. The angular positions of these maxima depend rather sensitively on the orbital angular momentum, $l_p\hbar$ or $l_n\hbar$, carried into the nucleus by the captured nucleon. It is usually possible to determine l_p or l_n experimentally by locating the angular position of the prominent first maximum, and this information is sufficient (a) to decide whether or not the parity of the residual nucleus is the same as that of the target, and (b) to indicate possible values for the spin of one of the two nuclei if that of the other is known. The theory involves a radius parameter r_0 which is approximately the sum of the deuteron and nuclear radii. In our work we have used $r_0=(2.06+1.22A^{\frac{1}{3}})10^{-13}$ cm, where A is the mass number of the target nucleus.

Since the publication of Butler's results, a considerable amount of experimental work has been done on angular distributions for stripping reactions. The (d,p) process has received the most attention because fast protons are much easier to study than fast neutrons. Two principal experimental methods have been invoked. In one, nuclear emulsions are used to detect the protons, whose energies are determined by track-length measurements. In the other, one or more proportional counters serve as detector, and energy measurements are made by determining the range of the protons in suitable absorbers. The former method has also been used to investigate (d,n) reactions, by studying the head-on recoil protons produced in the emulsions. A survey of all published reports shows that (d,p) angular distributions have been investigated for targets of just about every abundant stable isotopic species in the mass range from $A=6$ to $A=40$, with occasional forays into even higher masses. This preoccupation with low-mass targets is owing to Butler's neglect of Coulombic effects in the interests of simplicity, so that his results as originally presented are expected to become increasingly less valid as the atomic number of the target rises.

It is the purpose of this paper to describe a slightly different experimental approach to this problem. The technique, which is outlined in detail in the next section, is a kind of hybrid in the sense that it combines some features from each of the methods previously mentioned. Nuclear plates are used as detectors, but proton energies are determined by range measurements with suitable absorbers. The new method has been used to investigate proton angular distributions from stripping reactions with targets of Na^{23}, Ti^{47}, and Ti^{48}.

EXPERIMENTAL PROCEDURE

The principal features of our experimental arrangements are outlined in Fig. 1. A portion of the 10-Mev deuteron beam from the Washington University cyclotron is concentrated by a pair of strong-focusing magnetic lenses[2] and is conducted through evacuated tubing to a circular scattering chamber of conventional design. The chamber is approximately five meters from the nearest corner of the cyclotron, and is shielded by 32 inches of concrete.

The target material is supported on a 0.2-mil polyethylene foil which is mounted perpendicular to the beam at the center of the chamber. A series of 13 nuclear plates in holders is arranged in a circular pattern around

† Supported by the U. S. Air Force through the Office of Scientific Research of the Air Force Research and Development Command. The construction of some of the apparatus used, notably the magnetic lenses for focusing the deuteron beam, was supported by contract N6ori-11701 from the U. S. Office of Naval Research.

[1] S. T. Butler, Proc. Roy. Soc. (London) **208**, 559 (1951).

[2] Shull, MacFarland, and Bretscher, Rev. Sci. Instr. **25**, 364 (1954).

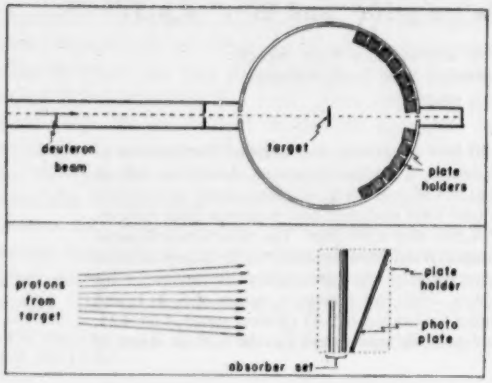

FIG. 1. Outline drawings of experimental arrangements.

the target and 20 cm from it; seven on one side of the beam cover the angular range 7.5° to 67.5° at 10° intervals; six on the other side similarly cover the 12.5° to 62.5° range. Each plate holder is machined with two pairs of slots. One pair accommodates a set of absorbing foils interposed between target and plate; the other pair supports the plate in a tilted position such that protons from the target enter the emulsion at approximately 20° from perpendicular (see Fig. 1).

The absorbing foils perform two functions: (1) they screen out deuterons, tritons, alpha particles, and low-energy protons, and (2) they act as a differential discriminator. The latter purpose is realized by assembling the upper and lower halves of each absorber set with different thicknesses, which cover different parts of a single nuclear plate one inch wide and 1.5 inches high. If the thinner half passes protons of incident energy E or higher, while the thicker half passes protons of energy $E+dE$ or higher, the difference between the fluxes of protons through the two halves is the flux of protons with energy between E and $E+dE$. Since only high-energy protons from the target can reach the emulsion, the microscopic analysis of the data is reduced to the very simple problem of counting the number of tracks per unit area in each half of each plate. This task is further simplified by the steep dip angle of the tracks, since a relatively dense concentration of tracks can be counted without undue confusion caused by overlapping.

With this technique, a prior knowledge of Q values for the reaction is necessary. The laboratory energy of each proton group must be computed for each angle of observation, and the absorber thicknesses must be selected accordingly. It is evident that only limited resolution of proton groups is possible; in view of the straggling of protons in the absorber, it seems unlikely that complete resolution can be obtained by this method if two adjacent proton groups differ in energy by less than 400 kev. A separate exposure is required to determine the angular distribution for each of the several proton groups from any target. Moreover, the method can be applied reliably only to the three or four most energetic proton groups, since at still lower energies one quickly encounters the difficulty of measuring the rather small difference between two comparatively large numbers. In spite of these drawbacks, the technique is an attractive one because of the enormously increased simplicity of the microscopic analysis required. It is not necessary to identify and reject the tracks of deuterons, alphas, and low-energy protons, and it is not necessary to measure track lengths. Moreover, the advantage of simultaneous collection of data at all angles is preserved, thus avoiding normalization difficulties.

By way of developing confidence in the method, it was first applied to a study of the $C^{12}(d,p)C^{13}$ reaction. Carbon was chosen because of the ease of preparing targets with polyethylene foil and because excellent earlier studies of this reaction have been made by Rotblat[3] using the conventional nuclear plate method, so that comparisons could be made. Our results were in excellent agreement with those of Rotblat for both the ground state and first excited state of C^{13}. The l_n values required for a good fit with Butler's theory are 1 and 0 respectively.

During the carbon experiments, it became apparent that the use of aluminum absorbers introduces a discrepancy at very small angles owing to bombardment of the aluminum foils by elastically scattered deuterons from the target. At very small angles, the flux of such deuterons is fairly high, and $Al^{27}(d,p)$ reactions in the absorbers lead to an extra component of protons appearing in the emulsions, over and above what comes directly from the target. To reduce this effect, we switched

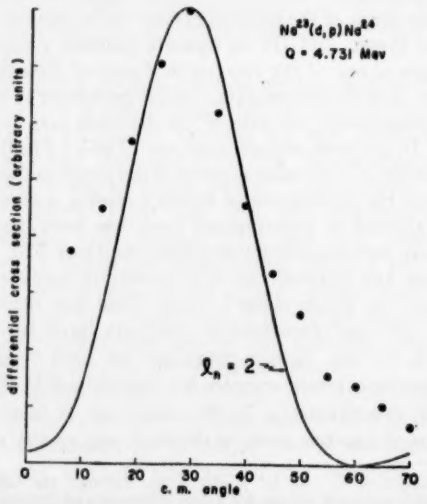

FIG. 2. Observed angular distribution of protons from deuteron bombardment of sodium, with Na^{24} formed in its ground state.

[3] J. Rotblat, Nature 167, 1027 (1951).

to the use of Pb foil for the front layer of absorber in each set, the remainder being aluminum as before. The Pb layer was made thick enough to stop the scattered deuterons. This minimizes the extra proton component because of the relatively small cross section and high threshold for the (d,p) reaction in Pb. With this modification of technique, we then proceeded with the investigation of protons from sodium and titanium targets.

RESULTS

$Na^{23}(d,p)Na^{24}$

Targets were prepared for most runs by evaporating a solution of Na_2CO_3 to dryness on a polyethylene foil, although NaOH was similarly used in a few instances. The residual deposit was crystalline and hygroscopic, and tended to be crusty around the edges. The deposition area was made large so that the area of intersection with the beam would be clear of the crusty edges. New targets were prepared just before each bombardment, so that hygroscopic action would have minimal effect. Target thicknesses were about one or two milligrams per square centimeter.

Absorber thicknesses were computed at each angle for each state of Na^{24} using Q values reported by Sperduto and Buechner.[4] We limited our investigations to the four lowest states of Na^{24}, corresponding to Q values of 4.731 (ground state), 4.259, 4.167, and 3.390 Mev. The presence of abundant amounts of carbon and oxygen in our target and its supporting foil precluded any examination of more highly excited states. Since the first and second excited states are separated by only 92 kev, we lumped them together as if they were a single state, in the hope that their superimposed angular distributions could be disentangled later.

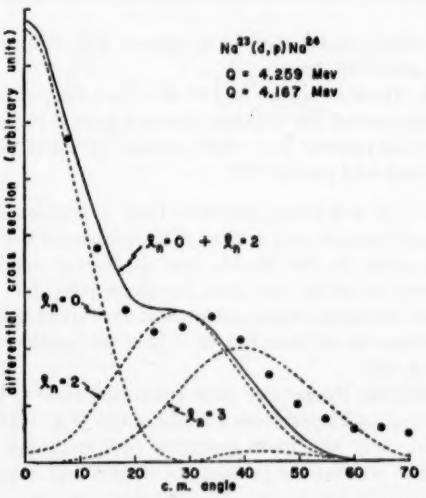

FIG. 3. Observed angular distribution of protons from deuteron bombardment of sodium, with Na^{24} formed in its first and second excited states.

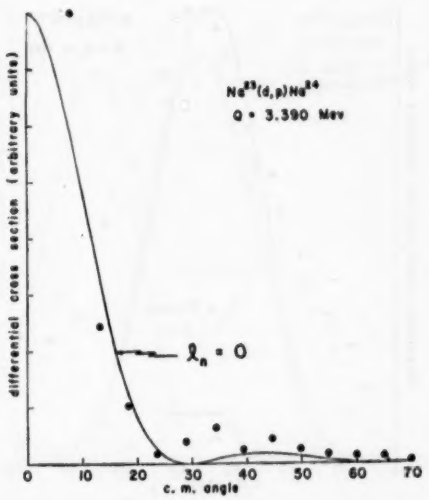

FIG. 4. Observed angular distribution of protons from deuteron bombardment of sodium, with Na^{24} formed in the third excited state.

The data are illustrated in Figs. 2–4, along with appropriate theoretical curves computed from Butler's theory. For the ground state and third excited state of Na^{24} the distributions can be unambiguously fitted by theoretical curves for $l_n=2$ and $l_n=0$, respectively. The lumped data for the first and second excited states in Fig. 3 show an abrupt rise near 0°, which indicates a strong $l_n=0$ component. The prominent subsidiary maximum at about 30° is probably a superposed component with higher l_n. We tried various combinations of $l_n=0$ with higher l_n, and conclude that the most promising combination is with $l_n=2$. We assume that the two l_n values are attributable to the two intermingled proton groups.

Kinsey, Bartholomew, and Walker[5] have measured the energies of gamma rays from Na^{24} which follow the capture of thermal neutrons by Na^{23}. Sperduto and Buechner[4] have fitted these gamma rays into a system of Na^{24} levels as determined from the $Na^{23}(d,p)Na^{24}$ reaction. No capture gamma-ray transitions directly to the ground state are observed; presumably this is because of the high spin ($I=4$) of the Na^{24} ground state compared with the initial capture state. In fact, the most energetic capture transition appears to go to the second excited state instead of to either the ground or first excited states. This suggests that the first excited state and the ground state are similar in that both have high spin, or at least that both have spins which differ by at least two units from that of the initial capture state. Moreover, the capture transitions to the second and third excited states occur with an 8

[4] A. Sperduto and W. W. Buechner, Phys. Rev. 88, 574 (1952).

[5] Kinsey, Bartholomew, and Walker, Phys. Rev. 83, 519 (1951).

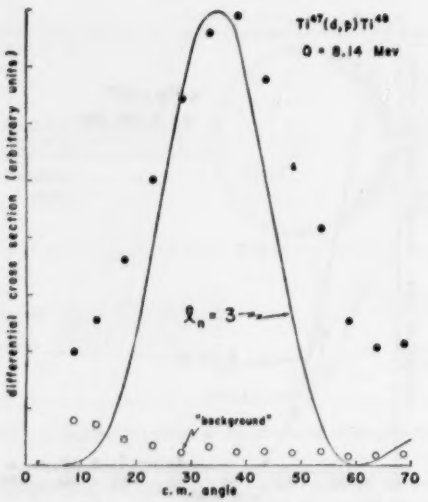

FIG. 5. Observed angular distribution of protons from deuteron bombardment of enriched Ti^{47} targets, with Ti^{48} formed in its ground (first excited?) state. The "background" represents the corresponding distribution of protons for which Q exceeds 8.35 Mev (approx.).

to 3 intensity ratio. This would be more or less consistent with the transition energies involved if both gammas were of the same multipole order and type. This behavior suggests that the second and third excited states of Na^{24} are quite similar, and may even have the same spin and parity. Combining these considerations with our own data leads us to conclude that the mixed $l_n=0$ and $l_n=2$ components in Fig. 3 are best identified with reactions leading to the second excited state ($Q=4.167$ Mev) and first excited state ($Q=4.259$ Mev), respectively, of Na^{24}.

The results for sodium targets are summarized in Table I, together with the parity and possible spin values for each corresponding level in Na^{24}. The spin of Na^{23} is $\frac{3}{2}$, and we assume that its parity is even, as predicted by the shell model. All of our conclusions are in agreement with those previously reported by Shapiro[6] and by Takemoto, Dazai, and Chiba.[7]

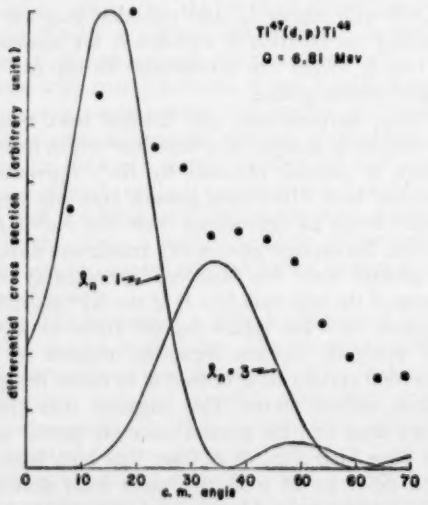

FIG. 6. Observed angular distribution of protons from deuteron bombardment of enriched Ti^{47} targets, with Ti^{48} formed in its first (second?) excited state. The data suggest that two different proton groups are involved, having similar Q values.

$Ti^{47,48}(d,p)Ti^{48,49}$

Three types of TiO_2 targets were used during this investigation:

(1) Those in natural form, in which the percentage abundances of the various titanium isotopes are 7.95 percent Ti^{46}, 7.75 percent Ti^{47}, 73.45 percent Ti^{48}, 5.51 percent Ti^{49}, and 5.34 percent Ti^{50}.

(2) Those enriched[8] in Ti^{47}, in which the percentage abundances of the titanium isotopes were 1.83 percent Ti^{46}, 82.05 percent Ti^{47}, 14.62 percent Ti^{48}, 0.81 percent Ti^{49}, and 0.69 percent Ti^{50}.

(3) Those enriched[8] in Ti^{48}, in which the percentage abundances of the titanium isotopes were 0.16 percent Ti^{46}, 0.32 percent Ti^{47}, 98.90 percent Ti^{48}, 0.48 percent Ti^{49}, and 0.14 percent Ti^{50}.

TABLE I. Summary of l_n values, together with the parity and possible spins for each level of the residual nuclei. The known ground-state spins are italicized.

Reaction	Q in Mev	Excit. energy of final nucleus (Mev)	l_n	Spin and parity of final nucleus
$Na^{23}(d,p)Na^{24}$	4.731	ground	2	*0, 1, 2, 3, 4* even
	4.259	0.472	2	0, 1, 2, 3, 4 even
	4.167	0.564	0	1, 2 even
	3.390	1.341	0	1, 2 even
$Ti^{47}(d,p)Ti^{48}$	8.14	ground? 1.27?	3	*0*, 1, 2, 3, 4, 5, 6 even
	6.81	1.33? 2.60?	1 (and 3?)	1, 2, 3, 4 even
	5.83	2.31? 3.58?	1	1, 2, 3, 4 even
	4.83	3.31? 4.58?	1	1, 2, 3, 4 even
$Ti^{48}(d,p)Ti^{49}$	5.81	ground	3	*5/2, 7/2* odd
	4.46	1.35	1	1/2, 3/2 odd
	4.11	1.70	1	1/2, 3/2 odd
	3.40	2.41	(1 or 2)	???

The oxide was finely ground to form a semisuspension in amyl acetate, and a trace of a commercial coil dope was added to the liquid. The suspended oxide was allowed to settle out onto the supporting foil, after which the excess liquid was allowed to evaporate slowly. The trace of coil dope helped to hold the powdery oxide on the foil.

Absorber thicknesses were computed from Q values reported by Pieper[9] from a study of the (d,p) reactions. Again, only the more energetic proton groups were studied, so that the presence of carbon and oxygen in

[6] P. Shapiro, Phys. Rev. **93**, 290 (1954).
[7] Takemoto, Dazai, and Chiba, Phys. Rev. **91**, 1024 (1953).
[8] Enriched samples were loaned through the courtesy of the Isotopes Division of the U. S. Atomic Energy Commission.
[9] G. F. Pieper, Phys. Rev. **88**, 1299 (1952).

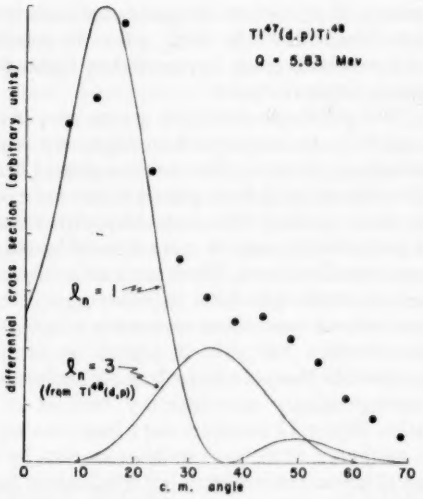

FIG. 7. Observed angular distribution of protons from deuteron bombardment of enriched Ti^{47} targets, with Ti^{48} formed in its second (third?) excited state. The presence of 14.6 percent Ti^{48} in the target is responsible for the $l_n=3$ contribution (compare with Fig. 9).

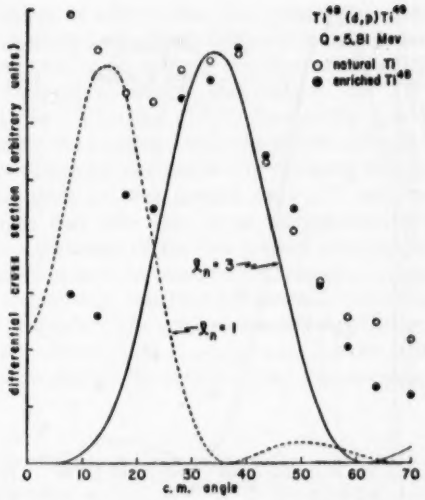

FIG. 9. Observed angular distribution of protons from deuteron bombardment of natural titanium and enriched Ti^{48} targets, with Ti^{49} formed in its ground state. The presence of 7.75 percent Ti^{47} in natural titanium is responsible for an $l_n=1$ contribution (compare with Fig. 7).

the target offered no difficulty. With the Ti^{47} target, proton groups for $Q=8.14$, 6.81, 5.83, and 4.83 Mev were investigated. With the natural titanium and enriched Ti^{48} targets, proton groups for $Q=5.81$ (ground state), 4.46, 4.11, and 3.40 Mev were investigated. The data are displayed in Figs. 5 through 12, together with appropriate Butler curves. In all but two cases, which are discussed below, the decision as to the value of l_n seems reasonably clear-cut. The results are tabulated in Table I, together with such deductions as can be made concerning parity and possible spin values for each state of a residual nucleus. The spins[10] of Ti^{47} and Ti^{49} are 5/2 and 7/2, respectively, while that of Ti^{48} is presumed to be zero because it is an even-even nuclide. The parity of Ti^{48} is assumed to be even for the same reason, while our own data on the $Ti^{47}(d,p)Ti^{48}$ reactions indicate that the Ti^{47} parity is odd, as expected from the shell model.

In $Ti^{47}(d,p)Ti^{48}$, the proton groups for Q values of 8.14 and 4.83 Mev show angular distributions for which

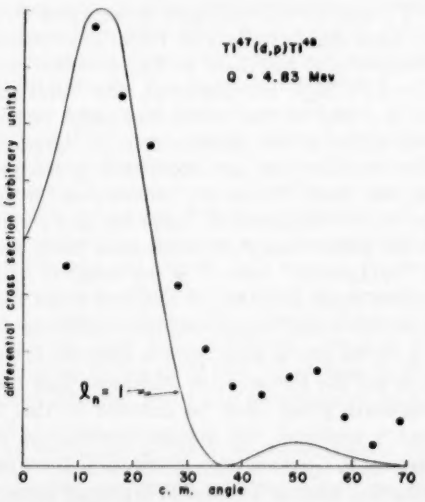

FIG. 8. Observed angular distribution of protons from deuteron bombardment of enriched Ti^{47} targets, with Ti^{48} formed in its third (fourth?) excited state.

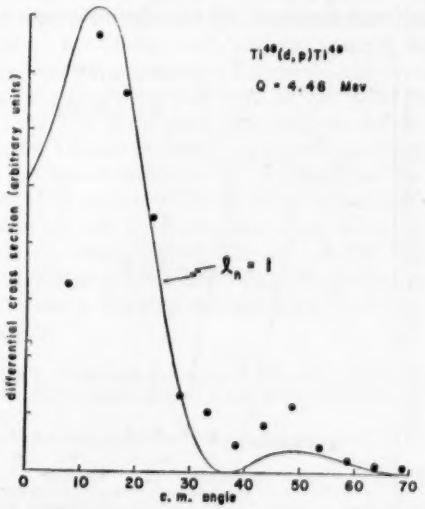

FIG. 10. Observed angular distribution of protons from deuteron bombardment of natural titanium targets, with Ti^{49} formed in its first excited state.

[10] C. D. Jeffries, Phys. Rev. **92**, 1262 (1953).

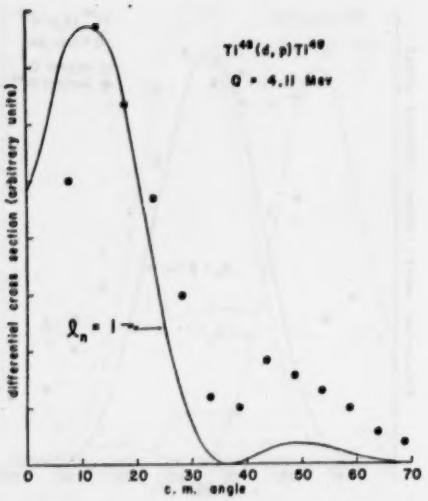

FIG. 11. Observed angular distribution of protons from deuteron bombardment of natural titanium, with Ti^{49} formed in its second excited state.

l_n values of 3 and 1 respectively can be identified unambiguously. The same is true also with the group for $Q=5.83$ Mev, for which $l_n=1$, but this appears with a small admixture of an $l_n=3$ component owing to the ground-state reaction with Ti^{48} in the target. When natural titanium is used, the two superposed groups show up with their relative intensities roughly reversed (see Figs. 7 and 9). The distribution for $Q=6.81$ Mev can be fitted by an $l_n=1$ curve, but in this case the unusually strong secondary component, which may also be fitted with $l_n=3$, cannot be attributed to the presence of other isotopes in the target. This may indicate another excited state in Ti^{48} with about the same excitation energy. If so, the new state probably has a Q value somewhat less than 6.81 Mev, since we specifically looked for a proton group having slightly higher Q with completely negative results.

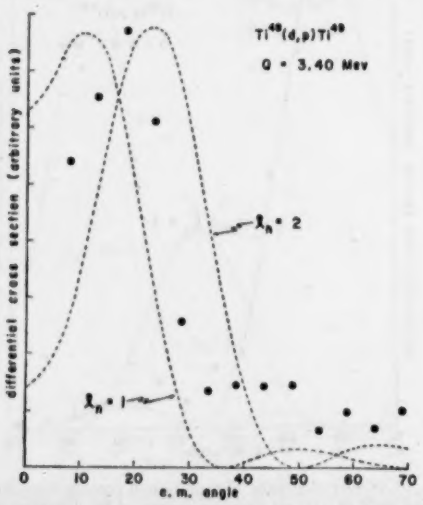

FIG. 12. Observed angular distribution of protons from deuteron bombardment of enriched Ti^{48} targets, with Ti^{49} formed in its third excited state.

In $Ti^{48}(d,p)Ti^{49}$, the first three groups have distributions which can be interpreted unambiguously. It should be pointed out, however, that the close spacing between the $Q=4.46$ and 4.11-Mev groups taxes the resolving power of our method. It is undoubtedly true that the latter group in particular is contaminated by degraded protons from the former. There is no indication of any component other than $l_n=1$ in either group, and we believe that our conclusions are correct in spite of the possible overlap. The yield of protons in the fourth group ($Q=3.40$ Mev) is relatively small, and our results are correspondingly unsatisfactory because of poor statistics. Figure 12 combines data from two separate trials, neither of which gave satisfactory data by itself. A peak at low angles is evident but it falls about halfway between the theoretical curves for $l_n=1$ and $l_n=2$. For this reason, we have listed no conclusions with respect to this state. For almost every other group, however, the experimental data seem to be shifted slightly toward larger angles relative to the Butler curve. For this reason it seems more likely that $l_n=1$ should be assigned in this questionable case. This opinion is strengthened by a comparison of the data points in Fig. 12 with the data points in Figs. 8, 10, and 11, where the assignments of $l_n=1$ seem to be correct.

There is some evidence, summarized by Pieper,[9] which indicates that $Q=8.14$ Mev does not correspond to the ground-state reaction in $Ti^{47}(d,p)Ti^{48}$. Collins, Nier, and Johnson[11] have measured the atomic masses of Ti^{47} and Ti^{48} with considerable precision, and the mass difference leads to an expected ground-state Q of 9.41 Mev. Moreover, their mass differences for Ti^{46}-Ti^{47}, Ti^{48}-Ti^{49}, and Ti^{49}-Ti^{50} all lead to expected Q values which agree satisfactorily with Pieper's conclusions for the related (d,p) reactions. In Fig. 5, where our data for $Q=8.14$ Mev are displayed, the "background" curve is a plot of the proton flux which passed the thicker halves of the absorber sets; it represents the yield of protons from the target with Q greater than about 8.35 Mev. We do not believe that the general shape of the "background" curve has any connection with the Butler theory. It seems more likely that the high "background" near 0° is the result of scattered deuterons which initiate (d,p) reactions in the absorber foils, an effect which we attempted to minimize by our use of Pb foil for the front layer in each set. If $Q=8.14$ Mev is not the ground-state transition, then the true ground-state group must be included in the "background"; moreover, its angular distribution should correspond to $l_n=3$ and thus resemble the $Q=8.14$-Mev distribution, because Ti^{47} and Ti^{48} (ground states) have different parities and their spins differ by 5/2. When we

[11] Collins, Nier, and Johnson, Phys. Rev. 86, 408 (1952).

try to visualize an $l_n=3$ distribution buried in the "background" of Fig. 5, we conclude that, at best, this hypothetical proton group cannot amount to more than about 3 percent of the $Q=8.14$-Mev group in intensity. Even so, this may represent the proper identification of the proton groups from Ti^{47}, since it is difficult to gainsay the evidence for a ground-state Q greater than 8.14 Mev. We can find no reason to distrust the mass data, and so, in Table I, two alternatives have been listed in the column headed "excitation energy of final nucleus," one of which assumes $Q=8.14$ Mev is the ground state while the other assumes that it is the first excited state, with a very uncertain excitation energy of about 1.27 Mev. If $Q=8.14$ Mev is not the ground-state transition, we can only speculate about the failure to observe the true ground-state reaction. One argument, which can lead only to qualitative conclusions, has to do with the peculiar nature of Ti^{47}. By the independent-particle shell model, the Ti^{47} spin should be 7/2 instead of 5/2. Presumably spin 5/2 is the result of an unusual coupling of five neutrons in $f_{7/2}$ orbits. If another neutron is to be captured directly into an $f_{7/2}$ orbit to form ground state Ti^{48} with six $f_{7/2}$ neutrons and zero spin, some rearrangement of the angular momenta of the five original neutrons will be necessary in order to conserve total angular momentum. It is undoubtedly true that this necessity for rearrangement will reduce the cross section for the reaction, but it is not obvious that it can account for our complete failure to observe the corresponding proton group.

PHYSICAL REVIEW VOLUME 96, NUMBER 1 OCTOBER 1, 1954

Two-Step Cascades in Chlorine-36 and Cadmium-114 Neutron-Capture Gamma-Ray Spectra*

ARTHUR L. RECKSIEDLER AND BERNARD HAMERMESH
Argonne National Laboratory, Lemont, Illinois

(Received June 23, 1954)

Two NaI(Tl) crystals were used in conjunction with a twenty- and a single-channel pulse-height analyzer and a 5-microsecond coincidence circuit to determine cascade branches in the neutron-capture gamma-ray emission from Cl^{36} and Cd^{114}. Several two-step cascades in Cl^{36} and one in Cd^{114} have been verified by the present methods.

INTRODUCTION

THE use of NaI(Tl) crystals has provided a method of measuring photon energy values in the lower range of neutron-capture gamma-ray energies. The most prominent capture gamma energies in several elements have been determined by the use of such crystals.[1] Higher-energy photons have been measured accurately by the use of a pair spectrometer.[2]

A single neutron capture by an element X^A forms the isotope X^{A+1} in an excited state corresponding to the neutron binding energy for the element. In decaying to the ground state, intermediate states may be involved and the energy difference between each state then corresponds to the energy of the capture gamma rays emitted by the isotope. In a time on the order of 10^{-13} second the new nucleus is at the ground state unless an isomer is formed. In chlorine-36 several two-step cascades had been predicted according to the data collected by the use of NaI(Tl) crystals by Hamermesh and Hummel, and a pair spectrometer by Kinsey *et al.* The sum of the two gamma rays constituting each supposed cascade branch is in agreement with the neutron binding energy as shown in Table I.

The cadmium high-energy spectrum has been investigated by Kinsey *et al.*, and the neutron binding energy reported as corresponding to the highest-energy gamma ray of 9.046 ± 0.008 Mev. Several other gamma rays have been determined including one at 8.48 Mev. The lower (50 kev to 5 Mev) energy range of the spectrum has been investigated in noncoincident runs with the NaI(Tl) crystal. The spectrum was found to be complicated and no lines other than the 0.558-Mev gamma ray were resolved. The sum of the 8.48-Mev and 0.558-Mev gamma rays equals the neutron binding energy, and a two-step cascade branch was also predicted here.

TABLE I. Combined pair-spectrometer and scintillation-spectrometer data on the capture γ rays from chlorine-36. Energies in Mev.

	Kinsey	Hamermesh	Sum (Neutron binding energy)
A	8.56 ± 0.03	...	8.56 ± 0.03
B	7.77 ± 0.03	0.784 ± 0.010	8.55 ± 0.03
C	7.42 ± 0.03	$1.15\ \pm0.010$	8.57 ± 0.03
D	6.98 ± 0.03	$1.59\ \pm0.013$	8.57 ± 0.03
E	6.62 ± 0.06	$2.00\ \pm0.025$	8.62 ± 0.06

* Part of a thesis submitted by A. L. Recksiedler as a requirement for the Master's Degree in Engineering Physics from the Michigan College of Mining and Technology. Work performed under the Participating Institution Program of the Argonne National Laboratory.

[1] B. Hamermesh and V. Hummel, Phys. Rev. **88**, 916 (1952).

[2] Kinsey, Bartholomew, and Walker, Phys. Rev. **85**, 1012 (1952).

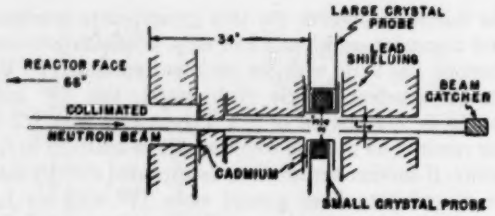

FIG. 1. Schematic diagram of coincident capture gamma-ray detectors (top view).

APPARATUS

The reactor CP3 at the Argonne National Laboratory was used as a source from which a collimated neutron beam was taken. The sample was placed in the beam approximately 100 inches from the reactor face. For the chlorine runs, a sample of C_2Cl_6 (hexachlorethane) was used as target material. Although there was no attempt made to separate isotopes, chlorine-35 is present to 75 percent in natural chlorine, with a neutron capture cross section of 32 barns. The remaining 25 percent is chlorine-37 with a cross section of 0.14 barn. Carbon in the sample also has a low capture cross section, so that the spectrum found is chiefly due to neutron capture processes by Cl^{35} nuclei. A target of metallic cadmium was placed in the beam to obtain the cadmium-114 spectrum. Although present to only 12.3 percent, the large capture cross section, on the order of several thousand barns, is sufficient to effectively minimize the contributions to the spectrum of the other cadmium isotopes.

A large NaI(Tl) crystal ($3\frac{1}{2}\times3\frac{1}{2}$ inch right circular cylinder) was placed 90° from the direct beam in a horizontal plane while a similar smaller crystal (1-inch height by $1\frac{3}{4}$-inch diameter) was placed approximately $2\frac{3}{4}$ inches apart from and opposing the larger crystal as shown in Fig. 1. Two-inch bismuth blocks were used as lining around the crystals and lead blocks were used for further shielding. Cadmium sheets were then placed over the lead shielding. The smallest shielding thickness

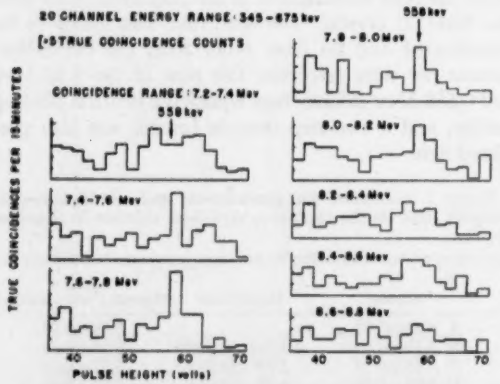

FIG. 2. Cadmium capture gamma-ray histograms; 0.558–8.48 Mev cascade; Method A.

was 4 inches, except at the face of the crystals. Only a sheet of cadmium separated the probe face from the sample. Background was further cut by means of cadmium and lead jaws placed about 18 inches from the crystals. The crystals were packaged by a method devised by Swank and Moenich.[3] The crystal arrangement was chosen for the best geometry available with a minimum of loss in effective shielding and in resolution.

A bank of three RCA 5819 photomultipliers was placed behind the large crystal with the output fed to a two-stage preamplifier. The small crystal was backed by a single 5819 and a similar preamplifier. The output from either probe could be connected to a single- or twenty-channel pulse-height analyzer. A coincidence circuit with a resolving time of 5 microseconds was connected so that the pulses from the single-channel analyzer would trigger the gate and the twenty-channel coincident pulses would be recorded. All single-channel pulses would also be recorded. Noncoincident trials were necessary to determine the noncoincident 20-channel counting rates.

METHOD

Increased background at lower energies combined with a greater crystal efficiency determined that the large crystal be used only in the high-energy region being investigated. At approximately 4 Mev the background represented 40 percent of the noncoincident counting rates. The large crystal was placed on the high-energy region while the smaller crystal recorded the low-energy region of the spectrum. The background did not arise as a major problem with the smaller crystal. The ratio of true coincident counts to accidental counts was between $1\frac{1}{2}$ and 2 at the expected coincident energies. True coincident counts are considered to be the total recorded counts less the accidental counts. Calibration was obtained from known gamma-ray energies in Au^{198} (0.411 Mev), Cs^{137} (0.662 Mev), Na^{24} (1.38 Mev and 2.76 Mev), and a PoBe source (4.5 Mev).

By exchanging the large and small crystal probes between the single- and twenty-channel analyzers, two methods of obtaining data were available. The first, Method A, was to set the twenty-channel analyzer on the low-energy range containing the full-energy peak and its maximum Compton energy. The range was varied on repeated trials to account for any individual channel variations. A channel width of approximately 20 kev was used below 1 Mev and 50 kev above 1 Mev. The single-channel analyzer was then varied over the energy range corresponding to the high-energy step in the cascade in widths of 200 kev. Due to the effects of pair production, it is possible for the high-energy gamma-ray to produce pulses in an energy range corresponding to approximately 1.2 Mev. Thus, six 200-kev intervals cover the energy range in which coincident

[3] R. K. Swank and J. S. Moenich, Rev. Sci. Instr. 23, 512 (1952).

pulses caused by the cascade can be expected. The high-energy counting rate decreased gradually with increasing energy, and no actual peaking effects were observed. A series of histograms may be made showing the true coincidence counts in each energy interval for the length of the run (15 minutes per interval), as shown for cadmium in Fig. 2. The low photoelectric peak is shown to appear as the high-energy ranges corresponding to the high-energy gamma-ray minus one and two annihilation quanta appear in the single-channel analyzer. The peak dies out after the full high-energy peak is passed. By adding the actual counts in the proper energy range and subtracting accidental counts, a curve of the low-energy region in coincidence with a high-energy range is obtained with fair statistics.

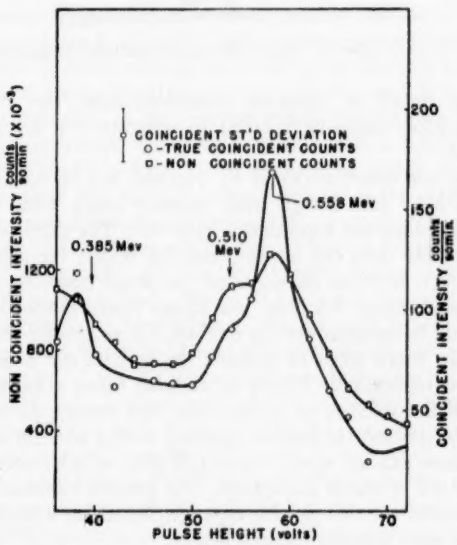

FIG. 3. Cadmium capture gamma-ray spectra, Method A; 0.558–8.48 Mev cascade, 7.4–8.6 Mev coincident range; calibration 9.62 kev/v.

Method B consisted of placing the large crystal's pulses on the twenty-channel analyzer and the small crystal's output on the single-channel analyzer. The low-energy range was then covered in successive 20- or 50-kev intervals. Due to the multiplicity of cascade possibilities the direct results of the run provided little useful information. As the full low-energy peak appeared in the single-channel analyzer, increased counts in the proper range seemed to appear in coincidence counting, but results were indefinite. Assuming the low-energy peak is sitting on a background of Compton distributions from slightly higher-energy gamma rays, which also form cascades within the high-energy range, the energy interval containing the low-energy photopeak will provide coincidences over a greater range than the 1.2-Mev range of the cascade being checked. To evaluate the Compton background on which the low-energy

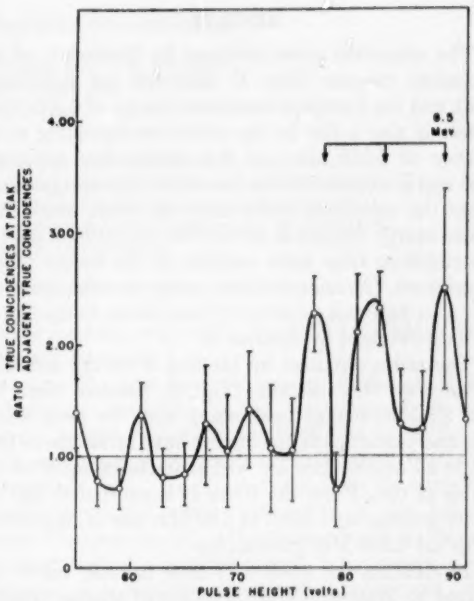

FIG. 4. Cadmium capture gamma-ray spectrum, Method B, 0.558–8.48 Mev cascade; calibration 91 kev/v.

gamma ray is sitting, an average was taken of the true coincident rates on either side of the photopeak, and the result was then divided into the true coincidences at the photopeak. Lines actually forming cascades should then have large ratios, while all other ratios are essentially one. The method, although yielding poor statistics, essentially has confirmed the results of Method A.

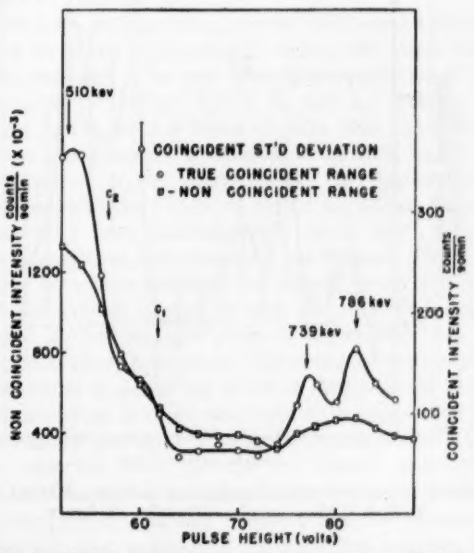

FIG. 5. Chlorine-36 capture gamma-ray spectra, Method A, 0.784–7.77 Mev cascade, 6.6–7.8 Mev coincident range; calibration 9.60 kev/v.

RESULTS

The coincident curve obtained by Method A on the cadmium cascade (Fig. 3) indicates the full-energy peak and the Compton maximum energy of 0.385 Mev. There is also a rise in the curve corresponding to an energy of 0.510 Mev, or the annihilation quantum, and this is coincident with the entire high-energy range. That the coincident curve does not reach zero in the other energy regions is attributed largely to Compton distributions from other cascades in the energy ranges considered. The noncoincident energy distribution without a background correction is also shown in the figures of data obtained by Method A.

The ratios obtained by Method B on the cadmium 0.558–8.48 Mev cascade (Fig. 4) indicate that the full 8.5-Mev energy peak along with the peak minus one and two annihilation quanta have ratios above two, while all other ratios are within statistics equal to the value of one. From the curve it is concluded that no other gamma rays down to 5.00 Mev are in coincidence with the 0.558-Mev gamma ray.

In chlorine the 0.784–7.77-Mev cascade curve obtained by Method A (Fig. 5) indicated another possible coincident gamma ray at 0.735 Mev, along with the expected photopeak at 0.784 Mev and its Compton edge (C_1). The Compton maximum (C_2) of the second gamma ray should also appear, but is obscured by the 0.510-Mev annihilation radiation. The extra peak has been found on repeated coincident runs, but noncoincident trials have failed to separate two distinct lines.

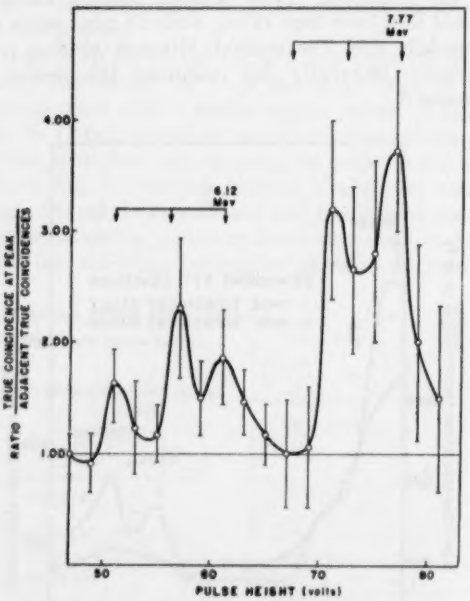

FIG. 6. Chlorine-36 capture gamma-ray spectrum, Method B, 0.784–7.77 Mev cascade; calibration 100 kev/v.

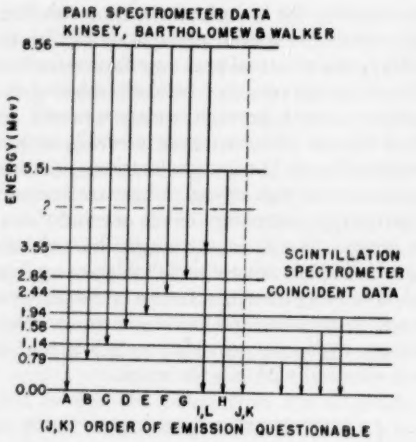

FIG. 7. Level scheme, chlorine-36 capture gamma-ray spectrum.

In the curve obtained by Method B (Fig. 6), the 7.77-Mev full energy peak appears along with the peak minus one annihilation quantum. The third peak definitely does not appear, and the reason for this is unclear. In trials on the other predicted cascades, the region around 6.5 Mev has shown lower ratios than would be expected for the method. There are also three peaks which seem to indicate the gamma ray of 6.12 Mev, reported by Kinsey *et al.*, also forms a cascade with the 0.784-Mev gamma-ray. The energy discrepancy between the neutron binding energy and the sum of these gamma rays is about 1.58 Mev, which could be emitted in one or more steps. The present information indicates the two gamma rays mentioned are a portion of a more complex cascade branch.

The curves on the other cascade branches in chlorine indicate only the predicted results, i.e., that the 1.15-Mev and 7.42-Mev gamma rays form a two-step cascade branch, and that the 1.59-Mev with the 6.98-Mev, and the 2.00-Mev with the 6.62-Mev gamma rays form similar two-step cascades.

CONCLUSIONS

The cascade branches of chlorine-36 which have been confirmed by the present study are indicated in the capture gamma-ray level scheme as shown in Fig. 7. There is yet to be resolved the significance of the 0.735-Mev gamma ray, and the reason for the apparent interference in the present methods of determining coincident energies around 6.5 Mev. A portion of a more complex cascade branch containing the 0.784-Mev and 6.12-Mev branch has also been found by the present methods.

Ratio of $\bar{\Gamma}_n^0/\bar{D}$ for Slow Neutron Resonances*

R. S. CARTER, J. A. HARVEY, D. J. HUGHES, AND V. E. PILCHER†
Brookhaven National Laboratory, Upton, New York

(Received June 28, 1954)

A survey has been made of resonance parameters of the heavy elements which have been measured recently. The variation of the ratio $\bar{\Gamma}_n^0/\bar{D}$ with atomic weight has been compared with theoretical predictions. A maximum was found in the ratio $\bar{\Gamma}_n^0/\bar{D}$ at atomic weight of approximately 160 in fair agreement with the more recent theories of neutron scattering by nuclei. The experimental data, however, are not sufficiently accurate to make a choice between the new theories which have been proposed.

THE extreme compound nucleus models proposed by Feshbach, Peaslee, and Weisskopf,[1] Feshbach and Weisskopf,[2] and Teichmann and Wigner[3] predicted that the ratio $\bar{\Gamma}_n^0/\bar{D}$ would be constant, independent of atomic weight. In the black-nucleus model[1] $\bar{\Gamma}_n^0/\bar{D}$ equals $2k_0/\pi K$, where $\bar{\Gamma}_n^0$ is the average reduced neutron width, $\bar{D}$ is the average level spacing for the spin state, k_0 is the wave number of a 1-ev neutron, and K is the wave number of the neutron inside the nucleus. The reduced neutron width of a resonance, Γ_n^0, is defined by $\Gamma_n^0=\Gamma_n/\sqrt{E_0}$, where Γ_n is the neutron width of the resonance and E_0 is the kinetic energy of the incident neutron at resonance expressed in electron volts. The value of $\bar{\Gamma}_n^0/\bar{D}$ depends on the nuclear well depth, V_0, and is 1.4×10^{-4} or 1.0×10^{-4} for well depths of 19 or 42 Mev, respectively. Recently, however, theories have been proposed by Feshbach, Porter, and Weisskopf,[4] Bohr and Mottelson,[5] and Thomas[6] which predict a variation of the $\bar{\Gamma}_n^0/\bar{D}$ ratio with atomic weight. The cloudy crystal-ball model[4] assumes a complex nuclear potential well with $V=V_0(1+i\xi)$ and a nuclear radius equal to $r_0A^{\frac{1}{3}}$($r_0=1.45\times10^{-13}$ cm). A well depth of 42 Mev was found by Adair[7] to best fit the low-energy neutron cross-section data. For this well depth, the model predicts maxima in $\bar{\Gamma}_n^0/\bar{D}$ for S-wave neutrons at atomic weights 11, 55, and 155. A fit of the theory to measured total neutron cross sections in the Mev energy region[8] requires ξ to have the value 0.03,[4] for $V_0=42$ Mev. With this choice of parameters the peak in the ratio $\bar{\Gamma}_n^0/\bar{D}$ at atomic weight 155 is 6 times the black-nucleus value. Between maxima the value is about $\frac{1}{6}$ the black-nucleus value. In the cloudy crystal-ball model, $\bar{\Gamma}_n^0/\bar{D}$ is independent of the distribution of the reduced neutron widths and is equal to $(\sum\Gamma_n^0)/\Delta E$, where ΔE is the energy interval over which the Γ_n^0's for a single spin state are summed.

During the past year the energy resolution of the instruments available for the measurement of low-energy neutron resonances has been greatly improved. It is now possible to obtain Breit-Wigner[9] resonance parameters ($g\Gamma_n$, E_0, Γ, and σ_0) from transmission measurements for many resonances of the heavier nuclei. The quantity $g\Gamma_n$ is the neutron width multiplied by the statistical weight factor g, E_0 is the energy of the resonance, Γ is the total width, and σ_0 is the peak cross section. The factor g equals $\frac{1}{2}[1\pm1/(2I+1)]$; for the zero spin target nuclei ($I=0$), g equals unity; for target nuclei of high spin, g is approximately $\frac{1}{2}$. Since $g\Gamma_n=\sigma_0\Gamma/4\pi\lambda_0^2$, where $2\pi\lambda_0$ is the de Broglie wavelength of a neutron of energy E_0, $\sigma_0\Gamma$ is a direct measure of $g\Gamma_n$. The product $\sigma_0\Gamma$ is obtained directly from the area above a transmission curve for a thin sample. When it is necessary to use thick samples the quantity $\sigma_0\Gamma^2$ is obtained. It is then necessary to know Γ to obtain $g\Gamma_n$. A detailed discussion of the area method is given in the paper by Seidl *et al.* and Melkonian *et al.* (references *a* and *k* of Table I).

We have made a critical survey of resonance parameters for nuclei above atomic weight 100 which have been measured in the past year. The compilation of the evaluated parameters $\bar{\Gamma}_n^0/\bar{D}$, $\bar{D}$, and $\bar{\Gamma}_n^0$ is given in Table I. The table is based on data from the Brookhaven fast chopper, supplemented by data from the Brookhaven crystal spectrometer, the Argonne fast chopper, and the Columbia pulsed cyclotron. Parameters have been tabulated only when more than 3 resonances have been measured per element. The number of resonances measured per element varies from 4 to 30. The average spacing for each spin state, $\bar{D}$, is determined at low energies where it is believed that no resonances have been missed. For example, 16 resonances were found in $_{69}\mathrm{Tm}^{169}$ up to 160 ev, but only the first 9 resonances up to 65 ev were used to determine the observed level spacing. For zero spin-target nuclei, $\bar{D}$ is just the observed level spacing; for nonzero spin-target nuclei, $\bar{D}$ is taken to be twice the observed level spacing. In the case of $_{63}$Eu and of $_{75}$Re where the resonances have not been assigned to the individual isotopes, the

* Work carried out under contract with U. S. Atomic Energy Commission.

† Doctoral candidate from North Carolina State College, Raleigh, North Carolina.

[1] Feshbach, Peaslee, and Weisskopf, Phys. Rev. **71**, 145 (1947).
[2] H. Feshbach and V. F. Weisskopf, Phys. Rev. **76**, 1550 (1949).
[3] T. Teichmann and E. P. Wigner, Phys. Rev. **87**, 123 (1952).
[4] Feshbach, Porter, and Weisskopf, Phys. Rev. **90**, 166 (1953); their extensive treatment of this model for a 42-Mev well depth will be published in the *Physical Review*.
[5] A. Bohr and B. R. Mottelson, Kgl. Danske Videnskab. Selskab Mat.-fys. Medd. **27**, 159 (1953).
[6] R. G. Thomas (private communication).
[7] R. K. Adair, Phys. Rev. **94**, 737 (1954).
[8] H. H. Barschall, Phys. Rev. **86**, 431 (1952).
[9] G. Breit and E. P. Wigner, Phys. Rev. **49**, 519 (1936).

level spacing was assumed to be the same for the 2 isotopes. In the original formulation, $\bar{\Gamma}_n^0/\bar{D}=(\sum\Gamma_n^0)/\Delta E$, the summation is taken over a single spin state. If, however, $\bar{\Gamma}_n^0/\bar{D}$ is assumed to be the same for both spin states, it can be shown that $\bar{\Gamma}_n^0/\bar{D}=(\sum g\Gamma_n^0)/\Delta E$ where the summation is taken over both spin states. The summation can extend to a higher energy than was used to calculate $\bar{D}$ because small resonances which might be missed at higher energies contribute very little to the sum of $g\Gamma_n^0$'s. For elements containing two isotopes it can also be shown that if $\bar{\Gamma}_n^0/\bar{D}$ has the same value for each isotope and spin state, then $\bar{\Gamma}_n^0/\bar{D}=(\sum fg\Gamma_n^0)/\Delta E$ where f is the fractional abundance of the isotope. It was necessary to make this assumption to determine $\bar{\Gamma}_n^0/\bar{D}$ for $_{63}$Eu and $_{75}$Re. In the case of $_{50}$Sn where only one or two resonances are present in each isotope below 180 volts, the ratio $\bar{\Gamma}_n^0/\bar{D}$ given in Table I is the average for the isotopes. The probable errors on parameters listed in Table I are calculated from the deviation of the individual values from the mean.

TABLE I. Compilation of $\bar{\Gamma}_n^0/\bar{D}$ ratio for slow neutron resonances.

Isotope	$(\bar{\Gamma}_n^0/\bar{D})\times10^4$	$\bar{D}$ per spin state per isotope (ev)	$\bar{\Gamma}_n^0$ (10^{-3} ev)	Reference
$_{47}$Ag^{107}	0.5±0.2	40±10	2.0±0.9	a
$_{47}$Ag^{109}	1.0±0.3	31±6	3.1±0.9	a
$_{49}$In^{113}	0.55±0.12	15±2	0.8±0.2	b, c
$_{49}$In^{115}	0.20±0.05	16±3	0.32±0.10	b, c
$_{50}$Sn^{112,6,7,8,0}	0.20±0.10	200±100	4±2	c
$_{51}$Sb^{121}	0.45±0.12	28±5	1.3±0.4	d
$_{51}$Sb^{123}	0.6±0.2	55±15	3.3±1.4	d
$_{53}$I^{127}	1.2±0.4	25±5	3.0±1.0	a
$_{55}$Cs^{133}	0.7±0.2	50±10	3.5±1.2	c, e
$_{63}$Eu^{151,3}	1.9±0.2	2.4±0.3	0.46±0.08	f, g
$_{65}$Tb^{159}	1.8±0.4	10.5±1.0	1.9±0.5	g
$_{67}$Ho^{165}	2.9±0.5	12.0±1.0	3.5±0.6	h, i
$_{69}$Tm^{169}	1.8±0.3	15±2	2.7±0.5	h, i
$_{71}$Lu^{175}	1.7±0.2	8±2	1.4±0.5	h, i
$_{72}$Hf^{177}	2.7±0.7	9.0±1.0	2.4±0.7	j
$_{72}$Hf^{179}	1.6±0.4	11±2	1.8±0.6	j
$_{73}$Ta^{181}	1.0±0.4	12±3	1.2±0.5	k, l
$_{75}$Re^{185,7}	0.9±0.3	7±3	0.6±0.3	k
$_{79}$Au^{197}	0.8±0.2	60±10	4.8±1.3	a
$_{90}$Th^{232}	0.8±0.2	22±4	1.8±0.5	a

[a] F. Seidl *et al.*, Phys. Rev. **95**, 476 (1954).
[b] V. L. Sailor and L. B. Borst, Phys. Rev. **87**, 161 (1952) and private communication.
[c] R. S. Carter and J. A. Harvey, Phys. Rev. **95**, 645 (1954) and private communication.
[d] L. M. Bollinger (private communication). The authors wish to thank Dr. Bollinger for making his results available prior to publication.
[e] H. H. Landon and V. L. Sailor, Phys. Rev. **93**, 1030 (1954).
[f] Sailor, Landon, and Foote, Phys. Rev. **93**, 1292 (1954) and private communication.
[g] V. E. Pilcher and R. S. Carter (private communication).
[h] Foote, Landon, and Sailor, Phys. Rev. **92**, 656 (1953).
[i] Pilcher, Carter, and Stolovy, Phys. Rev. **95**, 645 (1954).
[j] Hughes, Kato, and Levin, Phys. Rev. **92**, 1094 (1953) and private communication.
[k] Melkonian, Havens, and Rainwater, Phys. Rev. **92**, 702 (1953).
[l] R. L. Christensen, Phys. Rev. **92**, 1509 (1953).

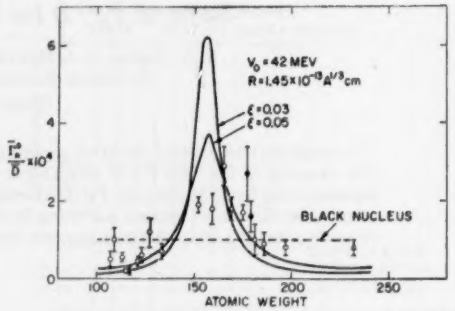

FIG. 1. Comparison of experimental values of $\bar{\Gamma}_n^0/\bar{D}$ *vs* atomic weight of the target nucleus with the theoretical predictions of black and cloudy crystal-ball models of the nuclear scattering. The symbols [○ odd Z-odd N, ● even Z-even N, △ even Z-odd N, and × the average for even Z-even N and even Z-odd N] refer to the compound nucleus. The errors represent the probable errors of the experimental points.

Figure 1 shows a plot of the experimental $\bar{\Gamma}_n^0/\bar{D}$ points as a function of atomic weight. The theoretical curves for a 42-Mev well depth are shown for the black nucleus model and for the cloudy crystal-ball model with $\xi=0.03$ and $\xi=0.05$.[10] The experimental points exhibit a maximum, in disagreement with the black nucleus picture. The experimental peak at about mass 160 is lower than the theoretical curve for $\xi=0.03$ which is the value of ξ giving the best fit for the total neutron cross sections in the Mev-region.[4] The experimental values off the peak are somewhat larger than predicted. Preliminary calculations by Choudhury[11] including the influence of the coupling to the nuclear rotational motion have shown that the maximum predicted in reference 4 at mass 155 would be depressed by a factor of about 2 and a secondary maximum would occur at approximately mass 120. In conclusion, the experimental data are in fair agreement with the recent theories[4–6] of neutron scattering; however, the present data are insufficient to select the best model.

The authors wish to thank Dr. C. E. Porter, Dr. V. F. Weisskopf, Dr. H. Feshbach, Dr. B. R. Mottelson, and Dr. R. G. Thomas for many stimulating discussions.

[10] The two theoretical curves for $\xi=0.03$ and $\xi=0.05$ were obtained from Dr. C. E. Porter (private communication).
[11] D. C. Choudhury (private communication from B. R. Mottelson, and A. Bohr (July, 1954).

Total Cross Sections of Liquefied Gases for High-Energy Neutrons*

PETER HILLMAN,† R. H. STAHL,‡ AND N. F. RAMSEY
Harvard University, Cambridge, Massachusetts

(Received June 9, 1954)

Total neutron cross sections of liquid H, He, N, O, A, and several solid elements have been measured at effective energies of 88±2 and 47.5±2 Mev. A liquid scintillation neutron counter was used. Results are in good agreement with previous experiments, where applicable.

1. INTRODUCTION

THE total neutron cross sections of many elements at neutron energies of about 100 Mev have been measured in the past.[1] No measurement exists, however, for helium or argon, nor for hydrogen except in the form of compounds. In order to obtain appreciable attenuation for pure helium or hydrogen, it is necessary to use these elements in the liquid state; 70 cm of either liquid constituting a 25-percent neutron attenuator at approximately 90 Mev. Such short attenuators are statistically disadvantageous, so that many counts are required in an accurate cross section measurement. This must be done in a short time, moreover, since a liquid helium target will keep for no more than 15 hours. It is therefore desirable to use an efficient neutron detector.

A simple liquid scintillation counter has been constructed and has been used to count neutrons with an efficiency of 15 percent. Although it has rather poor energy discrimination, it is possible to narrow the counted neutron spectrum by passing the cyclotron neutron beam[2] through "hardening" material which preferentially scatters low-energy neutrons. Two neutron beams have been used, with effective energies of 88±2 Mev and 47.5±2 Mev, 25 and 20 Mev wide, respectively, at half-height. The effects of γ-ray and low-energy neutron contamination of the beams are discussed below, and have been found to be small.

2. EXPERIMENTAL EQUIPMENT

A diagram of the geometry of the experiment is given in Fig. 1. The source of neutrons is a $\frac{1}{4}$-in. thick Be target bombarded by the circulating proton beam. Neutrons emitted at angles of 0° and 2° to the proton direction are collimated by lead and by 1-in. diameter tubes in the water shielding tank. Polyethylene rods inserted in the beam near the cyclotron tank harden the beam by scattering out preferentially the low-energy component (see Sec. 3). Identical neutron detectors are inserted into the beams; the "monitor" in the 2° beam close to the collimator, and the "counter" in the 0° beam behind another collimator. Attenuators are inserted roughly halfway from the neutron source to the counter.

Each neutron counter—Fig. 2—consists of an RCA 5819 photomultiplier sealed in a polished aluminum tube filled with scintillation solution (5 g/l terphenyl in reagent grade xylene). Teflon-wrapped O rings make a satisfactory glass to metal seal. Pulses from the photomultiplier are fed by a cathode follower to the control room, and there pass through an Atomic Instrument Company amplifier and discriminator into a scaler. Phototube high voltage is stabilized to better than $\frac{1}{10}$ percent[3] to reduce drift in gain.

The liquid helium and hydrogen attenuators consist of cylinders 30 and 70 cm long held in the target cryostat shown in Fig. 3. The attenuator container H is a $1\frac{5}{8}$-in. diameter tube soft-soldered from 0.005-in. shim stock with $\frac{1}{32}$-in. flat brass end plates (also soft-soldered). It is attached through tube G to a $2\frac{1}{2}$-liter reservoir ABE, and filled through 1-in. stainless steel access tube D. The cold parts are surrounded by a vacuum space and a radiation shield $JKNOP$ maintained at approximately liquid nitrogen temperature by conduction from the liquid nitrogen reservoir III. A guard vacuum for the liquid nitrogen completes the structure, the outer tube Q being a 10-in. diameter stainless steel tube 40-in. long. In the beam direction, windows are 0.005-in. Al (R) for the vacuum wall and 0.001-in. Al (P) for the radiation shield. The cryostat with its vacuum system and a gas-handling system for the target are mounted on a movable carriage positioned from the control room. Also mounted on this carriage is a dummy target assembly, experimentally normalized to the empty target tube, and used during the run to subtract the effects of that tube. Finally, there is provision on the carriage for mounting two 2-in. diameter solid targets.

Pure liquid helium was obtained from a Collins helium liquefier. Owing to the size of the target cryostat, it was necessary to use intermediate transfer vessels. In preparing the target and transfer bottles, in the siphoning, and in storage, care was taken to prevent contamination of the liquid by air. Hydrogen was supplied by A. D.

* Supported by the joint program of the U. S. Office of Naval Research and the U. S. Atomic Energy Commission.

† Now at the Atomic Energy Research Establishment, Harwell, England.

‡ Now at the University of California Radiation Laboratory, Livermore, California.

[1] Summarized *Neutron Cross Sections*, Atomic Energy Commission Report AECU-2040 (Technical Information Division, Department of Commerce, Washington, D. C., 1952), Supplement 2, (1953); also A. E. Taylor and E. Wood, Phil. Mag. 44, 95 (1953); W. I. Linlor and B. Ragent, Phys. Rev. 92, 835 (1953).

[2] J. A. Hofmann and K. Strauch, Phys. Rev. 90, 449 (1953); J. A. Hofmann, thesis, Harvard University, 1952 (unpublished).

[3] R. L. Smith (private communication).

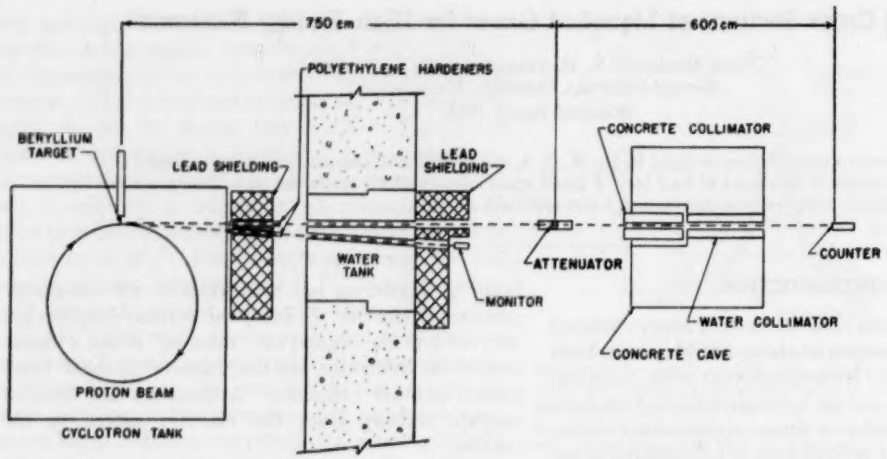

FIG. 1. Arrangement of apparatus.

Little, Inc., from a new liquefier under test and handled the same way. For this run the carriage was placed inside a timber and canvas house connected to an external exhaust fan to vent explosive gas from the cyclotron room.

Purity of the liquid target materials was checked by collecting the gas remaining after most of the liquid had boiled off, and measuring its density. The total contamination, if assumed to be air and uniformly distributed in the attenuator container, would introduce an error of $\frac{1}{2}$ percent in the hydrogen cross section, and 3 or 4 percent in that of helium. However, most of the impurity should be trapped in the reservoir, and much of the rest should settle out below the beam line, so that the actual effect on the cross section is believed much smaller—not more than 1 percent on the helium result. The absence of heaps reaching into the beam line from the bottom of the target was confirmed by taking a cross section of the rather dense He gas remaining with the liquid He level below the beam line. This agreed within statistics with the cross section of the liquid.

Liquid nitrogen and oxygen were obtained with high nominal purity from the Linde Air Products Company, and handled carefully. These liquids are much less likely to become contaminated than hydrogen or helium, and the neutron cross sections less sensitive to the presence of foreign matter. Argon was liquefied from high purity bottled gas under pressure in thermal contact with liquid oxygen.

The effect of bubbling on the liquid helium density has been investigated by cooling to produce He II, which does not bubble. The resultant cross section showed a bubbling effect of (0.3 ± 2.0) percent. The evaporation rate is about 150 cm³ per hour for liquid helium, 40 cm³ per hour for hydrogen, and much less for other liquids, so that the bubble effect should be greatest for helium.

Various lengths of solid 2-in. diameter attenuators were cut from nominally pure CH_2, C, Al, Cu, and Pb stock. C absorbers were cut down to beam diameter after use to test uniformity of density.

3. EFFECTIVE ENERGY DETERMINATION: BEAM AND COUNTER PROPERTIES

The determination of the exact composition of the counted beam and the effective energy of the measurements is made difficult by the characteristics of the neutron counter used. It has a very broad energy-sensitivity curve for neutrons, as well as high sensitivity to gammas and protons. The original cyclotron neutron beam has an unknown component of protons, gammas, and low-energy neutrons in addition to a large spread of neutron energies above 40 Mev.[2] The protons are easily

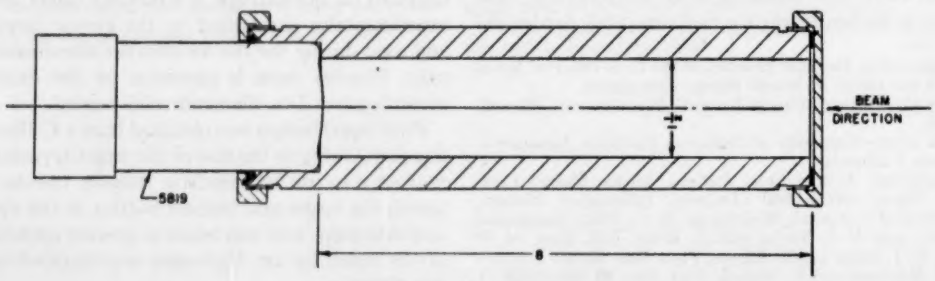

FIG. 2. Liquid scintillation counter.

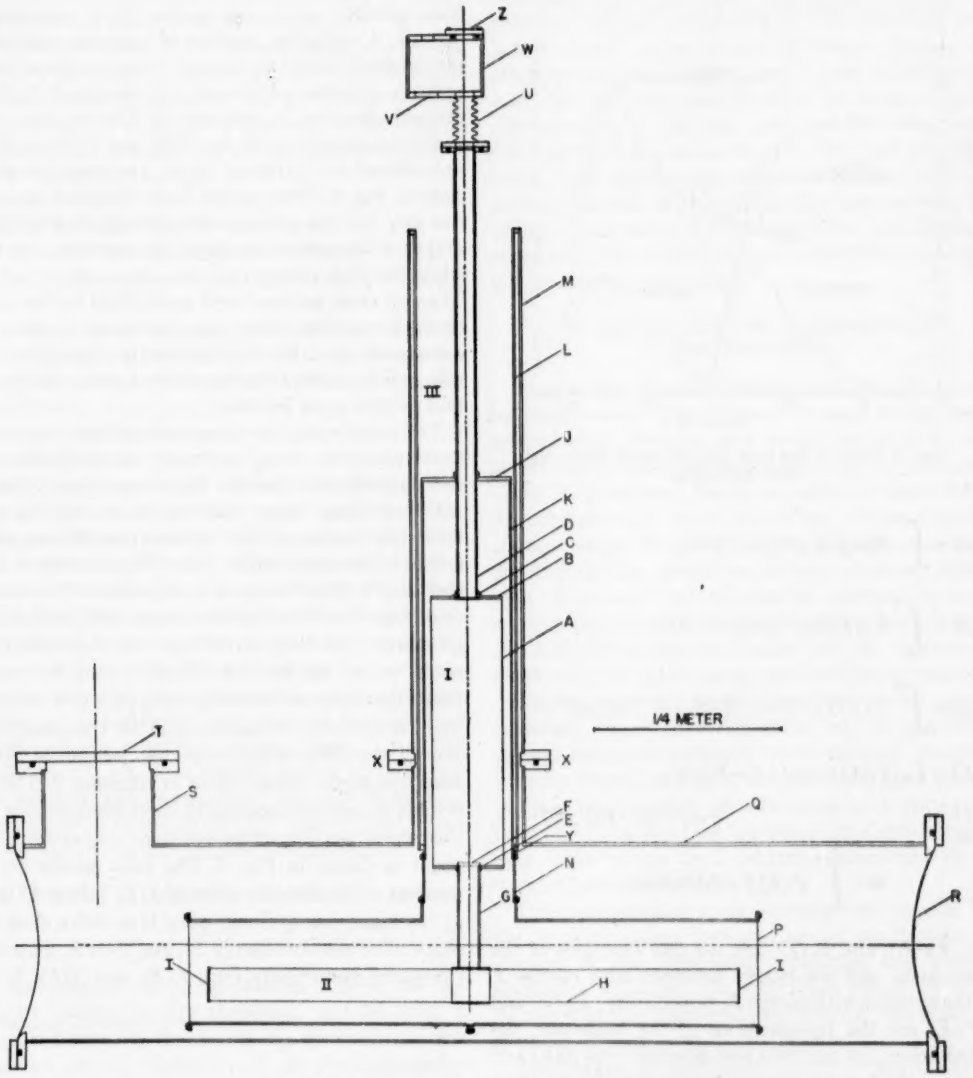

FIG. 3. Schematic diagram of low-temperature attenuator.

removed by a lead beam cleaner, but the other components require greater care.

A straightforward calculation shows that the true total cross section for pure material A will be

$$\sigma_A(E') = (-1/n_A)\{\ln[(1+X_N+X_\gamma)T_A - X_N T_A(E_N') - X_\gamma T_A^{(\gamma)}(E_\gamma')] - \ln(1+\alpha_A^{(2)}K)\}, \quad (1)$$

where n_A is the number of A atoms per cm^2, T_A is the experimental transmission, and $T_A(E_N')$ and $T_A^{(\gamma)}(E_\gamma')$ are the transmissions for neutrons and gammas of energies E_N' and E_γ', respectively. E_N', E_γ', and E' are the effective energies of the neutron and gamma contaminations and main beam respectively; X_N and X_γ, the fractional amounts of neutron and gamma contamination. K and $\alpha_A^{(2)}$ are defined by the following:

$$\int_0^\infty F(E)T_H(E)S(E)[(E-E')/E']dE=0,$$

$$\int_0^\infty F_N(E)T_H(E)S(E)[(E-E_N')/E_N']dE=0,$$

$$\int_0^\infty F_\gamma(E)T_H^{(\gamma)}(E)S_\gamma(E)[(E-E_\gamma')/E_\gamma']dE=0,$$

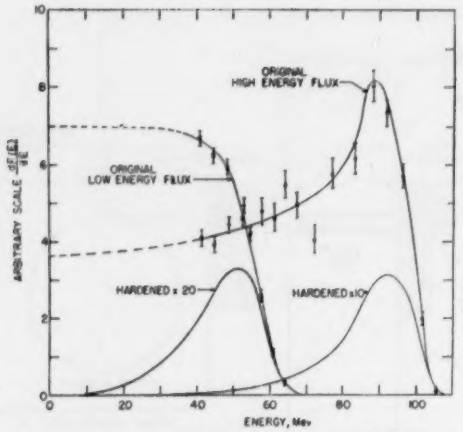

FIG. 4. Neutron flux from ¼-in. Be target before and after hardening.

$$X_N B = \int_0^\infty F_N(E) T_H(E) S(E) dE,$$

$$X_\gamma B = \int_0^\infty F_\gamma(E) T_H^{(\gamma)}(E) S_\gamma(E) dE,$$

$$KB = \int_0^\infty F(E) T_H(E) S(E) [(E-E')/E']^2 dE,$$

$$T_A(E) = T_A(E_0)\{1+\alpha_A^{(1)}(E-E_0)/E_0 + \alpha_A^{(2)}(E-E_0)^2/E_0^2 \cdots\},$$

where

$$B = \int_0^\infty F(E) T_H(E) S(E) dE.$$

$F(E)$, $F_N(E)$, and $F_\gamma(E)$, are the flux functions of the known high- and low-energy neutrons with energy E and the gammas with energy E, respectively; $T_H(E)$ and $T_H^{(\gamma)}(E)$ are the transmissions of the hardeners, described below, for neutrons and gammas; and $S(E)$ and $S_\gamma(E)$ are the counter-sensitivity functions for neutrons and gammas. The determination of n_A, the number of nuclei/cm^2 has been discussed in the previous section. T_A is the experimentally measured transmission. The remaining relevant quantities are E', X_N, X_γ, E_N', E_γ', and K. From these, and from known cross-section curves, it is possible to determine $T_A(E_N')$ and $T_A^{(\gamma)}(E_\gamma')$.

The high efficiency of the neutron counters used in this experiment made it possible to harden the beam with some three mean free paths of polyethylene at each energy. Rods 121 cm and 72 cm long were used at the two energies. This greatly reduced the neutron energy spread and hence the correction term $(1+\alpha_A^{(2)}K)$. Since the hardened flux, $F(E)T_H(E)$, has too low an intensity for direct determination, the unhardened flux $F(E)$ is measured, and the hardening effect $T_H(E)$ calculated from existing total cross section data, including the present. A negligible number of neutrons scattered in the hardener should be counted. A seven-crystal proton-recoil range telescope[4] is used to determine $F(E)$, by the method described in reference 2. The resultant points and extrapolated curves for $F(E)$ and $F(E)T_H(E)$, the unhardened and hardened fluxes, are shown for the two cases in Fig. 4. These curves were measured during one run only, and the assumption was made that the general shapes of the curves remained the same from run to run while the peak energy may vary as much as ±2 Mev. Then all cross sections were normalized to the energies of these runs by noting any variations in the carbon cross sections taken intermittently throughout each run, and by using the adequately known energy variation of each cross section.

Two points on the counter-sensitivity curve $S(E)$ were measured, using hardened beams similar to the two experimental beams. The seven-crystal telescope with a radiator larger than the beam and placed immediately in front of the neutron counter was used to monitor the total neutron flux. The counter is always reset to the same bias level by adjustment to a standard counting rate with a radium source held in a standard geometry. The only corrections that have then to be made to get the relative efficiencies are for neutrons below the telescope threshold (using the now sufficiently well-known neutron spectra) and for the energy variation of the differential $n-p$ cross section at 20°, the telescope angle, calculated as in reference 2. The curve is filled in and extrapolated to lower energies by a rough theoretical analysis of the counters' properties, and the result is shown in Fig. 5. The final results are independent of the absolute value of $S(E)$ (about 15 percent at the higher energy) and quite insensitive even to the shape. The effective energy E', and then K, may now be calculated numerically from $F(E)$, and $S(E)$. It is im-

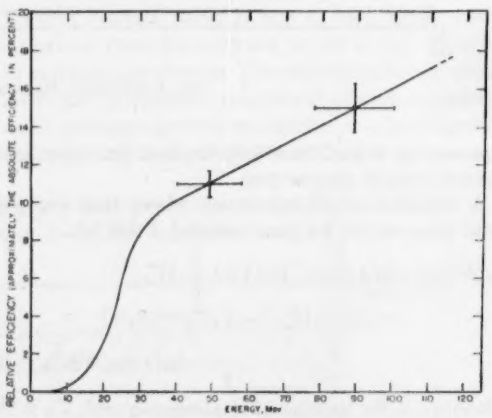

FIG. 5. Variation of counter sensitivity with energy.

[4] Kindly lent by K. Strauch and W. Titus.

portant to note that E' and K are functions of the beam only and are the same for all attenuators.

In order to measure the fractional gamma contamination X_γ, we choose a material whose neutron cross section is roughly the same for the low-energy neutron contamination (if any) as for neutrons of the experimental energies, namely lead. If we then let $T_A(E_N')=T_A(E')$ in Eq. (1), we get

$$X_\gamma \simeq [(1+X_\gamma+\alpha_A{}^2K)T_A(E') - (1-X_N)T_A]/T_A-T_A{}^{(\gamma)}(E_\gamma') \simeq [(1+\alpha_A{}^2K)T_A(E')-T_A]/T_A-T_A{}^{(\gamma)}(E_\gamma') \quad (2)$$

if X_N is small. If we measure the experimental transmission T_A for two thicknesses of lead, chosen as 2 in. and 6 in., we can eliminate $T_{A1}(E')$ and $T_{A2}(E')=T_{A1}(E')^{n_{A2}/n_{A1}}$ from the resulting Eqs. (2). E_γ' is difficult to determine for small contaminations, but is estimated as follows.

A carbon cyclotron target was found to give a much higher proportion of gammas than the beryllium, enabling a determination of the apparent lead cross section with counter bias and with hardener length. The former indicated an average gamma energy of less than about 10 Mev, the latter an energy of well above 5 Mev. (The hardener is too long for the observed increase of lead cross section with hardener length to be due to gammas originating in the hardener.) E_γ' is therefore estimated at 9 ± 3 Mev for the higher and 9 ± 5 Mev for the lower energy beryllium beams, giving $X_\gamma=0.007\pm0.009$ and 0.02 ± 0.02 for the two beams, respectively.

Two polyethylene attenuators 14 in. and 36 in. long are now used to eliminate $T_{A1}(E')$ and $T_{A2}(E')$ from similar equations for the neutron contamination,

$$X_N=\{[1+\alpha_A{}^{(2)}K]T_A(E')-T_A + X_\gamma[T_A{}^{(\gamma)}(E_\gamma')-T_A]\}T_A-T_A(E_N').$$

If we then assume E_N to be between 5 Mev, the approximate counter proton threshold, and 20 Mev, a reasonable maximum in view of the observed neutron spectra, we get $X_N=0.000\pm0.007$ for the high-energy beam. The fact that this figure did not increase detectably when the hardener at both energies was radically shortened, however, indicates very strongly that the contamination is in fact zero. Multiple or inelastic scattering in the hardener should yield a negligible contamination, and a check made by means of a "total absorber" of copper showed that within 0.3 percent statistics all of the counted beam passed through the hardeners. The error (giving a 3 percent error on the final high-energy hydrogen cross section) was therefore neglected for both energies.

The determination of $\alpha_A{}^{(2)}$ is the only one that relies at all sensitively on outside data. A smooth variation of $\alpha_A{}^{(2)}$ both with energy and with atomic number seems indicated by the existing data but is also explicitly assumed. Fairly comprehensive curves exist for six materials,[5] and are used directly to calculate any corresponding $\alpha_A{}^{(2)}$'s, choosing $E_0=E'$. From this data a curve of $\alpha_A{}^{(2)}$ *versus* atomic number is drawn, with attenuations used equal to that of each desired attenuator. All plots were smooth except for breaks at points corresponding to the fine structure first observed at Harwell,[5] and the unknown $\alpha_A{}^{(2)}$'s are read directly off them, with appropriate errors attached. Corrections were of the order of 3 percent on the cross sections, with errors of the order of 1 percent. The contribution of terms in $\alpha_A{}^{(3)}$ and higher cannot be accurately estimated but seems to be very small.

4. CALCULATION OF EXPERIMENTAL TRANSMISSIONS

The counters used in this experiment have of course no gain plateaus. Over a period of hours during runs of several days, counting rate variations of up to ±0.4 percent were noted (corresponding to gain variations of about $\pm1\frac{1}{2}$ percent). Liquid and dummy runs of up to 20 minutes each were, therefore, always taken in opposite order. The scatter of resulting ratios has with a few explainable exceptions always appeared random with magnitude not appreciable greater than that statistically expected. Dummy counting rates averaged 100 and 200 counts per second for the counter and monitor at the higher energy, and half that at the lower.

Counter noise averaged 3 counts per second and was measured regularly throughout a run. It was plotted against time and a smooth curve through the points (usually approximating a straight line) used for subtracting "noise" from all other data with appropriate error. All data was then corrected for electronic dead-time losses of up to 2 percent, determined by the standard two-source technique.

The cyclotron duty cycle was estimated visually from the neutron pulses displayed on an oscilloscope. An analysis of the pulse-height spectrum and amplifier properties indicates that electronic pileup of pulses smaller than the discrimination level will contribute less than 0.3 percent to the counting rate.

The leakage rate per monitor count is then determined and plotted, and a smooth curve used for subtraction. Leakage is the counting rate (typically 2 and 0.1 counts per second at the two energies) with a copper "total absorber" of the same diameter as the attenuators in the beam. The leakage flux consists predominantly of low-energy particles.

The full-empty ratios are then the final experimental transmissions T_A for the solid targets. For the liquid targets, the ratios are corrected for the experimental normalization of the dummy to the empty target performed before or after the run.

The maximum correction for neutrons scattered by the attenuators into the counter was 0.1 percent. To investigate the possible existence of a delayed beam-

[5] See Taylor and Wood, reference 1.

TABLE I. Results of total cross-section measurements, in millibarns.

Material\Energy	88±2 Mev	47.5±2 Mev
Liquid H	86.1± 2	
CH_2−C	84.5± 2	196± 10
He	199 ± 6	377± 12
C	560 ± 8	984± 20
N	636 ±10	1110± 25
O	743 ±15	1220± 25
Al	1200 ±25	1750± 35
A	1480 ±20	2080± 45
Cu	2265 ±35	2810± 70
Pb	4830 ±40	4460±100

dependent counting rate due to radioactivation of the counter or surrounding bodies, the counter was bombarded with the full beam and the decay of the noise rate determined. Only the 20-minute $C^{12}(n,2n)C^{11}$ activity was observed, with an intensity corresponding to a negligible 0.03 counts per second for the hardened beam.

In addition to these checks, no effect on the corrected cross sections of carbon and lead could be found when the second collimator was removed, or when the following were varied: (1) cyclotron beam strength, (2) counter bias level (except for a possible slight increase in the fractional gamma contamination at low bias), (3) attenuator and hardener position and diameter, and (4) counter size (a counter 3 in. long and 2 in. in diameter was used).

5. RESULTS AND ERRORS

Results of the experiment have been summarized on Table I. There is general agreement with previous experimental results where they exist, or with smoothly interpolated values. At the higher energy, the cross sections are in good agreement with the optical model,[6] notably including helium, but of course not hydrogen. The lower-energy results should fit $\sigma_A = 2\pi(R+\lambda)^2$ with $R = R_0 A^{\frac{1}{3}}$ according to the Feshbach-Weisskopf opaque model with sharp edges.[7] When this formula is used, the experimental σ's yield a value for R_0 of $(1.50\pm0.06)\times10^{-13}$ cm for all elements except lead (1.31×10^{-13}), helium (1.12×10^{-13}), and hydrogen (1.12×10^{-13}).

Errors listed are estimated total mean deviations arising from several sources. (1) Errors in the determinations of the experimental transmission: These are primarily counting statistics, less than 1 percent except for the hydrogen cross section from CH_2. An estimated 25 percent uncertainty in the dead-time correction gives a small error—typically 0.3 percent. (2) Errors in the density and purity of targets: These are quite small, except for liquid helium where the lowering of the density due to bubbling is estimated at (0.3 ± 2.0) percent and the error due to contamination about ±1 percent. (3) Errors in the effective beam energy and constitution. During the test run, the effective energies of measurement were determined to be 88 ± 2 Mev and 47.5 ± 2 Mev. The errors quoted were determined using reasonable "extreme curves" of the neutron spectra and counter sensitivity. Results of other runs have been normalized to these energies, and the errors arising in these adjustments have been added to the cross section errors.

The γ contamination was measured to be $X_\gamma = (0.7\pm0.9)$ percent for the 88-Mev neutron beam, with an estimated γ energy of 9 ± 3 Mev. For the 47.5-Mev neutron beam, the contamination is $X_\gamma = (2\pm2)$ percent at 9 ± 5 Mev. All results have been corrected for this effect. This is a major source of error in the lower-energy measurements.

ACKNOWLEDGMENTS

This experiment would not have been possible without the advice and cooperation of many persons. We are greatly indebted to Dr. C. A. Swenson for low temperature advice, to Mr. Earl Wilkie who ran the Collins liquefier, to Mr. Richard Wharton and the cyclotron operating crew, and to Mr. P. F. Cooper, Jr., for many services at late hours. Special thanks are due A. D. Little, Inc., for a gift of 100 liters of liquid hydrogen when most needed. During most of the period covered by this experiment, one of us (R. H. S.) held an U. S. Atomic Energy Commission Predoctoral Fellowship.

[6] Fernbach, Serber, and Taylor, Phys. Rev. **75**, 1352 (1949), using the parameters as for Cook's data.

[7] H. Feshbach and V. F. Weisskopf, Phys. Rev. **76**, 1550 (1949).

Production of Nb^{93m} by the Pile Irradiation of Niobium

R. P. SCHUMAN
Knolls Atomic Power Laboratory, Schenectady, New York*
(Received June 7, 1954)

Low-energy electrons and Nb K x-rays, believed to be due to the decay of the isomer Nb^{93m}, have been found in neutron-irradiated niobium. The electrons have energies of about 8.5 kev and 23 kev and are believed to be K and L conversion electrons from a 27-kev gamma ray. The half-life of the activity is about four years.

ADDITIONAL measurements have been made on the samples of niobium which had been irradiated for a long time in the Chalk River reactor and subsequently carefully purified. These measurements have shown the presence of low-energy electrons and x-rays, in addition to the 0.50-Mev beta and 0.70-, 0.87-, and 1.57-Mev gammas previously described.[1]

When some of the niobium was counted with a 4π counter, it showed a much higher specific activity then could be attributed to the 0.50-Mev Nb^{94} beta. An absorption curve taken with a low absorption counter showed that the additional activity is a very weak electron activity with a half-thickness of about 0.36 mg/cm^2 in aluminum. By using the top half of a 4π counter as a proportional counter spectrometer, the energy spectrum of the weak electrons was determined; two peaks were found, the larger one at about 23 kev and the smaller one at about 8.5 kev. The energies were determined by comparison with the energy of the MnK x-ray from Fe^{55}.

An aluminum absorption curve of the niobium radiations taken through sufficient beryllium to absorb all the beta rays showed the presence of a photon of about 15-kev energy in addition to the gamma rays. A proportional counter spectrometer showed an x-ray peak at 16 kev as determined by comparison with MnK x-rays. By the use of Rb, Sr, Y, Zr, Nb, and Mo critical absorbers, it was shown that the photons are niobium K x-rays.

The niobium samples have been followed for decay on an internal sample counter for a period of eight months, and a half-life of about four years has been obtained for the weak electron activity.

Since the x-rays are niobium x-rays, the electrons must be conversion electrons emitted during the isomeric transition of a niobium isotope. The isomer decays by the emission of an almost completely converted ($\sim$27 kev) gamma with L conversion ($\sim$23-kev e^-) more probable than K conversion ($\sim$8.5 kev e^-).

The isomer is most likely the 3.65-year isomer of Nb^{93} that has been reported by Glendenin and Steinberg.[2] They found that the isomer is produced by the decay of Zr^{93} and decays by the emission of conversion electrons with $K/L=0.14$ from a 29.2-kev gamma.

We feel that the weak electron activity in the niobium samples is due to Nb^{93m} which is produced from Nb^{93} by the inelastic scattering of fast neutrons. If so, the Chalk River pile neutron cross section for its formation is about 0.8 millibarn. The author wishes to give special thanks to the Chalk River Laboratories for making possible the long-term irradiation of the niobium, and also to thank Mrs. A. C. Mewherter for her help with the preparation of the counting samples.

* Operated for the U. S. Atomic Energy Commission by the General Electric Company.

[1] Douglas, Newherter, and Schuman, Phys. Rev. **92**, 369 (1953).

[2] Hollander, Perlman, and Seaborg, Revs. Modern Phys. **25**, 520 (1953).

Excited States in B^{10} and Be^{8}†

T. W. Bonner and C. F. Cook
The Rice Institute, Houston, Texas
(Received June 16, 1954)

A new technique for detecting neutron thresholds by using a slow neutron counter and a conventional long counter is described. By means of this technique, neutron thresholds from the deuteron bombardment of Li^7 have been studied at energies from 0.4 Mev to 4.7 Mev. Thresholds were observed at energies of 1.34, 2.18, 3.37, 3.6, and 4.07 Mev. These thresholds indicate excitation levels in Be^8 at 16.06, 16.72, 17.65, 17.8, and 18.19 Mev.

By the same method, excited states of B^{10} from the $Be^9(d,n)B^{10}$ reaction were found at 4.78, 5.11, 5.17, 5.93, 6.06, 6.16, 6.43, and 6.57 Mev.

INTRODUCTION

PRECISE energy determinations of excited states of nuclei have been made by using magnetic and electrostatic analyzers, which measure the energies of charged particles such as protons, deuterons, and alpha particles. Similar measurements of the energies of fast neutrons with comparable accuracy are not possible. However, in experiments measuring the energies of "neutron thresholds," Bonner and Butler[1] were able to obtain precise measurements of Q values in a number of reactions of the (p,n) and (d,n) type. Extension of this method to other reactions depends on the sensitivity of detection of a relatively small number of "threshold neutrons" with energies of from 5 to 50 kev in the presence of neutrons with higher energies.

APPARATUS

Considerable improvements in the techniques have been possible in the new Nuclear Research Laboratory where a 6-Mev Van de Graaff accelerator, built by the High Voltage Engineering Corporation, has recently been installed. Improvements have been made in two ways. In our old laboratory the target which was bombarded by protons or deuterons was only 4 feet above a thick concrete floor which moderated the fast neutrons and scattered these back to our "threshold detector," which was a BF_3 proportional counter surrounded by approximately 4 cm of paraffin. A smaller thickness of paraffin gives a detector with a better discrimination for kev-neutrons relative to Mev-neutrons, but is only useful if relatively few scattered neutrons reach the counter. Our new laboratory was designed so that the target is 4 feet above a floor of $\frac{1}{4}$-in. aluminum which is relatively transparent to fast neutrons. There is a pit 8 feet deep below the aluminum floor and so the target is 12 feet from an effective neutron moderator. Another improvement is derived from placing the target 20 feet away from our analyzing magnet. Some neutrons are always made when the diatomic and triatomic beams strike materials, especially when deuterons are accelerated. The inverse square law is especially helpful in reducing the effects of these background neutrons. Figure 1 shows the experimental arrangement which has been used. A paraffin layer $1\frac{3}{4}$ in. long and $\frac{3}{8}$ in. thick covers the middle portion of a BF_3 counter which has a diameter of 1 in. This threshold counter C_1 is placed 2 in. from the target and so subtends a cone of half-angle 24°. A second counter C_2 is placed 14 in. from the target and subtends approximately the same solid angle as C_1. This counter is the inner part of the usual "long counter" which has about equal efficiency for detecting neutrons of all energies from 0 to 5 Mev. The ratio of the number of counts in C_1 and C_2, taken at the same time, gives a measure of the relative number of slow neutrons to total neutrons. This ratio is independent of the beam current and of the uniformity of the target which is being bombarded.

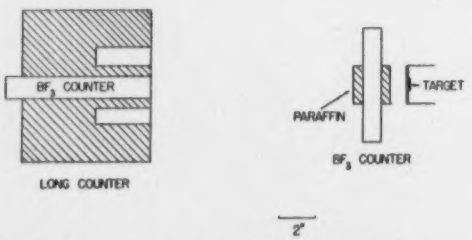

FIG. 1. Experimental arrangement of conventional long counter and BF_3 counter for neutron-threshold detection.

RESULTS

Experiments have been carried out with this technique when a thin lithium target is bombarded by protons. The results are shown in Fig. 2. The threshold for the nuclear reaction $Li^7(p,n)Be^7$ is at 1.883 Mev. When protons with energies lower than this strike the lithium target no neutrons are produced and the counting rate in counters C_1 and C_2 is very small. Above this threshold the counting rates in both counters increase rapidly; the ratio of the counting rates C_1/C_2 shows a threshold at 1.883 Mev and decreases as the bombarding energy is increased. The counting ratio decreases to $\frac{1}{2}$ its maximum rate when the proton energy is increased to 50 kev above the threshold. The ratio continues to drop smoothly until it is $\frac{1}{10}$ the threshold value when

† Supported in part by the U. S. Atomic Energy Commission.
[1] T. W. Bonner and J. W. Butler, Phys. Rev. 83, 1091 (1951).

the neutrons have energies of 0.6 Mev. The second curve shown in Fig. 2 is that of the counting rate in the long counter C_2 as a function of proton energy. The long-counter yield curve shows the neutron threshold at 1.883 Mev followed by a decrease in the neutron flux through this counter as the cone of neutrons opens to 180°. At a proton energy of 2.3 Mev, the known resonance caused by an excited state in the compound nucleus Be^8 is observed with the long counter. However, the ratio curve does not show any irregularity because of this resonance. This fact makes it possible to differentiate between neutron thresholds and resonances.

$Be^9(d,n)B^{10*}$

Experiments with the reaction $Be^9(d,n)B^{10*}$ have been carried out by means of the same techniques as described above. The evaporated beryllium target was 10 kev thick for 2-Mev deuterons. Threshold neutrons were investigated when the deuteron beam was increased from 0.45 Mev to 5.4 Mev. Data obtained below 3 Mev are shown in Fig. 3. Neutron thresholds observed are indicated in Fig. 3 at *A*, *B*, *C*, *D*, *E*, and *F*.

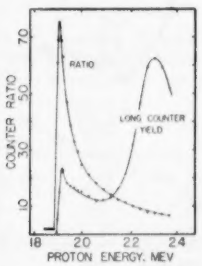

FIG. 2. Neutrons from the reaction $Li^7(p,n)Be^{7*}$. The solid circles give the ratio of the number of slow neutrons to the total number of neutrons from the reaction as a function of proton energy. The open circles give the long-counter yield in arbitrary units as a function of proton energy.

There is also a small effect at *H* caused by a "wide threshold" and a weak threshold at *G*.

Table I lists the thresholds shown in Fig. 3, the deuteron-bombarding energy at each threshold, the calculated *Q* values, the corresponding energies of the excited states of B^{10}, and the observed half-width. The last column of Table I lists excited states of B^{10} from measurements of recoil protons in photographic plates obtained by Ajzenberg.[2] Data taken with deuteron energies of 3–5.4 Mev indicate no additional thresholds. The states at 5.11, 5.17, and 5.93 Mev were obtained by Bonner and Butler.[1] The results reported here are in agreement with the results of Ajzenberg,[2] except that we do not observe the weak lines at 5.58 and 6.77 Mev and with higher-energy resolution we have resolved the doublet at 5.11 and 5.17 Mev, and the triplet at 5.93, 6.06, and 6.16 Mev.

All of the states of B^{10*} above 4.45 Mev can break up with α-particle emission, and so the widths of these states will be much greater than in the case of the lower states where γ emission only takes place. The widths of the states will be expected to increase with excitation

[2] Fay Ajzenberg, Phys. Rev. **82**, 43 (1951); **88**, 298 (1952).

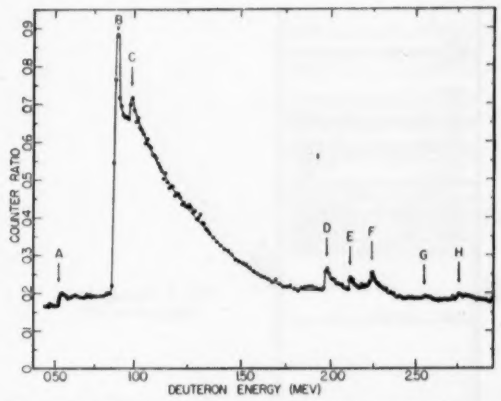

FIG. 3. Neutrons from the reaction $Be^9(d,n)B^{10*}$. The curve gives the ratio of the number of slow neutrons to the total number of neutrons from the reaction as a function of deuteron energy.

because of the increased penetrability of the α particle. Widths will also depend on the angular momentum carried away by the α particles and the isotopic spin. The states near 6-Mev excitation are unstable for α emission by ~1.5 Mev and so would be expected to have widths ~100 kev if *s* α-particle decay is possible. Since their widths are less than 10 kev, this would indicate that the *J* values of these states are probably $J=2$ or greater.

An energy-level diagram for B^{10} is given in Fig. 4. Spin, parity, and isotopic spin assignments are shown where known. The two levels at 5.11 and 5.17 Mev appear to form a doublet, the splitting between them being only 60 kev while the distance to the next levels above and below are 760 kev and 330 kev, respectively; the three levels at 5.93, 6.06, and 6.16 Mev appear to form a triplet with separations of 130 kev and 100 kev. Figure 3 also shows that the intensities of the two lines in the doublet at 5.11 Mev are nearly equal, also the three lines of the triplet at 6.06 Mev appears to have nearly equal intensities in the forward yield of low-

TABLE I. Neutron thresholds—excited states of B^{10}. Energies of excited states are based on a Q_0 value of 4.360 Mev.

Thresholds	Deuteron energy (Mev)	*Q* value Mev	Excitation energy B^{10} Mev	Level width Mev	Excitation energy B^{10} Ajzenberg[a] Mev
A	0.52	−0.42	4.78	<0.010	4.78
B	0.92	−0.75	5.11	<0.010	
					5.14
C	0.99	−0.81	5.17	<0.010	
					5.58
D	1.92	−1.57	5.93	<0.010	5.93
E	2.08	−1.70	6.06	<0.010	
					6.12
F	2.20	−1.80	6.16	<0.020	
G	2.53	−2.07	6.43		6.38
H	2.70	−2.21	6.57	~0.030	6.57
					6.77

[a] See reference 2.

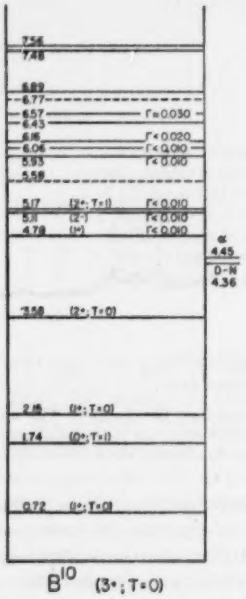

FIG. 4. Energy level diagram of B^{10}.

energy neutrons. Inglis[3] has pointed out that the two lines of the doublet may correspond to the two orientations of an s-proton spin relative to another j or J_p; however, the possibility seems to be at variance with the recent results of Wilkinson and Jones[4] which indicate that the 5.11-Mev level is $2(-)$ and the 5.17-Mev level is $2(+)$ and $T=1$. Both levels would be expected to have odd parity and J's of 1 and 2 when produced by s deuterons according to the suggestion of Inglis. The group of levels at 5.93, 6.06, and 6.16 Mev seem more likely to be physically significant instead of an accidental juxtaposition than does the doublet.

The small relative yield of threshold neutrons from the 4.78-Mev state is expected if it has even parity, since s deuterons will be predominant at a bombarding energy of 0.5 Mev, and then s-neutron emission is forbidden. The fact that the ratio curve does not fall off rapidly above the 0.52-Mev threshold indicates that p-neutron emission is involved.

$Li^7(d,n)Be^{8*}$

Experiments with neutrons from the (d,n) reaction on normal lithium were carried out using metallic lithium evaporated onto the target in the vacuum system of the accelerator. From threshold measurements with the (p,n) reaction, the lithium target was found to be 20-kev thick at 2 Mev. Under similar conditions to the experiments already described, the counting rates in the two counters C_1 and C_2 were observed as deuteron energy was increased from 0.45 Mev to 4.8 Mev. Figure 5 shows the results of the yield of neutrons in the long counter and the ratio of the counts in the two counters. The known resonances in the yield of neutrons at deuteron energies 0.7 and 1.0 Mev were observed but are not shown. Above 1.5 Mev there is evidence for a broad resonance at 2.0 Mev, and another broad resonance at 3.2 Mev which correspond to wide states in Be^9 at ~18.2 Mev and ~19.6 Mev.

The ratio curve is flat from 0.45 to 0.80 Mev and then rises slowly until it becomes flat again at 1.5 Mev. This shape of curve is that expected from a broad state in Be^{8*}; in this case the yield of threshold neutrons should follow the shape of the energy state. The maximum number of threshold neutrons from this level in Be^8 occurs at A. Another rise in the ratio curve begins at 1.7 Mev and reaches a peak value at B. The third rise in the curve at C indicates a neutron threshold at the same energy as an intense threshold in oxygen, so it seems probable that it is caused by a small amount of oxygen on the target. Other thresholds are indicated at D, E, and F in Fig. 5.

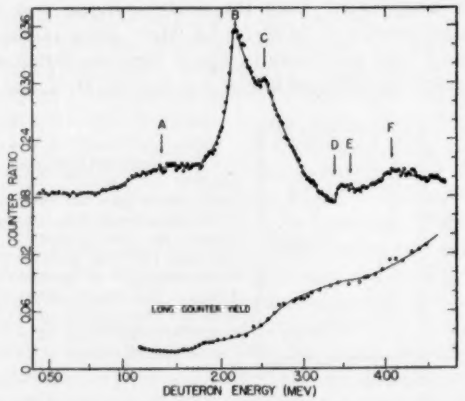

FIG. 5. Neutrons from the reaction $Li^7(d,n)Be^{8*}$. The upper curve gives the ratio of the number of slow neutrons to the total number of neutrons from the reaction as a function of deuteron energy. The lower curve gives the long-counter yield in arbitrary units as a function of deuteron energy.

Table II lists the thresholds shown in Fig. 5, the deuteron-bombarding energy at each threshold, the calculated Q values, the corresponding energies of the excited states of Be^8, and the observed half-width of each level.

All of the thresholds found are wide except that at 3.37 Mev, which has a width less than 20 kev. The Q value obtained for this narrow threshold agrees well with the known level[5] in Be^8 at 17.63 Mev (width 12 kev) made by 440-kev protons on Li^7. The width of this neutron threshold is less than the target thickness of 20 kev, and so it seems very likely that the two levels are the same. The level at 18.19 Mev has also been observed[6] in elastic scattering of protons on Li^7; a level

[3] D. R. Inglis, Revs. Modern Phys. **25**, 390 (1953).
[4] D. H. Wilkinson and G. A. Jones, Phys. Rev. **91**, 1575 (1953).
[5] T. W. Bonner and J. E. Evans, Phys. Rev. **73**, 666 (1948).
[6] Brown, Snyder, Fowler, and Lauritsen, Phys. Rev. **82**, 159 (1951).

width of 0.17 Mev was found. The state at 16.72 Mev can only emit a γ ray or break up into two α particles; the observed width of 0.19 Mev indicates α emission. The α particles have a total energy of 16.72 Mev and the level in Be^8 would be expected to show a width of $\sim$1 Mev unless the isotopic spin selection rule made the α emission considerably slower. A level in Be^8 with isotopic spin $T=1$ is expected[7] near 16.7 Mev. It seems likely that the level at 16.72 Mev with a width of 0.19 Mev is the first $T=1$ state in Be^8. From the 0.6-Mev width of the level at 16.06 Mev, it seems probable that this level is a $T=0$ state with $J=2+$ or $4+$; this follows from the fact that the $J=2+$ level at 19.9 Mev has a width of 1 Mev.

Wilkins and Goward[8] have presented evidence for states in Be^8 from the photo reactions $C^{12}(\gamma,3\alpha)$ which were observed in nuclear emulsions. They reported levels in Be^8 at 16.8 ± 0.2 Mev and 17.6 ± 0.2 Mev with widths <0.3 Mev. From the angular distribution of the α particles, they were able to conclude that the 16.8-Mev state has $J=2$. It seems likely that the level which we observed at 16.72 ± 0.01 Mev is the same as that observed by Wilkins and Goward. It seems improbable

TABLE II. Neutron thresholds—excited states Be^8. Energies of excited states are based on a Q_0 value of 15.02 Mev.

Threshold	Deuteron energy Mev	Q value Mev	Excitation energy Be^8 Mev	Level width Mev
A	1.34	−1.04	16.06	0.6
B	2.18	−1.70	16.72	0.19
C	2.5	···	Oxygen contamination	
D	3.37	−2.63	17.65	<0.02
E	3.6	−2.8	17.8	0.1
F	4.07	−3.17	18.19	0.17

that the level that we observe at 17.65 Mev is the same as reported by Wilkins and Goward at 17.6 Mev. They suggest that this level is $J=4+$ and $T=1$. Such a state would be expected to be narrower than the 16.72-Mev level ($J=2+$, $T=1$), but a width less than 20 kev is unexpected. The threshold at *D* (17.65-Mev state) is sharp on the low-energy side but does not drop off as fast as expected on the high-energy side. The best explanation is that the threshold at *D* is a doublet including a sharp level at 17.65 Mev and a wider one

[7] T. Lauritsen, Ann. Revs. Nuclear Sci. **1**, 67 (1952).
[8] J. J. Wilkins and F. K. Goward, Proc. Phys. Soc. (London) **66**, 661 (1953).

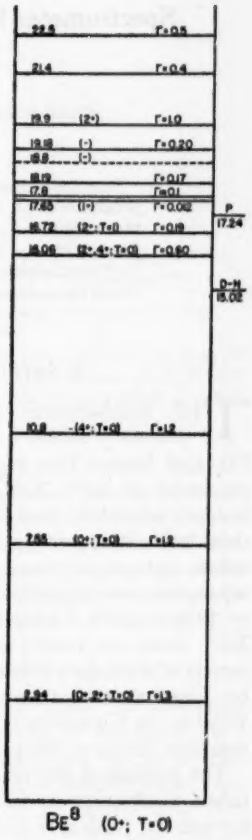

FIG. 6. Energy level diagram of Be^8.

at 17.8 Mev (*E*) with a width of approximately 0.1 Mev.

An energy-level diagram for Be^8 is given in Fig. 6. A number of the previously reported levels between 3 and 7 Mev are omitted. Evidence for the nonexistence of several of these levels comes from several sources.[9] There is still some question about levels at 4.05 and 5.3 Mev.[10] The experimental levels fit in very well with the intermediate coupling calculations of Inglis, except for the unpredicted levels at 7.75 and 16.06 Mev.

[9] R. F. Sinclair, Phys. Rev. **93**, 1082 (1954); R. Malm and D. R. Inglis, Phys. Rev. **92**, 1326 (1953); Kunz, Moak, and Good, Phys. Rev. **91**, 676 (1953); C. C. Trail and C. H. Johnson, Phys. Rev. **95**, 640A (1954); F. E. Steigert and M. B. Sampson, Phys. Rev. **92**, 660 (1953).
[10] E. W. Titterton, Phys. Rev. **94**, 206 (1954).

Spectrometer Studies of the Radiations of Some Neutron-Deficient Isotopes of Xenon and Iodine*

HIRDAYA B. MATHUR† AND EARL K. HYDE
Radiation Laboratory and Department of Chemistry, University of California, Berkeley, California
(Received June 28, 1954)

Neutron-deficient isotopes of xenon have been produced by (p,xn) reactions with high-energy protons on potassium iodide targets. The xenon activities were deposited on foils by the glow discharge technique and their radioactive properties were measured. Nineteen-hour Xe^{122} decays by electron capture to 3.5-minute I^{122}. Gamma rays of 182 and 235 kev accompany this decay. I^{122} decays by emission of 3.12-Mev positrons. Xe^{120} decays with a 1.8-hour half-life into 13-hour I^{120}. Positrons of 1.7±0.1 Mev, 150-kev gamma rays, and x-rays are associated with this decay. Xe^{121} has a half-life of 40±10 minutes for decay into 1.6-hour I^{121}.

I. INTRODUCTION

THE bombardment of iodine with high-energy protons produces xenon isotopes of mass number 127 and lower. This report is concerned with the properties of Xe^{123}, Xe^{122}, and Xe^{121}, and the iodine isotopes formed by their decay. Isolation and study of these iodine isotopes revealed the presence of the known iodine isotopes of mass 123, 122, and 121. Timed separations established the genetic relationship of these to 19-hour Xe^{122}, 1.8-hour Xe^{120}, and an ~40-minute Xe^{121}. Since our results agree with the published abstracts of work done independently and simultaneously by Tilley[1] at McGill University and of Dropesky and Wiig[2] at the University of Rochester, we shall not give complete details of this part of our work.

The purpose of this paper is to record some unpublished observations on the radiations of these isotopes carried out with a scintillation spectrometer and a beta-ray spectrometer. In these studies we took advantage of a novel method for the deposition of xenon activity on thin metallic foils suitable for beta-ray spectroscopy. This method and the spectrometers are briefly discussed at the end of the paper.

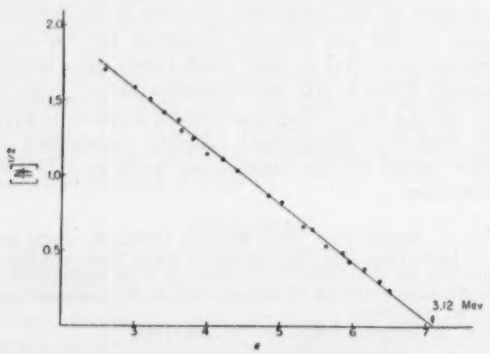

FIG. 1. Fermi-Kurie plot of positron spectrum of I^{122} obtained on Xe^{122}-I^{122} sample. [Data by T. O. Passell (unpublished).]

II. EXPERIMENTAL RESULTS

Xe^{122} and I^{122}

Potassium iodide targets were bombarded for 1 hour with 100-Mev protons. The xenon fraction was isolated 24 hours later and deposited on aluminum foil as described below. At this time the xenon activity was virtually pure Xe^{122}. Decay curves showed a straight-line decay of 19±0.5 hours over more than 5 half-lives. The amount of 18-hour Xe^{125} is slight because the $(p,3n)$ reaction cross section is down at this high proton energy. Separation of iodine activity at this time showed only the 3.5-minute I^{122} activity originally reported by Marquez and Perlman[3] and studied more completely by Young, Pool, and Kundu.[4]

The positron spectrum of the Xe^{122}-I^{122} mixture mounted on 0.1-mil aluminum foil was studied in the double-focusing beta-ray spectrometer by T. O. Passell.

Figure 1 is the Fermi-Kurie plot of this spectrum showing a single component with an end-point energy of 3.12±0.04 Mev. The calibration of the spectrometer was checked with the 1.97-Mev positron of Cs^{130}.[5] Xe^{122} decays by K capture and the 3.12-Mev positron group is assigned to the 3.5 minute I^{122} in equilibrium with it. Our positron energy agrees with the 3.08±0.1-Mev value determined by Young, Pool, and Kundu[4] who used absorption methods.

Figure 2 shows the gamma spectrum taken with the sodium iodide scintillation spectrometer. The only prominent peaks are a 182-kev gamma peak, a smaller gamma peak at 235 kev, and the annihilation gamma ray peak resulting from the positrons of I^{122}. No gamma rays of higher energy were observed. The 182- and 235-kev gamma peaks may be assigned to the decay of Xe^{122} as proved by the curves of Fig. 3. The upper curve taken on the Xe^{122}-I^{122} mixture shows these two peaks while the lower curve taken on a pure sample of I^{122} shows only the Compton smear of the Compton-

* This work was supported by the U. S. Atomic Energy Commission.

† On leave of absence from the Department of Chemistry, University of Delhi, Delhi, India.

[1] D. E. Tilley, Abstract 77, June Meeting of the Royal Society of Canada, 1952 (unpublished).

[2] B. Dropesky and E. O. Wiig, Phys. Rev. 88, 683 (1952).

[3] L. Marquez and I. Perlman, Phys. Rev. 78, 189 (1950).

[4] Young, Pool, and Kundu, Phys. Rev. 83, 1060 (1951).

[5] Smith, Mitchell, and Caird, Phys. Rev. 87, 454 (1952).

scattered annihilation radiation. This result is not surprising since Te^{122} is an even-even nuclide with an excited state at 568 kev[6] which in all likelihood is the first excited state, according to the systematics of the excited states of even-even nuclei as discussed by Scharff-Goldhaber.[7] The conversion electrons of the 182-kev gamma ray were observed (see below).

Xe^{123}–I^{123}

When the xenon fraction was separated from the potassium iodide target about 4 hours after the end of the bombardment 1.8-hour Xe^{123} and 19-hour Xe^{122} accounted for the greater part of the activity. It was possible to study the radiations of Xe^{123} in such mixtures, but samples which were much purer, although less intense, could be isolated by an alternate method; namely, isolation of Xe^{123} daughter activity from the decay of Cs^{123}.

In a previous publication[8] it was shown that 6-minute Cs^{123} is produced by the bombardment of calcium iodide

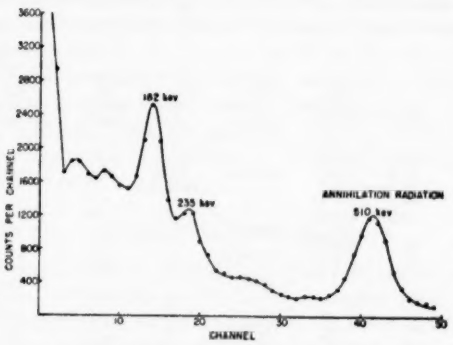

FIG. 2. Gamma spectrum of Xe^{122} taken on scintillation spectrometer.

with 130-Mev helium ions. From cesium fractions isolated quickly immediately after bombardment it is possible to separate Xe^{123} activity >90 percent pure by radioactivity. Some 18-hour Xe^{125} is present from the decay of 45-minute Cs^{125} also produced in the bombardment.

The decay of the activity as followed in a GM tube showed the 1.8-hour decay of Xe^{123} superimposed on the growth and decay of the 13-hour I^{123} daughter.

The gamma spectrum of Xe^{123} shows a major peak of K x-rays from the electron capture decay of Xe^{123}, a gamma ray of 150-kev energy, and a small peak of annihilation radiation (not shown) (see Fig. 4). Repeat runs on the gamma spectrum over a period of 24 hours showed the emergence of the 159-kev gamma peak[9] of

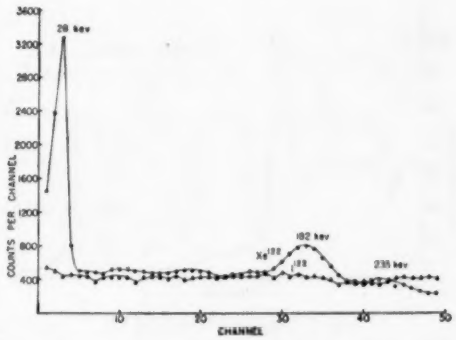

FIG. 3. Gamma spectrum of Xe^{122}-I^{122} mixture and on pure I^{122} showing assignment of 180-kev gamma radiation to Xe^{122}. Triangular points represent pure I^{122}. The 28-kev peak is K x-radiation.

I^{123} as the 150-kev gamma radiation of Xe^{123} decayed. The conversion electrons of these two gamma rays were also observed (see below).

A beryllium absorption curve on the positron activity gave a value of 1.8 Mev as the end-point energy of the positron. The energy of the positron as determined by the anthracene crystal spectrometer is 1.7±0.1 Mev.

Xe^{121} and I^{121}

Xenon samples isolated immediately after bombardment contained a high proportion of 40-minute Xe^{121}. Iodine daughter activity isolated from the xenon fraction within 1 hour of the end of bombardment contained 3.5-minute I^{122}, 1.5-hour I^{121}, and 13-hour I^{123}, but after the rapid decay of the I^{122} the principal activity was I^{121}. A gamma spectrum of such an iodine sample is shown in Fig. 5. In addition to the annihilation radiation a gamma ray of 210 kev is observed; the conversion electrons of the gamma ray were also observed as reported below. Marquez and Perlman[3] had reported conversion electrons of this gamma ray in the original report on the properties of I^{121}.

It was determined that Xe^{121} emits positrons by plotting the decay of the annihilation peak of gamma

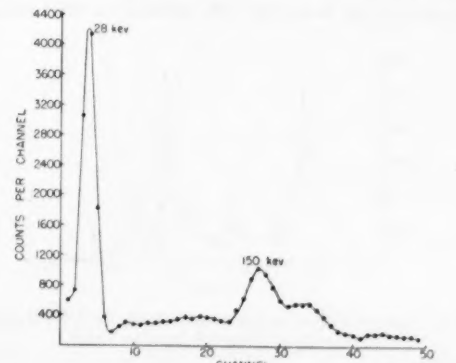

FIG. 4. Gamma spectrum of Xe^{123} sample isolated from Cs^{123}.

[6] M. Goldhaber and R. D. Hill, Revs. Modern Phys. **24**, 179 (1952).
[7] G. Scharff-Goldhaber, Phys. Rev. **90**, 587 (1953).
[8] H. B. Mathur and E. K. Hyde, Phys. Rev. **95**, 708 (1954).
[9] Mitchell, Mei, Maienschein, and Peacock, Phys. Rev. **76**, 1450 (1950).

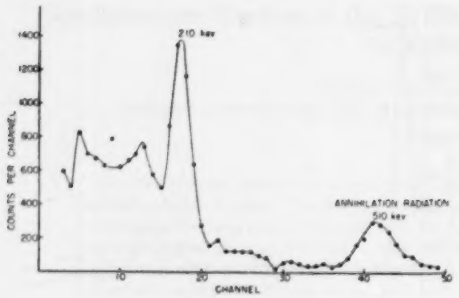

FIG. 5. Gamma spectrum of I^{121}.

spectra determined on xenon samples isolated within 1 hour of the end of the bombardment. A 40±10 minute component was resolved from this curve.

Conversion Electrons of $Xe^{121}Xe^{122}Xe^{123}$ Mixture

The conversion electrons of several of the gamma rays mentioned above were measured in the beta-ray spectrometer using a xenon sample collected on a ¼-mil aluminum foil 1 hour after the finish of a 1-hour bombardment of potassium iodide with 100-Mev protons. The conversion electron spectrum was determined about 2 hours after the end of the bombardment (see Fig. 6) and this determination was repeated 5 times over the next 24-hour period. The numbered peaks of Fig. 6 are listed in Table I. The observed half-life and the probable assignment of the isotopes and conversion shell are listed in Table I.

III. EXPERIMENTAL METHODS

Deposition of Xenon on Counting Foils

Samples of xenon radioactivity were deposited on thin metallic foils by the method developed and used extensively by Momyer and Hyde for the study of isotopes of emanation.[10] This method makes use of a glow discharge tube of the type shown in Fig. 7.

Figure 8 shows the glass vacuum system used to isolate the xenon from the cyclotron targets. The base pressure in the manifold was reduced to 10^{-5} mm Hg

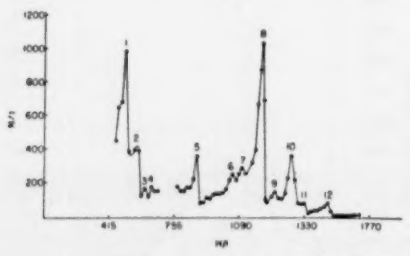

FIG. 6. Conversion electron spectrum in Xe^{121}, Xe^{122}, Xe^{123} mixture. The numbered peaks are listed in Table I.

[10] F. F. Momyer, University of California Radiation Laboratory Report UCRL-2060, 1953 (unpublished).

by a mercury diffusion pump and Cenco Hyvac mechanical forepump. The potassium iodide was dissolved in the closed dissolver flask *A* by introducing water from the dropping funnel. The off gases were pumped through trap *C* cooled with a dry ice-acetone cooling bath which removes water vapor and through traps *D*, *E*, and *F* cooled with liquid nitrogen which condensed the xenon. After 2 or 3 minutes stopcock *B* was closed and the total pressure in the entire system including the glow discharge tube was reduced to 10^{-4}–10^{-5} mm Hg. Then that part of the system including traps *D*, *E*, *F*, and the discharge tube were isolated from the rest of the system by suitable manipulation of the stopcocks and the xenon activity was distilled into the discharge tube by placing a liquid nitrogen cooling bath on the freeze down tip and by warming traps *D*, *E*, and *F* to room temperature. Then stopcock *G* was closed and the xenon and other condensed material was allowed to vaporize in the glow discharge tube. Usually enough inert vapors were condensed during this crude fractionation that the total pressure in the tube rose to the region 100–400 microns mercury. When this was not true, air was bled in until the pressure rose to this value as read on a thermocouple gauge, not shown. A dc potential of 300–800 volts with a limiting resistor of 50 000 ohms was placed across the electrodes (see Fig. 7) to initiate and maintain a glow discharge in the tube. The xenon atoms were ionized and collected on aluminum foils of 0.1-mil thickness clipped to the negative electrode. A collection time of 5 minutes served to affix a variable percentage (2–10 percent) of the xenon activity to both sides of this foil. The excess activity was pumped back into trap *F* and condensed with liquid nitrogen. The glow discharge tube was then removed from the line and opened. The xenon activity on the foil remained affixed indefinitely unless the foil was warmed above room temperature. It is believed that proper redesign of this method to allow better cooling of the electrodes during deposition

TABLE I. Conversion electrons of Xe^{121}-Xe^{122}-Xe^{123} mixture.

Peak No.	Energy (kev)	Approximate observed half-life	Assignment of parent isotope	Conversion shell	Gamma-ray energy (kev)	Gamma-ray energy from scintillation spectrometer (kev)
1	22.2	4 hr	mixture	Auger electrons	...	...
2	27.0	3 hr				
3	31.0	2 hr				
4	34.5	0.5 hr	?	...	...	...
5	63.2	45 min	Xe^{121}	*K*	95	...
6	91	50 min		*L*	96	
7	97	1.8 hr	Xe^{123}(?)	...	...	...
8	115.5	2.5 hr	Xe^{122}	*K*	148	150
10	144	2 hr		*L*	147	
9	128	20 hr[a]	I^{123}	*K*	160	160
11	155	14 hr	Xe^{122}	*K*	187	182
12	180	3 hr	I^{121}	*K*	212	210

[a] The limited number of points taken and the imperfect resolution of the electron peaks made it impossible to observe the *growth* of this peak from its 1.8-hour parent.

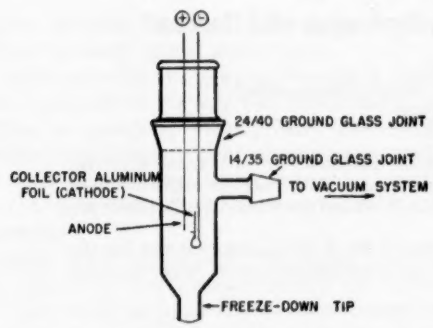

FIG. 7. Glow discharge tube used to deposit xenon on aluminum foils.

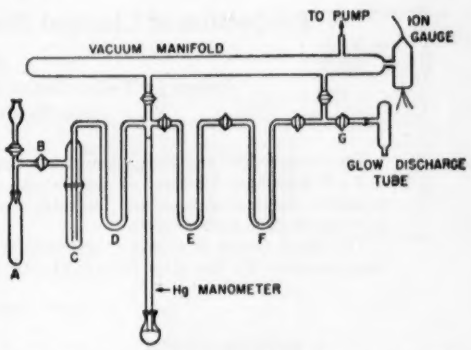

FIG. 8. Glass vacuum system used to isolate xenon activity.

would make possible near quantitative collection of tracer xenon activity.

Beta-Ray Spectrometer

The spectrometer used in this research was one of the double-focusing type proposed by Svartholm and Siegbahn[11] and by Shull and Dennison.[12] A side window GM tube with a thin vinyl plastic window filled with an argon-ethylene mixture was used as a detector. A more complete description of the instrument is given by O'Kelley.[13] We are indebted to Dr. Thomas O. Passell for major assistance in obtaining the data on this instrument.

Scintillation Spectrometer

The gamma-ray scintillation spectrometer was assembled by Ghiorso and Larsh of this laboratory. The initial gamma detection occurred in a 1.5-inch diameter by 1-inch thick crystal of sodium iodide mounted below a Dumont 6292 photomultiplier tube by the methods of Borkowski.[14] The crystal photomultiplier assembly was mounted above a 5-position shelf assembly and encased in an aluminum-lined lead shield.

The photomultiplier output was amplified in a preamplifier and linear amplifier and then introduced to a 50-channel differential pulse-height analyzer. This analyzer is of a new design of Ghiorso and Larsh. The channel-width stability was better than 1 percent operating at a 5-volt channel width and remained so for periods of weeks. Gain and bias controls permitted the inspection of any desired energy interval with the full 50 channels. Energy calibrations were carried out with known radiations from Na^{22}, Cs^{137}, Am^{241}, Cd^{109}, U^{235}, and other isotopes. Further details on the spectrometer and pulse-height analyzer will be given later by Ghiorso and Larsh.[15]

IV. ACKNOWLEDGMENTS

The authors are indebted to T. O. Passell for assistance with the beta-ray spectrometer. The bombardments were carried out by James T. Vale, Lloyd B. Houser, and the 184-inch cyclotron crew.

[11] N. Svartholm and K. Siegbahn, Arkiv Mat. Astron. Fysik **A33**, No. 21 (1946); see also Hedgran, Siegbahn, and Svartholm, Proc. Phys. Soc. (London) **A63** (1950).

[12] F. Shull and D. Dennison, Phys. Rev. **71**, 681 (1947); **72**, 256 (1947).

[13] G. D. O'Kelley, University of California Radiation Laboratory Report UCRL-1243, March 15, 1951 (unpublished).

[14] C. J. Borkowski, Oak Ridge National Laboratory Report ORNL-1336, September, 1952 (unpublished).

[15] A. Ghiorso and A. E. Larsh (to be published).

Production of Charged Pions from Hydrogen and Carbon*

A. H. ROSENFELD
Institute for Nuclear Studies, University of Chicago, Chicago, Illinois
(Received June 4, 1954)

The cross sections and energy spectra of pions produced in the reactions $P+P\rightarrow\pi^+ +D$ and $P+P\rightarrow\pi^+ +N+P$ have been measured at three angles using 440-Mev protons. Both reactions contribute about equally to the total cross section. The total cross section is (4 ± 1) mb and the angular distribution is proportional to $(0.15\pm0.06+\cos^2\theta)$.

The energy spectra of π^+ and π^- produced in a carbon target at 90° in the laboratory system has also been measured. We find $(d\sigma_{\pi^+}/d\Omega)=(0.83\pm0.11)$ mb sterad^{-1} per C nucleus and a π^+/π^- ratio of 7.2 ± 1.5.

I. INTRODUCTION

THE total production of pions in P-P collisions has been studied up to 50 Mev above threshold in the c.m. system.[1] It is of interest to extend the range of these measurements in order to get more information on the excitation function and also to allow direct comparison with the reactions $N+P\rightarrow\pi^{+,-,0}$ which are currently being studied using beams from the Chicago synchrocyclotron.

The importance of this excitation function and of this comparison is discussed in reference 1, in which an attempt is made to describe all the cross sections for pion production in nucleon-nucleon collisions in terms of the Watson-Brueckner[2] phenomenological treatment. This treatment assumes the conservation of isotopic spin, which by now has a sound experimental basis.

We have studied pion production 63.7 Mev above threshold in the c.m. system using nuclear emulsions exposed to targets of polyethylene and carbon bombarded by the internal 440-Mev beam of the Chicago synchrocyclotron. The pion energy spectrum and absolute cross section have been measured at three angles. The spectrum consists of a continuum associated with the reaction

$$P+P\rightarrow\pi^+ +N+P \qquad (A')$$

and in addition, just above the high-energy cutoff of the continuum, a line associated with

$$P+P\rightarrow\pi^+ +D. \qquad (B)$$

Our results show that reactions (A′) and (B) contribute about equally to the cross section and that the pion angular distribution is proportional to $0.15+\cos^2\theta$. Our total cross section is (4 ± 1) mb. Within the large experimental error this agrees with a reasonable extrapolation of the available data, which are compiled and discussed in reference 1.

For the purpose of making the polyethylene-carbon subtraction it is necessary to study the production of π^+ in proton-carbon collisions. It was relatively easy to extend the scanning to cover the entire π^+ and π^- spectra at an angle of 90° in the laboratory system. Our results are compared with similar data for lower energies. We attempt to interpret the cross section in terms of a model which assumes that pions are produced in collisions between a beam proton and an individual nucleon in carbon. This approach gives agreement with experiment within about 30 percent for the lower half of the spectrum, but fails at higher energy.

II. EXPERIMENTAL ARRANGEMENT

This experiment was undertaken before a high-intensity proton beam was extracted from the Chicago synchrocyclotron. The low intensity of the scattered external beam made it necessary to work with the circulating beam inside the vacuum chamber, despite difficulties that will be discussed.

The target is a $\frac{1}{8}$-inch rod of polyethylene or carbon. The total flux of protons through the target is determined by counting the 20.5-min C^{11} activity produced in the target. Pions emitted at three downward angles from the target are slowed down in absorber and come to rest in a well-shielded nuclear emulsion.

Immediately after the irradiation the film must be withdrawn from the vacuum chamber so that it will not be fogged by gamma radiation and the target must be withdrawn so that it can be counted. Even after the cyclotron has been standing idle for several hours the general radiation level at the tank walls is $\sim\frac{1}{2}$ r/hr, so that photographic emulsions cannot be kept there more than a few minutes.

The over-all physical design of the experiment was determined by the largest air-lock available, which was 8 in. long and designed to permit the passage of a 4-inch diameter probe.

Figure 1 shows the target and absorber-emulsion holder. The hinged holder lies horizontal while traversing the air-lock and then falls into the vertical position shown. The absorber was made of "pseudite," a material designed to have the same linear stopping power and "scattering power" as emulsion (see subsection D).

A. Proton Beam

The energy spectrum under study will be meaningful only if the bombarding proton beam is nearly mono-

* Work supported in part by the U. S. Atomic Energy Commission and the U. S. Office of Naval Research.

[1] References may be found in Table III of the following paper [A. H. Rosenfeld, Phys. Rev. **95**, 139 (1954)].

[2] K. M. Watson and K. A. Brueckner, Phys. Rev. **83**, 1 (1951).

energetic. We shall describe the Chicago proton beam and how its energy spread was reduced.

A proton spiraling out in an orbit which is almost a perfect circle will hit the target at 75½-in. radius when it attains an energy of 444±1½ Mev. The energy is calculated from magnetic field measurements, and the uncertainty in this energy arises from the uncertainty as to how well the beam is centered about the axis of the pole faces.

Actually, most protons do not simply spiral out slowly, but rather they oscillate radially and vertically about their stable orbit. At 75½-in. radius in our cyclotron the average amplitude of the vertical oscillations is about 0.6 in., and some of the radial amplitudes are greater than 4 in. The vertical oscillations are not serious, but the radial oscillations cause the energy of the protons hitting a target to be decreased by as much as 35 Mev. This comes about because a proton can hit the target when its instantaneous radius is greater than that of its stable orbit.

These radial oscillations were suppressed by placing a vertical 0.1-in. tungsten rod along the magnetic center of the cyclotron, bathed by the ion beam emerging from the arc source. This rod, suggested by R. H. Hildebrand, reduced the radial oscillation to <1 in. (9 Mev);[3] it also reduced the beam intensity by a factor of ~1000. This reduction is no disadvantage for photographic work, since even with this low intensity our exposures took only a few seconds.

During the exposures, oscillograms were taken of the time at which protons hit the target. Since there is an almost unique correspondence between time and proton kinetic energy, these oscillograms can be interpreted to show that all but 8 percent of the protons hitting the target had oscillations corresponding to <8 Mev; the remainder had energy deficiencies rather uniformly distributed between 8 and 32 Mev. These figures apply to the 90° exposures. At the time the irradiations were performed for the other two angles the vacuum was poor and the radial oscillations larger, resulting in an energy spread of 12 Mev.

A proton may make repeated traversals through the target before it is multiply scattered enough to collide with the dee. The proton loses some energy with each traversal, so that unless precautions are taken the beam energy will be degraded over about 20 Mev. We reduced this spread to about 1.5 Mev by placing a "clipper" 0.7 in. below the median plane. About one third of the protons had such large vertical oscillations that they hit the clipper before they ever hit the target, but we were willing to take a 30 percent increase in background in the interest of energy resolution.

The beam was also clipped ½ in. out radially from the tip of the target. This kept protons from hitting the brass probe tip and making background pions and protons. It also helped reduce multiple traversals, but radial clipping is rather ineffective for this purpose when there are radial oscillations.

[3] A. H. Rosenfeld and S. D. Warshaw, Rev. Sci. Instr. (to be published).

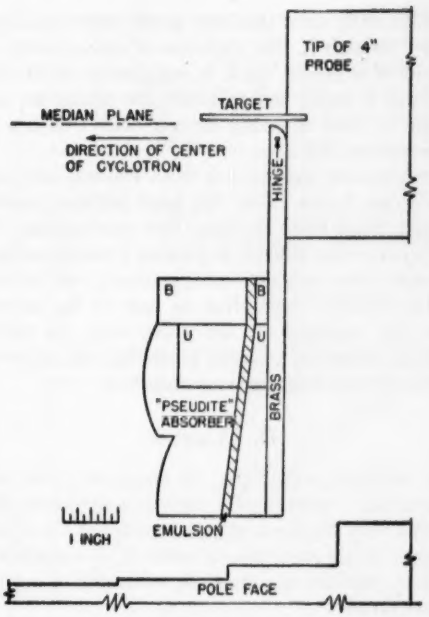

FIG. 1. Target and absorber, side view, looking into the proton beam. The energy of a pion is determined by the distance it goes through absorber before coming to rest in nuclear emulsion. As shown, the absorber will stop pions with energy up to 100 Mev. To investigate higher energies, the pieces of absorber labelled B and U, and the emulsion between them, were replaced with solid pieces of brass and uranium.

B. Shielding

The emulsion holder was shielded on three sides by 8 in. of nonradioactive lead. This primary shielding was entirely inadequate protection from protons coming from the beam direction; it was necessary to add another 8 in. of secondary shielding, extending ½ in. nearer the median plane, so as completely to shield the primary shielding.

C. Emulsions

The choice of emulsion was governed by several rather severe requirements. It had to be insensitive to unavoidable gamma exposure of about 0.1 r, and yet the meson tracks had to be heavy enough and the variation in grain density near the end of the track rapid enough to produce distinctive π-μ decays. It was also necessary that the processed emulsion be quite transparent, since a thickness of 1800 μ was desired.

The gamma background ruled out the possibility of using Ilford G5 emulsion, and thick layers of processed C2 or B2 emulsion are often not very transparent. Mr. C. Waller, of Ilford, Ltd., was kind enough to supply us with a new emulsion, G-special, which is similar to G5 except that it has a sensitivity only slightly higher than that of C2. The processed emulsion

was sufficiently clear that mm graph paper could easily be read through it. The variation of grain density near the end of a meson track is sufficiently rapid that a π-μ decay is easily recognizable; the tracks are heavy enough to allow scanning for π-μ decays with a 12× oil-immersion objective.

Our scanning technique is most efficient with emulsions about 2 mm thick. We used pellicles (emulsion stripped from glass backing) for two reasons—first, 1800-μ plates are difficult to process if the solutions can penetrate from only one side; secondly, we wished to use the pellicles themselves as part of the absorber; hence the presence of the glass, with its different stopping power for charged particles, was undesirable in an otherwise homogeneous absorber.

D. Absorber

We wish first to show that the energy of a pion cannot be accurately determined if there is a significant difference between the linear stopping power of the absorber and that of the emulsion. In order to demonstrate this we must consider the multiple scattering of a pion as it slows down.

The pion will deviate from its original line of flight. The root mean square of the deviation projected on a plane which passes through the original line of flight is given by

$$y_{\text{rms}} = 0.18R^{0.95} \approx 0.18R,$$

where R is the range, and all distances are measured in cm. The formula applies for energy <100 Mev. This effect is illustrated in Fig. 2, where the shaded area is a triangle with half-angle 0.18 radian and represents the projection of a cone through which most pions of 90 Mev pass as they slow down. The half-angle is comparable with the angle between the plane of the emulsion and the original pion direction. It is therefore inevitable that some of the pions coming to rest in a thick emulsion will have travelled some considerable distance through the emulsion rather than through the absorber proper. The thicker the emulsion used, the more stringent is the requirement that the linear stopping power of the absorber be matched to that of emulsion.

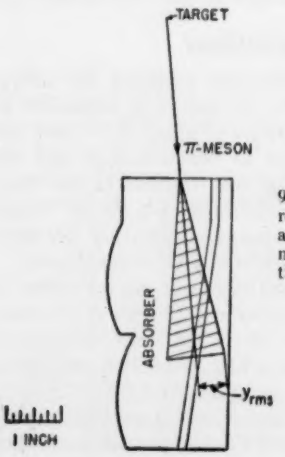

FIG. 2. Scattering of a 90-Mev pion as it comes to rest in emulsion. The shaded area indicates the region most probably traversed by the pion.

The absorber should also be chosen with Coulomb scattering properties close to those of emulsion. This minimizes preferential in- or out-scattering from the emulsion to the absorber. This effect is not quite negligible. For example, a crude estimate shows that if the average Z of the absorber were 13, even though its stopping powers were equal to that of the emulsion, the density of endings in the emulsion would be reduced by about 5 percent. This correction is uncertain and hard to estimate, and would vary rapidly with position in the emulsion. We preferred to make an absorber, "pseudite," which matches emulsion both in linear stopping power and in radiation length.

Pseudite

This is a machinable moulded mixture of fine copper, tin, and Lucite powders, 150 mesh or smaller. Each cc of the sample used contains 1.28 g Cu, 1.94 g Sn, and 0.71 g Lucite, and has a total density of 3.93 ± 2 percent. This is actually about 2.5 percent greater than was desired for a perfect match, so that the linear stopping power is 2.5 percent higher than that of emulsion of density 3.83. Pion ranges in pseudite were obtained by using Aron's[4] range-energy tables for Cu, assuming that Cu and pseudite (and emulsion) have the same mass stopping power. This recipe is accurate to 1 percent for pions with energy >10 Mev. It was arrived at by using the average ionization potentials of Mather and Segrè[5] and ignoring multiple scattering, which will be discussed separately in Sec. II-H.

E. Nuclear Absorption of Pions

We next consider the errors introduced by attenuation of the pions while they are being brought to rest. While traversing the absorber some pions will collide with nuclei and be absorbed. Others will be scattered, and if this scattering angle is $>40°$ they will probably never be seen during scanning, and if seen they will be discarded.

The top part of Fig. 3 displays a collection of data on the total cross section for $\pi^{\pm}$ in nuclear emulsion. At high energy the π^- cross section approaches about 1.3 times geometrical cross section, whereas attenuation cross sections determined using scintillation counters seem to approach geometrical. This discrepancy need not concern us because of our large statistical error for π^- (we found only 25 π^-). The solid curves which merge with the geometrical cross section at high energy represent the cross sections assumed for the purpose of computing attenuation.

[4] W. A. Aron, University of California Radiation Laboratory Report UCRL-1325, 1951 (unpublished).
[5] R. Mather and E. Segrè, Phys. Rev. **84**, 191 (1951).

The bottom part of the figure shows the computed attenuation. The corrections for losses are small (5.5 percent for the highest energy pion which can come from hydrogen at 90°, and less than 30 percent for the 55° case) so some error in the assumed cross section produces a negligible error in our final result.

F. Irradiation and Monitoring

The number of protons hitting the carbon and CH_2 targets was determined by counting the C^{11} nuclei formed in the target. The cross section for the reaction $C^{12}(p,pn)C^{11}$, (41 ± 3) mb at 440 Mev as measured by Rosenfeld, Swanson, and Warshaw,[6] was adopted.

The targets were monitored by slipping them into a positron-to-gamma converter with wall thickness just sufficient to stop the 0.95-Mev positrons from C^{11}. The annihilation radiation escaping from the converter was counted with a Geiger counter. An absolute (±1 percent) 4-π flow counter, kindly lent by V. L. Telegdi, was used to determine the efficiency of monitoring; this was 1.70×10^{-3} with a precision of 1 percent.

TABLE I. Effect upon pion energy resolution of multiple scattering, spread in beam energy, and straggling.

Laboratory angle	55°	90°	124°
Spread[a] due to			
Imperfect angular resolution	8.0	3.0	0.5
Spread in proton beam energy	3.35	1.42	1.50
Straggling	1.40	0.76	0.44
Multiple scattering	2.25	1.25	0.67
Total spread	9.15	3.63	1.73

[a] Standard deviation, measured in Mev, of a Gaussian in the laboratory system.

A suitable exposure produced from 5×10^6 to 130×10^6 C^{11} nuclei and took only a few seconds. The statistical error in monitoring was ≈1 percent, which is smaller than the other errors of about 2 percent introduced by uncertainties in time measurements, geometry, etc.

G. Energy Resolution

The theoretical energy spectrum for $P+P\rightarrow\pi^+$ is sketched at the bottom of Fig. 6. It consists of a continuum populated mainly at the high-energy end and then, a few Mev above the high-energy cutoff, a line associated with the production of bound deuterons [reaction (B)]. We wish to discuss in order of decreasing importance three experimental effects which will broaden the line so that it overlaps the continuum.

1. Angular Resolution

Because of the multiple scattering illustrated in Fig. 2, a pion coming to rest on a line making a given angle with the proton beam may have been emitted at a slightly different angle. The angular spreads are as follows: for the exposure at 55°, half-width 5.15°; for 90°, 3.2°; for 124°, 1.3°. In the laboratory system the energy of a pion emitted in reaction (B) is a sensitive function of the angle at which it is observed. The first row of Table I gives the energy spread arising from the angular spread. This spread could be reduced if it were possible to place the absorber farther from the target, but this was ruled out by the 8-in.-long air-lock.

[6] Rosenfeld, Swanson, and Warshaw (to be published).

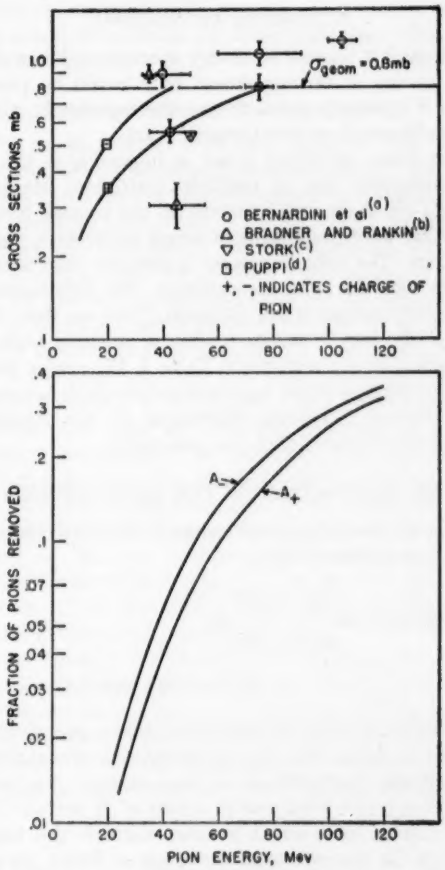

FIG. 3. Total cross section and attenuation of pions in emulsion. The crosses represent observed total cross sections in nuclear emulsion; the smooth curves are the cross sections assumed for computing the attenuation. The curves A_+ and A_- at the bottom give the computed attenuation for π^+ and π^-.

References:
[a] G. Bernardini, Booth, and Lederman, Phys. Rev. **83**, 1075 (1951); **84**, 610 (1951).
[b] H. Bradner and B. Rankin, Phys. Rev. **87**, 547 (1952).
[c] D. H. Stork, Phys. Rev. **92**, 538 (1953).
[d] G. Bernardini (private communication).

2. Spread in the Initial Proton Energy

A spread in the energy of the proton beam causes spread in pion energy which depends upon the angle at which the pion is observed. This latter spread is given in the second row of Table I.

3. Scattering and Straggling

These last sources of energy spread are inherent to the process of slowing down; they would be present even if it were possible to run the experiment with a monochromatic external proton beam.

For pions, straggling is not as important as the loss in resolution due to multiple scattering. Measured ranges are shortened 5 percent on the average because they are only projections of longer paths with wiggles in them. The value 5 percent applies for pion energies up to 100 Mev, and for emulsion. The distribution of shortened ranges is not Gaussian,[7] but we treat it as such. The loss in energy resolution resulting from the spread in range is shown in Table I. We used a range-energy relation which was corrected to take into account the average 5 percent shortening of the measured range as compared with the true range.

III. CALCULATION OF THE CROSS SECTION

The number of pions of energy T observed coming to rest in a volume $ds \cdot dx$ is

$$dn = 0.982 N_H J \frac{d^2\sigma}{d\Omega dT} \frac{ds}{x^2} \frac{dT}{dx} dx \times [1-A(T)](1+\delta)(1-\epsilon). \quad (1)$$

The factor 0.982 is the probability that a pion shall not decay in flight. For our geometry this probability is remarkably independent of pion energy. N_H is the effective target thickness in atoms of H per cm^2. J is the number of protons passing through the target; $x(T)$ is the distance from the target at which the pion comes to rest in emulsion; ds is an element of area perpendicular to the pion orbit; $A(T)$ is the fractional attenuation of pions as they pass through the absorber, as given in Fig. 3; δ is a small correction arising from the focussing of orbits in the magnetic field of the cyclotron; it is almost independent of T; ϵ is the difference of the scanning efficiency from unity (it is small; see Sec. IV).

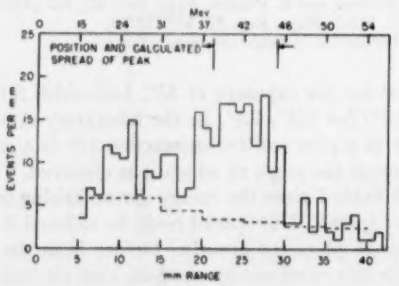

FIG. 4. π^+ endings per mm range at 90° lab. The solid histogram represents pions from polyethylene; the dashed one, which has been smoothed by grouping the data, represents the contribution from carbon. The calculated position and experimental spread of the line associated with deuterium formation is taken from Table I.

[7] M. F. Cartwright, Richman, Whitehead, and Wilcox, Phys. Rev. 91, 677 (1953).

For pions produced by P-P collisions in polyethylene, $(CH_2)_n$, $N_H J$ can be re-expressed as $2N_{11}/\sigma_{11}$. Here N_{11} is the number of C^{11} nuclei produced during the bombardment and $\sigma_{11}=41$ mb is the cross section for C^{11} production.

Equation (1) may now be written

$$\frac{d^2\sigma}{d\Omega dT} = (1-\delta+\epsilon)\frac{1}{N_{11}K(x)} \frac{dn}{dv}(x), \quad (2)$$

where

$$K(x) = 0.982 \cdot \frac{2}{\sigma_{11}} \cdot \frac{1}{x^2} \cdot \frac{dT}{dx}(1-A),$$

and $dx \cdot ds$ has been called dv.

$$\delta_{55°}=0.0425, \quad \delta_{90°}=0.0146, \quad \delta_{124°}=0.047.$$

The functions dT/dx and $x(T)$ were computed assuming a 5 percent shortening of range by projection.

IV. SCANNING

The emulsions were scanned for the endings of both pions and muons using either 12× or 22× oil-immersion objectives. Our microscopes were adapted so that it was easy to confine scanning to the middle third of an emulsion originally 1800 μ thick. This insured that whenever a π-μ decay was found it was possible to follow the muon to the end of its range, $(597\pm28)\mu$, and thus identify the event unambiguously in less than a minute.

Scanning Efficiency

Another advantage of scanning a thick layer is that it permits a truly objective test of scanning efficiency. If a π-μ decay is found in the layer of emulsion comprising the middle third of the pellicle, there is about a 50 percent probability that the associated muon will also end in the layer, though not necessarily in the strip currently being scanned. Similarly about one-half of the muon endings observed should lead back to pions in the same layer. Thus pions are found in two independent ways—by direct scanning and via muons; the same applies to muons. If the scanning efficiency were 100 percent it should never happen that a pion is seen only by tracking the corresponding muon, and is missed by direct search. The scanning efficiency for pions found by direct scanning is then given by $1-\epsilon = 1-N_{\text{missed}}/N_{\text{tracked}}$, where N_{missed} is the number of pions missed by direct observation but found by tracking, and N_{tracked} is the total number of pions found by tracking. We also kept a similar check on scanning efficiency for muons. As an example we give the result for the 90° exposures. About 200 pions and 200 muons were tracked; N_{missed} was 3 pions and 5 muons. We conclude that the scanning efficiency is 98½ percent for pions, 97½ percent for muons.

The greatest advantage to this running efficiency

TABLE II. Cross section in mb/sterad for pion with c.m. kinetic energy between 50 and 75 Mev. Errors are statistical standard deviations.

$\theta_{c.m.}$	90°	127°	152°
θ_{lab}	55°	90°	124°
$(d\sigma/d\Omega)_{lab}$	0.12±0.04	0.21±0.02	0.16±0.03
$(d\sigma/d\Omega)_{c.m.}$	0.08±0.03	0.30±0.03	0.48±0.09

check is that one can learn to scan rapidly at an efficiency very slightly less than unity and not waste time scanning too carefully.

Scanning Rate

Near the peaks in the range distribution corresponding to deuterium formations, the number of pions and proton endings is comparable. An experienced scanner can find and identify an ending in 10 minutes.

V. PION PRODUCTION FROM HYDROGEN—EXPERIMENTAL RESULTS

The results are most interesting after transformation to the c.m. system, but we first present the data in the laboratory system. Three angles were studied.

90° Lab

Figure 4 is a histogram of the data. It shows that the carbon subtraction introduces no serious complication, particularly at the high-energy end of the spectrum, which contributes most to the cross section. Figure 4 also illustrates an internal check on the validity of the subtraction. This check is based on consideration that it is kinematically impossible for the hydrogen in polyethylene to contribute to the production of pions with a range of more than 30 mm. At greater ranges the histogram from polyethylene and carbon should agree within experimental error. In the range from 30 to 55 mm we indeed found 50 π^+ from polyethylene, 59 from carbon.

Only 15 percent of the cross section from hydrogen lies below 25 Mev, which corresponds to about 12-mm range. At ranges smaller than 12 mm a reduced area of emulsion was scanned, so that only about two-thirds as many events were actually found as are indicated. The statistical errors shown have been appropriately corrected.

Figure 5 (top) gives the data converted to $d^2\sigma/(d\Omega dT)$.

124° Lab

No histogram is shown, but Fig. 5 (bottom) gives the cross section per steradian-Mev.

55° Lab

The cross section is small at this angle, which corresponds to 90° c.m. Moreover the peak in the hydrogen spectrum falls at an energy where the carbon spectrum is a maximum. No attempt was made to obtain a meaningful energy distribution. However, enough pions were found to establish the cross section per steradian given in Table II.

Transformation to the c.m. System

The transformation from lab. angle to c.m. angle does not depend strongly upon pion energy. Thus at 90° lab. the energy of the high-energy pions associated with deuteron production is 45 Mev, and the corresponding c.m. angle is 127°; for 30-Mev pions, 90° lab. corresponds to 131°; for 10 Mev, 144°. It can be seen that the pion-energy dependence of the transformation can be neglected, particularly since most of the cross section is concentrated in a peak at the high-energy end of the pion spectrum and there are experimental angular spreads of a few degrees arising from multiple scattering and from the fact that a finite volume of emulsion was scanned. The conversion from laboratory angle to c.m. angle was therefore taken to be that for pions of energy corresponding to the deuteron peak.

In Fig. 6 the lab. cross sections of Figs. 5 are transformed to the c.m. system. This transformation is easily calculated by making use of the fact that the quantity $(1/p)(d^2\sigma/d\Omega dT)$ is an invariant. Here p stands for the meson momentum.

It can be seen that about half the endings are found in the region where we would expect to find the experimentally spread line spectrum associated with deuteron formation. This is also true of the third angle.

In Sec. VI we shall estimate what fraction of the spectrum is really a line, but first we discuss the results

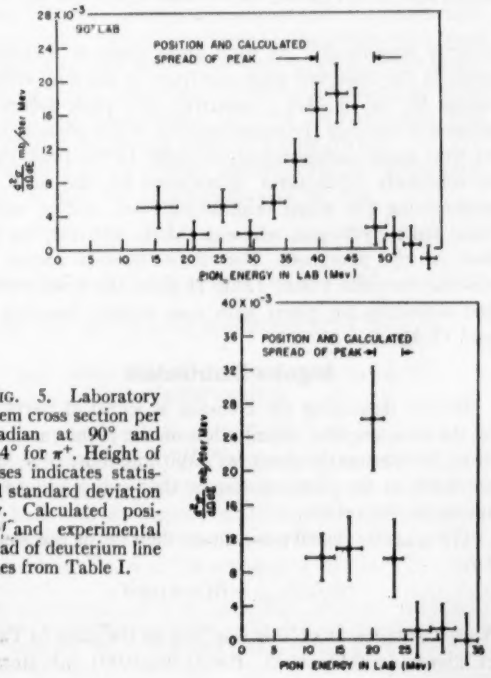
28 X 10⁻³
90° LAB
POSITION AND CALCULATED SPREAD OF PEAK
PION ENERGY IN LAB (Mev)
40 X 10⁻³
POSITION AND CALCULATED SPREAD OF PEAK
PION ENERGY IN LAB (Mev)

FIG. 5. Laboratory system cross section per steradian at 90° and 124.4° for π^+. Height of crosses indicates statistical standard deviation only. Calculated position and experimental spread of deuterium line comes from Table I.

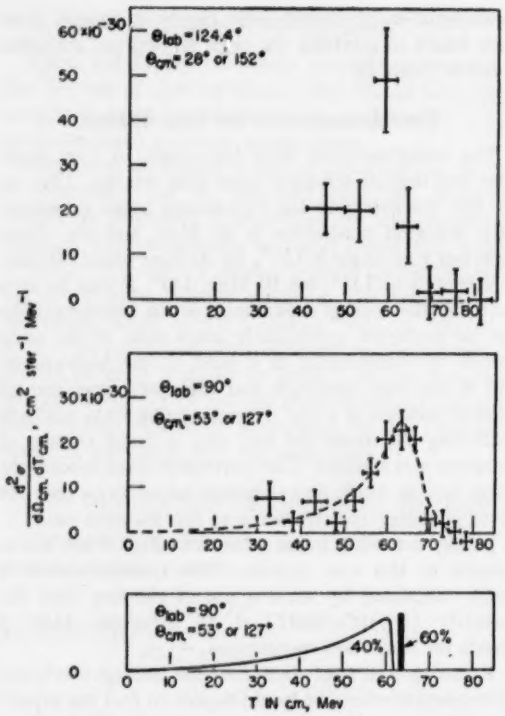

FIG. 6. Pion energy spectra in the c.m. system. These are the data of Figs. 5 converted to the c.m. system. The continuum and line spectrum at the bottom of the figure is the theoretical spectrum for pions accompanied by ^3S nucleons. The dashed line plotted along with the 90° lab. data is this theoretical spectrum folded in with the experimental resolution at 90°. (See Sec. VI.)

strictly empirically. At each angle there is a definite peak in the observed pion spectrum in the c.m. energy range 50 to 75 Mev; moreover this peak seems to represent roughly the same fraction of the cross section at that angle, independent of angle. In the peak there is relatively little error introduced by the need for subtracting the pions originating from carbon rather than from hydrogen, whereas this is not true for the rest of the spectrum. For these reasons above we discuss the peak alone. Table II gives the cross section per steradian for pions with c.m. energy between 50 and 75 Mev.

Angular Distribution

We are describing the collision of identical particles, so the c.m. angular distribution of the pions produced must be symmetric about 90°. With at most 65.4 Mev available to the pion, we assume that only s and p final states are important.

The angular distribution must then be of the simple form

$$(d\sigma/d\Omega)_{\text{c.m.}} = B(A+\cos^2\theta).$$

A least-squares fit of this function to the data in Table II gives $A=0.15\pm0.06$, $B=(0.56\pm0.09)$ mb/sterad. These errors are still only statistical. The fit is shown in Fig. 7.

Most of the experimental errors already discussed increase the uncertainty in B much more than in A. The 8 percent error in the C^{11} cross section is the largest single error, but we have assumed that all experimental errors amount to 10 percent. Combining these errors we find for pions with c.m. kinetic energy between 50 and 75 Mev,

$$(d\sigma/d\Omega)_{\text{c.m.}} = (0.63\pm0.12)(0.15\pm0.06+\cos^2\theta) \text{ mb/sterad.}$$

Integration over solid angle yields

$$\sigma_{50\text{–}75 \text{ Mev}} = (3.4\pm0.5) \text{ mb.} \quad (3)$$

VI. ANALYSIS OF THE SPECTRUM

We return to the problem of estimating the total cross section knowing only the partial cross section from 50 to 75 Mev c.m. We had hoped also to estimate the cross section corresponding to the deuteron line, but our conclusions are too ambiguous to be of value.

We shall use the phenomenological considerations described in reference 1. There it is shown that at the energy of our experiment the final nucleons are usually in S states, with ^3S about 10 times more probable than ^1S (in the notation of reference 1, $\sigma_{10}\approx 10\sigma_{11}$ at $\eta=1$). It is further shown that the formation of unbound ^3S nucleons relative to bound ^3S nucleons (deuterons) should be in the ratio 4:6 almost independent of angle. We have plotted at the bottom of Fig. 6 the predicted spectrum (continuum+line) for pions accompanied by ^3S nucleons. This spectrum, along with a similar spectrum representing the small ^1S contribution, has been folded into the calculated experimental resolution, and the result is plotted as a dashed line along with the 90° lab. data of Fig. 6. We have attempted to fit only the 90° data since this is the exposure that was most thoroughly scanned. In folding we took into account that during the exposure 92 percent of the protons were in the nominal energy interval (440±4) Mev, but that the remaining 8 percent had energies from 408 to 436 Mev, spread about evenly.

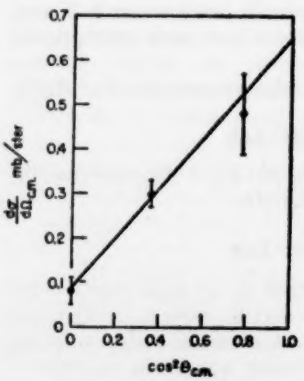

FIG. 7. Cross section per steradian vs $\cos^2\theta$. The solid line is a least-squares fit.

The height of the folded curve has been adjusted so that in the c.m. energy interval 50 to 75 Mev the area under the curve agrees with the experimental cross section. The agreement between the experimental spectrum and the folded curve is within statistical error, although if the continuum-to-line ratio had been arbitrary we would have chosen a somewhat larger fraction for the continuum, (50±16) percent of the total cross section rather than the value 40 percent obtained from phenomenological considerations.

If we assume that the theoretical spectrum is correct, we can calculate that the total cross section (including the pions associated with ^1S nucleons) is (4.0±0.8) mb, and the cross section for deuteron formation is (2.0 ±0.5) mb.

These results may be compared with similar results at other energies, which are displayed in Fig. 3 of reference 1. It can be seen that our total cross section (4.0±0.8) mb is in agreement with other results, but the value of 2 mb for deuterium formation does not agree with the other cross sections, which show that the correct value can hardly be more than 1.4 mb at our energy ($\eta=1.06$). We conclude that if there is no gross error in our experiment then the ratio of unbound to bound nucleons formed must be considerably greater than suggested by the phenomenological treatment; our data would suggest almost a factor two.

In reference 1 we show that other experiments do indeed indicate that the unbound-to-bound ratio is higher than predicted; but it is not clear from the evidence presented there whether the phenomenological treatment is inadequate, or whether the extra unbound nucleons are simply nucleons formed in P states, which we have neglected. P-state nucleons will be associated with low energy pions, and in our experiment the unexpected pions all have energy greater than 50 Mev, leaving less than 15 Mev for the nucleons. Hence we do not believe that the discrepancy can be fully resolved by invoking P-state nucleons.

In the light of the discussion above, we cannot state a cross section for the production of pions associated with deuterons, but our value of (4.0±0.8) mb for the total cross sections is still meaningful. The fraction of pions with energy less than 50 Mev certainly depends upon the ratio of unbound-to-bound nucleons formed, but we have assumed that this fraction is only 23 percent (see Fig. 6) so that even a fairly serious error in the unbound-to-bound ratio will not seriously affect our estimate for the total cross section.

We must increase the uncertainty in our value for the total cross section to allow for errors in going from the partial cross section above 50-Mev pion energy to the total cross section; we then find

$$\sigma(P+P\rightarrow\pi^+ + \text{nucleons}) = (4\pm1) \text{ mb},$$

where nucleons may be either bound or unbound and may be in any angular momentum state.

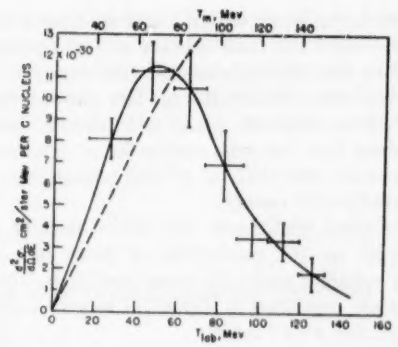

FIG. 8. Energy spectrum of π^+ from carbon at 90° lab. A smooth solid line has been drawn through the data. The scale at the top of the figure and the dashed curve refer to the discussion of Sec. VIII.

VII. PION PRODUCTION FROM CARBON—EXPERIMENTAL RESULTS

The cross section per Mev per steradian for π^+ production per C nucleus is shown in Fig. 8. No energy spectrum is given for π^- production. We scanned for π^- endings, but in a volume containing 250 π^+ endings we found only 25 π^- stars. Their energy distribution seems qualitatively to be similar to that for π^+. In order to state the total cross section for π^- production, the number of π^- stars found with one or more prongs was multiplied by 1.37 to account for zero-prong stars.[8]

It was necessary to correct the data for pions which did not originate in the target. Below 100 Mev this background amounted to less than 5 percent, but above 100 Mev its relative importance increases with energy and it becomes as large as the production from the target by 135 Mev. If we were to repeat the experiment we would use a larger target which could increase the signal-to-background ratio by perhaps four and still impair the energy resolution very little.

Including a 10 percent uncertainty for systematic error, we find, for π^+ production at 90° lab.,

$$d\sigma/d\Omega = (0.83\pm0.11) \text{ mb/sterad per C nucleus.}$$

Production of π^- is lower by a factor 7.2±1.5, so that

$$d\sigma/d\Omega = (0.11\pm0.03) \text{ mb/sterad per C nucleus.}$$

VIII. PION PRODUCTION FROM CARBON, DISCUSSION

Figure 9 gives the available data (including our own) on the production of pions from carbon as a function of bombarding proton energy. It is of interest to compare this with the analogous excitation functions for the production of pions in nucleon-nucleon collisions; these are given in Fig. 3 of the accompanying paper.[1]

[8] F. L. Adelman and S. B. Jones, Phys. Rev. **75**, 1468 (1949). An independent determination of the fraction of 0-prong stars was made by W. F. Fry and the author. This corroborated Adelman *et al.*

The nucleons in carbon have internal kinetic energy, and this raises the cross section at low bombarding energy,[9] so that the carbon excitation function is less steep than that for hydrogen. The general features illustrated in reference 1 are still present, however, in the sense that the cross section for π^- production is much smaller than that for π^+ and probably increases more rapidly with energy.

The authors who report the carbon data of Fig. 9 also report on the production of pions in nucleon-nucleon collisions under the same conditions. The cross sections are combined in Table III to give carbon-to-hydrogen and π^+/π^- ratios.

TABLE III. Carbon-to-hydrogen and positive-to-negative ratios for pions produced in proton-carbon collisions as a function of bombarding energy. $T_{c.m.}$ would be the c.m. energy of a pion produced in the reaction $p+p\rightarrow\pi^++d$ if the target nucleon were stationary.

$T_{c.m.}$, Mev	29.5	29.5–38	63.7
$\frac{d\sigma_C^+/d\Omega}{d\sigma_H/d\Omega}$	8 ±3	11±1	3.6 ±0.7
$\frac{d\sigma^+/d\Omega}{d\sigma^-/d\Omega}$	5.1±1.0	10±3	7.25±1.5

Analysis in Terms of Nucleon-Nucleon Collisions

This model is similar to that used by Passman, Block, and Havens.[10] It assumes that the bombarding proton interacts with only one nucleon in the target nucleus and that the main effect of the other nucleons is to have given the struck nucleon a momentum distribution. Of course the other nucleons may scatter the incoming proton[11] and the outgoing pion.

We have computed the dashed curve of Fig. 8 using this model with the following assumptions.

1. The momentum distribution of the nucleons is Gaussian, and the mean kinetic energy is 24 Mev.[12]

2. Provided that the maximum energy T_m available to the pion in the appropriate c.m. system is less than 100 Mev, then $\sigma(P+P\rightarrow\pi^+)$ is given by the dashed line in Fig. 3 of reference 1. We ignore P-N collisions. For simplicity we make the entirely unjustified assumption that each pion is created with energy $0.8T_m$. The angular distribution is proportional to $0.2+\cos^2\theta_{c.m.}$ (see reference 1).

3. If a pion is scattered or absorbed as it leaves the nucleus it will not be seen at 90° lab. We used the interaction cross sections reported by Stork.[13]

Although about one-half of the incoming protons will be scattered by carbon, we ignored this possibility, but we did take into account the suppression of π^+ production by Coulomb repulsion.

It can be seen that the computed curve falls below the experimental results at low energy, and above for $T_m>80$ Mev. There appear to be two main reasons for this:

1. The reduction of energy of incident protons due to scattering will tend to reduce high-energy and increase low-energy pion production.

2. Our approximation of representing the pion spectrum in the reaction $(P+P\rightarrow\pi^++\text{nucleon})$ by a δ function obviously underestimates the number of low-energy pions.

We have not attempted to extend the calculation beyond 100 Mev because the extrapolation from lower energies of both the cross section $\sigma(P+P\rightarrow\pi^+)$ and the pion absorption mean free path becomes quite dubious.

It might be noted that when data on $P+P\rightarrow\pi^+$ at high energies become available one might be able to solve for the absorption mean free path, a quantity which is not easily accessible to direct measurement.

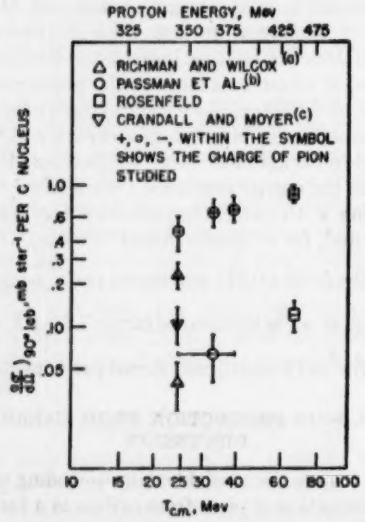

FIG. 9. Excitation function for pions produced at 90° lab. from carbon bombarded with protons. References: (a) G. Richman and H. A. Wilcox, Phys. Rev. 78, 496 (1950); (b) Passman, Block, and Havens, Phys. Rev. 88, 1247 (1952); (c) W. E. Crandall and B. J. Moyer, Phys. Rev. 92, 749 (1953).

IX. CONCLUSIONS AND ACKNOWLEDGMENTS

In 440-Mev P-P collisions, pions are produced with a differential and total cross section which is in fair agreement with extrapolation of the lower-energy results. Both the lower-energy data and ours indicate that the fraction of pions produced along with bound deuterons is lower than predicted by the phenomeno-

[9] W. McMillan and E. Teller, Phys. Rev. 72, 1 (1947).
[10] Passman, Block, and Havens, Phys. Rev. 88, 1247 (1952).
[11] S. Gasiorowicz, Phys. Rev. 93, 843 (1954).
[12] Cladis, Hess, and Moyer, Phys. Rev. 87, 425 (1952).
[13] D. H. Stork, Phys. Rev. 93, 868 (1954).

logical theory of Brueckner and Watson. This is discussed in reference 1.

We wish to thank Professor E. Fermi for his continued help. S. B. Treiman assisted greatly in the design of the experiment, and W. E. Slater and F. T. Solmitz contributed valuable help. Thanks are due to J. E. Boyce of the Argonne National Laboratory for the loan of the uranium absorber. We are indebted to the entire cyclotron staff, and to the scanners, Enid Bierman, J. T. Lach, and W. E. Slater, for their cooperation.

PHYSICAL REVIEW VOLUME 96, NUMBER 1 OCTOBER 1, 1954

Production of Pions in Nucleon-Nucleon Collisions at Cyclotron Energies

A. H. ROSENFELD
Institute for Nuclear Studies, University of Chicago, Chicago, Illinois
(Received June 7, 1954)

All available data on the production of pions in nucleon-nucleon collisions at cyclotron energies are compiled and are compared with the phenomenological theory of Watson and Brueckner. The principle of conservation of isotopic spin allows all these cross sections to be written in terms of only three independent cross sections, whose excitation functions are predicted by the phenomenological model. The theory represents satisfactorily the excitation functions and the angular distributions that are known experimentally; however the experimental ratio $\sigma(P+P\rightarrow\pi^+ +N+P)/\sigma(P+P\rightarrow\pi^+ +D)$ appears to be about a factor 2 larger than predicted.

Using a notation for total cross section in which the first subscript indicates the isotopic spin of the initial state, and the second that of the final state of the two nucleons, and expressing all cross sections in millibarns, we find:

$$\begin{aligned}
&\sigma_{10}(D) &&=\sigma(P+P\rightarrow\pi^+ +D) && =0.14\eta+1.0\eta^3,\\
&\sigma_{10}(N+P) &&=\sigma(P+P\rightarrow\pi^+ +N+P)-\sigma_{11} && \approx 1.5\eta^4,\\
&\sigma_{01} &&=2\sigma(N+P\rightarrow\pi^\pm)-\sigma_{11} && \lesssim 0.3\eta^4,\\
&\sigma_{11} &&=\sigma(P+P\rightarrow\pi^0) && \approx 0.2\eta^5.
\end{aligned}$$

η is the maximum c.m. momentum available to the pion, measured in units of μc.

I. INTRODUCTION

IN 1951 several authors[1-3] succeeded in interpreting satisfactorily the data then available on the production of pions near threshold. The only reaction that had been studied extensively was $P+P\rightarrow\pi^+ +D$, mainly using 340-Mev protons, corresponding to a pion energy of 22 Mev in the c.m. system. By assuming that the pions are created mainly in p states and by treating the nucleon-nucleon interaction phenomenologically it was possible to explain the energy spectrum and angular distribution of the pions, and to predict the excitation function for the reaction.

Since 1951 the information available on pion production has been greatly extended.[4] There are now data on N-P as well as P-P collisions; the energy range studied has been extended downwards to 10 Mev above threshold (where s-state production of pions should become relatively important) and cross sections have been published up to 50 Mev above threshold. Currently the Pittsburgh and Chicago synchrocyclotrons are being used to study the energy region 46 to 92 Mev. At Chicago eight experiments either are in progress or else have been recently completed.

There is by now some experimental confirmation of the principle of conservation of isotopic spin in pion production.[5-7] According to this principle it is possible to express all pion production data for each energy in terms of only three independent differential cross sections;[3] moreover the phenomenological treatment makes certain predictions about the excitation functions for these cross sections. We mean "phenomenological" to include the assumption of charge independence and also all the selection rules that will be discussed below.

We shall show that the new data are consistent with the phenomenological model, even when the pions are relativistic. The only appreciable discrepancy is that the experimental ratio $\sigma(P+P\rightarrow\pi^+ +N+P)/\sigma(P+P\rightarrow\pi^+ +D)$ seems to be about twice as large as predicted.

We have compiled the available cross sections for pion production in nucleon-nucleon collisions at cyclotron energies, and we have adjusted unknown parameters in the phenomenological treatment so as to give a best fit to the data.

Several authors[8,9] have proposed that various reactions could be sorted out by polarization experiments.

[1] K. Brueckner, Phys. Rev. **82**, 598 (1951).
[2] Chew, Goldberger, Steinberger, and Yang, Phys. Rev. **84**, 581 (1951).
[3] K. M. Watson and K. A. Brueckner, Phys. Rev. **83**, 1 (1951).
[4] References to all experiments are given in Table III.
[5] R. H. Hildebrand, Phys. Rev. **89**, 1090 (1953).
[6] R. A. Schluter, Phys. Rev. **95**, 639(A) (1954).
[7] R. H. Hildebrand and A. H. Rosenfeld (to be published).
[8] K. M. Watson and C. Richman, Phys. Rev. **83**, 1256 (1951).
[9] R. E. Marshak and A. M. L. Messiah, Nuovo cimento **11**, 337 (1954).

Inserting our parameters into their expressions we find how large a polarization effect can be expected and at what energy it can most easily be detected. We discuss the results of such experiments.

II. SUMMARY OF THE THEORY

The conservation of isotopic spin places severe restrictions on the production of pions in nucleon-nucleon collisions.

All the possible reactions can be expressed in terms of only three independent reactions, whose cross sections we shall denote by σ_{10}, σ_{01}, and σ_{11}. The notation is the following: the first index represents the isotopic spin of the initial state, and the second that of the final state of the two nucleons. There is no σ_{00}, since this reaction cannot conserve isotopic spin.

The simplest results are obtained for the total cross sections and are given in Table I. The word "nucleons" indicates that the final nucleons may be either bound or unbound; the symbol D is reserved for a deuteron and we shall use $N+P$ to indicate unbound nucleons; for example $\sigma(P+P\to\pi^++\text{nucleons})=\sigma(P+P\to\pi^++D)+\sigma(P+P\to\pi^++N+P)=\sigma_{10}(D)+\sigma_{10}(N+P)+\sigma_{11}$.

Exactly the same table applies to cross sections (integrated over angle) per unit pion energy. Thus the unbound part of reaction (A) can be written

$$\frac{d\sigma}{dT}(P+P\to\pi^++N+P)=\frac{d\sigma_{10}}{dT}+\frac{d\sigma_{11}}{dT}, \qquad (A')$$

where T is the c.m. energy of the pion.

By chance, none of the reactions listed in Table I involves more than two of the fundamental cross sections. This fact simplifies the discussion. It may seem surprising that σ_{11} does not contribute to reaction (E), but the appropriate Clebsch-Gordan coefficient is zero.

Note that reactions (B) and (H) are experimentally accessible in two different ways; i.e., $\sigma_{10}(D)$ can be determined directly in a pion production experiment, but it can also be inferred from $\sigma(\pi^++D\to P+P)$ using the principle of detailed balancing.

A table equivalent to Table I can be constructed for cross sections *per steradian*, but is slightly more complicated.[10]

TABLE I. Pion production cross sections in terms of the three independent cross sections.

$\sigma(P+P\to\pi^++\text{nucleons})$	$=\sigma_{10}+\sigma_{11}$	(A)
$\sigma(P+P\to\pi^++D)$	$=\sigma_{10}(D)$	(B)
$\sigma(P+P\to\pi^0)$	$=\sigma_{11}$	(C)
$\sigma(N+P\to\pi^+)$	$=\frac{1}{2}[\sigma_{11}+\sigma_{01}]$	(D)
$\sigma(N+P\to\pi^0+\text{nucleons})$	$=\frac{1}{2}[\sigma_{10}+\sigma_{01}]$	(E)
$\sigma(N+P\to\pi^0+D)$	$=\frac{1}{2}[\sigma_{10}(D)]$	(F)
$\sigma(N+N\to\pi^-+\text{nucleons})$	$=\sigma_{10}+\sigma_{11}$	(G)
$\sigma(N+N\to\pi^-+D)$	$=\sigma_{10}(D)$	(H)

[10] Van Hove, Marshak, and Pais, Phys. Rev. **88**, 1211 (1952).

It should be noted that even if charge independence should be essentially valid, all the relations above are subject to correction because of Coulomb forces and the π^+-π^0 and N-P mass differences.

Selection Rules

All of the experimental information available is at energies such that the pion has 65 Mev or less in the c.m. system, with the exception of Stadler's work which extends to 94 Mev. A 65-Mev pion has a momentum η, measured in units of μc, of 1.1. Figure 6 of an accompanying paper[11] gives the experimental pion spectrum when 63.7 Mev is available in the c.m. system; it shows that a typical pion carries away 50 Mev, leaving an internal energy of the residual two-nucleon system of only 10 to 15 Mev. Now we may imagine the phenomenon of pion production to take place at a characteristic distance R from the center of collision, where R must be of the order of $\hbar/\mu c$. (Arguments based on the data in this paper in fact indicate that R is slightly less than $\frac{1}{2}\hbar/\mu c$.) Therefore, in the energy region under consideration, the product $k_\pi R$ or $k_{\text{nuc}}R$ is $\lesssim 1$. We may suppose, then, that the pion will be emitted in an s or p state with respect to the two-nucleon system, and that the two nucleons will be in an S or P state relative to one another.[12] In the case of the nucleons the strong attractive force in the S state (as contrasted with the relatively weak interaction between P-state nucleons at low energies) will strongly favor S states as well as enhancing the preference for low nucleon energies. In the case of the pions, experiment indicates that the p state is preferred (except close to threshold). This is consistent with the large p-state interaction found for pion-proton scattering, and with the fact that the pion is a pseudoscalar particle.

Let us adopt a shorthand notation for the final states in which the first letter stands for the orbital angular momentum of the two-nucleon system and the second for the orbital angular momentum of the pion. The discussion above can then be summarized as follows. If pion production near threshold is analyzed in terms of the angular momentum of the final states, angular momentum 2 or more may be neglected, and the remaining partial waves can be classified in order of decreasing intensity Sp, Ss, Pp, and Ps.

In Table II, all the allowed reactions of class Sp and Ss (and some others) are listed, grouped according to isotopic spin of the initial and final nucleons (see Table I) and then further grouped according to intensity class. The notation is defined in the caption. The construction of the table will be described by discussing the first few rows. We shall show below that the most important elementary cross section is σ_{10}, so the reactions contributing to this cross section are taken first.

[11] A. H. Rosenfeld, preceding paper [Phys. Rev. **95**, 130 (1954)].

[12] We use lower-case letters to indicate the angular momentum of the pion, capitals for the angular momentum of the two-nucleon system.

Among these we list first the most important intensity class Sp. The pion is a pseudoscalar particle, so this class will have even parity. If the final nucleons are to have isotopic spin $T=0$, the S state must have spin 1 and be a triplet with over-all angular momentum $J=0$, 1, or 2. There is only one possible initial state ($^1S_0$) that has $T=1$, $J=0$, and even parity. This feeds the $^3S_1\,p_0$ final state and is accordingly listed in front of it. There is no appropriate initial state with $J=1$, so this reaction is absent. Only $^1D_2$ can feed $^3S_1\,p_2$. In the absence of interference between the various final states, any reaction with $J=0$ must be isotropic, and any reaction $^1D_2 \rightarrow {}^3S_1\,p_2$ must have an angular distribution proportional to $\frac{1}{3}+\cos^2\theta$. We may point out that this latter anisotropic reaction should dominate over the isotropic one because it is favored by a statistical factor $2J+1=5$. Experimentally this is found to be the case. So far the only assumptions incorporated into the table are that the pion is pseudoscalar and that isotopic spin is conserved. In calculating the total cross sections, however, excitation functions are derived taking into account nuclear forces, and undetermined parameters are then adjusted to fit the data of Sec. III.

Table II shows that for σ_{11} the intense reaction class Sp is absent. It turns out to be impossible to explain the experimental excitation function by invoking class Ss alone. Therefore, for σ_{11} only, we must consider also reactions of class Pp and Ps.

TABLE II. Analysis of pion production near threshold in terms of the angular momentum (S or P) of the final two-nucleon system and the angular momentum (s or p) of the pion. The spin and angular momentum of the two-nucleon system are indicated in the conventional way. The last subscript to the final-state symbols indicates the over-all angular momentum. The "Initial state" column gives all the two-nucleon states that have the same isotopic spin, angular momentum, and parity as a given final state. The angular distributions are those which would apply in the absence of interferences. The total cross sections are calculated in Secs. II and III. Classes which are intensified by the $(\frac{3}{2},\frac{3}{2})$ pion-nucleon interaction are in boldface.

Isotopic reaction	Class	Initial state	Final state	Angular distribution	Total cross section in mb
σ_{10}	**Sp**	$^1S_0$	$^3S_1\,p_0$	isotropic	$\left\{\begin{array}{l}1.0\eta^2 \text{ for deuteron formation}\\ 1.5\eta^4 \text{ for } N+P\end{array}\right.$
		none	$^3S_1\,p_1$	...	
		$^1D_2$	$^3S_1\,p_2$	$\frac{1}{3}+\cos^2\theta$	
	Ss	$^3P_1$	$^3S_1\,s_1$	isotropic	0.14η
σ_{01}	Sp	$^3S_1$ or $^3D_1$	$^1S_0\,p_1$	$\left\{\begin{array}{l}\text{isotropic}\\ \frac{1}{3}+\cos^2\theta\end{array}\right\}$	$0.3\eta^4$
	Ss	none	$^1S_0\,s_0$	...	0
σ_{11}	Sp	none	$^1S_0\,p_1$	...	0
	Ss	$^3P_0$	$^1S_0\,s_0$	isotropic	$\sim 0.01\eta^2$
	Pp	$^3P_{0,1}$ $^3P_{0,1,2}$ or $^3F_2$ $^3P_{1,2}$ or $^3F_{2,3}$	$^3P_0\,p_1$ $^3P_1\,p_{0,1,2}$ $^3P_2\,p_{1,2,3}$	$\left.\begin{array}{l}\\ c+\cos^2\theta\\ \\ \end{array}\right\}$	$0.2\eta^6$
	Ps	$^1S_0$ none $^1D_2$	$^3P_0\,s_0$ $^3P_1\,s_1$ $^3P_2\,s_2$	$\left.\begin{array}{l}\text{isotropic}\\ ...\\ \text{isotropic}\end{array}\right\}$	$\propto \eta^6$

Angular Distributions

Two or more of the reactions listed in Table II can interfere in the pion angular distribution only if the final nucleon states are identical. This immediately rules out the possibility of interference between σ_{10} and the other two cross sections. Even if the final nucleons are in the same state, there can be no interference unless the initial nucleons are in the same spin state (for an unpolarized beam). These rules, applied to Table II, show that there can be interference between the reactions within a given intensity class, but the only possibility of interference between classes is between the Sp reaction contributing to σ_{01} and the Ss reaction of σ_{11}. Only this interference can produce a forward-backward asymmetry, as is discussed below.

Relative Intensities

At the energies of interest here, σ_{10} is found experimentally to be considerably larger than the other two cross sections. There are two reasons why this should be the case. First there is the possibility of the production of deuterons; this added possibility roughly doubles the cross section. Second there is the effect of the strong interaction between a pion and a nucleon when they are in a two-particle state characterized by isotopic spin $\frac{3}{2}$ and angular momentum $\frac{3}{2}$, the state which is known to have a large cross section for pion-proton scattering. Although there are six possible reactions of class Sp or Ss the $^1D_2 \rightarrow {}^3S_1\,p_2$ reaction (associated with σ_{10}) is the only one in which this $(\frac{3}{2},\frac{3}{2})$ state is represented. The $(\frac{3}{2},\frac{3}{2})$ interaction can also enhance the reactions of class Pp and Ps which contribute to σ_{10} and σ_{11}. It does not affect σ_{01} because a nucleon-pion state with isotopic spin $\frac{3}{2}$ cannot combine with a nucleon to give overall isotopic spin 0.

Using meson theory, Aitken *et al.*[13] have calculated the increase in cross section resulting from the $(\frac{3}{2},\frac{3}{2})$ interaction. They assume that the effect is energy-independent, and find an enhancement of two or three. Experimentally we find a factor of about 5 (see the discussion following Eq. (27).

In discussing Table II we pointed out that the $^1D_2 \rightarrow {}^3S_1\,p_2$ reaction was already favored by a statistical factor 5. With the extra $(\frac{3}{2},\frac{3}{2})$ enhancement it should be even more dominant.

The Pion Spectrum and Excitation Function for σ_{10}

We shall now discuss in greater detail the most important reaction, namely the production of p-state pions associated with ^3S nucleons.

Watson[14] takes into account phenomenlogically the attraction between the final nucleons; neglecting terms of order $\mu/2M$ he finds a pion production cross section

[13] A. Aitken *et al.*, Phys. Rev. **93**, 1349 (1954).
[14] K. M. Watson, Phys. Rev. **88**, 1163 (1952).

per unit pion energy, integrated over angle,

$$\frac{d\sigma_{10}'}{dT}=b_{10}(2\mu)^{-\frac{1}{2}}\frac{P^2(T_0-T)^{\frac{1}{2}}}{B+T_0-T}, \tag{1}$$

where b_{10} is a constant, T and P are the c.m. kinetic energy and momentum of the pion, T_0 is the kinematic maximum for T for the continuous part of the spectrum, and B is the binding energy of the deuteron. We have adopted the convention of writing a prime after cross sections derived from the phenomenological model. The numerator of (1) is the product of P^2 from the square of the matrix element for the production of a p-state pion and $P(T_0-T)^{\frac{1}{2}}$ which is the phase space available to the three final particles. The nuclear force introduces the denominator $|B|+T_0-T$. The spectrum is plotted at the bottom of Fig. 6 of the accompanying paper.

Equation (1) can be integrated over pion energy to give a total cross section for the production of pions associated with unbound ^3S nucleons. Using the nonrelativistic relation $P^2/2\mu=T$ we get the simple result

$$\sigma_{10}'(N+P,\ p\text{-state})=b_{10}\pi T_0^2F(y), \tag{2*}$$

where

$$F(y)=\tfrac{2}{3}-y^{\frac{1}{2}}(1+y)^{\frac{1}{2}}+\tfrac{2}{3}y+y^2, \tag{3}$$

and $y=|B|/T_0$. (An asterisk after the number of an equation means that it applies in the nonrelativistic limit.) Note that the nuclear force serves not only to raise the cross section, but also to change the form of the excitation function, which would otherwise be proportional to T_0^3.

Exactly the same set of assumptions give a cross section for the formation of deuterons:

$$\sigma_{10}'(D,\hat{p})=b_{10}(2\mu)^{-\frac{1}{2}}2\pi B^{\frac{1}{2}}P_m^3\equiv\beta_{10}\eta^3, \tag{4}$$

where P_m is the c.m. momentum of the pions and η is $P_m/\mu c$. It should be emphasized that the ratio σ_{N+P}/σ_D is fixed by the theory without the introduction of any arbitrary parameters. Nonrelativistically, (4) can be better compared with (2*) by writing $P_m^2=2\mu T_m=2\mu T_0(1+y)$, so

$$\sigma_{10}'(D,\hat{p})=b_{10}2\pi T_0^2y^{\frac{1}{2}}(1+y)^{\frac{1}{2}},$$

and

$$\frac{\sigma_{10}'(N+P)}{\sigma_{10}'(D)}=\frac{F(y)}{2y^{\frac{1}{2}}(1+y)^{\frac{1}{2}}}. \tag{5*}$$

In writing (1) and (4) we have used Watson's results, but have tried to write them in a form that applies to relativistic pions, i.e., to distinguish between $P^2/2\mu$ and T. Phase space is treated relativistically, and we assume that the matrix element for the production of a p-state pion is $\hat{p}/\sqrt{w}$, where w is the pion energy (it enters because of the normalization of the wave function), $\hat{p}$ comes from a gradient operator, and we have neglected terms in higher powers of $\hat{p}$ because we do not know what they are. Even the expression $\hat{p}/\sqrt{w}$, while reasonable, is only a guess. It has the virtue, however, that it fits the experimental results and leads to some particularly simple algebraic expressions.

The approximations which are used to treat the S-wave nucleon-nucleon interaction also become worse if there is an appreciable probability that the nucleons may acquire more than about 20 Mev. Watson's expression (1) is derived on the assumption that the presence of the pion does not affect the nuclear force. It is then reasonable that the enhancement of the cross section by this force should be proportional to $|\psi(R)|^2$, where $\psi(R)$ is the amplitude of the nucleon wave function at the small distance R characteristic of pion production. The simple denominator $|B|+T_0-T$ of (1) comes from writing $\psi(R)$ in terms of effective-range parameters and dropping terms involving the square of the nucleon energy. It can be shown that the approximations used to obtain (1) result in an underestimate of the enhancement when the nucleon energies are large particularly if R is really much smaller than $\hbar/\mu c$. To estimate the error, we computed $|\psi(0)|^2$ exactly (assuming a square potential well of effective range 1.7×10^{-13} cm) and averaged it over the pion energy spectrum for a single representative high-energy case, $T_0=57.8$ Mev ($\eta=1$). This calculation gives a branching ratio $\sigma'(N+P)/\sigma'(D)$ which is 20 percent larger than given by (5*). (The relatively good agreement arises from the cancellation of errors from several approximations.) We feel that an approximation that is good to 20 percent is adequate, particularly since there is probably a much larger error introduced by the assumption that the pion has no effect upon the nuclear force. This difficulty is discussed in Sec. III.

Equation (1) can be integrated over pion energy to give the relativistic version of (2*),

$$\sigma_{10}'(N+P,\ \hat{p})=b_{10}\pi T_0^2\left\{F(y)-\frac{3z}{32(2+z)}\right\}(1+z/2)^2, \tag{6}$$

where $z=T_0/\mu c^2$, and $F(y)$ is given by (3). This differs from the nonrelativistic expression (2*) by somewhat less than 50 percent at $\eta=1$.

Using expressions (6) and (4), we calculate the fraction of unbound nucleons which should be formed at various energies. We find for 341-Mev protons (Berkeley) $\sigma'(N+P,\hat{p})/[\sigma'(N+P,\hat{p})+\sigma'(D,\hat{p})]=17$ percent; for 400-Mev neutrons (Chicago) 32 percent; for 440-Mev protons (Chicago and Pittsburgh) 35 percent.

We have so far considered only the production of pions in $\hat{p}$ states. The equivalent expressions for s-state production are obtained by replacing η^3 by η in the expressions for the cross section since the matrix element involved is constant rather than proportional to P. We then have

$$\sigma_{10}'(D,s)=\alpha_{10}\eta, \tag{7}$$

and

$$\frac{\sigma_{10}'(N+P,\ s)}{\sigma_{10}'(D)}=\frac{G(y)}{2y^{\frac{1}{2}}(1+y)^{\frac{1}{2}}}, \tag{8}$$

where

$$G(y)=\tfrac{1}{2}+y-y^{\frac{1}{2}}(1+y)^{\frac{1}{2}}, \quad y=|B|/T_0. \tag{9}$$

Because s-state production is relatively important only at low energy there is no point in treating (8) relativistically. The fraction (8) of unbound nucleons is higher for s- than for p-state production. From (8) we find for 341-Mev protons (Berkeley) the fraction is 27 percent, for 440-Mev protons (Chicago), 47 percent.

In Sec. III we shall determine the p-state parameter β_{10} by fitting (4) to the experimental cross sections, but the s-state parameter α_{10} has already been determined indirectly by Brueckner, Serber, and Watson.[15] They make use of the known branching ratio between the two processes $\pi^-+D\to 2N$ and $\pi^-+D\to 2N+\gamma$, following the capture (from an s state) of π^- by deuterium.[16] Using detailed balancing and taking the exclusion principle into account, they relate α_{10} to experimental information on photopion production near threshold. Taking the latest information available, $\sigma(\gamma+D\to\pi^-)=(1.4\pm0.2)\sigma(\gamma+D\to\pi^+)$;[17] and $\sigma(\gamma+P\to\pi^++N)=0.14$ mb $\times\eta$,[18] we find

$$\alpha_{10}=(0.14\pm0.05)\text{ mb}. \tag{10}$$

The Angular Distribution for $\sigma_{10}(D)$

We now want to consider the addition and interference of the three reactions which contribute to $\sigma_{10}(D)$, i.e.,

$J=0$,	${}^1S_0\to{}^3S_1\,p_0$,	(isotropic),	amplitude $\mu_0\propto\eta$
$J=2$,	${}^1D_2\to{}^3S_1\,p_2$,	$\frac{1}{3}+\cos^2\theta$,	amplitude $\mu_2\propto\eta$
$J=1$,	${}^3P_1\to{}^3S_1\,s_1$,	isotropic,	amplitude $\mu_1\propto$ const.

To each reaction has been assigned a complex transition amplitude μ_J. These amplitudes are understood to be proportional to S-matrix elements, so that the partial cross sections $\sigma_J\propto(2J+1)|\mu_J|^2$. Thus

$$\frac{\sigma_{10}(D,s)}{\sigma_{10}(D,p)}=\frac{\sigma_1}{\sigma_0+\sigma_2}=\frac{3|\mu_1|^2}{|\mu_0|^2+5|\mu_2|^2}=\frac{\alpha_{10}}{\beta_{10}\eta^2}.$$

Angular distributions and polarization relations depend only upon ratios of transition amplitudes; to simplify the equations we define

$$r_0=\frac{\mu_0}{(5)^{\frac{1}{2}}i^2\mu_2}; \quad r_1=\frac{(3)^{\frac{1}{2}}i\mu_1}{(5)^{\frac{1}{2}}i^2\mu_2}.$$

Note that r_0 is independent of pion energy, but $r_1\propto\eta^{-1}$.

The $J=0$ and $J=2$ reactions, which both arise from an initial singlet state, interfere to give an angular distribution of the form $X+\cos^2\theta$, where

$$X=\left\{\left|\frac{2-\sqrt{2}r_0}{1+\sqrt{2}r_0}\right|^2-1\right\}^{-1}. \tag{11}$$

Equation (4), which describes the Sp contribution to $\sigma_{10}(D)$ can now be written in the form of an angular distribution,

$$4\pi\frac{d\sigma_{10}'(D,p)}{d\Omega}=\beta_{10}\eta^3\frac{X+\cos^2\theta}{X+\frac{1}{3}}. \tag{12}$$

Adding the contribution (7) of the noninterfering s wave, we find

$$4\pi\frac{d\sigma_{10}'(D)}{d\Omega}=(\alpha_{10}\eta+\beta_{10}\eta^3)\frac{A+\cos^2\theta}{A+\frac{1}{3}}, \tag{13}$$

where

$$A=X+(X+\tfrac{1}{3})\frac{\alpha_{10}}{\beta_{10}}\frac{1}{\eta^2}. \tag{14}$$

For the energy range in which this treatment is valid A should be a linear function of η^{-2}. In Sec. III (Fig. 2) we plot the experimental values of A *vs* η^{-2} and obtain a best fit value of X.

The discussion has been restricted to the case of deuteron formation because of the simple form of the excitation functions and because there are no good experimental angular distributions for the "unbound" reaction. Equation (11) still applies to the unbound case, however, and the isotropic contribution A to the angular distribution should resemble that drawn in Fig. 2.

Pion Spectrum and Excitation Function for σ_{01}

Of the reactions considered in Table II, only those two leading to the final state ${}^1S_0\,p_1$ can contribute to σ_{01}. The pion spectrum is of the same form as (1) except that $B=2.227$ Mev must be replaced by $|B_{\text{singlet}}|\approx 70$ kev. Because of the low value of $|B|$ the pion spectrum is very peaked near T_0 and the quantity $y=|B|/T_0$ in (2*) and (3) becomes almost zero, so that the expression for the excitation function (2*) reduces to

$$\sigma_{01}'\approx b_{01}\pi T_0^2\cdot\tfrac{2}{3}\equiv\beta_{01}\eta^4. \tag{15*}$$

A similar simplification arises in the relativistic expression (6).

Excitation Function for σ_{11}

For σ_{11} reactions of class Sp are absent. Reactions of class Ss give a cross section

$$\sigma_{11}'(Ss)=\alpha_{11}\eta^2. \tag{16*}$$

We shall see in Sec. III that (16*) fails utterly to describe the experimental excitation function, which is very steep, proportional to $\approx\eta^8$. We must therefore discuss class Pp and Ps. The relative importance of

[15] Brueckner, Serber, and Watson, Phys. Rev. **81**, 575 (1951).
[16] Panofsky, Aamodt, and Hadley, Phys. Rev. **81**, 565 (1951).
[17] Beneventano, Lee, Stoppini, Hanson, Yamagata, and Bernardini, quoted by G. Bernardini at 1954 Rochester Conference on High-Energy Nuclear Physics (University of Rochester, Rochester).
[18] G. Bernardini, 1954 Rochester Conference Report on High-Energy Nuclear Physics (University of Rochester, Rochester).

these classes is not surprising since they are reinforced by the strong pion-nucleon interaction (see Table II).

The effect of nuclear forces is relatively unimportant for reactions of class Pp or Ps, so that the excitation functions are simple. For class Ps the cross section is proportional to η^6, and for class Pp:

$$\sigma_{11}'(Pp)=\beta_{11}\eta^8. \qquad (17^*)$$

Mather and Martinelli[19] discuss the possibility of explaining the steep experimental excitation function in terms of a cross section $\propto\eta^6$. They note that a pion, created in a pure s state at a distance R from the center of mass has an s-state component kR about the center of mass. This cross section must certainly be present, but it can be shown to be somewhat too small to explain the data.

Angular Distribution for σ_{01} and σ_{11}

Inspection of Table I shows that only in the case of reaction D is a forward-backward asymmetry not ruled out by the principle of charge symmetry. According to the more restrictive principle of charge independence none of the various reactions contributing to a given elementary cross section (like σ_{01}) can interfere asymmetrically *among themselves*. (According to charge independence a neutron and a proton in a pure isotopic spin state behave like indistinguishable particles, so there is no distinction between forwards and backwards.)

It is experimentally observed that σ_{01} and σ_{11} do interfere to give a large forward-backward asymmetry in reaction D. We can account for this asymmetry by invoking only the interference between reactions associated with S-state nucleons. Although this is what we do, it may not be correct. We have just mentioned that σ_{11} (Ss) is smaller than σ_{11} (Pp or Ps), which can interfere with σ_{01} (Pp or Ps). Until experimental data on σ_{01} become available at more than one energy we have no information on σ_{01} (Pp or Ps); if it should turn out that these Pp and Ps reactions contribute more than about 10 percent to σ_{01}, then the relations given below will have to be replaced with more complicated ones.

The only interfering reactions that we consider are

$$\sigma_{01},\ {}^3S_1\rightarrow{}^1S_0\,p_1,\text{ amplitude }\mu_3;$$
$$\sigma_{01},\ {}^3D_1\rightarrow{}^1S_0\,p_1,\text{ amplitude }\mu_4;$$
$$\sigma_{11},\ {}^3P_0\rightarrow{}^1S_0\,s_0,\text{ amplitude }\mu_5.$$

In the present case the subscripts to the transition amplitudes do not correspond to any physical quantity, they simply distinguish the three reactions. We have again normalized the μ_i so that $(2J+1)|\mu_i|^2\propto\sigma_i(\eta)$.

Let us write the angular distribution for reaction (D) in the form

$$4\pi\frac{d\sigma}{d\Omega}\propto a+b\cos\theta+c\cos^2\theta. \qquad (18)$$

Then we find

$$a=-3\sqrt{2}\,\mathrm{Re}\mu_3^*\mu_4+3|\mu_3|^2+\tfrac{3}{2}|\mu_4|^2+|\mu_5|^2 \qquad (19)$$

$$b=2\sqrt{3}\,\mathrm{Im}\mu_5^*(\mu_3+\sqrt{2}\mu_4) \qquad (20)$$

$$c=g/2|\mu_4|^2+g\sqrt{2}\,\mathrm{Re}\mu_3^*\mu_4 \qquad (21)$$

$$\sigma\propto a+c/3=3|\mu_3|^2+3|\mu_4|^2+|\mu_5|^2 \qquad (22)$$

$$\sigma=\sigma_{01}(Sp)+\sigma_{11}(Ss). \qquad (23)$$

We must again caution that pion production associated with the formation of P-state nucleons has been ignored. While there is some hope that the equation for the asymmetry b may still be meaningful, the expressions for a and c are certainly incomplete; for example we shall see in Sec. III that at $\eta=0.9$ σ_{11} (Pp or Ps) represents about $\frac{1}{3}$ of the total cross section for reaction (D).

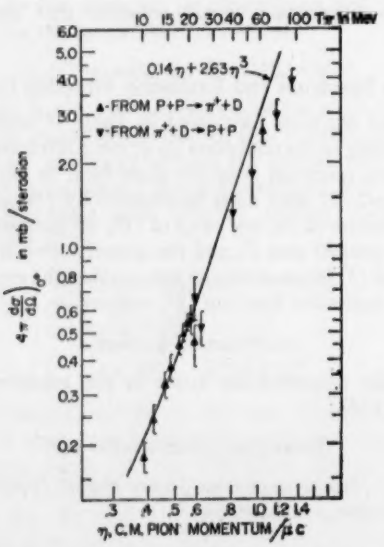

FIG. 1. Cross section per steradian in the c.m. at 0° for $P+P\rightarrow\pi^++D$. The lowest six points are the relative excitation results of Schulz and have been normalized to the absolute point of Crawford and Stevenson at $\eta=0.54$ (see Table III).

[19] J. W. Mather and E. A. Martinelli, Phys. Rev. **92**, 780 (1953).

III. COMPARISON OF THEORY AND EXPERIMENT

In this section we shall show that there is reasonably good agreement between the experimental data and the excitation functions set forth in the last section.

Determination of Parameters for $\sigma_{10}(D)$

Equation (13) gives the energy and angular dependence of $d\sigma(D)/d\Omega$ in terms of the three parameters α_{10}, β_{10}, and X. To determine these parameters, we shall first make use of the 0° data, which are comparatively abundant at low energy. Figure 1 gives all the available 0° differential cross sections for reaction (B) and also the results from the inverse reaction con-

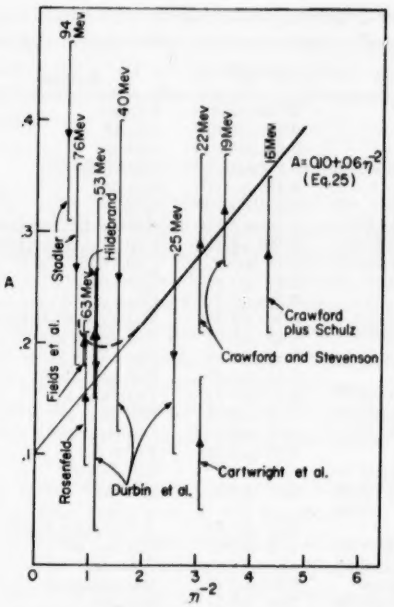

FIG. 2. Experimental values of A *vs* η^{-2}, where A is defined by $d\sigma_{10}'/d\Omega \propto A+\cos^2\theta$. The straight line comes from inserting into Eq. (14) the values $X=0.1$, $\alpha_{10}/\beta_{10}=0.14$. The dashed curve indicates that experimentally A deviates from (14). References are in Table II. Durbin *et al.* report values of A but not their errors; we have computed the errors using their published data.

verted by detailed balancing. The solid line was obtained by assuming $\alpha_{10}=0.14$ mb [see (10)], and adjusting the coefficient of η^3 to give a good fit at low energy. In this manner we obtain the relation $\beta_{10}(X+1)/(X+\frac{1}{3})=2.63$ mb [see (12)]. The data on the angular distribution as a function of energy, as shown in Fig. 2, can now be used to determine X. The data are evidently not adequate to confirm the linear dependence of A on η^{-2} given by (14); in fact they show that (14) does not apply for $\eta \gtrsim 1$. We have, however, drawn a straight line of A *vs* η^{-2}, with its slope determined by (14), which is a fair fit to the low-energy data. We find $X=0.10\pm0.03$. Then for the total cross section we find

$$\sigma_{10}'(D)=0.14\eta+1.0\eta^3, \tag{24}$$

and Eq. (14) becomes

$$A=1.0+0.06\eta^{-2}. \tag{25}$$

The only experimental result in serious disagreement with (25) is that of Cartwright *et al.*[20] at $\eta^{-2}=3$, but this is presumably to be superseded by the more recent work of Crawford and Stevenson[20] at the same energy. Nevertheless we must repeat that (25) should not be taken very seriously.

It should be noted that our fit to the experimental data is not too sensitive to the value of α_{10} assumed because at the energies and angles which we have considered so far the Sp reactions dominate over the Ss. To obtain more information on α_{10} we need more data at low energy and at 90° c.m. At 0° class Ss contributes more than Sp only from threshold to ≈4 Mev; however at 90° c.m. the Ss contribution dominates for energies up to ≈37 Mev.

We can now test our semiempirical excitation function (24) by comparing it with experimental total cross sections. The values of $d\sigma_{10}(D)/d\Omega$ displayed in Fig. 1 are given in Fig. 3 and Table III in the form of total cross sections, along with all other available total cross sections for the single production of charged and neutral pions in nucleon-nucleon collisions below 510 Mev. When only a differential cross section is published and an angular distribution is not reported, then the cross section is computed using the angular distribution (25). It can be seen that (24) fits the experimental data very well up to $\eta \approx 1$.

We believe that the parameters we have chosen give a good over-all fit to the data. Different parameters could, for example, improve the apparent fit in Fig. 3 for the total cross sections, but only at the expense of

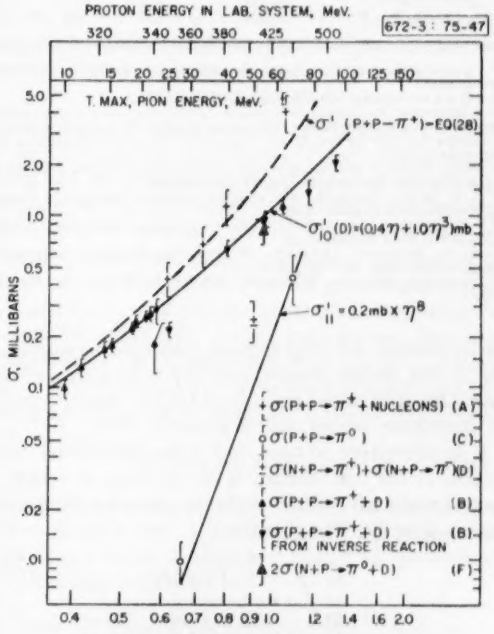
PROTON ENERGY IN LAB. SYSTEM, Mev.
320 340 360 380 425 500
672-3: 75-47
10 15 20 25 30 40 50 60 80 100 125 150
T. MAX, PION ENERGY, Mev.
σ' (P+P→π⁻)=EQ(28)
σ'10(D)=(0.14η+1.0η³)mb
σ'11=0.2mb×η⁸
σ MILLIBARNS
σ(P+P→π⁺+NUCLEONS) (A)
σ(P+P→π⁰) (C)
σ(N+P→π⁺)+σ(N+P→π⁻) (D)
σ(P+P→π⁺+D) (B)
σ(P+P→π⁺+D) (B)
FROM INVERSE REACTION
2σ(N+P→π⁰+D) (F)
0.4 0.5 0.6 0.7 0.8 0.9 1.0 1.2 1.4 1.6 2.0
η, MAX. C.M. PION MOMENTUM IN UNITS OF μc

FIG. 3. Excitation function for the production of charged and neutral pions in nucleon-proton collisions in both direct and inverse reactions.

The abscissa η is the maximum momentum available to a pion in the particular reaction plotted. Note that the scale labelled "Proton Beam Energy" applies only to reaction (A); it cannot apply to all reactions because of the mass differences between neutral and charges pions, etc.

Note also that in the case of pion production by neutrons, twice the cross section has been plotted so as to display more directly the fundamental cross sections as defined in Table I.

References are in Table III.

[20] See Table III.

TABLE III. Production of charged and neutral pions in nucleon-proton collisions.

Reaction	Elementary cross section	T_{proton} Mev	$T_{\pi\ pion}$[a] Mev	η[b]	A[c]	$\sigma_{pion\ production}$ mb	Reference
$P+P\to\pi^++D$	$\sigma_{10}(D)$	311	10.1	0.386		0.100±0.013[d]	Schulz[e]
$P+P\to\pi^++D$	$\sigma_{10}(D)$	315	11.7	0.418		0.133±0.016[d]	Schulz[e]
$P+P\to\pi^++D$	$\sigma_{10}(D)$	321	14.3	0.462		0.168±0.018[d]	Schulz[e]
$P+P\to\pi^++D$	$\sigma_{10}(D)$	324	15.5	0.482	0.28±0.07	0.178±0.016	Crawford[f]
$P+P\to\pi^++D$	$\sigma_{10}(D)$	330	18.1	0.523		0.228±0.017[d]	Schulz[e]
$P+P\to\pi^++D$	$\sigma_{10}(D)$	336	20.6	0.560		0.264±0.019[d]	Schulz[e]
$P+P\to\pi^++D$	$\sigma_{10}(D)$	332	19.0	0.535	0.32±0.05	0.245±0.013	Crawford,[f] Stevenson[g]
$P+P\to\pi^++D$	$\sigma_{10}(D)$	338	21.5	0.575	0.29±0.08	0.269±0.026	Crawford,[f] Stevenson[g]
$P+P\to\pi^++D$	$\sigma_{10}(D)$	340	22.3	0.585	0.11±0.06	0.18 ±0.06	Cartwright *et al.*[h]
$P+P\to\pi^++$nucl.	$\sigma_{10}+\sigma_{11}$	340	22.3	0.585		0.28 ±0.10	Cartwright[i]
$\pi^++D\to P+P$	$\sigma_{10}(D)$	341	22.8	0.590		0.284±0.050	Clark *et al.*[j]
$P+P\to\pi^0+P+P$	σ_{11}	341	27.8	0.660	isotropic	0.010±0.003	Mather and Martinelli[k]
$P+P\to\pi^++$nucl.	$\sigma_{10}+\sigma_{11}$	345	24.5	0.618		0.43 ±0.10	Passman *et al.*[l]
$P+P\to\pi^++$nucl.	$\sigma_{10}+\sigma_{11}$	365	33.0	0.728		0.68 ±0.18	Passman *et al.*[l]
$P+P\to\pi^++$nucl.	$\sigma_{10}+\sigma_{11}$	381	39.5	0.806		1.15 ±0.27	Passman *et al.*[l]
$\pi^++D\to P+P$	$\sigma_{10}(D)$	346.5	25	0.625	0.19+0.09	0.22 ±0.02	Durbin *et al.*[m]
$\pi^++D\to P+P$	$\sigma_{10}(D)$	382	40	0.815	0.26±0.14	0.66 ±0.07	Durbin *et al.*[m]
$\pi^++D\to P+P$	$\sigma_{10}(D)$	413.5	53	0.960	0.18±0.15	0.97 ±0.10	Durbin *et al.*[m]
$N+P\to\pi^\pm+$nucl.	$\frac{1}{2}(\sigma_{01}+\sigma_{11})$	405	48	0.915		0.16 ±0.04[n]	Yodh[o]
$N+P\to\pi^0+D$	$\frac{1}{2}\sigma_{10}(D)$	400	53	0.970	0.21±0.06		Hildebrand[p]
$N+P\to\pi^0+D$	$\frac{1}{2}\sigma_{10}(D)$	400	53	0.960	0.28+0.24 −0.14	0.41 ±0.07	Schluter[q]
$P+P\to\pi^++$nucl.	$\sigma_{10}+\sigma_{11}$	437	63.0	1.05		4.75 ±0.24	de Carvalho *et al.*[r]
$P+P\to\pi^++D$	$\sigma_{10}(D)$	437	63.0	1.05	0.20±0.02	1.15 ±0.13	Fields *et al.*[s]
$P+P\to\pi^++$nucl.	$\sigma_{10}+\sigma_{11}$	440	63.7	1.07	0.15±0.06	4.0 ±1.0	Rosenfeld[t]
$P+P\to\pi^0+P+P$	σ_{11}	430	64.4	1.11	isotropic	0.45 ±0.15	Marshall *et al.*[u]
$\pi^++D\to P+P$	$\sigma_{10}(D)$	470	76	1.17	0.27±0.09	1.39 ±0.23	Stadler[v]
$\pi^++D\to P+P$	$\sigma_{10}(D)$	515	94	1.33	0.39±0.08	2.04 ±0.22	Stadler[v]

[a] T_π pion is the maximum energy available to the pion in the center-of-mass system.
[b] η is the momentum corresponding to T_π in units of μc.
[c] A represents the fraction of isotropic contribution on the assumption that $d\sigma/d\Omega\propto(A+\cos^2\theta)$. Where the angular distribution was not measured, we assume Eq. (25) for $d\sigma_{10}/d\Omega$ and isotropy for $d\sigma_{11}/d\Omega$ in calculating the total cross section.
[d] Schulz measured only an excitation function, which is here normalized to Crawford and Stevenson's absolute cross sections.
[e] A. H. Schulz, University of California Radiation Laboratory Report UCRL-1756, 1952 (unpublished).
[f] F. S. Crawford, University of California Radiation Laboratory Report UCRL-2187, 1953 (unpublished).
[g] M. L. Stevenson, University of California Radiation Laboratory Report UCRL-2188, 1953 (unpublished).
[h] Cartwright, Richman, Whitehead, and Wilcox, Phys. Rev. 91, 677 (1953).
[i] W. F. Cartwright (private communication).
[j] Clark, Roberts, and Wilson, Phys. Rev. 83, 649 (1951).
[k] J. W. Mather and E. A. Martinelli (reference 19).
[l] Passman, Block, and Havens, Phys. Rev. 88, 1247 (1952).
[m] Durbin, Loar, and Steinberger, Phys. Rev. 84, 581 (1951).
[n] Yodh's cross section represents the average value for π^+ and π^- production. This is a preliminary result.
[o] G. B. Yodh (to be published).
[p] R. H. Hildebrand (see reference 5).
[q] R. A. Schluter (see reference 6).
[r] de Carvalho *et al.* (to be published).
[s] Fields, Fox, Kane, Stallwood, and Sutton, Phys. Rev. 95, 638(A) (1954).
[t] A. H. Rosenfeld, Phys. Rev. 95, 638(A) (1954).
[u] Marshall, Marshall, Nedzel, and Warshaw, Phys. Rev. 88, 632 (1952).
[v] H. L. Stadler, Phys. Rev. (to be published).

the agreement with the angular distributions shown in Fig. 2. We should remark that the ratio $\alpha_{10}/\beta_{10}=0.14$ from (24) is in close agreement with the estimate made by Brueckner, Serber, and Watson[21] in 1951.

It is interesting to note that if the differential cross section in the c.m. system is of the form $A+\cos^2\theta$, a measurement at a single angle can give the total cross section directly: The quantity,

$$\frac{d\sigma}{d\Omega}\Big/\sigma=\frac{1}{4\pi}\,\frac{A+\cos^2\theta}{A+\frac{1}{3}},$$

becomes independent of A for $\cos^2\theta=\frac{1}{3}$ (55° or 125°). For the reaction $P+P\to\pi^++D$, the "representative" c.m. angle of 125° transforms to an angle close to 90° in the laboratory system (87° for a bombarding energy of 440 Mev, and 83° for 380 Mev). The experiments of Passman *et al.*[20] which were done at 90° in the lab., thus give a total cross section comparatively insensitive to assumptions about the angular distribution.

[21] Brueckner, Serber, and Watson, Phys. Rev. 84, 258 (1951).

(3/2, 3/2) Interaction

We can insert our value of X into (11) and obtain an expression for the ratio r_0 of the transition amplitudes relating the two reactions of class Sp. It should be remembered that the important pion-nucleon state of isotopic spin $\frac{3}{2}$ and angular momentum $\frac{3}{2}$ is not represented at all in one of these reactions ($^1S_0\to{}^3S_1\,p_0$), but is important for the other ($^1D_2\to{}^3S_1\,p_2$).

Equation (11) restricts r_0 to a circle in the complex plane, i.e.,

$$r_0=-\sqrt{\tfrac{1}{2}}(1+3X)+(3/\sqrt{2})(X^2+X)^{\frac{1}{2}}e^{i\omega_0}. \quad (26)$$

For $X=0.10$,

$$r_0=-0.92+0.70e^{i\omega_0}, \quad (27)$$

and the circle lies entirely to the left of the origin. Near the threshold for pion production it can be shown that the phase of r_0 is related to proton-proton scattering phase shifts. We consider it more probable that the phase is closer to 0° or 180° than to 90°. Making the assumption that r_0 is real and less than unity, we find $r_0\approx0.2$, so that the relative intensity of the $J=2$

(enhanced) and $J=0$ (unenhanced) reactions is $r_0^{-2}\approx 25$. Part of this factor ≈ 25 must arise from the purely statistical factor $2J+1=5$, but the remaining factor ≈ 5 probably arises from the strong $(\frac{3}{2},\frac{3}{2})$ pion-nucleon interaction.

Conservation of Isotopic Spin

In Fig. 2 we should call attention to the result of Hildebrand[5,20] which is an established piece of evidence for the conservation of isotopic spin. According to this principle, only one of the three independent cross sections, namely σ_{10}, can lead to deuteron formation (thus Table I shows that reactions (B) and (F) should be identical except for a factor two). Hildebrand has measured the isotropic contribution A for reaction (F) at 53 Mev c.m. His result is seen to be in good agreement with all the rest of the data, which come from reaction (B).

A new piece of evidence is shown in Fig. 3; this is Schluter's total cross section for reaction (F). It is plotted as an open triangle at $\eta=0.96$. If isotopic spin were not conserved, there would be no reason why the cross sections for reactions (F) and (B) should agree. They do agree within the experimental error which however is still large for the neutron reaction. Schluter also reports a value for A, but his statistical error is large, so that we have not plotted his result in Fig. 2.

σ_{10}—The Branching Ratio of Unbound to Bound Nucleons

Reaction (A) of Table I can be written

$$\sigma(P+P\rightarrow\pi^+ + \text{nucleons}) = \sigma_{10}(D)+\sigma_{10}(N+P)+\sigma_{11}. \quad (28)$$

We now have phenomenological expressions for the three cross sections on the right-hand side. $\sigma_{10}(D)$ is given by (24), $\sigma_{10}(N+P)$ is computed by inserting the known parameters α_{10} and β_{10} from (24) into (6), (7), and (8); σ_{11} will be given by (30′).

The sum of these three phenomenological cross sections is plotted as a dashed line in Fig. 3. It is not a simple power law, but may be approximated by

$$\sigma(P+P\rightarrow\pi^+ + \text{nucleons})\approx 1.8\eta^5, \quad (29)$$

in the energy region of interest.

It can be seen that the dashed line falls somewhat below the experimental points, although no discrepancy is indicated at low energy. There is however a discrepancy which does not show up in Fig. 3. Certain experiments, which do not necessarily establish a total cross section, give the ratio $\sigma(D)/\sigma(N+P)$ directly. Such results are not displayed in Fig. 3, but are summarized in Table IV.

Cartwright *et al.* and Peterson *et al.* measured the pion energy spectrum, and were thus able to determine, or at least put a lower limit on, the branching ratio. Hildebrand counts the protons or deuterons in coincidence with the π^0; knowing the range and angle of the proton or deuteron, he can distinguish between them and measure the branching ratio directly. All three experiments give measured branching ratios about twice as large as those computed.

Thus both Table IV and the high-energy data of Fig. 3 give considerable evidence that the branching ratio $\sigma(N+P)/\sigma(D)$ is about twice as big as predicted by the phenomenological treatment. Some of this discrepancy can be explained in terms of P-state nucleon production, which we have neglected; we also pointed out in the discussion preceding Eq. (5) that we have made approximations which indeed do underestimate the probability of formation of unbound nucleons by about 20 percent. These two effects, combined with some experimental error, could conceivably explain the discrepancy, but more likely the error lies with the phenomenological treatment. The presence of the pion might, for instance, slightly decrease the interaction of the final-state nucleons. Equation (5*) shows that the branching ratio depends sensitively on $|B|/T_0$; in fact it is almost inversely proportional to $|B|$. If the presence of the pion reduced the effective deuteron binding energy from 2.227 Mev to, say, 1 Mev, the phenomenological equations would again fit all the available data.

Determination of σ_{11}

Reference to Table I shows that σ_{11} should in principle be easy to measure, since $\sigma_{11}=\sigma(P+P\rightarrow\pi^0)$. Unfortunately the cross section is small and the reaction has not been studied extensively. Cross sections are available at only two energies, and the accuracy is low.

In our phenomenological discussion of the excitation function [Eqs. (16*) and (17*)], we predicted a sum of $\alpha_{11}\eta^2$ and $\beta_{11}\eta^5$, with perhaps some additional terms in η^6 from the "displaced" s-state cross section discussed by Mather and Martinelli[19] and from reactions of class (Ps). For the high-energy experimental point $(\eta=1.1)$ the term $\beta_{11}\eta^5$ should be dominant. We have accordingly drawn a line

$$\sigma_{11}'(Pp)=0.2\text{ mb}\times\eta^5, \quad (30^*)$$

passing through this point. This line fits the meager data sufficiently well that we conclude the production of pions in s states is small and cannot be determined quantitatively at present.

TABLE IV. Measured and predicted branching fractions $\frac{\sigma(N+P)}{\sigma(N+P)+\sigma(D)}$.

Reaction	Measured fraction %	Predicted fraction %	η	Reference
$P+P\rightarrow\pi^+$	35±10	20	0.59	Cartwright[a]
$P+P\rightarrow\pi^+$	45±10	20	0.49	Peterson *et al.*[b]
$N+P\rightarrow\pi^0$	60±15	32	0.95	Hildebrand[c]

[a] See reference 20.
[b] Peterson, Iloff, and Sherman, Phys. Rev. **84**, 372 (1951).
[c] R. H. Hildebrand (to be published).

Both Wright and Schluter[22] and Yodh[23] find a large experimental forward-backward asymmetry for reaction (D); if the angular distribution is written in the form $4\pi d\sigma/d\Omega = a+b\cos\theta+c\cos^2\theta$, then the ratio of b to the total cross section $a+c/3$ is probably about one-half. We must now show that this asymmetry is consistent with our conclusion that s-state production contributes little to σ_{11}.

The transition amplitude μ_s for s-state production is related to the coefficient of $\cos\theta$ in the angular distribution by (20) and (22). Using these two equations and the two semiempirical formulas (30*) and (32*) it follows that

$$\sigma'_{11}(Ss) > 0.01 \text{ mb} \times \eta^2. \tag{31*}$$

Thus $\sigma'_{11}(Ss)$ can be as small as 0.01 mb$\times\eta^2$ and still be large enough to account for the observed asymmetry. Such a small coefficient of η^2 would not modify the observed steep excitation for σ_{11}, which is proportional to η^6 or η^8.

Determination of σ_{01}

The only elementary cross section that cannot be measured directly is σ_{01}. It can best be determined by subtracting σ_{11} from $2\sigma(N+P\to\pi^+)$. Two experimental determinations of this latter cross section are now in progress using the Chicago neutron beam, and Yodh's tentative result[20] is plotted in Fig. 3. Adjusting the parameter β_{01} of (15*) to fit Yodh's cross section, we get

$$\sigma_{01}' = (0.3\pm0.1) \text{ mb} \times \eta^4. \tag{32*}$$

There is as yet no experimental way to test (32*) since data are available at only one energy.

IV. POLARIZATION

In the discussion entitled "Angular Distribution for $\sigma_{10}(D)$" in Part II of this paper, we established relations (11) and (14) between the two transition amplitude ratios r_0 and r_1 and the experimentally measurable quantities X and A in the angular distribution of σ_{10}, but we could not determine uniquely the magnitudes and phases of r_0 and r_1.

This can in principle be done by polarization experiments. Most of the relations which we give below have been derived previously,[8,9] but it may be worth while to restate them in our notation and to insert our values of X and A so as to see at what energies and angles interesting effects may be observed, and how large these effects may be. Two experiments are discussed below, and the second of these is now underway at several laboratories. The results will be summarized in a note-in-proof.

Polarized Deuterons

We first discuss that polarization experiment which is in practice the most difficult. The deuterons associated with the $\sigma_{10}(Ss)$ reaction are not polarized perpendicular to the plane of the reaction, but the two Sp reactions produce deuterons which are polarized perpendicular to this plane, with a degree of polarization given by

$$P_P = \frac{\sin\omega_0}{1+2X+2(X^2+X)^{\frac{1}{2}}\cos\omega_0} \cdot \frac{2(X^2+X)^{\frac{1}{2}}\sin\theta\cos\theta}{X+\cos^2\theta}, \tag{33}$$

where $-1<P_P<1$, and ω_0 [defined by (26)] is a parameter of the ratio r_0 relating the two Sp reactions. The first factor can vary from -1 to $+1$, and thus establishes the phase ω_0. The second factor can also vary from -1 to $+1$, depending upon the angle θ at which the deuterons are detected. The second factor is largest when $\cos2\theta=-1/(2X+1)$; for $X=0.1$ this corresponds to $\theta=73°$. If the phase ω_0 happens to be propitious (for $X=0.1$ this is 56°, which is a rather improbable angle), deuterons leaving the collision at about 73° could be completely polarized. On the other hand it should be pointed out that at 73° the cross section per steradian is not very large ($X+\cos^2\theta=0.18$), and despite the large possible polarization the experiment would probably be extremely difficult.

Polarized Beam of Protons

We have not yet discussed the phase of the transition amplitude μ_1 governing the Ss contribution to σ_{10}. According to (4) and (10), the magnitude of μ_1 is determined by the relation:

$$\frac{\alpha_{10}}{\beta_{10}\eta^3} = \frac{3|\mu_1|^2}{|\mu_0|^2+5|\mu_2|^2} = \frac{|r_1|^2}{1+|r_0|^2}, \tag{34}$$

but we have no information on its phase. Marshak and Messiah[9] have pointed out that it may be found by measuring the angular distribution of the reaction $P+P\to\pi^++D$ using polarized protons. Since the reactions of class Sp arise from initial singlet states, any asymmetry must be due to the Ss reaction. If the proton beam has a degree of polarization P_1 in the $+x$ direction then the angular distribution of the pions is given by

$$\frac{d\sigma_{10}}{d\Omega} \propto A+\cos^2\theta+P_1QA\sin\theta\sin\phi, \tag{35}$$

where

$$Q = \sqrt{\tfrac{1}{2}}\frac{2b}{1+b^2}\sin(\psi-\tau_1), \tag{36}$$

$$r_1 = |r_1|e^{i\tau_1}, \tag{37}$$

$$b = \left|\frac{r_0+\sqrt{\tfrac{1}{2}}}{r_1}\right|, \tag{38}$$

$$\psi = \arg(r_0+\sqrt{\tfrac{1}{2}}). \tag{39}$$

[22] S. C. Wright and R. A. Schluter (to be published).
[23] G. B. Yodh (to be published).

Unfortunately, (35) shows that the fractional asymmetry is the greatest at 90° where the cross section is a minimum.

For simplicity we shall adopt the point of view that quantities do not vary appreciably with energy in the limited range under consideration unless a variation is indicated by the phenomenological model. Thus, while we assume that $r_1 \propto \mu_1/\mu_2 \propto \eta^{-1}$, we shall consider the phases of r_1 and r_0 to be constant. The parameter of maximum asymmetry Q will reach its maximum value of $\sqrt{\frac{1}{2}}\sin(\psi-\tau_1)$ when $b=1$, i.e., when

$$|r_1| = |r_0+\sqrt{\tfrac{1}{2}}|\,; \tag{40}$$

or, using (34), when

$$\eta=\eta_c=\left(\frac{\alpha_{10}}{\beta_{10}}\right)^{\frac{1}{2}}\frac{(1+|r_0|^2)^{\frac{1}{2}}}{|(r_0+\sqrt{\frac{1}{2}})|}=\left(\frac{\alpha_{10}}{\beta_{10}}\right)^{\frac{1}{2}}\left(1+\frac{1}{3X}\right)^{\frac{1}{2}}. \tag{41}$$

This last equality can be checked using (11). Inserting the value $X=0.1$, we find

$$\eta_c=0.78\pm0.2, \tag{42}$$

which corresponds to a pion energy of 35 Mev. Equation (38) may now be rewritten as $b=\eta/\eta_c$. Putting this into (36), we obtain an energy-dependence of the asymmetry:

$$Q/Q_{\max}=2\eta\eta_c/(\eta^2+\eta_c^2). \tag{43}$$

The experiment under consideration has now been completed by three groups. Crawford and Stevenson[24] find a large asymmetry; they report $|Q|=0.39\pm0.05$ at $\eta=0.41$, with the pions produced preferentially to the right of a proton beam which had been polarized by a left scatter. Sutton *et al.*[25] find a very similar result at $\eta=0.96$, namely $|Q|=0.41\pm0.07$. Here too the majority of pions were found on the side opposite from the original scatter.

de Carvalho *et al.*[26] have a result obtained as a by-product of another experiment. Their arrangement was such as to detect not only the pions formed in association with deuterons, but also about 78 percent of the rest. We can hope that both reactions show the same asymmetry and try to interpret the experimental results merely by inserting into (43) an average value of η which we take to be 0.8. Then at 85° c.m. they find $|Q|=-0.22\pm0.12$, and at 98° $|Q|=-0.08+0.11$.

[24] F. S. Crawford and M. L. Stevenson, Phys. Rev. **95**, 1112 (1954).
[25] Roger Sutton (private communication).
[26] de Carvalho, Heiberg, Marshall, and Marshall, Phys. Rev. **94**, 1796 (1954).

If we express these four results in terms of $\sin(\psi-\tau_1)$ they should be independent of the energy at which the experiment was performed. We then find for $\sin(\psi-\tau_1)$:

$+0.67\pm0.03$ (Crawford and Stevenson)
$+0.6\ \pm0.1$ (Sutton *et al.*)
$+0.22\pm0.12$ (de Carvalho *et al.*, 85°)
-0.08 ± 0.11 (de Carvalho *et al.*, 98°).

If all of these results are correct it would indicate that the asymmetry of pions associated with unbound nucleons is almost equal and opposite to that of pions associated with deuterons.

V. CONCLUSIONS

We have compiled the available data on pion production in nucleon-nucleon collisions and have analyzed them using the approach of Watson and Brueckner, which uses the fact that the pion is a pseudoscalar particle, assumes that isotopic spin is conserved, and treats nuclear forces phenomenologically.

By adjusting undetermined parameters which give the relative amplitude and phase of several partial reactions, we establish semiempirical formulas which fit the available information within experimental error (see Fig. 3). This statement should not be taken as too striking, since none of the reactions except $P+P\rightarrow\pi^++D$ has been extensively studied. For the latter reaction, however, the agreement is good, even considerably above threshold.

There is probably a discrepancy in that the fraction of unbound nucleons formed per deuteron is higher than predicted.

Evidence is given for the conservation of isotopic spin in cases where the data are good enough to permit meaningful comparison of pion production in P-P and N-P collisions.

Using our best values for the relevant parameters we discuss the information attainable by experimenting with polarized beams.

Many of the ideas in the paper came from cooperation with Murray Gell-Mann and there is considerable overlap in content between this paper and a chapter on pion production by M. Gell-Mann and K. M. Watson to appear in Vol. 4 of *Annual Reviews of Nuclear Science* (1954); we have used similar notation.

We must thank all those who are working on pion producton here and at other laboratories for many helpful discussions and for permission to use yet-unpublished data. In particular we wish to thank E. Fermi, M. Gell-Mann, R. H. Hildebrand, F. T. Solmitz, and G. B. Yodh for their active help and support.

Inelastic Scattering of 500-Mev Negative Pions in Emulsion Nuclei*

M. BLAU, *Brookhaven National Laboratory, Upton, New York*

AND

MARTIN CAULTON,† *Rensselaer Polytechnic Institute, Troy, New York*

(Received June 17, 1954)

Inelastic scattering of 500-Mev negative pions has been investigated in 1700 meson-induced events in emulsion nuclei. Large energy losses and strong angular relationships of the emitted mesons have been observed, similar to those in experiments with lower energy mesons. The possible causes for this behavior are discussed. In 1–3 percent of the events, production of charged mesons has been found. The cross section for meson production on free nucleons is estimated to be between 3.5 and 10 mb, considering the possible absorption of one or both mesons. The angular and energy distributions of mesons and recoiling nucleons in events with meson production are discussed. Six events of π^0 production on free protons (or edge nucleons) have been found. The results are compared with observations on meson scattering and meson production in cosmic-ray experiments.

I. INTRODUCTION

INVESTIGATIONS on the interaction of nucleons with complex nuclei have contributed considerably to the knowledge of nucleon-nucleon collisions. Particularly, the ideas on meson production are, up to date, almost entirely based on these experiments.

It seemed promising to apply the same methods for high energy meson interactions—500-Mev negative pions—and to explore, in general, problems connected with these interactions.

Experiments using lower meson energies (30 to 210 Mev) have been performed by various authors[1–9] in cloud chamber and emulsion experiments. Elastic scattering, meson absorption, and inelastic scattering events have been found;[10] and the cross section and characteristics of these types of events have been discussed. It has been established that absorption of low energy mesons takes place in nucleon pairs or larger nucleon complexes. The process of inelastic meson scattering at all these energies is characterized by great energy losses and strong angular dependence and is not fully understood.

It was expected that at higher energies the prevailing interaction would be quasi-elastic scattering—elastic scattering on single nucleons within the nucleus. However, the interaction process turned out to be actually more complex. The investigation of this process was one of the objects of this paper. The main purpose, however, was the attempt to detect meson production by mesons and to find the laws governing this process.

II. EXPERIMENTAL PROCEDURE

A. Plate Exposure

Two different types of exposures were used.

(1) The plates were exposed to the "500-Mev meson beam" of the Brookhaven Cosmotron; mesons of 620-Mev/c momentum, analyzed and focused by the Cosmotron magnet, leave through a hole in the Cosmotron shield. These mesons were further deflected by a second analyzing magnet. The plates were placed parallel to the beam behind a lead collimator and shielded by lead bricks from background radiation.

(2) Particles emitted from the Cosmotron target (beryllium) at an angle of 32° with the proton direction pass directly through the Cosmotron shield. After collimation, particles of the desired momentum and charge were selected by an analyzing magnet. Again the plates were placed parallel to the direction of the selected beam and properly shielded. The "focused" beam had higher intensity than the "direct" beam, but the latter had less contamination. The angular spread of the focussed beam was approximately $\pm 4°$, which was the same as that exhibited by incident minimum tracks found on the exposed plates. The angular spread in the direct beam was less than $\pm 2°$.

400-micron Ilford G-5 emulsions with glass backing were used in the first series of experiments. In latter exposures stacks of a dozen 400-micron Ilford G-5 stripped emulsions were used. The processing of the emulsions followed standard development techniques.

B. Search

Meson interactions were found by area scanning under 300 times magnification. Under high magnification, only about 20 meters of minimum tracks have been followed, mainly to check the efficiency of the area scanning search and to compare the distribution of certain types of events found in both methods.

* Research carried out under auspices of the U. S. Atomic Energy Commission.

† Now at Brookhaven National Laboratory.

[1] Bernardini, Booth, Lederman, and Tinlot, Phys. Rev. **80**, 924 (1950); Bernardini, Booth, and Lederman, Phys. Rev. **82**, 105 (1951); G. Bernardini and F. Levy, Phys. Rev. **84**, 610 (1951).

[2] H. Bradner and B. Rankin, Phys. Rev. **81**, 916 (1951).

[3] Blau, Oliver, and Smith, Phys. Rev. **91**, 949 (1953).

[4] G. Goldhaber and S. Goldhaber, Phys. Rev. **91**, 674 (1953).

[5] W. F. Fry, Phys. Rev. **91**, 1576 (1953).

[6] A. H. Morrish, Phys. Rev. **90**, 674 (1953).

[7] A. H. Morrish, Phil. Mag. **45**, 47 (1954).

[8] Byfield, Kessler, and Lederman, Phys. Rev. **86**, 17 (1952).

[9] J. O. Kessler and L. M. Lederman, Phys. Rev. **94**, 689 (1954).

[10] The term inelastic scattering is commonly used to describe stars with one emitted meson.

The efficiency in area scanning for picking up events with 2 or more black tracks was almost 100 percent, for 1 black prong only 50±10 percent. Events without black prongs and 1 or 2 light tracks have only been picked up occasionally. This fact immediately limits the scope of the experiments to inelastic scattering events.

In total, 1700 events have been found in about 8 cc of emulsion. In the beginning of this investigation all observed events were measured and the grain count and angular relation of light tracks determined. After 460 interactions were found, only stars were measured with at least one fast particle or a black track which seemed a meson by its apparent scattering. After a total of approximately 700 interactions were found, only special events (having at least two tracks, which were possible mesons) were measured and recorded. The other events were only counted, in order to keep account of the total number of observed events.

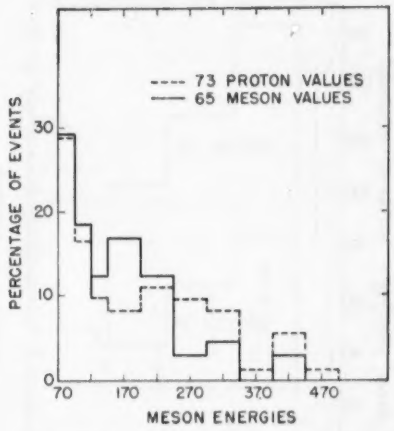

FIG. 1. Histogram of average multiple scattering angles (expressed in corresponding meson energies) for mesons and protons.

C. Measurements

Nature and energy of particles were determined by the usual methods: grain count, multiple scattering, and range measurements. Sample tracks of incoming mesons have been scattered for each set of exposures; the mean energy determined from scattering measurements was 520±30 Mev, in agreement with the value expected from experimental conditions (current of the analyzing magnet, position, etc.).

Grain count and scattering measurements on light tracks emitted in the interactions have been performed, whenever track length or ionization made this procedure meaningful. In this way for about 30 percent of all light tracks the nature and energy of the particle could be determined. In experiments with emulsion stacks the ionization loss per unit path length could be used as an additional criterion, especially in cases where excessive dip angle or distortion made scattering measurements unreliable. Scattering measurements on heavily ionizing tracks were performed, when they were suspected by apparent scattering to be π mesons or by other unusual features to be heavy mesons. However, no single case of a meson heavier than π could be established. Likewise, the investigation of several two-prong stars without an incoming particle, suspected to be Λ^0, gave no positive results.

D. Measurement Considerations

In the interactions described in this paper the presence of mesons with energies greater than 100 Mev (minimum grain count) can be established by kinematic considerations alone, since the maximum energy a proton can acquire in an elastic collision with 500-Mev mesons is 420 Mev (including 22-Mev Fermi energy), and therefore, the corresponding tracks have grain counts higher than minimum. Based on similar considerations, tracks emitted in the backward hemisphere, with grain counts less or equal to 1.4 minimum grain count, cannot be protons, but must be mesons.

In order to establish the energy distribution of the mesons, scattering measurements are necessary. The question arises, whether the scattering measurements made on 30 percent of light tracks (sample comprising about 1000 events) represent the true distribution of mesons in number and energy. Since the track lengths necessary for adequate scattering measurements increases with the particle energy, i.e., with smaller multiple scattering angles, it is important to investigate if the distribution in the measured sample is deficient of high-energy mesons. While the true energy distribution of mesons is not known, the energy distribution of protons can be calculated in an approximate manner.[11]

The probability of finding a track adequate for scattering measurements depends on: (1) the dip angle of track, (2) position in the plate, and (3) the mean multiple scattering angle of the track. (1) and (2) are obviously independent of the nature of the particle causing this track (whether meson or proton). (3), the multiple scattering angle of the most energetic recoil protons (420 Mev), is about equal to the multiple scattering angle of the incoming mesons (500 Mev), and, therefore, equal to or smaller than the multiple scattering angle of emitted mesons.

The histogram of protons—73 protons with energies >60 Mev—is plotted in Fig. 1 (dotted lines) *versus* the

[11] The calculations are based on the well-known energy dependance of mean free paths in nucleon matter for $p-p$ and $p-n$ collisions and the average number of collisions in emulsion nuclei [Bernardini, Booth, and Lindenbaum, Phys. Rev. **85**, 826 (1952); **88**, 1017 (1952)]. It is assumed that the fast protons are produced in elastic meson-nucleon collisions with energies corresponding to the experimentally observed angular distribution of the mesons (Fig. 2). The ratio of neutron to proton recoils has been determined by the ratio of neutrons to protons in emulsion nuclei and the statistical weight of $\pi^-+p\rightarrow\pi^-+p$ and $\pi^-+n\rightarrow\pi^-+n$ interactions.

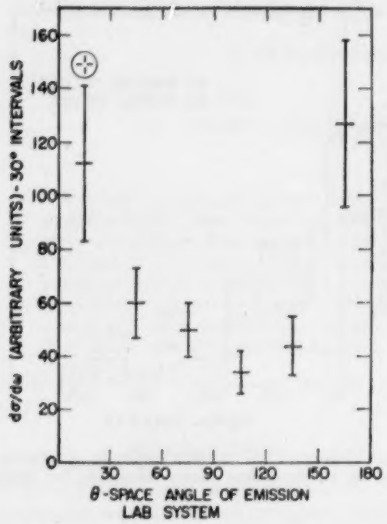

FIG. 2. Differential cross section of emitted mesons *versus* space angle of emission in laboratory system.

angle of multiple scattering; the scattering angle, however, is expressed in corresponding meson energies. In this sample, 8 percent of all protons (>60 Mev—corresponding to 70-Mev meson energy) have energies >280 Mev (corresponding in scattering angle to mesons >350 Mev). Calculating[11] the percentage of protons with energies >280 Mev among protons of energies >60 Mev yielded the value 7.5 percent.

The solid lines in Fig. 1 correspond to the energy distribution of mesons in a nearly equal sample (65 mesons). There is a greater number of large multiple scattering angles in the meson distribution than in the proton distribution.

Because of the approximate character of the calculation of fast emerging protons, the agreement between experimental and calculated values (7.5 percent and 8 percent, respectively) does not necessarily prove that the sample really embraces all fast protons. However, the fact that the meson sample has relatively fewer high energy particles than the proton distribution makes it probable that the former sample represents the true meson energy distribution.

Furthermore, the ratio (minimum tracks scattered)/(total number of minimum tracks) is nearly equal for forward (presumably higher energy mesons) and backward-scattered mesons.

On the other hand, some fast mesons, scattered strongly forward (small energy of the recoil nucleon) may have been missed because of the inefficiency in finding small events (1 and 0 prong stars). The percentage of missing forward-scattered (Fig. 2), and therefore, possibly high energy mesons (Figs. 3 and 4), has been estimated by comparing the frequency of finding small events in area scanning and scanning along incident tracks. The dotted lines in Fig. 2 and Fig. 4 are corrected for this loss assuming that the missing events are entirely connected with high energy meson emission; the dotted lines in Fig. 4, therefore, probably represent an overestimate of high energy mesons.

III. EXPERIMENTAL RESULTS AND DISCUSSION

From a phenomenological standpoint the interactions observed can be divided into 3 groups. (1) Stars with 1 meson—38±6 percent of all cases, (2) stars with 2 mesons—1–3 percent, and (3) stars without mesons. Presumably, in all three types of events the primary process is meson interaction with a single nucleon; interactions with nucleon complexes, if present at all, will be less probable because of the small wavelength of 500-Mev pions.

The number of stars with mesons—usually called inelastic scattering events—has increased in comparison to experiments with lower-energy mesons. Only 10 percent of all interactions with 70-Mev mesons[1] have mesons emerging, 22 percent with 135-Mev mesons,[4] and 31 percent with 210-Mev mesons.[7]

A. Stars without Mesons

In a certain percentage of mesonless stars charge exchange scattering may have occurred. In order to estimate this percentage the energy dissipation in stars with and without charged mesons has been compared and found distinctly different. The mean number of black prongs is 4.3±0.2 in mesonless stars and about 66 percent of all stars have a fast proton; in stars with mesons the mean prong number is 2.7±0.1, and only 40 percent have a proton more energetic than 30 Mev.

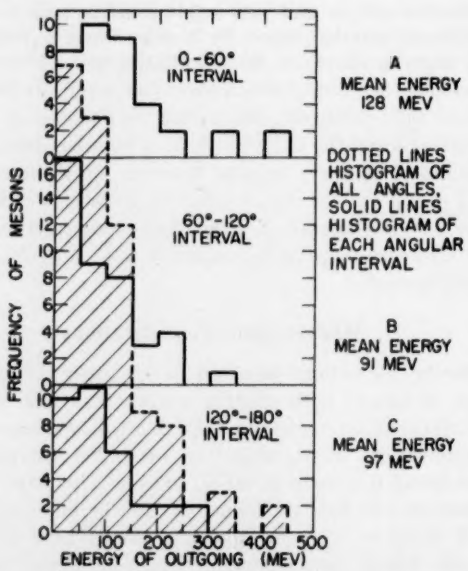
FREQUENCY OF MESONS
0-60° INTERVAL
60°-120° INTERVAL
120°-180° INTERVAL
A MEAN ENERGY 128 MEV
DOTTED LINES HISTOGRAM OF ALL ANGLES, SOLID LINES HISTOGRAM OF EACH ANGULAR INTERVAL
B MEAN ENERGY 91 MEV
C MEAN ENERGY 97 MEV
ENERGY OF OUTGOING (MEV)

FIG. 3. Energy distribution of emitted mesons.

The mean energy of the emitted charged mesons is 110 Mev and the energy distribution is assumed to be equal for charged and neutral mesons;[12] therefore, the mean energy dissipation in mesonless stars should be greater by 110+140 Mev. This energy increase expressed in black and gray tracks has been estimated from the known prong distribution of sigma stars[13] and stars produced by negative mesons in the energy interval of 50–100 Mev.[1] According to this estimate, charge exchange should have occurred in 29 percent of all mesonless stars or in 18 percent of all interactions observed. Another rough estimate of the frequency of charge exchange can be obtained by considering the frequency of events with electron pairs. Among 1700 events 2–4 have been observed with pairs emerging from the vertex of the interaction.[14] Assuming these pairs to be conversion electrons from π^0 disintegrations, charge exchange would have taken place in 10–20 percent of all events. A value of 20 percent would be expected from statistical spin considerations,[15] the near equality of $\pi^+ + p$ and $\pi^- + p$ cross sections at this energy, and the ratio of neutrons to protons in emulsion nuclei.

After subtracting 20 percent of the events as charge exchange, 44 percent of the stars are still mesonless. This percentage is astonishingly high considering the high energy of mesons involved. It seems reasonable to assume that meson capture in nucleon pairs will occur only if the meson wavelength is comparable with the distance of nucleons within the nucleus (smaller meson energies).[16] Therefore, the meson must lose an appreciable amount of its original energy before being captured. If the energy degradation takes place gradually through repeated scatterings, the frequency of meson escape should be higher, considering the finite size of the nucleus.

B. Stars with One Meson

Figure 2 gives the angular distribution (differential cross section in arbitrary units) for 112 inelastically scattered mesons leaving the nucleus, and Fig. 3, the energy distribution of these mesons. *A*, *B*, and *C* in Fig. 3 refer to angular intervals 0–60°, 60–120°, and 120–180° (solid lines), while the dotted lines of the histogram comprise all three angular regions.

The energy distribution is peaked at low energies and only a few mesons have energies greater than 200 Mev. The distribution is quite similar in *A*, *B*, and *C*, with the exception of a few high energy mesons in *A*. It seems, therefore, that there is no relation between meson energy and angle of emission. One would, however, expect such a relation on the obvious assumption that the primary process within the nucleus will be meson-nucleon scattering. Therefore, the observed distribution strongly suggests that the original distribution is obliterated by other processes, for instance, repeated scattering or meson production and reabsorption. The fact that repeated scattering or meson reabsorption may have occurred in at least several of the events can be demonstrated by observation of fast protons in the backward hemisphere in 9 out of 112 cases. However, at least 3 of these cases can be interpreted as reabsorption of positive mesons since in addition to the backward ones, forward protons are observed and the angles between protons are ≥ 150 degrees.

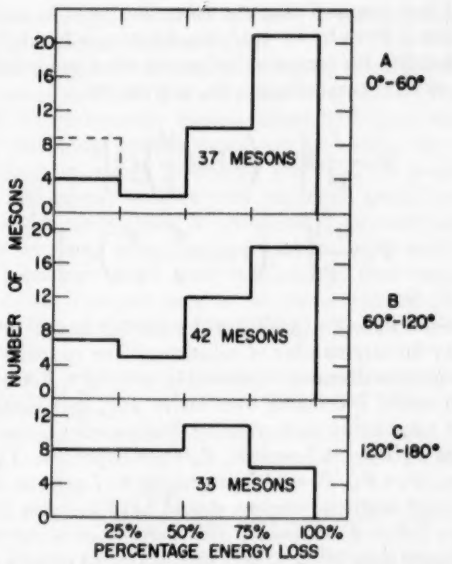

FIG. 4. Number of mesons *versus* percentage energy loss for three space intervals.

1. *Energy Degradation of Observed Mesons*

The number of collisions necessary to explain the observed energy degradation would be rather high, especially if one considers that for high-energy mesons the probability of forward scattering (small energy loss) will be at least as high as that of backward scattering. For instance, three consecutive scatterings at 60° would decrease the initial energy to about 200 Mev; but only 14 percent (or 18 percent after correction) of all observed mesons have energies ≥ 200 Mev.

For mesons scattered in the forward direction (up to 60°), it is possible to estimate the probabilities for escape after one or two repeated collisions, respectively. In this angular interval the changes in energy are relatively small and lead to energy regions in which the mean free path in nuclear matter is nearly constant (small increase).

[12] Carlson, Hooper, and King, Phil. Mag. **41**, 701 (1950).
[13] Menon, Muirhead, and Rochat, Phil. Mag. **41**, 583 (1950).
[14] In two cases the nature of the particles causing the pair of minimum tracks could not be established with certainty. A small additional number of events with electron pairs having 1 or 0 black prongs may have been missed in area scanning.
[15] K. A. Brueckner, Phys. Rev. **86**, 109 (1952).
[16] Proton pairs accelerated in the absorption of a π^+ meson in a nucleon pair rarely have energies greater than 70 Mev.

If it is assumed that the mean free path in nuclear matter is given by $\lambda=4\pi r_0^3/3\sigma_\mu$, where $\sigma_\mu=26$ mb,[17] the probability for escape of the meson after one collision, P_1, or after two collisions, P_2, is given by

$$P_1=\frac{2}{a^2}\cdot 2\left[1-\left(1+a+\frac{a^2}{2}\right)e^{-a}\right],$$

$$P_2=\frac{2\cdot 3}{a^2}\left[1-\left(1+a+\frac{a^2}{2}+\frac{a^3}{2\cdot 3}\right)e^{-a}\right].$$

$P_T=1-P_0=\{1-(2/a^2)[1-(1+a)e^{-a}]\}$ is the probability for any number of collisions.[18] The quantity a is the nuclear diameter expressed in units of λ. For emulsion nuclei (averaging over heavy and light elements and considering their relative transparency), one obtains $P_1/P_T=34.7$ percent. $P_2/P_T=29$ percent. Therefore, $(P_1+P_2)/P_T=63.7$ percent, or 63.7 percent of all forward scattered mesons should have energies ≥ 260 Mev (after 2 collisions). This percentage is an overestimate since initially backward-scattered mesons may enter the forward hemisphere by being scattered a second time at angles greater than 90°. However, since the mean free path for backward-scattered mesons is much smaller than for forward mesons, one would expect that mesons scattered twice at great angles will not contribute greatly to the frequency of mesons observed at forward angles.[19]

Figure 4 compares for 3 angular intervals the energy loss suffered by the emerging mesons. The energy loss in percent is defined by $L=1-W_{i\gamma}/W_{e\gamma}$, where $W_{i\gamma}$ is the kinetic energy of a meson observed at an angle γ and $W_{e\gamma}$ is the kinetic energy expected at this angle in the case of elastic scattering. (The Fermi momentum distribution has been taken into account.) The results are in obvious contradiction to the above calculations and considerations. Only 17 percent of all mesons or 10 percent in the angular interval 0–60° can be considered first or second collisions according to Fig. 4. If the events missed because of incomplete scanning efficiency are taken into account, the above percentages would be 22 percent or 25 percent, respectively. Since in about one-half of all events no meson leaves the nucleus, these figures can be smaller by one-half the stated amount.

Another fact, in disagreement with the great observed energy losses, is the small size of stars observed.

[17] L. Yuan and S. Lindenbaum, Phys. Rev. **92**, 1578 (1953), found a cross section of 25±3 mb for 450-Mev negative pions on hydrogen and 27 mb for positive mesons of equal energy. In the calculation of the total cross section, the mean cross section per nucleon has been assumed to be 26 mb.

[18] S. A. Wouthuysen, University of Rochester Technical Report No. 5 on the 130″ cyclotron (unpublished).

[19] The calculation for backward-scattered mesons is more difficult, because the mean free path is strongly dependent on energy for meson energies near 200 Mev.

2. *Angular Distribution of Mesons*

Figure 2 shows a strong angular dependence of inelastic scattered mesons and that again is difficult to reconcile with a model of frequent repeated scatterings.

Similar features (great energy losses and strong angular dependence of inelastic scattered mesons) have also been observed in experiments with mesons of lower energy.[1–8] Kessler and Lederman[9] compare for 120-Mev negative incident pions the angular distribution of mesons inelastically scattered in carbon and lead with the differential cross section of the elementary process $\pi^+ + p \rightarrow \pi^+ + p$ at equal energy. The distribution from carbon simulates closely the elementary process and even in the large nucleus, lead, the features of the elementary distribution are recognizable although here the distribution is smoother and obviously somewhat obliterated by multiple scattering processes. Emulsion experiments with 135-Mev negative mesons[4] show similar results. While the relative loss in meson energy is considerable, the absolute amount of energy loss in both experiments is relatively small. The energy of the emitted mesons may be depressed because of the momentum distribution within the nucleus.[20] On the other hand, the angular distribution (predominantly backward) may be partly affected by the small mean free path of the incident meson, favoring an interaction near the beginning of its travel through the nucleus; therefore, the scattered mesons may preferentially escape the nucleus in the backward direction.

With 210-Mev mesons,[7] great energy losses of emitted mesons are observed. Because of the small mean free path, repeated scatterings are expected. However, a definite angular distribution is found; the ratio of forward- to backward-scattered mesons increases as compared with lower energy experiments. This is indicative of the influence of a primary nucleon process.

For the experiments described here no comparison with the elementary scattering process can be made, since the differential scattering cross section for 500-Mev mesons is not known. Because of the great absolute energy loss suffered by the majority of mesons in the present experiment, any angular distribution differing from an isotropic one seems incompatible with the assumption of gradual energy loss by frequently repeated scatterings.

It is, therefore, believed that there exists another mechanism, by which the meson energy is reduced in larger steps in one single or at least relatively few collisions.

Meson production, eventually followed by reabsorption, could lead to sudden energy changes. The cross section for production of charged mesons has been estimated within rather wide limits[21] (14–40 percent of the elastic cross section). If the actual value is appreciably larger than the lower limit and if the π^0 production

[20] M. H. Johnson, Phys. Rev. **83**, 510 (1951).

[21] Section III: C-3 of this paper.

cross section is of comparable magnitude, the combined effect of meson production, scattering, and absorption may be sufficient to explain the experimental results—great energy losses and strong angular preference of mesons.

C. Events with Two Mesons—Meson Production by Mesons

1. *Production of Charged Mesons*

Among 1700 events, 20 cases with 2 mesons leaving the nucleus have been identified with certainty. There are 24 more cases which probably represent meson production. In the established events the mesons have been identified by grain count, scattering, and range. Fifteen of these events are tabulated in Table I. In some cases the minimum tracks at backward laboratory angles have been denoted mesons from kinematic considerations alone. Whenever the possibility existed that a track considered a meson could be a proton, the event was classified as only possible. It is likely that more than 50 percent of these possible cases represent meson production. About 10 more cases with steeply dipping tracks have been observed, which possibly could be events with meson production, but because of the uncertainty, these events have not been considered.

The events with two emitted mesons represent most probably meson production by mesons; meson production by recoil nucleons produced in the primary scattering process is very unlikely because of the low energy of these recoil nucleons.[22] Furthermore, the kinematics of only 15 out of 44 events would be in agreement with meson production by recoil nucleons.

Only 3 events, Numbers 2, 9, and 15 in Table I, can be explained by meson production on free protons, since no other tracks besides the two mesons are visible. These events have been analyzed. If the momenta and angles of the incoming and both emitted mesons are known, the momentum and the angle of the recoil nucleon can be found. An event, representing meson production on a single nucleon, balances if $T_{\mu 1}+T_{\mu 2}+T_N = T_{\mu i}-140$ Mev $=360$ Mev. Here, $T_{\mu i}$, $T_{\mu 1}$, and $T_{\mu 2}$ are the kinetic energies of incoming and both emitted mesons, and T_N is the kinetic energy of the nucleon derived from the momentum diagram. In event 2 the sum of energies of both mesons and the calculated nucleon add up to 360 Mev and in No. 9 to 320 Mev, and therefore, these events agree kinematically with the assumption of meson production on a free proton. In event No. 15 the forward scattered particle was too short to be identified with certainty. However, since only one other particle (identified as a meson) is emitted, the event can be assumed to have occurred on a free proton. In this case the energy of one of the mesons together with both emission angles determines the kinematics of the event. The event balances with a meson energy for the forward track in good agreement with grain count measurements.

The energies of the emitted mesons, determined by the usual methods, are only known within a certain limit. For low-energy mesons, where both grain count and scattering measurements can be made, the uncertainty in energy is usually less than 10 percent. For high-energy mesons with minimum grain count, the upper energy limit is sometimes 35 percent higher than the mean value. In cases 2 and 9 and in many of the cases mentioned later, balance has been reached for meson energies near or at the calculated mean value. If higher energy values within the fiducial limits

TABLE I. Description of established two-meson events (mesons in kinematic balance with a single nucleon encounter). Angles are given in degrees.

(1) Event[a]	(2) Kin. energy T (lab) Mev	(3) Lab angle θ	(4) Kin. energy T (c.m.) Mev	(5) C.m. angle $\bar{\theta}$	(6) Lab angle $\pi-\pi$	(7) Lab angle $\pi-N$	(8) C.m. angle $\pi-\pi$	(9) C.m. angle $\pi-N$	(10) Other tracks[b]
1 *I*	500	0							1 *B*
A (π^+)	8.4	39	5	125		31		35	
B	280	35	178	33	71	76	145	160	
N	55	41	37	126					
2 *A*	16	7	0.4	35		20		66	None
B	125	102	169	125	105	123	130	177	
N	220	20	48	52					
3 *A*	53	145	117	159		137		153	4 *B*
B	38	66	35	106	149	68	93	114	
N	230	2	55	6					
4 *A*	55	32	23	60		55		170	1 *R*
B	115	96	147	123	71	122	73	103	1 *B*
N	185	26	46	49					1 *e*
5 *A*	3.1	12	3.3	168		15		136	1 *B*
B	105	115	164	138	119	131	46	175	
N	250	15	51	37					
6 *A*	60	128	116	148		130		150	5 *B*
B	42	90	58	125	104	105	39	173	
N	250	12	48	33					
7 *A*	57	60	45	95		72		128	3 *B*
B	86	154	176	165	107	159	79	159	
N	230	13	42	35					
8 *A*	70	126	128	147		138		150	1 *R*
B	40	95	60	128	82	108	58	153	3 *R*
N	280	13	62	31					
9 *A*	2.8	46	7	154		72		60	None
B	280	14	152	24	32	39	129	170	
N	34	25	21	147					
10 *A*	90	70	84	100		86		144	1 *B*
B	49	159	119	168	90	176	68	148	
N	230	17	47	43					
11 *A*	120	62	99	90		100		175	2 *B*
B	94	51	64	79	12	90	14	168	
N	145	39	60	92					
12 *A*	2.5	124	22	166		145		146	2 *B*
B	122	95	154	121	30	115	45	168	1 *R*
N	240	20	56	49					
13 *A*	4	52	8	146		74		141	1 *R*
B	150	84	164	108	50	109	46	171	
N	210	25	54	61					
14 *A*?[c]	40	43	20	81	*AB* 62	47	*AB* 78	105	1 *B*
B	3.1	95	17	155	*AC* 46	92	*AC* 141	95	
C	95	41	54	66	*BC* 75	48	*BC* 126	115	
N	92	12	4	83					
15 *A*	100	156	198	165		162		155	None
B	17	17	2	76	149	20	110	72	
N	260	5	46	13					

[a] In column (1), *I*—incident particle; *A*, *B*, *C*—mesons; *N*—nucleon.
[b] In column (10), *B*—black track, *R*—recoil, and *e*—electron.
[c] Track *A* causes a star after traveling 958 microns.

[22] Argument presented in paper by Blau, Caulton, and Smith, Phys. Rev. **92**, 516 (1953).

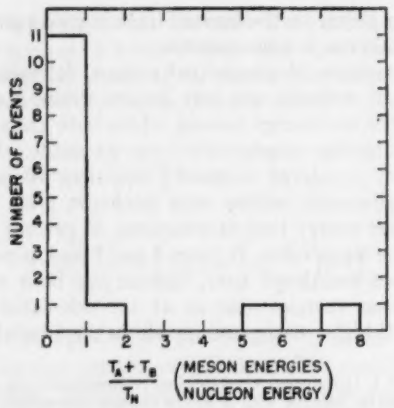

FIG. 5. Distribution of meson and nucleon energies in events with meson production in laboratory system. (Ratio of sum of meson energies to nucleon energy.)

(67 percent probability) have been used, this procedure seemed justified because of cell length or other considerations connected with the measurement. An event was assumed to be balanced when the sum of energies of both mesons and the nucleon energy did not differ by more than 10 percent from the calculated value. The energy values in Table I correspond to energy values for which "balancing" was found.

In all the other "established events" in Table I, evaporation particles in addition to both mesons are emitted. Meson production may have occurred on protons or neutrons, with the exception of 2 cases where the charge of one of the mesons could be identified as positive, so that collision with a proton is certain. Under the assumption that these tracks are caused by subsequent interactions of the recoil nucleon a kinematic investigation similar to that described has been made. Energy and momentum balance within the error limit has been found for the events of Table I.

Event No. 14 in Table I is a case where possibly 3 mesons emerge from the vertex. B and C have been identified as mesons; track A has 1.8 times minimum grain count and travels 958μ before causing a star; the star has only a few black prongs and could have been caused by either a 40-Mev meson or 260-Mev proton. If A is assumed to be a meson, a single nucleon is needed to balance energy and momentum. Total energy is $500-2(140)=220$ Mev. In columns 5, 6, and 7 of Table I, the energies and angles in the center-of-mass system are listed. Five more events with unmistakably identified mesons could not be balanced; in these events the energy of both mesons was small, and therefore, one or both of the mesons might have suffered a subsequent scattering before emerging. One of these events has 8 black tracks and 3 others have fast protons; in two of these cases emission of a π^0 is not excluded.

In the case of "possible events," energy and momentum balance was attempted, whenever energy determination of the emitted particles was possible. Eleven of these events could be balanced and nucleon energies and angles have been calculated. In 6 events with minimum tracks (multiple scattering angle not measurable) balance was not even attempted because the energy of these mesons is not known. In these cases only emission angles have been calculated in the laboratory and c.m. systems;[23] 5 more cases could not be balanced, and finally in 2 cases not enough information was available for an analysis.

In most of the events described, the nucleon receives in the laboratory system a great amount of the energy available. Figure 5 is a histogram showing the frequency of events *versus* the ratio $(T_{\mu 1}+T_{\mu 2})/T_N$, the sum of the kinetic energy of both mesons divided by the nucleon energy. In the two events with a ratio ≥ 5, one of the mesons is produced with nearly the maximum available meson energy. One of these events is No. 9 without evaporation tracks while both of the other "proton events" lie in the interval with a ratio around 0.5. The angular distribution of both mesons is plotted in Fig. 6 (laboratory system) and Fig. 7 (c.m. system). The dotted lines comprise both established and probable events. No differentiation between produced and original mesons can be made; only 2 cases of positive mesons have been observed, and both are emitted backwards in the c.m. system.[24] Figures 8(a) and 8(b) show for 14 events the distribution of the angles between both

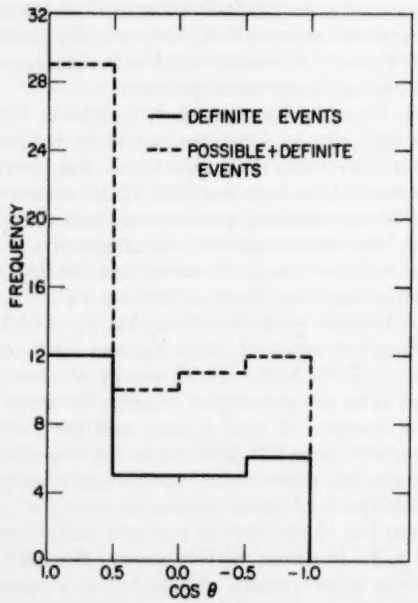

FIG. 6. Angular distribution of mesons in events with meson production—laboratory system.

[23] The relation between laboratory and c.m. angles depends very little on energy for meson energies greater than 80 Mev.

[24] One event observed with incident mesons of 750 Mev, without evaporation tracks, also has a positive meson emitted backward.

mesons in the laboratory and c.m. systems. The statistics are too poor to draw any conclusion, although small angles between mesons (c.m. system) seem to be more frequent. Finally, Fig. 9 gives the histogram of nucleons in the c.m. system. (Dotted lines refer again to established+possible events.) The trend in forward emission of nucleons follows from the backward trend of meson emission. In two of the alleged proton events the nucleon is emitted forward, while in the case of No. 9 with a high ratio (meson energies/nucleon energy) the nucleon is in the backward hemisphere.

The differentiation between events with evaporation tracks and the "free proton events" without visible prongs has been made for the following reason. It is felt that in some of the former cases the nucleus excitation might not be caused entirely by the recoil nucleon but also by subsequent scattering of one or both of the emitted mesons. The argument of balance would not be stringent, if something like coincidence balance exists. Calculations have been made on constructed and observed cases in order to determine the probability of chance balance. If the energy of both of the mesons is ≥ 100 Mev, chance balance seems impossible; for 1 meson ≥ 100 and the other < 100, chance balance is possible; that means that there exists another meson energy and angle from which one of the mesons could have been scattered to its actual position. The limits for chance balance are very narrow from a theoretical standpoint, but are widened by uncertainties in energy and angular (for high dip angles) measurements. If, however, the second meson has a very small energy,

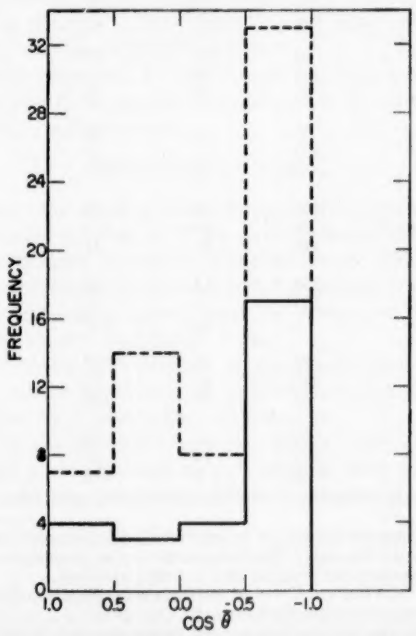

FIG. 7. Angular distribution of mesons in events with meson production—c.m. system.

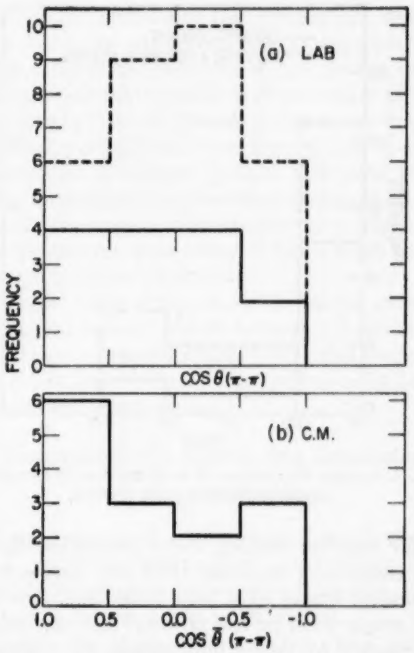

FIG. 8. Distribution of angles between the two emitted mesons in cases of meson production. (a) Laboratory system; (b) c.m. system.

then even if it should have been scattered from an original position, parameters like nucleon energy or angle will be only slightly affected.[25] Most suspicious are events with both mesons of energies below ~ 100 Mev; then, cases can be constructed allowing for both mesons the possibility of having been scattered from another produced angle and energy. Five cases out of the 14 events used for the histograms (Figs. 6–9) belong in this group. Assuming that there are cases where the energy connected with the emitted mesons was originally higher, then the energy of the recoil nucleons would have been overestimated, and, consequently, the angle of emission (c.m. system) would have been shifted towards the forward direction. The nucleon angular distribution may actually become more isotropic and the ratio of backward- to forward-emitted mesons smaller.[26] The angular distribution of nucleons and mesons again may have been altered to some degree by the momentum distribution within the nucleus. This could affect the "free proton events" in the same way, since there is a certain possibility that the events took place on bound nucleons (edge of nucleus) and not on free protons. Crussard, Walker, and Koshiba,[27] studying meson production (charged and neutral mesons) with

[25] This argument is not valid if the original meson has suffered more than 1 scattering; the high capture cross section for mesons in this energy interval and the small star sizes observed do not favor such an assumption, however.

[26] Lal, Pal, Peters, and Swami, Proc. Indian Acad. Sci. **36**, 75 (1952).

[27] Crussard, Walker, and Koshiba, Phys. Rev. **94**, 736 (1954).

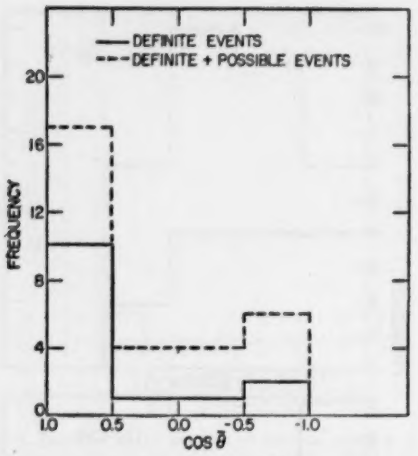

FIG. 9. Angular distribution of recoil nucleons in events with meson production (c.m. system).

1.5-Bev negative mesons, found predominantly backward emission of nucleons. Here only events without evaporation tracks have been considered. One-half of these events occur on free protons; this conclusion has been reached by taking into account the known cross section for 1.5-Bev mesons.

It cannot be decided if the different angular distribution of the recoil nucleons found with 500-Mev mesons is attributable to: (1) the difference in energy, (2) the fact that the production takes place in complex nuclei, or (3) the fact that in some cases coincidence balance leads to false conclusions. Backward asymmetry of emitted mesons in showers produced by high-energy mesons has been observed by Lal *et al.*[26]

2. *Production of Neutral Mesons*

Very little can be said about neutral meson production in the reaction $\pi^-+p\rightarrow p+\pi^-+\pi^0$; reactions on free protons are necessary for the unambiguous identification of this process, and such reactions can only rarely be found in area scanning techniques.

In all, 6 events corresponding to the above reaction were found; the respective energies and angles are given in Table II. In 5 of the 6 events the proton is emitted in the backward direction in the c.m. system. Strongly peaked backward emission of the protons in π^0 production has been found by Crussard *et al.*[27] with 1.5-Bev negative pions. However, the number of events here is too small to draw any conclusions. Furthermore, the area scanning technique will favor events with low-energy protons (backward in the c.m. system) which give black or dark grey tracks.

It is difficult to evaluate the number of cases where π^0 emission may have occurred in collisions with bound protons or neutrons (events with evaporation tracks). In a certain percentage of events with charged mesons, the energy degradation observed may have been caused by this type of collision. At least 6 percent of all events with a single charged meson most probably belong to this type of interaction. This value is found by considering only events with a single evaporation prong and a forward emitted meson (charged),[28] which apparently has lost a large amount of energy. From statistical considerations[29] the number of events with two charged mesons should be about equal to the frequency of events with 1 charged and 1 neutral meson.

3. *Approximate Cross Section for Production of Charged Mesons*

As stated before, in only 1–3 percent of all events production of charged mesons has been found.[30] It is thought that this figure can at the most be doubled in order to account for inefficiency in scanning. This, however, is only valid for meson production in nuclei with at least 1 evaporation track; events occurring in hydrogen or edge nucleons may have been missed in a greater proportion.

It is obvious that the actual fraction of interaction leading to meson production will be higher than 1–3 percent, since both or at least one of the mesons can be captured within the nucleons, and therefore, not be observable. The absorption coefficient will be appreciable, if one takes into account the low energy of mesons (mean energy) observed in this process.

TABLE II. Description of events representing π^0 production on a free proton. ($\pi^-+p\rightarrow p+\pi^-+\pi^0$.) Angles are in degrees.

Event	Lab energy Mev	Lab angle θ	C.m. angle $\bar{\theta}$	Lab angle π-π
1 π^-	90	63	93	
π^0	200	56	81	104
p	86	23	99	
2 π^-	80	34	58	
π^0	280	12	19	47
p	5	10	177	
3 π^-	165	48	72	
π^0	76	81	112	37
p	138	10	42	
4 π^-	240	15	24	
π^0	165	37	47	51
p	6	46	112	
5 π^-	150	38	59	
π^0	150	47	71	50
p	71	47	120	
6 π^-	100	32	53	
π^0	256	16	25	49
p	6	6	178	

[28] Backward mesons can be associated with fast recoil neutrons to take up the energy. Since discernment of π^0 production among such events is not possible, they are not considered.

[29] C. N. Yang and E. Fermi (private communication). See Blau, Caulton, and Smith, Phys. Rev. **92**, 516 (1953).

[30] Calculations based on $\pi-\mu-e$ decays observed in plates and stacks lead to a value of 0.4±0.1 percent for the production of positive mesons alone (in the energy interval 0–30 Mev).

An estimate of the probability of meson production per nucleon can be obtained by considerations similar to those in the case of photomeson production.

Francis and Watson[31] describe the relation between the photomeson production cross sections σ_π from a nucleus of atomic weight A, and σ_f, the cross section for production on free nucleons. The equation

$$\sigma_\pi = A\eta\sigma_f(\lambda/V_A)\sigma_{abs}$$

represents this relationship, where λ is the mean free path in nuclear matter, σ_{abs} is the absorption cross section for mesons, V_A is the nuclear volume, and η is a factor smaller than one.

In applying this equation to the present case, the value of λ, 3×10^{-13} cm, found by Kessler and Lederman[9] for 120-Mev mesons, has been used since this energy is comparable with the mean energy of emitted mesons. σ_π is assumed to be 2 percent of σ_{total}, where $\sigma_{total}=610$ mb[32] calculated from the mean free path of 500-Mev mesons[33] averaging over all emulsion nuclei, taking into account their transparency. Furthermore, one has to consider that not only the produced, but also the scattered mesons are subject to additional scattering and absorption (square of absorption factor). Finally, contrary to the problem of photomeson production, the attenuation of the incident mesons has to be accounted for. This has been done in an approximate manner by multiplying the number of nucleons per atom by a factor P_A. P_A is the probability that a 500-Mev meson suffers exactly one collision in passing through a nucleus of atomic mass number, A. This assumption implies that mesons having suffered more than 1 collision in passing through the nucleus no longer have sufficient energy to produce further mesons.

If one takes into account heavy and light emulsion nuclei and their respective abundance in the emulsion, the final result becomes:

$$0.02\times610\times10^{-27}=3.4\sigma_{pr},$$

and σ_{pr}, the cross section for production of charged mesons per nucleon, is 3.5 mb or 14 percent of the total meson-nucleon interaction cross section at 500 Mev. The calculated meson production cross section probably has been underestimated, since the mean free path λ may be smaller than 3×10^{-13} cm.

A probable overestimate of the meson production cross section based only on experimental data can be obtained by the following considerations.

With 135-Mev incident meson energy,[4] only 22 percent of all interactions in the emulsion have a single meson leaving the nucleus. Since in the case of meson production, the probability that two mesons leave the nucleus has to be considered, one would expect that only 5 percent of all cases with meson production can be observed and that actually in 40 percent of all interactions production of charged mesons takes place. This estimate would lead to a cross section of 10 mb for production of charged mesons. The value 10 mb, however, is considered an overestimate since an incident meson, on the average, has to traverse a larger path within the nucleus than either of the mesons emitted in the case of meson production.

The actual value of the meson production cross section (charged mesons) will lie between 3.5 and 10 mb. From statistical considerations,[29] the cross section for meson production by mesons is expected to be 12 percent of the total cross section.

D. Comparison with Cosmic-Ray Experiments

1. *Meson Scattering*

The mean energy of mesons emitted as shower particles in cosmic-ray experiments is 640 Mev.[34] Therefore, a comparison with experiments using only slightly lower energy mesons should be of interest.

In cosmic-ray investigations it had been assumed that for mesons the interaction mean free path is geometric over a wide range of energies. With artificial mesons (based mainly on counter measurements), strong energy dependence of the cross section has been found. For 500-Mev mesons the mean free path in nuclear emulsions is about twice geometric. Some calculations connected with transition effects and the mean free path of the star-producing components will have to be revised because of these data.

Interactions of single mesons have been studied by the Bristol group. Lock and Yekutieli[35] compile results on this subject; 86 meson interactions in the energy range of 0.1 to 1 Bev are discussed. The conclusion is reached that mesons below 160 Mev are strongly absorbed, while at higher energies, charge exchange prevails. This conclusion is based on the relatively low excitation energy of stars induced by mesons of energy higher than 160 Mev. It is assumed that more than 50 percent of all mesons suffer charge exchange, a value which seems high in comparison to observations with artificial mesons.

Sixteen meson induced events have been found (in the majority of the cases the incoming meson energy was higher than 300 Mev), where an identified meson leaves the nucleus. As in the cases with artificial mesons, great energy losses in the emitted mesons have been observed; an attempt was made to explain these energy losses on the basis of repeated scattering. This explanation makes it necessary to assume a high interaction cross section for mesons and this assumption is in dis-

[31] N. C. Francis and K. M. Watson, Phys. Rev. **89**, 328 (1953); **92**, 291 (1953); compare with I. Reff, Phys. Rev. **91**, 150 (1953).

[32] S. J. Lindenbaum and L. C. L. Yuan, Phys. Rev. **92**, 1578 (1953), see also reference 17.

[33] 610 mb is in fair agreement with an experimental value found by comparing the number of stars and inelastic events with the number of incident particles corrected for μ-meson and electron contamination.

[34] M. Sands, Phys. Rev. **77**, 180 (1950).

[35] W. O. Lock and G. Yekutieli, Phil. Mag. **43**, 231 (1952).

agreement not only with the cross section found for artificial mesons in this energy interval, but also with observations on mesons in showers produced by high energy nucleon-nucleon collisions; the mean energy of these shower particles is 640 Mev, and therefore, comparable with the energy of the single mesons, observed by the Bristol group[36] and in the experiments with 500-Mev mesons.

From the number of mesons scattered backward in nucleon-nucleon collisions, the interaction cross section of shower particles is estimated to be not greater than 10 percent of the geometrical cross section. The number of black and grey tracks in stars connected with shower particles increases only very slowly with the increasing number of shower particles and that again favors the assumption of a small interaction cross section and a small probability for meson reabsorption.

The discrepancy between the interaction of single mesons and mesons produced in "showers" is difficult to understand. Several hypotheses[36] have been put forward to clarify this problem, but none of them is entirely satisfactory. The mean free path for mesons of energy ≥ 300 Mev is equal or even smaller than the mean free path of relativistic nucleons; therefore, mesons produced in nucleon-nucleon collisions traverse in the average the same nuclear path as secondary mesons scattered or produced in meson-nucleon collisions.

The difference in the behavior of single incident mesons and shower mesons may be connected with the production mechanism of the latter, the formation of excited nucleons. Not enough is known about this process to discuss the consequences this phenomenon may have on the scattering of produced mesons. If it should be possible to assume that the excited nucleons have a finite lifetime $\sim 10^{-23}$ sec, for example, then excited nucleons (great mass, and, therefore, less subject to scattering), not single mesons, will traverse at least part of the nuclear path.

One has reason to believe that also in meson-nucleon collisions excited nucleon formation may take place[37]; however, the probability of this process will be smaller (only one nucleon as compared with two in nucleon-nucleon collisions).

2. *Meson-Meson Production*

Indirect evidence on meson-meson production has been obtained in absorption experiments. Rosser and Swift[38] exposed sensitive emulsions at mountain altitudes below and above 30 cm of lead. By comparing the ratio of charged and neutral primaries producing shower particles ($n_s \geq 2$), a ratio twice as large has been found in absorber plates. This effect, if explained entirely on the basis of meson-meson production, would lead to a production cross section nearly equal to the geometric cross section of the average emulsion nucleus. This result is in disagreement with observations on artificial mesons.

One event of meson-meson production initiated by a 1-Bev meson has been identified by Camerini *et al.*[36] The cross section of meson production per nucleon has been estimated to be 10 percent of the elastic cross section.

Lal *et al.*[26] found 7 meson showers produced by relativistic shower particles from very high-energy primary collisions. The showers are of the jet type (few evaporation tracks) and have a large angular spread. Since this type of shower is not observed in nucleon collisions, production by mesons has been assumed. The low excitation of the nucleus makes it improbable that scattering may have occurred. Therefore, some of the mesons are emitted originally with rather large angles to the primary meson. In the c.m. system more than half of all mesons are emitted in the backward hemisphere.

From experiments with artificial mesons of lower energy, not enough information is yet available to decide if, actually, the produced mesons are emitted preferentially in the backward direction.

IV. ACKNOWLEDGMENTS

The authors are especially grateful to Mrs. Elizabeth Medd for the very competent plate scanning, without which the experiment could not have been completed. The authors particularly thank Dr. George Snow for many interesting and helpful discussions.

Thanks are due the Brookhaven Cosmotron staff for their cooperation in making the exposures, especially Dr. S. J. Lindenbaum and Dr. L. C. L. Yuan for their advice and aid in this respect and John Quinn for his assistance in the preparation of the exposures. The assistance of Mrs. Elsie Schwarzer and Mrs. Margaret Carter in processing the emulsions is appreciated. We gratefully acknowledge the aid of Mrs. Barbara Cozine, who performed a great deal of the plate scanning during the early stages of the work. The assistance of Mrs. Jeanne Dennison with much of the multiple scattering calculations is acknowledged. The contribution and assistance of Joseph E. Smith in the early stages of the work is acknowledged with pleasure.

The authors wish to thank Dr. C. N. Yang for interesting discussions. One of the authors (MC), wishes to thank Professor W. A. McKinley of Rensselaer Polytechnic Institute for sponsoring his stay at Brookhaven.

[36] Camerini, Fowler, Lock, and Muirhead, Phil. Mag. 41, 413 (1950); Camerini, Davies, Fowler, Franzinetti, Lock, Perkins, and Yekutieli, Phil. Mag. 42, 1261 (1951).
[37] Crussard, Walker, and Koshiba (private communication).
[38] W. G. Rosser and M. I. Swift, Phil. Mag. 42, 856 (1951).

Electron Density Distribution near Large Air Shower Axes at Sea Level*†

R. E. HEINEMAN‡
H. M. Randall Laboratory, University of Michigan, Ann Arbor, Michigan
(Received April 15, 1954)

A large, multiple-wire ionization chamber has been used to sample 20 separate areas of the plane of observation to obtain detailed "profiles" of the structure of large air showers within about 2 meters of their axes. Interpretation of the data is based on (1) quantitative calculations of the transition effect in 0.305 radiation lengths of dural, and (2) a semiquantitative discussion of the fluctuations in the lateral-distribution function. Lateral distribution functions for electrons and photons of various energies have been calculated for $r<10$ meters at the shower maximum and the function for electrons of all energies turns out to be essentially equal to the one given by Molière. No drastic revision of the calculated distribution function is indicated by the data, but a flatter distribution than that calculated is not ruled out. Evidence for a multiple-core structure in a small percentage of cases is presented.

I. INTRODUCTION

IT has been supposed[1] for some time that a neutral π meson, the π^0, which decays into two photons after a very short lifetime, initiates the high-energy electronic cascades commonly called large air showers. This belief grew stronger as the existence of the π^0 was confirmed in the laboratory[2] and as experimental evidence was obtained in cloud-chamber work[3–5] which showed that π^0 mesons are the main, if not the exclusive, source of photons associated with cosmic-ray nuclear events. If a cascade shower is produced from each high-energy photon created in the decay of an energetic π^0 meson, and if there is a multiplicity of π^0's similar to the multiplicity of charged π mesons produced in high-energy nuclear events,[6] then it would be expected that, in general, large air showers would be composed of multiple shower cores. The lack of experimental confirmation of such multiple-cored events does not disprove the suspected π^0-meson origin since the numbers of such particles produced, their angular distribution, and their energy distribution are probably not known.[7] It seemed, therefore, that a more detailed study of the electron density in *individual* high-energy events than had been performed[8,9] previously might produce evidence as to their origin and shed some light on the characteristics of π^0 production.

At the time the work to be described here[10] was begun it could only be stated that the available data[8,9] on the electron-density distribution in large air showers at distances from 2 to 100 meters from the core gave no indication of a multiple-core structure, and, moreover, showed no incompatibility with the theoretical distribution obtained by Molière[11] for a single shower core. More recent studies[12,13] of the electron distributions found by using a large cloud chamber or a cloud chamber in conjunction with five ionization chambers presented evidence of a "lumpy" distribution near the axes of the showers in a small percentage of cases. The experimental shower "profiles" to be presented here (some of which appeared in reference 10) are in substantial agreement with the foregoing conclusion.

The present experiment was designed to obtain the electron-density distribution within 2 meters of the core in each useful shower event recorded by using a multiple-wire ionization chamber. The chamber has a sensitive area of 0.97 m^2 and a wire separation of 10 cm for each of the 20 pulse channels. The use of such a chamber combines the well-defined density measurement obtainable with an ion chamber (as compared to geiger-counter arrays) with the resolution of a cloud chamber. This apparatus is capable of resolving two cores, each having equal energies and "$1/r$" density distributions, separated by 30 to 60 cm in a direction perpendicular to the chamber wires. The actual resolution is dependent upon the local size of the shower and the distance of the axes from the center of the chamber.

The data were obtained at an elevation of about 280 meters and, therefore, at a depth in the atmosphere 26.4-radiation lengths where the characteristic scatter-

* Supported in part by the U. S. Office of Naval Research and the U. S. Atomic Energy Commission.

† Based on a thesis submitted in partial fulfillment of the requirements for a Ph.D. degree at the University of Michigan, Ann Arbor, Michigan.

‡ Present address: General Electric Company, Hanford Atomic Products Operation, Richland, Washington.

[1] Lewis, Oppenheimer, and Wouthuysen, Phys. Rev. **73**, 127 (1948).

[2] Bjorklund, Crandall, Moyer, and York, Phys. Rev. **77**, 213 (1950); Panofsky, Aamodt, Hadley, and Phillips, Phys. Rev. **80**, 94 (1950); Steinberger, Panofsky, and Steller, Phys. Rev. **78**, 802 (1950).

[3] B. Gregory and J. Tinlot, Phys. Rev. **81**, 675 (1951).

[4] P. R. Barker, Phys. Rev. **81**, 291 (1951).

[5] G. Salvini and Y. B. Kim, Phys. Rev. **88**, 40 (1952).

[6] Kaplan, Ritson, and Walker, Phys. Rev. **90**, 716 (1953); Lal, Pal, Peters, and Swami, Proc. Indian Acad. Sci. **36**, 75 (1952); Lord, Fainberg, and Schein, Phys. Rev. **80**, 970 (1950); see also, E. Fermi, Progr. Theoret. Phys. **5**, 570 (1950).

[7] Hazen, Heineman, and Lennox, Phys. Rev. **86**, 198 (1952).

[8] R. W. Williams, Phys. Rev. **74**, 1689 (1948).

[9] Cocconi, Tongiorgi, and Greisen, Phys. Rev. **76**, 1020 (1949).

[10] Some of the work and results contained here have been briefly outlined previously: R. E. Heineman and W. E. Hazen, Phys. Rev. **90**, 496 (1953).

[11] G. Molière, *Cosmic Radiation* (Dover Publications, New York, 1946).

[12] W. E. Hazen, Phys. Rev. **85**, 455 (1952).

[13] Hazen, Williams, and Randall, Phys. Rev. **93**, 578 (1954).

ing length r_1 is 80 m. We have used $X_0=37.7$ g/cm^2 for the radiation length in air. The sensitive volume of the chamber was shielded from the upper hemisphere by the chamber cover plate of 1-in. dural and an additional 0.05 in. of aluminum. The transition effect in this material is calculated in Sec. III. The chamber was placed with its long axis in a north-south direction, which thus minimizes the effect (only recently pointed out by Cocconi[14]) of the earth's magnetic field on the electron lateral distribution.

II. EXPERIMENTAL

A. General

A block diagram of the equipment used is presented in Fig. 1.

When all 4 Geiger counters are discharged within the resolving time (45 μsec) of the coincidence circuit, the probability is great that a shower core has hit within a few meters of the center of the ionization chamber. The output of the coincidence circuit trips the sweep and brightener circuits of a 20-channel synchroscope which displays the amplified pulses from the ion chamber. The electron pulses induced on the central wires of the chamber by the passage of shower electrons through the chamber are separately amplified, first by preamps having a clipping time constant of about 700 μsec, and then by a 20-channel amplifier. The latter amplifier was purposely constructed to be moderately nonlinear to accommodate a larger range of input voltage pulses. After the array of pulses appearing on the cathode-ray tubes are recorded on 35-mm film, a trigger from the synchroscope rewinds the camera in preparation for the next 4-fold coincidence and records a count on a mechanical register. The time of each event is also recorded by briefly illuminating the face of a clock mounted on the synchroscope chassis. The long time constants in the amplifiers are necessary because of the poor photographic properties of the light output from the green-phosphor cathode-ray tubes used. The Geiger counters have a sensitive area of 350 cm^2 and were positioned at the ends and sides of the ionization chamber, 132 and 67 cm from the center of the chamber, respectively. Since the selection of interesting events can easily be made by looking at the photographic record, a more selective triggering system is not necessary.

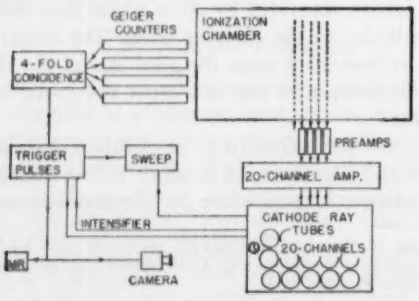

FIG. 1. Block diagram of experimental apparatus.

B. Ionization Chamber

The ionization chamber, shown schematically in Fig. 2 with the top plate removed, has $\frac{5}{16}$-in. steel sides, 1-in. dural top and bottom, and has a collecting volume of 7 ft 6 in.$\times$25 in.$\times$8 in. To make end effects small (transition effect in the steel walls and capacitance to the end walls), a dummy collecting wire is placed at each end of the chamber. Grounded cylindrical guard rings are used on both ends of each of the remaining 20 collecting wires which are connected to the ground through separate 100-meg resistors. The chamber itself is connected to the high-voltage supply and shielded by a grounded aluminum and galvanized-iron box.

Calibration polonium-α sources were deposited on a copper rod which lies inside a brass cylinder on the bottom of the chamber. The rod can be turned so that α particles are emitted through holes in the cylinder beneath each of the 20 wires or turned so that they are completely absorbed in the walls of the cylinder. In addition, one source is so constructed that it can be moved vertically from the bottom plate up to the wire above it in order to test for electron attachment in impurities in the argon filling the chamber. This test

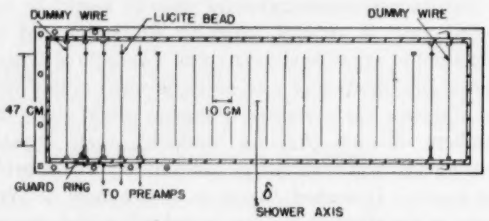

FIG. 2. Schematic diagram of the ion chamber with its 1-in. dural top removed. The parameter δ locates the shower axis in a direction perpendicular to the long axis of the chamber.

was suggested by Driggers,[15] and his results are confirmed as described below.

The α-pulse heights which were recorded as the movable source was positioned at varying distances from the central wire, before and after successive attempts at purification of the argon, are shown in Fig. 3. The argon was purified by circulating it through a heated cylinder containing calcium turnings. Positive circulation was ensured by connecting a centrifugal fan to the rotor of an induction motor within the pressurized system. For the case in which there is no attachment the α-pulse heights should decrease as the source is moved closer to the wire, because of the ionization being deposited in regions of lower potential. This

[14] G. Cocconi, Phys. Rev. **93**, 646 (1954).

[15] F. E. Driggers, Phys. Rev. **87**, 1080 (1952).

decrease should not be very drastic since the range of the α particles is only 0.5 cm (37 psia of argon) and the rod is in contact with the high voltage shell of the chamber. To predict the decrease quantitatively is difficult since the field geometry is complicated and the source emits particles in any direction within the upper hemisphere. For the latter reason, it is expected that widely varying pulse heights should be observed for source-to-wire distances that are of the order of the range of the alpha particles. This was indeed observed and makes the uncertainty in the pulse-height determinations relatively large for these small distances. The decrease in pulse height from curve I to II is assumed to be caused by outgassing of the calcium turnings and

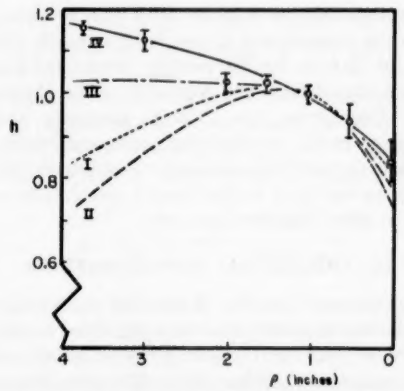

FIG. 3. Relative polonium α-pulse height h *vs* distance ρ of an α source from a central collecting wire. The curves are normalized to 1.0 at $\rho=1$. The data in curve I were taken before attempting purification, and the data for the other curves were taken after the purifier had been operated for 4 hours at 250 watts (II), 2 hours at 500 watts (III), and 3 hours at 500 watts (IV). Typical estimated errors are given for curve IV.

purifier, while curves III and IV indicate a decreasing attachment probability with further purification.

In Fig. 4 are presented typical saturation curves of a single channel taken before and after purification. They show the α-pulse height for a stationary source *vs* the chamber high-voltage. From the shapes of these curves it is evident that the saturation of the α-pulse height as the chamber voltage is increased does not necessarily, in itself, indicate the absence of electron attachment.

C. Measurement of Ionization

The passage of a high-energy shower electron through the chamber produces ionization, low-energy electrons, and positive argon ions. The quantities measured directly for each event are the numbers of these secondary electrons which are liberated within the sensitive volumes of each of the 20 wires, as described in this section. It will be shown in the next section that there is a simple relationship between these

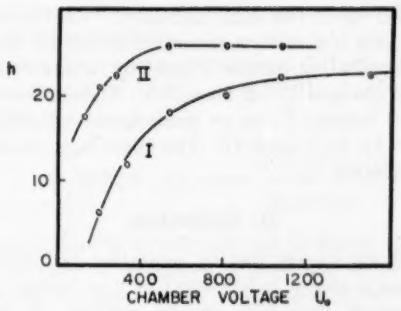

FIG. 4. Saturation curves taken with an α source at the bottom of the chamber before (I) and after (II) purification of the argon: α-pulse height h *vs* chamber voltage U_0.

numbers and the numbers of shower electrons passing through each of these volumes.

Rossi and Staub[16] have shown that the voltage pulse appearing across the collecting electrode and ground of an ion chamber is

$$V=\frac{e}{C}\frac{1}{U}\sum_{i=1}^{N_0}U_i,$$

if the output-time constant of the chamber is so long that all the electrons are collected but short enough so that the positive ions have not moved appreciably from their position of formation when the pulse begins to decay. In this expression, C is the output capacitance of the collecting electrode, e is the charge on an electron, U is the high voltage on the chamber, N_0 is the number of ion pairs formed in the sensitive volume of the collecting electrode, and U_i is the potential at the position of formation of the ith ion pair. Since the number of shower electrons passing through the chamber in each recorded event will be rather large, it is reasonable to assume that little error will be incurred by using the value of $\sum_i U_i$ which would be found for a uniform distribution of ionization throughout each sensitive volume. Then we may write

$$V=\frac{eN_0}{C}\frac{\bar{U}_i}{U}=\frac{eN_0}{C}f,$$

where $f=0.87$, as calculated for our chamber geometry. It can easily be shown that the presence of one dummy wire on each end of the chamber is sufficient to make the value of f essentially the same for all collecting volumes.

It is obvious that the foregoing method of finding the voltage pulse on a wire may be validly applied to our chamber only insofar as the ionization which is collected solely on that wire does not affect the potentials of the other wires. The magnitude of the

[16] B. Rossi and H. Staub, *Ionization Chambers and Counters* (McGraw-Hill Book Company, Inc., New York, 1949).

induction effect has been calculated[17] for the case in which there is a uniform density of ionization throughout the collecting volume of one wire, whose voltage is thereby changed by an amount V. Then it was found that the voltage V_1 on an immediately adjacent wire is given by $V_1=-0.027V$. The effect is so small that it is neglected.

D. Calibration

Since the energy loss by ionization for relativistic electrons is almost independent of their energy, it can be assumed that each shower electron, in passing through the chamber of height l centimeters, liberates the same number of ion pairs $N_0=lj\delta$. δ is the density of argon in g/cm³ and j is the average specific ionization of the electron in ion pairs per g/cm². Then, from the previous section the voltage pulse produced by Π shower electrons whose ionization is all collected on one wire is given by

$$V=\Pi N_0 ef/C=\Pi efl j\delta/C.$$

To calibrate the output voltage V, either a known amount of ionization must be placed in the chamber or the capacitance C determined. Since C is very difficult to evaluate, the former method is used. It has been shown[18] that the number of ion pairs formed by an alpha particle in argon is proportional to its energy. If we let W_0 be the energy necessary to form one ion pair, the pulse height V_α observed because of the collection of the charge produced by an alpha particle of energy E_α is $Q_\alpha/C=(E_\alpha/W_0)/C$. The factor f does not appear because the α sources are located near the shell of the chamber where the potential changes only slightly within a distance equal to the range of the α particles. Eliminating the capacitance in the above expressions, we find

$$\Pi=\frac{E_\alpha}{efl\delta jW_0}\frac{V}{V_\alpha}.$$

Since it is believed[19] on theoretical grounds that the energy W_0 expended to form one ion pair is independent of the type of ionizing particle, jW_0 may be considered to be the energy dissipated in collision processes by the shower electron. Since the average energy of shower electrons is 100 Mev,[20] jW_0 is found to be 2.1×10^6 ev g/cm². It is to be noted that the *total* energy loss by collision should be used since shower theory, which is used to interpret the data, does not count energetic secondary electrons produced by collision as separate shower electrons. Though some collisions give rise to secondary electrons so energetic that they do not dissipate all their energy before leaving the argon, there are a compensating number of secondary electrons entering the chamber since the collision probabilities and energy loss in argon and in air (or aluminum) are almost the same.

Calibration pulses are recorded by uncovering the sources and tripping the sweep circuit at random. Since the alphas are released at random also, the superposition of a large number of sweeps produces a row of pulses whose heights can easily be measured. As a secondary calibration for the nonlinear amplifiers, a precision pulser is used to pulse the shell of the chamber, inducing pulses of identical voltages on all 20 channels, and to trip the sweep circuit simultaneously.

By comparing an α pulse with the induced-pulse heights the capacitance C can be calculated. Using a value[15] of 26.4 ev for W_0, we find that $C=4.2\ \mu\mu$f. A value calculated from the geometry of the chamber is $4.3\ \mu\mu$f. Considering the difficult geometry and the uncertainty in W_0, we find the agreement better than could be expected. This calculation is of interest because it increases our faith in the similar calculations of the induction effect between channels.

III. THEORETICAL CONSIDERATIONS

It was shown in section II that the pulse heights on the cathode-ray tubes could be interpreted in terms of numbers of electrons traversing the sensitive volumes of the ionization-chamber wires. However, because of the transition effect in the 1.05 in. of dural above the collecting volume of the chamber, these numbers are not necessarily the same as the numbers of electrons in the air shower incident on the dural. Since this effect is dependent upon the energies and the relative numbers of electrons and photons, it depends also upon r, distance from the shower axis. Therefore, in part A below we use the results of shower theory to calculate the lateral distribution of electrons under 1.05-in. dural, and from this distribution we calculate, in B, the response of the ion-chamber channels to such a distribution. We must then look for consistency between observed data and the calculated response curves. If inconsistencies are found, they could conceivably be explained by assuming that (1) shower theory, as used here, inadequately describes the showers observed; (2) there is a multiplicity of cores associated with a particular event; or (3) the fluctuations in the lateral development of showers are large. These possible departures from the response curves calculated for the average single shower core are discussed in C and D.

A. Lateral Distribution of Electrons Under 1.05 in. Dural

A general description of the method used to find this distribution will first be given. The calculations of the

[17] R. E. Heineman, thesis, University of Michigan, 1953 (unpublished).
[18] Jesse, Forstat, and Sadauskis, Phys. Rev. 77, 782 (1950).
[19] B. Rossi, *High Energy Particles* (Prentice-Hall, Inc., New York, 1952).
[20] B. Rossi and K. Greisen, Revs. Modern Phys. 13, 240 (1941).

specific functions and constants required by this method are outlined in the succeeding subsections.

Let $P_r(E,r,s)rdrdE$ be the average relative number of electrons of energy E in dE passing through the plane of observation in an annular ring between r and $r+dr$ from the axis, and in a direction making any angle ϑ with the axis, of a shower of age s. Let this function be normalized such that

$$\int_0^\infty P_r(E,r,s)rdr=\frac{\pi(E_0,E,t)}{\Pi(E_0,0,t)},$$

and (1)

$$\int_0^\infty\int_0^\infty P_r(E,r,s)rdrdE=1,$$

where $\pi(E_0,E,t)dE$ is the number of electrons of energy E in dE found at a depth t from the origin of a shower of total energy E_0 and $\Pi(E_0,0,t)$ is the number of electrons in the shower at depth t having energies $E>0$. The age parameter s is a function of E_0 and t, defined by Eq. (2.104) of reference 19. Let $Q_r(W,r,s)rdrdW$ be a similar function for the photons of energy W, where

$$\int_0^\infty Q_r(W,r,s)rdr=\frac{\gamma(E_0,W,t)}{\Pi(E_0,0,t)}, \qquad (2)$$

and γ is the differential photon spectrum. Q_r is normalized with respect to Π because, in the usual shower theory approximations, the corresponding integral photon function, $\lim_{W\to 0}\Gamma(E_0,W,t)$, is infinite.

Let $\mathfrak{N}(E_1,E_2;r,s,\tau)$ be the relative number of electrons of energy between E_1 and E_2 found in an annular ring between r and $r+dr$ under a thickness of absorber τ when a shower of age s is incident above the absorber; and let $n(E',r,s,\tau)dE'$ be the corresponding number of electrons of energy E' in dE'. Then we may write

$$\mathfrak{N}(E_1,E_2;r,s,\tau)=\int_{E_1}^{E_2} n(E',r,s,\tau)dE,$$

and (3)

$$n(E',r,s,\tau)=\int_0^\infty T(E,E',\tau)rP_r(E,r,s)dE + \int_0^\infty T(W,E',\tau)rQ_r(W,r,s)dW.$$

The function $T(E,E',\tau)$ is the number of electrons of energy E' created in the absorber, relative to the number of electrons of energy E which were incident on the absorber and led to their creation. Similarly, $T(W,E',\tau)$ is the number of electrons of energy E' produced relative to the number of incident photons of energy W which led to their creation. It is assumed that neither a particle nor any of its secondary electrons experiences a displacement in r in traversing the layer. For the great majority of all electrons, this displacement is small compared to the separation of the detector areas in this experiment.

The function we want to calculate, $\mathfrak{N}(0,\infty;r,s,\tau)$, for τ equal to 1.05-in. dural, or $0.304X_0$, is normalized such that

$$\int_0^\infty \mathfrak{N}(0,\infty;r,s,\tau)dr=\frac{\Pi(E_0,0,t+\tau)}{\Pi(E_0,0,t)}.$$

The dependence of $\mathfrak{N}$ on τ will not be shown hereafter since we shall be interested in only one value of this parameter. Because very little is known about P_r and Q_r for any point in the shower development except the maximum, it will be assumed that all showers incident on the chamber are at their maximum. The dependence on s need not be shown explicitly since $s=1$ will be understood.

The integrations in (3) must be performed numerically since good analytical functions for P_r and Q_r are not available for all energies. The functions $T(E,E')$ and $T(W,E')$ vary slowly with E and W. We may therefore use a small number of energy intervals ΔE_i and ΔW_i, and represent the functions T in each interval by constants, which are called *transition factors*. They are the values of the functions calculated at an energy equal to the median electron energy of each interval. With the above simplications, we use (3) and obtain

$$\mathfrak{N}(0,\infty;r)=\sum_j n(\Delta E_j;r),$$

and (4)

$$n(\Delta E_j,r)=\sum_i\{T(\bar{E}_i,\Delta E_j)N_e(\Delta E_i;r) + T(\bar{W}_i,\Delta E_j)N_p(\Delta W_i;r)\},$$

where

$$N_e(\Delta E_i;r)=\int_{\Delta E_i} rP_r(E,r)dE \qquad (5)$$

is the distribution function for incident electrons having energies in the energy range ΔE_i. $N_p(\Delta E_i;r)$ is a similar function for the incident photons. Equation (4) may be rewritten, so that the distribution function for electrons of all energies under the layer of dural is

$$\mathfrak{N}(0,\infty;r)=\sum_i\{\sum_j[T(\bar{E}_i,\Delta E_j)]N_e(\Delta E_i;r) + \sum_j[T(\bar{W}_i,\Delta E_j)]N_p(\Delta W_i;r)\}. \qquad (6)$$

(1) *Lateral Distributions of Incident Electrons*—$N_e(E_1,E_2;r)$

The incident electrons have been divided into five energy ranges, and the corresponding radial distribution functions which have been calculated are shown in Fig. 5.

From Eqs. (1) and (5), it is seen that these functions must satisfy the condition that

$$\int_0^\infty N_e(E_1,E_2;r)dr\cong\frac{P_0(E_0,E_2)-P_0(E_0,E_1)}{P_0(E_0,0)}, \qquad (7)$$

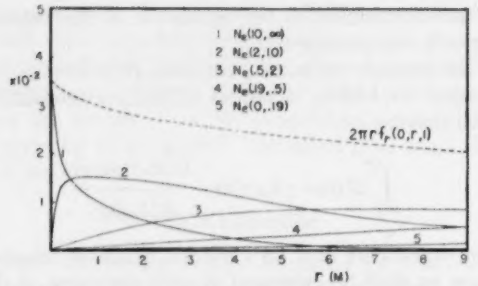

FIG. 5. Lateral distribution functions for shower electrons of energy in the range ΔE_i, $N_e(E_1,E_2;r)$, and the Molière function, $2\pi r f_r$, for electrons of all energies. The curves refer to showers at their maximum in air where $r_1=80$ m. Energies are in units of the critical energy ϵ_0.

where $P_0(E_0,E)$ is the integral track length of electrons of energy greater than E, used in shower theory.[19,20] The approximation indicated is best when E_0 and t are such that the shower is at its maximum. To evaluate (7) we have connected the numerical results of Richards and Nordheim,[21] for $E\leq 3\epsilon_0$, to the results of shower theory Approximation A, where ϵ_0 is the critical energy in air, 84.2 Mev.[19] These results allow a normalization of the functions $P_r(x)$, where $x=(Er)/\epsilon_0 r_1$, given by Eyges and Fernbach.[22]

Since the method used by EF did not give the behavior of the functions $P_r(x)$ near $x=0$, they did not prescribe their functions in this region except for very high energies, $E>10\epsilon_0$. In this case they used the similar high-energy function obtained by Molière to continue their function to $x=0$. Since the Molière function does not fit smoothly with the distributions given by EF for lower energies, we have continued the latter to zero (on a log-log plot in which the curvature is minimized) in such a way that they preserve the general shape of Molière's high-energy function. It is to be noted, however, that the normalization is found independently and that there is little freedom left in the process of continuing the curves smoothly to zero.

It is perhaps surprising that the sum of our distribution functions is essentially equal to the total-distribution function of Molière[11] since different approximations have been used in each. The form of this function which has been given by Bethe[8] is

$$2\pi r f_r(0,r,1)=0.454(2\pi r_1)(1+4r/r_1)\exp[-4(r/r_1)^{\frac{1}{2}}],$$

and is shown in Fig. 5 also. Actually, we might hope that our treatment is better than that of Molière for the range of r considered. For high energies, $E>10\epsilon_0$, the functions used here are probably better, though equal to Molière's high-energy function near $r=0$. For intermediate energies, $2\epsilon_0\leq E\leq 10\epsilon_0$, the functions used are similar to Molière's high-energy function for $r<10$ m, but differ in their normalization. For low energies, $E<2\epsilon_0$, the function used was that constructed from the EF function for $E=2\epsilon_0$. Though this function would again be similar to the one used by Molière, the relative numbers of low-energy electrons should be quite reliable in our calculations as compared with the rather poor approximations available to Molière (see Blatt[23]). Though there has been some controversy recently[24,25] concerning the assumptions underlying the calculations of EF and Molière, our use of the results of the former can be regarded as a choice of a first-order approximation which seems to have given at least fair agreement with experiment in the past.

(2) *Lateral Distributions of Incident Photons*—$N_p(W_1,W_2;r)$

The calculated lateral photon distributions for the four ranges of photon energies above $0.19\epsilon_0$ are shown in Fig. 6, together with Molière's electron distribution for $E>0$ (dotted). The photon distributions were obtained as follows.

A comparison of the renormalized Molière photon distribution,[26] for energies $W\gg\epsilon_0$, with the numerical photon distributions, for energies $W>10\epsilon_0$ and $W=10\epsilon_0$, $5\epsilon_0$, and $2\epsilon_0$, given by Eyges and Fernbach,[22] showed good agreement for the range of r to be considered. The renormalized,[22] analytical distribution $Q_r'(x)$ of Molière was therefore used, since it could be integrated easily. This distribution is

$$Q_r'(x)=\frac{31.94\exp\left(-\dfrac{2x}{(0.1)^{\frac{1}{2}}}\right)}{\dfrac{2x}{(0.1)^{\frac{1}{2}}}}+\frac{0.806}{3.25}\exp\left(-\frac{2x}{(3.25)^{\frac{1}{2}}}\right)$$

where $x=(Wr)/\epsilon_0 r_1$ and $\int_0^\infty Q_r'(x)x\,dx=1$. This function

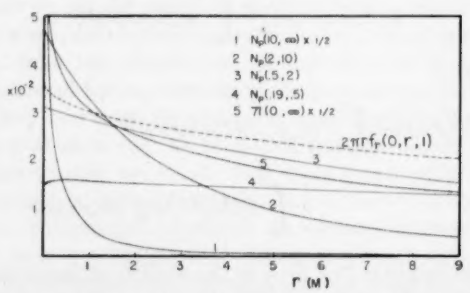

FIG. 6. Lateral distribution functions for shower photons of energy in the range ΔW_i, $N_p(W_1,W_2;r)$; the Molière electron distribution, $2\pi r f_r$; and the distribution function for electrons of all energies under 1.05-in. dural, $\mathfrak{N}(0,\infty;r)$. The curves refer to showers at their maximum in air where $r_1=80$ m. Energies are in units of the critical energy ϵ_0.

[21] J. Richards and L. Nordheim, Phys. Rev. **74**, 1106 (1948).
[22] L. Eyges and S. Fernbach, Phys. Rev. **82**, 23 (1951), hereinafter referred to as EF.
[23] J. M. Blatt, Phys. Rev. **75**, 1584 (1949).
[24] H. S. Green and H. Messel, Phys. Rev. **88**, 331 (1952).
[25] G. Molière, Phys. Rev. **93**, 636 (1954).
[26] G. Molière, Phys. Rev. **77**, 715 (1950).

is normalized correctly for high energies where the Approximation A of shower theory is correct. Since it does not give the correct numbers of photons at lower energies, we introduce a correction function $\sigma(W)$ given by

$$\sigma(W)=\frac{r_1^2}{0.437}\frac{Q_r(W,r)}{Q_r'(x)}.$$

By comparing the normalization of $Q_r'(x)$ with that for $Q_r(W,r)$ given by (2), we find

$$\sigma(W)=\frac{1}{0.437}\left(\frac{W}{\epsilon_0}\right)^2\frac{\gamma(E_0,W,t)}{\pi(E_0,W,t)}\frac{\pi(E_0,W,t)}{\Pi(E_0,0,t)},$$

from which $\sigma(W)$ will be calculated. At high energies under Approximation A, it is found that $\gamma/\pi=9/7$ and $\pi/\Pi=0.437(\epsilon_0/W)^2$. At lower energies we equate γ/π to $g_0(E_0,W)/p_0(E_0,W)$, where g_0 and p_0 are the differential track lengths of photons and electrons of energy W, respectively; and π/Π to $p_0(E_0,W)/P_0(E_0,0)$, where $P_0(W,0)$ is the integral track length of all electrons having energy $W>0$. Using values for the track lengths calculated by Richards and Nordheim,[21] we plot g_0/p_0 as curve I and $(\pi/\Pi)_{\text{Approx A}}/(p_0/P_0)$ as curve II in Fig. 7. It is seen that both curves vary much more rapidly with energy than $1/\sigma(W)$, shown as curve III in Fig. 7.

The incident photon distributions can then be written

$$N_p(W_1,W_2;r)=\frac{0.437}{r_1^2}\sigma(\bar{W}_i)\int_{x_1}^{x_2}Q_r'(x)dx, \qquad (8)$$

where $\sigma(W)$ has been replaced by an average value, $\sigma(\bar{W}_i)$, over the energy range considered. The values of $\sigma(\bar{W}_i)$ which were used are given in Table I.

In calculating the distribution for the highest energy range, $(10\epsilon_0,\infty)$, W_2 in (8) should not, of course, be ∞, but some upper limit $W_{\max}<E_0$. Even though the lower limit, W_1, is much less than $W_{\max}$ in our case, the detailed behavior of the integral for r less than 5 or perhaps 10 cm is dependent upon $W_{\max}$. Since our ionization chamber is insensitive to changes in the distribution function at such small distances from the shower core, we have made suitable assumptions concerning the height of production of the showers, their energies, and the degradation of this energy. The approximations made should give an adequate representation of the distribution near $r=0$ for all showers observed.

TABLE I. The average values of $\sigma(W)$, $\sigma(\bar{W}_i)$, for the energy ranges (W_1,W_2). Energies are in units of the critical energy ϵ_0.

(W_1,W_2)	$(10,\infty)$	(2,10)	(0.5,2)	(0.19,0.5)
$\bar{W}_i$	20	3.75	0.92	0.31
$\sigma(\bar{W}_i)$	1.22	1.06	0.81	0.55

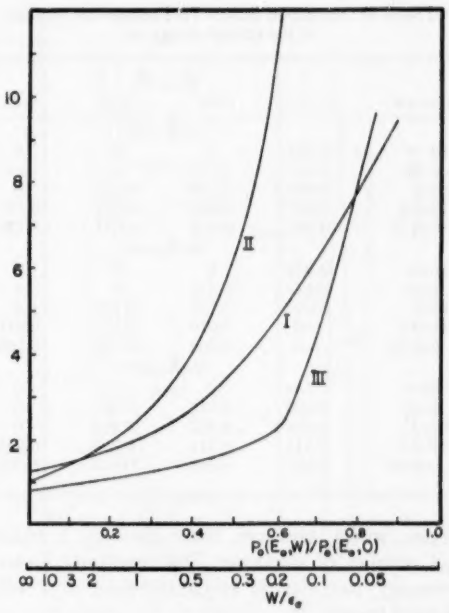

FIG. 7. Curve I: $g_0(E_0,W)/p_0(E_0,W)$. Curve II: $[\pi(E_0,W)/\Pi(E_0,0)]_{\text{Approx. A}}/[p_0(E_0,W)/P_0(E_0,0)]$. Curve III: $1/\sigma(W)$. $\sigma(W)$ is a slowly varying function which ensures a correct normalization of the photon distribution functions for photon energies $W<10\epsilon_0$ and is equal to [Curve I/Curve II].

(3) *Transition Factors*—$T(\bar{E}_i,\Delta E_j)$ and $T(\bar{W}_i,\Delta E_j)$

The calculations to be outlined in this section can be grouped into two portions. First, under the assumption that the secondary particles produced in the dural do not cause further multiplication we find transition factors which are labeled T_0. Second, the factors T_0 are used to obtain the transition factors T, which take account of the interactions of the secondaries. For example, we must find the numbers of photons in an energy range ΔW_j, which are radiated by electrons in any other possible energy range, of median energy $\bar{E}_i$, and which materialize before reaching the bottom of the dural layer. The inclusion of secondary interactions does not necessitate a revision of our general method as summarized in Eq. (6), since, for the example above, the electron pairs will be counted in the end as if they were created directly by the incident electrons.

The results of the first part of this work are shown in Table II. It is to be noted that though we calculate $T_0(\bar{E}_i,\Delta W_j)$, the number of photons in the energy range ΔW_j produced by electrons having a median energy $\bar{E}_i$ (so that their secondary electrons may be found), we do not present factors $T_0(\bar{W}_i,\Delta W_j)$ since processes in which photons are simply degraded in energy are not significant at these high energies.

The results of the second portion of the calculations are presented in Table III. By comparing the results of Tables II and III it is easily seen that the corrections for secondary interactions are small except at low

TABLE II. Transition factors T_0. Energies are in units of the critical energy ϵ_0.

ΔE_j or ΔW_j	$\bar{E}_i$ or $\bar{W}_i$ 20	3.75	0.92	0.31
	$T_0(\bar{W}_i,\Delta E_j)$			
10–∞	0.207	0	0	0
2–10	0.158	0.172	0	0
0.5–2	0.036	0.144	0.160	0
0.19–0.5	0.007	0.034	0.101	0.112
0–0.19	0.004	0.013	0.051	0.130
	$T_0(\bar{E}_i,\Delta E_j)$			
10–∞	0.834	0	0	0
2–10	0.147	0.823	0	0
0.5–2	0.019	0.149	0.842	0
0.19–0.5	~0	0.019	0.122	0.831
0–0.19	~0	0.008	0.036	0.169
	$T_0(\bar{E}_i,\Delta W_j)$			
10–∞	0.168	0	0	0
2–10	0.490	0.141	0	0
0.5–2	0.495	0.402	0.115	0
0.19–0.5	0.342	0.341	0.262	0.068
0–0.19	0.607	0.588	0.555	0.393

energies, where, however, there are only a relatively small number of electrons. The treatment given the low-energy particles is straightforward and will be discussed briefly.

We neglect the incident electrons in the range $(0,0.19\epsilon_0)$ entirely, since it has been shown by Barker[27] that the average effective range of electrons of energy 16 Mev $=0.19\epsilon_0$ is 1.05-in. dural if ionization and radiation losses are fully taken into account. As we shall see below, the small numbers of incident photons in this energy range will scatter few electrons or produce few pairs of electrons having sufficient energy to penetrate the rest of the dural; and they have been neglected also. Thus, we must consider further only the low-energy secondaries produced in the dural.

It can easily be estimated that only about 20.2 percent of those electrons *produced* in the energy interval $(0,0.19\epsilon_0)$, by either pair production or radiation, from particles in higher energy ranges would be observed under the dural. It can also be shown that the number of observable electrons arising from Compton scattering of secondary photons in the energy range $(0.04\epsilon_0,0.19\epsilon_0)$ is about 3.3 percent of the number of photons, and almost independent of their energy, in this range. Since the probability of pair production is equal to the total probability for Compton scattering at about 16 Mev $=0.19\epsilon_0$, the Compton scattering factor has been doubled to give an approximate upper limit for both processes. The transition factors for these low-energy particles were then computed and listed in Table III.

The lateral distribution of electrons under 1.05-in. dural, $\mathfrak{N}(0,\infty;r)$, is then obtained, according to (7), by multiplying each lateral distribution curve found in Secs. III.A(1) and III.A(2) by the sum of the appropriate transition factors from Table III and adding. The result is shown in Fig. 6.

[27] P. R. Barker, thesis, University of Michigan, 1952 (unpublished).

B. Ionization Chamber Response Curves

A set of curves has been prepared which gives the number of shower electrons passing through the sensitive volume of each wire when showers characterized by a lateral distribution function $\mathfrak{N}(0,\infty;r)$ pass through the plane of observation in the vicinity of the chamber. The coordinates in the plane of observation have been designated "wire number" and δ. The ion-chamber wires are labeled with consecutive integers from the shower axis outward. δ is the distance of the shower core from the center of the chamber in a direction perpendicular to the long axis of the chamber (see Fig. 2). This set of response curves is shown in Fig. 8 and assumes a total number of electrons $\Pi(E_0,0,t)=2\times10^4$. Since the number of electrons N_i per channel is directly proportional to Π, curves for different values of Π are easily obtained from those of Fig. 8.

In general, Fig. 8 presents 2 curves for every value of δ, though the curves differ only near the shower axis. Each peaked curve is for a shower that hits one wire (numbered 0) directly. Each flat-topped curve is for a shower which hits between 2 wires. The dotted curve shows the response of the chamber, for $\delta=0$, to a Molière distribution, which is not corrected for the transition effect. If all ordinates of this response curve are multiplied by a factor 2, then the curve is almost identical to the response curve, corrected for the transition effect, for $\delta=23.5$ cm. We see that the transition effect sharpens the distribution by increasing the peak height and decreasing the half-width slightly. This is to be expected since: (1) the spread of a shower is proportional to the characteristic scattering length, which is 80 m for air and 4 cm for Al; and (2) the multiplication of the high-energy particles is inversely proportional to the radiation length, which is 37.7 g/cm² for air and 24.5 g/cm² for Al, while the energy loss by collision for the low-energy electrons per g/cm² is almost the same for air and aluminum.

C. Systematic Departures from the Response Curves

The response curves were obtained under the assumption of a lateral distribution function for a cascade shower, initiated by one particle and observed at its maximum. Thus, it would be expected that the experi-

TABLE III. Transition factors $T(\bar{E}_i,\Delta E_j)$ and $T(\bar{W}_i,\Delta E_j)$. Energies are in units of the critical energy ϵ_0.

ΔE_j	$\bar{E}_i$ 20	3.75	0.92	0.31	$\bar{W}_i$ 20	3.75	0.92	0.31
10–∞	0.85	0	0	0	0.19	0	0	0
2–10	0.19	0.83	0	0	0.17	0.16	0	0
0.5–2	0.11	0.18	0.85	0	0.06	0.15	0.15	0
0.19–0.5	0.05	0.06	0.12	0.83	0.02	0.05	0.10	0.10
0–0.19	0.06	0.05	0.05	0.06	0.01	0.01	0.02	0.03
	$\Sigma_j T(\bar{E}_i,\Delta E_j)$				$\Sigma_j T(\bar{W}_i,\Delta E_j)$			
0–∞	1.26	1.12	1.02	0.89	0.45	0.37	0.27	0.13

mental data will exhibit systematic departures from the theoretical curves.

First, if one considers the region around the shower axis where the majority of all electrons have energies $E \gg \epsilon_0$, that is, $r \ll r_1$, it has been shown[28] that the total distribution function has a singularity which behaves as $1/r^{2-s}$ where, of course, $s=1$ for the shower maximum. Though it would be difficult to ascertain the exact effect which would result from our attempt to analyze data from relatively old showers on the basis of curves calculated for the shower maximum, it is plausible that, if δ may be used as a variable parameter, the distribution in the assigned values of δ would not be random; i.e., there would be no events which fit the response curve for $\delta=0$, but there would be a disproportionate number which fit the curves for rather large values of δ.

Second, it is to be expected as discussed in Sec. I that the large air showers are, in general, superpositions of showers of various energies initiated by decay photons from more than one π^0 meson. In order to be able to resolve multiple maxima in this experiment, the separate showers giving rise to the individual maxima must have (1) comparable energies, (2) separations $d \gtrsim 30$ cm, and (3) their cores lying on a line nearly parallel to the long axis of the ion chamber. With these requirements in mind, we shall consider single and multiple π^0 production.

If a single π^0 meson is the precursor of a shower, a double core would be expected. In order to ascertain whether or not the structure should be observed experimentally, the energies and angular separations of the decay photons must be determined. In the extreme relativistic case, $E_{\pi^0} \gg m_0c^2$, where E_{π^0} is the energy of the meson and m_0 its rest mass, it can easily be shown that to a very good approximation the angular separation is $2m_0c^2/E_{\pi^0}$. The approximation becomes poor only when most of the energy of the π^0 is carried off by one of the photons. However, the resulting shower structure would not be resolvable under this condition because of statistics. If the neutral mesons are assumed to have been produced at an altitude of 15 km, the above expression implies a lateral separation of π^0-decay-photon showers of

$$d(\text{cm}) = 4.1 \times 10^{14}/E_{\pi^0}(\text{ev}).$$

The question of the separations to be expected between cores produced by two or more neutral mesons is, probably, still unanswered. The suggestion of Lewis *et al.*[1] is not satisfying because, contrary to experiment, it predicts multiplicities of about 100 at the usual shower energies with core separations of about 10 meters at the observation level. By using the thermodynamic approximation[29] of Fermi's statistical theory of multiple meson production, estimates closer to experimental observations have been obtained.[7] The predicted separations are still too large—about 1 to 10 meters—to be in agreement with shower data.

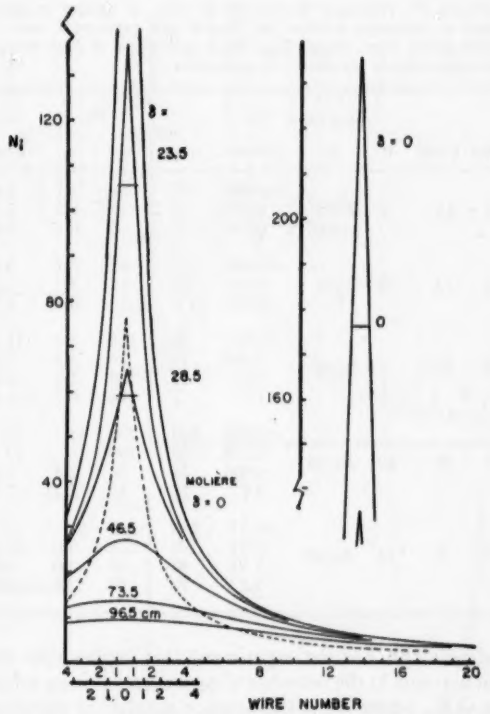

FIG. 8. Chamber response curves: the number of electrons N_i passing through the sensitive volume of wire number i when the axis of a shower containing $\Pi = 2\times10^4$ electrons passes through the plane of observation at a perpendicular distance δ from the long axis of the chamber. The dotted curve is the response assuming a Molière distribution uncorrected for the transition effect in the dural above the chamber volume.

The possible roles which the highly interacting N component of the showers may play in the production of a soft component related only indirectly to the showers produced in the initial primary interaction have not been discussed so far. A quantitative estimate of its contribution to the electronic distribution function is impossible at present. It can be expected, however, that a general background of lower-energy showers is added to the initial shower, or showers. The low energy is a result of the degradation of the energy reaching the soft component via the nucleonic cascade.

D. Fluctuations

A given density distribution found in the ion chamber may be interpreted adequately only if the fluctuations in the lateral distribution function are known or can be estimated. Blatt[23] has concluded in a qualitative way that the fluctuations should not be much larger than those expected if the shower particles are completely

[28] I. Pomeranchuk, J. Phys. (U.S.S.R.) **8**, 17 (1944); A. Migdal, J. Phys. (U.S.S.R.) **9**, 183 (1945); J. Nishimura and K. Kamata, Progr. Theoret. Phys. (Japan) **5**, 899 (1950).

[29] E. Fermi, Phys. Rev. **81**, 683 (1951).

TABLE IV. Numbers of fluctuation cores of various energies found at distances r from the shower axis between r_1 and r_2 which result from single, large-angle scattering of high-energy electrons early in the shower development.

					E_0 10^{13} ev		10^{14} ev	
$t(X_0)$	h(km)	Π	E	$N(r_1,r_2)$	r_1	r_2	r_1	r_2(cm)
1	13	2	$E_0/2$	<0.009	17	34	1.7	3.4
				0.035	8	17	0.8	1.7
				0.139	4	8	0.4	0.8
2	12	2	$E_0/4$	<0.009	31	62	3.1	6.2
				0.035	15	31	1.5	3.1
				0.139	8	15	0.8	1.5
3	10.8	6	$E_0/8$	<0.027	56	112	5.6	11.2
				0.105	28	56	2.8	5.6
				0.41	14	28	1.4	2.8
				1.7	7	14	0.7	1.4
4	10	10	$E_0/16$	<0.044	100	200	10	20
				0.174	50	100	5	10
				0.695	25	50	2.5	5.0
				2.8	12.5	25	1.25	2.5
5	9	22	$E_0/32$	<0.10	180	360	18	36
				0.38	90	180	9.0	18.0
				1.53	40	90	4.0	9.0
				6.2	20	40	2.0	4.0

independent. For our experiment this implies that the fluctuations in the response of each detector area would be $\sqrt{\bar{N}_i}$, where $\bar{N}_i$ is the average number of electrons passing through the ith area.

As Blatt points out, the fluctuations in the lateral distribution feature (1) a "short memory" and (2) a "small amplification." The short memory is a result of the large displacement ($\gg$10 cm, the wire spacing of our chamber) of electrons from their point of origin caused by multiple scattering when their energy is low enough for them to be found an appreciable distance (many wire spacings in this experiment) from the shower axis. If their energy is this low, then these electrons produce few secondaries and show a small amplification for fluctuations. Illustrative examples of the above statements are readily obtained by picking an energy for the electrons, finding their rms displacement from the shower axis, and calculating their rms displacement per radiation length due to multiple scattering. It is then seen that the electrons must have an energy $\gg\epsilon_0$ in order for their progeny to appear to be related in their lateral position. Since we shall have a detailed view of the structure near the shower axis in this experiment, it is necessary to consider the possible consequences of fluctuations of the very high-energy electrons found near the shower axis. We shall therefore calculate the probability that one of the high-energy electrons found in the early development of the shower undergoes a single, large angle scattering, so that its progeny resembles an auxiliary shower having an independent origin.

Since a model of the shower development is required, we assume that a photon of energy E_0, produced 3 radiation lengths ($\gtrsim$125 g/cm^2) down from the top of the atmosphere, initiates a shower in which each electron and photon produces two equally energetic particles by radiative and pair production processes, respectively, for each radiation length of air traversed. Table IV is a collection of the numbers which have been obtained[17] from this model for two initiating energies. Π is the total number of electrons at depth t, and E is their energy. The numbers of such cores $N(r_1,r_2)$ found at a distance r between r_1 and r_2 from the main shower axis are negligibly different if primary electrons are assumed.

As an example, it is seen that in 3.5 percent of the cases of 10^{13}-ev showers, two equally energetic "fluctuation cores" (as these fluctuations will be called) of energy 5×10^{12} are found separated by distances of from 8 to 17 cm, with the majority having the smaller separation ($N\sim1/r^2$). An upper limit of 0.9 percent have separations of from 17 to 34 cm. For comparison, the most probable separation for two π^0 decay-photon showers at this energy is 41 cm. It is also seen that, for this experiment, fluctuations of this type are negligible for energies $E_0\gtrsim10^{14}$ ev.

From the above discussion it appears justifiable to assume that, except in the rare case in which a fluctuation core is found, the rms fluctuations in the numbers of electrons per channel in the chamber are only negligibly larger than $\sqrt{N_i}$. Actually, since there is a spacial dependency introduced in the positions of the pairs of electrons produced in the materialization of photons in the dural, the transition effect increases the fluctuations to about $2\sqrt{N_i}/\sqrt{3}=1.15\sqrt{N_i}$.

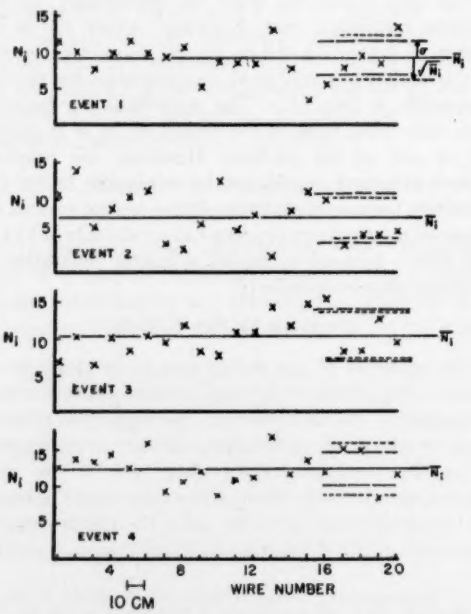

FIG. 9. Events showing a flat distribution of ionization and no systematic fluctuations.

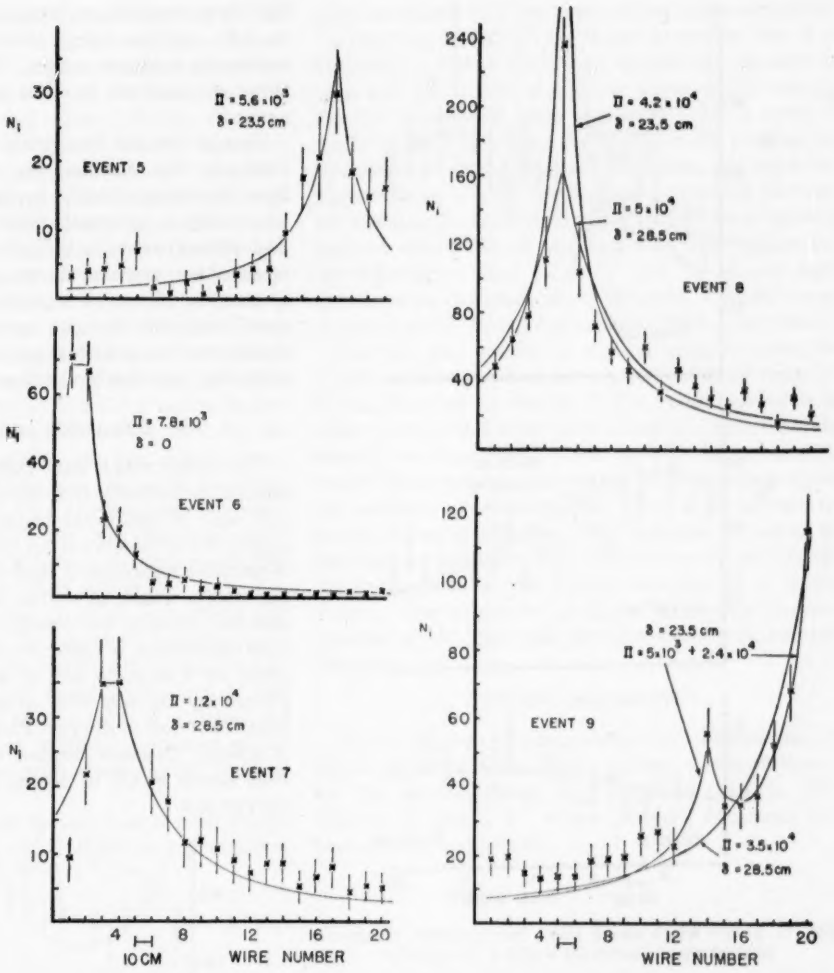

FIG. 10. Events showing marked changes in electron density over the length of the chamber.

IV. EXPERIMENTAL RESULTS

A. Individual Events

The four-fold coincidence rate of the Geiger counter arrangement described in II was 4.10 ± 0.13 hr^{-1}; in a total running time of 109 hours about 430 shower events were recorded. The reduced data for the most interesting events are shown in Figs. 9–12. In plotting these results the wires have been numbered consecutively from one end of the chamber and the number of electrons passing through the sensitive volume of wire i is denoted by N_i. In almost every case the indicated errors are $1.15\sqrt{N_i}$.

The first group, events 1–4, showed no systematic change in density over the chamber and were selected because they were the largest of their type observed. They are assumed to be caused by high-energy showers whose axes pass through the plane of observation relatively far from the chamber. The close agreement between $\sqrt{\bar{N}_i}$ and σ, the rms deviation from the mean, show that at least far from the shower axis the fluctuations are not larger than expected.

The second group, events 5–9, exhibit rather striking changes in density over the chamber, and have been interpreted to be the result of showers whose axes passed through the chamber area or were immediately adjacent thereto. Response curves from Fig. 8 have been selected which can perhaps best represent the data and are shown on the figures. In general, the agreement is not too unsatisfactory and appears to require no drastic revision of the lateral distribution function calculated in III. In event 6 a shower core was assumed to have passed between the first two wires of the chamber since N_1 and N_2, the numbers of electrons passing through the first and second detector areas, were so nearly equal while the ratio N_2/N_3 is so very large. Event 8 was the largest obtained, and the height of the peak has not been determined very

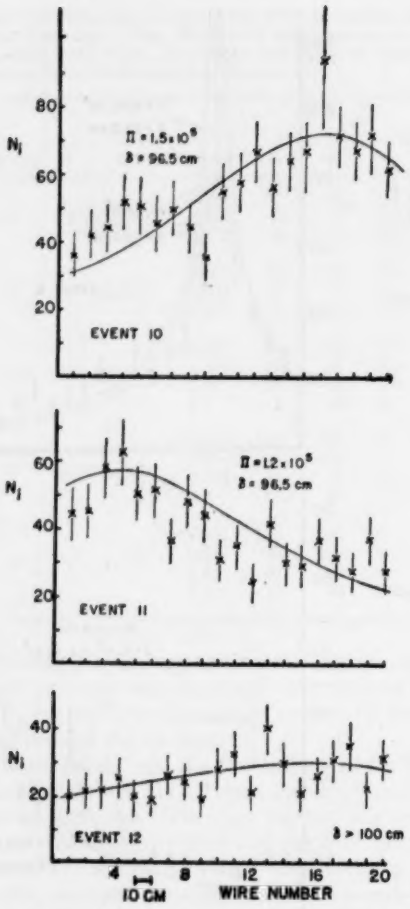

FIG. 11. Events which exhibit small, but consistent, changes in electron density across the length of the chamber.

accurately since the center channel was overloaded and its response could only be estimated by the amount of undershoot. The two immediately adjacent channels were just at the overload level. Therefore, two curves have been chosen, but they show too little difference to make a choice between them readily apparent. The attempt to fit event 9 with a single response curve from Fig. 8 is less satisfactory than for the other events in this group. Adding an auxiliary shower whose core hits wire No. 14 gives a better fit over the region nearest the main core, but does not provide any improvement in fitting the tail. By fitting events 8 and 9 with a single shower curve it has been necessary to make a compromise between picking a response curve which had a half-width narrow enough (δ small) and a tail which was high enough (δ large).

The next three events, 10–12, have been ascribed to showers whose axes hit relatively too far from the chamber area to show a very pronounced maximum. For the showers shown here, the statistics are too poor to rule out fits using monotonically increasing or decreasing response curves. There is relatively poor agreement between the data and the curve shown for event 11.

Though the last two events shown, 13 and 14, have relatively flat distributions, they have fluctuations from the average which are almost twice $1.15\sqrt{\bar{N}_i}$ and which show a systematic behavior across the chamber. The former event is difficult to interpret except in terms of two separate shower axes, presumably due to π^0 mesons. Event 14 is particularly difficult because more than two response curves must be utilized to obtain very much better agreement than that obtained using only one slowly varying curve.

B. Discussion and Conclusions

The events which have been studied in detail were selected individually from the events recorded either on the basis of significant changes in density over the length of the chamber or on the basis of a large density of particles regardless of their distribution. The triggering system would, of course, tend to introduce such a selection already, but introduces no serious bias. The coincidence rate is about 16 percent higher than that found by Cocconi *et al.*[30] at sea level, but can be explained by the somewhat closer counter spacing used here. The effect of the $\frac{1}{4}$-in. Pb shielding on the counters is difficult to assess because the transition effect has been shown in III to depend upon distance from the shower axis.

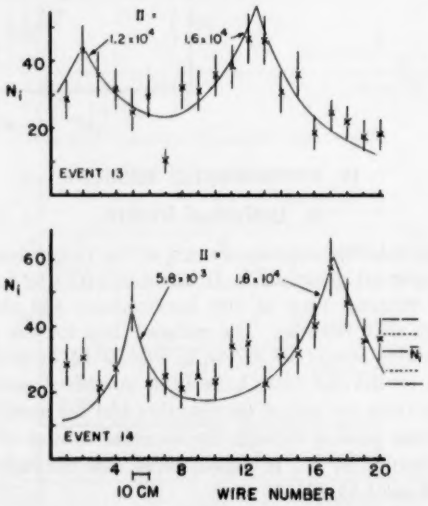

FIG. 12. Events which show electron density distributions which are (a) unlike those expected from single showers whose axes pass through or close by the chamber and (b) difficult to attribute to showers whose axes pass far from the chamber because of the large, systematic fluctuations observed in the chamber response.

[30] Cocconi, Tongiorgi, and Greisen, Phys. Rev. **75**, 1063 (1949).

Since the showers observed here would be quite far beyond their maximum if they were initiated about one mean free path (for nuclear interaction of the cosmic-ray N-component) down in the atmosphere, it is perhaps surprising to find electron density distributions which are as sharp as those of events 5–9. This is especially true since previous experiments[8,13] at mountain altitudes have indicated that the showers found there are less peaked within about one meter of the shower axis than predicted by the Molière distribution. A reconciliation can be made if event 6 is attributed to either a very young shower or a few highly ionizing rays emerging from the dural lid of the chamber. Then, the curves fitted to the other 4 events in the chamber have values of δ which are about equal to the half width of the chamber. Such a distribution in δ values implies a structure function flatter than that assumed. On the other hand, it was found that for the two largest events, 8 and 9, that the half-width was too small compared to the height of the tails for a good fit with our theoretical curves. It is possible that the transition effect in the high-energy core of older showers differs strongly from that for showers at their maximum. It is also possible that a large number of widely scattered small showers created by the N-component cascade could account for the high density found in the tails. Though there appear to be several large fluctuations in the tails of events 8 and 9 which tend to support the latter possibility, it is not profitable to pursue either of the above alternative explanations on the basis of the data presented here.

An attempt to attribute the auxiliary shower drawn in event 9 to either a π^0-decay photon or a fluctuation core associated with the main shower fails completely. By referring to Sec. III.C., it can be shown that if a π^0 meson of energy 2×10^{15} ev decays into photons of $\frac{1}{4}E_{\pi^0}$ and $\frac{3}{4}E_{\pi^0}$, then a multiple curve which exactly fits the response of wires numbered 6–19 in event 5 would be obtained. Since the statistics are too poor in this event to distinguish such structure, and since for higher energy π^0's the core separations would be even smaller than 20 cm, it can be seen that π^0-decay photon showers would not be resolved with this apparatus. By referring to Sec. III.D., it can be shown that the structure discussed above for event 5 would occur in only 2 out of 100 cases because of "fluctuation cores."

The last two events, 13 and 14, appear to be the profiles of showers which have been described[13] recently in the literature as "lumpy." The percentage of such cases found in this experiment (2 out of 7) corresponds roughly to that found in reference 13 (8 out of 39), though these figures are probably quite dependent upon the methods of selection used. Since it is difficult to accept the conclusion that the systematic deviations in the chamber response found in these events are caused by fluctuations in the lateral structure of a single shower, these events are attributed to cascade showers initiated by at least two particles having comparable energies.

ACKNOWLEDGMENTS

It is a pleasure to acknowledge my indebtedness to Professor W. E. Hazen, who suggested this experiment, for his encouragement and guidance; and to Mr. William P. Davis, Jr., whose generous assistance has been greatly appreciated.

Elastic Scattering of 26-Mev Negative Pions by Hydrogen in Emulsion*

JAY OREAR† AND WILLIAM SLATER, *Institute for Nuclear Studies, University of Chicago, Chicago, Illinois*

AND

J. J. LORD, S. L. EILENBERG, AND A. B. WEAVER, *Department of Physics, University of Washington, Seattle, Washington*

(Received June 21, 1954)

Standard Ilford G5 plates were exposed to a fairly monoenergetic 30-Mev π^--meson beam obtained by slowing down the Chicago 90-Mev beam with absorber and then using magnetic analysis. Range curves were taken indicating a 35 percent contamination from muons and electrons in this geometry. This figure was independently determined from the grain density distribution of tracks in the emulsion. A flux of 2.2×10^5 tracks per cm^2 was used for area scanning. The average beam energy in the plates is (26±2) Mev as determined from measuring the recoil proton energies in the 5 pion-proton scatterings which were found. An equivalent pion path length of 13×10^4 cm was scanned giving a cross section of (1.15±0.6) mb for the 5 events. This cross section is for scatterings greater than 50°. Smaller angle scatterings were not considered because of the possibility that such short recoil protons might be missed by area scanning. Various scanning efficiency checks indicate a scanning efficiency above 90 percent. The data are analyzed to give (4.7°±2.7°) for the phase shift combination $(2\alpha_1+\alpha_3)$.

I. INTRODUCTION

PION–PROTON elastic scattering experiments using hydrogen targets and counters have been limited to energies above 30 Mev because of the short range of pions under 30 Mev. Two other techniques have been used successfully in the low-energy region: the hydrogen diffusion cloud chamber[1] and the nuclear emulsion technique of area scanning for hydrogen collisions.[2]

The energy region below 30 Mev is quite important in that such information is necessary for a reliable determination of the scattering lengths for the phase shifts in pion-nucleon scattering. At the time this experiment was initiated the experimental evidence led some workers to discuss the possibility that the s-wave phase shifts were proportional to the pion momentum only for energies under 10 Mev. There was some speculation that the s-wave phase shift $\alpha_3(T=\frac{3}{2})$ might change sign in the region of 20 to 30 Mev.[3] Such a phase shift behavior would predict roughly 8 mb as the result for this experiment rather than the observed 1.15 mb.

The results of this experiment, along with other recent information, now permit the simpler interpretation that α_3, α_1, and α_{33} behave as momentum to the power $(2l+1)$ up to 80 Mev. This interpretation is discussed in detail in the following paper.[4]

This experiment gives (1.15±0.6) millibarns for the elastic $(\pi^-$-$p)$ scattering cross section between 50° and 180° in the center-of-mass system. Such a low value would be expected by extrapolating down the phase shifts obtained at 40,[5] 61.5,[6] or 120 Mev[7] using the momentum to the power $(2l+1)$ dependence. At the low energies studied by the Columbia cloud chamber group,[1] one would expect this cross section to increase considerably due to a constructive Coulomb interference. Quantitatively, the Columbia cloud chamber preliminary results are consistent with our 26-Mev result.[4]

Details of exposure geometry and beam analysis are given in Sec. II. As described in Sec. III, the plates were area scanned under 350× magnification for single proton beginnings. Then each proton beginning was examined for an incoming and scattered pion. Three-pronged events of this type, but not due to hydrogen, were rejected on the basis of two tests: coplanarity of the three prongs, and angular correlation of the two scattering angles to satisfy energy-momentum conservation. A total of 5 hydrogen events with $\chi>50°$ was found. χ is the pion scattering angle in the center-of-mass system. In each of these events the recoil proton did not leave the emulsion, thus permitting a measurement of the incoming pion energy.

II. EXPOSURE

Since there is no external pion beam of the Chicago cyclotron under 40 Mev, it is necessary to slow down higher-energy pions with absorber. Slowing down a higher-energy beam to the region of 26 Mev results in a considerable energy and angular spread of what was initially a fairly monoenergetic and parallel beam. In order to obtain a workable degree of energy resolution and parallelism of tracks, we found it necessary to use magnetic analysis after the beam leaves the absorber. In order to achieve parallelism of beam tracks suitable for area scanning, it is necessary to expose the plates a

* Supported by the joint program of the U. S. Atomic Energy Commission and the U. S. Office of Naval Research.

† Now at Physics Department, Columbia University, New York City, New York.

[1] Rinehart, Sargent, Rogers, and Lederman in *Proceedings of the Fourth Rochester Conference* (University of Rochester Press, Rochester, 1954); and (private communication).

[2] Orear, Lord, and Weaver, Phys. Rev. **93**, 575 (1954).

[3] H. P. Noyes and A. E. Woodruff, Phys. Rev. **94**, 1401 (1954).

[4] J. Orear, following paper, Phys. Rev. **96**, 176 (1954).

[5] J. Tinlot and A. Roberts, Phys. Rev. **95**, 137 (1954).

[6] Bodansky, Sachs, and Steinberger, Phys. Rev. **93**, 1367 (1954).

[7] Anderson, Fermi, Martin, and Nagle, Phys. Rev. **91**, 155 (1953).

considerable distance behind the absorber. Both the 45-Mev and 90-Mev π^- beams were tried with the 90-Mev beam giving much better results. The intensity and energy resolution were improved somewhat by making use of the horizontal focusing properties of the Chicago 45° magnetic wedge. The absorber and plates were placed at conjugate foci as shown in Fig. 1. This geometry gave an intensity of about 1/80 of the intensity with no absorber. A six-hour exposure was required to obtain a flux of 2.2×10^5 tracks per cm^2.

Another difficulty in obtaining external low-energy pion beams is the high contamination of muons and electrons. In our case this contamination was determined by two independent methods. An absorption curve was taken at the time of the exposure using thin counters. Analysis of this curve gave a pion content of (64±3) percent. Then both scanning groups independently counted grain densities of 100 successive tracks over a length of 480 microns each. Figure 2 shows the histogram obtained by the Chicago group. The grain densities cluster into three distinct groups as would be expected for electrons, muons, and pions of the same momentum. This analysis gives a pion content of (65±4) percent.

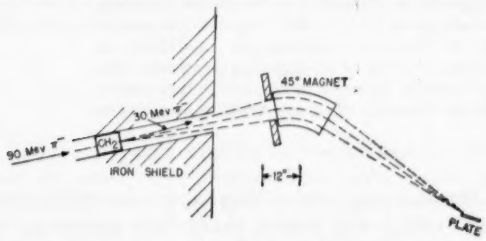

FIG. 1. Experimental setup. Paraffin absorber and plate are at conjugate foci of 45° magnetic wedge.

III. SCANNING

The scanning technique is the same as described in previous papers.[2,8] This technique is quite time-consuming for cross sections as low as was encountered in this experiment. Scanning continued until all the emulsion which had been exposed was covered. The scanners were responsible for observing all proton beginnings confined to a square region 250×250 microns which is defined by a whipple disk reticle. Since there is some possibility of overlooking short proton tracks, we limited ourselves to scatterings greater than 50°, or proton tracks greater than 40 microns in length. Also the regions within 15 microns of either surface were excluded. All scanning was done by the authors who have previous experience in this type of pion-proton scanning. The scanners personally felt that their scanning efficiencies were greater than 90 percent. In addition two types of quantitative checks were made. Strips were rescanned independently by a second scanner. Also scanning tests were devised by selecting strips which contained events which either were pion-proton scatterings or else looked similar to them. Out of 15 possibilities, no events were missed.

[8] J. Orear, Phys. Rev. **92**, 156 (1953).

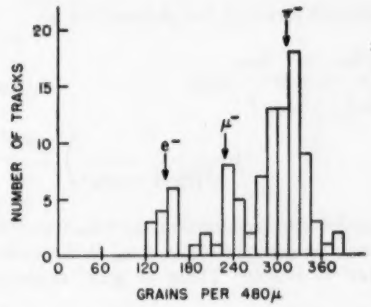

FIG. 2. Grain density distribution of beam tracks.

IV. RESULTS

If L_τ is the total pion path scanned, n_H the density of hydrogen in the plates, and N the number of events found, then

$$\sigma=(1/L_\tau n_H)N.$$

The value $n_H=(3.34\pm0.1)\times10^{22}$ protons/cm^2 is specified by Ilford, where the uncertainty is that caused by moisture content of the emulsion. For the region scanned L_τ was determined to be $(1.3\pm0.1)\times10^5$ cm. Five pion-proton scatterings were found with $\chi>50°$. This gives

$$\sigma(\chi>50°)=(1.15\pm0.6)\text{ millibarns.}$$

The 5 events are listed in Table I.

The energies of the incoming pions were calculated by measuring the range of the recoil protons. Fortunately in all 5 cases the protons stopped in the emulsion. This method of determining the pion beam energy superimposes an artificial energy spread mainly due to inaccuracies in the determination of χ. According to the range curves taken at the time of the exposure, the primary beam was about 30 Mev. Since this beam entered 600-micron emulsion at about 8° inclination to the surface, the average value of (26±2) Mev obtained from the five events is consistent with the range curve determination.

These results can give some useful information about the s-wave phase shifts. At these low energies the elastic

TABLE I. Energies and angles of the $(\pi^- - p)$ scatterings.

Event	χ, deg	Pion energy, Mev
1	55	32
2	87	22
3	97	26
4	97	22
5	104	26

π^- scattering in terms of the phase shifts is

$$\frac{d\sigma}{d\omega}=\lambda^2\left[\left(\frac{2\alpha_1}{?}+\frac{\alpha_3}{3}+\frac{2\alpha_{33}}{3}\cos\chi\right.\right.$$
$$\left.\left.+\frac{1}{137\beta\pi(1-\cos\chi)}\right)^2+\frac{\alpha_{33}^2}{9}\sin^2\chi\right].$$

This is under the assumption $\alpha_{31}=\alpha_{13}=\alpha_{11}=0$. This equation can be solved for $(2\alpha_1+\alpha_3)$ if the value of α_{33} at 26 Mev is known. There is good evidence that $\alpha_{33}=0.235\eta^3$ in this energy region.[4] Using this value for α_{33} we have $2\alpha_1+\alpha_3=(4.7°\pm2.7°)$ at 26 Mev. The upper and lower limits are the values corresponding to a cross section of 1.7 and 0.6 mb, respectively, for scatterings greater than 50°.

This result when combined with other recent results lead to the conclusion that the simple energy dependence of momentum to the power $(2l\pm1)$ is quite reasonable for the phase shifts α_3, α_1 and α_{33} up to 80 Mev. The following paper develops this conclusion in detail.

PHYSICAL REVIEW VOLUME 96, NUMBER 1 OCTOBER 1, 1954

Low-Energy Behavior of the Phase Shifts in Pion-Proton Scattering*

JAY OREAR†
Institute for Nuclear Studies, University of Chicago, Chicago, Illinois
(Received June 21, 1954)

A best fit has been made to all pion-proton scattering phase-shift information under 80 Mev assuming the energy dependence of the phase shifts is momentum to the power $(2l+1)$ which would be the case for strong short-range interactions. The values obtained for the Fermi-type solutions are $\alpha_{33}=0.235\eta^3$, $\alpha_3=-0.11\eta$, and $\alpha_1=0.16\eta$. These phase shifts, along with Coulomb forces, fit all scattering experiment data quite closely including the 5-Mev cloud chamber results at Columbia. However, at zero energy they predict $(\alpha_1-\alpha_3)=0.27\eta$, while recent photoproduction results and the Panofsky effect as evaluated here predict $(\alpha_1-\alpha_3)=0.21\eta$ with rather large uncertainties.

INTRODUCTION

NECESSARY parameters for devising a theory of meson-nucleon forces are the scattering lengths, which in principle can be determined from low-energy pion-proton scattering experiments. Recently, considerable low-energy pion-proton scattering information has become available, and has been analyzed in terms of s- and p-wave phase shifts. At low energies the energy dependence of such phase shifts can be expanded in powers of the momentum, where the first term is the power $(2l+1)$. Furthermore, wave mechanics shows that if the two particle interaction is strong compared to the kinetic energy in a region $r<r_0$ and if there is essentially no interaction beyond this region, then for $kr_0\ll1$ the first term of the expansion in momentum is much larger than the higher order terms. In this energy region we would expect

$$\alpha_l\propto\eta^{2l+1}, \tag{1}$$

where η is the center-of-mass momentum divided by $m_\pi c$. Empirically the phase shifts up to 80 Mev seem to follow this energy dependence. We have taken such an empirical approach in selecting 80 Mev as the upper energy limit of the available data which is used in obtaining a best fit to the theoretical shape η^{2l+1}.

The scattering results have fairly successfully been fitted with s- and p-wave phase shifts assuming conservation of isotopic spin. In the various phase shift solutions at low energies there are two fairly large s-wave phase shifts α_3 and α_1 (corresponding to $T=\frac{3}{2}$ and $T=\frac{1}{2}$) and one large p-wave phase shift. We shall consider only that type solution (commonly called the Fermi-type solution) where α_{33} $(T=\frac{3}{2}, J=\frac{3}{2})$ is the largest p-wave phase shift.[1] We shall make the additional restriction that α_{33} be positive. This choice is based on preliminary 115-Mev π^+-p scattering results which show a destructive Coulomb interference.[2] Also the solutions with negative α_{33} are inconsistent with Eq. (1).

At the 1954 Rochester Conference, Bethe[3] and Noyes[3] discussed the possibility of a Jastrow-type potential for α_3 which had previously been suggested by Marshak.[4] Such a potential would cause α_3 to depart violently from Eq. (1) at about $\eta=0.3$ and in some of the proposals it would change sign at about $\eta=0.5$.[3,5] Bethe and de Hoffman discuss the possibility that $\alpha_3\sim0$ up to $\eta\sim0.3$ in their forthcoming book.[6] One of the motiva-

* Research supported in part by the U. S. Office of Naval Research and the U. S. Atomic Energy Commission.
† Now at Physics Department, Columbia University, New York, New York.

[1] Anderson, Fermi, Martin, and Nagle, Phys. Rev. **91**, 155 (1953).
[2] J. Orear (to be published).
[3] *Proceedings of the Fourth Rochester Conference on High Energy Physics* (University of Rochester, Rochester, 1954).
[4] R. E. Marshak, Phys. Rev. **88**, 1208 (1952).
[5] H. P. Noyes and A. E. Woodruff, Phys. Rev. **94**, 1401 (1954).
[6] H. A. Bethe and F. de Hoffmann, *Mesons and Fields* (Row, Peterson and Company, Evanston, to be published).

tions for such phase-shift behavior is an attempt to fit a zero-energy prediction from earlier photoproduction data of $(\alpha_1-\alpha_3)=0.16\eta$ with a value of $(\alpha_1-\alpha_3)=0.3\eta$ predicted by the scattering experiments. Also the preliminary 5-Mev cloud chamber results of Lederman[7] in some cases were possibly misinterpreted (the actual data have not yet been published). We find that the most recent scattering data is consistent with the simpler approach of Eq. (1) and that the zero-energy prediction of $(\alpha_1-\alpha_3)$ as reevaluated in the Appendix is not unreasonably off from this.

At present there is useful low-energy information at 0,[8] 5,[7] 20,[9] 26,[10] 30,[9] 40,[11] 45,[12] 61.5[13] and 78 Mev.[1] Fermi-type phase shift solutions have been obtained from the experiments at 40, 45, 61.5, and 78 Mev. The remaining information, although in the form of certain phase-shift combinations, is still quite useful and will be utilized fully in our analysis. The results of this analysis are $\alpha_{33}=0.235\eta^3$, $\alpha_3=-0.11\eta$, and $\alpha_1=0.16\eta$. As can be seen from Figs. 1 and 2, these values fit all the scattering data well within the errors which are usually about 20 percent. At energies above 80 Mev it appears that α_1 varies slower and that α_3 varies faster than the η^{2l+1} law.

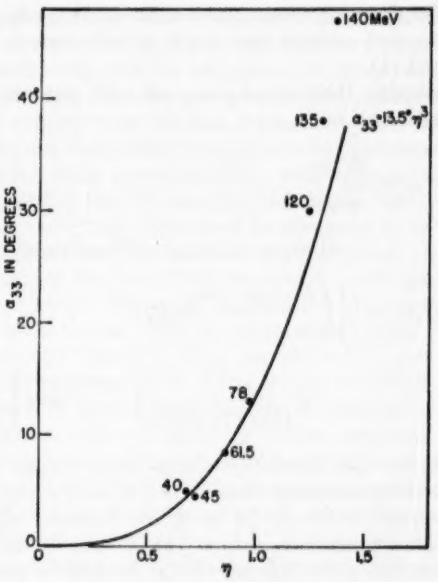

FIG. 1. α_{33} in degrees vs η of the pion in the center-of-mass system. Only the first 4 points were used in making the fit.

DISCUSSION

p-Waves

In the Fermi-type solution, α_{33} is considerably larger than the other three p-wave phase shifts. So far α_{33} is the only p-wave phase shift which can be established by the experiments to any degree of accuracy. It is given by π^+-meson scattering experiments at 40, 45, 61.5, and 78 Mev. In the case of the 40 and 61.5 Mev solutions, π^- data is also used. In our analysis equal weights are given to these four independent results, even though the phase shifts are less well determined at the lower energies. This is compensated by the possibility that at higher energies departures from the η^{2l+1} law might begin to appear.

TABLE I. Phase-shift values.

Energy Mev	$a=\alpha_1/\eta$	$b=\alpha_3/\eta$	$(a-b)$	$(2a+b)$	α_{33}/η^3	Reference
0			0.21			8
20			0.25			9
26				0.141		10
30			0.26			9
40	0.164	−0.112			0.260	11
45		−0.138			0.206	12
61.5	0.191	−0.11			0.228	13
78		−0.109			0.248	1

[7] Rinehart, Sargent, Rogers, and Lederman (private communication) and reference 3.
[8] See Appendix for discussion and references.
[9] W. J. Spry, Phys. Rev. **95**, 1295 (1954).
[10] Orear, Slater, Lord, Eilenberg, and Weaver, preceding paper [Phys. Rev. **96**, 174 (1954)].
[11] J. Tinlot and A. Roberts, Phys. Rev. **95**, 137 (1954).
[12] Orear, Lord, and Weaver, Phys. Rev. **93**, 575 (1954).
[13] Bodansky, Sachs, and Steinberger, Phys. Rev. **93**, 1367 (1954).

At the lowest energy the phase shifts are least well specified. For example, the paper of Roberts and Tinlot[11] quotes a preliminary Fermi-type analysis of H. P. Noyes: $\alpha_{33}=4.9°$, $\alpha_3=-3.7°$, and $\alpha_1=8.3°$. Bethe and de Hoffmann,[6] in section 33 of their forthcoming book, give $\alpha_{33}=4.5°$, $\alpha_3=-5°$, $\alpha_1=4.4°$ for the same Fermi-type solution to the 40-Mev data. Both these solutions give values less than 1.7° for the other p-wave phase shifts. The main explanation for the differences in these two solutions is the room available for personal judgments in handling the various 40-Mev data. In our analysis we have always used the average of these two solutions for the 40-Mev phase shifts.

These four values of α_{33}/η^3 are given in Table I. The average gives as our best fit:

$$\alpha_{33}=0.235\eta^3. \tag{2}$$

The standard deviation due to the spread of the four values used is only 4.7 percent. This supports our choice of η^3 as the energy dependence since each of these values of α_{33} is probably only determined within limits of 20 percent. Equation (2) and the experimental values of α_{33} up to 140 Mev are plotted in Fig. 1.

s Waves

As in the above case, α_3 is determined at 40, 45, 61.5, and 78 Mev. α_1 is determined at 40 and 61.5 Mev with large errors. More information about α_1 can be obtained from low-energy measurements of the total charge-exchange cross section and the total elastic π^- cross section in the energy region below 40 Mev. In this energy region the p-wave phase shifts become

smaller than the s-wave phase shifts and the effects of α_{31}, α_{13}, and α_{11} have been neglected as is done in Eqs. (3) and (4).

Assuming that $\alpha_{31}=\alpha_{13}=\alpha_{11}=0$ and that $\sin\alpha\approx\alpha$, we have

$$\frac{d\sigma}{d\omega}(\pi^-,\pi^0)=\frac{2\lambda^2}{9}\frac{v_0}{v_-}\times[(\alpha_3-\alpha_1+2\alpha_{33}\cos\chi)^2+\alpha_{33}^2\sin^2\chi], \quad (3)$$

$$\frac{d\sigma}{d\omega}(\pi^-,\pi^-)=\lambda^2\left[\left(\frac{2\alpha_1+\alpha_3}{3}+\frac{2\alpha_{33}}{3}\cos\chi+\frac{1}{137\beta_\pi(1-\cos\chi)}\right)^2+\frac{\alpha_{33}^2}{9}\sin^2\chi\right], \quad (4)$$

where $\beta_\pi c$ = initial velocity of pion in lab system.[14] The total charge-exchange cross section at zero energy can be inferred indirectly by using the Panofsky effect[15] and photoproduction results. This is done in the Appendix and gives $(\alpha_1-\alpha_3)=0.21\eta$. Because of various uncertainties, this evaluation should be considered less reliable than the direct experiments. Also the total charge-exchange cross section has been measured at 20 Mev and 30 Mev by Spry.[9] If the values for α_{33} given by Eq. (2) are used in Eq. (3), and an additional correction made for the process $(\pi^-+p\rightarrow\gamma+n)$, Spry's results give $(\alpha_1-\alpha_3)=0.25\eta$ at 20 Mev and 0.26η at 30 Mev.

Likewise Eqs. (2) and (4) give a determination of $(2\alpha_1+\alpha_3)$ at 26 Mev based on the results of the preceding paper.[10] Preliminary results of total π^- elastic cross section at an average energy of about 5 Mev using the diffusion cloud-chamber technique were reported by Lederman[7] at the 1954 Rochester Conference. Since these data have not been presented in a final form, they will not be used in making the best-fit determination. However, the predictions from our best-fit phase shifts compare favorably with Lederman's data. This also holds for the more extensive 12-Mev experiments[16] now in progress.

A least-squares analysis is made to all these data (shown in Table I) which gives the best-fit values of α_1 and α_3 assuming the theoretical forms $\alpha_1=a\eta$ and $\alpha_3=b\eta$. In the least-squares method assumptions must be made about the errors of each of the pieces of data. We have assumed the 40 Mev and above data to have the same relative errors, and the lower energy data to have relative errors twice this amount.

The results of this calculation are

$$\alpha_3=-0.11\eta, \quad \alpha_1=0.16\eta. \quad (5)$$

These curves are plotted in Fig. 2 along with the data

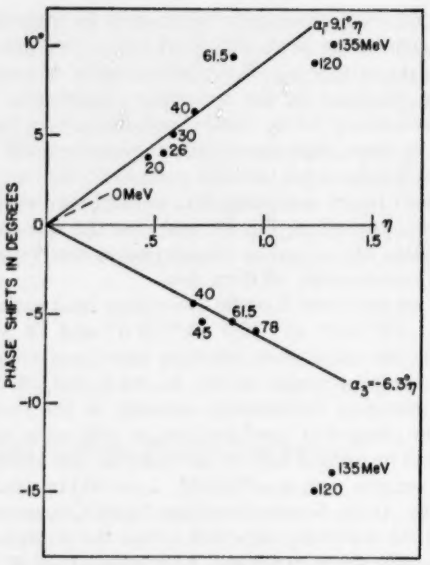

FIG. 2. α_1 and α_3 *vs* η. The 0 Mev slope and the 20, 26, and 30 Mev values of α_1 are obtained from experiments when α_3 is assumed $=-0.11\eta$.

of Table I. The values of $(a-b)$ and $(2a+b)$ are shown by plotting the α_1 obtained when using $\alpha_3=-0.11\eta$. The zero-energy value of $(\alpha_1-\alpha_3)=0.21\eta$ is expressed by a dotted line showing the predicted slope of α_1 when using $\alpha_3=-0.11\eta$. It is encouraging that all phase shifts and phase-shift combinations below 80 Mev fit these curves within their experimental errors. If the phase shifts of Eq. (5) are inserted in Eq. (4) and integrated from 60° to 180° at 5 Mev one gets a π^- elastic cross section of 6.5 mb. The preliminary Columbia cloud chamber results[3] are 4 events in 610 g/cm² of hydrogen which is a cross section of 10.9 mb. This value does not agree very well with the phase-shift energy dependence proposed by others.[4,5] For example, sets I and III of Noyes and Woodruff[5] predict 25 mb for 5 Mev. As mentioned earlier, the Columbia cloud chamber 12-Mev experiments, which involve about 4½ times more track, so far show no sign of disagreement with our choice of phase shifts.

Although the Rochester 40-Mev phase shifts fit in fairly well with this scheme, the π^- transmission experiment[17] might seem out of line. Subtracting the total charge-exchange cross section from the transmission cross section gives (5±2.5) mb (using their errors). This still includes the contribution from $(\pi^-+p\rightarrow\gamma+n)$. Assuming an energy-independent matrix element over the region of photon energy from 130 to 160 Mev, this contribution can be evaluated to be 1.8 mb using our phase shifts and the Panofsky effect.[15] This leaves (3.2±2.5) mb for elastic scattering between 55° and 180°. Our values of α_{33}, α_3, and α_1 give 1.7 mb when the

[14] F. T. Solmitz, Phys. Rev. **94**, 1799 (1954).
[15] Panofsky, Aamodt, and Hadley, Phys. Rev. **81**, 565 (1951).
[16] Rinehart, Sargent, Rogers, and Lederman (private communication).
[17] C. E. Angel and J. P. Perry, Phys. Rev. **92**, 835 (1953).

other p-wave phase shifts are neglected. This may no longer be justified at 40 Mev.

CONCLUSIONS

All possible data relevant to the low-energy dependence of the phase shifts α_{33}, α_3, and α_1 can be fitted within experimental errors by $\alpha_{33}=0.235\eta^3$, $\alpha_3=-0.11\eta$, and $\alpha_1=0.16\eta$. Furthermore, potential models which make α_3 approach zero in the region $\eta=0.5$ do not give any better fit and actually tend to contradict the 5-Mev and 26-Mev total elastic π^- cross sections. If α_3 is to be zero at 26 Mev, the largest permissible value for α_1 within the errors of the experiment is 3.7°. This is considerably lower than the value such fits give for α_1. As already pointed out, the phase shifts given by the model of Noyes and Woodruff predict a 5-Mev cross section considerably larger than observed. Also their phase shifts at 26 Mev predict 8 mb as opposed to the observed (1.15±0.6) mb.[10] The behavior of α_3 at $\eta=0.5$ can be settled once and for all by a measurement of the total (π^+-p) cross section at 20 Mev. This experiment is now in progress using the techniques described in the preceding paper.[10] This cross section for angles greater than 60° should be 5.5 mb if our phase shifts are used. If α_3 were zero or positive, then this cross section would be less than 1.1 mb.

The biggest discrepancy at present to our best fit is the zero-energy prediction of $(\alpha_1-\alpha_3)=0.21\eta$ using Panofsky effect and photoproduction data. Our phase shifts give $(\alpha_1-\alpha_3)=0.27\eta$. This evaluation could be made independent of the photoproduction links by a direct measurement of $\pi^-+p\rightarrow\gamma+n$. Conversely, such a measurement would help explain what happens in photoproduction on deuterium since the photoproduction on free neutrons would then be established by detailed balancing.

The author wishes to thank Mr. Wm. Slater for helping with the calculations and is grateful to Professor Enrico Fermi for the interest he has shown in this work.

APPENDIX

Zero-Energy Charge Exchange

The value of $(\alpha_1-\alpha_3)/\eta$ at zero energy can be obtained indirectly by making use of several other experiments and making assumptions about their interpretation. One of these experiments, photoproduction on deuterium, has rather large errors, at least in the sense that independent measurements have given different numbers. Of the several assumptions involved in the reasoning, perhaps the weakest is that one can obtain the threshold photoproduction on free neutrons $(\gamma+n\rightarrow\pi^-+p)$ by multiplying the threshold cross section $(\gamma+p\rightarrow\pi^++n)$ by the π^- to π^+ ratio from threshold photons on deuterium. We feel at least one should make a Coulomb correction due to the presence of the extra proton in $(\gamma+d\rightarrow\pi^-+p+p)$. A reasonable model is to assume that in π^- production the photon has interacted only with the neutron in the deuteron. This neutron then becomes a proton with a rather small recoil velocity when the pion is produced. Thus it will also have a fairly small relative velocity (compared to the total phase space available) with respect to the other proton, and its wave function in the final state will be accordingly suppressed as compared to the π^+ production case. We find that our knowledge of the structure of the proton and deuteron is insufficient to make a precise calculation of this effect. We estimate a 10 to 30 percent effect. A suppression greater than 30 percent is obtained when $2\pi\alpha/(e^{2\pi\alpha}-1)$ is used for the Coulomb penetration factor, where $\alpha=e^2/\hbar v$.[18] We will use a 20 percent suppression as an educated guess. The latest results obtained by nuclear emulsions exposed at the University of Illinois[19] give an average π^- to π^+ ratio of 1.53±0.1 in the photon energy region of 180 Mev. The Coulomb correction makes this ratio 1.9. This emulsion result of 1.53 is somewhat higher than the recent (May 1954) California Institute of Technology result of 1.3 at 200 Mev.[20]

Bernardini and Goldwasser[21] have made an analysis of the s-wave component of the reaction $(\gamma+p\rightarrow\pi^++n)$. Their value is $1.55\times10^{-28}\eta$ cm^2. Multiplying by 1.9 gives $\sigma(\gamma+n\rightarrow\pi^-+p)=2.94\times10^{-28}\eta$ cm^2 at threshold. Detailed balancing gives for very low-energy pions

$$\sigma(\pi^-+p\rightarrow\gamma+n)=2\left(\frac{p_\gamma}{p_\pi}\right)^2\sigma(\gamma+n\rightarrow\pi^-+p)$$
$$=\frac{1}{\beta_{\pi^-}}(5.1\times10^{-28}).$$

From the Panofsky effect[15] branching ratio of 0.94, we have

$$\sigma(\pi^-+p\rightarrow\pi^0+n)=\frac{0.94}{\beta_{\pi^-}}\times5.1\times10^{-28}.$$

Now making the final assumption that all violations of isotopic spin conservation for pion kinetic energies much lower than the π^--π^0 mass difference are explicitly taken into account in Eq. (3), we obtain $(\alpha_1-\alpha_3)=0.21\eta$. The more recent Columbia result for the pion mass difference is used.[22]

We feel that a 25 percent error should be assigned to this determination of $(\alpha_1-\alpha_3)$ at zero energy due to the experimental uncertainties alone. In addition there are unknown uncertainties in the assumptions made.

---

[18] Saito, Matanabe, and Yamaguchi, Progr. Theoret. Phys. (Japan) **7**, 103 (1952).
[19] Beneventano, Lee, and Stoppini, Nuovo cimento (to be published).
[20] Sands, Teasdale, and Walker, Phys. Rev. **95**, 592 (1954).
[21] G. Bernardini and E. L. Goldwasser, Phys. Rev. **95**, 857 (1954).
[22] W. Chinowsky and J. Steinberger, Phys. Rev. **93**, 586 (1954).

Suppression of Coherent Radiation by Electrons in a Synchrotron*

JOHN S. NODVICK† AND DAVID S. SAXON
University of California, Los Angeles, California
(Received May 25, 1954)

Approximate expressions are obtained for the coherent radiation loss by electrons in a synchrotron in the presence of finite parallel plate metallic shields, such as the pole faces of the magnet. The results would seem to provide a useful interpolation between the two simple limiting cases of shielding by infinite plates and no shielding at all.

INTRODUCTION

As is well known, the coherent radiation loss by electrons in a synchrotron, although independent of energy, increases with decreasing bunch size as the $(-4/3)$ power.[1] In some of the extremely high-energy synchrotrons reportedly under consideration, the bunching is likely to be sufficiently marked so that the coherent radiation loss could become serious. As is also well known, the coherent radiation has a spectrum mainly in the short-wave radio and microwave regions and hence can be suppressed in part by the use of metallic shields.[1] It is our purpose to extend some unpublished results of Schwinger,[2] in which this radiation was calculated assuming the orbit to lie midway between two plane parallel sheets of metal of infinite extent, to the case in which these metallic sheets are finite, as would be the case, for example, if the shielding were produced by the pole faces of the race track magnet itself. Our results, although necessarily rough, would seem to provide a useful interpolation between the two simple limits of shielding by infinite plates and no shielding at all.

POWER RADIATED BY ONE ELECTRON

We begin by writing an expression for the power P_n radiated in the nth harmonic by an electron moving in the $z=0$ plane in a circular orbit of radius R with angular velocity ω; namely,

$$P_n=\mathrm{Re}\left\{4in\omega e^2\int_{-\pi}^{\pi}d(\varphi-\varphi')G_n(R,\varphi,0;R,\varphi',0)\times[1-\beta^2\cos(\varphi-\varphi')]e^{-in(\varphi-\varphi')}\right\},\quad(1)$$

where $\beta=\omega R/c$. In the above, the Green's function $G_n(r,\varphi,z;r',\varphi',z')$, which is to be evaluated on the orbit as indicated, is the outgoing wave solution of

$$(\nabla^2+k_n^2)G_n=-\delta(z-z')\delta(\varphi-\varphi')\delta(r-r')/r,\quad(2)$$

with

$$k_n=n\omega/c=n\beta/R.$$

In addition, G_n must satisfy appropriate boundary conditions if a metallic shield is present. We consider three cases as follows:

I. No Shielding

In this case G_n is just the free-space Green's function $G_n^{(0)}$ which, when evaluated on the orbit, is given by

$$G_n^{(0)}(R,\varphi,0;R,\varphi',0)=\frac{1}{4\pi}\frac{\exp[2in\beta|\sin\tfrac{1}{2}(\varphi-\varphi')|]}{2R|\sin\tfrac{1}{2}(\varphi-\varphi')|}.\quad(3)$$

Substitution into Eq. (1) yields, after the angular integration is performed, the well known result[3,4]

$$P_n^{(0)}=(n\omega e^2/R)\left[2\beta^2J_{2n}'(2n\beta)-(1-\beta^2)\int_0^{2n\beta}J_{2n}(x)dx\right].\quad(4)$$

II. Infinite Parallel Plate Shields

In this case G_n must satisfy the boundary condition that it vanish on the metal plates. Taking these plates to be separated by a distance a, with the electron orbit midway between the plates, we thus require a solution of Eq. (2) subject to

$$G_n=0;\quad z=\pm a/2.\quad(5)$$

This function, which we denote by $G_n^{(\infty)}$, is easily derived[5] and can be expressed as

$$G_n^{(\infty)}(r,\varphi,z;r',\varphi',z')=(i/2a)\sum_{j=1}^{\infty}\sum_{m=-\infty}^{\infty}\sin j\pi(\tfrac{1}{2}+z/a)\times\sin j\pi(\tfrac{1}{2}+z'/a)\times e^{im(\varphi-\varphi')}J_m(\gamma_{nj}r_<)H_m^{(1)}(\gamma_{nj}r_>),\quad(6)$$

* Supported in part by the joint program of the U. S. Office of Naval Research and the U. S. Atomic Energy Commission.
† Present address: California Institute of Technology, Pasadena, California.
[1] L. I. Schiff, Rev. Sci. Instr. **17**, 6 (1946). See also Eq. (23) below.
[2] J. Schwinger, "On radiation by electrons in a betatron," 1945 (unpublished). We wish to thank L. Jackson Laslett who called our attention to this material.
[3] G. A. Schott, *Electromagnetic Radiation* (Cambridge University Press, Cambridge, 1912).
[4] J. Schwinger, Phys. Rev. **75**, 1912 (1949). Our starting point, Eq. (1), with G_n given by Eq. (3), is essentially Eq. (III.7) of this reference.
[5] See, for example, P. M. Morse and H. Feshbach, *Methods of Theoretical Physics* (McGraw-Hill Book Company, Inc., New York, 1953), Chap. 7, particularly p. 892. A detailed derivation is given in reference 2.

where

$$\gamma_{nj}=[k_n^2-(j\pi/a)^2]^{\frac{1}{2}}=[(n\beta/R)^2-(j\pi/a)^2]^{\frac{1}{2}},$$

and where $r_<$ is the lesser of the two radii r and r', $r_>$ the greater of the two. Substitution into Eq. (1), then yields after performance of the angular integration,

$$P_n^{(\infty)}=(n\omega e^2/R)(4\pi R/a)\mathrm{Re}\{\sum_{j=1,3,\cdots}^{\infty}[-H_n^{(1)}J_n+\tfrac{1}{2}\beta^2(H_{n-1}^{(1)}J_{n-1}+H_{n+1}^{(1)}J_{n+1})]\},\quad(7)$$

where the argument of all the cylinder functions is

$$\gamma_{nj}R=[(n\beta)^2-(j\pi R/a)^2]^{\frac{1}{2}}.$$

The power radiated into the attenuated modes is of course zero since for these modes the arguments of the cylinder functions, and also therefore the products $H_n^{(1)}J_n$, become purely imaginary. Only those terms for which $j\leq n\beta a/\pi R$ consequently contribute to Eq. (7).

III. Finite Parallel Plate Shields

Imagine now that the shielding plates of Case II, instead of being infinite, extend from an inner radius R_1 to an outer radius R_2 (with $R_1<R<R_2$ of course) as would be the case if the pole pieces of the ring magnet itself were the shielding plates. In this case, the Green's function in the region between the plates must satisfy appropriate (and very complicated) boundary conditions at the surfaces $r=R_1$ and $r=R_2$ in addition to the boundary conditions of Eq. (5). These extra conditions can be satisfied only if a general solution of the homogeneous equations is added to the Green's function of Eq. (6). Thus for this case we must have

$$G_n=G_n^{(\infty)}+F_n,\quad(8)$$

where we write F_n in the form

$$F_n=(i/2a)\sum_{j=1}^{\infty}\sum_{m=-\infty}^{\infty}\sin j\pi(\tfrac{1}{2}+z/a)\times\sin j\pi(\tfrac{1}{2}+z'/a)e^{im(\varphi-\varphi')}\times[A_{mj}H_m^{(1)}(\gamma_{nj}r)+B_{mj}H_m^{(2)}(\gamma_{nj}r)],\quad(9)$$

where the factor $(i/2a)e^{-im\varphi'}\sin j\pi(\frac{1}{2}+z'/a)$ is included for convenience. The important fact is that F_n is a general solution of

$$(\nabla^2+k_n^2)F_n=0,$$

and satisfies Eq. (5). The coefficients A_{mj} and B_{mj} are exactly determinable only upon consideration of an extremely difficult, if not insoluble, boundary value problem. However, F_n represents essentially reflected waves at the boundaries R_1 and R_2, and hence these coefficients can be roughly estimated from physical arguments. In particular, we shall seek to stay on the safe side by looking for something like an upper limit to the power radiated. As a first step, we assume that as far as the propagating modes are concerned, the power radiated is not less than it would be for an infinite shield, i.e., we set $A_{nj}, B_{nj}=0$ for propagating modes. It is then necessary only to consider the power radiated into the attenuated modes. As mentioned previously, $G_n^{(\infty)}$ contributes nothing for attenuated modes and only F_n enters. Thus we have

$$P_n\lesssim P_n^{(\infty)}+P_n^{(\mathrm{att})},\quad(10)$$

where $P_n^{(\infty)}$ is given by (7) and where

$$P_n^{(\mathrm{att})}=\mathrm{Re}\left\{4in\omega e^2\int_{-\pi}^{\pi}d(\varphi-\varphi')F_n(\mathrm{orbit})\times[1-\beta^2\cos(\varphi-\varphi')]e^{-im(\varphi-\varphi')}\right\}.\quad(11)$$

In order to evaluate Eq. (11), we must estimate the remaining A_{nj} and B_{nj}. The easiest way to do this is as follows. In any high-energy synchrotron, the length R_2-R_1 and the plate separation a are very small compared to the orbit radius R. Thus the cylindrical waves behave very much like plane waves, i.e., the Bessel functions can be replaced by their asymptotic values. To this approximation, a typical attenuated mode of G_n of Eq. (8) has the form of attenuated plane waves emitted by the source plus waves reflected at the boundaries with amplitudes expressible in terms of a complex reflection coefficient of order of magnitude unity. The power transmitted in the attenuated modes is easily calculated in terms of such reflection coefficients and an "upper limit" estimated by choosing the phase of these reflection coefficients properly while setting their magnitudes equal to unity. The simple result is then the following:

$$P_n^{(\mathrm{att})}\simeq(n\omega e^2/R)(4\pi R/a)\sum_{\substack{j=1,3,\cdots\\ j>n\beta/\pi R}}(2/\pi)(a/j\pi R)\times[e^{-2j\pi(R-R_1)/a}+e^{-2j\pi(R_2-R)/a}].$$

In obtaining this result, multiple reflections have been neglected and the argument $\gamma_{nj}R$ of the Bessel functions in Eq. (9) has been approximated by $i(j\pi R/a)$, both being permissible for highly attenuated modes. The various terms which appear are then easily identified. The factor $(n\omega e^2/R)(4\pi R/a)$ is the same normalization factor as in Eq. (7); the factor $(2/\pi)(a/j\pi R)$ arises from the asymptotic expansion of the Bessel functions, while the first exponential gives the attenuation of a wave of unit amplitude originating at the source and then being reflected back to it by the surface at R_1 and similarly for the second exponential term with reflection at R_2. In any event, if we now introduce the dimensionless parameters,

$$\delta_1=(R-R_1)/a,\quad \delta_2=(R_2-R)/a,\quad(12)$$

we obtain finally

$$P_n^{(\mathrm{att})}\simeq(8n\omega e^2/\pi R)\sum_{\substack{j=1,3,\cdots\\ j<n\beta/\pi R}}(1/j)(e^{-2j\pi\delta_1}+e^{-2j\pi\delta_2}).\quad(13)$$

The procedure described above is admittedly crude, but in fact we have obtained the same result by a much more careful treatment in which the shield was regarded as a section of a radial transmission line with proper care being given to asymptotic representations of the Bessel functions in the various domains of order and argument which occur. We shall not reproduce that treatment here except to say that it shows that Eq. (13) is adequate provided $\delta \lesssim 2$ and $(R/a) \gtrsim 20$. This restriction on δ is relaxed somewhat if R/a is larger, as might be expected for actual synchrotrons. For example, if $R/a \gtrsim 100$, then $\delta \lesssim 5$ is suitable. However, as we shall see, the shield behaves very much as if it were infinite when δ appreciably exceeds 2 and hence this is not a serious restriction.

COHERENT RADIATION

Having obtained expressions for the power radiated in the nth harmonic by a single electron for each of the three cases, we now desire expressions for the power radiated by, say, N electrons distributed in a specified way around the circular orbit.[1-3] In particular, suppose the kth electron to have the angular coordinate $\varphi_k + \omega t$ at time t. In the Fourier decomposition of the fields, the contribution of each electron thus contains a phase factor $e^{-in\varphi_k}$ for the nth harmonic. It is then easily established that the power radiated in the nth harmonic by the N electrons is

$$P_n \left| \sum_1^N e^{-in\varphi_k} \right|^2 = NP_n + P_n \sum_{k \neq q}^N \cos n(\varphi_k - \varphi_q). \quad (14)$$

The first term gives just the incoherent power loss. Since the spectrum of this radiation is mostly in the visible or ultraviolet region, it is of course unaffected by the presence of the shields, i.e., when summed over n, it gives the usual results[1-4] in all cases and we shall not discuss it further.

Our interest is in the second term, representing the coherent radiation, which we express as

$$N(N+1)P_n f_n \simeq N^2 P_n f_n, \quad (15)$$

where the form factor f_n is

$$f_n = [1/N(N+1)] \sum_{k \neq q} \cos n(\varphi_k - \varphi_q). \quad (16)$$

Assuming that the electrons are symmetrically distributed about the same mean angle, say zero, and that each electron is independent, we then have at once

$$f_n = \left(\int \cos n\varphi \cdot S(\varphi) d\varphi \right)^2,$$

where $S(\varphi)d\varphi$ is the probability that a given electron is found in the angular interval between φ and $\varphi + d\varphi$. For example, if the electrons are uniformly distributed over an angular interval α, then

$$S(\varphi) = 1/\alpha, \quad -\alpha/2 \leq \varphi \leq \alpha/2$$
$$= 0, \text{ otherwise}$$

and

$$f_n = [\sin(\tfrac{1}{2}n\alpha)/(\tfrac{1}{2}n\alpha)]^2. \quad (17)$$

As a second example, if the electrons are distributed according to a Gaussian law, then

$$S(\varphi) = (1/\alpha\sqrt{\pi}) \exp(-\varphi^2/\alpha^2)$$

and

$$f_n = \exp[-(n\alpha/2)^2]. \quad (18)$$

In any event, the total coherent radiation is obtained by summing Eq. (15) over all harmonics and we then have, for the three cases under consideration:

I. No Shielding

$$P_{\text{coh}}^{(0)} = N^2 \sum P_n^{(0)} f_n. \quad (19)$$

II. Infinite Parallel Plate Shields

$$P_{\text{coh}}^{(\infty)} = N^2 \sum P_n^{(\infty)} f_n. \quad (20)$$

III. Finite Parallel Plate Shields

$$P_{\text{coh}} = P_{\text{coh}}^{(\infty)} + P_{\text{coh}}^{(\text{att})}, \quad (21)$$

$$P_{\text{coh}}^{(\text{att})} = N^2 \sum P_n^{(\text{att})} f_n. \quad (22)$$

Using the fact that $P_n^{(0)} \sim n^{\frac{1}{3}}$, Eq. (19) has been evaluated for a uniform distribution by Schwinger[2] and for a Gaussian distribution by Schiff,[1] with the results

$$P_{\text{coh}}^{(0)} = (N^2\omega e^2/R)(\sqrt{3}/\alpha)^{4/3} \text{ (uniform)} \quad (23)$$

and

$$P_{\text{coh}}^{(0)} = (N^2\omega e^2/R)(\sqrt{3}/\alpha)^{4/3} \times (4/\pi\sqrt{3})2^{\frac{1}{3}}[\Gamma(2/3)]^2 \text{ (Gaussian)}.$$

It is seen that the results are not terribly sensitive to the detailed character of the form factor, and henceforth we shall consider only the uniform distribution. For this distribution, Schwinger[2] has also evaluated Eq. (20), but only under the assumption that the size of the bunch is at least of the order of the plate separation (i.e., that $R\alpha \gtrsim a$), with the result[6]

$$P_{\text{coh}}^{(\infty)} = (N^2\omega e^2/R)(\sqrt{3}a/2R\alpha^2). \quad (24)$$

This restriction on the size of the bunch is not as serious as it seems at first glance, since for $R\alpha$ much less than a the shielding effects become very small and hence are not of significance. Additionally, examination of Schwinger's derivation leads one to the conclusion that Eq. (24) represents essentially an upper limit to the coherent radiation loss as α becomes smaller than a/R. Presumably, therefore, Eq. (24) can be safely used until α becomes small enough that the result is numerically equal to that of Eq. (23), which is the result in the absence of shielding.[7]

[6] See the Appendix for details.

[7] Actually one can do considerably better than this as follows: As the bunch size α decreases toward zero, for fixed plate separation a, the shielding effect becomes negligible. In other words,

Finally, we calculate the correction term for finite shields from Eq. (22), using Eq. (17) and Eq. (13):

$$P_{\rm coh}^{(\rm att)} = (8N^2\omega e^2/\pi R) \sum_{j=1,3,\cdots} (1/j) \times (e^{-2j\pi\delta_1}+e^{-2j\pi\delta_2}) \sum_{n=1}^{j\pi R/a} n\left(\frac{\sin\frac{1}{2}n\alpha}{\frac{1}{2}n\alpha}\right)^2.$$

For $\delta \geq \frac{1}{2}$, only the $j=1$ term contributes significantly, as is easily verified, so that, using

$$\sum_{1}^{\pi R/a} (1/n)\sin^2(\tfrac{1}{2}n\alpha) \simeq \int_0^{\pi R\alpha/a} (1/x)\sin^2(x/2)dx = S(\pi R\alpha/a) \quad (25)$$

we obtain

$$P_{\rm coh}^{(\rm att)} \simeq (N^2\omega e^2/R)(32/\pi\alpha^2) \times [e^{-2\pi\delta_1}+e^{-2\pi\delta_2}]S(\pi R\alpha/a). \quad (26)$$

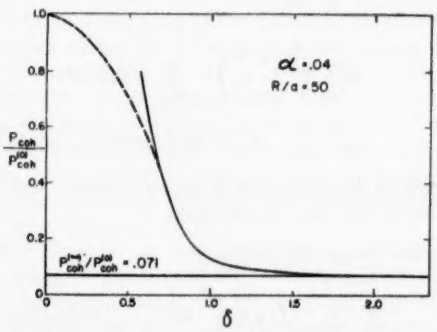

FIG. 1. Coherent power loss, relative to the loss in the absence of shielding, *vs* plate width in units of the plate separation.

This result is valid under the conditions $R/a \gtrsim 20$ and $\frac{1}{2} \leq \delta \leq 2$. Although this may seem to be a small domain of validity, it actually covers the most important region. The quantity $S(\pi R\alpha/a)$ is easily expressed in terms of known functions;[8] viz.,

$$S(y) = \tfrac{1}{2}[C+\log y - \mathrm{Ci}(y)], \quad (27)$$

where $C = 0.577\cdots$ = Euler's constant, and $\mathrm{Ci}(y)$ is the cosine integral; so that the final result is extremely simple.

As an example, in Fig. 1, we present a plot of the coherent power loss, relative to the loss in the absence of shielding, against plate width for the special case $\delta_1 = \delta_2 = \delta/2$ and for $\alpha = 0.04$ and $R/a = 50$. Although only a portion of the curve can be calculated [using (21), (23), and (26)] we do know the limit points when $\delta = 0$ (no shielding) and $\delta = \infty$ (infinite parallel plate shielding) and hence the remainder of the curve can be sketched in without serious error. The dotted portion in the figure has been so sketched, while the solid portion has been calculated according to the above.

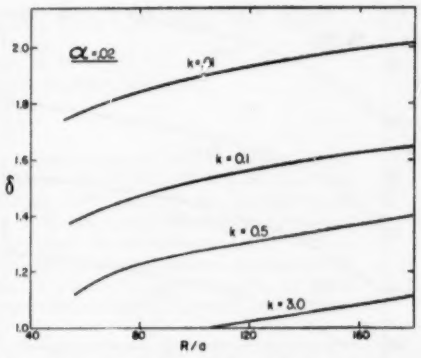

FIG. 2. Plate width *vs* orbit radius, both in units of the plate separation, for constant ratio of coherent power loss to that for infinite parallel plate shields and for the electrons bunched uniformly over an angular interval 0.02 radian.

In Figs. 2, 3, and 4, we present the results in convenient form by introducing the parameter $k(\delta,\alpha,R/a)$ defined by

$$P_{\rm coh} = [1+k(\delta_1,\alpha,R/a)+k(\delta_2,\alpha,R/a)]P_{\rm coh}^{(\infty)}, \quad (28)$$

where $P_{\rm coh}^{(\infty)}$ is given by Eq. (23). Values of δ *vs* R/a for constant k have been plotted for $\alpha = 0.02$, 0.04, and 0.06. These curves enable one to estimate the width of shielding required to reduce the coherent radiation loss to a given amount in units of the loss for infinite shields. As an example, given $R/a = 60$ and $\alpha = 0.02$, it might be desirable to know the plate widths necessary to reduce the coherent power to twice $P_{\rm coh}^{(\infty)}$. Selecting $\delta_1 = \delta_2$ so that $k(\delta_1,\alpha,R/a) = k(\delta_2,\alpha,R/a) = 0.5$, we find from the curves

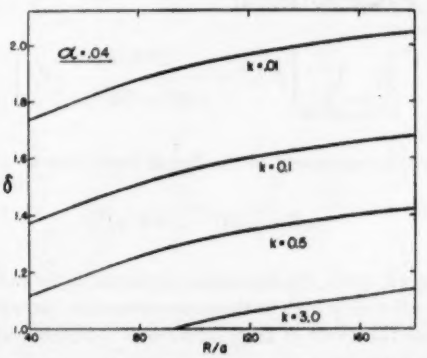

FIG. 3. Plate width *vs* orbit radius, both in units of the plate separation, for constant ratio of coherent power loss to that for infinite parallel plate shields and for the electrons bunched uniformly over an angular interval 0.04 radian.

regarded as a function of α, $P_{\rm coh}^{(\infty)}$ approaches $P_{\rm coh}^{(0)}$ as α approaches zero. Knowing that the result (24), valid for large α, is essentially an upper limit for small α, one can then easily sketch in the entire curve to reasonable accuracy.

[8] See, for example, E. Jahnke and F. Emde, *Tables of Functions* (Dover Publications, New York, 1943), pp. 2–6.

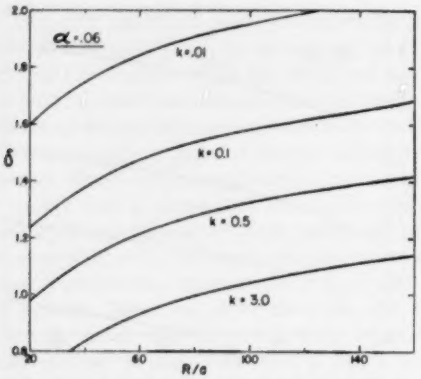

FIG. 4. Plate width *vs* orbit radius, both in units of the plate separation, for constant ratio of coherent power loss to that for infinite parallel plate shields and for the electrons bunched uniformly over an angular interval 0.06 radian.

of Fig. 2 that $\delta_1=\delta_2=1.15$; and hence, from (12), $R-R_1=R_2-R=1.15a$.

ACKNOWLEDGMENT

We should like to express our appreciation to L. Jackson Laslett for calling this problem to our attention and for providing us with some of his own unpublished material as well as the material of reference 2.

APPENDIX

Because of the unavailability of reference 2, we give an outline of Schwinger's derivation of Eq. (24). Taking the indicated real part of (7) we have

$$P_n^{(\infty)}=(n\omega e^2/R)(4\pi R/a)\times\sum_{\substack{j=1,3,\cdots\\ j<n\alpha\beta/\pi R}}[-J_n{}^2+\tfrac{1}{2}\beta^2(J_{n-1}{}^2+J_{n+1}{}^2)]$$

$$=(n\omega e^2/R)(4\pi R/a)\times\sum_{\substack{j=1,3\cdots\\ j<n\alpha\beta/\pi R}}\left[\beta^2 J_n{}'^2+\frac{(j\pi R/a)^2}{(n\beta)^2-(j\pi R/a)^2}J_n{}^2\right], \quad \text{(A1)}$$

where the argument of the Bessel Functions is

$$\gamma_{nj}R=[(n\beta)^2-(j\pi R/a)^2]^{\frac{1}{2}}.$$

Since $\pi R/a\gg 1$, the harmonics involved in the radiation are sufficiently high so that approximation formulas for Bessel functions of large order are applicable and we write,[9] placing $\beta=1$,

[9] G. N. Watson, *Bessel Functions* (The MacMillan Company, New York, 1945), p. 248.

$$J_n([n^2-(j\pi R/a)^2]^{\frac{1}{2}})=\frac{1}{\sqrt{3}\pi}\left(\frac{j\pi R/a}{n}\right)K_{\frac{1}{3}}[(j\pi R/a)^3(1/3n^2)],$$

$$J_n'([n^2-(j\pi R/a)^2]^{\frac{1}{2}})=\frac{1}{\sqrt{3}\pi}\left(\frac{j\pi R/a}{n}\right)^2 K_{\frac{2}{3}}[(j\pi R/a)^3(1/3n^2)]. \quad \text{(A2)}$$

Recognizing that the contributions to $P_n^{(\infty)}$ are negligible unless $n\gtrsim(j\pi R/a)(j\pi R/a)^{\frac{1}{2}}$, so that n must exceed $j\pi R/a$ by a rather large factor, we simplify the second term of (A-1) accordingly and obtain

$$P_n^{(\infty)}=(\omega e^2/R)(4R/3\pi a)\sum_{\substack{j=1,3,\cdots\\ \gamma_j<n}}(\gamma_j{}^4/n^3)\times[K_{\frac{1}{3}}{}^2(\gamma_j{}^3/3n^2)+K_{\frac{2}{3}}{}^2(\gamma_j{}^3/3n^2)],$$

where

$$\gamma_j=j\pi R/a.$$

The total coherent power is then given by

$$P_{\text{coh}}^{(\infty)}=(N^2\omega e^2/R)(4R/3\pi a)\times\sum_{n=1}\left(\frac{\sin\frac{1}{2}n\alpha}{\frac{1}{2}n\alpha}\right)^2\sum_{\substack{j=1,3,\cdots\\ \gamma_j<n}}(\gamma_j{}^4/n^3)\times[K_{\frac{1}{3}}{}^2(\gamma_j{}^3/3n^2)+K_{\frac{2}{3}}{}^2(\gamma_j{}^3/3n^2)].$$

Replacing the sum over n by an integral, and introducing $x=\gamma_j{}^3/3n^2$, we then have

$$P_{\text{coh}}^{(\infty)}=(N^2\omega e^2/R)(12R/\pi a\alpha^2)\times\sum_{j=1,3,\cdots}(1/\gamma_j{}^2)\int_0^\infty\sin^2([\gamma_j{}^3/3x]^{\frac{1}{2}}\alpha/2)\times[K_{\frac{1}{3}}{}^2(x)+K_{\frac{2}{3}}{}^2(x)]x\,dx, \quad \text{(A3)}$$

where the correct upper limit of the integral, $\gamma_j/3$, which is large compared to unity, has been replaced by infinity. Now the main contribution to the integral comes for values of x in the interval $0\leq x\lesssim 1$. In this interval the argument of the $\sin^2$ term in the integral is at least of order $\alpha\gamma_j\sqrt{\gamma_j}\simeq(jR\alpha/a)(jR/a)^{\frac{1}{2}}\gg R\alpha/a$. Hence, if $R\alpha/a$ is at least of order unity, the $\sin^2$ term can be replaced by its average value $\frac{1}{2}$, the known integrals[8] and sums performed and the result of Eq. (24) follows.

Without this restriction on $R\alpha/a$, the evaluation of Eq. (A3) seems possible only numerically. However, we remark that if α is small enough that the argument of the $\sin^2$ term is rather small over the important range, then this term is considerably less than its average value and hence, as indicated in the text, one errs only on the conservative side in extending Schwinger's result. Needless to say, an absolute upper limit is obtained by replacing the $\sin^2$ term by unity, thus giving twice the result of Eq. (24), but this seems unnecessarily conservative.

Reactions of Cesium with Protons at 60, 80, 100, 150, and 240 Mev*

RICHARD W. FINK† AND EDWIN O. WIIG
Department of Chemistry, University of Rochester, Rochester, New York

(Received April 26, 1954)

Absolute production cross sections have been determined for certain isotopes of barium, cesium, iodine, and tellurium produced by reactions of cesium with protons of energies 60, 80, 100, 150, and 240 Mev. The yields are based on the known cross section for the monitor reaction $Al^{27}(p,3pn)Na^{24}$. In the region up to 100 Mev the data indicate that the yields are largely explained on the basis of an evaporation mechanism which competes with the prompt knock-on optical model to an extent which decreases rapidly with increasing energy because of increasing nuclear transparency. The neutron pick-up reaction manifests itself in extraordinarily large yields of Cs^{128} and to a lesser extent in the yields of Cs^{131}. Formation of small amounts of neutron-excess iodine isotopes argues for alpha-particle fragmentation especially at the lower bombardment energies.

INTRODUCTION

PREVIOUSLY[1] we have reported on the spallation of cesium with 240-Mev protons from the Rochester 130-inch cyclotron. The results indicated that a majority of reactions at 240 Mev occur as primary knock-on collisions in which the incident proton interacts with only a few nucleons. This primary interaction is followed by dissipation of the residual nuclear excitation, whose energy spread is quite broad, leading to a distribution of products which reach far down the nuclide chart. At an energy of 240 Mev those yields due to the knock-on process largely predominate over those due to an evaporation mechanism because of the nuclear transparency[2] which increases with energy rapidly up to roughly 200 Mev and then much more slowly up to about 400 Mev.

In this paper we report the behavior at a variety of proton energies; namely, 60, 80, 100, 150, and 240 Mev. The experimental techniques are identical with those reported earlier,[1] as are all of the assumptions and correction factors which are applied to obtain the yield of each nuclear species.

The results are given in Table I, which also lists the counting efficiency used for each nuclide. This efficiency is defined as the ratio of the number of events recorded in the beta-proportional methane flow counting chamber to the total number of events occurring within the sensitive volume of the chamber. The values are identical to those given previously with the exception of Cs^{132}. We have reconsidered the value of the counting efficiency for this nuclide and have used a value of 0.01 in place of the value of 0.005 used formerly. The yield of Cs^{132} at 240 Mev given in our first paper should therefore be revised to that given in Table I.

BARIUM YIELDS

Figure 1 depicts the yield data for barium isotopes taken from Table I. It is seen that the yield of Ba^{128} has a threshold of about 60 Mev and a maximum at approximately 80 Mev. The relative shape of these yield curves must be attributed to differences in average excitation energies imparted to the struck target nuclei by the incident protons. In general, lower bombardment energies result in lower average excitation energies left to the struck nuclei. Consequently, the broad peaks must result from a rather wide distribution of smaller excitation energies given to the excited nuclei following an initial knock-on reaction. Subsequent evaporation ejects protons and neutrons either singly or in fragments such as alpha particles. The maximum yield of each barium isotope in Fig. 1 occurs in the expected sequence Ba^{131}, Ba^{129}, and Ba^{128}. Apparently the hump

TABLE I. Absolute production cross sections of spallation products resulting from irradiation of cesium with protons at various energies.[a]

Nominal half-life	Nuclide	Counting efficiency	60 Mev	80 Mev	100 Mev	150 Mev	240 Mev
				(Yields in millibarns)			
2.4 days	Ba^{128}	1.0	0	67	58	14	8.1
2.0 hr	Ba^{129}	1.0	173	3.1	4.7	11	3.6
12.5 days	Ba^{131}	0.72	20	4.8	13	3	5.3
42.5 hr	Ba^{128m}	0.78	31	—	—	—	—
5.5 hr	Cs^{127}	1.0	0	7.1	15.4	6.4	4.5
31 hr	Cs^{129}	0.4	83	123	116	36	15
30 min	Cs^{130}	1.0	137	46	—	12	—
9.8 days	Cs^{131}	0.0025	470	—	500	320	460
7.1 days	Cs^{132}	0.01	790	1120	890	570	59
1.6 hr	$I^{126+131}$	1.0	0	0	0	3.6	11
13 hr	I^{128}	0.17	0	0	0	8.5	21
4.0 days	I^{126}	0.30	0	0	0.9	5.7	8.4
12.5 days	I^{124}	0.53	0.05	0.94	2.4	2.5	5.0
25.0 min	I^{125}	0.95	0.36	0.4	0.44	—	—
12.6 days	I^{130}	1.0	0.004	0.02	0.04	—	—
2.5 hr	Te^{117}	1.0	0	0	—	0.2	2.4
6.0 days	Te^{119}	1.0	0	0	—	1.1	4.8
17.0 days	Te^{121}	0.1	—	—	7.3	5.1	—

[a] Energies quoted are nominal beam energies of the Rochester 130-inch cyclotron as estimated from radius. Places in the table showing a yield of 0 millibarns signify that in those instances the nuclide should have been observed had it been present, so that a 0 yield signifies a lack of production of detectable amounts of the nuclide. Places showing a dash (—) signify that in those instances the nuclide might have been present in small amounts but could not be detected and identified because of experimental difficulties such as (a) the time for chemical separation was too long; (b) other species of similar half-life or stronger radiations were produced at that energy, causing masking; or (c) the yield was too small to be detected or identified.

* This investigation was supported by the U. S. Atomic Energy Commission. Part of this work is taken from the doctoral thesis of R. W. Fink, who also acknowledges with appreciation the award of a Post-doctoral Fellowship at the University of Rochester, 1953.

† Present address: Department of Chemistry, University of Arkansas, Fayetteville, Arkansas.

[1] R. W. Fink and E. O. Wiig, Phys. Rev. **94**, 1357 (1954).

[2] J. DeJuren and N. Knable, Phys. Rev. **77**, 606 (1950); J. DeJuren, Phys. Rev. **80**, 27 (1950).

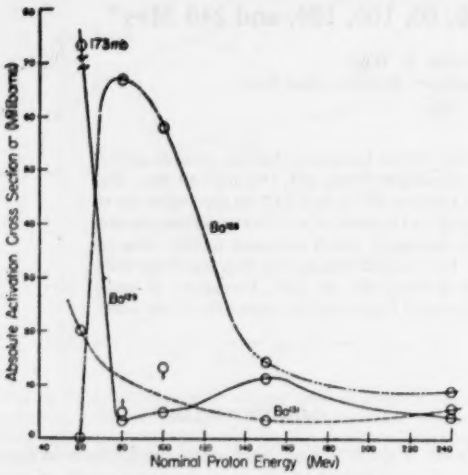

FIG. 1. Variation of the yields of barium isotopes with proton bombardment energy.

in the yield curve of Ba^{129} in the 150-Mev region is real. Caretto[3] has observed a similar maximum in the region of 175 Mev for the yields of several nuclides produced by the reaction of protons on yttrium. If this maximum is real, it might be explained on the basis that at energies between 80 and 100 Mev, the production cross sections of Ba^{128}, Cs^{129}, Cs^{131}, and Cs^{132} compete severely with that of Ba^{129}, lowering the yield of the latter in this region. As the excitation energy is increased, this competition becomes less pronounced and a rise occurs in the Ba^{129} yield curve above 100 Mev.

CESIUM YIELDS

Figure 2 presents the yield data for cesium isotopes from Table I. The yield of Cs^{132} is seen to be extraordinarily high, especially in the neighborhood of 80 to 100 Mev, compared to the yields of its immediate neighbors, Cs^{131} and Cs^{130}. This observation can probably be explained on the basis of the neutron pick-up reaction, $Cs^{133}(p,d)Cs^{132}$. Several investigators at Berkeley[4] have observed that irradiations of elements with 90-Mev neutrons result in unexpectedly large yields of deuterons of energy of the same order as the incident neutrons and sharply peaked in the forward direction. The high yield, high emission energy, and the angular distribution peaked sharply forward all suggest that a production mechanism is responsible which involves the "pick-up" of a neutron by an incident proton, or vice versa, according to the suggestions of Chew and Goldberger.[5] To a much smaller extent the pick-up process also operates to form tritons, in which the incident proton and two neutrons in the target nucleus happen to possess momenta relative to each other which is compatible with the internal motion of a triton. To a certain extent then, we expect a contribution to the yield of Cs^{131} from the pick-up reaction $Cs^{133}(p,t)Cs^{131}$, but the effect is much less pronounced than that due to the (p,d) reaction in Fig. 2. One would expect a gradual decrease in the contribution from pick-up reactions with increasing energy, which is borne out experimentally by the yield curve of Cs^{132} which falls off only gradually as compared with the yield curves of barium and other cesium nuclides which fall off rapidly. A reaction threshold for the formation of Cs^{127} of about 55 Mev is also indicated by the data in Fig. 2. The other general features of the cesium yield curves can be explained on the same basis of average excitation energies as the barium curves.

IODINE YIELDS

Figure 3 indicates the yield pattern of the $(Z-2)$ product, iodine, from the data in Table I. These curves, very different from the yield curves for barium and cesium in the region below 150 Mev, show that the formation of neutron-deficient iodine isotopes occurs only at higher energies. There are no salient peaks at lower energies, indicating little if any contribution from an evaporation mechanism below 100 Mev. This is in marked contrast to cesium and barium yields which show large contributions from the evaporation model below 100 Mev. It is clear that the neutron-deficient iodine isotopes are formed above about 100 Mev chiefly from the knock-on process, although some evaporation may redistribute the iodine yields following the initial knock-on reaction. In the case of the neutron-excess isotope I^{128} the yield which appears in Table I below 150 Mev probably can be attributed to alpha-particle emission, due to lower excitation energies in the struck nucleus, as well as to evaporation. The yield of I^{130} is still smaller by at least one order of magnitude and would require the emission of the equivalent of He^3 from

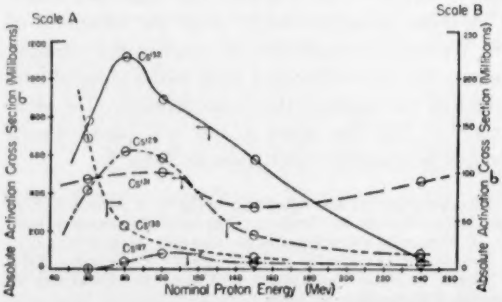

FIG. 2. Variation of the yields of cesium isotopes with proton bombardment energy. Note that two ordinates are used; the arrows indicate which scale applies to a particular curve.

[3] A. A. Caretto, Jr., Ph.D. thesis, University of Rochester, 1953 (unpublished).

[4] A. Bratenahl, University of California Radiation Laboratory Report UCRL-1842, 1952 (unpublished); J. Hadley and H. F. York, Phys. Rev. 80, 345 (1950); K. Brueckner and W. M. Powell, Phys. Rev. 75, 1274 (1949); H. Bradner, Phys. Rev. 75, 1467 (1949).

[5] G. Chew and M. Goldberger, Phys. Rev. 77, 470 (1950).

the excited target nucleus. Emission of alpha particles increases the neutron/proton ratio of the product which may account for the augmented yield of I^{126} at the lower energies. Formation at these energies of such shielded isotopes as I^{124}, I^{126}, and I^{128} is also an indication of alpha-particle fragmentation.

The apparent threshold for formation of $I^{120+121}$ and I^{123} is about 100 Mev; for formation of I^{124}, about 80 Mev; and for I^{126}, about 60 Mev. The reason that the yields of I^{123} are larger than those of its neighbors up to the highest energy studied, 240 Mev, must be associated with the assumption that in the range 140 to 240 Mev, the average excitation energy given to the struck target nucleus must be such as to favor the reaction leading to I^{123}. Thus, as the bombardment energy is increased to 240 Mev from the lowest value, each iodine isotope starting from stable I^{127} is in turn the product of a favored reaction, the yields first rising successively and then eventually flattening out. Thus, in Fig. 3, the yield of I^{126} rises first and flattens out soonest; next comes I^{124}, rising and then flattening out; then I^{123}, the most favored product between 140 and 240 Mev, which possibly would flatten out at still higher energies; finally, the yield of the most neutron-deficient isotope(s) $I^{120+121}$ is still rising at 240 Mev and presumably would reach and surpass that of I^{123} at much higher energies. Consequently, it is clear that the iodine yield curves can be explained qualitatively on the picture of successively higher average excitation energies imparted to the target nuclei with a particular reaction being favored over the others at a given average excitation energy.

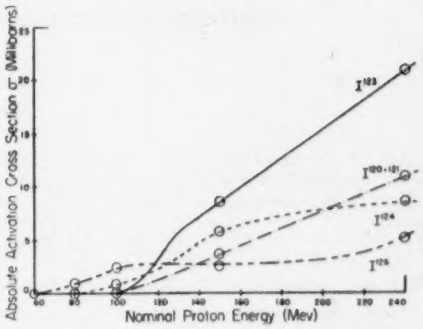

FIG. 3. Variation of the yields of iodine isotopes with proton bombardment energy.

TELLURIUM YIELDS

Yields of tellurium isotopes are given in Table I, but are not plotted. In common with the iodine results, the data for the more neutron-deficient isotopes Te^{117} and Te^{118} indicate a production threshold near 100 Mev and yields that increase with energy.

ACKNOWLEDGMENTS

We are happy to acknowledge the cooperation of Professor S. W. Barnes, Mr. William Coombs, Mr. Kurt Enslein, and the crew of the Rochester 130-inch cyclotron.

Relativistic Coulomb Scattering of Electrons and Positrons*

G. PARZEN AND T. WAINWRIGHT
Department of Physics, University of Notre Dame, Notre Dame, Indiana
(Received June 4, 1954)

The numerical tables of Feshbach for the relativistic Coulomb scattering of electrons and positrons by a nucleus of charge Z have been fitted with an analytic function. The accuracy of the analytic function is equivalent to that of the tables.

THE relativistic pure Coulomb scattering of electrons and positrons by a nucleus of charge Z was solved exactly by Mott.[1] The result was expressed in the form of a slowly convergent Legendre series. This series was summed numerically by Bartlett and Watson,[2] McKinley and Feshbach,[3] and Feshbach.[4]

In the course of some work on electron scattering, we have fitted the numerical tables of Feshbach, which are valid for positron and electron energies above about 4 Mev, with an analytical function. Such an analytical representation may be of some use, and we would like to give our result in this note. The accuracy with which our analytic function represents the numerical results is very good. The accuracy of the analytic function is as good as the accuracy of Feshbach's tables, which is about 0.1 percent except where the cross section gets small.

The cross section $\sigma(\theta)$ for the scattering of particles obeying the Dirac equation can be expressed in terms of the two scattering amplitude functions[1] $f_3(\theta)$ and $f_4(\theta)$ as

$$\sigma(\theta)=|f_3|^2+|f_4|^2. \tag{1}$$

At high energies, f_3 and f_4 are related and can be expressed in terms of a single function, $F(\theta)$:

$$f_3=\tfrac{1}{2}(1+\cos\theta)F(\theta), \tag{2}$$

$$f_4=\tfrac{1}{2}\sin\theta e^{i\varphi}F(\theta). \tag{3}$$

This relationship is given by the Born approximation[5] and is also exact in the high-energy limit.[6] In the Born approximation $F(\theta)$ would be given by

$$F=(-2E/4\pi)\cdot\int d\tau\,\exp(-i\mathbf{k}\cdot\mathbf{r})V(\mathbf{r})\exp(i\mathbf{k}_0\cdot\mathbf{r}), \tag{4}$$

where $\mathbf{k}_0$ and $\mathbf{k}$ are the incident and final momenta of the particle, $V(\mathbf{r})$ is the potential, and E is the incident energy of the particle. ($\hbar=c=1$ throughout.)

In terms of F, the cross section is given by

$$\sigma=\cos^2\tfrac{1}{2}\theta|F|^2. \tag{5}$$

We have computed the exact values of $F(\theta)$ from Feshbach's tables and have fitted $F(\theta)$ with an analytic function. In attempting to fit $F(\theta)$ with an analytic function, we have been guided by the fact that the form of $F(\theta)$ is known for small Z and for small scattering angles.

For small Z, which means small α, $\alpha=Ze^2/\hbar c$ and $F(\theta)$ is given by[3]

$$F=\left(\frac{-Ze^2}{2k}\right)\frac{1}{\sin^2\tfrac{1}{2}\theta}\left\{\exp[i(2\alpha\ln\sin\tfrac{1}{2}\theta+2\eta)]\right.$$
$$\left.+\tfrac{1}{2}\pi\alpha\frac{\sin\tfrac{1}{2}\theta}{1+\sin\tfrac{1}{2}\theta}+i\alpha\tan^2\tfrac{1}{2}\theta\ln\sin\tfrac{1}{2}\theta\right\}, \tag{6}$$

where $\exp(2i\eta)=\Gamma(1-i\alpha)/\Gamma(1+i\alpha)$, and k is the incident momentum of the particle.

For small scattering angles, F is given by[2]

$$F=\frac{-Ze^2}{2k}\frac{1}{\sin^2\tfrac{1}{2}\theta}\exp[i(2\alpha\ln\sin\tfrac{1}{2}\theta+2\eta)]$$
$$\times(1+\tfrac{1}{2}\pi\alpha\sin\tfrac{1}{2}\theta e^{i\chi}), \tag{7}$$

where $\exp(2i\chi)=\Gamma(\frac{1}{2}-i\alpha)\Gamma(1+i\alpha)/\Gamma(\frac{1}{2}+i\alpha)\Gamma(1-i\alpha)$. Here, as in all our results, Z is positive for electrons, negative for positrons.

Our analytic expression for $F(\theta)$ must reduce to Eq. (6) for small Z and to Eq. (7) for small θ. A function that will reduce to (6) and (7) in the small-Z and small-θ limits is the function defined by,

$$F_S=\frac{-Ze^2}{2k}\frac{1}{\sin^2\tfrac{1}{2}\theta}\exp\{i[2\alpha(1+\tfrac{1}{2}\tan^2\tfrac{1}{2}\theta)\ln\sin\tfrac{1}{2}\theta$$
$$+2\eta+\tfrac{1}{2}\pi\alpha(\sin\chi)y]+\tfrac{1}{2}\pi\alpha(\cos\chi)y\}, \tag{8}$$

$$|F_S|^2=\frac{Z^2e^4}{4k^2}\frac{1}{\sin^4\tfrac{1}{2}\theta}\exp[\pi\alpha(\cos\chi)y], \tag{9}$$

where $y=\sin\tfrac{1}{2}\theta/(1+\sin\tfrac{1}{2}\theta)$.

It turns out that F_S does represent $F(\theta)$ fairly well in the cases of positron scattering and small-Z ($Z\leq 30$) electron scattering. However, for large-Z electron scattering, $F(\theta)$ departs considerably from F_S at the larger angles. For the large-Z large-angle scattering, $F(\theta)$ is well represented by the function F_L defined by

$$F_L=F_S\cdot A\exp(By+i\delta), \tag{10}$$

* Supported in part by the joint program of the U. S. Office of Naval Research and the U. S. Atomic Energy Commission.

[1] N. F. Mott, Proc. Roy. Soc. (London) A124, 426 (1929).
[2] J. H. Bartlett and R. E. Watson, Proc. Am. Acad. Arts Sci. 74, 53 (1940).
[3] W. A. McKinley and H. Feshbach, Phys. Rev. 74, 1759 (1948).
[4] H. Feshbach, Phys. Rev. 88, 295 (1952).
[5] G. Parzen, Phys. Rev. 80, 261 (1950).
[6] Yennie, Ravenhall, and Wilson, Phys. Rev. 95, 500 (1954).

where A, B, and δ depend only on Z and are tabulated below.

In the general case, $F(\theta)$ can be accurately represented by a combination of the small-angle function F_S and the large-angle function F_L as

$$F=\exp(-ay^2)F_S+[1-\exp(-by^2)]F_L, \qquad (11)$$

where a and b depend only on Z.

In Tables I and II, the values of the various parameters are given as functions of Z. We found that to the accuracy of Feshbach's tables we could put $A=1$,

TABLE I. Table of χ and η as functions of Z for electron scattering. For positron scattering, the sign is changed. χ and η were computed with help of *Tables of Coulomb Wave Functions*, National Bureau of Standards, Applied Mathematics Series (U. S. Government Printing Office, Washington, D. C. 1952), No. 17, Vol. I.

Z	χ	η
0	0.0000	0.0000
13	0.2590	0.0544
29	0.5459	0.1184
47	0.8011	0.1827
62	0.9585	0.2275
80	1.0938	0.2687

$B=0$ for all Z in positron scattering. $F(\theta)$ was rather insensitive to the choice of the parameters a and b, particularly in the positron and small-Z electron cases. Thus the values of a and b can be varied by as much as 10 percent in some cases and we will still get the same $F(\theta)$ to the accuracy of Feshbach's tables.

Although Eq. (11) represents $F(\theta)$ with considerable accuracy, it is somewhat complicated mathematically. There are some special cases where we can find mathematically simpler expressions for $F(\theta)$ which are still fairly accurate.

TABLE II. The parameters A, B, δ, a, and b, as functions of Z for electron and positron scattering. Z is positive for electron scattering.

Z	A	B	δ	a	b
80	0.6172	2.352	0.218	21.1	24.0
62	0.7834	1.316	0.076	27.5	33.4
47	0.9154	0.625	0.019	45.6	49.2
29	0.9764	0.205	−0.009	37.6	38.0
13	0.9928	0.026	−0.0048	7.5	7.5
0	1.0000	0	0		
−13	1.0000	0.0000	−0.0062	10.5	10.5
−29	1.0000	0.0000	−0.030	8.3	8.3
−47	1.0000	0.0000	−0.045	13.8	13.8
−62	1.0000	0.0000	−0.058	13.2	13.2
−80	1.0000	0.0000	−0.062	14.9	14.9

POSITRON SCATTERING

In this case, $F(\theta)$ is given to within a few percent by

$$F=F_S, \qquad (12a)$$

$$|F|^2=\frac{Z^2e^4}{4k^2}\frac{1}{\sin^4\frac{1}{2}\theta}\exp[\pi\alpha(\cos\chi)y]. \qquad (12b)$$

ELECTRON SCATTERING

For small-Z, that is, $Z\leq 30$, $F(\theta)$ is given to within a few percent by

$$F=F_L \qquad (13a)$$

$$|F|^2=\frac{Z^2e^4}{4k^2}\frac{1}{\sin^4\frac{1}{2}\theta}\exp\{(\pi\alpha\cos\chi+2B)y\}. \qquad (13b)$$

For the large-Z electron scattering Eq. (13) is valid at the larger angles but is considerably in error at the smaller angles, where $F=F_S$. However, one can say that for large Z, at angles larger than $\theta=60°$, F is given by Eq. (13) to within a few percent.

Excitation Function of the $C^{12}(p,pn)C^{11}$ Reaction in the Bev Region*

R. L. WOLFGANG AND G. FRIEDLANDER
Chemistry Department, Brookhaven National Laboratory, Upton, New York
(Received June 29, 1954)

The ratio of the cross section of the $C^{12}(p,pn)C^{11}$ reaction to the cross section of the $Al^{27}(p,3pn)Na^{24}$ reaction has been measured in the energy range 400 Mev to 3 Bev. This ratio as well as the excitation curve of the $C^{12}(p,pn)C^{11}$ reaction appear to be quite insensitive functions of the energy in the range studied. A possible interpretation is discussed.

THE excitation function of the $C^{12}(p,pn)C^{11}$ reaction between threshold and 390 Mev has previously been the subject of detailed studies.[1,2] In the present paper we report cross section measurements for this reaction in the energy range from 400 Mev to 3 Bev. The irradiations were carried out in the circulating proton beam of the Brookhaven Cosmotron.

Targets were made up of several layers of polythene of thicknesses varying from 5 mg/cm² to 10 mg/cm² and one or two layers of aluminum foil 1 mil or 3 mils thick. The Na^{24} induced in the aluminum served as the monitor of irradiation intensity. Multiple layers of foils were used to check the possibility of recoil losses and to obtain duplicate values. The total thickness of the sandwiches was in all cases less than 50 mg/cm², so that the contribution of secondary reactions to the measured activities would be negligible. The irradiations were carried out at the desired proton energy in the Cosmotron by means of the pulsed moving target technique described elsewhere.[3]

After irradiation identical sections of the foils in each sandwich were cut out and counted with end-window proportional counters. The polythene foils were counted immediately and showed a pure 20.5-min C^{11} decay and the aluminum foils were counted after the C^{11} and F^{18} activities had died out to leave the pure 15-hour decay of Na^{24}. Small corrections for self-absorption effects were applied to the data obtained.

TABLE I. Ratio of $C^{12}(p,pn)$ to $Al^{27}(p,3pn)$ cross sections.

Energy Bev	$\sigma C^{11}/\sigma Na^{24}$
2.95	2.38
2.2	2.24, 2.38
1.8	2.14
1.4	2.20
1.0	2.29
0.6	2.31
0.42	2.69, 2.85
0.44[a]	2.63
0.35[a]	2.88
0.35[b]	2.76
0.39[b]	2.84

[a] Determinations by A. Turkevich using Chicago synchrocyclotron (private communication).
[b] Determinations by J. Miller using Nevis synchrocyclotron (private communication).

The ratio of the $C^{12}(p,pn)C^{11}$ cross section to the $Al^{27}(p,3pn)Na^{24}$ cross section is given in Table I for each energy investigated. We consider these data to be reliable to ±5 percent. To convert these ratios to absolute cross sections for the $C^{12}(p,pn)C^{11}$ reaction we use the measured values of 10.8 mb at 420 Mev[4] and 9.0 mb at 2.2 Bev[5] for the $Al^{27}(p,3pn)Na^{24}$ reaction and assume the cross section for this reaction to vary linearly with energy between 400 Mev and 3 Bev. The values thus obtained for the $C^{12}(p,pn)C^{11}$ cross section are plotted in Fig. 1. Since the cross sections of the reference reaction $Al^{27}(p,3pn)$ above 400 Mev are tentative, the $C^{12}(p,pn)C^{11}$ excitation curve given in Fig. 1 may have to be revised somewhat when better absolute values for the $Al^{27}(p,3pn)Na^{24}$ reaction become available.

It should be noted that the excitation function reported here does not join smoothly with the lower-energy data (up to 390 Mev) of Aamodt *et al.*[1] and Warshaw *et al.*[2] The discrepancy may arise from an error in one of the absolute cross section measurements or an error in our cross section ratio in the 400-Mev region. To check on the latter possibility it seemed desirable to obtain independent checks of the ratio of $C^{12}(p,pn)$ to $Al^{27}(p,3pn)$ cross sections at ~400 Mev. J. M. Miller using the Nevis synchrocyclotron, and A. Turkevich using the Chicago synchrocyclotron, very kindly made such independent determinations of this ratio. Their results, shown in Table I, confirm the authors' work. The possibility that the measured ratios are too low because of production of Na^{24} by secondary neutrons [$Al^{27}(n,\alpha)$ reaction] was eliminated by experiments both by J. M. Miller at Nevis and by J. Hudis at the Cosmotron. In these experiments the cross section for Na^{24} production from aluminum was shown to be essentially independent of target thickness in the region of interest so that neutrons produced in the target itself cannot produce any significant fraction of the Na^{24} observed. Other experiments in the Cosmotron showed Na^{24} production from aluminum due to general neutron flux in the target region to be quite negligible. Accepting the validity of our ratio measurements, we

* Research performed under the auspices of the U. S. Atomic Energy Commission.
[1] Aamodt, Peterson, and Phillips, Phys. Rev. **88**, 739 (1952). This paper gives references to earlier work.
[2] Warshaw, Swanson, and Rosenfeld, Phys. Rev. **95**, 649 (1954).
[3] Friedlander, Miller, Wolfgang, Hudis, and Baker, Phys. Rev. **94**, 727 (1954).
[4] L. Marquez, Phys. Rev. **86**, 405 (1952).
[5] A. Turkevich, Phys. Rev. **94**, 775 (1954).

must then consider either the absolute value of the $C^{12}(p,pn)$ cross section or that of the $Al^{27}(p,3pn)$ cross section (or both) to be in error. We have rather arbitrarily chosen to base our data on the 10.8-mb value for the $Al^{27}(p,3pn)$ cross section at 420 Mev.

Figure 1 shows that the cross section of the $C^{12}(p,pn)C^{11}$ reaction is a fairly insensitive function of the energy of the incident proton in the energy range studied here. Since similar results were found for the production of Na^{24}, Na^{22}, and F^{18} from aluminum and for Be^{7} formation from carbon,[6] it appears to be generally true that the probability of ejecting a small number of nucleons from a small nucleus remains substantially constant over a range of bombarding energies from a few hundred Mev to at least 3 Bev. This implies that the probability that the incident particle leaves behind a relatively small amount of energy ($\lesssim$100 Mev) in the *initial* interaction with the nucleus is relatively constant over the wide energy range studied. However within this energy range meson production increases very markedly with energy and becomes a probable process. If the nucleus is large these mesons would have a good chance of being reabsorbed in the nucleus in which they were produced. This would result in a shift of the maximum in the total energy deposition spectrum to higher values, and reactions in which only a small number of particles are ejected would become less likely. Such an effect has been observed in our studies on heavier nuclei.[3] However, in a small nucleus reabsorption of mesons would be a much less important mode of depositing excitation energy because of their greater escape probability. Thus it becomes plausible that while the increasing dominance of meson processes decreases the cross sections for relatively simple reactions in heavy target nuclei, the cross sections for similar reactions of light nuclei remain almost unchanged.

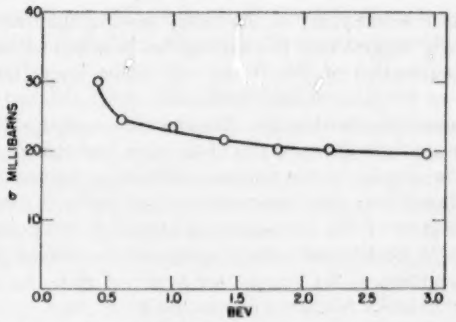

FIG. 1. Excitation function of the $C^{12}(p,pn)C^{11}$ reaction.

The help of the Cosmotron operating staff is gratefully acknowledged.

[6] Hudis, Wolfgang, and Friedlander (unpublished).

PHYSICAL REVIEW VOLUME 96, NUMBER 1 OCTOBER 1, 1954

Conservation of Isotopic Spin and Isotopic Gauge Invariance*

C. N. YANG † AND R. L. MILLS
Brookhaven National Laboratory, Upton, New York

(Received June 28, 1954)

It is pointed out that the usual principle of invariance under isotopic spin rotation is not consistant with the concept of localized fields. The possibility is explored of having invariance under local isotopic spin rotations. This leads to formulating a principle of isotopic gauge invariance and the existence of a **b** field which has the same relation to the isotopic spin that the electromagnetic field has to the electric charge. The **b** field satisfies nonlinear differential equations. The quanta of the **b** field are particles with spin unity, isotopic spin unity, and electric charge $\pm e$ or zero.

INTRODUCTION

THE conservation of isotopic spin is a much discussed concept in recent years. Historically an isotopic spin parameter was first introduced by Heisenberg[1] in 1932 to describe the two charge states (namely neutron and proton) of a nucleon. The idea that the neutron and proton correspond to two states of the same particle was suggested at that time by the fact that their masses are nearly equal, and that the light stable even nuclei contain equal numbers of them. Then in 1937 Breit, Condon, and Present pointed out the approximate equality of $p-p$ and $n-p$ interactions in the ^1S state.[2] It seemed natural to assume that this equality holds also in the other states available to both the $n-p$ and $p-p$ systems. Under such an assumption one arrives at the concept of a total isotopic spin[3] which is conserved in nucleon-nucleon interactions. Experi-

* Work performed under the auspices of the U. S. Atomic Energy Commission.

† On leave of absence from the Institute for Advanced Study, Princeton, New Jersey.

[1] W. Heisenberg, Z. Physik **77**, 1 (1932).

[2] Breit, Condon, and Present, Phys. Rev. **50**, 825 (1936). J. Schwinger pointed out that the small difference may be attributed to magnetic interactions [Phys. Rev. **78**, 135 (1950)].

[3] The total isotopic spin **T** was first introduced by E. Wigner, Phys. Rev. **51**, 106 (1937); B. Cassen and E. U. Condon, Phys. Rev. **50**, 846 (1936).

ments in recent years[4] on the energy levels of light nuclei strongly suggest that this assumption is indeed correct, An implication of this is that all strong interactions such as the pion-nucleon interaction, must also satisfy the same conservation law. This and the knowledge that there are three charge states of the pion, and that pions can be coupled to the nucleon field *singly*, lead to the conclusion that pions have isotopic spin unity. A direct verification of this conclusion was found in the experiment of Hildebrand[5] which compares the differential cross section of the process $n+p\rightarrow\pi^0+d$ with that of the previously measured process $p+p\rightarrow\pi^+ +d$.

The conservation of isotopic spin is identical with the requirement of invariance of all interactions under isotopic spin rotation. This means that when electromagnetic interactions can be neglected, as we shall hereafter assume to be the case, the orientation of the isotopic spin is of no physical significance. The differentiation between a neutron and a proton is then a purely arbitrary process. As usually conceived, however, this arbitrariness is subject to the following limitation: once one chooses what to call a proton, what a neutron, at one space-time point, one is then not free to make any choices at other space-time points.

It seems that this is not consistent with the localized field concept that underlies the usual physical theories. In the present paper we wish to explore the possibility of requiring all interactions to be invariant under *independent* rotations of the isotopic spin at all space-time points, so that the relative orientation of the isotopic spin at two space-time points becomes a physically meaningless quantity (the electromagnetic field being neglected).

We wish to point out that an entirely similar situation arises with respect to the ordinary gauge invariance of a charged field which is described by a complex wave function ψ. A change of gauge[6] means a change of phase factor $\psi\rightarrow\psi'$, $\psi'=(\exp i\alpha)\psi$, a change that is devoid of any physical consequences. Since ψ may depend on x, y, z, and t, the relative phase factor of ψ at two different space-time points is therefore completely arbitrary. In other words, the arbitrariness in choosing the phase factor is local in character.

We define *isotopic gauge* as an arbitrary way of choosing the orientation of the isotopic spin axes at all space-time points, in analogy with the electromagnetic gauge which represents an arbitrary way of choosing the complex phase factor of a charged field at all space-time points. We then propose that all physical processes (not involving the electromagnetic field) be invariant under an isotopic gauge transformation, $\psi\rightarrow\psi'$, $\psi'=S^{-1}\psi$, where S represents a space-time dependent isotopic spin rotation.

To preserve invariance one notices that in electrodynamics it is necessary to counteract the variation of α with x, y, z, and t by introducing the electromagnetic field A_μ which changes under a gauge transformation as

$$A_\mu'=A_\mu+\frac{1}{e}\frac{\partial\alpha}{\partial x_\mu}.$$

In an entirely similar manner we introduce a B field in the case of the isotopic gauge transformation to counteract the dependence of S on x, y, z, and t. It will be seen that this natural generalization allows for very little arbitrariness. The field equations satisfied by the twelve independent components of the B field, which we shall call the **b** field, and their interaction with any field having an isotopic spin are essentially fixed, in much the same way that the free electromagnetic field and its interaction with charged fields are essentially determined by the requirement of gauge invariance.

In the following two sections we put down the mathematical formulation of the idea of isotopic gauge invariance discussed above. We then proceed to the quantization of the field equations for the **b** field. In the last section the properties of the quanta of the **b** field are discussed.

ISOTOPIC GAUGE TRANSFORMATION

Let ψ be a two-component wave function describing a field with isotopic spin $\frac{1}{2}$. Under an isotopic gauge transformation it transforms by

$$\psi=S\psi', \tag{1}$$

where S is a 2×2 unitary matrix with determinant unity. In accordance with the discussion in the previous section, we require, in analogy with the electromagnetic case, that all derivatives of ψ appear in the following combination:

$$(\partial_\mu-i\epsilon B_\mu)\psi.$$

B_μ are 2×2 matrices such that[7] for $\mu=1$, 2, and 3, B_μ is Hermitian and B_4 is anti-Hermitian. Invariance requires that

$$S(\partial_\mu-i\epsilon B_\mu')\psi'=(\partial_\mu-i\epsilon B_\mu)\psi. \tag{2}$$

Combining (1) and (2), we obtain the isotopic gauge transformation on B_μ:

$$B_\mu'=S^{-1}B_\mu S+\frac{i}{\epsilon}S^{-1}\frac{\partial S}{\partial x_\mu}. \tag{3}$$

The last term is similar to the gradiant term in the gauge transformation of electromagnetic potentials. In analogy to the procedure of obtaining gauge invariant field strengths in the electromagnetic case, we

[4] T. Lauritsen, Ann. Rev. Nuclear Sci. 1, 67 (1952); D. R. Inglis, Revs. Modern Phys. 25, 390 (1953).
[5] R. H. Hildebrand, Phys. Rev. 89, 1090 (1953).
[6] W. Pauli, Revs. Modern Phys. 13, 203 (1941).

[7] We use the conventions $\hbar=c=1$, and $x_4=it$. Bold-face type refers to vectors in isotopic space, not in space-time.

define now

$$F_{\mu\nu}=\frac{\partial B_\mu}{\partial x_\nu}-\frac{\partial B_\nu}{\partial x_\mu}+i\epsilon(B_\mu B_\nu-B_\nu B_\mu). \tag{4}$$

One easily shows from (3) that

$$F_{\mu\nu}'=S^{-1}F_{\mu\nu}S \tag{5}$$

under an isotopic gauge transformation.‡ Other simple functions of B than (4) do not lead to such a simple transformation property.

The above lines of thought can be applied to any field ψ with arbitrary isotopic spin. One need only use other representations S of rotations in three-dimensional space. It is reasonable to assume that different fields with the same total isotopic spin, hence belonging to the same representation S, interact with the same matrix field B_μ. (This is analogous to the fact that the electromagnetic field interacts in the same way with any charged particle, regardless of the nature of the particle. If different fields interact with different and independent B fields, there would be more conservation laws than simply the conservation of total isotopic spin.) To find a more explicit form for the B fields and to relate the B_μ's corresponding to different representations S, we proceed as follows.

Equation (3) is valid for any S and its corresponding B_μ. Now the matrix $S^{-1}\partial S/\partial x_\mu$ appearing in (3) is a linear combination of the isotopic spin "angular momentum" matrices T^i $(i=1, 2, 3)$ corresponding to the isotopic spin of the ψ field we are considering. So B_μ itself must also contain a linear combination of the matrices T^i. But any part of B_μ in addition to this, $\bar{B}_\mu$, say, is a scalar or tensor combination of the T's, and must transform by the homogeneous part of (3), $\bar{B}_\mu'=S^{-1}\bar{B}_\mu S$. Such a field is extraneous; it was allowed by the very general form we assumed for the B field, but is irrelevant to the question of isotopic gauge. Thus the relevant part of the B field is of the form

$$B_\mu=2\mathbf{b}_\mu\cdot\mathbf{T}. \tag{6}$$

(Bold-face letters denote three-component vectors in isotopic space.) To relate the $\mathbf{b}_\mu$'s corresponding to different representations S we now consider the product representation $S=S^{(a)}S^{(b)}$. The B field for the combination transforms, according to (3), by

$$B_\mu'=[S^{(b)}]^{-1}[S^{(a)}]^{-1}BS^{(a)}S^{(b)}+\frac{i}{\epsilon}[S^{(a)}]^{-1}\frac{\partial S^{(a)}}{\partial x_\mu}+\frac{i}{\epsilon}[S^{(b)}]^{-1}\frac{\partial S^{(b)}}{\partial x_\mu}.$$

But the sum of $B_\mu^{(a)}$ and $B_\mu^{(b)}$, the B fields corresponding to $S^{(a)}$ and $S^{(b)}$, transforms in exactly the same way, so that

$$B_\mu=B_\mu^{(a)}+B_\mu^{(b)}$$

(plus possible terms which transform homogeneously, and hence are irrelevant and will not be included). Decomposing $S^{(a)}S^{(b)}$ into irreducible representations, we see that the twelve-component field $\mathbf{b}_\mu$ in Eq. (6) is the same for all representations.

To obtain the interaction between any field ψ of arbitrary isotopic spin with the $\mathbf{b}$ field one therefore simply replaces the gradiant of ψ by

$$(\partial_\mu-2i\epsilon\mathbf{b}_\mu\cdot\mathbf{T})\psi, \tag{7}$$

where T^i $(i=1, 2, 3)$, as defined above, are the isotopic spin "angular momentum" matrices for the field ψ.

We remark that the nine components of $\mathbf{b}_\mu$, $\mu=1, 2, 3$ are real and the three of $\mathbf{b}_4$ are pure imaginary. The isotopic-gauge covariant field quantities $F_{\mu\nu}$ are expressible in terms of $\mathbf{b}_\mu$:

$$F_{\mu\nu}=2\mathbf{f}_{\mu\nu}\cdot\mathbf{T}, \tag{8}$$

where

$$\mathbf{f}_{\mu\nu}=\frac{\partial\mathbf{b}_\mu}{\partial x_\nu}-\frac{\partial\mathbf{b}_\nu}{\partial x_\mu}-2\epsilon\mathbf{b}_\mu\times\mathbf{b}_\nu. \tag{9}$$

$\mathbf{f}_{\mu\nu}$ transforms like a vector under an isotopic gauge transformation. Obviously the same $\mathbf{f}_{\mu\nu}$ interact with all fields ψ irrespective of the representation S that ψ belongs to.

The corresponding transformation of $\mathbf{b}_\mu$ is cumbersome. One need, however, study only the infinitesimal isotopic gauge transformations,

$$S=1-2i\mathbf{T}\cdot\delta\omega.$$

Then

$$\mathbf{b}_\mu'=\mathbf{b}_\mu+2\mathbf{b}_\mu\times\delta\omega+\frac{1}{\epsilon}\frac{\partial}{\partial x_\mu}\delta\omega. \tag{10}$$

FIELD EQUATIONS

To write down the field equations for the $\mathbf{b}$ field we clearly only want to use isotopic gauge invariant quantities. In analogy with the electromagnetic case we therefore write down the following Lagrangian density:[8]

$$-\tfrac{1}{4}\mathbf{f}_{\mu\nu}\cdot\mathbf{f}_{\mu\nu}.$$

Since the inclusion of a field with isotopic spin $\frac{1}{2}$ is illustrative, and does not complicate matters very much, we shall use the following total Lagrangian density:

$$\mathfrak{L}=-\tfrac{1}{4}\mathbf{f}_{\mu\nu}\cdot\mathbf{f}_{\mu\nu}-\bar{\psi}\gamma_\mu(\partial_\mu-i\epsilon\boldsymbol{\tau}\cdot\mathbf{b}_\mu)\psi-m\bar{\psi}\psi. \tag{11}$$

One obtains from this the following equations of motion:

$$\begin{aligned}&\partial\mathbf{f}_{\mu\nu}/\partial x_\nu+2\epsilon(\mathbf{b}_\nu\times\mathbf{f}_{\mu\nu})+\mathbf{J}_\mu=0,\\&\gamma_\mu(\partial_\mu-i\epsilon\boldsymbol{\tau}\cdot\mathbf{b}_\mu)\psi+m\psi=0,\end{aligned} \tag{12}$$

‡ *Note added in proof.*—It may appear that B_μ could be introduced as an auxiliary quantity to accomplish invariance, but need not be regarded as a field variable by itself. It is to be emphasized that such a procedure violates the principle of invariance. Every quantity that is not a pure numeral (like 2, or M, or any definite representation of the γ matrices) should be regarded as a dynamical variable, and should be varied in the Lagrangian to yield an equation of motion. Thus the quantities B_μ must be regarded as independent fields.

[8] Repeated indices are summed over, except where explicitly stated otherwise. Latin indices are summed from 1 to 3, Greek ones from 1 to 4.

where

$$\mathbf{J}_\mu = i\epsilon\bar{\psi}\gamma_\mu\boldsymbol{\tau}\psi. \tag{13}$$

The divergence of $\mathbf{J}_\mu$ does not vanish. Instead it can easily be shown from (13) that

$$\partial\mathbf{J}_\mu/\partial x_\mu = -2\epsilon\mathbf{b}_\mu\times\mathbf{J}_\mu. \tag{14}$$

If we define, however,

$$\mathfrak{J}_\mu = \mathbf{J}_\mu + 2\epsilon\mathbf{b}_\nu\times\mathbf{f}_{\mu\nu}, \tag{15}$$

then (12) leads to the equation of continuity,

$$\partial\mathfrak{J}_\mu/\partial x_\mu = 0. \tag{16}$$

$\mathfrak{J}_{1,2,3}$ and $\mathfrak{J}_4$ are respectively the isotopic spin current density and isotopic spin density of the system. The equation of continuity guarantees that the total isotopic spin

$$\mathbf{T} = \int \mathfrak{J}_4 d^3x$$

is independent of time and independent of a Lorentz transformation. It is important to notice that $\mathfrak{J}_\mu$, like $\mathbf{b}_\mu$, does not transform exactly like vectors under isotopic space rotations. But the total isotopic spin,

$$\mathbf{T} = -\int \frac{\partial \mathbf{f}_{4i}}{\partial x_i} d^3x,$$

is the integral of the divergence of $\mathbf{f}_{4i}$, which transforms like a true vector under isotopic spin space rotations. Hence, under a general isotopic gauge transformation, if $S \to S_0$ on an infinitely large sphere, $\mathbf{T}$ would transform like an isotopic spin vector.

Equation (15) shows that the isotopic spin arises both from the spin-$\frac{1}{2}$ field ($\mathbf{J}_\mu$) and from the $\mathbf{b}_\mu$ field itself. Inasmuch as the isotopic spin is the source of the $\mathbf{b}$ field, this fact makes the field equations for the $\mathbf{b}$ field nonlinear, even in the absence of the spin-$\frac{1}{2}$ field. This is different from the case of the electromagnetic field, which is itself chargeless, and consequently satisfies linear equations in the absence of a charged field.

The Hamiltonian derived from (11) is easily demonstrated to be positive definite in the absence of the field of isotopic spin $\frac{1}{2}$. The demonstration is completely identical with the similar one in electrodynamics.

We must complete the set of equations of motion (12) and (13) by the supplementary condition,

$$\partial\mathbf{b}_\mu/\partial x_\mu = 0, \tag{17}$$

which serves to eliminate the scalar part of the field in $\mathbf{b}_\mu$. This clearly imposes a condition on the possible isotopic gauge transformations. That is, the infinitesimal isotopic gauge transformation $S = 1 - i\boldsymbol{\tau}\cdot\delta\boldsymbol{\omega}$ must satisfy the following condition:

$$2\mathbf{b}_\mu\times\frac{\partial}{\partial x_\mu}\delta\boldsymbol{\omega} + \frac{1}{\epsilon}\frac{\partial^2}{\partial x_\mu^2}\delta\boldsymbol{\omega} = 0. \tag{18}$$

This is the analog of the equation $\partial^2\alpha/\partial x_\mu^2 = 0$ that must be satisfied by the gauge transformation $A_\mu' = A_\mu + \epsilon^{-1}(\partial\alpha/\partial x_\mu)$ of the electromagnetic field.

QUANTIZATION

To quantize, it is not convenient to use the isotopic gauge invariant Lagrangian density (11). This is quite similar to the corresponding situation in electrodynamics and we adopt the customary procedure of using a Lagrangian density which is not obviously gauge invariant:

$$\mathfrak{L} = -\frac{1}{2}\frac{\partial\mathbf{b}_\mu}{\partial x_\nu}\cdot\frac{\partial\mathbf{b}_\mu}{\partial x_\nu} + 2\epsilon(\mathbf{b}_\mu\times\mathbf{b}_\nu)\frac{\partial\mathbf{b}_\mu}{\partial x_\nu}$$

$$-\epsilon^2(\mathbf{b}_\mu\times\mathbf{b}_\nu)^2 + \mathbf{J}_\mu\cdot\mathbf{b}_\mu - \bar{\psi}(\gamma_\mu\partial_\mu + m)\psi. \tag{19}$$

The equations of motion that result from this Lagrangian density can be easily shown to imply that

$$\frac{\partial^2}{\partial x_\nu^2}\mathbf{a} + 2\epsilon\mathbf{b}_\nu\times\frac{\partial}{\partial x_\nu}\mathbf{a} = 0,$$

where

$$\mathbf{a} = \partial\mathbf{b}_\mu/\partial x_\mu.$$

Thus if, consistent with (17), we put on one space-like surface $\mathbf{a} = 0$ together with $\partial\mathbf{a}/\partial t = 0$, it follows that $\mathbf{a} = 0$ at all times. Using this supplementary condition one can easily prove that the field equations resulting from the Lagrangian densities (19) and (11) are identical.

One can follow the canonical method of quantization with the Lagrangian density (19). Defining

$$\boldsymbol{\Pi}_\mu = -\partial\mathbf{b}_\mu/\partial x_4 + 2\epsilon(\mathbf{b}_\mu\times\mathbf{b}_4),$$

one obtains the equal-time commutation rule

$$[b_\mu^i(x),\ \Pi_\nu^j(x')]_{t=t'} = -\delta_{ij}\delta_{\mu\nu}\delta^3(x-x'), \tag{20}$$

where b_μ^i, $i = 1, 2, 3$, are the three components of $\mathbf{b}_\mu$. The relativistic invariance of these commutation rules follows from the general proof for canonical methods of quantization given by Heisenberg and Pauli.[9]

The Hamiltonian derived from (19) is identical with the one from (11), in virtue of the supplementary condition. Its density is

$$H = H_0 + H_{\text{int}},$$

$$H_0 = -\tfrac{1}{2}\boldsymbol{\Pi}_\mu\cdot\boldsymbol{\Pi}_\mu + \frac{1}{2}\frac{\partial\mathbf{b}_\mu}{\partial x_j}\cdot\frac{\partial\mathbf{b}_\mu}{\partial x_j} + \bar{\psi}(\gamma_j\partial_j + m)\psi, \tag{21}$$

$$H_{\text{int}} = 2\epsilon(\mathbf{b}_i\times\mathbf{b}_4)\cdot\boldsymbol{\Pi}_i - 2\epsilon(\mathbf{b}_\mu\times\mathbf{b}_j)\cdot(\partial\mathbf{b}_\mu/\partial x_j) + \epsilon^2(\mathbf{b}_i\times\mathbf{b}_j)^2 - \mathbf{J}_\mu\cdot\mathbf{b}_\mu.$$

The quantized form of the supplementary condition is the same as in quantum electrodynamics.

[9] W. Heisenberg and W. Pauli, Z. Physik **56**, 1 (1929).

PROPERTIES OF THE *b* QUANTA

The quanta of the **b** field clearly have spin unity and isotopic spin unity. We know their electric charge too because all the interactions that we proposed must satisfy the law of conservation of electric charge, which is exact. The two states of the nucleon, namely proton and neutron, differ by charge unity. Since they can transform into each other through the emission or absorption of a **b** quantum, the latter must have three charge states with charges $\pm e$ and 0. Any measurement of electric charges of course involves the electromagnetic field, which necessarily introduces a preferential direction in isotopic space at all space-time points. Choosing the isotopic gauge such that this preferential direction is along the z axis in isotopic space, one sees that for the nucleons

$$Q=\text{electric charge}=e(\tfrac{1}{2}+\epsilon^{-1}T^z),$$

and for the **b** quanta

$$Q=(e/\epsilon)T^z.$$

The interaction (7) then fixes the electric charge up to an additive constant for all fields with any isotopic spin:

$$Q=e(\epsilon^{-1}T^z+R). \tag{22}$$

The constants R for two charge conjugate fields must be equal but have opposite signs.[10]

FIG. 1. Elementary vertices for **b** fields and nucleon fields. Dotted lines refer to **b** field, solid lines with arrow refer to nucleon field.

We next come to the question of the mass of the **b** quantum, to which we do not have a satisfactory answer. One may argue that without a nucleon field the Lagrangian would contain no quantity of the dimension of a mass, and that therefore the mass of the **b** quantum in such a case is zero. This argument is however subject to the criticism that, like all field theories, the **b** field is beset with divergences, and dimensional arguments are not satisfactory.

One may of course try to apply to the **b** field the methods for handling infinities developed for quantum electrodynamics. Dyson's approach[11] is best suited for the present case. One first transforms into the interaction representation in which the state vector Ψ satisfies

$$i\partial\Psi/\partial t=H_{\text{int}}\Psi,$$

where H_{int} was defined in Eq. (21). The matrix elements of the scattering matrix are then formulated in terms of contributions from Feynman diagrams. These diagrams have three elementary types of vertices illustrated in Fig. 1, instead of only one type as in quantum electrodynamics. The "primitive divergences" are still finite in number and are listed in Fig. 2. Of these, the one labeled a is the one that effects the propagation function of the **b** quantum, and whose singularity determines the mass of the **b** quantum. In electrodynamics, by the requirement of electric charge conservation,[12] it is argued that the mass of the photon vanishes. Corresponding arguments in the **b** field case do not exist[13] even though the conservation of isotopic spin still holds. We have therefore not been able to conclude anything about the mass of the **b** quantum.

FIG. 2. Primitive divergences.

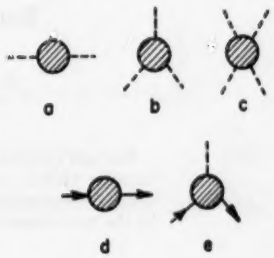

A conclusion about the mass of the **b** quantum is of course very important in deciding whether the proposal of the existence of the **b** field is consistent with experimental information. For example, it is inconsistent with present experiments to have their mass less than that of the pions, because among other reasons they would then be created abundantly at high energies and the charged ones should live long enough to be seen. If they have a mass greater than that of the pions, on the other hand, they would have a short lifetime (say, less than 10^{-20} sec) for decay into pions and photons and would so far have escaped detection.

[10] See M. Gell-Mann, Phys. Rev. **92**, 833 (1953).
[11] F. J. Dyson, Phys. Rev. **75**, 486, 1736 (1949).
[12] J. Schwinger, Phys. Rev. **76**, 790 (1949).
[13] In electrodynamics one can formally prove that $G_{\mu\nu}k_\nu=0$, where $G_{\mu\nu}$ is defined by Schwinger's Eq. (A12). ($G_{\mu\nu}A_\nu$ is the current generated through virtual processes by the arbitrary external field A_ν.) No corresponding proof has been found for the present case. This is due to the fact that in electrodynamics the conservation of charge is a consequence of the equation of motion of the electron field alone, quite independently of the electromagnetic field itself. In the present case the **b** field carries an isotopic spin and destroys such general conservation laws.

Bound States and the Formal Theory of Scattering

M. N. HACK
Palmer Physical Laboratory, Princeton University, Princeton, New Jersey
(Received May 20, 1954)

The exact expression for the transition rate for quantum-mechanical scattering problems is derived formally without recourse to adiabatically switching on the interaction or averaging the initial state in time. The equivalence is shown of the stationary definition of the S matrix and an appropriate definition by the time-dependent method.

INTRODUCTION

IN the derivation of the expression for the transition rate in the formal theory of scattering, a certain difficulty arises in connection with oscillatory terms in the time development of the state vector, which is due to the assumption of an initial "plane wave state" for the incident system, and which has sometimes been circumvented by a mathematical device usually described as "adiabatically switching on the interaction." This has been avoided in a recent treatment by Gell-Mann and Goldberger,[1] in which they introduced instead an averaging of the initial state in time. This has the effect of removing the oscillatory terms, which arise from the presence of bound states (if any) of the total Hamiltonian. In the following formal derivation of the expression for the transition rate, neither of the above devices, which are artificial from the standpoint of their physical interpretation in terms of the principles of quantum mechanics, is employed.

We assume that the total Hamiltonian H is the sum of two parts,

$$H=K+V, \tag{1}$$

where K, the "noninteracting part," and V, the "interacting part" of the total Hamiltonian are Hermitian time-independent operators in the Schroedinger representation. We will denote by φ_a a continuum eigenfunction of K of energy E_a,

$$K\varphi_a=E_a\varphi_a. \tag{2}$$

H is assumed to have the same continuous spectrum as K; and ψ_a^+ and ψ_a^-, the outgoing and incoming wave eigenfunctions of H corresponding to φ_a, satisfy the Lippmann-Schwinger equations[2]

$$\psi_a^{\pm}=\varphi_a+\lim_{\epsilon\to 0+}\frac{1}{E_a-K\pm i\epsilon}V\psi_a^{\pm}, \tag{3}$$

and

$$H\psi_a^{\pm}=E_a\psi_a^{\pm}. \tag{4}$$

H may have in addition discrete eigenstates ψ_l,

$$H\psi_l=E_l\psi_l, \tag{5}$$

where the ψ_l will be assumed not to overlap the continuous spectrum.

THE TRANSITION RATE

We start from the general relation (in units $\hbar=1$),

$$U(t_2,t_1)=e^{iKt_2}e^{-iH(t_2-t_1)}e^{-iKt_1}, \tag{6}$$

where $U(t_2,t_1)$ is the operator that generates the wave function at time t_2 from the wave function at time t_1 in the interaction representation,[3] and are interested in the convergence as $t\to-\infty$ of

$$U(0,t)\varphi_a=e^{iHt}e^{-iE_at}\varphi_a.$$

Expanding[4] φ_a in the complete set of eigenfunctions of H,

$$\varphi_a=\int dc\psi_c^+(\psi_c^+,\varphi_a)+\sum_l\psi_l(\psi_l,\varphi_a),$$

we obtain

$$\begin{aligned}U(0,t)\varphi_a&=\gamma_a(t)+\beta_a(t),\\ \beta_a(t)&=\textstyle\sum_l e^{i(E_l-E_a)t}\psi_l(\psi_l,\varphi_a)\end{aligned} \tag{7}$$

$$\gamma_a(t)=\int dc\left(\varphi_c+\frac{1}{E_c+i\epsilon-K}V\psi_c^+,\varphi_a\right)\psi_c^+e^{i(E_c-E_a)t},$$

where in the last line we have substituted from (3) and the limit as $\epsilon\to 0+$ is understood. By the orthonormality of the φ_c's, we have

$$\gamma_a(t)=\psi_a^++\rho_a^+(t), \tag{8}$$

$$\rho_a^+(t)=\int dc^0\int dE_c\frac{1}{E_c-i\epsilon-E_a}\times(V\psi_c^+,\varphi_a)\psi_c^+e^{i(E_c-E_a)t}, \tag{9}$$

where, following Watson,[5] we have explicitly separated out the integration over the energy in the integration over all physical quantities needed to specify the states

[1] M. Gell-Mann and M. L. Goldberger, Phys. Rev. **91**, 398 (1953).
[2] B. A. Lippmann and J. Schwinger, Phys. Rev. **79**, 469 (1950).
[3] See, e.g., reference 1, Sec. III.
[4] The expansion coefficients (ψ_c^+,φ_a) are singular. However, see below where a wave packet is taken for initial state; this introduces an integration over these quantities.
[5] K. M. Watson and K. A. Brueckner, U. S. Atomic Energy Commission Document AECU-2765 (unpublished).

ψ_c^+. We put (suppressing the dependence on a):

$$(V\psi_c^+,\varphi_a)\psi_c^+ \doteq f(c^0,E_c),$$

and

$$x=(E_a-E_c)t.$$

Using the limit-integration theorem denoted symbolically by

$$\lim_{\eta\to 0+}\frac{1}{x\mp i\eta}=\mathrm{P}\left(\frac{1}{x}\right)\pm i\pi\delta(x), \tag{10}$$

where P denotes principal-value integration, we have for fixed $t<0$:

$$\rho_a^+(t)=\int dc^0\mathrm{P}\int_{E_a t}^{\infty}dx\frac{e^{-ix}}{x}f\left(c^0,E_a-\frac{x}{t}\right)$$

$$+i\pi\int dc^0\int_{E_a t}^{\infty}dx\delta(x)e^{-ix}f\left(c^0,E_a-\frac{x}{t}\right).$$

The second integral is immediately

$$+i\pi\int dc^0 f(c^0,E_a).$$

(We have assumed E_a definitely greater than the lower limit of the continuous spectrum, which we have taken, without loss of generality, equal to zero.) The principal value term is, in the limit $t\to-\infty$,

$$-i\pi\int dc^0 f(c^0,E_a).$$

Thus

$$\lim_{t\to-\infty}\rho_a^+(t)=0. \tag{11}$$

It remains to look at the contribution (7) from the bound states. This oscillates as $t\to-\infty$, unless all the (ψ_l,φ_a) vanish. Thus in the case where the total Hamiltonian H admits bound states, the limit of $U(0,t)\varphi_a$ as $t\to-\infty$ does not exist in general.[6]

Suppose, however, we take as initial state a wave packet $\bar{\varphi}_i$ which being normalizable can therefore be expanded in the φ_a's. We shall assume that this expansion contains a superposition of φ_a's over a small range of energies. We have

$$U(0,t)\bar{\varphi}_i=\int da(\varphi_a,\bar{\varphi}_i)[\psi_a^+ +\rho_a^+(t)+\beta_a(t)]$$

$$\equiv\bar{\psi}_i^+ +\bar{\rho}_i^+(t)+\bar{\beta}_i(t), \tag{12}$$

where the last equality defines the barred quantities. Now

$$E_l(\psi_l,\varphi_a)=(H\psi_l,\varphi_a)=(\psi_l,H\varphi_a)=E_a(\psi_l,\varphi_a)+(\psi_l,V\varphi_a),$$

so that, by (12) and (7),

$$\bar{\beta}_i(t)=\sum_l\int da\frac{e^{i(E_l-E_a)t}}{E_l-E_a}\psi_l(\psi_l,V\varphi_a)(\varphi_a,\bar{\varphi}_i).$$

Since we assume that the bound states do not overlap the continuous spectrum, the denominator never vanishes. By our assumption that $\bar{\varphi}_i$ involves a superposition of φ_a's over a range of energies, we therefore obtain, because of the rapidly varying exponential,

$$\lim_{t\to-\infty}\bar{\beta}_i(t)=0. \tag{13}$$

Also

$$\lim_{t\to-\infty}\bar{\rho}_i^+(t)=0, \tag{14}$$

so that

$$\lim_{t\to-\infty}U(0,t)\bar{\varphi}_i=\bar{\psi}_i^+. \tag{15}$$

By the definition (12) of $\bar{\psi}_i^+$,

$$(\varphi_b,e^{iKt}e^{-iHt}\bar{\psi}_i^+)=\left(\varphi_b,e^{iEbt}\int da(\varphi_a,\bar{\varphi}_i)\psi_a^+e^{-iE_at}\right)$$

$$=\int da(\varphi_b,\psi_a^+)(\varphi_a,\bar{\varphi}_i)e^{i(E_b-E_a)t}, \tag{16}$$

$$(\varphi_b,e^{iKt}Ve^{-iHt}\bar{\psi}_i^+)$$

$$=\int da(\varphi_b,V\psi_a^+)(\varphi_a,\bar{\varphi}_i)e^{i(E_b-E_a)t}. \tag{17}$$

By (6) and (12),

$$\frac{d}{dt}|(\varphi_b,U(t,t_0)\bar{\varphi}_i)|^2$$

$$=2\,\mathrm{Re}\{-i(\varphi_b,e^{iKt}Ve^{-iHt}[\bar{\psi}_i^+ +\bar{\rho}_i^+(t_0)+\bar{\beta}_i(t_0)])$$

$$\times(\varphi_b,e^{iKt}e^{-iHt}[\bar{\psi}_i^+ +\bar{\rho}_i^+(t_0)+\bar{\beta}_i(t_0)])^*\}. \tag{18}$$

We now obtain, from (13), (14), (16), (17), and (18), and the orthonormality of the φ_a's,

$$w_{ba}\equiv\lim_{\bar{\varphi}_i\to\varphi_a}\lim_{t_0\to-\infty}\frac{d}{dt}|(\varphi_b,U(t,t_0)\bar{\varphi}_i)|^2$$

$$=2\,\mathrm{Re}\{-i(\varphi_b,V\psi_a^+)(\varphi_b,\psi_a^+)^*\},$$

[6] In their treatment of this problem, Gell-Mann and Goldberger (see reference 1) introduced an averaging of the initial state in time. They were led to define

$$U(0,-\infty)\varphi_a=\lim_{\epsilon\to 0+}\epsilon\int_{-\infty}^{0}dte^{\epsilon t}U(0,t)\varphi_a.$$

The fact that the contribution from the continuum has a limit by the ordinary definition implies that the limit exists and has the same value (ψ_a^+) by this generalized definition. However, it is clear from (7) that with this generalized limit, the contribution from the bound states vanishes.

independent of t. By (3) and (10), we have[7]

$$(\varphi_b,\psi_a^+)=\delta(b-a)+\left[P\left(\frac{1}{E_a-E_b}\right)-i\pi\delta(E_a-E_b)\right](\varphi_b,V\psi_a^+).$$

Noting that the principal value term does not contribute to the real part, and defining

$$\mathbf{T}_{ba}=(\varphi_b,V\psi_a^+),$$

we finally get

$$w_{ba}=2\delta(b-a)\,\mathrm{Im}\mathbf{T}_{ba}+2\pi\delta(E_b-E_a)|\mathbf{T}_{ba}|^2, \quad (19)$$

which is the well-known exact expression for the transition rate.

EQUIVALENCE OF THE STATIONARY AND THE TIME-DEPENDENT DEFINITIONS OF THE S MATRIX

Snyder[8] has pointed out the necessity for a demonstration of the equivalence of the stationary and time-dependent definitions of the S matrix. This can be achieved by the methods of the preceding section.[9] In case we had expanded in terms of the ψ^-'s instead of the ψ^+'s,[10] we would have obtained, instead of (8) and (9),

$$\gamma_a(t)=\psi_a^-+\rho_a^-(t),$$

$$\rho_a^-(t)=\int dc\frac{1}{E_c+i\epsilon-E_a}(V\psi_c^-,\varphi_a)\psi_c^-e^{i(E_c-E_a)t}.$$

Proceeding as in the derivation of (11), we find that the principal value term and delta function term no longer cancel, but have the same sign, and we get

$$\lim_{t\to-\infty}\rho_a^-(t)=-2\pi i\int dc^0(V\psi^-(c^0,E_a),\varphi_a)\psi^-(c^0,E_a). \quad (20)$$

Taking the limit as $t\to-\infty$ of

$$\gamma_a(t)=\psi_a^++\rho_a^+(t)=\psi_a^-+\rho_a^-(t)$$

thus provides, by (11) and (20), the relation

$$\psi_a^+=\psi_a^--2\pi i\int dc^0(V\psi^-(c^0,E_a),\varphi_a)\psi^-(c^0,E_a).$$

Because the inner product occurs between states of the same energy, we can apply the reciprocity theorem,[2]

$$(V\psi^-(c^0,E_a),\varphi_a)=(\varphi(c^0,E_a),V\psi_a^+),$$

so that

$$\psi_a^+=\psi_a^--2\pi i\int dc\delta(E_c-E_a)(\varphi_c,V\psi_a^+)\psi_c^-.$$

Making use of the orthonormality of the ψ^-'s, we obtain from the stationary definition of the S matrix introduced by Gell-Mann and Goldberger,

$$S_{ba}\equiv(\psi_b^-,\psi_a^+)=\delta(b-a)-2\pi i\delta(E_b-E_a)\mathbf{T}_{ba}.$$

In the treatment of the S matrix by the time-dependent method the same difficulty arises that was discussed in the preceding section. It is now clear that we should take a wave packet for the initial state and at the end of the calculation let the wave packet approach a plane wave. Thus we define

$$S_{ba}\equiv\lim_{\bar\varphi_i\to\varphi_a}\lim_{t\to\infty}\lim_{t_0\to-\infty}(\varphi_b,U(t,t_0)\bar\varphi_i). \quad (21)$$

By (6), (15), and (16),

$$\lim_{t_0\to-\infty}(\varphi_b,U(t,t_0)\bar\varphi_i)=(\varphi_b,e^{iKt}e^{-iHt}\bar\psi_i^+)$$
$$=(\varphi_b,\bar\varphi_i)+\int da\frac{e^{i(E_b-E_a)t}}{E_a+i\epsilon-E_b}(\varphi_b,V\psi_a^+)(\varphi_a,\bar\varphi_i),$$

where the last line follows from substituting (3) into (16), and the limit as $\epsilon\to0+$ is understood. Thus, making use again of (10),

$$\lim_{t\to\infty}\lim_{t_0\to-\infty}(\varphi_b,U(t,t_0)\bar\varphi_i)$$
$$=(\varphi_b,\bar\varphi_i)-2\pi i\int da\delta(E_b-E_a)(\varphi_b,V\psi_a^+)(\varphi_a,\bar\varphi_i),$$

and we therefore again obtain

$$S_{ba}=\delta(b-a)-2\pi i\delta(E_b-E_a)\mathbf{T}_{ba}. \quad (22)$$

Thus the definition (21) of the S matrix by the time-dependent method also leads to (22), whether or not there are bound states of H, provided these do not overlap the continuous spectrum.

ACKNOWLEDGMENT

It is a pleasure to thank for discussions Professor Marvin L. Goldberger, Professor Arthur S. Wightman, Dr. John S. McIntosh, and Mr. William M. MacDonald.

[7] There is still an integration over final states to be performed eventually. In fact, inserting (19) into the relation expressing conservation of probability,

$$\int dbw_{ba}=0$$

provides, as Snyder has noted (see reference 8), an immediate proof of the well-known "optical theorem" [reference 8, Eq. (45)].

[8] H. S. Snyder, Phys. Rev. **83**, 1154 (1951).

[9] S. T. Ma [Phys. Rev. **87**, 652 (1952)], has considered this problem from a different point of view, making use of a concept of "conditional equality." Necessary integrations required for the validity of "conditional equalities" arise naturally when a wave packet is taken for the initial state. (See, e.g., Eq. (36a) of reference 8, and note that an integration over E_μ is required there.)

[10] I owe this suggestion to Professor Goldberger. It is assumed here that the ψ^+'s and ψ^-'s span the same space.

Note added in proof.—After completing this work, I received unpublished notes of Professor F. Low in which Eq. (15) and Eq. (22) are derived by the same method as used here. I have also been informed that similar methods have been employed in unpublished work of Professor J. Ashkin.

Families of Spinor Fields

TOICHIRO KINOSHITA*
The Institute for Advanced Study, Princeton, New Jersey
(Received June 3, 1954)

It is shown that a system of spinor fields can be classified uniquely into several sets, called families, when the interaction is given. This is made possible by noting that an interaction imposes some restriction on the commutation relation between different spinor fields. The fermion system is then classified, by a method of construction, into a set of families characterized by the following conditions. (1) Spinor fields of the same family anticommute with each other. (2) Commutation relations between any pair of spinor fields of different families are completely unspecified. To this end, we use a mathematical device which is derived from the self-evident requirement that equations of motion for fermions are determined unambiguously by the variation principle. We have applied the present method to the classification of observed spinor fields and discussed the structure of families in some detail.

I. INTRODUCTION

IT is known that reactions of various elementary particles which have heretofore been discovered are subject to several selection rules. One of them is the so-called conservation law of heavy particles which has been noticed in connection with the stability of matter.[1] Although the deeper cause of this law is still beyond our comprehension, it seems to indicate at least that nucleons and V particles form a distinct set from other fermions. Thus, these particles are usually said to form a "nucleon family." Of course the notion of a nucleon family is expected to represent implicitly certain features of the interaction of heavy particles with other elementary particles. It has, however, been a rather obscure concept. It will be worth while to ask whether or not it is possible to give a definite physical meaning to the nucleon family. Furthermore, it will be useful if one can extend the concept to establish the notion of a general family which is applicable to any spinor field.

It was first noticed by Nishizima[2] that a restriction is imposed on the commutation relation between different spinor fields by the integrability condition of the Schrödinger equation in the interaction representation. Generalizing his idea, Oneda and Umezawa[3] tried to use the commutation property of various spinor fields to define the family. Their method is incomplete, however, since they did not give a prescription to determine the commutation relation between different spinor fields. The purpose of this paper is to improve their method and give a satisfactory and unambiguous definition of family on the basis of empirical knowledge about the interaction. We do not intend, however, to give any explanation for the existence of the conservation law of heavy particles.

In Sec. II, we shall give a lemma based on a fundamental requirement of the usual quantized field theory which is useful in studying the interacting spinor fields. In Sec. III, we shall see how a given interaction Lagrangian restricts the commutation relations between different spinor fields and how this result is used to classify them into several families. We shall apply our method to the classification of the actual fermion system observed in recent experiments.

II. PRELIMINARY REMARKS

Let us consider an assembly of n fermion fields described by the operators $\psi^1, \psi^2, \cdots, \psi^n$ and their conjugates interacting with each other and with several boson fields. To describe this, one can of course start from a c-number Lagrangian and introduce commutation relations afterwards so that one obtains a consistent picture of field quantization. Instead, however, we shall use here a q-number Lagrangian L from the beginning.[4] This is a Lorentz-invariant polynomial of fermion and boson operators. It is composed of the free part L_0 and the interaction part L_I. We shall assume that the anticommutation relations,

$$\begin{aligned}&\{\psi_\alpha{}^i(\mathbf{x},t),\ \psi_\beta{}^{i*}(\mathbf{x}',t)\}=\delta_{\alpha\beta}\delta(\mathbf{x}-\mathbf{x}'),\\&\{\psi_\alpha{}^i(\mathbf{x},t),\ \psi_\beta{}^i(\mathbf{x}',t)\}=0,\ \text{etc.},\ i=1,2,\cdots,n,\end{aligned}\tag{2.1}$$

are already proved to hold for the free fermion fields and that the ordinary commutation relations hold for the free boson fields. On the other hand, the commutation relation between different kinds of spinor fields is not determined by L_0.[5]

In order to study how a given L_I imposes restriction

---

* Now at the Department of Physics, Columbia University, New York.

[1] It was first noticed by Wigner that a sum of the number of protons, neutrons, and V particles, or more exactly, the difference of the number of these particles and their antiparticles, is conserved in any known reactions, see E. P. Wigner, Proc. Am. Phil. Soc. **93**, 521 (1949); Proc. Nat. Acad. Sci. U. S. **38**, 449 (1952).

[2] K. Nishizima, Progr. Theoret. Phys. (Japan) **5**, 187 (1950).

[3] S. Oneda and H. Umezawa, Progr. Theoret. Phys. (Japan) **9**, 685 (1953).

[4] J. Schwinger, Phys. Rev. **82**, 914 (1951); **91**, 713 (1953).

[5] For example, a transformation of free-field variables like

$$\psi_c^1=\psi^1,\quad \psi_c^2=C\psi^2=\psi^3C,\quad C\psi^1=-\psi^1C,$$

with

$$C=\exp\Big[i\pi\int_{\sigma_x}d\sigma_\mu'\bar{\psi}^1(x')\gamma_\mu{}^1\psi^1(x')\Big],$$

transforms a commutation relation of ψ^1 and ψ^2 (for $n=2$) into an anticommutative one and vice versa without changing any other relations, where σ_x is a space-like surface which passes through the point x. See O. Klein, J. phys. et radium (7), **9**, 1 (1938). L. Michel, Proc. Phys. Soc. (London) **A63**, 514 (1950).

on the commutation relation between different spinor fields, it is convenient to make use of the following lemma:

Lemma 1. *Each term of L_I has to involve an even number of operators (including ψ^i) which anticommute with $\psi^i (i=1, 2, \cdots, n)$.*

This is derived in the following way from the requirement that the equations of motion for all field operators must be determined uniquely from the Lagrangian L by the principle of stationary action. Making use of a two-valued function ϵ_{ij} defined by[6]

$$\psi^i\psi^j=\epsilon_{ij}\psi^j\psi^i, \quad \psi^{i*}\psi^j=\epsilon_{ij}\psi^j\psi^{i*}, \text{ etc.}, \tag{2.2}$$

with

$$\epsilon_{ij}=\begin{cases}1 \text{ if } \psi^i \text{ and } \psi^j \text{ commute,}\\ -1 \text{ if } \psi^i \text{ and } \psi^j \text{ anticommute,}\end{cases} \tag{2.3}$$

one can rearrange L in such a way that $\bar{\psi}^i$ stands on the left end of all terms. Let us call it L_l. In the same way, $\bar{\psi}^i$ can be brought to the right end of all terms which we shall call L_r. By varying L_l and L_r with respect to $\bar{\psi}^i$, one obtains two equations of motion for ψ^i. The uniqueness postulate requires that they should be identical. It is easy to see that this is satisfied if and only if the relation

$$\Pi_j \epsilon_{ij}=-1 \tag{2.4}$$

holds for each term of L_I which involves $\bar{\psi}^i$. The left-hand side is a product of functions ϵ_{ij} for the term of L_I considered, and -1 on the right-hand side is the value of the function ϵ_{ii} for L_0. Lemma 1 follows immediately from (2.4). Obviously the same result is obtained for any product of terms of L_I when they are space-like relative to each other.

This lemma is equivalent to the one used by Oneda and Umezawa but is derived in a much simpler way. We shall also notice that Nishizima's result is involved in this lemma since an integrability condition like $[H_1(x), H_2(x')]=0$ for space-like $x-x'(x\neq x')$ follows immediately from it.

III. CLASSIFICATION OF SPINOR FIELDS

We are now ready to classify the spinor fields with a given interaction Lagrangian into several families. Because of the Lorentz invariance, L_I can be written as follows:

$$L_I=L^{(2)}+L^{(4)}+\cdots+L^{(2k)}+\cdots, \tag{3.1}$$

where $L^{(2k)}$ is a sum of all terms which are products of $2k$ spinors.[7] In considering the effect of L_I on the commutation relation, we shall take account of the terms of this expansion successively.

Let ψ^a be an operator which appears in at least one term of $L^{(2)}$. Consider all $\psi^{a'}$ that are partners of ψ^a in $L^{(2)}$. Then consider all $\psi^{a''}$ that are partners of at least one of $\psi^{a'}$ in $L^{(2)}$ and so on. Let us call an assembly of all spinors thus obtained a "2-family" and denote it as

$$F_a^{(2)}\equiv\{\psi^a, \psi^{a'}, \cdots, \psi^{a''}, \cdots\}. \tag{3.2}$$

This is uniquely determined irrespective of which spinor in this set one starts from. By Lemma 1, a pair of spinors forming together a term of $L^{(2)}$ must anticommute with each other. It can further be shown that all spinors belonging to $F_a^{(2)}$ anticommute with each other. One can construct another 2-family $F_b^{(2)}$ starting from a spinor which appears in $L^{(2)}$ but does not belong to $F_a^{(2)}$. Obviously $F_a^{(2)}$ and $F_b^{(2)}$ have no common element. In this manner, one can construct successively several 2-families. When there are spinors which do not appear in $L^{(2)}$, however, they do not belong to any of these families. The commutation property of such a spinor with other spinors cannot be determined by $L^{(2)}$. We shall adopt the definition that each of them forms a 2-family by itself. Then the entire set of spinor fields are classified into several 2-families having the following properties. (1) Spinor fields of the same 2-family anticommute with each other. (2) Commutation relations between spinors of different 2-families are unspecified as far as $L^{(2)}$ is concerned.

The effect of $L^{(4)}$ can be taken into account in a similar but more complicated way. We first notice that if three spinors in a term of $L^{(4)}$ belong to the same 2-family, the fourth spinor must anticommute with the three spinors even if it does not belong to the same 2-family. This can be proved by solving Eq. (2.4) for this term. By Lemma 1, it is easily shown that any pairs of operators from these two 2-families are anticommutative with each other. In general, if there is a term of $L^{(4)}$ which involves three spinors (or one spinor) from a 2-family $F_a^{(2)}$ and one spinor (or three spinors) from a set of 2-families in which any pair of spinors are proved to anticommute with each other, it can be shown that all spinors of $F_a^{(2)}$ anticommute with all spinors of the latter set.

In this way one can construct a maximum set of 2-families in which any pair of spinor fields are anticommutative. We shall call it a 4-family. By the same procedure we shall construct as many 4-families as possible. If there still remain several 2-families which do not belong to any of these 4-families, we shall consider that each such 2-family forms a 4-family by itself. Then the whole set of 2-families can be classified into a set of 4-families in an unambiguous way. Obviously, spinor fields of the same 4-family anticommute with each other. Furthermore, it is easy to see that commutation relations between spinor fields belonging to different 4-families cannot be determined by $L^{(4)}$. Thus, as far as $L^{(4)}$ is concerned, a 4-family defined above is actually maximal in the sense that it cannot be extended to a larger set in which any pair of operators are anticommutative.

The same reasoning can be applied to $L^{(6)}$, $L^{(8)}$, and so on, leading to the classification of spinor fields into

[6] In the case $i=j$, an additional c number may appear in (2.2). We can neglect it, however, since it is not necessary for our purpose.

[7] Being unnecessary, terms involving only boson operators are dropped in (3.1).

6-families, 8-families, and so on. If terms beyond $L^{(2k)}$ do not provide us with a new restriction on the commutation relations, the $2k$-families will be the most precise classification of spinor fields which one can expect from the study of a given L_I. We shall then define a $2k$-family as a *family*. Summarizing the above argument, one can conclude that *when the interaction Lagrangian is given, an assembly of spinor fields is classified uniquely into several families having the following properties. (1) Spinor fields of the same family anticommute with each other. (2) Commutation relations between spinors of different families are completely unspecified.*

It is to be noticed that the distinction between spinor operators and their conjugates is not essential in this result More detailed information about the fermion system will be obtained if one takes their difference into account. For this purpose it is useful to observe the behavior of ψ and ψ^* with respect to the transformation of their phases. We shall not go into the details of this problem, however, but simply refer to one of the results obtained. It is the following: If there is a conservation law of the number of particles at all, it must be applied to a family or an assembly of families and not to a smaller set of spinor fields.

In applying our method to the actual problem, we must note that what we find from the study of various reactions is in general not the Lagrangian itself but the S matrix. Accordingly, the foregoing discussion might have to be somewhat modified. In fact, however, one can develop essentially the same argument as before making use of the following lemma:

Lemma 2. *Each term in the normal product expansion*[8] *of the S matrix involves an even number of operators which anticommute with* ψ^i.

This can be derived at once by applying Lemma 1 to the operators of the interaction representation.

The existence of the following fermions has been more or less established: electron (e), neutrino (ν), muon (μ), κ particle (κ), proton (p), neutron (n), and V particles (V^0 and V^{ch}). Some of them might turn out to be bosons by further investigation. For the sake of definiteness, we shall assume that they are all fermions. Furthermore, we shall adopt only those interactions which are customarily assumed.[9] Then, it is easy to see that the fermions are classified into the following four 2-families:

$$F_e^{(2)}=\{e\},\quad F_\nu^{(2)}=\{\nu,\mu\},\quad F_\kappa^{(2)}=\{\kappa\},\quad F_p^{(2)}=\{p,n,V^0,V^{\mathrm{ch}}\}. \tag{3.3}$$

By making use of the direct interactions of fermions, they are further classified into the *lepton and nucleon families* as follows:

$$F_e^{(4)}=\{\nu,e,\mu,\kappa\},\quad F_p^{(4)}=\{p,n,V^0,V^{\mathrm{ch}}\}. \tag{3.4}$$

Since we have, at present, no evidence for the existence of any more complicated elementary interaction, this is the most precise classification we can expect from our knowledge about the reactions between various elementary particles.

From our general argument, it is clear that if some new fermions are added to $F_p^{(4)}$ in the future, the conservation of heavy particles should be extended to include them. On the other hand, if an interaction is found which makes the lepton and nucleon family anticommutative, it is impossible to apply the conservation law to nucleons and V particles.[10] It is not known yet whether or not the conservation of particle number should hold for the lepton family too. It is interesting to notice, however, that there are two possible cases characterized by the interactions

$$f\psi^{\mu *}\psi^{\nu *}\psi^{e}\psi^{\nu}+\mathrm{cc}, \tag{3.5}$$

and

$$f'\psi^{\mu *}\psi^{\nu}\psi^{e *}\psi^{\nu}+\mathrm{cc}, \tag{3.6}$$

in which the conservation law can be true for the leptons. Their difference lies in the point that two neutrinos are distinguishable in (3.5) while they are identical in (3.6). Since the electric charge is known to be conserved absolutely in any process, (3.6) is forbidden if ψ^μ and ψ^e have the same electric charge while (3.5) is forbidden if ψ^μ and ψ^e have electric charges of opposite signs. Evidently they are mutually exclusive. An advantage in adopting (3.6) was stressed by Konopinski and Mahmoud[11] since it automatically forbids several unobserved processes like

$$\begin{aligned}&\mu^\pm \leftrightarrow e^\pm+\gamma,\\ &\mu^\pm \leftrightarrow e^\pm+e^++e^-,\\ &\mu^\pm+p\ (\text{or } n) \leftrightarrow e^\pm+p\ (\text{or } n),\end{aligned} \tag{3.7}$$

under the assumption of validity of the conservation law for the lepton family. It is to be noticed, however, that it is impossible to explain other unobserved processes such as the $\pi-e$ decay in this way.

The author would like to express his gratitude to Professor R. Oppenheimer for his kind hospitality at the Institute for Advanced Study. He is very greatly indebted to Professor Y. Nambu for many valuable discussions.

[8] G. C. Wick, Phys. Rev. **80**, 268 (1950).

[9] In this paper, we shall not discuss such problems as the neutral muon, the Majorana neutrino, or the assumption of the existence of heavy bosons in beta decay suggested by Y. Tanikawa and K. Saeki, Progr. Theoret. Phys. (Japan) **10**, 232 (1953).

[10] Tanikawa proposed just such an interaction in his theory of beta decay. By assuming a special interaction, he could avoid the collapsing of matter though the conservation law of heavy *spinor* particles does not hold in his theory. See reference 9.

[11] E. J. Konopinski and H. M. Mahmoud, Phys. Rev. **92**, 1045 (1953).

Evaluation of the Collision Matrix for Dirac Particles in an External Potential*

B. ZUMINO
Institute of Mathematical Sciences, New York University, New York, New York
(Received June 7, 1954)

The collision matrix for a quantized Dirac field in an external electromagnetic potential is evaluated by a method which utilizes the close relation between the theory of positrons and the formal one-particle Dirac theory. The main mathematical tool employed is a theorem by Baker and Hausdorff on exponentials of noncommuting quantities. One obtains the collision matrix expressed as a product of exponentials, involving creation and destruction operators in a way suitable for the calculation of matrix elements in the occupation number representation. In the Appendix the evaluation of the collision matrix for a real scalar field in interaction with a given source distribution is carried out by means of a similar technique.

1. INTRODUCTION

THE purpose of the present note is to evaluate the collision matrix for a Dirac field subject to an external time-dependent (unquantized) electromagnetic potential. This problem can be solved by means of the techniques developed by Feynman[1] and Dyson,[2] and has been treated repeatedly by various authors.[3] We shall present here an alternative solution, based on the definition of the collision matrix in the Heisenberg representation given by Yang and Feldman.[4] Our presentation emphasizes the close correspondence between the formal one-particle theory, in which negative energy states are allowed, and the quantized theory of positrons. In Sec. 3 we obtain an exponential and obviously unitary form for the collision matrix and in Sec. 4 we proceed to order the creation and destruction operators. The developments of these two sections parallel those of Friedrichs,[5] and are indeed the relativistic analog of the treatment he devised for the solution of a similar and related problem. In particular we also achieve the ordering of the creation and destruction operators by the use of a theorem by Baker[6] and Hausdorff[7] on exponentials of noncommuting quantities. Although the formula given by Baker and Hausdorff has been occasionally used in field theory in simple cases when the higher commutators vanish (as it happens for instance in the problem of a given source distribution treated in the Appendix of this paper), it will become clear that our use of the theorem is of completely different nature. One of the aims of this paper is just to illustrate this particular type of application.

Our main result is expressed by the ordered form of the collision matrix given in formulas (41) and (42) or (43) below. It is not an S-ordered expression as defined by Wick[8] (in our formulas not all creation operators act after the destruction operators), although it could be transformed into an S-ordered expression. We shall not carry out the transformation, which involves some algebra, since, as we shall see, our solution is useful as it stands.

The problem treated here is the most significant one which we were able to solve in this way. It does not seem easy to generalize the present method to the more complex case of truly nonlinear interactions of quantized fields.

One of the motivations for the present work was the hope that it may represent a first step to a rigorous mathematical treatment of the problem in consideration. However we shall not investigate here the conditions under which our expressions are meaningful and our equations have solutions. In particular this applies to the reciprocals, exponentials and logarithms of the singular operators used in this paper; for small strengths of the potentials one can define these expressions by series expansions. We shall make use without justification of simple formal properties of these expansions.

2. STATEMENT OF THE PROBLEM

We first consider a c-number Dirac field subject to an external potential

$$(\gamma\partial/\partial x+m+Q)\psi=0, \tag{1}$$

$$\gamma\partial/\partial x=\gamma^\mu\partial/\partial x^\mu, \quad Q(x,x')=-ie\gamma^\mu\Phi_\mu(x)\delta(x-x'), \tag{2}$$

$$\gamma^\mu\gamma^\lambda+\gamma^\lambda\gamma^\mu=2g^{\lambda\mu}.$$

Our time coordinate x^0 is real, $c=\hbar=1$, $g^{00}=-1$, $g^{11}=g^{22}=g^{33}=1$, $g^{\lambda\mu}=0$ for $\lambda\neq\mu$; the matrix γ^0 is anti-Hermitian; γ^1, γ^2, and γ^3 are Hermitian. It has some formal advantages to write the potential, as we have done, as a singular integral operator. We shall also use symbolic integral operators associated with the well known singular functions S, S^+, $S^{\rm ret}$, etc.: an expression such as $S^{\rm ret}Q\psi(x)$, for instance, stands for

$$\int\int S^{\rm ret}(x-x')dx'Q(x',x'')dx''\psi(x'').$$

* Supported by the U. S. Office of Naval Research.
[1] R. P. Feynman, Phys. Rev. 76, 749 (1949).
[2] F. J. Dyson, Phys. Rev. 75, 1736 (1949).
[3] For instance, K. Yamazaki, Progr. Theoret. Phys. (Japan) 7, 449 (1952); Yamazaki uses the operator calculus of R. P. Feynman, Phys. Rev. 84, 108 (1951). His results bear some similarity to our formula (41).
[4] C. N. Yang and D. Feldman, Phys. Rev. 79, 972 (1950).
[5] K. O. Friedrichs, Communications on Pure and Applied Mathematics 6, 1 (1953); see also the appendix of *Quantum Theory of Fields* (Interscience Publishers, Inc., New York, 1953).
[6] H. F. Baker, Proc. London Math. Soc. (2) 3, 24 (1905).
[7] F. Hausdorff, Berichte Saechsischen Akad. Wiss. (Math. Phys. Kl.) Leipzig 58, 19 (1906).
[8] G. C. Wick, Phys. Rev. 80, 268 (1950).

(The integrations extend over all space-time and the spinor matrices are multiplied in the usual way.) Besides the Pauli adjoint of a spinor $\bar{\psi}=\bar{\psi}_\rho=-\psi_\sigma^*\gamma_{\sigma\rho}^0$ (sum over repeated spinor indices) we shall define the adjoint of an integral operator

$$\bar{R}=(\bar{R})_{\rho\sigma}(x,x')=-\gamma_{\rho\tau}^0 R_{\lambda\tau}^*(x',x)\gamma_{\lambda\sigma}^0$$

(notice the interchange of x and x'). Expressions like $\int\bar{\chi}(x')R(x',x)dx'$ and $\int\bar{\chi}(x')R(x',x'')\psi(x'')dx'dx''$ will then be abbreviated respectively as $\bar{\chi}R$ and $\bar{\chi}R\psi$. In the particular case of our potential we have

$$\bar{Q}=Q. \tag{3}$$

The following relations involving the singular kernels will be used[9]

$$S=S^{\text{adv}}-S^{\text{ret}}=S^+ +S^-,$$

$$\bar{S}=-S,\quad \bar{S}^{\text{ret}}=S^{\text{adv}},\quad \overline{S^+}=-S^+,\quad \overline{S^-}=-S^-,$$

$$\left(\gamma\frac{\partial}{\partial x}+m\right)S^{\text{ret}}=\left(\gamma\frac{\partial}{\partial x}+m\right)S^{\text{adv}}=-1.$$

For any solution ψ of (1) we define the incoming and outgoing fields,

$$\psi^{\text{in}}=\psi-S^{\text{ret}}Q\psi, \tag{4}$$

$$\psi^{\text{out}}=\psi-S^{\text{adv}}Q\psi. \tag{5}$$

It is clear from this definition that both ψ^{in} and ψ^{out} satisfy the free-field equation,

$$(\gamma\partial/\partial x+m)\psi^{\text{in}}=0, \tag{6}$$
$$(\gamma\partial/\partial x+m)\psi^{\text{out}}=0.$$

In scattering problems one considers (4) as an integral equation for ψ, to be solved for given ψ^{in} satisfying (6). We shall not investigate here the conditions for the existence and the uniqueness of the solution of (4). It is likely that, with suitable restrictions on the potential, both existence and uniqueness will be ensured, and the homogeneous equations corresponding to (4) and (5) will have no solutions.

Eliminating ψ from (4) and (5), the relation between ψ^{in} and ψ^{out} can be written as

$$\psi^{\text{out}}=\psi^{\text{in}}-SQ(1-S^{\text{ret}}Q)^{-1}\psi^{\text{in}}. \tag{7}$$

The linear operator transforming ψ^{in} into ψ^{out} can be identified with the collision matrix for the formal one particle theory. As we shall see in Sec. 3, it is unitary with respect to the appropriate inner product.

If the Dirac field is quantized all the above relations are still valid as relations between the operators ψ, ψ^{in} and ψ^{out}. The operators ψ^{in} and ψ^{out} both satisfy the free-field equation and the free-field (anti-) commutation relation and we are led to the problem to find a unitary operator $\mathbf{S}$ such that

$$\mathbf{S}^{-1}\psi_\rho^{\text{in}}(x)\mathbf{S}=\psi_\rho^{\text{out}}(x). \tag{8}$$

According to Yang and Feldman, $\mathbf{S}$ is the collision matrix; we should like to express it in terms of the incoming fields only. We also should like to find a form for $\mathbf{S}$, in which the creation and destruction operators are ordered in such a way that it is possible to evaluate the effect of the application of $\mathbf{S}$ to a state vector in the occupation number representation.

3. EXPONENTIAL FORM OF THE COLLISION MATRIX

In this section and in Sec. 4 we want to investigate the relation between equations of the type of (7) and (8). We consider general linear transformations operating in the space D of the solutions of

$$(\gamma\partial/\partial x+m)\phi=0. \tag{9}$$

We shall first assume that the fields are unquantized.

Every solution of (9) and its adjoint can be written, respectively, as

$$\phi=S\phi_1,\quad \bar{\phi}=\bar{\phi}_1\bar{S}=-\bar{\phi}_1 S.$$

Here the spinor ϕ_1 is not uniquely determined by ϕ since it can be changed into $\phi_1+\eta$ where $S\eta=0$. The operator S projects a general spinor function of x onto D. We can define the inner product of two solutions ϕ and ξ of (9) in the following way:

$$(\xi,\phi)=-i\bar{\xi}_1 S\phi_1. \tag{10}$$

This inner product depends only upon the solutions ξ and ϕ themselves; it is a complex number, and it would not be difficult to show that it is equal to the more customary expression $\int\xi^*\phi d^3x$ where the three-dimensional integration is extended over a manifold $x^0=$ constant.

If ϕ is in D, a linear relation such as

$$\chi=(1+SY)\phi=(1+SY)S\phi_1, \tag{11}$$

$$\bar{\chi}=\bar{\phi}(1-\bar{Y}S)=-\bar{\phi}_1 S(1-\bar{Y}S), \tag{12}$$

insures that χ also is in D. If we are interested only in linear operations in D we can consider Y to be to a certain extent arbitrary; it could be changed and still give the same linear relation in D provided SYS remains the same. This situation will come up in various instances because of the presence of a projection operator, such as S, in the formulas.

We shall now require that the linear operator $1+SY$ in (11) is unitary with respect to the inner product (10). The operator is length-preserving if

$$(\xi,\phi)=((1+SY)\xi,(1+SY)\phi)$$
$$=-i\bar{\xi}_1(1-S\bar{Y})S(1+YS)\phi_1,$$

for arbitrary ξ_1 and ϕ_1, which means

$$(1-S\bar{Y})S(1+YS)=S. \tag{13}$$

[9] The symbol $\bar{S}$ is used here to denote the adjoint of the integral operator S, and not, as it is customary in the literature, the singular kernel $\frac{1}{2}(S^{\text{adv}}+S^{\text{ret}})$ for which we reserve the letter G (see Sec. 5).

The operator is also unitary if, in addition,

$$(1+SY)S(1-\bar{Y}S)=S. \tag{14}$$

The relation (7) between ψ^{in} and ψ^{out} is a particular case of (11) for

$$Y=-Q(1-S^{ret}Q)^{-1}, \tag{15}$$

and one could check, using (3), that for this particular choice of Y both (13) and (14) are verified.

As a consequence of relations (13) and (14) we can assume the existence of an operator P such that

$$(1+SY)S=e^{SP}S \tag{16}$$

and

$$S\bar{P}S=SPS \tag{17}$$

hold; condition (17) means that P is anti-Hermitian in D in the sense of the inner product (10).

We now go over to the case of quantized fields. The conditions (13) and (14) are necessary and sufficient to insure that χ satisfies the free-field commutation relations if ϕ does, and vice versa. For instance, if

$$\{\phi,\tilde{\phi}\}=-iS, \tag{18}$$

we have from (14)

$$\{\chi,\tilde{\chi}\}=(1+SY)\{\phi,\tilde{\phi}\}(1-\bar{Y}S)$$
$$=-i(1+SY)S(1-\bar{Y}S)=-iS.$$

We can express the relation between χ and ϕ by means of a transformation analogous to (8). With the definition

$$[P]=\tfrac{1}{2}i\int\int P_{\rho\lambda}(x,x')\{\tilde{\phi}_\rho(x)\phi_\lambda(x')$$
$$-\phi_\lambda(x')\tilde{\phi}_\rho(x)\}dxdx', \tag{19}$$

the commutator identities

$$[\phi_\rho(x),[P]]=(SP\phi)_\rho(x), \tag{20}$$

$$[\tilde{\phi}_\rho(x),[P]]=-(\tilde{\phi}PS)_\rho(x), \tag{21}$$

follow from (18). [No use is made here of (17), but we shall assume that (17) is satisfied.] As will be shown below, one has as a consequence

$$\chi=e^{SP}\phi=\mathbf{S}^{-1}\phi\mathbf{S}, \tag{22}$$

$$\tilde{\chi}=\tilde{\phi}e^{-PS}=\mathbf{S}^{-1}\tilde{\phi}\mathbf{S}, \tag{23}$$

with

$$\mathbf{S}=\exp[P]. \tag{24}$$

Owing to (17), $\mathbf{S}$ is unitary; formula (24) solves the problem of finding an exponential form for the collision matrix. We see that the operator in the exponent of (24) is the second quantized operator of the operator P in the exponent of (16) in the sense of the theory of positrons (Heisenberg's rule). It should be noted that for $[P]$ only the value of SPS is relevant.

To verify (22), for instance, consider the derivative of the operator

$$f(\lambda)=e^{\lambda[P]}e^{\lambda SP}\phi(x)e^{-\lambda[P]}$$

with respect to the parameter λ. We have

$$f'(\lambda)=e^{\lambda[P]}e^{\lambda SP}\{SP\phi(x)-[\phi(x),[P]]\}e^{-\lambda[P]}$$

and because of (20), $f'(\lambda)=0$; therefore $f(1)=f(0)=\phi$.

4. ORDERED FORM OF THE COLLISION MATRIX

We now proceed to the separation of the creation and destruction operators by suitably decomposing (24) into a product of exponentials. We define as "Lie polynomial" a homogeneous polynomial in certain variables α, β, $\cdots$, which can be constructed from Lie polynomials of lower order by forming commutators and linear combinations with constant coefficients. Any formal series of Lie polynomials will be called a "Lie function."

Making use of (20) and (21) one can easily verify the second commutator identity,

$$[[P_1],[P_2]]=[P], \tag{25}$$

where P satisfies

$$SP_1SP_2S-SP_2SP_1S=SPS. \tag{26}$$

It is then apparent, by repeated application of (25), that, if $l(\alpha,\beta)$ is a Lie function, the relation $SPS=l(SP_1,SP_2)S=Sl(P_1S,P_2S)$ entails $[P]=l([P_1],[P_2])$, and vice versa. This result can be obviously generalized to Lie functions of more than two variables.

Following Friedrichs, we shall now make use of a theorem discovered independently by Baker and Hausdorff: if α, β, and γ satisfy the formal relation $e^\alpha e^\beta=e^\gamma$, then

$$\gamma=\alpha+\beta+\tfrac{1}{2}[\alpha,\beta]+(1/12)([[\alpha\beta]\beta]+[[\beta\alpha]\alpha])+\cdots$$

is a Lie function of α and β.[10] The generalization to the product of more than two exponentials is obvious. The observation of the preceding paragraph allows us to conclude that if

$$e^{SP_1}e^{SP_2}e^{SP_3}S=e^{SPS}, \tag{27}$$

then

$$e^{[P_1]}e^{[P_2]}e^{[P_3]}=e^{[P]}, \tag{28}$$

and vice versa.

Equation (28) can be used to obtain the form of the operator $\mathbf{S}$ ordered in the desired way with respect to creation and destruction operators by having each of the exponentials in the left-hand side contain only certain creation or destruction operators. More precisely, let us define the two projection operators E^+ and E^- which transform a function of the space-time variable x into its positive- and negative-frequency parts, respectively. They satisfy

$$E^+f(x)=f^+(x),\quad E^-f(x)=f^-(x),$$
$$E^++E^-=1,\quad (E^+)^2=E^+,\quad (E^-)^2=E^-, \tag{29}$$
$$E^+E^-=E^-E^+=0,\quad E^+=\overline{E^+},\quad \overline{E^-}=E^-.$$

[10] It is not possible to give an explicit formula for γ, but one can give a recursive construction of it. For details see, for instance, W. Magnus, Report No. BR-3, New York University Mathematics Research Group, 1953 (unpublished).

It follows that

$$\tilde{f}(x)E^+=\tilde{f}^-(x), \quad \tilde{f}(x)E^-=\tilde{f}^+(x), \tag{30}$$

and that

$$E^+S=S^+=SE^+, \quad E^-S=S^-=SE^-. \tag{31}$$

We shall require that P_1, P_2, and P_3 not only satisfy (27) with the right-hand side given by (16) but also be of the form

$$\begin{aligned} iP_1&=E^+AE^-,\\ iP_2&=E^+BE^+-E^-CE^-,\\ iP_3&=E^-DE^+. \end{aligned} \tag{32}$$

One can then easily see from (29) and (30) that

$$\begin{aligned} [P_1]&=\tilde{\phi}^-A\phi^-,\\ [P_2]&=\tilde{\phi}^-B\phi^+ +(C\phi^-)\tilde{\phi}^+ +\tfrac{1}{2}i\,\mathrm{Tr}BS^+ +\tfrac{1}{2}i\mathrm{Tr}CS^-,\\ [P_3]&=\tilde{\phi}^+D\phi^+; \end{aligned} \tag{33}$$

here we have made use of

$$\{\phi^-,\tilde{\phi}^+\}=-iS^-, \quad \{\phi^+,\tilde{\phi}^-\}=-iS^+, \tag{34}$$

and the symbol Tr denotes a trace taken by summing over the spinor indices and integrating over the four-dimensional variable x.

Our present problem is to find the operators A, B, C, and D such that (27) is satisfied. Substituting (32) into (27) we obtain the relation which these operators must satisfy. The first exponential in the left-hand side of (27) reduces to

$$\begin{aligned} e^{SP_1}&=\exp(-iSE^+AE^-)\\ &=\exp(-iE^+SAE^-)=1-iE^+SAE^-, \end{aligned}$$

because the higher-order terms in the development of the exponential vanish as a consequence of the property of the projection operators $E^-E^+=0$. Similarly, for the other two exponentials, one has (using also $E^+E^-=0$)

$$e^{SP_3}=\exp(-iSE^-DE^+)=1-iE^-SDE^+$$

and

$$\begin{aligned} e^{SP_2}&=\exp(-iSE^+BE^+ +iSE^-CE^-)\\ &=\exp(-iE^+SBE^+)\exp(iE^-SCE^-). \end{aligned}$$

From (16), the relation to be satisfied becomes

$$\begin{aligned} &(1-iE^+SAE^-)\exp(-iE^+SBE^+)\exp(iE^-SCE^-)\\ &\quad\times(1-iE^-SDE^+)S=(1+SY)S. \end{aligned} \tag{35}$$

The presence of the projection operators S, E^+, and E^- in this formula has again the consequence that A, B, C, and D are not uniquely determined by SYS; only their relevant projections are, and this agrees with the fact that only their projections occur in (33). Separation of the various frequency signs in (35) gives the four relations

$$\begin{aligned} &[\exp(iS^-C)-1]S^-=S^-YS^-,\\ &\exp(iS^-C)iS^-DS^+=S^-YS^+,\\ &iS^+A\exp(iS^-C)S^-=S^+YS^-,\\ &[\exp(-iS^+B)-1-S^+A\exp(iS^-C)S^-D]S^+=S^+YS^+. \end{aligned} \tag{36}$$

Before we can proceed to transform (36) we must derive some consequences of the unitarity conditions (13) and (14). We first have the relation

$$S(1-\bar{Y}S^+)YS=S\bar{Y}(1+S^-Y)S, \tag{37}$$

which is equivalent to (13), since $S=S^++S^-$. From (37) we obtain

$$S^+(1-\bar{Y}S^+)YS^-=S^+\bar{Y}(1+S^-Y)S^-,$$

and, multiplying by $(1+YS^-)^{-1}$ on the right and by $(1-S^+\bar{Y})^{-1}$ on the left, we have

$$S^+Y(1+S^-Y)^{-1}S^-=S^+\bar{Y}(1-S^+\bar{Y})^{-1}S^-. \tag{38}$$

In a similar way, from (14), we obtain

$$S^-Y(1+S^-Y)^{-1}S^+=S^-\bar{Y}(1-S^+\bar{Y})^{-1}S^+. \tag{39}$$

We can now proceed to solve the four equations (36). The first three of them give, without difficulty,

$$\begin{aligned} iS^-CS^-&=\{\log(1+S^-Y)\}S^-,\\ iS^-DS^+&=S^-(1+YS^-)^{-1}YS^+=S^-Y(1+S^-Y)^{-1}S^+\\ &=S^-\bar{Y}(1-S^+\bar{Y})^{-1}S^+,\\ iS^+AS^-&=S^+Y(1+S^-Y)^{-1}S^-=S^+\bar{Y}(1-S^+\bar{Y})^{-1}S^-. \end{aligned}$$

From the fourth, one has

$$\exp(-iS^+B)S^+=[1+S^+Y+S^+A\exp(iS^-C)S^-D]S^+;$$

substituting for S^+AS^- the expression just found, and for $\exp(iS^-C)S^-DS^+$ the value given by the third equation (36), one obtains

$$\begin{aligned} &\exp(-iS^+B)S^+\\ &\quad=\{1+S^+Y-S^+\bar{Y}(1-S^+\bar{Y})^{-1}S^-Y\}S^+\\ &\quad=(1-S^+\bar{Y})^{-1}\{(1-S^+\bar{Y})(1+S^+Y)-S^+\bar{Y}S^-Y\}S^+\\ &\quad=(1-S^+\bar{Y})^{-1}\{1+S^+(Y-\bar{Y}-\bar{Y}SY)\}S^+\\ &\quad=(1-S^+\bar{Y})^{-1}. \end{aligned} \tag{40}$$

Here we have used the fact that

$$S^+(Y-\bar{Y}-\bar{Y}SY)S^+=0,$$

which is a consequence of (13). Equation (40) can be solved in the form

$$iS^+BS^+=\{\log(1-S^+\bar{Y})\}S^+.$$

Summarizing our results, we now make use of (24), (28), and (33), and have for the collision matrix

$$\begin{aligned} \mathbf{S}=\exp(\tilde{\phi}^-A\phi^-)\exp[\tilde{\phi}^-B\phi^+ +(C\phi^-)\tilde{\phi}^+]\exp(\tilde{\phi}^+A\phi^+)\\ \times\exp(\tfrac{1}{2}i\,\mathrm{Tr}S^+B+\tfrac{1}{2}i\,\mathrm{Tr}S^-C), \end{aligned} \tag{41}$$

in which we can take

$$\begin{aligned} iA &= V(1+S^-V)^{-1}, \\ iS^-CS^- &= \{\log(1+S^-V)\}S^-, \\ iS^+BS^+ &= \{\log(1-S^+\bar{V})\}S^+. \end{aligned} \tag{42}$$

The ordered form (41) is not S-ordered, because not all destruction operators are to the right of all creation operators. Nevertheless, it can be directly used as it is to calculate matrix elements of $\mathbf{S}$ between a final and an initial state in which, let us say, only a finite number of particles are present. Expanding the first and third exponential in a power series it is clear that only a finite number of terms of each has to be retained, because the exponents contain only creation and destruction operators, respectively. As for the second exponential, it obviously commutes with the operator which gives the number of particles, and therefore its effect on any vector representing a state in which only a finite number of particles is present can be evaluated without much difficulty and without series expansions. The fourth exponential is just a numerical factor, the vacuum expectation value of the collision matrix. As compared with an S-ordering, the form (41) has the advantage that some terms of the S-ordered expansion are already summed together in the second exponential operator. It is possible, on the other hand, to S-order this second exponential; one would then obtain a closed expression for $\mathbf{S}$ equivalent to the Feynman-Dyson expansion. We shall not do it here, since it requires some manipulations, and does not represent an improvement over (41).

5. EVALUATION OF THE COLLISION MATRIX

The results of the preceding section can now be applied to the particular case of interest in which V is given by (15) and $\phi=\psi^{\text{in}}$.

By use of the Feynman function S^F, characterized by

$$\tfrac{1}{2}iS^F=S^{\text{ret}}+S^-=S^{\text{adv}}-S^+,$$

a straightforward calculation gives

$$\begin{aligned} 1+S^-V&=1-S^-Q(1-S^{\text{ret}}Q)^{-1} \\ &=(1-\tfrac{1}{2}iS^FQ)(1-S^{\text{ret}}Q)^{-1}, \\ 1-S^+\bar{V}&=1+S^+Q(1-S^{\text{adv}}Q)^{-1} \\ &=(1-\tfrac{1}{2}iS^FQ)(1-S^{\text{adv}}Q)^{-1}. \end{aligned}$$

Therefore the expressions given in (42) become

$$\left.\begin{aligned} A&=iQ(1-\tfrac{1}{2}iS^FQ)^{-1} \\ iS^-C&=\log\{(1-\tfrac{1}{2}iS^FQ)(1-S^{\text{ret}}Q)^{-1}\} \\ iS^+B&=\log\{(1-\tfrac{1}{2}iS^FQ)(1-S^{\text{adv}}Q)^{-1}\}, \end{aligned}\right\} \tag{43}$$

dropping a common factor S^+ or S^-.

We can evaluate the traces occurring in (37) making use of the identity $\operatorname{Tr}\log\alpha\beta=\operatorname{Tr}\log\alpha+\operatorname{Tr}\log\beta$, valid also if α and β do not commute. This identity is a consequence of the fact, stated in the Baker-Hausdorff theorem, that $\log\alpha\beta$ is a Lie function of $\log\alpha$ and $\log\beta$; indeed the trace of the commutator of two operators is zero. One has

$$\begin{aligned} \tfrac{1}{2}i\operatorname{Tr}S^+B+\tfrac{1}{2}i\operatorname{Tr}S^-C&=\operatorname{Tr}\log(1-\tfrac{1}{2}iS^FQ) \\ &\quad-\tfrac{1}{2}\operatorname{Tr}\log(1-S^{\text{ret}}Q)-\tfrac{1}{2}\operatorname{Tr}\log(1-S^{\text{adv}}Q). \end{aligned} \tag{44}$$

It is clear that so far in all our considerations we have not made use of the particular form (2) of the operator Q, i.e., our formulas would be true also if Q would not contain a δ-function factor (nonlocal interaction). If however (2) is valid, as we shall assume from now on, the sum of the second and third term in the right-hand side of (44) vanishes. To show this, consider the series development of the logarithms. The terms of first order give

$$\begin{aligned} &\tfrac{1}{2}\operatorname{Tr}S^{\text{ret}}Q+\tfrac{1}{2}\operatorname{Tr}S^{\text{adv}}Q \\ &\qquad=\operatorname{Tr}GQ=-ie\operatorname{tr}\{G(0)\gamma^\mu\}\int\Phi_\mu(x)dx, \end{aligned} \tag{45}$$

where we have introduced the singular function[9]

$$G=\tfrac{1}{2}(S^{\text{adv}}+S^{\text{ret}}),$$

used the definition (2) of Q, and denoted by tr the trace taken over the spin indices only. But the right-hand side of (45) is zero, owing to

$$\operatorname{tr}\{G(0)\gamma^\mu\}=0.$$

The higher-order terms are also zero. For instance

$$\begin{aligned} \operatorname{Tr}S^{\text{ret}}QS^{\text{ret}}Q&=-e^2\int\int S^{\text{ret}}(x-x')\gamma^\mu\Phi_\mu(x') \\ &\qquad\times S^{\text{ret}}(x'-x)\gamma^\lambda\Phi_\lambda(x)dxdx' \\ &=0, \end{aligned}$$

because $S^{\text{ret}}(x-x')$ is zero whenever the point x is outside the future light cone emanating from x', and therefore at least one of the two S^{ret} functions occurring in (46) vanishes.

The vacuum expectation value of the collision matrix now becomes simply $\exp\operatorname{Tr}\log(1-\tfrac{1}{2}iS^FQ)$. This expression has been previously given by various authors.[11] Its expansion is identical with the evaluation of the same quantity given by Feynman;[12] it is known from his work that $\operatorname{Tr}\log(1-\tfrac{1}{2}iS^FQ)$ has an infinite imaginary part, coming from the second term of the expansion (the first term is zero), and is otherwise finite. One can drop this infinite imaginary part; this amounts to a redefinition of the collision matrix by a phase factor, and does not affect transition probabilities. It is connected with the charge renormalization.

In conclusion, the author wishes to express his thanks to Professor K. O. Friedrichs and to Dr. H. E. Moses for many helpful discussions.

[11] For instance M. Neuman, Phys. Rev. **85**, 129 (1952).
[12] See reference 1, Sec. 5.

APPENDIX. GIVEN SOURCE DISTRIBUTION

We consider briefly the evaluation of the collision matrix for a real Bose field influenced by a given source distribution. For simplicity we take a scalar field

$$(\Box - m^2)\phi(x) = \rho(x). \tag{A.1}$$

The solution of this problem can be obtained, for instance, by use of Feynman's operator calculus,[13] and has been given also by other authors.[14] We want here to make use of the formula

$$e^{\alpha+\beta} = e^{\alpha} e^{\beta} e^{\frac{1}{2}[\beta,\alpha]}, \tag{A.2}$$

valid whenever α and β commute with their commutator, in particular if this commutator is a number. Equation (A.2) is an immediate consequence of the more general formula given by Baker and Hausdorff.

With a notation perfectly analogous to the one used in the main text, we define the incoming and outgoing fields:

$$\phi^{\text{in}} = \phi + \Delta^{\text{ret}}\rho, \tag{A.3}$$

$$\phi^{\text{out}} = \phi + \Delta^{\text{adv}}\rho. \tag{A.4}$$

Here the elimination of ϕ can be completely achieved

$$\phi^{\text{out}} = \phi^{\text{in}} + \Delta\rho, \tag{A.5}$$

and the collision matrix, defined by

$$\mathbf{S}^{-1}\phi^{\text{in}}\mathbf{S} = \phi^{\text{out}}, \tag{A.6}$$

is given by the exponential

$$\mathbf{S} = \exp[-i\rho\phi^{\text{in}}]. \tag{A.7}$$

In the following let us simply write ϕ for ϕ^{in}. To verify (A.7) one can introduce the operator,

$$f(\lambda) = e^{-i\lambda\rho\phi}(\phi + \lambda\Delta\rho)e^{i\lambda\rho\phi},$$

and notice that, as a consequence of

$$f'(\lambda) = e^{-i\lambda\rho\phi}(\Delta\rho - i[\rho\phi,\phi])e^{i\lambda\rho\phi} = 0,$$

one has

$$f(1) = f(0).$$

Application of (A.2) immediately gives an ordered form of the collision matrix, if we take $\alpha = -i\rho\phi^-$, $\beta = -i\rho\phi^+$, $[\beta,\alpha] = i\rho\Delta^-\rho$ which is a number. One has

$$\mathbf{S} = \exp[-i\rho(\phi^+ + \phi^-)] = \exp(-i\rho\phi^-)\exp(-i\rho\phi^+)\exp(\tfrac{1}{2}i\rho\Delta^-\rho). \tag{A.8}$$

From this ordered form one can easily derive an expression for the probability P_n that n particles are created from the vacuum. It is given by $\sum|(\Phi_n, S\Phi_0)|^2$, if we denote by Φ_0 the vacuum of incoming particles, by Φ_n a state in which n particles are present and sum over all states Φ_n. It is clear from (A.8) that

$$P_n = \sum\left|\left(\Phi_n, \frac{(-i\rho\phi^-)^n}{n!}\Phi_0\right)\exp(\tfrac{1}{2}i\rho\Delta^-\rho)\right|^2; \tag{A.9}$$

indeed, the destruction operator ϕ^+ in the second exponential applied to the vacuum gives zero, and the only term in the expansion of the first exponential which has a matrix element different from zero is the one which creates n particles. In (A.9) the sum $\sum$ can now be extended to states with any number of particles since only matrix elements which are zero are added. One then has

$$P = \frac{1}{(n!)^2}(\Phi_0, (i\rho\phi^+)^n(-i\rho\phi^-)^n\Phi_0)\exp(-\tfrac{1}{2}\rho\Delta^{(1)}\rho); \tag{A.10}$$

here use has been made of $(\Delta^-)^* = \Delta^+$ and of

$$i(\Delta^+ - \Delta^-) = \Delta^{(1)}.$$

One can bring the destruction operators in (A.10) to the right of the creation operators by use of the commutation relation. This gives $n!$ terms equal to $(i\rho\Delta^+\rho)^n$; observing that

$$\rho\Delta^+\rho = -\rho\Delta^-\rho,$$

one has finally for P_n the well-known Poisson distribution:[15]

$$P_n = \frac{1}{n!}W^n e^{-W}, \quad W = \tfrac{1}{2}\rho\Delta^{(1)}\rho.$$

[13] See Eq. (49) of Feynman's paper quoted in reference 3.

[14] W. Thirring and B. Touschek, Phil. Mag. (7) **42**, 244 (1951); R. J. Glauber, Phys. Rev. **84**, 395 (1951).

[15] See, for instance, reference 14.

Model of the Causal Interpretation of Quantum Theory in Terms of a Fluid with Irregular Fluctuations

D. BOHM, *Faculdade de Filosofia, Ciências e Letras, Universidade de São Paulo, São Paulo, Brazil*

AND

J. P. VIGIER, *Institut Henri Poincaré, Paris, France*

(Received June 14, 1954)

In this paper, we propose a physical model leading to the causal interpretation of the quantum theory. In this model, a set of fields which are equivalent in many ways to a conserved fluid, with density $|\psi|^2$, and local stream velocity, $d\xi/dt=\nabla S/m$, act on a particle-like inhomogeneity which moves with the local stream velocity of the equivalent fluid. By introducing the hypothesis of a very irregular and effectively random fluctuation in the motions of the fluid, we are able to prove that an arbitrary probability density ultimately decays into $|\psi|^2$. Thus, we answer an important objection to the causal interpretation, made by Pauli and others. This result is extended to the Dirac equation and to the many-particle problem.

1. INTRODUCTION

A CAUSAL interpretation of the quantum theory has been proposed,[1,2] involving the assumption that an electron is a particle following a continuous and causally defined trajectory with a well-defined position, $\xi(t)$, accompanied by a physically real wave field, $\psi(\mathbf{x},t)$. To obtain all of the results of the usual interpretation, the following supplementary assumptions had to be made:

1. $\psi(\mathbf{x},t)$ satisfied Schrödinger's equation.
2. $d\xi/dt=\nabla S/m$, where $\psi=R\exp(iS/\hbar)$.
3. The probability distribution in an ensemble of electrons having the same wave function, is $P=|\psi|^2$.

These assumptions were shown to be consistent.

Assumption (3), however, has been criticized by Pauli[3] and others[4] on the ground that such a hypothesis is not appropriate in a theory aimed at giving a causal explanation of the quantum mechanics. Instead, they argue it should be possible to have an arbitrary probability distribution [a special case of which is the function $P=\delta(\mathbf{x}-\mathbf{x}_0)$, representing a particle in a well-defined location], that is at least in principle independent of the ψ field and dependent only on our degree of information concerning the location of the particle.

In a more recent paper,[5] one of us has proposed a means of dealing with this problem by explaining the relation, $P=|\psi|^2$ in terms of random collision processes. It was shown in a simplified case that a statistical ensemble of quantum-mechanical system with an arbitrary initial probability distribution decays in time to an ensemble with $P=|\psi|^2$. This is equivalent to a proof of Boltzmann's H theorem in classical mechanics. Thus, we can answer the objection of Pauli, for no matter what the initial probability distribution may have been (for example, a delta function), it will eventually be given by $P=|\psi|^2$.

In the work cited above, however, certain mathematical difficulties make a generalization of the results to an arbitrary system very difficult. (The difficulties are rather analogous to these appearing in classical statistical mechanics when one tries rigorously to treat the approach of a distribution to equilibrium, by means of demonstrating a quasi-ergodic character of the motion). In the present paper, we shall avoid these difficulties by taking advantage of the fact that the causal interpretation of the quantum theory permits an unlimited number of new physical models, of types not consistent with the usual interpretation, which lead to the usual theory only as an approximation, and which may lead to appreciably different results at new levels (e.g., 10^{-13} cm). The model that we shall propose here furnishes the basis for a simple deduction of the relation, $P=|\psi|^2$; and in addition, gives a possible physical interpretation of the relation $d\xi/dt=\nabla S/m$ (postulate 2), which follows rather naturally from the model. This model is an extension of the causal interpretation of the quantum theory already proposed, which provides a more concrete physical image of the meaning of our postulates than has been available before, and which suggests new properties of matter that may exist at deeper levels.

2. THE HYDRODYNAMIC MODEL

The model that we shall adopt in this paper is an extension of a hydrodynamic model, originally proposed by Madelung[6] and later developed further by Takabayasi[7] and by Schenberg.[8] To obtain this model, we first write down Schrödinger's equation in terms of the

[1] L. de Broglie, Compt. rend. **183**, 447 (1926); **184**, 273 (1927); **185**, 380 (1927).
[2] D. Bohm, Phys. Rev. **85**, 166, 180 (1952).
[3] *Les Savants et le Monde*, Collection dirigée par André George, *Louis de Broglie, Physicien et Penseur* (Editions Albin Michel, Paris, 1953).
[4] J. B. Keller, Phys. Rev. **89**, 1040 (1953).
[5] D. Bohm, Phys. Rev. **89**, 1458 (1953).
[6] E. Madelung, Z. Physik **40**, 332 (1926).
[7] T. Takabayasi, Progr. Theoret. Phys. (Japan) **8**, 143 (1952); **9**, 187 (1953).
[8] M. Schenberg, Nuovo cimento (to be published).

variables, R and S, where $\psi = R\exp(iS/\hbar)$:

$$\partial R^2/\partial t + \operatorname{div}(R^2\nabla S/m) = 0, \tag{1}$$

$$\frac{\partial S}{\partial t} + \frac{(\nabla S)^2}{2m} - \frac{\hbar^2}{2m}\frac{\nabla^2 R}{R} + V = 0. \tag{2}$$

Now Madelung originally proposed that R^2 be interpreted as the density $\rho(\mathbf{x})$ of a continuous fluid, which had the stream velocity $\mathbf{v} = \nabla S/m$. Thus, the fluid is assumed to undergo only potential flow. Equation (1) then expresses the conservation of fluid, while Eq. (2) determines the changes of the velocity potential S in terms of the classical potential V, and the "quantum potential":

$$\frac{-\hbar^2}{2m}\frac{\nabla^2 R}{R} = \frac{-\hbar^2}{4m}\left[\frac{\nabla^2\rho}{\rho} - \frac{1}{2}\left(\frac{\nabla\rho}{\rho}\right)^2\right].$$

As shown by Takabayasi[7] and by Schenberg,[8] the quantum potential may be thought of as arising in the effects of an internal stress in the fluid. This stress depends, however, on derivatives of the fluid density, and therefore is not completely analogous to the usual stresses, such as pressures, which are found in macroscopic fluids.

The above model is, however, not adequate by itself; for it contains nothing to describe the actual location, $\xi(t)$, of the particle, which makes possible, as we have seen in previous papers,[2,5] a consistent causal interpretation of the quantum theory. At this point, we therefore complete the model by postulating a particle, which takes the form of a highly localized inhomogeneity that moves with the local fluid velocity, $\mathbf{v}(\mathbf{x},t)$. The precise nature of this inhomogeneity is irrelevant for our purposes. It could be, for example, a foreign body, of a density close to that of the fluid, which was simply being carried along with the local velocity of the fluid as a small floating body is carried along the surface of the water at the local stream velocity of the water. Or else it could be a stable dynamic structure existing in the fluid; for example, a small stable vortex or some other stable localized structure, such as a small pulse-like inhomogeneity. Such structures might be stabilized by some nonlinearity that would be present in a more accurate approximation to the equations governing the fluid motions than is given by (1) and (2).

3. FLUCTUATIONS OF THE MADELUNG FLUID

Thus far we have been assuming that the Madelung fluid undergoes some regular motion, which can in principle be calculated by solving Schrödinger's equation with appropriate boundary conditions. We know, however, that in all real fluids ever met with thus far (and indeed, in all physically real fields also) the motions never take precisely the forms obtained by solving the appropriate equations with the correct boundary conditions. For there always exist random fluctuations. These fluctuations may have many origins. For example, real fluids may be subject to irregular disturbance originating outside the fluid and transmitted to it at the boundaries. Moreover, because the equations of motion flow of the fluid are, in general, nonlinear, the fluid motion may be unstable, so that irregular turbulent motion may arise within the fluid itself. And finally, because of the underlying constitution of the fluid in terms of molecules in random thermal motion, there may exist a residual Brownian movement in the fluid, even for fluid elements that are large enough to contain a great many molecules. Thus, in a real fluid, there are ample reasons why the usual hydrodynamical equations will, in general, describe only some mean or average aspect of the motion, while the actual motion has an addition some very irregular fluctuating components, which are effectively random.

Since the Madelung fluid is being assumed to be some kind of physically real fluid, it is therefore quite natural to suppose that it too undergoes more or less random fluctuations in its motions. Such random fluctuations are evidently consistent within the framework of the causal interpretation of the quantum theory. Thus, there are always random perturbations of any quantum mechanical system which arise outside that system. (Indeed, as we have already shown in a previous paper,[5] the effects of such perturbations are by themselves capable of explaining the probability distribution, $P = |\psi|^2$, at least for certain simple systems.) We may also assume that the equations governing the ψ field have nonlinearities, unimportant at the level where the theory has thus far been successfully applied, but perhaps important in connection with processes involving very short distances. Such nonlinearities could produce, in addition to many other qualitatively new effects, the possibility of irregular turbulent motion. Moreover, we may conceive of a granular substructure of matter underlying the Madelung fluid, analogous to (but not necessarily of exactly the same kind as) the molecular structure underlying ordinary fluids.

We may therefore assume that for any or all of these reasons, or perhaps for still other reasons not mentioned here, our fluid undergoes a more or less random type of fluctuation about the Madelung motion as a mean. Thus, the velocity will not be exactly equal to $\nabla S/m$, nor will the density, ρ, be exactly equal to $|\psi|^2$. All that we require is that the relations $\rho = |\psi|^2$ and $\mathbf{v} = \nabla S/m$ be valid as averages. Indeed, it is not even necessary that the exact velocity be derivable from a potential. Thus, we would have $d\xi/dt = \nabla S'/m + \nabla\times\mathbf{A}$, more generally,[7-9] where $\langle\nabla\times\mathbf{A}\rangle_{Av} = 0$ and $\langle\nabla S'\rangle_{Av} = \langle\nabla S\rangle_{Av}$. Hence Schrödinger's equation will not apply to the fluctua-

[9] Such vortex components of the velocity may also explain the appearance of "spin" provided that they could have a regular component as well as a random component. Indeed, in another paper, the Pauli equation will be treated from this point of view. But here we concern ourselves only with a level of precision in which the spin can be neglected, so that Schrödinger's equation is a good approximation for the mean behavior of the fluid.

tions. However, the conservation equation $\partial\rho/\partial t + \mathrm{div}(\rho\mathbf{v}) = 0$ will be assumed to hold even during a fluctuation. Such an equation is implied almost by the very concept of a fluid; for if there were no conservation, then the model of a fluid would lose practically all of its content.

From the above assumptions, it is clear that if we followed a given fluid element, we would discover that it undergoes an exceedingly irregular motion, which is able in time to carry it from any specified trajectory of the mean Madelung motion to practically any other trajectory. Such a random motion of the fluid elements would, if it were the only factor operating, lead eventually to a uniform mean density of the fluid. For it would on the average carry away more fluid from a region of high density than it carried back. The fact that the mean density remains equal to $|\psi|^2$, despite the effects of the random fluctuations, implies then that a systematic tendency must exist for fluid elements to move toward regions of high mean fluid density, in such a way as to maintain the stability of the mean density, $\bar{\rho} = |\psi|^2$. As for the origin of such a tendency, the question is, of course, not important for the problem that we are treating in this paper. We may, however, suggest by way of a possible explanation that the internal stresses in the fluid are such that whenever ρ deviates from $|\psi|^2$, a kind of pressure arises that tends to correct the deviation automatically. Such a behavior is analogous to what would happen, for example, to a gas in irregular turbulent motion in a gravitational field, in which the pressures automatically adjust themselves in such a way as to maintain a local mean density close to $\rho = \rho_0 e^{-mgz/KT}$ if the temperature T is constant. (In this connection, note that as shown in theoretical treatments of turbulence, the irregular turbulent motions themselves raise the effective "pressure" in the fluid, so that the effective "temperature" T is equal to the sum of the mean kinetic energy of random molecular motion and that of irregular turbulent motion.)

We must now make some assumptions concerning the behavior of the particle-like inhomogeneity. We assume that *even in a fluctuation*, it follows the fluid velocity $\mathbf{v}(\mathbf{x},t)$. Such a behavior would result if the inhomogeneity were a very small dynamic structure in the fluid (e.g., a vortex, or a pulse-like inhomogeneity) or if it were a foreign body of about the same density as the fluid, provided that the wavelengths associated with the fluctuations were appreciably larger than the size of the particle. For in this case, the inhomogeneity would have to do more or less as the fluid did, since it would act, for all practical purposes, like a small element of fluid.

The presence of fluctuations with wavelengths smaller than the size of the body could complicate the problem, especially if we were considering inhomogeneities, such as vortices and pulses, which were dynamically maintained structures in the fluid itself. For, such fluctuations would treat different parts of the inhomogeneity differently, and thus, in general, would tend to lead to a dispersal of the inhomogeneity. Let us recall, however, that we are by hypothesis considering only equations having such nonlinearities in them as to lead to *stable* inhomogeneities. It is true that the equations of ordinary hydrodynamics do not do this. But it is not necessary that the sub-quantum-mechanical Madelung fluid should have exactly the same kinds of properties as are possessed by ordinary fluids. Indeed, we have already seen that instead of the usual classical pressure term, it has a quantum-mechanical internal stress, which depends on the derivatives of the fluid density, rather than on the density itself. Thus, we may reasonably postulate that it also has some characteristically new kind of nonlinear term which leads to stable inhomogeneities. Hence, small fluctuations of wave length much less than the size of the body will merely cause irregular oscillations in the inhomogeneities, the effects of which will, for practical purposes, cancel out. Large fluctuations may destroy the inhomogeneity or transform it into new kinds of inhomogeneity. This could, however, represent certain aspects of the "creation," "destruction," and transformation of "elementary" particles, which is characteristic of phenomena connected with very high energies and very short distances. But in the low-energy domain, which we are treating now, where Schrödinger's equation is a good enough approximation, such processes will not occur.

We see then that if there are fluctuations of wavelength a great deal shorter than the size of the body, they will have a negligible effect on the over-all motions of the body (whether it be a foreign body or a stable dynamic structure in the fluid). In this case, the body will follow the mean velocity of the fluid in a small region surrounding it. To take into account the possibility that such fluctuations may exist, we shall therefore hereafter let $\mathbf{v}(\mathbf{x},t)$ and $\rho(\mathbf{x},t)$ represent respectively the mean velocity and mean density in a small neighborhood surrounding the body, while $\nabla S(\mathbf{x},t)$ and $\rho(\mathbf{x},t)$ represent the means of these quantities in a region that is much larger than the size of the body, but still small enough so that $\psi(\mathbf{x},t)$ does not change appreciably within this region. The consistency of these assumptions evidently requires that the body be very small; but with a choice, for example, of something of the order of 10^{-13} cm for its size, one obtains ample opportunity to satisfy the above assumptions in a consistent way.

It is clear, of course, that fluctuations having a wavelength close to the size of the body will neither cancel out completely, nor will they necessarily cause the body to move exactly with the mean of the fluid velocity in a small neighborhood surrounding it. We may assume, however, that the magnitude of the longer-wavelength fluctuations is so great that we can neglect the effects of fluctuations of these intermediate wavelengths. Thus, a rather wide range exists of kinds of fluctuations that could lead to the type of motion that we are assuming for the inhomogeneity.

On the basis of the above assumptions, it is evident that the inhomogeneity will undergo an irregular motion, analogous to the Brownian motion.[10] Let us now consider a statistical ensemble of fluids, each having in it an inhomogeneity, and let us denote the probability density of such inhomogeneities in the ensemble by $P(\mathbf{x},t)$. Let us further assume that the fluid motion is so irregular that in time a fluid element initially in an arbitrary region $d\mathbf{x}'$ in the domain in which the mean fluid density $|\psi(\mathbf{x},t)|^2$ is appreciable, has a nonzero probability of reaching any other region $d\mathbf{x}$ in this domain. We can then quite easily see in qualitative terms that the probability density $P(\mathbf{x},t)$ must approach $|\psi(\mathbf{x},t)|^2$ as an equilibrium value.

First of all, it is clear that if, for any reason whatever, the distribution $P=|\psi|^2$, is once established, then it will be maintained for all time, despite the random fluctuations in the fluid motion. For the inhomogeneities simply follow the fluid velocity in a small neighborhood surrounding the body. Now by hypothesis the fluid fluctuations are just such as to preserve the equilibrium mean density of $P=|\psi|^2$. Therefore, they must also preserve the equilibrium probability density of particles in the same way.

Let us now consider what happens when P is not equal to $|\psi|^2$. Suppose, for example, that there were a larger number of particles in a specified element of volume than is given by $P=|\psi|^2$. Now, the random motions carry particles away from such an element at a rate proportional to their density in this element. The systematic tendency for particles to come back to the element, which results from their following the fluid, as it drifts back at a rate sufficient to maintain the mean equilibrium density of $\bar{\rho}=|\psi|^2$, will however be just large enough to cancel the loss that would have taken place if the probability density of particles had been $P=|\psi|^2$. Since the density was actually greater than this, more particles are lost than are compensated by the drift back and the density therefore approaches $P=|\psi|^2$. If the probability density of particles in this element had been less than $P=|\psi|^2$, the element would, of course, have tended to gain particles until it had a density of $|\psi|^2$.

In the next section, we shall give a mathematical demonstration of the above result, the correctness of which should however, already be evident from the qualitative considerations cited above.

Finally, we may mention that the picture of a fluid undergoing random motion about a regular mean is only one out of an infinite number of possible models leading to the same general type of theory. Indeed, all the properties that we have assumed for our fluid could equally well belong to some 4-vector field $(\rho,\mathbf{j})$ which was conserved, and which underwent random fluctuations about a mean given (in the nonrelativistic limit) by $\rho=|\psi|^2$ and $\mathbf{j}=(\hbar/2mi)(\psi^*\nabla\psi-\psi\nabla\psi^*)=R^2\nabla S/m$, where ψ is a solution of Schrödinger's equation. And if ρ and $\mathbf{j}$ were assumed to satisfy sufficiently nonlinear equations, there could also exist pulse-like solutions[11] for ρ and $\mathbf{j}$ that moved with a 4-velocity parallel to $(\rho,\mathbf{j})$.

Although it is important to keep in mind these more general possibilities when one is actually trying to formulate a more detailed theory, we have found it convenient in this paper to express our assumptions and results in terms of a hydrodynamical model, because this model not only provides a very natural and vivid physical image of the behavior of the ψ field, but also a simple explanation of the formula, $d\xi/dt=\nabla S/m$, (postulate 2) expressing the velocity of an inhomogeneity in terms of the local mean stream velocity.

4. PROOF THAT PROBABILITY DENSITY APPROACHES FLUID DENSITY IN RANDOM FLUCTUATIONS OF A FLUID

We shall now prove the following theorem. Suppose that we have a conserved fluid that undergoes random fluctuations of the velocity, $\mathbf{v}(\mathbf{x},t)$, and of the density, $\rho(\mathbf{x},t)$, about respective mean values $\mathbf{v}_0(\mathbf{x},t)$ and $\rho_0(\mathbf{x},t)$ [so that $\partial\rho/\partial t+\mathrm{div}(\rho\mathbf{v})=0$ and $\partial\rho_0/\partial t+\mathrm{div}(\rho_0\mathbf{v}_0)=0$]. Suppose in addition that there is an inhomogeneity that follows the fluid motions, with the local stream velocity, $\mathbf{v}(\mathbf{x},t)$. Then if the fluctuations are such that a fluid element starting in an arbitrary element of volume, $d\mathbf{x}'$, in the region where the fluid density is appreciable has a nonzero probability of reaching any other element of volume $d\mathbf{x}$ in this region, it follows that an arbitrary initial probability density of inhomogeneities will in time approach $P=\rho_0(\mathbf{x},t)$.

This theorem is seen to apply to our problems as a special case, in which we set $\rho_0=|\psi(\mathbf{x},t)|^2$ and $\mathbf{v}_0(\mathbf{x},t)=\nabla S(\mathbf{x},t)/m$, where $\psi(\mathbf{x},t)$ satisfies Schrödinger's equation, provided that we regard $\rho(\mathbf{x},t)$ and $\mathbf{v}(\mathbf{x},t)$ as the mean fluid density and velocity in a small region surrounding the inhomogeneity. This theorem is a generalization of a well-known theorem concerning the approach to equilibrium in a Markow process.[12] Essentially, we have generalized the theorem to treat the time-dependent probabilities of transition and time-dependent limiting distributions with which we have to deal in our problem.

To prove this theorem, we note that, as shown in the previous section, a given fluid element follows an extremely irregular trajectory, in which its density $\rho(\mathbf{x},t)$ fluctuates near the mean density $\rho_0(\mathbf{x},t)$. Now because the volume of a given fluid element is always

[10] Brownian motion models of the quantum theory have already been proposed elsewhere, but on a very different basis. See, I. Fenyes, Z. Physik **132**, 81 (1952); W. Weizel, Z. Physik **134**, 264 (1953); **135**, 270 (1953).

[11] See L. de Broglie, *La Physique Quantique, Restera-t-elle Indeterministe* (Gauthier-Villars, Paris, 1953), where the idea of L. de Broglie and J. P. Vigier on this subject are discussed.

[12] W. Feller, *Probability Theory and Its Applications* (John Wiley and Sons, Inc., New York, 1950).

changing in accordance with the changing mean fluid density in the new regions that it enters, it is rather difficult in rectangular coordinates to keep track of how much fluid is transferred on the average from one element of volume to another. To facilitate the treatment of the problem, we shall therefore take the preliminary step of introducing a new set of coordinates, $\xi_1(\mathbf{x})$, $\xi_2(\mathbf{x})$, $\xi_3(\mathbf{x})$, which are so defined that an elementary cell in the space of ξ_1, ξ_2, ξ_3 always contains a mean quantity of fluid proportional to its volume.

Such a set of coordinates is easily defined. For the mean quantity of fluid in a given volume element is

$$dQ=\rho_0(\mathbf{x},t)d\mathbf{x}=\rho_0(\mathbf{x},t)J(\partial x_\mu/\partial\xi_\nu)d\xi_1d\xi_2d\xi_3$$
$$=\rho_0 d\xi_1d\xi_2d\xi_3/J_0(\partial\xi_\nu/\partial x_\mu),$$

where $J(\partial\xi_\nu/\partial x_\mu)$ is the Jacobian of the transformation. Now we want to have $J(\partial\xi_\nu/\partial x_\mu)=c\rho_0(\mathbf{x},t)$ (where we shall choose c to be unity for convenience).

Since there is only one equation, it is clear that only one of the ξ_ν can be defined in this way, so that the other two can be chosen according to what is convenient. Thus, if we fix the forms of ξ_2 and ξ_3, we see that the above equation becomes a linear differential equation defining ξ_1, in terms of ξ_2, ξ_3, and ρ_0. Such an equation always has solutions wherever ξ_2, ξ_3, and ρ_0 are regular. There may exist singular points or curves, but we shall later show how these are to be dealt with.

As an example, consider a cylindrically symmetric density function $\rho(R)=e^{-R}/R$. We first express the volume element in cylindrical polar coordinates (with $R^2=X^2+Y^2$):

$$\rho(R)RdRd\phi dZ=e^{-R}dRd\phi dZ.$$

Now we want $e^{-R}dR=d\xi_1$, or $\xi_1=e^{-R}$. As for ξ_2 and ξ_3, we can in this case leave them equal to ϕ and Z respectively.

Here we see that when R goes from 0 to ∞, ξ_1 goes from unity to zero. This is an example of a characteristic property of the ξ_ν space to be limited in volume when the function $\rho_0(R)$ is appreciable only in a limited domain. Such a property is to be expected, because we are mapping the x_μ on the ξ_ν in just such a way that each region maps into a new volume proportional to the amount of fluid originally in that region. Thus even infinite regions of x_μ space may map onto negligible regions of ξ_ν space, if they contain negligible quantities of fluid.

The solution of the differential equation for ξ_1, will lead in general to multiple-valued functions. This, however, causes no trouble, as we need merely establish a convenient cut somewhere which defines which branch of the function that we are using. Thus the transition to cylindrical polar coordinates, $R^2=X^2+Y^2$; $\phi=\tan^{-1}\times(Y/X)$, leads to a multiple valued function for ϕ, but we deal with this problem by establishing a cut, say at $\phi=0$, and then defining the range of variation of ϕ as being from zero to 2π. In order to cover the entire XY plane only once, a similar definition can be made with any multiple-valued function.

If $\rho_0(\mathbf{x},t)$ vanishes at certain points, then at those points we cannot solve for all the ξ_ν in terms of the x_μ (as, for example, in cylindrical polar coordinates we cannot solve for ϕ at $R=0$). As long as $\rho_0(\mathbf{x},t)$ vanishes only at a set of isolated points, or at most, on a set of one-dimensional curves, where will be no real difficulty. For the vanishing of $\rho_0(\mathbf{x},t)$ means only (as in the case of cylindrical polar coordinates) that some of the ξ_ν are not defined along these curves. To avoid any ambiguities arising from the lack of definition, we may surround each of these curves with a tube, as small in radius as we please, and thus exclude them from the region under consideration without excluding any significant physical effects.

If, however, there are two-dimensional surfaces where $\rho_0(\mathbf{x},t)=0$, this creates more serious mathematical difficulties. Since such surfaces do not, in fact, arise in any real problem of interest to us,[13] we shall assume that $\rho_0(\mathbf{x},t)$ vanishes at most on a set of one-dimensional curves.

Finally, let us note that since ρ_0 changes with time, our ξ_ν will change with time correspondingly. Thus, we are adopting a moving set of coordinates (but not in general one that moves with the mean motion of the fluid elements).

In the space of the ξ_ν, the mean fluid density will be a constant which also does not change with time. As a result, the problem of describing the fluctuations will be greatly simplified. For in the ξ_ν space there is no tendency for the fluctuation to favor any special region since the equilibrium density, which was $\rho_0(\mathbf{x},t)$ in rectangular coordinate, is now a constant. Thus, in the ξ_ν space, the fluctuations have a truly random character, independent of the fluid density at any particular point.

We are now ready to set up the equations governing

[13] In the case of interest to us, $\rho_0=|\psi(\mathbf{x},t)|^2$. At first sight, it may seem that we shall have to be concerned with surfaces on which ρ_0 vanished, because in a perfectly stationary state, $\psi(\mathbf{x},t)$ can be zero on certain nodal surfaces. In the case of a perfectly stationary state, ψ can be real [or more generally, writing $\psi=U(\mathbf{x},t)+iV(\mathbf{x},t)$, we may have a functional relationship between $U(\mathbf{x},t)$ and $V(\mathbf{x},t)$ permitting both to vanish on some two-dimensional surface]. However, for the general complex function ψ, which we obtain in a nonstationary state, it may be shown that there is no such functional relation between U and V, so that ψ can vanish at most on a set of one-dimensional curves.

Now a *perfectly* stationary state is an abstraction that never really exists. For all systems that have ever been dealt with are perturbed to some extent by interactions with other systems. Thus, in a gas, a hydrogen atom suffers 10^{12} collisions per second. In a metal, the electrons suffer a correspondingly large number of collisions with each other and with the cores. In the nucleus, there is a continual process of perturbation due to the fluctuating electronic and ionic fields acting on the spin and quadripole moments of the nuclei. Even in interstellar space, atoms undergo at least one collision with electrons in 10^7 seconds. Thus, all states are slightly nonstationary, and no perfectly nodal planes of the ψ function ever really appear in nature.

A set of perfectly nodal surfaces could interfere with our proof that $P\rightarrow|\psi|^2$; for they would represent surfaces that would never be crossed so that the regions on different sides of these surfaces could be completely isolated from each other.

the changes of the probability density $P(\mathbf{x},t)$ for the inhomogeneities. We first transform to the ξ_ν space, writing

$$P(\mathbf{x},t)d\mathbf{x}=\frac{P(\mathbf{x},t)d\xi}{J(\partial\xi_\nu/\partial x_\mu)}=\frac{P(\mathbf{x},t)}{\rho_0(\mathbf{x},t)}d\xi=F(\xi,t)d\xi, \quad (3)$$

where we have defined the vector $\xi=(\xi_1,\xi_2,\xi_3)$ in the ξ_ν space, with the volume element, $d\xi=d\xi_1 d\xi_2 d\xi_3$. The probability density for the space of the ξ_ν is clearly $F=P/\rho_0$. To prove that $P\rightarrow\rho_0$, we then merely have to show that in ξ_ν space, $F(\xi,t)$ approaches a constant.

We now define the probability that fluid in an element $\delta\xi$, centered at the point ξ at the time t, has in the process of fluctuation come from an element $\delta\xi'$ at an earlier time t' with its center ξ' lying in a region $d\xi'$. (Note that $\delta\xi'$ is the magnitude of the volume element,[14] whereas $d\xi'$ is the size of the cell in which the center of the volume element was located at the time t'). This probability is

$$dP=K(\xi,\xi',t,t')d\xi'. \quad (4)$$

Clearly, by definition,

$$\int K(\xi,\xi',t,t')d\xi'=1. \quad (5)$$

Now the exact form of $K(\xi,\xi',t,t')$ will depend on the precise nature of the fluctuations that are taking place in the fluid. We shall see, however, that in order to prove that $F(\xi,t)\rightarrow 1$, it is sufficient to assume that $K(\xi,\xi',t,t')$ fails to be zero over the part of ξ space corresponding to the region of $\mathbf{x}$ space in which $\rho_0(\mathbf{x},t)$ is appreciable. This is clearly just a mathematical expression of the assumption appearing in the first part of this section that there is a nonzero probability that an element starting at any point $\mathbf{x}$ in this region has a nonzero probability of arriving at any other point x' in the region.

Note, however, that the region of $\mathbf{x}$ space in which ρ_0 is appreciable will include, for practical purposes, the whole of the ξ space (except for a region of negligible dimensions). Thus, we may postulate that $K(\xi,\xi',t,t')$ fails to be zero in the whole of ξ space (except possibly along some one-dimensional curves where $\rho_0(\mathbf{x},t)$ may be zero, which we can exclude by means of tubes of negligible dimensions).

As for other properties of K, they are irrelevant for our purposes here, although we shall discuss some of them in Sec. 6, in another connection.[15]

[14] On the average, $\delta\xi$ will not change as the fluid element moves because the fluid density fluctuates near a constant volume in space.

[15] It may be noted at this point that the kernel $K(\xi,\xi',t,t')$ already contains implicit within it a description of the mean fluid velocity $\nabla S/m$. To show this, consider $t-t'=\delta t$ to be a small interval of time. Then $K(x,x',t,t'-\delta t)$ will be large in only a small region of ξ space corresponding in $\mathbf{x}$ space to a region centered around $(x-x'-\nabla S\delta t/m)=0$. The motion of the center of this region describes the mean fluid velocity. The spread of this region describes the random deviations from the mean. In a typical random diffusion process, this width is given by $(\Delta x)^2\sim\delta t$, for short times. For longer times, the functional form of K is determined in a complicated way, which is however of no concern to us in this paper.

Let us now discuss the motions of the inhomogeneities. Since these latter follow the fluid in its fluctuations, it is easily seen that the probability density of inhomogeneities, $F(\xi,t)$, is just the average of $F(\xi',t')$ weighted with the probability $K(\xi,\xi',t,t')$. Thus,

$$F(\xi,t)=\int K(\xi,\xi',t,t')F(\xi',t')d\xi'. \quad (6)$$

Now, let $\xi_M(t)$ represent the value of ξ for which $F(\xi,t)$ is a maximum, $\xi_m(t)$ the value for which it is a minimum. (If there is more than one pair of such points, let us consider any single pair.) We also let $F_{\max}(\xi,t)=M(t)$, and $F_{\min}(\xi,t)=m(t)$. Setting $\xi=\xi_M(t)$ in Eq. (6), and using (5), we obtain

$$M(t)=\int K(\xi_M(t),\xi',t,t')F(\xi',t')d\xi' \leqq \int K(\xi_M(t),\xi',t,t')M(t')d\xi'=M(t'); \quad (7)$$

and with $\xi=\xi_m(t)$ in Eq. (6), we get similarly

$$m(t)=\int K(\xi_m(t),\xi',t,t')F(\xi',t')d\xi' \geqq \int K(\xi_m(t),\xi',t,t')m(t')d\xi'=m(t'). \quad (8)$$

Thus,

$$M(t)\leqq M(t'), \quad (9a)$$

$$m(t)\geqq m(t'). \quad (9b)$$

In order for the equal sign to hold in Eq. (9a), it is necessary that $F(\xi',t')$ be a constant. For by hypothesis, $K(\xi,\xi',t,t')$ fails to vanish anywhere in the ξ space; and if $F(\xi',t')$ is *not* a constant, then the integral (7) must obtain contributions from regions in which $F(\xi',t')<M$. Similarly, we can show that the equal sign can hold in (9b) only if $F(\xi',t')$ is a constant. But if $F(\xi',t')$ is a constant in ξ space, then by (6) we have

$$F(\xi,t)=F(\xi',t')\int K(\xi,\xi',t,t')d\xi'=F(\xi',t').$$

Thus, $F(\xi',t')=$ constant is also an equilibrium solution, since it does not change with the passage of time. The result, of course, is more or less to be expected from the physical argument given at the beginning of this section showing that $P=\rho_0(\mathbf{x},t)$ is an equilibrium solution, so that $F=P/\rho_0=$ constant must likewise be one. We conclude then that if $F(\xi',t')$ is not a constant, Eqs. (9a) and (9b) must be written as

$$M(t)<M(t'), \quad (10a)$$

$$m(t)>m(t'). \quad (10b)$$

Now we can show that Eqs. (10a) and (10b) imply that $F(\mathbf{x},t)$ must approach a constant, with the passage of time. To do this, let us consider a series of times, $t_1, t_2, t_3 \cdots t_n, t_{n+1} \cdots$. We apply (10a) and (10b) from one element of the series of times to the next. Thus

$$M(t_n) < M(t_{n-1}), \tag{11a}$$

$$m(t_n) > m(t_{n-1}). \tag{11b}$$

It is clear that $M(t_n)$ and $m(t_n)$ must each approach constant limits. For $M(t_n)$ is always decreasing and yet remains greater than some fixed number, $m(t_s)$, where t_s is any element of the series such that $t_n > t_s$. Similarly $m(t_n)$ is always increasing and yet less than $M(t_s)$. Now there are just two possibilities: (a) The two constant limits are different; (b) they are the same. We easily see that alternative (a) is self-contradictory. To do this, we denote the two limits by M and m, respectively. Then $M-m=\lim[M(t_n)-m(t_n)]$. But by (11a) and (11b), we have

$$M-m<\lim_{n\to\infty}[M(t_{n-1})-m(t_{n-1})]$$
$$=\lim_{n\to\infty}[M(t_n)-m(t_n)]=M-m.$$

Because this is a contradiction, alternative (b) must hold. Then $F(\xi,t)$ must approach a constant limit, and $P(\mathbf{x},t)$ must approach $a\rho_0(\mathbf{x},t)$, where a is a constant. If, as happens in quantum theory, the integral of $\rho_0(\mathbf{x},t)$ is normalized to unity, then since by definition the integral of P is also normalized to unity, we must have $a=1$, and

$$P(\mathbf{x},t)\to\rho_0(\mathbf{x},t). \tag{12}$$

5. APPLICATION TO DIRAC EQUATION AND EXTENSION TO MANY-PARTICLE PROBLEM

We may apply the preceding results to the causal interpretation of the Dirac equation,[16] where, as in the Schrödinger equation, we have a stream velocity, $\mathbf{v}_0=\psi^*\boldsymbol{\alpha}\psi/\psi^*\psi$, and a conserved density, $\rho_0=\psi^*\psi$. If we assume a fluid of the same kind as that treated in Sec. 4, and replace $\nabla S/m$ by $\psi^*\boldsymbol{\alpha}\psi/\psi^*\psi$ and $|\psi|^2$ by $\psi^*\psi$, then according to the results of Sec. 4, the probability density will ultimately approach $\psi^*\psi$.

Our results can also be extended very readily to the case of many particles. We first discuss this extension in a purely formal way. We have a wave function, $\psi(\mathbf{x}_1,\mathbf{x}_2\cdots\mathbf{x}_N,t)$, defined in a $3N$-dimensional configuration space. Writing $\psi=R\exp(iS/\hbar)$, we have a set of $3N$ velocity fields, $\mathbf{v}_n=\nabla_n S(\mathbf{x}_1,\mathbf{x}_2,\cdots\mathbf{x}_N,t)$, where ∇_n refers to differentiation with respect to the coordinates of the nth particle. We have a conservation equation in the configuration space.[17] We may now assume that each particle follows the line of flow given by $\mathbf{v}_n(\mathbf{x}_1,\mathbf{x}_2,\cdots\mathbf{x}_N,t)$. Thus, our model is formally just a $3N$-dimensional extension of the model given previously. Hence, if we assume random fluctuations of the $3N$-dimensional velocity field, we shall obtain the result that the probability density in configuration space, $P(\mathbf{x}_1,\mathbf{x}_2,\cdots\mathbf{x}_N,t)$, approaches $|\psi(\mathbf{x}_1,\mathbf{x}_2,\cdots\mathbf{x}_N,t)|^2$.

To obtain a possible physical picture of the meaning of this model, we may use the causal interpretation of the N-particle problem recently proposed by de Broglie.[18] De Broglie has shown that the usual formulation in terms of a wave function in the $3N$-dimensional configuration space can be replaced by an equivalent formulation, according to which each particle is accompanied by its own 3-dimensional wave field, which depends on the precise locations of the other $(N-1)$ particles. Since each wave field satisfies its own Schrödinger's equation, the preceding demonstration still applies.

The above model would imply that each particle moves in its own fluid, and that the fluids interpenetrate each other. For the case of equivalent particles, however, de Broglie has suggested that all particles can be regarded as moving in a common three-dimensional fluid, the velocity of which, at any point $\mathbf{x}$, is dependent on the locations of all the particles, $\mathbf{x}_n$. Thus, we would merely need as many fluids as there are types of particles.

6. ON THE RELATION BETWEEN THE THEORY OF MEASUREMENTS AND FLUCTUATIONS IN THE ψ FIELD

We have demonstrated that with time, the limiting distribution, $P=|\psi|^2$, will be established for any functional form of $K(\xi,\xi',t,t')$, at least within a region which is such that $K(\xi,\xi',t,t')$, does not vanish for any pair of points ξ' and ξ in the region in question. But without a further specification of the $K(\xi,\xi',t,t')$, the rate of approach to the limiting distribution cannot be estimated.

The very fact that no conclusion drawn from the assumption that $P=|\psi|^2$ has as yet been contradicted experimentally, suggests, however, that at least to a fairly high degree of approximation, P is equal to $|\psi|^2$ in all quantum-mechanical systems which have thus far been investigated. Hence, we are led in our model to assume that the existing fluctuations are at least rapid enough to insure the approximate maintenance of the relation, $P=|\psi|^2$ in the very wide variety of systems which has thus far been studied.

In connection with the theory of measurements, however, there arises an important case in which the rate of approach to the equilibrium distribution must be quite slow, if the theory as a whole is to be consistent. This is the case of two wave packets separated by a classical order of distance, throughout which the mean density $|\psi|^2$ is completely negligible.

To show why this case is important, let us recall

[16] D. Bohm, Progr. Theoret. Phys. (Japan) **9**, 273 (1953).
[17] See reference 2, Paper I, Eq. (16).
[18] See reference 11; also Compt. rend. **235**, 1345, 1372 (1953).

briefly some results of the theory of measurements given in a previous paper.[2]

It was shown that in a measurement process, the interaction between measuring apparatus and observed system breaks the wave function into a series of classically separated packets, corresponding to the various possible results of the measurement. The particle, however, enters one of the packets and thereafter remains in it. It is important that the particle remain in this packet; because if it does, the other packets will never play any physical role, so that they can thereafter be neglected and the complete wave function replaced by a simplified one corresponding to the actual result of the measurement. Thus, we understand how a measurement can come to have a definite result, despite the spread of the wave function over a range of possibilities.

Now, if the introduction of a random fluctuation of the ψ field led to an appreciable diffusion of the particle from one of these classically separated packets to another, the above definiteness of the result of a measurement would be destroyed. It is essential therefore for the over-all consistency of the theory that the probability that the particle diffuse across a large region where $\rho_0(\mathbf{x},t)$ is very small shall be negligible.[19]

It is easy to see, however, that almost any reasonable assumptions concerning the fluctuations will lead to this result. For the mean current of particles is $\langle \rho \mathbf{v} \rangle_{\text{Av}}$. Now ρ is everywhere of the order of magnitude of $\rho_0(\mathbf{x},t)$, which is by hypothesis very small in the region between the wave packets. Thus a large probability of a fluctuation that would carry a particle across this space would mean an enormous fluctuation velocity in this region. The mere assumption that fluctuation velocities do not differ by large orders of magnitude in different parts of the fluid is therefore sufficient to insure that the probability of diffusion across this space be very small.

7. CONCLUSION

The essential result of this paper has been to show that the probability density $P=|\psi|^2$ follows from reasonable assumptions concerning random fluctuations of the ψ field. Now, it has already been demonstrated[2] that once the probability distribution $P=|\psi|^2$ has, for any reason whatever, been set up in a statistical ensemble of quantum-mechanical systems, then the results predicted for all measurement processes will be precisely the same in the causal interpretation as in the usual interpretation. The difference between the two points of view, however, is this: in the usual interpretation, the irregular statistical fluctuations in the observed results[20] obtained in general when we make very precise measurements on *individual* atomic systems are assumed, so to speak, to be fundamental elements of reality, since it is supposed that they cannot be analyzed in more detail, and that they cannot be traced to anything else.[21] In the model that we have proposed here, however, the statistical fluctuation in the results of such measurements are shown to be ascribable consistently to an assumed deeper level of irregular motion in the ψ field.

In this paper we have proposed as a possible picture of this deeper level the more specific model of a fluid, undergoing a random fluctuation of its velocity and density about certain mean values determined from Schrödinger's equation, and having in it an inhomogeneity that follows the local stream velocity of the fluid. Of course, this proposal has not yet reached a definitive stage, since we have given only a very general description of the assumed fluctuations and of the properties of the inhomogeneity. Nevertheless, such a model, incompletely defined in character as it is, already suggests a number of interesting questions.

For example, the fluid may have vortex motion. In another paper[22] it will be shown that such vortex motion provides a very natural model for the nonrelativistic wave equation of a particle with spin (the Pauli equation). Work now in progress indicates that a generalization of such a treatment to relativity may yield a model of the Dirac equation.

Another interesting problem to be studied is the possible effects of the assumption of nonlinear equations for the ψ field, which could, as we have seen in Sec. 2, explain the existence of the irregular fluctuations that lead to $P=|\psi|^2$. Such nonlinear equations can lead to many qualitatively new results. For example, it is known that they have a spectrum of stable solutions having localized pulse-like concentrations of field,[23] which could describe inhomogeneities such as we

[19] Note that the slowness of this particular type of diffusion does not interfere with the validity of the relation $P=|\psi|^2$, for the wave function as a whole (i.e., over a whole set of wave packets). For the relation $P=|\psi|^2$ will already have been established by random fluctuations before the measurement took place; and as we have seen, once established, the relationship persists and is not thereafter altered by the fluctuations no matter what happens. But what we have been discussing is *another* probability; namely, the probability that if a particle has entered a given packet, it will within a given time diffuse to another packet. It is this probability that is negligible.

[20] Let us recall that as discussed in reference 5, Sec. 3, there exist real observable large-scale phenomena obtained in a measurement process, which depend on the properties of *individual* atoms (e.g., clicks of a Geiger counter, tracks in a Wilson chamber, etc.)

[21] For example, they cannot in general be ascribed to the uncontrollable actions of the measuring apparatus, as demonstrated by Einstein, Rosen, and Podolsky, Phys. Rev. **47**, 774 (1933) and also D. Bohm, *Quantum Theory* (Prentice Hall Publications, New York, 1951), p. 614. As Bohr has made clear [Phys. Rev. **48**, 696 (1935)] the measuring apparatus plus observed object must be regarded as a single indivisible system which yields a statistical aggregate of irregularly fluctuating observable phenomena. It would be incorrect, however, to suppose that these fluctuations originate in anything at all. They must simply be accepted as fundamental and not further analyzable elements of reality, which do not come from anything else but just exist in themselves. For a complete discussion of this problem, see, *Albert Einstein, Philosopher-Scientist*, Paul Arthur Schilpp, Editor (Library of Living Philosophers, Evanston, 1949).

[22] Bohm, Tiomno, and Schiller (to be published).

[23] Finkelstein, LeLevier, and Ruderman, Phys. Rev. **83**, 326 (1951).

have been assuming in this paper. Such pulse-like concentrations of field would also tend, for many types of field equations, to follow the local stream velocity.[11] The transitions between different possible forms of the inhomogeneous pulse-like part of the solution, combined with transitions between various modes of vibration in the rest of the fluid, could perhaps describe changes from one type of particle to another. Thus, we see that at least in its qualitative aspects, the model seems to have possibilities for explaining some of the kinds of phenomena that are actually found experimentally at the level of very small distances.

The authors would like to express their gratitude to the Conselho Nacional de Pesquisas of Brazil and the Section des Relations Culturelles of France, which provided grants that made this research possible.

PHYSICAL REVIEW VOLUME 96, NUMBER 1 OCTOBER 1, 1954

Expansion of Wave Packets

DANIEL S. LING, JR.
University of Kansas, Lawrence, Kansas
(Received April 16, 1954)

The Fourier coefficients of a wave packet are proved to be equal to the coefficients obtained when the wave packet is expanded in terms of a set of functions appropriate to a scattering problem.

IN a recent paper discussing the use of ingoing waves in scattering problems, Breit and Bethe[1] made use of the fact that when a wave packet is expanded in terms of a set of functions appropriate to a scattering problem, the expansion coefficients are in most cases identical with the Fourier coefficients of the packet. This note indicates a more precise proof of this theorem.

Let $\psi(\mathbf{r})$ be a wave packet which is well localized in both coordinate and momentum space; $\mathbf{r}^c$ and $\mathbf{k}^c$ denote the center of the packet in the two spaces. We assume that the spread of the packet in coordinate (momentum) space is small compared with $\mathbf{r}^c$,$(\mathbf{k}^c)$. Let $\psi_\mathbf{k}(\mathbf{r})$ be a complete set of wave functions appropriate to a scattering problem. As Breit and Bethe point out, we get a complete set of functions if we choose $\psi_\mathbf{k}$ to behave asymptotically as a plane wave plus an outgoing spherical wave; thus

$$\psi_\mathbf{k}(\mathbf{r})\sim e^{i\mathbf{k}\cdot\mathbf{r}}+f_\mathbf{k}(\theta,\varphi)e^{ikr}/r. \tag{1}$$

We will expand $\psi(\mathbf{r})$ in terms of $\psi_\mathbf{k}$ and denote the expansion coefficients by $B(\mathbf{k})$; the Fourier coefficients of $\psi(\mathbf{r})$ are $A(\mathbf{k})$. Thus

$$\psi(\mathbf{r})=(2\pi)^{-\frac{3}{2}}\int B(\mathbf{k})\psi_\mathbf{k}(\mathbf{r})d\mathbf{k}, \tag{2}$$

$$\psi(\mathbf{r})=(2\pi)^{-\frac{3}{2}}\int A(\mathbf{k})e^{i\mathbf{k}\cdot\mathbf{r}}d\mathbf{k}. \tag{2'}$$

It can now be proved that, except when $\mathbf{r}^c$ and $\mathbf{k}^c$ are parallel, $B(\mathbf{k})\simeq A(\mathbf{k})$. In particular, Breit and Bethe used the fact that $B(\mathbf{k})\simeq A(\mathbf{k})$ when $\mathbf{r}^c$ and $\mathbf{k}^c$ are antiparallel.

[1] G. Breit and H. A. Bethe, Phys. Rev. 93, 888 (1954).

Let $C(\mathbf{k})=B(\mathbf{k})-A(\mathbf{k})$, and form

$$J(\mathbf{r}^c,\mathbf{k}^c)=(2\pi)^{-\frac{3}{2}}\int|C(\mathbf{k})|^2d\mathbf{k}.$$

We assume that $\psi(\mathbf{r})$ is far enough removed from the origin so that the asymptotic form of $\psi_\mathbf{k}$ may be used in computing $B(\mathbf{k})$. This gives

$$C(\mathbf{k})=(2\pi)^{-\frac{3}{2}}\int\psi(\mathbf{r})f_\mathbf{k}^*(\theta,\varphi)e^{-ikr}/r d\mathbf{r}, \tag{3}$$

and

$$J(\mathbf{r}^c,\mathbf{k}^c)=(2\pi)^{-9/2}\int d\mathbf{r}\psi^*(\mathbf{r})\int d\mathbf{r}'\psi(\mathbf{r}')\times\int d\mathbf{k}f_\mathbf{k}(\theta,\varphi)f_\mathbf{k}^*(\theta',\varphi')\times\exp[ikr-ikr']/rr'. \tag{4}$$

The completeness relation for $\psi_\mathbf{k}$ combined with Eq. (1) yields the result

$$\int d\mathbf{k}f_\mathbf{k}(\theta,\varphi)f_\mathbf{k}^*(\theta',\varphi')(rr')^{-1}\exp[ikr-ikr']=-\int d\mathbf{k}f_\mathbf{k}(\theta,\varphi)\exp[ikr-i\mathbf{k}\cdot\mathbf{r}']/r-\int d\mathbf{k}f_\mathbf{k}^*(\theta',\varphi')\exp[-ikr'+i\mathbf{k}\cdot\mathbf{r}]/r'. \tag{5}$$

Inserting (5) into (4) and noting that one integration may now be performed, we find that J reduces to

$$J=-(2\pi)^{-3}\int d\mathbf{k}\int d\mathbf{r}\{[\psi^*(\mathbf{r})f_\mathbf{k}(\theta,\varphi)\times A(\mathbf{k})e^{ikr}/r]+(\text{cc})\}. \tag{6}$$

Since $\psi(\mathbf{r})$ is well localized and far removed from the origin in both coordinate and momentum space, we may write

$$J=-(2\pi)^{-3}\Big[(r^c)^{-1}f_{\mathbf{k}^c}(\theta_{\mathbf{r}^c},\varphi_{\mathbf{r}^c}) \times\int d\mathbf{k}d\mathbf{r}\psi^*(\mathbf{r})A(\mathbf{k})e^{ikr}+(\mathrm{cc})\Big],$$

and we may also expand kr as

$$kr=-k^cr^c+(\mathbf{k}\cdot\mathbf{k}^c)r^c/k^c+(\mathbf{r}\cdot\mathbf{r}^c)k^c/r^c.$$

Thus finally

$$J(\mathbf{r}^c,\mathbf{k}^c)=-[(r^c)^{-1}f_{\mathbf{k}^c}(\theta_{\mathbf{r}^c},\varphi_{\mathbf{r}^c})\exp(-ik^cr^c) \times A^*(\mathbf{r}^c(k^c/r^c))\psi(\mathbf{k}^c(r^c/k^c))+(\mathrm{cc})]. \quad (7)$$

Now since $\psi(\mathbf{r})$ vanishes unless $\mathbf{r}\simeq\mathbf{r}^c$ and since $(r^c/k^c)\mathbf{k}^c$ is a vector of magnitude r^c in the direction of $\mathbf{k}^c$, unless $\mathbf{r}^c$ and $\mathbf{k}^c$ are nearly parallel $\psi((r^c/k^c)\mathbf{k}^c)$ will be very small. A similar argument applies to $A^*((k^c/r^c)\mathbf{r}^c)$. In particular, if $\mathbf{k}^c$ and $\mathbf{r}^c$ are antiparallel J will be essentially zero.

Breit and Bethe make clear the fact that we would also have obtained a complete set for $\psi_{\mathbf{k}}$ by choosing the asymptotic behavior of $\psi_{\mathbf{k}}$ to be that of a plane wave plus an incoming spherical wave. Had we made this choice it is clear that J would be essentially zero except when $\mathbf{r}^c$ and $\mathbf{k}^c$ are antiparallel.

As pointed out by Breit and Bethe, these results may be argued physically by remarking that the outgoing (ingoing) spherical wave part of $\psi_{\mathbf{k}}$ can contribute to the expansion of $\psi(\mathbf{r})$ only if in the past (future) the wave packet passed close enough to the origin to be scattered. In view of this it would be expected that the size of $J(\mathbf{r}^c,\mathbf{k}^c)$ would be determined by the maximum of the probability of finding the particle at the origin at any time in the past (future). If a Gaussian packet is used for $\psi(\mathbf{r})$, it is indeed possible to demonstrate this. For a Gaussian packet with equal relative spread in coordinate and momentum space, $\Delta r/r^c=\Delta k/k^c$, the maximum of the probability of finding the particle at the origin at any time in the past is proportional to $\exp[-2(r^c/\Delta r)^2(1-\cos\gamma)]$, where γ is the angle between $\mathbf{k}^c$ and $\mathbf{r}^c$. For this same packet J is proportional to $\exp[-4(r^c/\Delta r)^2(1-\cos\gamma)]$. In applying this theorem, Breit and Bethe may choose $\Delta r/r^c$ as small as desired, and thus they may say with complete precision that J vanishes unless $\gamma=0$.

Generalized Variational Principle for the Scattering Amplitude*

S. I. RUBINOW
Massachusetts Institute of Technology, Cambridge, Massachusetts
(Received June 2, 1954)

The Schwinger variational principle in differential form for the S-wave phase shift has been generalized so as to be applicable to the entire scattering amplitude.

VARIATIONAL principles for the calculation of phase shifts in nuclear scattering problems were first introduced by Schwinger[1] and Hulthén[2] and have by now been given numerous other formulations.[3–6] All these depend upon Schrödinger's equation in its differential form. Schwinger[7] has also provided variational principles for both the phase shifts and the scattering amplitude which are based on the integral equation formulation of Schrödinger's equation, but sometimes the use of a varaitional principle involving the differential formulation is more feasible for numerical calculations. The generalization of Hulthén's method for the phase shift to the entire scattering amplitude has been given by Kohn.[8] In the present note it will be shown that a similar generalization exists for the corresponding Schwinger differential formulation.[1] This permits the use of trial functions involving the "inside" wave function[6] representing the difference between the wave function and its asymptotic form.

Let Schrödinger's equation be written as

$$\Delta\psi+k^2\psi-V(r)\psi=0, \tag{1}$$

and let the subscripts 1, 2 denote two particular solutions of Eq. (1) having the asymptotic form

$$\lim_{r\to\infty}\psi_i=e^{i\mathbf{k}_i\cdot\mathbf{r}}+f(\mathbf{k}_i,\mathbf{k})\frac{e^{ikr}}{r}, \quad i=1,2. \tag{2}$$

This represents an incident plane wave in the direction $\mathbf{k}_i$ and a scattered wave in the direction $\mathbf{k}$ with amplitude $f(\mathbf{k}_i,\mathbf{k})$. For simplicity, let $\psi_i=e^{i\mathbf{k}_i\cdot\mathbf{r}}+r^{-1}\phi_i$, and form the expression

$$\int d\tau\left(e^{i\mathbf{k}_2\cdot\mathbf{r}}+\frac{1}{r}\phi_2\right)\left(\Delta\frac{\phi_1}{r}+k^2\frac{\phi_1}{r}-V(r)\left[e^{i\mathbf{k}_1\cdot\mathbf{r}}+\frac{\phi_1}{r}\right]\right)=0. \tag{3}$$

By the use of Green's theorem,

$$\int d\tau e^{i\mathbf{k}_2\cdot\mathbf{r}}\left(\Delta\frac{\phi_1}{r}+k^2\frac{\phi_1}{r}\right)=\int dS\left(e^{i\mathbf{k}_2\cdot\mathbf{r}}\frac{\partial}{\partial n}\left(\frac{\phi_1}{r}\right)-\frac{\phi_1}{r}\frac{\partial}{\partial n}e^{i\mathbf{k}_2\cdot\mathbf{r}}\right), \tag{4}$$

where the surface integral extends over an infinitely large sphere. Consequently, the function ϕ_1 may be replaced by its asymptotic form $\chi_1=f(\mathbf{k}_1,\mathbf{k})e^{ikr}$. The resulting expression is readily evaluated[9] and is equal to $-4\pi f(\mathbf{k}_1,-\mathbf{k}_2)$. The terms in Eq. (3) involving ϕ_2 and $\Delta\phi_1$ may be integrated by parts, yielding the symmetric form

$$4\pi f(\mathbf{k}_1,-\mathbf{k}_2)=\int d\tau\frac{1}{r^2}\left\{-\frac{\partial\phi_1}{\partial r}\frac{\partial\phi_2}{\partial r}-\frac{1}{r^2}\frac{\partial\phi_1}{\partial\theta}\frac{\partial\phi_2}{\partial\theta}-\frac{1}{r^2\sin^2\theta}\frac{\partial\phi_1}{\partial\varphi}\frac{\partial\phi_2}{\partial\varphi}+k^2\phi_1\phi_2-V(r)[re^{i\mathbf{k}_1\cdot\mathbf{r}}+\phi_1]\times[re^{i\mathbf{k}_2\cdot\mathbf{r}}+\phi_2]\right\}+\int d\Omega\left[\phi_2\frac{\partial\phi_1}{\partial r}\right]_{r=0}^{r=\infty}. \tag{5}$$

Following Schwinger's analysis, the divergent contribution arising from the evaluation at infinity of the last term above is eliminated by subtracting an exactly similar contribution from the equation for the asymptotic function. Thus, the function χ_1 satisfies the equation

$$\frac{1}{r}\left(\frac{\partial^2}{\partial r^2}\chi_1+k^2\chi_1\right)=0. \tag{6}$$

After multiplying by $r^{-1}\chi_2$ and integrating over all space, one obtains

$$\int d\tau\frac{1}{r^2}\left(-\frac{\partial\chi_1}{\partial r}\frac{\partial\chi_2}{\partial r}+k^2\chi_1\chi_2\right)+\int d\Omega\left[\chi_2\frac{\partial\chi_1}{\partial r}\right]_{r=0}^{r=\infty}=0. \tag{7}$$

Subtracting (7) from (5), one obtains the following

* Supported in part by the joint program of the U. S. Atomic Energy Commission and the U. S. Office of Naval Research.

[1] J. Schwinger, Phys. Rev. **72**, 742 (1947); **78**, 135 (1950).
[2] L. Hulthén, Kgl. Fysiograf. Sällskap. Lund, Förh. **14**, No. 21, 257 (1944); Den 10. Skandinaviske Matematiker Kongres 1946 (Jul. Gjellerups Vorlag, Copenhagen, 1947), p. 201.
[3] L. Hulthén, Arkiv Mat. Astron. Fysik **35A**, 25-1 (1948).
[4] L. Hulthén and S. Skavlem, Phys. Rev. **87**, 297 (1952).
[5] T. Kato, Phys. Rev. **80**, 475 (1950).
[6] H. Feshbach and S. I. Rubinow, Phys. Rev. **88**, 484 (1952).
[7] J. Schwinger, hectographed notes, Harvard University, 1947 (unpublished). See also J. M. Blatt and J. D. Jackson, Phys. Rev. **76**, 18 (1949), and reference 8.
[8] W. Kohn, Phys. Rev. **74**, 1763 (1948).
[9] P. A. M. Dirac, *Principles of Quantum Mechanics* (Clarendon Press, Oxford, 1947), third edition, Sec. 50.

variational principle for $f(\mathbf{k}_1, -\mathbf{k}_2)$:

$$4\pi f(\mathbf{k}_1, -\mathbf{k}_2) = \int d\tau \frac{1}{r^2}\Big\{ -\frac{\partial\phi_1}{\partial r}\frac{\partial\phi_2}{\partial r} - \frac{1}{r^2}\frac{\partial\phi_1}{\partial\theta}\frac{\partial\phi_2}{\partial\theta} - \frac{1}{r^2\sin^2\theta}\frac{\partial\phi_1}{\partial\varphi}\frac{\partial\phi_2}{\partial\varphi} + k^2\phi_1\phi_2 - V(r)[re^{i\mathbf{k}_1\cdot\mathbf{r}} + \phi_1] \times [re^{i\mathbf{k}_2\cdot\mathbf{r}} + \phi_2]\Big\} - \int d\tau \frac{1}{r^2}\Big\{ -\frac{\partial\chi_1}{\partial r}\frac{\partial\chi_2}{\partial r} + k^2\chi_1\chi_2 \Big\} + ik\int d\Omega f(\mathbf{k}_1,\mathbf{k}) f(\mathbf{k}_2,\mathbf{k}), \quad (8)$$

the last term above being contributed by the last term in Eq. (7). This expression is stationary with respect to arbitrary variations in the functions ϕ_i, χ_i provided that these have the correct radial dependence at infinity, e.g.,

$$\lim_{r\to\infty}\delta\phi_i = \delta\chi_i = \delta f(\mathbf{k}_i,\mathbf{k}) e^{ikr}. \quad (9)$$

One can now introduce the "inside" wave function defined by

$$Y_i = \chi_i - \phi_i, \quad (10)$$

which satisfies the boundary conditions

$$\begin{aligned} Y_i(0) &= f(\mathbf{k}_i,\mathbf{k}), \\ Y_i(\infty) &= 0. \end{aligned} \quad (11)$$

Equation (8) may now be written as

$$4\pi f(\mathbf{k}_1, -\mathbf{k}_2) = 4\pi f_B(\mathbf{k}_1, -\mathbf{k}_2) + \int d\tau \frac{1}{r^2}\Big\{ -\frac{\partial Y_1}{\partial r}\frac{\partial Y_2}{\partial r} + k^2 Y_1 Y_2 - \frac{1}{r^2}\frac{\partial}{\partial\theta}(\chi_1 - Y_1)\frac{\partial}{\partial\theta}(\chi_2 - Y_2) - \frac{1}{r^2\sin^2\theta}\frac{\partial}{\partial\varphi}(\chi_1 - Y_1)\frac{\partial}{\partial\varphi}(\chi_2 - Y_2) - V(r)[re^{i\mathbf{k}_1\cdot\mathbf{r}}(\chi_2 - Y_2) + re^{i\mathbf{k}_2\cdot\mathbf{r}}(\chi_1 - Y_1)]\Big\} - ik\int d\Omega f(\mathbf{k}_1,\mathbf{k}) f(\mathbf{k}_2,\mathbf{k}), \quad (12)$$

where $f_B(\mathbf{k}_1, -\mathbf{k}_2)$ is just the Born approximation

$$4\pi f_B(\mathbf{k}_1, -\mathbf{k}_2) = -\int d\tau e^{i\mathbf{k}_1\cdot\mathbf{r}} V(r) e^{i\mathbf{k}_2\cdot\mathbf{r}}. \quad (13)$$

Equation (12) is stationary with respect to variations in Y_i.

I am indebted to Herman Feshbach for several illuminating conversations out of which this work developed.

Letters to the Editor

PUBLICATION of brief reports of important discoveries in physics may be secured by addressing them to this department. The closing date for this department is five weeks prior to the date of issue. No proof will be sent to the authors. The Board of Editors does not hold itself responsible for the opinions expressed by the correspondents. Communications should not exceed 600 words in length and should be submitted in duplicate.

Ultrasonic Attenuation in Superconducting Lead

H. E. BÖMMEL

Bell Telephone Laboratories, Murray Hill, New Jersey

(Received August 2, 1954)

IN a previous paper Bömmel and Olsen[1] described an attempt to find an influence of superconductivity on ultrasonic velocity and attenuation. Using a frequency of 1 Mc/sec, the authors could find only a not very reproducible increase of the sound attenuation during the penetration or ejection of the magnetic flux used to destroy superconductivity. Experiments are now being carried out in the frequency range from 9–27 Mc/sec and the preliminary results show marked effects.

The superconductive specimens used were two cylindrical single crystals of lead, about 1.25 cm in diameter, 2.2 cm and 0.63 cm long. The first one was used for measurements with longitudinal waves and the second for shear waves. Unfortunately, some recrystallization could not be avoided during cutting and surfacing of the originally perfect crystal specimens. The absolute values of the measured attenuations must, therefore, be too high, due to losses at grain boundaries, etc. In further experiments, the technique of preparing the specimens will be improved.

The measurements were made by an ultrasonic pulse technique with apparatus similar to one described by McSkimin.[2] With the samples used, the apparatus was sensitive enough to detect changes in attenuation in the order of 10^{-3} neper cm and changes in velocity in the order of 1 part in 10^5. A variable longitudinal magnetic field could be applied in order to keep the specimens normal-conducting below the transition temperature, T_c.

The results obtained with longitudinal and shear waves were very similar.

No change could be observed in sound velocity within the whole frequency range. This means that any change due to the superconducting transition must be of the order of 1 part in 10^5 or less. This is in agreement with what one would expect from thermodynamical reasons.[3]

The sound attenuation showed a very pronounced decrease in the superconducting state, the amount of which increased with increasing frequency. Figure 1 gives a typical result obtained with longitudinal waves at a frequency of 26.64 Mc/sec. When the specimen was cooled and kept normal conducting by a magnetic field, the attenuation curve, after passing through a flat minimum at about 9.8°K increased continuously, with no discontinuity at T_c, till about 4°K and then flattened out between 4°K and 1.5°K. When the specimen was cooled without application of a magnetic field, the attenuation dropped down very sharply at the transition temperature and seemed to remain constant between about 5°K and 1.5°K.

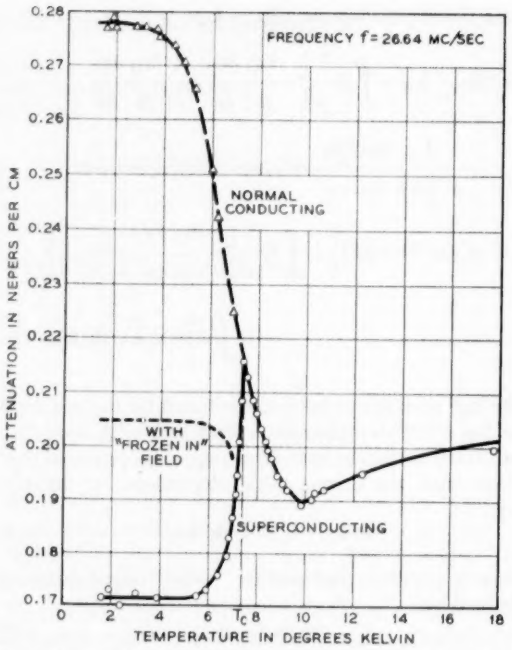

FIG. 1. Attenuation of longitudinal waves in superconducting lead as function of temperature.

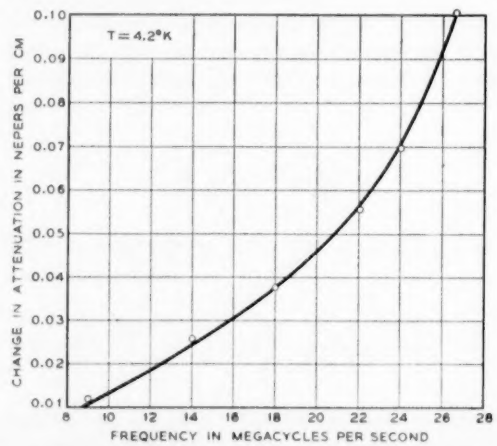

FIG. 2. Change in attenuation between normal and superconducting state for longitudinal waves as function of frequency.

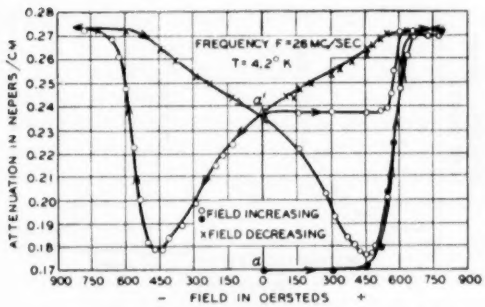

FIG. 3. Effect of "frozen in" field on attenuation in superconducting lead.

Figure 2 shows how the difference $\Delta\alpha$ in attenuation between the normal and superconducting states at 4.2°K changes with frequency, approximately a square law curve within the used frequency range. The ratio $\Delta\alpha/\alpha_n$ (α_n = total loss in normal conducting state at 4.2°K) changed from about 0.15 at 9 Mc/sec to 0.38 at 26.64 Mc/sec. These latter values must be regarded as minimum values since, for the reasons mentioned above, the actual values of α_n are probably smaller. For the same reason it has not yet been possible to make a statement about the actual value of the residual attenuation in the superconducting state which might be of great interest.

When superconducivity was destroyed by the magnetic field H and then re-established by turning off the field, the attenuation did not drop down to the original α, but (depending on the shape of the specimen and the speed of the field change) only to a 30–60 percent higher value α' (marked in Fig. 1 by the dotted line), indicating that a great part of the magnetic flux remained "frozen in." The attenuation as a function of H followed the curve given in Fig. 3. The form of this "magnetization curve" and the large hysteresis have not yet been fully explained and will be the subject of special investigation.

The curves in Fig. 1 look somewhat similar to the well known curves of thermal conduction as a function of temperature. This could suggest that a great part of the acoustic loss at low temperature might be due to loss from heat conduction, but since one gets the same effect with shear waves, this possibility seems to be ruled out.

Further experiments with better crystal samples, other elements, compounds, normal conducting materials, and a greater frequency range are in progress. The reported results might be a further support for the conception that superconductivity is mainly due to interactions between electrons and lattice vibrations, but it seems reasonable not to begin theoretical speculations about the observed effect before further experiments are carried out. Besides its theoretical interest, the effect might provide a very useful means for the study of superconducting properties, as, for example, observations in the intermediate state, etc.

The author wishes to express his gratitude to Mr. H. J. McSkimin for lending him his ultrasonic equipment and to Mr. T. B. Bateman for valuable help with the experiments.

[1] H. E. Bömmel and J. L. Olsen, Phys. Rev. **91**, 1017 (1953).
[2] H. J. McSkimin, J. Appl. Phys. **24**, 988 (1953).
[3] D. Schoenberg, *Superconductivity* (Cambridge University Press, Cambridge, 1952), p. 74.

New Minority Carrier Phenomenon in Germanium

STEPHEN J. ANGELLO AND THEODORE E. EBERT
Materials Engineering Department, Westinghouse Electric Corporation, East Pittsburgh, Pennsylvania
(Received June 29, 1954)

IT is now well known that minority carriers can be injected into germanium by means of a point contact or P-N junction biased in the direction of easy flow of current carriers. An experiment reported by Haynes and Shockley[1] is considered a classical illustration of this phenomenon.

We have discovered that a P-N junction of indium alloyed to germanium and biased in the high-resistance direction can withdraw minority carriers from a bar of N-type germanium, and that the deficit can be propagated down the bar by means of an electrical field. The phenomenon is the exact inverse of the Haynes-Shockley effect and consequently we have named the withdrawal of minority carriers "minority carrier egression."

In Fig. 1, a bar of N-type germanium is provided with two indium alloyed P-N junctions labeled emitter and collector. In the Haynes-Shockley experiment, the emitter is biased positively by the proper position of switch S_2. The synchroverter switch S_1 opens and closes the emitter circuit with a repetition rate of 1000 cps and

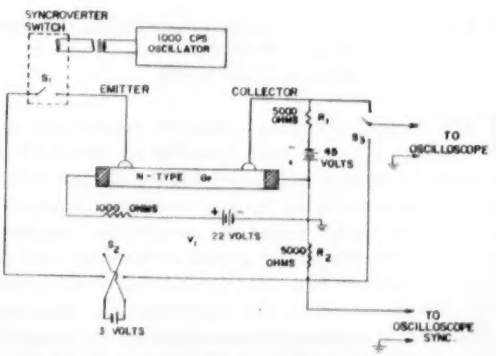

FIG. 1. Circuit used to compare minority carrier injection and egression.

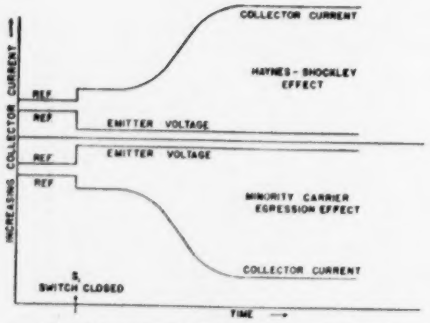

FIG. 2. Haynes-Shockley effect compared with minority carrier egression.

an oscilloscope sweep is synchronized with S_1 to give a repetitive presentation. The collector is biased negatively to attract positive holes. Positive holes in excess of the equilibrium density cause an increase in collector current which appears as an increased voltage across resistor R_1. This voltage is presented on the oscilloscope. A sweeping voltage V_1 causes positive holes to go from the emitter to the collector.

In Fig. 2, the upper trace is the Haynes-Shockley effect compared with the emitter voltage appearing across R_2 to show the switching instant. The lower trace appears when switch S_2 is reversed. In this case, the leakage current of the collector is decreased after a time delay for propagation of the effect and remains depressed as long as the emitter bias remains. It is to be noted that the sweeping voltage V_1 has the same polarity in both cases.

The phenomenon of electron egression has implications in the physical mechanism of the operation of transistor devices.

[1] J. R. Haynes and W. Shockley, Phys. Rev. **75**, 691 (1949).

Effective Masses of Electrons in Silicon*

R. N. DEXTER AND BENJAMIN LAX, *Lincoln Laboratory, Massachusetts Institute of Technology, Cambridge, Massachusetts*

AND

A. F. KIP AND G. DRESSELHAUS, *Department of Physics, University of California, Berkeley, California*

(Received August 9, 1954)

THE original cyclotron resonance experiments on germanium were made possible by virtue of rf ionization of carriers by the microwave electric field.[1] This technique could not be used on silicon because of the relatively large trapping energies for carriers. Recent experiments by the groups at Berkeley and at Lincoln Laboratory have used optical excitation of carriers.[2] We report here the independently obtained results of the two laboratories on the effective mass m^* of electrons in silicon. The principal values of m^* agree within the experimental error. The experiments were

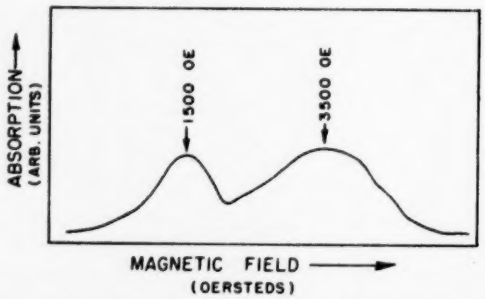

FIG. 1. Cyclotron resonance absorption of electrons in silicon as a function of magnetic field H when H is parallel to the [001] direction.

carried out on single crystals at liquid helium temperature. Microwave frequencies were in the 23-kMc/sec region.

The resonance peaks were observed when the magnetic field was parallel to the [001] and [110] directions and one peak was observed when the magnetic field was along the [111] axis. This suggests that the constant energy surfaces at the bottom of the conduction band in silicon can be represented by six ellipsoids of revolution along the cubic axes in the Brillouin zone, in agreement with the conclusions drawn from magnetoresistance[3] and piezoresistance[4] experiments.

The principal values of the mass tensor are conveniently obtained from the peak positions when the magnetic field is along the [001] direction. An absorption trace for this orientation is shown in Fig. 1; the peaks correspond to effective masses m_2 and $(m_1m_2)^{\frac{1}{2}}$. These data indicate a transverse mass $m_2=0.19\,m_0$ and a longitudinal mass $m_1=0.98\,m_0$, where m_0 is the free electron mass.[5] The average effective mass for these values is $\bar{m}^*=3\,m_1m_2/(2\,m_1+m_2)=0.26\,m_0$. The ratio $m_1/m_2=5.2$ is consistent with the value estimated from the magnetoresistance effect.[3] By using these values of m_1 and m_2, following Shockley,[6] two theoretical curves for m^*/m_0 as a function of θ were computed, where θ is

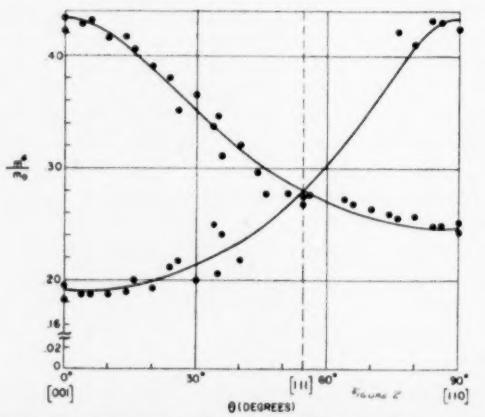

FIG. 2. Effective mass of electrons in silicon as a function of magnetic field orientation in the (1̄10) plane.

the angle between the [001] direction and the magnetic field in the (1̄10) plane. These curves are shown in Fig. 2 in comparison with experimental points obtained with several samples.

The half-widths of the resonance lines were of the order of 1000 oersteds. From this fact it was estimated that the mean collision time was about 2×10^{-11} sec. This is approximately $\frac{1}{3}$ the collision time found for pure Ge at 4°K.

The authors would like to express their appreciation for the samples of silicon kindly provided by General Electric Research Laboratories and Bell Telephone Laboratories. We would also like to thank Professor C. Kittel and Dr. H. J. Zeiger for several helpful discussions.

* The M.I.T. research reported in this document was supported jointly by the Department of the Army, the Department of the Navy, and the Department of the Air Force. The University of California research has been supported in part by the U. S. Office of Naval Research and the U. S. Signal Corps.

[1] Dresselhaus, Kip, and Kittel, Phys. Rev. **92**, 827 (1953); Lax, Zeiger, Dexter, and Rosenblum, Phys. Rev. **93**, 1418 (1954).
[2] Dexter, Zeiger, and Lax, Phys. Rev. **95**, 557 (1954).
[3] G. L. Pearson and C. Herring, Physica (to be published), paper presented at the International Conference on Semiconductors, Amsterdam, Netherlands, June 30, 1954.
[4] C. S. Smith, Phys. Rev. **94**, 42 (1954).
[5] The estimated error in the mass values is about ±5 percent.
[6] W. Shockley, Phys. Rev. **90**, 491 (1953).

Effective Masses of Holes in Silicon*

R. N. DEXTER, *University of Wisconsin, Madison, Wisconsin, and Lincoln Laboratory, Massachusetts Institute of Technology, Cambridge, Massachusetts*

AND

BENJAMIN LAX, *Lincoln Laboratory, Massachusetts Institute of Technology, Cambridge, Massachusetts*

(Received August 9, 1954)

CYCLOTRON resonance experiments have been carried out on p-type silicon at 23 kMc/sec and 4°K. Carriers were excited by infrared light as described for germanium.[1] The beam from the light source was chopped at 900 cps, with a resulting amplitude modulation of the absorption signal. High sensitivity was achieved by a phase-sensitive detection method.[2] The reference signal for the detector was obtained from a phototube in the chopped beam.

Two resonance peaks were observed corresponding to effective masses m_1^* and m_2^*. The effective masses measured in the principal directions are summarized in Table I; m_0 is the free electron mass. From these data, by means of simple statistics, the approximate average effective mass of holes was calculated to be $0.39m_0$.

The observations are consistent with the model used for germanium,[1,3] in which the top of the valence band occurs at $k=0$ and in which the constant energy surfaces in the Brillouin zone can be represented by two sets of warped surfaces centered about the origin. For these

TABLE I.

Magnetic field parallel to:	[001]	[111]	[110]
m_1^*/m_0	0.171	0.160	0.163
m_2^*/m_0	0.46	0.56	0.53

surfaces, the energy E is given as a function of the wave vector $\mathbf{k}$ by

$$E=(-\hbar^2/2m_0)\{ak^2\pm[b^2k^4-c(k_x^4+k_y^4+k_z^4)]^{\frac{1}{2}}\}, \quad (1)$$

where a, b, and c are constants. The approximate theoretical calculation of the resonance frequency and the effective mass at resonance was carried out as previously described[1,4] but a more exact expansion of the radical was used. The result is

$$1/m^*=(1/m_0)[A_\pm+B_\pm(1-3\cos^2\theta)^2], \quad (2)$$

where $A_\pm=a\pm b'\pm(c/12b')$, $B_\pm=\mp c/32b'$, $b'=(b^2-\frac{2}{3}c)^{\frac{1}{2}}$, and the plus and minus signs refer to the effective masses m_1^* and m_2^*, respectively. The constants can be determined from the values for m_1^* at $\theta=0$ and for m_2^* at $\theta=0°$ and 55°. The result for silicon is: $a=4.0$, $b^2=8.1$, and $c=6.5$. By using these values in Eq. (2), a theoretical curve was calculated for m_2^* and plotted in Fig. 1.

According to the perturbation theory[3] which describes the valence band structure of germanium around $\mathbf{k}=0$, three degenerate bands are split by spin-orbit interaction into the two bands described by Eq. (1) and a lower band for which the energy is

$$E_3=-E_0-(\hbar^2ak^2/2m_0)=-E_0-(\hbar^2k^2/2m_3^*), \quad (3)$$

where E_0 is the splitting at $\mathbf{k}=0$.[5,6] If this expression is correct for silicon, $m_3^*=0.25m_0$. We have not been able to detect holes in this normally filled band.

The authors would like to thank Mrs. Laura Roth and Dr. H. J. Zeiger for helpful suggestions and the

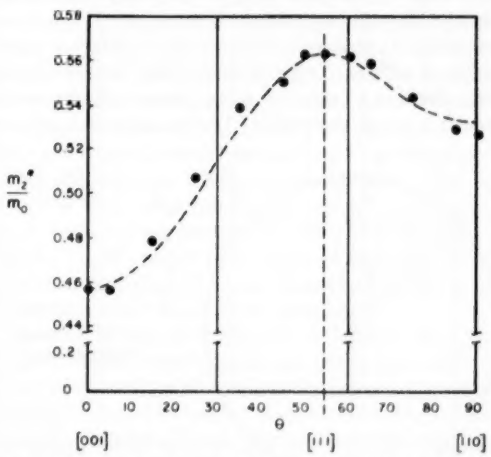

FIG. 1. The effective mass m_2^* of the heavy holes in silicon is plotted as a function of θ, the angle between the [001] direction and the magnetic field in the (110) plane. The points are experimental, and the curve is theoretical.

General Electric Research Laboratories and the Bell Telephone Laboratories for providing samples of silicon.

* The research reported in this document was supported jointly by the Department of the Army, the Department of the Navy, and the Department of the Air Force.

[1] Dexter, Zeiger, and Lax, Phys. Rev. **95**, 557 (1954).

[2] A similar technique was developed by A. F. Kip, Physica (to be published), paper presented at the International Semiconductor Conference, Amsterdam, Netherlands, June, 1954.

[3] Dresselhaus, Kip, and Kittel, Phys. Rev. **95**, 568 (1954).

[4] Lax, Zeiger, and Dexter, Physica (to be published), paper presented at the International Semiconductor Conference, Amsterdam, Netherlands, June, 1954.

[5] F. Herman, Physica (to be published), paper presented at the International Semiconductor Conference, Amsterdam, Netherlands, June, 1954.

[6] C. Kittel, Physica (to be published), paper presented at the International Semiconductor Conference, Amsterdam, Netherlands, June, 1954.

Finley-Freundlich Red-Shift Hypothesis

H. L. Helfer*

Department of Terrestrial Magnetism, Carnegie Institution of Washington, Washington, D. C.

(Received August 9, 1954)

In view of the possible serious physical implications[1,2] of the Finley-Freundlich hypothesis[3] that light, passing through an enclosure of energy density $u=bT^4$ and dimension h, suffers a red shift $\Delta\lambda/\lambda=AT^4h$ ($A=2\times10^{-29}$ cgs units), it appears desirable to state here two astronomical arguments preventing acceptance of this proposal unmodified.

Consider an eclipsing binary star system ($i=90°$) in which the relative orbit is circular with radius a. Take $u_i=b_iT_i^4$ as the energy density at the surface of star i, the radius of which is R_i. The energy density in space at a point at distance h from star i is $u=u_iR_i^2/h^2$. If θ is the angle introduced in Fig. 1, the integrated energy density along the line of sight towards star 2, due to its companion's presence,[4] is $U_2=(u_1R_1^2/a)[(\pi-\theta)/\sin\theta]$, outside of eclipse. A change in the total energy density along the line of sight of many times $u_1R_1^2/a$, would occur in a single revolution. The quantity $u_1R_1^2/a$ corresponds to a predicted Freundlich shift of amount $\Delta V=cAT_1^4R_1^2/a$.

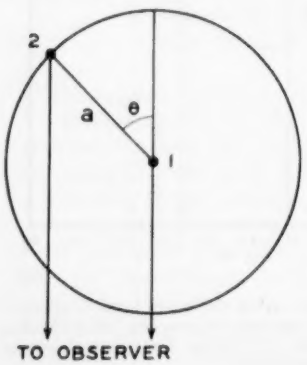

Fig. 1. A typical binary system.

Table I contains the predicted ΔV, together with other quantities of interest for five systems selected from the *Fourth Lick Catalog of Spectroscopic Binaries*,[5] Although there exists a slight uncertainty in spectral types and consequently in temperature, the predicted effect is certainly orders of magnitude too large and one can afford to be slightly uncritical of the observational data. Use of more recent spectral classifications[6] decreases ΔV by only 50 percent for the fainter star in *TX* Herculis, and not at all for the fainter star in *Z* Vulpeculae. The data for the system *Y* Cygni are particularly reliable.

It may be maintained that the hypothesis holds only in the presence of matter, the above argument then not being conclusive since the presence of matter in the orbital plane has not been demonstrated.

The unusual system of ϵ Aurigae[7] provides a natural test of this further possibility. While objections[8,9] have been raised to parts of the interpretation of this system, it still appears quite probable that during the eclipse, the light of the *cF* star passes *through* the outer part of its companion *I* star. During eclipse ionized lines arising from the outer parts of the *I* star indicate the presence of gaseous material. At eclipse, we therefore have the ideal situation of a long path length though matter in the presence of a radiation field.

Table I. Data for five systems. Column 1 gives the Fourth Lick Catalog number, Column 2 the star name, Column 3 the spectral type (*HD* Rev.) of each component (in all cases listed the spectral type being the same for both components), Column 4 the effective temperature corresponding to the spectral type, Column 5 the mean radius of the two components, the solar radius being taken as unity, Column 6 the semimajor axis of the relative orbit using the same unit of length, Column 7 the percentage contribution of each star to the total luminosity of the system, Column 8 the semiamplitudes of the two radial velocity curves, and Column 9 the predicted ΔV. In all cases the inclination of the orbital plane exceeds 86.5°.

1	2	3	4	5	6	7	8	9
No.	Star name	Type	Eff. temp. °K	Mean rad.	Semi-major axis	Lumin. contrib. percent	Semi-amplitudes km/sec	ΔV km/sec
78	*TT* Aur.	*B3*	18 000	4.3	11.7	68; 32	197; 246	70 000
115	*WW* Aur.	*A7*	8 000	2.1	12.5	55; 45	116; 135	610
251	*TX* Her.	*A2*	10 000	1.6	10.7	64; 36	121; 140	1 000
296	*Z* Vul.	*B3*	18 000	4.3	15.1	75; 25	96; 214	54 000
322	*Y* Cyg.	*O9*	25 000	5.9	28.4	50; 50	245; 241	200 000

If one uses the Yerkes model,[7] the maximum dip of the *cF* star below the *I* star's edge is 2.4×10^{13} cm and the radius of the *I* star is 2×10^{14} cm. If the *I* star was perfectly spherical, the *F* star's light would travel along a chord of the *I* star, 2×10^{14} cm long. If one uses $T_I=1200°$K, the predicted ΔV is 2400 km/sec. Judging from the observations, this is at least 200 times too large. If the path length is chosen so as to be equal to the effective length over which optical absorption occurs,[7] ΔV is decreased by a factor of ten. It is to be noted that the temperature used for this calculation is

quite conservative, the considerable ionizing radiation emanating from the *cF* star being ignored.

It is to be noted that ζ Aurigae systems such as the prototype and *VV* Cephei provide means for similar tests, and that Struve[10] has already pointed out the possibility of interpreting the observational bases of this theory by more conventional mechanisms.

* Carnegie Institution Fellow in Radio Astronomy, 1953–1954.
[1] M. Born, Proc. Phys. Soc. (London) **A67**, 193 (1954).
[2] D. ter Haar, Phil. Mag. **45**, 320 (1954).
[3] E. F. Freundlich, Proc. Phys. Soc. (London) **A67**, 192 (1954); Phil. Mag. **45**, 303 (1954).
[4] The contribution to the total energy density along the line of sight made by the star itself has been omitted. Its inclusion would imply a shift of the solar lines from their laboratory wavelength of 200 km/sec.
[5] J. H. Moore, Lick Observatory Bul. **18**, No. 483 (1935).
[6] F. B. Wood, Univ. Penn. Astron. Pub. **8**, 1 (1953).
[7] Kuiper, Struve, and Stromgren, Astrophys. J. **86**, 570 (1937).
[8] S. Gaposchkin, Publs. Astron. Soc. Pac. **66**, 112 (1954).
[9] Z. Kopal, Observatory **74**, 14 (1954).
[10] O. Struve, Sky and Telescope **13**, 225 (1954).

K Band in Additively Colored KCl

H. W. Etzel and F. E. Geiger, Jr.
United States Naval Research Laboratory, Washington, D. C.
(Received August 9, 1954)

THE *F*-band absorption in alkali halides is accepted to be the result of a $1s$-$2p$ transition of an electron trapped at a negative ion vacancy in the lattice. Mott and Gurney[1] first suggested that the shoulder on the high-energy side of the *F* band (the *K* band[2]) was associated with $1s$-np transitions and transitions to the ionization continuum. Dexter[3] has calculated the absorption cross section per electron at the *F* band, and at its presumed series limit using hydrogen like wave functions. No evidence has been presented definitely to contradict the assumption that the *K* band is an integral part of the *F* band, and for this reason the most recent review article on color centers[4] maintains this point of view. The data presented here indicate that the ratio of the absorption of the *F* and *K* bands is not a constant. Therefore the two bands are not a result of transitions from the ground state of the same center.

The KCl crystals used in the room temperature work were high purity crystals grown by the Kyropoulos technique. The crystals were additively colored at 600°C in potassium vapor. Next, thin crystals which were cleaved for absorption measurements (made in the Beckman Model DR Spectrophotometer) were wrapped in a light tight aluminum foil and heated to 500°C. After allowing sufficient time for the dispersal of any aggregate or colloidal bands the crystals were quenched. Curve *a* of Fig. 1 shows the absorption obtained without exposing the crystal to light. Curves *b*, *c*, *d*, and *e* were obtained after subsequent exposures of the same crystal to light of wavelengths greater than

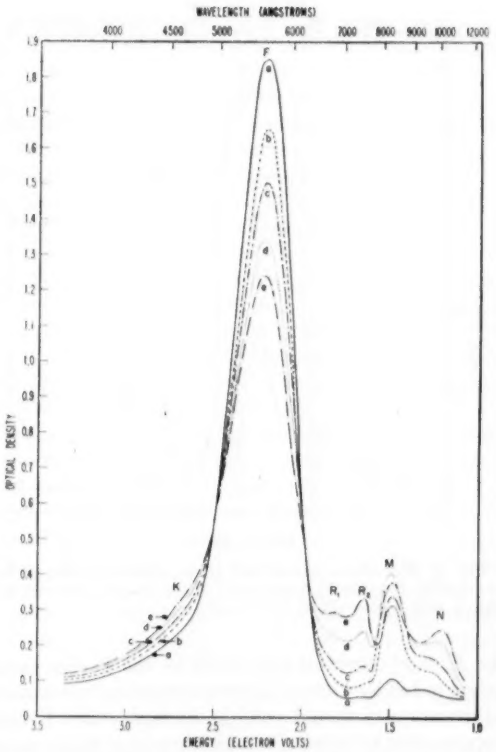

FIG. 1. A sequence of absorption measurements at room temperature of additively colored KCl ($\sim 4\times10^{17}$/cc). Irradiation made with a tungsten lamp through a Corning No. 3482 filter. Curve (*a*), no optical bleach; (*b*), illuminated 20 seconds; (*c*), 40 seconds; (*d*), 100 seconds; (*e*), 220 seconds.

5000A. The crystals used for the liquid nitrogen data were Harshaw crystals colored at 477°C for 28 hours, quenched immediately to room temperature and measured in a Cary automatic recording spectrophotometer. Curve *a* of Fig. 2 shows the absorption of the crystal measured at −160°C prior to bleaching. In curve *b* the same crystal after irradiation into the *F* band at +50°C, is measured again at liquid nitrogen temperature. The Cary spectrophotometer was used as a monochromator with a slit width of 1.5 mm or about 250A. Both sets of curves show after irradiation a partial bleaching of the *F* band and an unexpected growth of the *K* band. The R_1, R_2, *M*, and *N* bands grow as expected at room temperature, but at 50°C the R_1 and R_2 bands appear to decrease while the *M* band increases.

The data presented here do not yet allow a description of the *K* center, but indicate that the center is not due to a transition of an electron in the ground state of the *F* center to excited states or to the conduction band. It should be pointed out that the data of Molnar[5] indicate that the *K* band grows as the *F* band is bleached, but apparently no significance was attached to the increase in absorption in the *K* band region. It is unlikely that

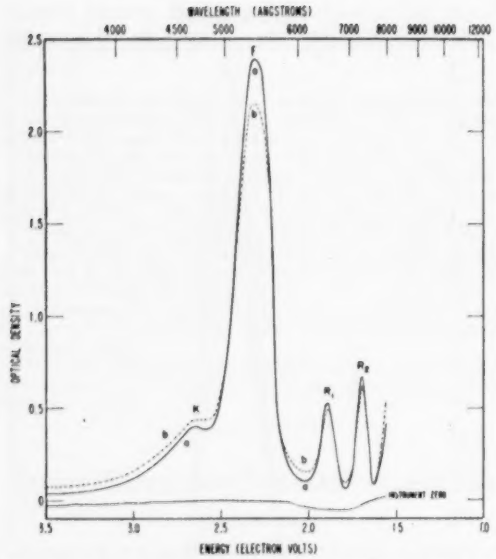

FIG. 2. Absorption measurements on additively colored KCl at −160°C. Curve (*a*), no optical bleach; Curve (*b*), after 2½-hour bleach with *F* light (5600 A) at +50°C.

the *K* band observed here could be the *V*-type center as suggested by Duerig[6] since the crystals were colored additively and should contain no holes. The *K* band appears then to be some combination of an electron and negative ion vacancy in such a way as not to form a normal *F* center. Further work is planned to determine the nature of the center.

The additive coloration, by R. J. Ginther, of the crystals used in the room temperature measurements is deeply appreciated.

[1] N. F. Mott and R. W. Gurney, *Electronic Processes in Ionic Crystals* (Oxford University Press, London, 1940), p. 114.
[2] F. G. Kleinschrod, Ann. Physik **27**, 97 (1936).
[3] D. L. Dexter, Phys. Rev. **83**, 435 (1951).
[4] F. Seitz, Revs. Modern Phys. **26**, 1 (1954).
[5] J. P. Molnar, thesis, Massachusetts Institute of Technology, 1940 (unpublished).
[6] W. H. Duerig, Phys. Rev. **94**, 65 (1954).

Injection Breakdown in Iron-Doped Germanium Diodes

W. W. TYLER

General Electric Research Laboratory, Schenectady, New York

(Received August 5, 1954)

IRON dissolved in germanium introduces two deep energy levels in the forbidden band. It is possible to produce both *n*- and *p*-type samples of Fe-doped Ge which exhibit high resistivity when cooled to liquid nitrogen temperature. Thermal ionization energies characteristic of *n* and *p* samples are ~0.27 ev and ~0.34 ev, respectively. Studies of the recovery of photoconductivity after exposure to light indicate that *n*-type samples are much more photosensitive and slower in recovery than are *p*-type samples, suggesting that states introduced by Fe act as hole traps in *n*-type crystals.[1] The purpose of this letter is to describe briefly an experiment with diodes which tends to confirm the presence of hole traps in high-resistivity *n*-type Fe-doped Ge.

Diodes were formed by fusing an indium contact on one face of an ~1/8-in. cube of germanium. The "ohmic" base contact on the opposite face was of fused tin. Sixty-cycle ac voltage was applied to the diodes and current-voltage characteristics were observed on a calibrated oscilloscope. At 300°K the diodes show normal behavior with high reverse saturation currents due to the low carrier lifetime (~5 μsec) in the Fe-doped crystals. When cooled to liquid nitrogen temperature (77°K), in the dark, a typical diode behaves like a high resistance for small voltages of either polarity. (The equilibrium value of resistivity for the Fe-doped Ge at this temperature is ~10^{12} ohm-cm.) On increasing the applied ac voltage (to ~15 volts peak) injection currents of several microamperes are seen on the forward cycle. At sufficiently high voltage (~50 volts peak) a breakdown process takes place after which the effective resistivity of the Ge drops to about 100 ohm-cm. This breakdown condition is maintained until the applied voltage is reduced to less than several volts. Light ($h\nu > 0.7$ ev) falling on the diode greatly reduces the voltage necessary to initiate the breakdown condition.

Figure 1 shows the current voltage characteristic of a typical diode before breakdown. The diode is immersed in liquid nitrogen. Pre-breakdown injection current of about 1 microampere is noticeable on the forward cycle. Breakdown is initiated by a short light pulse from a neon lamp. Figures 2 and 3 show current-

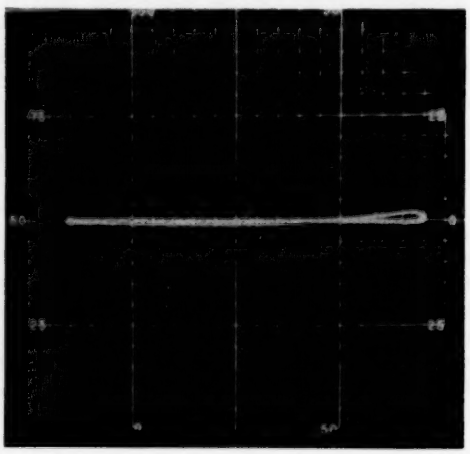

FIG. 1. Current-voltage characteristic before breakdown. Horizontal scale calibration is 2 volts per small division. Vertical scale calibration is 2 microamperes per small division.

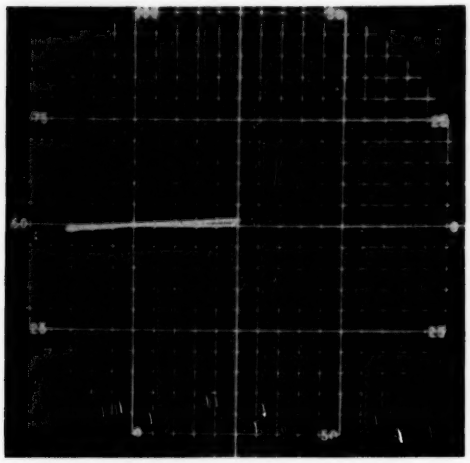

FIG. 2. Current-voltage characteristic after breakdown. Scale calibration is the same as in Fig. 1.

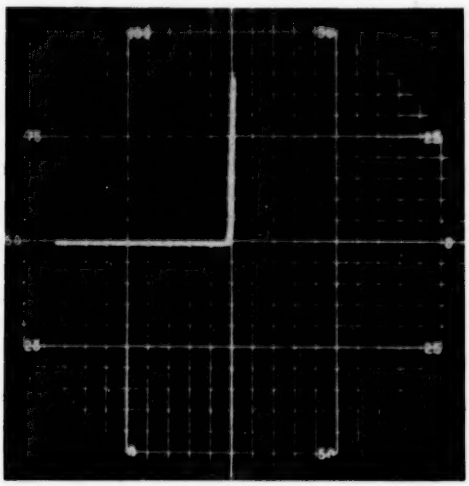

FIG. 3. The same characteristic shown in Fig. 2 except that the vertical scale calibration has been changed to 2 milliamperes per small division.

voltage characteristics after breakdown. In Fig. 3 current sensitivity has been decreased by a factor of 10^3. The peak forward current of 15 milliamperes is limited by external resistance. A thermocouple fused to the diode indicates no detectable ($<0.05°K$) increase in temperature after many minutes of operation under these conditions. The breakdown may be extinguished by decreasing the series resistance, permitting sufficiently high forward currents to heat the Ge to $\sim 100°K$.

The process described has been termed injection breakdown. Although the kinetics of the voltage-induced breakdown are not quantitatively understood, the steady-state breakdown condition may be explained by assuming high, nonequilibrium conduction in the Ge due to mobile electrons which neutralize trapped holes, with injected holes continuously being retrapped, replacing evaporation or recombination losses. On sixty-cycle operation, a sufficient number of nonequilibrium carriers remain after the reverse cycle so that applied forward voltage again localizes at the junction and injection saturates the traps during the first part of the forward cycle (assuming sufficient current density). Because of this reloading process, a small discontinuity is always observed in the current voltage characteristic during the first part of the forward cycle. This is barely discernible in Fig. 3 as a change in slope near the origin. Heating the Ge to $\sim 100°K$ increases the rate of hole evaporation sufficiently that it is difficult to maintain the breakdown condition.

Two observations of Newman support the model proposed for the steady-state operation of the breakdown diode. The infrared absorption of injected carriers in the breakdown diode does not show the structure characteristic of hole absorption which is found in most normal diodes.[2] With the applied voltage just greater than the minimum sustaining voltage, it is possible to extinguish the breakdown by irradiation of the diode with monochromatic light in the wavelength interval (~ 0.35 to 0.7 ev) which had previously been found effective in quenching intrinsic photoconductivity in n-type Fe-doped crystals.[3]

[1] Tyler, Woodbury, and Newman, Phys. Rev. **94**, 1419 (1954). The details of this work are being prepared for publication.
[2] R. Newman, Phys. Rev. (to be published).
[3] R. Newman and W. W. Tyler, Phys. Rev. (to be published).

Effect of Dislocations on the Optical Absorption Edge in Nonmetals*†

R. M. BLAKNEY AND D. L. DEXTER
Institute of Optics, University of Rochester, Rochester, New York
(Received August 16, 1954)

THE absorption spectra of many nonmetals exhibit a long-wavelength tail which has been attributed to lattice disorder.[1] Seitz[2] discussed the absorption spectra of the silver halides in the near ultraviolet and concluded on the basis of the magnitude of the radiation matrix element for a crystal containing edge type dislocations, that this type of lattice disorder can account for the long-wavelength tail observed.[3] This letter summarizes the results of calculations on the order of magnitude of the absorption coefficient to be expected in a crystal containing edge-type dislocations.

There are three ways in which dislocations can modify the fundamental absorption edge: (1) Optical (i.e., momentum) selection rules are relaxed by the deviation from periodicity. (2) Local density variations in the neighborhood of the dislocations change the local width of the forbidden gap, permitting lower-energy allowed

transitions to occur between the valence and conduction bands. (3) Various kinds of charged debris are created by and associated with the dislocations; as in the case of the α center, some of these imperfections would be effective in lowering the energy of the transition of the neighboring ions.

The absorption coefficient on the long-wavelength side of the fundamental absorption edge was calculated according to mechanism (1) for a crystal in which the energy contours in k space for the valence band are those for a p band, while those for the conduction band are for an s band. The calculation involved a summation over all k states in the two bands which could be evaluated only by means of simplifying assumptions which restrict the validity of the results to the region near the absorption edge. The length of the tail (measured from the absorption edge toward lower energies) cannot exceed the width of that branch of the valence band which bends upward.

For a dislocation density of 10^{12} lines per cm^2, a crystal with a valence band two volts wide, an energy gap of six volts, and with 0.4 taken to be the ratio of the effective mass of an electron in the conduction band to its mass in the valence band, an absorption coefficient of 20 cm^{-1} is calculated at 1 ev from the edge. In a crystal with a valence band one volt wide, an energy gap of nine volts, and 0.2 for the effective mass ratio, an absorption coefficient of 20 cm^{-1} is reached only 0.2 ev from the edge. The displaced oscillator strength per dislocation line intersection is about 0.2 in both cases. An alternative mechanism, considered by Bardeen and co-workers,[4] for obtaining nonvertical, or forbidden electronic transitions seems much more effective than that treated here for crystals of normal lattice disorder. (In the former mechanism, the transition occurs by the simultaneous emission of absorption of a phonon in order to conserve momentum.)

The shift in the absorption edge due to mechanism (2) was estimated by adopting the Heitler-London point of view and using deformation potential theory[5] to calculate the change in the absorption edge per atom as a function of the local density. This treatment shows that most of the absorption on the long-wavlength side of the edge occurs in the immediate vicinity of the edge and does not extend beyond about 0.5 ev beyond the edge. (This figure was obtained for a maximum dilatation of 0.1 and a reasonable value of 5 ev per unit dilatation for the deformation potential constant.)

It was concluded that neither mechanism (1) nor (2) can account for the long-wavelength tail extending into the visible as observed in the silver halides. However, in a cold-worked crystal, the vacancies, incipient vacancies, clusters, and other charged products of the moving dislocations represent regions of the crystal particularly effective in modifying the fundamental absorption edge. Measurements on the effects of cold working and annealing on good single crystals would be helpful in indicating the importance of mechanism (3).

* This paper was presented at the Bristol Conference on Defects in Crystalline Solids in July, 1954, and the details of these calculations will appear in the published proceedings of this meeting.

† Research supported in part by funds from the U. S. Air Force under a contract monitored by Headquarters, Air Research and Development Command, Baltimore, Maryland.

[1] N. F. Mott and R. W. Gurney, *Electronic Processes in Ionic Crystals* (Oxford University Press, London, 1948), p. 94.
[2] F. Seitz, Revs. Modern Phys. **23**, 328 (1951).
[3] H. Fesefeldt, Z. Physik **64**, 741 (1930); H. Fesefeldt and Z. Gyulai, Göttingen Nachr. **1929**, 226.
[4] Hall, Bardeen, and Blatt, Phys. Rev. **95**, 559 (1954).
[5] J. Bardeen and W. Shockley, Phys. Rev. **80**, 72 (1950).

Structure of the Intermediate State of Superconductors*

B. Serin
Rutgers University, New Brunswick, New Jersey
(Received August 6, 1954)

WE have qualitatively verified the observations of Meshkosky and Shalnikov[1,2] on the discontinuous structure of the intermediate state of superconductors. We used lead rather than tin for the sample, and employed a different technique for observing the normal and superconductive regions.

The discontinuous magnetic field changes at the normal-superconductive interfaces were detected by using commercially available magnetic recording tape.[3] After the tape was magnetized at low temperatures, the details of the magnetization were revealed by making a magnetic powder pattern[4] on the tape after it had been warmed to room temperature. A similar technique was tried without success by Shalnikov and Meshkovsky,[1] who finally used the changes in the electrical resistance of an extremely small bismuth wire to detect the discontinuous magnetic field changes.

The sample consisted of two polycrystalline lead hemispheres of 0.25-in. radius cast from Johnson-Matthey and Company lead. Each hemisphere was mounted in a Plexiglass holder, and the two holders were bolted together with the tape in between them so that flat sides of the hemispheres were pressed against the two surfaces of the magnetic tape. The tape is 0.002 in. thick. A small patch of tape was also placed in the bottom of one holder so that it pressed against the outside surface of the hemisphere in the neighborhood of the pole. A bismuth wire was mounted in one of the holders near the equator. Suitable leads were attached so that the electrical resistance of the wire could be measured, and the magnetic field at the surface of the sphere thereby determined.

The sample was cooled in liquid helium to about 1.4°K. A uniform magnetic field was then applied in a direction passing through the poles, and thus transverse to the long direction of the tape between the hemispheres. The field was increased slowly and the resistance of the bismuth wire measured. The initial penetration of the magnetic field into the sphere was

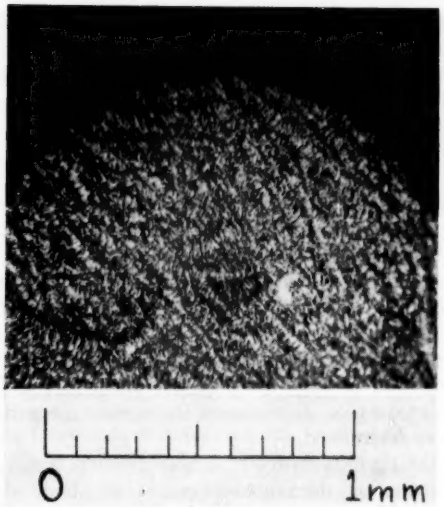

FIG. 1. Photomicrograph of powder pattern obtained on tape placed near the pole.

detected by the abrupt, large decrease in the slope of the resistance as a function of field. The field at which penetration occurs is $\frac{2}{3}$ of the threshold field value. The threshold field was thereby determined to be about 800 oersted. After initial penetration, the external field was further increased to about 0.8 of the threshold value, corresponding to a ratio of magnetic induction to critical field inside the sphere of about 0.4 The external field was then reduced to zero, and the apparatus warmed up.

Figure 1 is a photomicrograph of a powder pattern obtained on the tape placed at the pole on the outside of the hemisphere. The light areas are the magnetized regions where the iron powder has collected, and these correspond to the regions of normal phase in the sample. The pattern is complicated, but it is clear that the distances between the regions are about 0.05 mm. Similar patterns were obtained on the tape placed between the hemispheres, and qualitatively similar results were obtained with three different samples. The tape placed on the outside seems to become more strongly magnetized and thus exhibit clearer patterns, probably because the magnetic field at the outer surface has a component which lies in the tape as well as one transverse to it.

We hope that this extremely simple technique can be used to explore aspects of the intermediate state in which further investigations are needed.[5]

* This work has been supported by a joint program of the U. S. Office of Naval Research, the Rutgers University Research Council, and the Radio Corporation of America.

[1] A. Meshkovsky and A. Shalnikov, J. Phys. (U.S.S.R.) **11**, 1 (1947).

[2] For a review of the later work which is printed in Russian see D. Shoenberg, *Superconductivity* (Cambridge University Press, London, 1952), pp. 103–110.

[3] "Scotch" Brand Sound Recording Tape No. 111A, Minnesota Mining & Manufacturing Company, St. Paul, Minnesota.

[4] B. F. Murphy and H. K. Smith, Audio Engineering **33**, 12 (1949).

[5] *Note added in proof.*—Another technique, quite different from the one above, has been recently reported by Schawlow, Matthias, Lewis, and Devlin, Phys. Rev. **95**, 1344 (1954).

Magnetic Cloud Chamber Study of $V^{\pm}$ Events*

V. B. KIM, J. R. BURWELL, R. W. HUGGETT AND R. W. THOMPSON

Department of Physics, Indiana University, Bloomington, Indiana

(Received August 16, 1954)

THE object of this note is to give a preliminary report of the $V^{\pm}$ events observed to date with the rectangular magnet chamber.[1]

The transverse momentum p_y has been measured for 31 cases[2] with an average uncertainty of ± 5 percent.

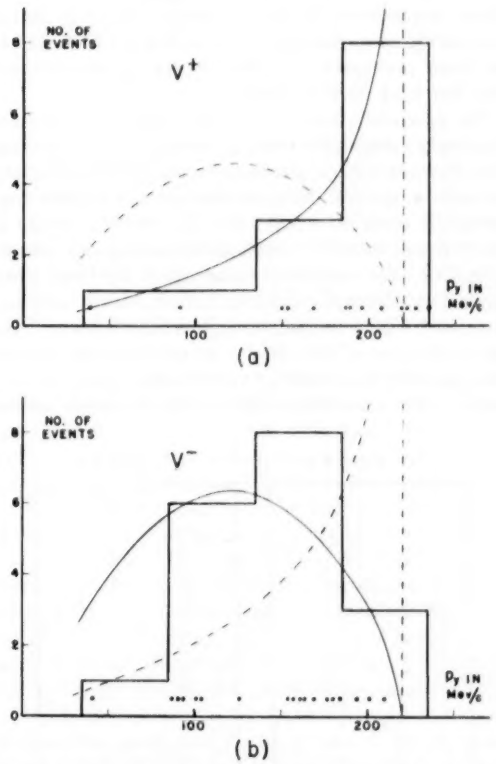

FIG. 1. The distributions of transverse momenta of $V^{\pm}$ events. The histograms give the number of events per 50-Mev/c interval. (a) is the distribution for V^+ (13 events) and (b) for V^- (18 events). The values of the individual p_y's are indicated by the dots. Events with $p_y \leq 35$ Mev/c are omitted in order not to include possible π–μ decays. The theoretical distributions for a two-body decay (with $p' = 220$ Mev/c) and for a three-body decay (with $p'_{max} = 220$ Mev/c) are shown by the solid line and by the dashed line in (a), and by the dashed line and by the solid line in (b). The average uncertainty in p_y is 5 percent and the errors are not folded into the theoretical distributions.

The distributions for V^+ (13 cases) and V^- (18 cases) are shown separately in Fig. 1. Although the statistics are limited, there is preliminary indication of a charge asymmetry. The distribution for V^+ is peaked near the highest observed values; for V^- the distribution appears to be broader and the center of gravity occurs at a lower value of p_y. Further indication for charge asymmetry is found in the distributions of decay points in the chamber shown in Fig. 2. The V^+ decays appear to be more or less uniformly distributed throughout the chamber, whereas the V^- decays appear to occur predominantly in the top half. Since the distributions of the longitudinal momentum of the secondary p_z are not much different for V^+ and V^- decays (the mean value of p_z is 575 Mev/c for V^+ and 732 Mev/c for V^-), this asymmetry in the distributions of decay points probably reflects a difference in lifetime. A detailed lifetime analysis will be reported in a later publication. Taken together, the two effects (difference in p_y distribution and in lifetime) provide reasonable evidence for a charge asymmetry in the $V^\pm$ events. Such a charge asymmetry in p_y distribution as well as in lifetime has not been previously observed in the magnetic cloud chamber work on $V^\pm$ events.[3-6]

The p_y distribution of V^+ events suggests, or at least is entirely compatible with, a two-body decay process with $p' \sim 220$ Mev/c, the momentum of the secondary in the c.m. system. This interpretation is further supported by three V^+ events (R-112,[7] R-390,[8] R-521) in which the primaries are well measurable and p' can be computed. The computed values of p' for these three events are 231 ± 15, 222 ± 6, 219 ± 8 Mev/c and are consistent with a unique value $p' = 222\pm5$ Mev/c (the weighted mean of the three values).[9] Thus the present data provides preliminary evidence for a long-lived K^+ particle with mass about 1000 m_e which decays into an L^+ meson and one neutral fragment of mass not greater than that of a π^0.

Gregory *et al.*[10] present evidence for a long-lived positive particle, $K_\mu{}^+ \rightarrow \mu^+ + \nu$, with a directly measured mass of $914\pm20 m_e$. In two cases, the ranges of the positive secondary are in the intervals (83.5–90.5) and (88–101) g/cm² of lead. These are consistent with a unique value of 90 g/cm² which corresponds to $p' = 220$ Mev/c for a muon. Hodson *et al.*[11] report a remarkable photograph which may represent $\theta^+ \rightarrow \pi^+ + (\pi^0 \rightarrow 4e)$ $\pm212\pm20$ Mev. Bridge *et al.*[12] report three S-particle secondaries with ranges in the intervals (100–140), (92–108), and (100–104) g/cm² of lead. These are consistent with a unique range of 102 g/cm² which corresponds to $p' = 236$ Mev/c for a muon and $p' = 266$ Mev/c for a pion. In this work the signs of the particles are not determined.

If the V^- data represent a homogeneous group, the p_y-distribution does not suggest a two-body decay process. This conclusion is confirmed by one event (R-156; $p_y = 87\pm2$ Mev/c) in which the primary is measurable and the computed value of p' is less than 140 Mev/c.

In another V^- event (R-423;[8] $p_y = 101\pm4$ Mev/c) the charged secondary is identified to be a π^- meson from π-μ decay. This event is entirely compatible with the suggested alternate decay mode of the τ meson, $\tau^\pm \rightarrow \pi^\pm + 2\pi^0$,[13] for which $p'_{\max} = 132$ Mev/c. However, there is difficulty in explaining the majority of V^- events with $p_y \leqslant 132$ Mev/c in this way since the observed decay points in the chamber suggest that the lifetime is much shorter than that of the τ (about 10^{-8} sec).[14] There is, in fact, a tendency for V^- events with low p_y to decay near the very top of the chamber, but the statistics are insufficient to regard this as more than the most preliminary sort of evidence for two groups.

We have not, as yet, observed an example of the cascade decay,[4,15] $Y^- \rightarrow \Lambda^0 + \pi^-$. In view of the lifetime of Λ^0 it is very unlikely that more than a few V^- events are decays of this type.

The highest p_y values observed so far by us are in the neighborhood of 220 Mev/c. A K particle with mass substantially greater than $1000 m_e$[16] would give p_y values substantially greater than 220 Mev/c,[17] providing the neutral fragments (or fragment) are light. The absence of any much higher p_y values indicates that at most very few of the present $V^\pm$ events can be attributed to such a decay.

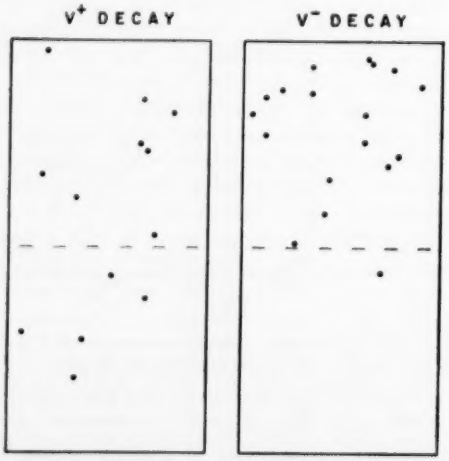

FIG. 2. The distributions of decay points in the chamber. The illuminated region of the chamber is 11 in. wide, 22 in. high and 5 in. deep. The decay points as seen from the central camera are shown by the dots.

* Assisted by the U. S. Office of Ordnance Research and by grant of the Frederick Gardner Cottrell Fund of the Research Corporation.

[1] Thompson, Buskirk, Etter, Karzmark, and Rediker, Phys. Rev. **90**, 329 (1953).

[2] Exclusive of (a) π–μ decays, (b) angular deflections with visible recoil blobs at the points of deflection, (c) events with $p_y \leqslant 35$ Mev/c. The last condition is imposed in order not to include possible π–μ decays. Also five $V^\pm$ events (two V^+, two V^-, one $V^?$) are not suitable for measurement and are excluded from analysis.

[5] Proceedings of the Bagnères Conference, 1953 (unpublished).
[6] Armenteros, Barker, Butler, Cachon, and York, Phil. Mag. **43**, 597 (1952).
[6] Buchanan, Cooper, Millar, and Newth (private communication). We are indebted to Dr. Newth for sending us a prepublication copy of this paper.
[6] York, Leighton, and Bjornerud, Phys. Rev. **95**, 159 (1954). These authors report two groups of $V^{\pm}$ events. One group consists predominantly of a very short-lived positive particle with a probable two-body decay process and can be interpreted in terms of the hyperonic decay, $V^{+}\rightarrow(\text{nucleon})^{+,0}+\pi^{0,+}$. The other group with a longer mean lifetime is concluded to be consistent, in every respect, with the decay process $K^{\pm}\rightarrow\mu^{\pm}+2$ light neutral particles ($M_K\sim1000m_e$). From the consideration of lifetime, our data should be compared to the latter group in which York *et al.* do not report a charge asymmetry apart from a negative excess.
[7] Thompson, Buskirk, Karzmark, and Rediker, Phys. Rev. **92**, 209 (1953).
[8] Kim, Burwell, Cohn, Karzmark, and Thompson, Phys. Rev. **95**, 661 (1954).
[9] In two events (R-112, R-390) the primaries are heavily ionizing and our mass estimates are consistent with the value of $1000m_e$. However, in all three events, the p_y values are high and p' is not very sensitive either to the primary mass or to whether the secondary is π or μ. The value of p' obtained in the present experiment may be used as a basis for calculation of the $K^{\pm}$ particle mass for various assumptions as to the nature of the decay fragments. The results are: $917\pm19m_e$ for $(\mu^{+}+\nu$ or $\gamma)$, $948\pm18m_e$ for $(\pi^{+}+\nu$ or $\gamma)$, $991\pm17m_e$ for $(\mu^{+}+\pi^{0})$, and $1022\pm17m_e$ for $(\pi^{+}+\pi^{0})$.
[10] Gregory, Lagarrigue, Leprince-Ringuet, Muller, and Peyrou, Nuovo cimento **11**, 292 (1954).
[11] A. L. Hodson *et al.*, post deadline paper, Washington Meeting of the Am. Phys. Soc. ,May, 1954.
[12] Bridge, Courant, Dayton, DeStaebler, Rossi, Safford, and Willard (private communication). We are indebted to Dr. Bridge for sending us a prepublication copy of this paper.
[13] Crussard, Kaplon, Klarmann, and Noon, Phys. Rev. **93**, 253 (1954), also Phys. Rev. **95**, 584 (1954). Report on the Padua Conference, 1954 (unpublished).
[14] This point is further supported by the frequency of the ordinary τ decays observed in our chamber. We have observed only one τ^{+} decay.
[15] Anderson, Cowan, Leighton, and van Lint, Phys. Rev. **92**, 1089 (1953).
[16] The possible existence of a particle of mass about $1400m_e$ has been reported by D. H. Perkins and P. H. Fowler, Proceedings of the Duke Conference, 1953.
[17] Such an example is reported in reference 5.

Alpha-Emitting Isomer Polonium 211†

W. JENTSCHKE, A. C. JUVELAND, AND G. H. KINSEY
University of Illinois, Urbana, Illinois
(Received August 9, 1954)

SPIESS[1] has recently found that the α-particle bombardment of $_{82}Pb^{208}$ produces two short-lived α emitters belonging to $_{84}Po^{211}$, with $E_\alpha^{(1)}=7.14$ Mev, $T_{\frac{1}{2}}^{(1)}=25$ sec, and $E_\alpha^{(2)}=7.43$ Mev, $T_{\frac{1}{2}}^{(2)}=0.52$ sec. He concluded that these two states are isomeric states of $_{84}Po^{211}$, the 25-sec state being the ground state and the 0.52-sec state being an excited state having a low spin and an excitation energy of 0.3 Mev. He points out, however, that this explanation leads to a difficulty; in the K-capture decay $_{85}At^{211}\rightarrow{}_{84}Po^{211}$ only the 0.52-sec activity is observed. Since, according to shell theory, the ground state of both $_{84}Po^{211}$ and $_{85}At^{211}$ have spin 9/2, it is hard to understand why the 25-sec activity is not also found. Spiess also observed long-range α particles of low intensity, but did not identify them. We have investigated these long-range α particles and have shown that they are from $_{84}Po^{211}$. Our results lead to the revised decay scheme shown in Fig. 1. The 0.52-sec state appears as the ground state, and the difficulty mentioned by Spiess thus disappears. The 7.14-Mev α decay does not take place from the ground state of $_{84}Po^{211}$ but occurs from a 1.30-Mev 25-sec level and goes to the $i_{13/2}$ state of $_{82}Pb^{207}$.

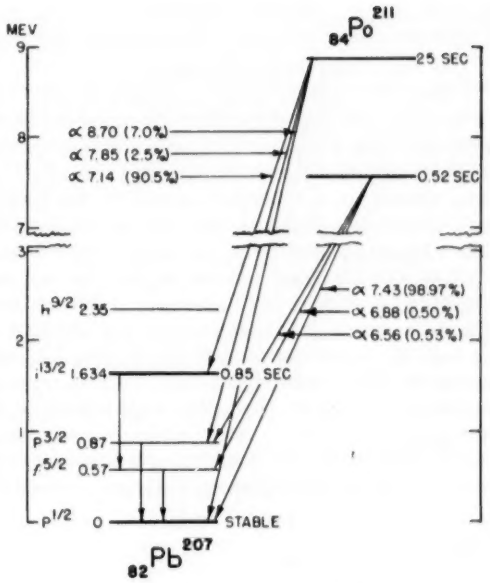

FIG. 1. Decay scheme of $_{84}Po^{211}$.

The decay scheme shown in Fig. 1 was deduced from the experiments 1–5 described below. In all of these experiments a thin lead foil was bombarded by α particles for 1 minute and measurements were started about 30 seconds after the end of the bombardment.

(1) The measurements of the energy of the α particles, made with an ionization chamber, gave peaks at 7.14 ± 0.05 Mev, 7.85 ± 0.05 Mev, and 8.70 ± 0.05 Mev. Figure 2 shows the pulse-height distribution. The differences in the α-disintegration energies: $8.87-7.28=1.59\pm0.07$ Mev and $8.87-8.00=0.87\pm0.07$ Mev agree with the excitation energies of the $i_{13/2}(E=1.63$ Mev) and the $p_{3/2}(E=0.87$ Mev) states of $_{82}Pb^{207}$.[2]

(2) The three α groups ($E=7.14$, 7.85, and 8.70 Mev) all have the same half-life of 25 sec. A fourth weak group at 6.58 ± 0.05 Mev decays with a half-life of about 2.1 minutes and probably belongs to $_{83}Bi^{211}$.

(3) The intensity ratios of the three groups remain unchanged while varying the bombarding α energy from 21.3 to 24 Mev, thereby changing the cross sections by a factor of about 3. These results indicate that all three groups are emitted from the same level of $_{84}Po^{211}$.

(4) γ-ray measurements with sodium iodide scin-

tillation counters showed the presence of a 0.56-Mev and a 1.06-Mev γ ray, both decaying with a half-life of 25 sec. The two γ rays are in coincidence.

(5) Since the half-life of the $i_{13/2}$ state of $_{82}Pb^{207}$ is 0.84 sec,[3] the 7.14-Mev alpha particles should not be in coincidence with γ rays. α–γ coincidence experiments with pulse-heights election confirmed this conclusion.

The absence of a 7.43-Mev α-peak in the pulse-height distribution indicates that the partial half-life of the γ transition from the 25-sec state to the 0.52-sec state is at least a hundred times as large as that for the α transition. From Weisskopf's formula[4] it follows that a transition with $L \geq 5$ is necessary to explain such a long half-life. According to shell theory, the 0.52-sec level should have a spin of 9/2. The 25-sec state then must have a spin of at least 19/2. This conclusion is also supported by α-decay considerations. Calculations of the α-decay half-lives, made using a semiempirical formula,[5] yield the result that spin changes of about 9,

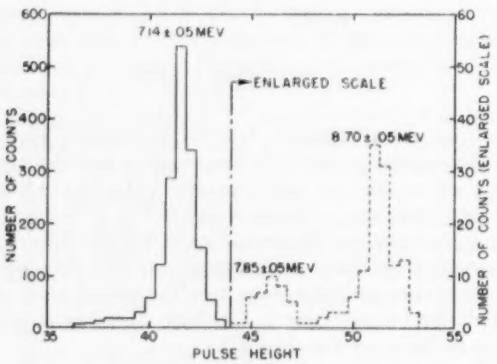

FIG. 2. Pulse-height distribution of the α particles from the 25-sec state of $_{84}Po^{211}$.

8, and 5 units accompany the 8.70, 7.85, and 7.14-Mev α decays of the 25-sec level and that the 7.43-Mev α decay occurs with a spin change of about 4 in agreement with the shell theory assignment of 9/2 for the spin of the 0.52-sec level. These results show that the spin of the 25-sec state very probably lies between 19/2 and about 23/2.

The simple single-particle model cannot explain the high spin of this excited state, since the highest reasonable spin for a low excited level of $_{84}Po^{211}$ would occur for the 127th neutron in a $j_{15/2}$ state. Spiess' suggestion that the excited state of $_{84}Po^{211}$ is due to "core isomerism"[6] is consistent with our decay scheme. By exciting the proton core to a $(h_{9/2}f_{7/2})$ configuration, and assuming the 127th neutron in the $g_{9/2}$ state,[7] the maximum spin of the 25-sec state would be 25/2.

It is somewhat surprising that the expected 25-sec α-particle group which decays to the $f_{5/2}$ state of $_{82}Pb^{207}$ could not be found. There seems to be some consistency, however, since the decay of the 0.52-sec level of $_{84}Po^{211}$ to the $f_{5/2}$ state of $_{82}Pb^{207}$ is also unexpectedly weak.[8]

According to these results the 8.70-Mev α particles decay with a partial half-life of about 360 sec from a state with a spin of at least 19/2 into a $p_{\frac{1}{2}}$ state. This is probably the largest spin change known for a nuclear decay.

The authors are grateful to Professor E. Segrè for suggesting this investigation. We thank Professor Hans Frauenfelder and Professor Peter Axel for valuable discussions and Mr. Sidney Singer for advice and help during the experiments.

† Assisted by the joint program of the U. S. Office of Naval Research and the U. S. Atomic Energy Commission.

[1] F. N. Spiess, Phys. Rev. **94**, 1292 (1954).
[2] D. E. Alburger and M. H. L. Pryce, Phys. Rev. **95**, 1482 (1954). A. H. Wapstra, Arkiv Fysik **7**, 279 (1954).
[3] E. C. Campbell, Oak Ridge National Laboratory Report ORNL-1620, 1953 (unpublished).
[4] J. M. Blatt and V. F. Weisskopf, *Theoretical Nuclear Physics* (John Wiley and Sons, Inc., New York, 1952).
[5] N. Feather, *Nuclear Stability Rules* (Cambridge University Press, London, 1952).
[6] M. Goldhaber, Phys. Rev. **89**, 1146 (1953).
[7] Fred, Tomkins, and Barnes, Phys. Rev. **92**, 1324 (1953).
[8] Hollander, Perlman, and Seaborg, Revs. Modern Phys. **25**, 469 (1953).

Vacuum Polarization in a Strong Coulomb Field*

EYVIND WICHMANN AND NORMAN M. KROLL
Columbia University, New York, New York
(Received August 17, 1954)

IN the interpretation of recent experiments with x-rays from μ-mesonic atoms, some reference has been made to the role of vacuum polarization both in connection with the μ-mass determination[1] and in connection with nuclear radius determinations.[2–5] The estimates made have been based on the Uehling formula,[6] which is merely the first term of an expansion in powers of αZ. Since the experiments have been carried out in elements as heavy as lead, for which $\alpha Z = 0.6$, the role of higher-order corrections may be significant.

Another situation in which such effects may play an experimentally significant role is in connection with the x-ray fine-structure separation $(2P_{\frac{1}{2}} - 2P_{\frac{3}{2}})$ in the heavy elements. The large value of the nuclear radius deduced by Schawlow and Townes[7] from the anomalous Z dependence of this fine structure might be brought into agreement with values determined by other methods by including electrodynamic effects. One must in this case, of course, include the effects of the mass operator as well as those of the polarization charge.

There is, of course, also some general theoretical interest in the treatment of such quantities, by techniques which either avoid power series expansions in certain quantities, usually treated as small, or which establish the convergence of these power series. Ac-

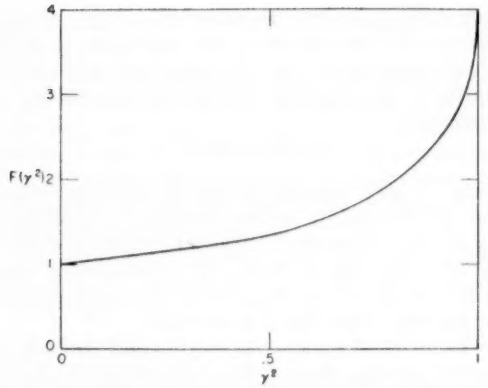

FIG. 1. The function $F(\gamma^2)$ defined in Eq. (4) plotted as a function of γ^2.

cordingly, a new attack has been made on the polarization charge problem with these objectives in view.

It is well known that the polarization charge density in a static electric field can, apart from radiative corrections, be expressed in terms of the solutions to the Dirac equation in that field. Starting from such an expression, making use of a contour integral representation of the summation over the radial eigenstates for a given angular momentum state, and making use of the fact that the solution of the Dirac equation for the case of the Coulomb field are known, one can show that the Laplace transform of $r^2\rho(r)$ is given by

$$Q(p)=\int 4\pi r^2\rho(r)e^{-pr}dr$$

$$=\frac{q}{\pi Z}\sum_{k=1}^{\infty}k\int_0^{\infty}dt\int_0^1 dz\Bigg[\Bigg(\frac{1}{(1-z)(1+uz)}+\frac{1}{1-z+uz}\Bigg)\frac{\gamma\cos g}{(1+t^2)^{\frac{1}{2}}}+\frac{2ts(k)\sin g}{(1+t^2)(1+uz)}+\frac{2\gamma t^2\cos g}{(1+t^2)^{\frac{1}{2}}(1+uz)}\Bigg]P^{-s(k)}, \quad (1)$$

with

$$P=(1+uz)(1-z+uz)(1-z)^{-1},$$

$$g=\gamma t(1+t^2)^{-\frac{1}{2}}\ln(1-z)(1+uz)(1-z+uz)^{-1},$$

$$s(k)=(k^2-\gamma^2)^{\frac{1}{2}},\quad u=\tfrac{1}{2}p(1+t^2)^{-\frac{1}{2}},\quad \gamma=\alpha Z=|eq|/hc,$$

where $\rho(r)$ is the polarization charge density induced by the potential q/r. Renormalization, divergence, and gauge difficulties are dealt with by examining the behavior of $Q(p)$ at small p and removing a term of the form $ap^{-2}+bp^{-1}+c\ln p+d$, with the coefficients chosen to yield $Q(0)=0$. It can be shown that this procedure is equivalent to regularization. It is worth noting that $Q(p)$ is virtually as useful a quantity as $\rho(r)$ itself. For example, the behavior of the polarization potential at small distances is determined by $Q(p)$ at large p, while the expectation values of the potential for Schrödinger wave functions can be expressed in terms of the derivatives of the Laplace transform of the potential multiplied by the radial variable r. This quantity is related to $Q(p)$ through

$$u(p)=\int rV(r)e^{-pr}dr=\frac{1}{p^2}\int_0^p Q(p')dp'. \quad (2)$$

Equation (1) serves as a convenient starting point for expansion in powers of γ. We have confirmed that $Q^{(1)}(p)$, the lowest-order term (linear in γ) is precisely the Uehling term, while for the third-order term we find

$$\begin{aligned}Q^{(3)}(p)&=q(\alpha\gamma^2/\pi)[-0.115(p/2)+0.166(p/2)^2\\&\quad-0.274(p/2)^3+0.303(p/2)^4\\&\quad-0.187(p/2)^4\ln p+\cdots];\quad p\ll 1\\&=-0.0209\alpha q\gamma^2\ \text{for}\ p\to\infty.\end{aligned} \quad (3)$$

The computational problem of obtaining (3) from (1) seems to be orders of magnitude simpler than obtaining the corresponding results from Feynmann integrals. The appearance of the $p^4\ln p$ term corresponds to an asymptotic $1/r^7$ behavior at infinity for $\rho(r)$. This result can, in fact, be deduced from the Euler-Heisenberg Hamiltonian.[8] The coefficient obtained by the two methods are in agreement.

Finally we note that similar results can be obtained without expanding in powers of γ. In particular, we find

$$\begin{aligned}\delta Q&=\operatorname*{Lim}_{p\to\infty}[Q(p)-Q^{(1)}(p)]\\&=(q/\pi Z)\Bigg(\frac{2}{3}\sum\frac{1}{n^3}-\frac{\pi^2}{6}+\frac{7}{9}\Bigg)\gamma^3\\&\quad-(2q/\pi Z)\sum_{k=1}^{\infty}k\Bigg(\sin^{-1}\frac{\gamma}{k}-\frac{\gamma}{k}-\frac{\gamma^3}{6k^3}\Bigg)\\&\quad+(4q/\pi Z)\sum_{k=1,n=1}^{\infty}\Bigg(\frac{nk\gamma}{[n+s(k)]^2+\gamma^2}\\&\qquad-k\tan^{-1}\frac{\gamma}{n+s(k)}+\frac{k^2\gamma}{(n+k)^2}-\frac{3n^2-k^2}{(n+k)^4}\gamma^3\Bigg)\\&=-0.0209\alpha q\gamma^2-0.0071\alpha q\gamma^4F(\gamma^2),\end{aligned} \quad (4)$$

where $F(\gamma^2)$ is plotted in Fig. 1. The small-r behavior of the polarization potential is given by

$$V(r)=\frac{2\alpha q}{3\pi r}\Bigg(\ln\frac{1}{rC}-\frac{5}{6}\Bigg)+\frac{\delta Q}{r}, \quad (5)$$

$$C=0.577\cdots.$$

It is clear from Eq. (4) that a perturbation theory expansion of δQ converges[9] with radius of convergence $\gamma=1$. It is also interesting to note that δQ remains finite in the limit $\gamma\rightarrow 1$.

The corrections to the Uehling formula for $V(r)$ at small r are very small, even for lead, so that its use for the μ-meson work appears to be well justified.

Formulas like (4) can be obtained for all of the coefficients in the small-p expansion of $Q(p)$, although the labor involved increases with the order of the coefficient. In view of the smallness of (4), however, it is unlikely that the terms beyond the cubic are ever important.

A fuller account of the work described above, together with some applications, will be subsequently submitted for publication.

* Work partially performed at Brookhaven National Laboratory, under the auspices of the U. S. Atomic Energy Commission.

[1] Koslow, Fitch, and Rainwater, Phys. Rev. **95**, 291 (1954).
[2] V. Fitch and J. Rainwater, Phys. Rev. **92**, 789 (1953).
[3] L. W. Cooper and E. M. Henley, Phys. Rev. **92**, 801 (1953).
[4] H. C. Corben, Phys. Rev. **94**, 787 (1954).
[5] D. L. Hill and K. W. Ford, Phys. Rev. **94**, 1617 (1954).
[6] E. A. Uehling, Phys. Rev. **48**, 55 (1935); R. Serber, Phys. Rev. **48**, 49 (1935).
[7] A. L. Schawlow and C. H. Townes, Science **115**, 284 (1952).
[8] W. Heisenberg and H. Euler, Z. Physik **98**, 714 (1936); H. Euler, Ann. Physik **26**, 398 (1936).
[9] One can also show that for a given value of p, $Q(p)$ is an analytic function of γ within the circle $|\gamma|=1$.

Polarization of Arsenic Nuclei in a Silicon Semiconductor*

A. Honig

Department of Physics, University of California, Berkeley, California

(Received August 12, 1954)

A NEW mechanism capable of producing nearly 100 percent polarization of nuclear spins under moderate conditions of field and temperature has been found in the course of electron spin resonance studies.

Electron spin resonances exhibiting resolved hyperfine structure have recently been observed by Fletcher *et al.*[1] on a number of impurity-doped silicon samples. This note is concerned with a similar sample of arsenic-doped silicon; it is reported to contain 1.3×10^{17} As atoms per cm^3. The sample was generously provided by Dr. F. J. Morin of Bell Telephone Laboratories.

At a temperature of 4°K and at a frequency of about 9000 Mc/sec, the four resonances reported by Fletcher were observed. These lines correspond to each of the four possible orientations in the magnetic field of the As^{75} nucleus, which has a spin of $\frac{3}{2}$. The lines were approximately 3 oersteds broad, were spaced about 73 oersteds apart, and exhibited inhomogeneous saturation behavior.[2]

On each one of the resonances, the following observations were made: If the magnetic field was swept twice through the same resonance with a time t elapsing between the two traversals, the amplitude A_2 of the second traversal of the resonance line is decreased relative to the amplitude of the first traversal by approximately

$$A_2/A_1=1-e^{-t/T},$$

where T is about 16 seconds. Also, by sweeping through two neighboring hyperfine components sufficiently rapidly, an *enhancement* of the second line relative to the first line was obtained, this enhancement being about a factor of two larger if the first line was one of the extrema of the hyperfine multiplet.

The proposed explanation of this effect utilizes the process whereby electron spin relaxation can effect a nuclear spin reorientation through the $\mathbf{I}\cdot\mathbf{S}$ magnetic hyperfine interaction. In sweeping through a resolved hyperfine resonance line using sufficient rf power, we suppose that virtually all of the relevant As nuclei undergo a Δm_I of ±1, thus depopulating the m_I level associated with the particular line. Then, if the nuclear spin relaxation time is about 16 seconds, the observed effect results. However, in order for the net depopulation of the m_I level to occur during the electronic resonance, it is necessary to have a mechanism whereby the number of nuclear spins flipped by electron spin relaxations is greatly enhanced when *on the electronic resonance*. A mechanism for this was suggested by J. I. Kaplan and is described in the following Letter. It consists essentially of a broadening of the power spectrum of the electron relaxation, centered at the electron spin Larmor frequency, due to the shortened lifetime of an electron spin state during resonance; this produces a larger Fourier amplitude at the nuclear Larmor frequency, thereby increasing the probability of a nuclear spin flip. In the present As-doped sample, it is estimated that, for an rf amplitude of $H_1=0.010$ oersted, the time for a nuclear spin flip would be of the order of 10^{-2} second due to this mechanism, as contrasted with 16 seconds under no rf.

Manifestations of this effect are also seen in sweeping through a single line. The shape of the line shows an asymmetry and large g shift due to a progressive depopulation of the associated nuclear m_I state. The *inhomogeneous* line width and spin diffusion time of the Si^{29} nuclei enter into the quantitative analysis of this behavior.

In the present case, to polarize completely the As nuclei in a particular m_I state, one has to sweep through the resonances corresponding to the other three m_I states in a time small compared to the nuclear relaxation time. In the case of Si doped with an impurity having a spin of $\frac{1}{2}$, such as phosphorus, satisfying the resonance condition for one m_I state would completely polarize the other state. The general requirement is that sufficient rf power be used so that the nuclear spin flip time in the presence of the rf will be short compared to the nuclear relaxation time in the absence of rf. It is to be

noted that saturation of the electronic resonance is not necessarily required.

It should be possible to apply this effect toward obtaining polarized samples for the study of nuclear level decay schemes. Another consequence is that it is possible to measure nuclear relaxation times in systems where the nuclear resonance cannot be observed because of the strong and fluctuating local magnetic field at the nucleus due to the electrons.

It is a pleasure to thank the members of the solid state group at the University of California for many stimulating discussions.

* This work has been assisted in part by the U. S. Office of Naval Research and the U. S. Signal Corps.

[1] Fletcher, Yager, Pearson, Holden, Read, and Merritt, Phys. Rev. **94**, 1392 (1954).
[2] A. M. Portis, Phys. Rev. **91**, 1071 (1953).

Nuclear Electric Quadrupole Moment of Na^{23}

S. SENGUPTA
Government College, Darjeeling, West Bengal, India
(Received August 2, 1954)

IT has recently been reported by Sagalyn[1] that the nuclear electric quadrupole moment of Na^{23} is $+0.1\times10^{-24}$ cm^2. On Mayer's single-particle level scheme, there are three possible configurations for the ground state of Na^{23}. They are $[(d_{5/2})^3]_{3/2}$, $[(d_{5/2})^2 s_{1/2}]_{3/2}$, $[(d_{3/2})^3]_{3/2}$. The actual level order here, as given by Mayer,[2] is $d_{5/2}$, $s_{1/2}$, $d_{3/2}$. The last assignment, though giving a positive Q, is extremely improbable, because of the large departure of the observed magnetic moment from the Schmidt limit. Mayer herself preferred the first assignment, especially because a calculation of μ with jj coupling gives for this configuration a value of 2.87 nm, in fairly good agreement with the experimental value of 2.22 nm. However, as has been shown by Sagalyn,[1] the quadrupole moment in this configuration with jj coupling comes out to be zero. Hence the $(d_{5/2})^3$ configuration also cannot be accepted. We are thus left with the second alternative. Calculations for both magnetic and quadrupole moments have been carried out for this configuration with jj coupling. The wave functions for the $(d_{5/2})^2$ configuration are calculated by the method of Gray and Wills[3] and the total wave function for $(d_{5/2})^2 s_{1/2}$ is then antisymmetrized by the method given in Condon and Shortley.[4] The $(d_{5/2})^2$ state is coupled with the $s_{1/2}$ state to give the observed spin of 3/2. The result gives

$$\mu = 1.78 \text{ nm},$$

$$Q = +(8/35)\langle r^2\rangle_{Av} = +0.041\times10^{-24} \text{ cm}^2,$$

where $\langle r^2\rangle_{Av}$ is calculated from the formula $r = 1.5A^{\frac{1}{3}}\times10^{-13}$ cm. Thus the observed magnetic dipole and electric quadrupole moments of Na^{23} are found to support the assignment $[(d_{5/2})^2 s_{1/2}]_{3/2}$ for its ground state.

[1] P. L. Sagalyn, Phys. Rev. **94**, 885 (1954).
[2] M. G. Mayer, Phys. Rev. **78**, 16 (1950).
[3] N. M. Gray and L. A. Wills, Phys. Rev. **38**, 248 (1931).
[4] E. U. Condon and G. H. Shortley, *Theory of Atomic Spectra* (Cambridge University Press, London, 1953), p. 213.

K Mesons and a Charged Hyperon Produced by 3-Bev Protons in Emulsions*

W. F. FRY AND M. S. SWAMI
Department of Physics, University of Wisconsin, Madison, Wisconsin
(Received August 4, 1954)

A GROUP of glass backed plates and pellicles were exposed inside the Cosmotron to 3-Bev protons. The proton flux was greatly reduced from the normal operating intensity, and the plates were exposed to about 5 pulses from the Cosmotron. The proton track density in the plates is about 5×10^5 tracks/cm^2.

The emulsions were area scanned with an over-all magnification of about 100×, looking for slow heavy mesons, hyperons, and bound Λ^0 particles. In this note we describe three events which are interpreted as two K mesons and a hyperon. These three events were found in 4.5 cc of emulsion. A detailed description of bound Λ^0 particles will be given elsewhere.

The essential characteristics of the three events are given in Table I.

A photograph of the production and decay of particle K_1 is shown in Fig. 1. The track of the K meson is 7000 microns long and stops in the same plate, giving rise to a secondary track which is nearly in the plane of the emulsion and is 24 000 microns long in the same plate. The ionization along the secondary track was measured by blob counting and was compared with 3-Bev proton tracks at the same depth in the emulsion. The ionization of the secondary particle was found to be 1.08 ± 0.06 times that of the 3-Bev protons. The scattering parameter, $\rho\beta$, of the secondary particle was found to be 180 ± 13 Mev/c by using cells of 200 microns. The kinetic energy of the secondary particle is 121 ± 9 Mev, 109 ± 8 Mev, or 180 ± 13 Mev if we assume it to be a μ meson, a π meson, or an electron respectively. The expected relative ionization,[1] compared with 3-Bev protons, is 1.1 ± 0.02 for a μ meson and 1.2 ± 0.02 for a π meson. The measured ionization and multiple scattering strongly indicate that the secondary particle is a μ meson or an electron. If the secondary particle is assumed to be a π meson, the expected ionization differs from the measured value by about two standard deviations. The mass of the K_1 particle was found to be $850\pm150m_e$ by using the constant sagitta method.[2,3] The event is consistent with the decay of a meson of

TABLE I. Characteristics of heavy mesons.

Event	Range of primary (microns)	Mass of primary (m_e)	Range of secondary (microns)	Ionization ratio I/I_0	$\rho\beta$ of decay particle in Mev/c	Identity of secondary
K_1	7000	850±150	>24 000	1.08±0.06	180±13	μ or e
K_2	4400	920±200	>200	μ_1	...	...
Y_1	820	2300±1000	1783±20	(black)	191±1	p

mass about $900m_e$ into a μ meson and a single neutrino or into an electron and two neutrinos.

The K_2 particle entered the emulsion from the glass backing and stopped in the plate after 4.4 mm. The decay track dips steeply in the emulsion, therefore no reliable measurements can be obtained. The ionization is about minimum. The measurement of the mass of particle K_2 by the constant sagitta method gives 920 $\pm 200m_e$.

A projection drawing of event Y_1 appears in Fig. 2. The increase in the amount of small angle scattering, the absence of gaps and δ rays along track Y^+ near point A strongly implies that the particle stopped at point A (Fig. 2). The mass measurement along track Y^+, by the constant sagitta method, gives a value of $2300\pm1000m_e$. The secondary particle p stopped in the adjacent emulsion, and the characteristics of the track indicate that it is a proton. The total range of the proton is 1783±30 microns, corresponding to an energy

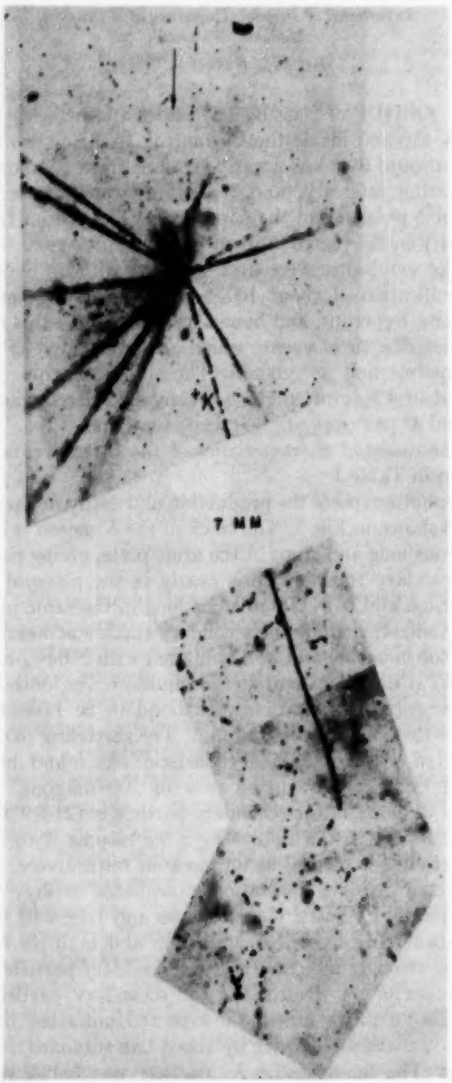

FIG. 1. The production and decay of a K meson by a 3-Bev proton is shown in the projection drawing.

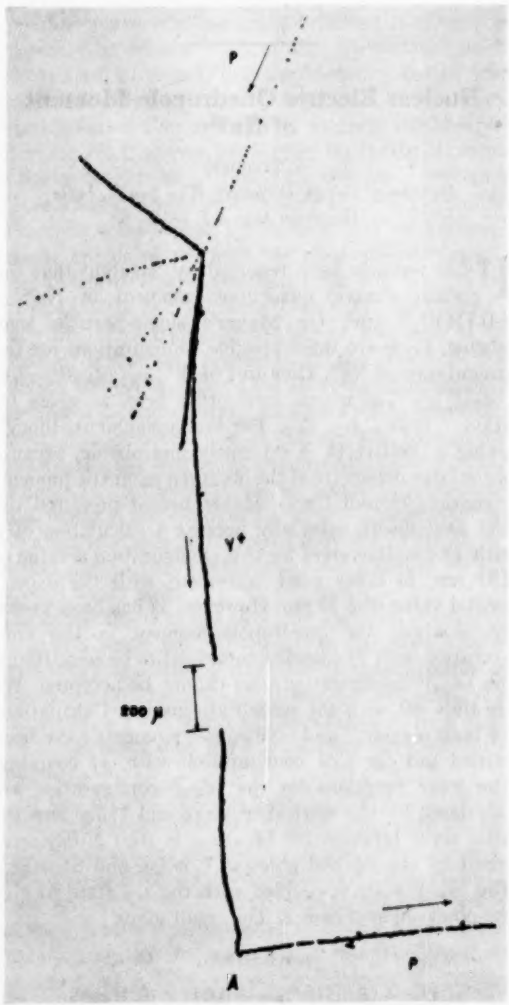

FIG. 2. A charged hyperon (Y^+) is produced in the collision of a 3-Bev proton. The hyperon appears to have stopped at point A and decayed into a proton.

of 19.5±0.2 Mev.[4] There are no associated low-energy electron or recoil tracks at point A (Fig. 2). The absence of a recoil and low energy electron in conjunction with the mass measurements along the primary make it improbable that the proton was ejected by the nuclear capture of a negative π or K meson. In terms of known decay schemes, it seems reasonable to interpret the event as the decay, from rest, of a charged hyperon[5] (V^+) into a proton and a neutral π meson:

$$V^+ \rightarrow p + \pi^0 + Q.$$

The Q value for this reaction is found to be 117±2 Mev. From the measured Q value, the mass of the hyperon is found to be $2329\pm5m_e$. The Q value is in excellent agreement with two other similar events reported by the Genoa-Milan and the Padua groups.[6] In these two events, the proton energies were found to be 18.7±0.2 Mev and 18.5±0.3 Mev, respectively. The consistency in the ranges of the protons among the three events (the Genoa-Milan, the Padua event, and the above event) strongly indicate that these three hyperons decayed from rest and that only two particles were involved in the decay.

The authors are greatly indebted to the Cosmotron group for their assistance in exposing the plates and particularly to Dr. R. K. Adair for his continued interest and cooperation.

* Supported in part by the Graduate School from funds supplied by the Wisconsin Alumni Research Foundation.

[1] E. Pickup and L. Voyvodic, Phys. Rev. **80**, 89 (1950) and private communications (1954).

[2] Biswas, George, and Peters, Proc. Indian Acad. Sci. **38**, 418 (1953).

[3] Dilworth, Goldsack, and Hirschberg, Nuovo cimento **11**, 113 (1953).

[4] The range-energy data of Wilkins were used. J. J. Wilkins, Atomic Energy Research Establishment Report AERE G/2 664 (unpublished).

[5] We use the notation proposed at the Bagneres Congress [See Physics Today **6**, No. 12, 24 (1553)].

[6] Reported at the Padua Conference, 1954 and private communication.

Theory of Coulomb Excitation

K. ALDER* AND A. WINTHER

Institute for Theoretical Physics, University of Copenhagen, Copenhagen, Denmark

(Received August 11, 1954)

THE theory of Coulomb excitation has been considered earlier by many authors. Especially helpful for the interpretation of the experiments is a semiclassical calculation by Ter-Martirosyan.[1,2] In this theory the trajectory of the impinging particle is described by a classical hyperbolic orbit.

We have obtained a somewhat more accurate description of the process by approximating the Coulomb wave function, entering in the quantum-mechanical treatment, by means of the WBK method. The results of this calculation are very similar to the results of the semiclassical theory. The cross sections for electric dipole and electric quadrupole excitation are:

$$\sigma(E1)=\frac{2\pi^2 Z_1^2 e^2}{9\hbar^2 v_i^2}B(E1)g_{E1}(\xi), \tag{1}$$

$$\sigma(E2)=\frac{2\pi^2 m_1^2 v_f^2}{25 Z_2^2 e^2 \hbar^2}B(E2)g_{E2}(\xi), \tag{2}$$

with the following new definition of the parameter:

$$\xi=\alpha_f-\alpha_i=\frac{Z_1 Z_2 e^2}{\hbar}\left(\frac{1}{v_f}-\frac{1}{v_i}\right), \tag{3}$$

where Z_1e and Z_2e are the charges of the impinging projectile and the nucleus, respectively. The initial and final relative velocities are denoted by v_i and v_f, while m is the reduced mass. $B(E\lambda)$ is the reduced transition probability for electric 2^λ-pole radiation in the notation of Bohr and Mottelson.[3] The functions $g_{E\lambda}(\xi)$ are the same as those entering in the semiclassical expression.[1,2] For small excitation energies ΔE, the formulas (1), (2), and (3) reduce to the corresponding semiclassical formulas. We have then $v_f \sim v_i \sim v$, and

$$\xi=\frac{Z_1 Z_2 e^2}{\hbar v}\frac{\Delta E}{2E}. \tag{4}$$

The expression (1) for electric dipole excitation has been compared with the exact quantum mechanical formula[4]

$$\sigma(E1)=-\frac{128\pi^4}{9}\frac{Z_1^2 e^2}{\hbar^2 v_i^2}B(E1)\left(\frac{\alpha_f}{\alpha_i}\right)^2 \times\frac{e^{2\pi\alpha_i}}{(e^{2\pi\alpha_i}-1)(e^{2\pi\alpha_f}-1)}\frac{d}{dx_0}|F(x_0)|^2,$$

where

$$x_0=-4\alpha_i\alpha_f/(\alpha_i-\alpha_f)^2, \tag{5}$$

and

$$F(x_0)={}_2F_1(-i\alpha_i, -i\alpha_f, 1, x_0)$$

in terms of ${}_2F_1$, the ordinary hypergeometric function. In the range $\alpha_i \gtrsim 1$ and $0 \leqslant \alpha_f-\alpha_i=\xi \leqslant 1$, the WBK expression (1) agrees within 2 percent with the quantum mechanical calculation, which represents a considerable improvement over the semiclassical treatment.

In the case of the quadrupole excitation, no exact quantum mechanical treatment has been given, but the adequacy of the WBK treatment for the $E1$ case, suggests that (2) should also represent a good approximation when the effects resulting from penetration of the bombarding particle into the nucleus itself can be neglected.

Indeed, it is found that (2) satisfactorily represents all the experimental yield curves available to us at the present time.

Other kinds of electromagnetic excitations have also been considered and a detailed account of all the calcu-

lations will be published in the proceedings of the Danish Academy.[5,6]

* Theoretical Study Group, European Council for Nuclear Research. On leave from Physikalisches Institut der Eidgenössischen Technischen Hochschule, Zürich, Switzerland.

[1] K. A. Ter-Martirosyan, J. Exptl. Theoret. Phys. (U.S.S.R.) **22**, 284 (1952).

[2] K. Alder and A. Winther, Phys. Rev. **91**, 1578 (1953).

[3] A. Bohr and B. Mottelson, Kgl. Danske Videnskab. Selskab, Mat.-fys. Medd. **27**, No. 16 (1953).

[4] R. Huby and H. C. Newns, Proc. Phys. Soc. (London) **A64**, 619 (1951); C. T. Mullin and E. Guth, Phys. Rev. **82**, 141 (1951).

[5] K. Alder and A. Winther, Kgl. Danske Videnskab. Selskab (to be published).

[6] A review article on the theory of Coulomb excitation, containing also an analysis of experimental data, is being prepared in collaboration with A. Bohr, T. Huus, B. Mottelson, and C. Zupančič.

Rf-Induced Transitions of Nuclear Spins at the Electronic Resonance Frequency*

JEROME I. KAPLAN
Department of Physics, University of California, Berkeley, California

(Received August 12, 1954)

A REASONABLE explanation is offered to account for the observed increased transition rate of nuclear spins at the electronic spin resonance frequency, as reported in the preceding Letter by Honig. It is known from the work of Bloembergen[1] that an important mechanism of nuclear spin-lattice relaxation in solids is through the coupling of the nuclear magnetic moments to the electron magnetic moments of paramagnetic impurities. The power spectrum associated with the relaxation of the electron moment determines the rate at which nuclear spins are flipped. If the electron spin-lattice relaxation time is very long, even a weak rf field at the electron resonance frequency will have a major effect on the power spectrum. In this way nuclear flips are enhanced when the electron resonance is observed."

The Hamiltonian for a single arsenic site, when the dipolar interactions are neglected, is

$$\mathcal{H}=a\mathbf{I}\cdot\mathbf{S}+H_0(g_e\mu_B S_z-g_N\mu_N I_z)+H_x e^{i\omega t}g_e\mu_B S_z-H_x e^{i\omega t}g_N\mu_N I_x, \quad (1)$$

where the nuclear moment is considered to be positive. For the experimental magnetic field of 3000 oersteds the use of I_z and S_z as good quantum numbers gives the correct energy levels within 2 to 3 percent. The off-diagonal interaction term $\frac{1}{2}aS^+I^-$ can be made to induce nuclear transitions to first order in the sense of time-dependent perturbation theory, by considering the rf-induced transitions of S^+ as a source of power. This is similar to the argument made by Bloembergen, Purcell, and Pound[2] in which they use the time dependence of the magnetic dipolar interactions caused by the rotational and translational motion of the spins to obtain the power necessary for a nuclear spin relaxation. The correlation function for $S^+(t)$ is assumed, following Bloembergen,[1] to be proportional to

$$|S^+|^2 e^{i\omega_0 t}\exp(-t/T_{rf}^{e1}),$$

where T_{rf}^{e1} is the electronic transition time given as[2]

$$T_{rf}^{e1}=(\tfrac{1}{2}\mu_B{}^2H_1{}^2T_2{}^{e1}/\hbar^2)^{-1}, \quad (2)$$

and $T_2{}^{e1}$ is the half-maximum value of the electronic line shape function.

Corresponding to this correlation function is the power spectrum,

$$|S^+|^2\frac{2T_{rf}^{e1}/\pi}{1+4(T_{rf}^{e1})^2(\omega-\omega_0)^2}, \quad (3)$$

where ω_0 is the electronic Larmor frequency. Substituting into the standard formula for transition probability,[3] we have for the nuclear transition time,

$$T_{nuc}=\left[\frac{2\pi}{\hbar^2}\left|\frac{a}{2}S^+I^-\right|^2\frac{2T_{rf}^{e1}/\pi}{1+4(T_{rf}^{e1})^2(\omega_0'-\omega_0)^2}\right]^{-1}. \quad (4)$$

Note that the component of the power spectrum is taken at the nuclear Larmor frequency ω_0'.

Next we will show how the same result can be obtained by second-order perturbation theory. Here we consider the transition between the initial spin state, $m_S=\frac{1}{2}$, $m_I=\frac{3}{2}$, and the final state, $m_S=\frac{1}{2}$, $m_I=\frac{1}{2}$. If standard perturbation theory is used, the expansion coefficient for the final state satisfies the equation,

$$\dot{a}_f{}^{(2)}=(ih)^{-1}\sum_n H_{fn}a_n{}^{(1)}e^{i\omega_{fn}t}, \quad (5)$$

where

$$H=H_1g_e\mu_BS_xe^{i\omega t}+\tfrac{1}{2}aS^+I^-+\tfrac{1}{2}aS^-I^+,$$

and

$$a_n{}^{(1)}=(ih)^{-1}\Big\{\langle n|H_1g_e\mu_BS_x|i\rangle\times\left[\frac{\exp[i(\omega+\omega_{ni}{}^{(1)}+i/2T_{rf}^{e1})t]-1}{i(\omega+\omega_{ni}{}^{(1)}+i/2T_{rf}^{e1})}\right]+\langle n|\tfrac{1}{2}aS^+I^-+\tfrac{1}{2}aS^-I^+|i\rangle\times\left[\frac{\exp[i(\omega_{ni}{}^{(2)}+i/2T_{rf}^{e1})t]-1}{i(\omega_{ni}{}^{(2)}+i/2T_{rf}^{e1})}\right]\Big\}.$$

It is to be noted that we have represented the initial state by a decaying exponential.[4] The only intermediate state which gives a nonzero contribution is $m_S=-\frac{1}{2}$, $m_I=\frac{3}{2}$, and thus only the matrix element containing H_1 contributes to $a_n{}^{(1)}$. Therefore we set $\omega_{ni}{}^{(1)}=-\omega_0$ and $\omega_{fn}=\omega_0-\omega_0'$. The transition probability is wanted at the electronic renance frequency, so setting $\omega=\omega_0$ the expansion coefficient then satisfies the equation

$$\dot{a}_f{}^{(2)}=-(ih)^{-2}(2T_{rf}^{e1})\langle f|\tfrac{1}{2}aS^+I^-|n\rangle\langle n|H_1g_e\mu_BS_x|i\rangle\times[\exp(-t/2T_{rf}^{e1}+i\omega_0t-i\omega_0't)-\exp(i\omega_0t-i\omega_0't)]. \quad (6)$$

The first two terms can be made to conserve energy between the initial and final states by choosing the Fourier component of $\exp(-t/2T_{rf}^{e1})\exp(i\omega_0t)$ at the frequency ω_0'. Formally carrying this out gives just the transition probability in Eq. (4).

By taking the local field at the electrons as due to the electronic dipoles on the other arsenics, a $T_2^{el} \approx 4\times10^{-6}$ sec is found, yielding $T_{rf}^{el} \approx \frac{1}{2}\times10^{-4}$ from Eq. (2) (if one takes $H_1 = 10^{-2}$ oersted). The hyperfine splitting of 73 oersteds gives a value of the hyperfine parameter a equal to $\frac{3}{2}\times10^{-18}$ erg. Then, with an applied frequency of 9×10^9 cps and an rf field of 10^{-2} oersted, the value for the rf-induced nuclear transition time becomes, from Eq. (4),

$$T_{nuc} = [(6\times10^{24})(2\times10^{-36})(4\times10^{-18}/3)]^{-1} \approx 6\times10^{-2} \text{ sec.}$$

This is to be compared to the nuclear spin relaxation time of 16 sec.

I wish to acknowledge very helpful discussions with Mr. A. Kahn, Dr. R. D. Lawson, and Dr. A Honig.

* Supported in part by the U. S. Office of Naval Research and the U. S. Signal Corp.

[1] N. Bloembergen, Physica **15**, 386 (1949).
[2] Bloembergen, Purcell, and Pound, Phys. Rev. **73**, 679 (1948).
[3] L. I. Schiff, *Quantum Mechanics* (McGraw-Hill Book Company, Inc., New York, 1949), p. 193.
[4] V. Weisskopf and E. Wigner, Z. Physik **63**, 54 (1930).

Results of a Phase Shift Calculation of High-Energy Electron Scattering*

D. G. RAVENHALL AND D. R. YENNIE
Stanford University, Stanford, California
(Received August 6, 1954)

USING the phase shift analysis described previously,[1] an attempt has been made to fit the experimental data of Hofstadter *et al.*[2] on the elastic scattering of electrons on gold at energies of 84, 126, 154, and 183 Mev. Only scattering from a static spherically symmetric charge distribution is considered; all other interactions are neglected. The one-parameter charge distributions such as uniform, Gaussian, and exponential considered earlier[1] are clearly ruled out by the experimental data because of both the shape of the individual cross sections and their energy dependence. The present results are for "smoothed uniform" distributions, characterized by a central region of almost constant density and a surface region in which the density drops to zero. Of the two parameters required to identify a distribution of this type (a radius and a surface thickness), it turns out that the surface thickness is small enough compared with the electron's de Broglie wavelength λ that the detailed surface structure is unimportant; this is not true at higher energies, of course.

We define[3] a radius c by

$$c = \int_0^\infty \rho(r)dr/\rho(0), \tag{1}$$

and a surface thickness s by

$$s^2 = -4\int_0^\infty (r-c)^2(d\rho/dr)dr/\rho(0). \tag{2}$$

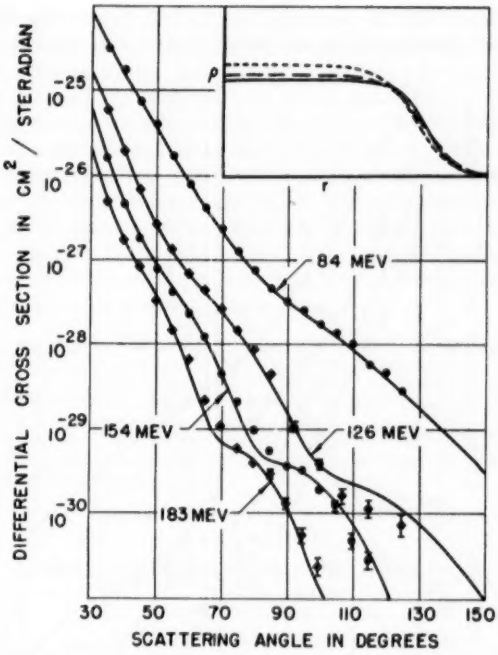

FIG. 1. Cross sections at 84, 126, 154, and 183 Mev for the elastic scattering of electrons by gold, using the charge distribution (4) with the parameters $K = 2.20$, $c = 6.63$ ($r_0 = 1.20$, $s = 1.65$). (Distances are in units of 10^{-13} cm.) Inset is the charge distribution (full line), together with that for Fig. 2 (dashed line) and Fig. 3 (dotted line). The experimental values are of Hofstadter *et al.* (reference 2).

To relative order $(s/c)^4$, the root-mean-square radius is then given by

$$\langle r^2\rangle^{\frac{1}{2}} = \left(\frac{3}{5}\right)^{\frac{1}{2}} c\left(\frac{1+(5/2)(s/c)^2}{1+(3/4)(s/c)^2}\right)^{\frac{1}{2}}$$

$$= (3/5)^{\frac{1}{2}} r_0 A^{\frac{1}{3}} \times 10^{-13} \text{ cm.}$$

In the results presented here, we have used for the charge density the form

$$\rho = \rho_0[1+e^{K(r-c)}]^{-1}. \tag{4}$$

For $e^{Kc} \gg 1$ the c of Eq. (4) is the same as that defined by Eq. (1). The surface thickness s is $2\pi/\sqrt{3}K\,(=3.63/K)$, which is slightly smaller than the previously defined "smoothing distance"[1] $(=4.40/K)$. To confirm theoretical arguments that the cross section depends only on c and s, and is independent of the surface shape,[3] calculations at 183 Mev have been carried out for several shapes having the same value of s and c as those of Fig. 1. The most extreme of these has a surface which varies linearly with r. For angles less than 105° the cross section for all of these shapes agreed to within 10 percent; by a slight alteration of parameters to allow for the terms in $(s/c)^4$ this agreement could be improved still further.

In Figs. 1–3 we compare the results of the phase shift calculations with the experimental data, which have

been arbitrarily normalized for each energy to give the best agreement with the theory. Perhaps the best fit is

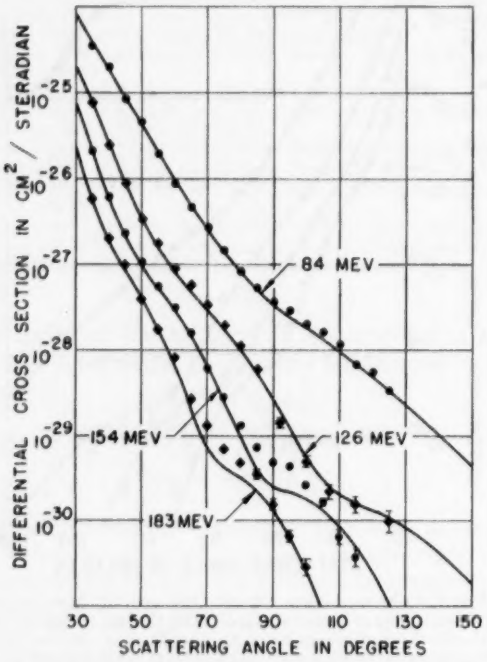

FIG. 2. Cross sections for the parameters $K=1.85$, $c=6.51$ ($r_0=1.20$, $s=1.96$).

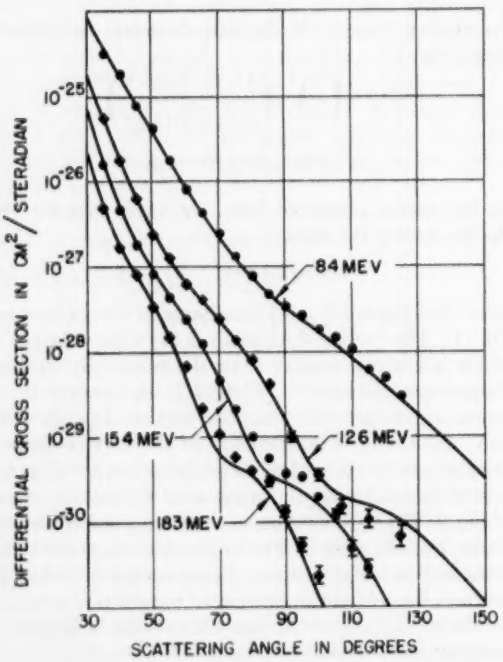

FIG. 3. Cross sections for the parameters $K=1.85$, $c=6.19$ ($r_0=1.16$, $s=1.96$).

that of Fig. 1, where $s=1.65\times10^{-13}$ cm, $r_0=1.20$ ($c=6.63\times10^{-13}$ cm).[4] The charge distributions of Figs. 2 and 3, which are for slightly different values of s and r_0, show that the cross section depends rather sensitively on these parameters.

The slight differences between the experiments and the results of Fig. 1, if significant, can be due to a number of different effects. Perhaps a more complicated charge distribution is required; preliminary calculations indicate that a decrease in the central charge density alters the cross sections in such a way as to improve the fit with the 183-Mev data.[5] There may also be appreciable contributions from the static quadrupole moment, nuclear excitations, and radiative corrections. L. I. Schiff and B. Downs[6] have considered the first of these, together with quadrupole excitations to low-lying levels, on the basis of a modified Born approximation.[3] They find that in gold these effects add at most three percent to the elastic cross section. The other effects have not yet been estimated.

For values of s and r_0 quoted above, the cross sections in Pb^{208} also agree very well with the data of Hofstadter *et al.*[2]

These calculations were made on the computer Univac at the University of California Radiation Laboratory at Livermore. We thank the authorities of this Laboratory, particularly Dr. S. Fernbach, for permission to use Univac, and Mr. H. Hanerfeld for instruction and advice in coding. We wish to thank Professor R. Hofstadter, Dr. B. Hahn, and Dr. J. A. McIntyre for discussions about their work and ours, and Professor L. I. Schiff and Professor G. C. Wick for helpful conversations. We also thank Dr. G. E. Brown for communicating his results and those of Drs. S. Brenner and L. R. B. Elton prior to their publication.

* Supported in part by the Office of Scientific Research, Air Research and Development Command.

[1] Yennie, Ravenhall, and Wilson, Phys. Rev. **95**, 500 (1954).

[2] Hofstadter, Hahn, Knudsen, and McIntyre, Phys. Rev. **95**, 512 (1954).

[3] An elaboration of the following results will be presented later, together with some applications.

[4] This is slightly larger than the tentative value of r_0 ($r_0=1.1\pm0.1$) obtained in reference 2.

[5] Dr. G. E. Brown informs us that he and Drs. S. Brenner and L. R. B. Elton have come to a similar conclusion.

[6] L. I. Schiff, Phys. Rev. (to be published) and private communications.

Acquirement of Cosmic-Ray Energies by Electromagnetic Induction in Galaxies*

W. F. G. SWANN

Bartol Research Foundation of The Franklin Institute, Swarthmore, Pennsylvania

(Received August 10, 1954)

IN 1933, the present writer applied to a special case[1] the principle of acceleration of charged particles to cosmic-ray energies through electromagnetic induction.

The present communication represents an extension and generalization to changing magnetic fields in galaxies. Attention is confined to problems of axial symmetry about the axis of z, i.e., to problems in which the electric and magnetic fields E and H show no variation with the θ coordinate.

If one applies Lagrange's equations to the Lagrangian function, L, given in cylindrical coordinates by

$$L=-mc^2(1-r^2\dot{\theta}^2/c^2-\dot{r}^2/c^2-\dot{z}^2/c^2)^{\frac{1}{2}}+er\dot{\theta}U_\theta/c,$$

where the scalar potential ϕ is zero in our problem, and where U_θ is the vector potential and m the rest mass of the particle, it readily follows that:

(1) If a charged particle starts to acquire kinetic energy at $t=0$, and if the magnetic field is zero at $t=0$, then the particle acquires energy continually.

(2) If, at $t=0$, the magnetic field is finite, a sufficient, but by no means necessary, condition for continual gain of energy is that $|E|\geqslant|H|$ for all positions and times.

It can be readily shown that when the magnetic field and kinetic energy T are both zero at $t=0$,

$$\frac{d}{dt}(T+mc^2)^2=e^2\frac{\partial U_\theta^2}{\partial t}=e^2\left(\frac{dU_\theta^2}{dt}-\dot{r}\frac{\partial U_\theta^2}{\partial r}-\dot{z}\frac{\partial U_\theta^2}{\partial z}\right).$$

Further, it can readily be shown that the terms $(-\dot{r}\partial U_\theta^2/\partial r)$ and $(-\dot{z}\partial U_\theta^2/\partial z)$ are always positive, so that

$$\frac{d}{dt}(T+mc^2)^2\geqslant e^2\frac{dU_\theta^2}{dt},$$

and consequently, since T and U_θ are zero at $t=0$,

$$(T^2+2mc^2T)^{\frac{1}{2}}\geqslant eU_\theta.$$

From this result, and neglecting $2mc^2T$ in comparison with T^2, for convenience but not of necessity, it appears that the kinetic energy T acquired by a proton which finds itself at the cylindrical radius r, where the average z component of magnetic field is $\bar{H}_z$ within that radius is such that

$$T\geqslant 150r\bar{H}_z \text{ electron volts.}$$

If $r\sim25\,000$ light years, as for Andromeda, and $\bar{H}\sim7\times10^{-6}$ gauss, $T\sim2.3\times10^{19}$ ev.

It also appears that the particle, in its motion, spirals outwards, inwards or remains on a circle, according as $\bar{H}_z>2H_z$, $\bar{H}_z<2H_z$, $\bar{H}_z=2H_z$, respectively, where $\bar{H}_z$ is the average z component within the radius r at which the z component of the magnetic field has the value H_z. If in its journey through places where $\bar{H}_z\neq2H_z$ the particle reaches a place where $\bar{H}_z=2H_z$, then it will asymptotically approach a circular orbit for that value of r.

A strict application of the foregoing to a case where the growth of the magnetic field has occurred uniformly throughout the life of the universe ($\sim5\times10^9$ years) would encounter the difficulty that since the mean life of a cosmic ray as determined by nuclear collisions is of the order 10^8 years, the rays which started to acquire energy at $t=0$ would no longer be with us. The difficulty can be surmounted by assuming that the magnetic field has a period of less than 4×10^8 years, or by considering the case of neutral particles which become ionized and start to acquire energy after the magnetic field has grown to a finite value. The latter problem requires more intricate mathematical considerations which will be dealt with in a later communication.

* Assisted in part by the joint program of the U. S. Office of Naval Research and the U. S. Atomic Energy Commission.

[1] W. F. G. Swann, Phys. Rev. **43**, 217 (1933); J. Franklin Inst. **215**, 273 (1933). A simplified version of the original problem is given by the writer in the September, 1954 issue of the *Journal of The Franklin Institute*, and the full details associated with the *present* communication will be published in the November, 1954 issue of that Journal.

Gamma Radiation from the Reactions $Na^{23}+p$

J. O. NEWTON

Atomic Energy Research Establishment, Harwell, England

(Received July 26, 1954)

THERE are three reactions which produce gamma radiation when sodium is bombarded with protons; these are $Na^{23}(p,p'\gamma)Na^{23}$, $Na^{23}(p,\alpha\gamma)Ne^{20}$, and $Na^{23}(p,\gamma)Mg^{24}$. Sodium iodide scintillation detectors have been used to study the gamma rays from these processes at most of the resonances in the range of proton bombarding energy from 0.7–1.5 Mev. The targets were of sodium bromide. Both thin-target and thick-target excitation functions were measured.

The energies of the gamma rays from the inelastic scattering process and from the $(p,\alpha\gamma)$ reactions were found to be 444 ± 5 kev and 1.629 ± 0.008 Mev, respectively, in agreement with other work.[1,2]

The observed capture gamma rays can be related to transitions to the ground state of Mg^{24}, to and from the well-known levels at 1.37 Mev and 4.12 Mev, and to and from the level recently reported by Hausman *et al.*[3] at 4.24 Mev (see Fig. 1). It seems likely that this level decays both to the ground state and to the 1.37-Mev level, since gamma rays of energy 4.24 ± 0.04 Mev and 2.8 ± 0.05 Mev, with relative intensities of about 1 and 0.2, respectively, always occurred together when this mode of decay was observed.

In addition, a gamma ray of energy 3.86 ± 0.04 Mev was definitely observed at one resonance and less definitely at two others. It was found to be in coincidence with gamma rays of energy 1.37 Mev and 7.9 Mev. A possible interpretation is that it arises from a triple cascade transition through a level at 5.23 ± 0.04 Mev. Such a level could be reached in the β decay of Na^{24}.

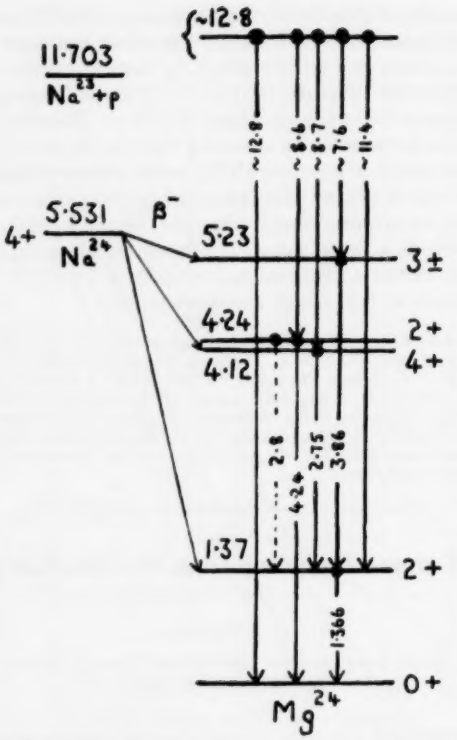

FIG. 1. Proposed energy level scheme for Mg^{24}. Observed gamma rays are shown. Only a few of these occur with appreciable intensity at a given resonance.

Cavanagh and Turner[4,5] have observed a gamma ray from this process having an energy of 3.9 Mev and an intensity of 1 in 2000 disintegrations. It has also been reported by Beghian, Bishop, and Halban,[6] who gives a value of 3.7±0.1 Mev for the energy. There is no evidence from any of the other reactions leading to Mg^{24} to suggest that there is a level at ~3.8 Mev, although such evidence would be expected if the level did in fact exist. The decay scheme of Na^{24} therefore gives some support for the assumption that there is a level in Mg^{24} at 5.23 Mev. The proposed level scheme for this nucleus is shown in Fig. 1.

At the 1.392-Mev resonance, gamma rays were observed which could be interpreted as arising from two parallel cascades, one through the 4.24-Mev level and the other through the 5.23-Mev level. Angular distribution and correlation measurements were made, and it was deduced from these that the 4.24 and 5.23-Mev levels had spins 2 and 3, respectively. From the upper limit of 2×10^{-6} per disintegration set by Beghian *et al.*[6] to the intensity of a ~4.14-Mev gamma ray in the beta decay of Na^{24}, it follows that the beta transition to the 4.24-Mev state is second or higher forbidden, and therefore that if the spin of the 4.24-Mev state is 2 it must have even parity.

TABLE I. Widths and partial widths in the reactions $Na^{23}+p$. Decays to the ground state are indicated by A, to the first excited state by B, etc. The relative intensities of the weaker modes of decay are indicated in brackets (strongest = 1). Γ, Γ_c', Γ_a' and $\Gamma_{pp'}'$ are the total level width and the partial widths for the capture, $(p,\alpha\gamma)$, and (p,p') processes, respectively. The errors in the absolute values of the widths are estimated at ±25 percent.

Bombarding energy Mev	Γ(kev)	Γ_c'(ev)	Mode of decay	Γ_a'(ev)	$\Gamma_{pp'}'$(ev)	J
0.742		...	D, B (0.26)	$\sim0.1\Gamma_c'$	$0.2\Gamma_c'$	1, 2
0.869		13	A, B (0.23)	~1	<0.2	1
0.985	<2	4.6	C, B (0.15)	<0.4	<1.5	3, 4
1.008	5	3		80	140	2+
1.017	6	18	D, B (0.3)	<1	130	1, 2
1.080	<5	1		<4	<16	
1.088	11	<0.8		30	60	2+
1.162	<4	2.7	A, B (0.8)	170	180	1−
1.172	<4	13	A, B (0.5), D (0.7)	<2	9	
1.201	<4	6.4	D, B (0.3)	<6	<5	
1.210	<3	<1		110	130	
1.253	<3	<1		80	100	1+[a]
1.281	9	8	E, B (0.26), D (0.75)	9	1300	
1.319	4	54	B, A (0.2)	<15	<90	
1.328	5	<3		340	1700	
1.358	<4	<3		<2	100	
1.392	<2	20	E, B (0.35), B (0.07)	<4	150	3+
1.415	<1.5	70	C	<22	80	4, 5
1.455	11	10	E, D (1), B (0.1)	50	3000	2−

[a] J. Seed, Phil. Mag. **44**, 921 (1953).

The partial widths $\Gamma'=(2J+1)\Gamma$ for the three processes have been estimated from the thick-target excitation curves on the assumption that the main contribution to each level width arises from the re-emission of the incident protons. Spins J are suggested for a number of the resonance levels. These results are shown in Table I.

Other work on the $Na^{23}+p$ reactions has been reported by a number of authors.[1,7-10] A more compregensive description of these experiments and a discussion of the results will be published elsewhere. A brief description of some of this work was given at the Birmingham Nuclear Physics Conference, 1953.

[1] Stelson, Preston, and Goodman, Phys. Rev. **86**, 629 (1952).
[2] Donahue, Jones, McEllistrom, and Richards, Phys. Rev. **89**, 824 (1953).
[3] Hausman, Allen, Arthur, Bender, and McDole, Phys. Rev. **88**, 1296 (1952).
[4] J. F. Turner and P. E. Cavanagh, Phil. Mag. **42**, 636 (1951).
[5] P. E. Cavanagh and J. F. Turner (private communication).
[6] Beghian, Bishop, and Halban, Phys. Rev. **83**, 186 (1951).
[7] Turner, Seagondollar, and Krone, Phys. Rev. **93**, 1035 (1954).
[8] O. H. Turner, Australian J. Phys. **6**, 380 (1953).
[9] H. Casson, Phys. Rev. **89**, 809 (1953).
[10] R. L. Burling, Phys. Rev. **60**, 340 (1941).

Contents—Continued

. . . . . H. P. Broida 220

. . . . . Stephen J. Angello and Theodore E. Ebert 221

. . . . . Benjamin Lax, A. F. Kip, and G. Dresselhaus 222

. . . . . R. N. Dexter and Benjamin Lax 223

. . . . . H. L. Helfer 224

. . . . . H. W. Ehrat and F. E. Geiger, Jr. 225

. . . . . W. W. Tyler 226

. . . . . R. M. Bishop and D. L. Dexter 227

. . . . . B. Serin 228

. . . . . Y. S. Kim, J. S. Russell, R. W. Huggett, and R. W. Thompson 229

. . . . . W. Hutchin, A. C. Juveland, and G. H. Kinsey 231

. . . . . Eyvind Wichmann and Norman M. Kroll 232

. . . . . A. Honig 234

. . . . . B. Senguppa 235

. . . . . W. F. Fry and M. S. Swami 236

. . . . . K. Rüdy and A. Winther 237

. . . . . Jerome I. Kaplan 238

. . . . . D. G. Rawson and D. R. Yennie 239

. . . . . W. F. G. Swann 240

. . . . . J. O. Newton 241

CONTENTS

THE PHYSICAL REVIEW SECOND SERIES, VOLUME 96, NO. 1 OCTOBER 1, 1954

Secondary Electron Emission by Photoelectric Action and Ion Bombardment at the Cathode in Corona Breakdown of Argon . . . Laura Colli and Ugo Facchini 1
Spherically Symmetric Solutions in Nonsymmetrical Field. Theories. II . . . P. C. Vaidya 5
Space Charge Formation and the Townsend Mechanism of Spark Breakdown in Gases . . . R. W. Crowe, J. K. Bragg, and Virginia G. Thomas 10
Properties of the Quantum Statistical Impedance . . . J. L. Jackson and M. C. Yovits 15
Virial Series of the Ideal Bose-Einstein Gas . . . B. Widom 16
Approximate Variational Principle in Quantum Statistics . . . William M. MacDonald, III and John M. Richardson 18
Mobility of Impurity Ions in Germanium and Silicon . . . C. S. Fuller and J. C. Severiens 21
Adiabatic Magnetization of a Superconducting Sphere . . . R. L. Dolecek 25
Electrical Properties of Silicon Containing Arsenic and Boron . . . F. J. Morin and J. P. Maita 28
Secondary Electron Yield from Al by High-Energy Primary Electrons . G. W. Tautfest and H. R. Fechter 35
Paramagnetic Resonance in Uranium Salts . . . S. N. Ghosh, Walter Gordy, and D. G. Hill 36
Paramagnetic Resonance in Chromous Sulfate Pentahydrates . . . Kazuo Ono, Shoichiro Koide, Hisao Sekiyama, and Hidetaro Abe 38
Properties of Zinc-, Copper-, and Platinum-Doped Germanium . . . W. C. Dunlap, Jr. 40
Thermal Effects on Lifetime of Minority Carriers in Germanium . . . R. A. Logan and M. Schwartz 46
Optical Properties of Lead Telluride . . . Marvin E. Lasser and Henry Levinstein 47
Magnetic Resonance Absorption of Diphenyl-Picryl Hydrazyl at Low Magnetic Fields . . . M. A. Garstens, L. S. Singer, and A. H. Ryan 53
Vibrational Anharmonicity and Lattice Thermal Properties . . . J. S. Dugdale and D. K. C. MacDonald 57
Probability Curves near Threshold for the Formation of He^{+}, Ne^{++}, A^{++}, Kr^{++}, and Xe^{++} by Electron Impact . . . W. M. Hickam, R. E. Fox, and T. Kjeldaas, Jr. 63
Improved Theory of the Zeeman Effect of Atomic Oxygen . . . K. Kambe and J. H. Van Vleck 66
Decay Scheme of I^{128} . . . H. L. Finston and W. Bernstein 71
Coulomb Wave Functions in the Transition Region . . . Milton Abramowitz and H. A. Antosiewicz 75
Evaluation of Coulomb Wave Functions along the Transition Line . . . Milton Abramowitz and Philip Rabinowitz 77
Elastic Scattering of Deuterons by He^{4} . . . R. J. S. Brown, K. F. Famularo, H. D. Holmgren, D. Rankin, and T. F. Stratton 80
Absolute Cross Section *Versus* Energy of the $Cu^{63}(\gamma,n)$ and $Cu^{63}(\gamma,2n)$ Reactions . . . Arthur I. Berman and Karl L. Brown 83
Identification of Platinum-188 . . . Robert A. Naumann 90
Multiple Scattering of Neutrons . . . George H. Vineyard 93
Indirect Exchange Coupling of Nuclear Magnetic Moments by Conduction Electrons . . . M. A. Ruderman and C. Kittel 99
Identification of Gadolinium and Terbium Radioisotopes as Fission Products of U^{235} . . . E. C. Freiling, L. R. Bunney, and N. E. Ballou 102
Angular Distributions of Protons from $Na^{23}(d,p)Na^{24}$ and $Ti^{47,48}(d,p)Ti^{48,49}$ . . . M. M. Bretscher, J. O. Alderman, A. Elwyn, and F. B. Shull 103
Two-Step Cascades in Chlorine-36 and Cadmium-114 Neutron-Capture Gamma-Ray Spectra . . . Arthur L. Recksiedler and Bernard Hamermesh 109
Ratio of Γ_n^0/D for Slow Neutron Resonances . . . R. S. Carter, J. A. Harvey, D. J. Hughes, and V. E. Pilcher 113
Total Cross Sections of Liquefied Gases for High-Energy Neutrons . . . Peter Hillman, R. H. Stahl, and N. F. Ramsey 115
Production of Nb^{93m} by the Pile Irradiation of Niobium . . . R. P. Schuman 121
Excited States in B^{10} and Be^{8} . . . T. W. Bonner and C. F. Cook 122
Spectrometer Studies of the Radiations of Some Neutron-Deficient Isotopes of Xenon and Iodine . . . Hirdaya B. Mathur and Earl K. Hyde 126
Production of Charged Pions from Hydrogen and Carbon . . . A. H. Rosenfeld 130
Production of Pions in Nucleon-Nucleon Collisions at Cyclotron Energies . . . A. H. Rosenfeld 139
Inelastic Scattering of 500-Mev Negative Pions in Emulsion Nuclei . . . M. Blau and Martin Caulton 150
Electron Density Distribution near Large Air Shower Axes at Sea Level . . . R. E. Heineman 161
Elastic Scattering of 26-Mev Negative Pions by Hydrogen in Emulsion . . . Jay Orear, William Slater, J. J. Lord, S. L. Ellenberg, and A. B. Weaver 174
Low-Energy Behavior of the Phase Shifts in Pion-Proton Scattering . . . Jay Orear 176
Suppression of Coherent Radiation by Electrons in a Synchrotron . John S. Nodvick and David S. Saxon 180
Reactions of Cesium with Protons at 60, 80, 100, 150, and 240 Mev . Richard W. Fink and Edwin O. Wiig 185
Relativistic Coulomb Scattering of Electrons and Positrons . . . G. Parzen and T. Wainwright 188
Excitation Function of the $C^{12}(p,pn)C^{11}$ Reaction in the Bev Region . R. L. Wolfgang and G. Friedlander 190
Conservation of Isotopic Spin and Isotopic Gauge Invariance . . . C. N. Yang and R. L. Mills 191
Bound States and the Formal Theory of Scattering . . . M. N. Hack 196
Families of Spinor Fields . . . Toichiro Kinoshita 199
Evaluation of the Collision Matrix for Dirac Particles in an External Potential . . . B. Zumino 202
Model of the Causal Interpretation of Quantum Theory in Terms of a Fluid with Irregular Fluctuations . . . D. Bohm and J. P. Vigier 208
Expansion of Wave Packets . . . Daniel S. Ling, Jr. 216
Generalized Variational Principle for the Scattering Amplitude . . . S. I. Rubinow 218

(*continued on cover three*)

LANCASTER PRESS, INC., LANCASTER, PA.